



AALBORG UNIVERSITY
DENMARK

Aalborg Universitet

Nyere metoder til projektering af moler

Frigaard, Peter

Publication date:
1998

Document Version
Publisher's PDF, also known as Version of record

[Link to publication from Aalborg University](#)

Citation for published version (APA):
Frigaard, P. (1998). *Nyere metoder til projektering af moler*. Dansk Vandbygningsteknisk Selskab.

General rights

Copyright and moral rights for the publications made accessible in the public portal are retained by the authors and/or other copyright owners and it is a condition of accessing publications that users recognise and abide by the legal requirements associated with these rights.

- Users may download and print one copy of any publication from the public portal for the purpose of private study or research.
- You may not further distribute the material or use it for any profit-making activity or commercial gain
- You may freely distribute the URL identifying the publication in the public portal -

Take down policy

If you believe that this document breaches copyright please contact us at vbn@aub.aau.dk providing details, and we will remove access to the work immediately and investigate your claim.

Michael Brorssen

DANSK VANDBYGNINGSTEKNISK SELSKAB

DANISH SOCIETY OF HYDRAULIC ENGINEERING

v/ Helge Gravesen, Carl Bro Anlæg a/s, Granskoven 8, 2600 Glostrup

Tlf. +45 43 48 63 28, Fax +45 43 63 65 67, email hlganl@carlbro.dk



Nyere metoder til projektering af moler.



DANSK VANDBYGNINGSTEKNISK SELSKAB

DANISH SOCIETY OF HYDRAULIC ENGINEERING

v/ Helge Gravesen, Carl Bro Anlæg a/s, Granskoven 8, 2600 Glostrup
Tlf. +45 43 48 63 28, Fax +45 43 63 65 67, email hlganl@carlbro.dk

Nyere metoder til projektering af moler.

Onsdag den 25 marts 1998.

Aalborg Universitet, Sohngaardsholmvej 57, Lokale F108

Tid	Foredragsholder	Titel
10.45	Hans F. Burcharth, Aalborg Universitet	Velkomst og introduktion af seminar
11.00	Thomas Jensen, DHI Arne Hansen, Portconsult	Design and model tests with Tuban breakwater, Indonesia
11.30	Tue Hald, Aalborg Universitet	Rock armoured single layer Rubble Mound Breakwaters in Norway
12.00	Mogens Hebsgaard, DHI Peer Smed, Rambøll	An Accropode Breakwater in Beirut
12.30		Frokost
13.30	Jens Peter Kofoed, Aalborg Universitet	Wave Loading and Overtopping on Vertical wall breakwaters in Multidirectional Breaking Seas
14.00	Peter Frigaard, Aalborg Universitet	Berm Breakwaters
14.30	Zhou Liu, Aalborg Universitet	Stresses in Tetrapod and Dolos armour blocks
15.00		Kaffe
15.15	Mutlu Sumer, DTU	Scour around Breakwater heads
15.45	Jan Pedersen, Rambøll	Wave Forces and overtopping of rubble mound Breakwaters.
16.15	Hans F. Burcharth, Aalborg Universitet	Failure Modes and Reliability evaluations of breakwaters
17.00		Seminar slut.

Nærværende publikation er udgivet i forbindelse med afholdelse af seminaret **Nyere metoder til projektering af moler** afholdt på Aalborg Universitet marts 1998. Dansk Vandbygningsteknisk Selskab takker alle foredragsholdere og forfattere for deres bidrag til seminaret.

Peter Frigaard

DANSK VANDBYGNINGSTEKNISK SELSKAB

DANISH SOCIETY OF HYDRAULIC ENGINEERING

v/ Helge Gravesen, Carl Bro Anlæg a/s, Granskoven 8, 2600 Glostrup
Tlf. +45 43 48 63 28, Fax +45 43 63 65 67, email hlganl@carlbro.dk

UDKAST

Seminar: Nyere metoder til projektering af moler.
Aalborg Universitet, onsdag den 25 marts 1998.

Tid	Foredragsholder	Titel
10.45	Hans F. Burcharth, Aalborg Universitet	Velkomst og introduktion af seminar
11.00	Thomas Jensen, DHI Arne Hansen, Port Consult	Model tests with Tuban breakwater, Indonesia
11.30	Tue Hald, Aalborg Universitet	Rock armoured single layer Rubble Mound Breakwaters in Norway
12.00	Mogens Hebsgaard, DHI Per Smed, Rambøll	An Accropode Breakwater in Beirut
12.30		Frokost
13.30	Peter Frigaard, Aalborg Universitet	Wave Loading and Overtopping on Vertical wall breakwaters in Multidirectional Breaking Seas
14.00	Peter Sloth, DHI	Design of Berm Breakwaters
14.30	Zhou Liu, Aalborg Universitet	Stresses in Tetrapod and Dolos armour blocks
15.00		Kaffe
15.15	Mutlu Sumer, DTU	Scour around Breakwater heads
15.45	Jan Pedersen, Rambøll	Wave Forces and overtopping of rubble mound Breakwaters.
16.15	Hans F. Burharth, Aalborg Universitet	Failure Modes and Reliability evaluations of breakwaters

*Kilbøge fyldt
glad 12*

Seminaret er afpasset så det passer med flyveren fra København 9.30.

I forbindelse med seminaret udgives der en publikation med de forskellige indlæg.



State of the Art in the Design of Coastal Structures

by

BURCHARTH H. F.
Hydraulics and Coastal Engineering Laboratory
Dept. of Civil Engineering, Aalborg University, Denmark

Dansk Vandbygningsteknisk Selskabs seminar om
"Nyere metoder til projektering af moler"
Aalborg Universitet, den 25. marts 1998

State of the Art in the Design of Coastal Structures

Contributions from MAST, PIANC and some national projects

by

Prof., Dr.techn., Dr. h.c. Hans F. Burcharth
Department of Civil Engineering, Aalborg University, Denmark

Contents

1	Introduction	2
2	Design procedure	4
3	Important recent projects	4
4	Hydraulic responses	6
4.1	Run-up	6
4.2	Wave transmission	6
4.3	Wave overtopping	6
4.4	Wave reflection	7
4.5	Internal porous flow and pore pressure built up	7
5	Wave loads and related responses	8
5.1	Scale and model effects	8
5.2	Wave loads on sloping rubble structures	9
5.3	Wave loads on monolithic vertical wall structures	9
5.4	Wave loads on crown walls	11
6	Probabilistic failure mode analysis and safety coefficients	12
6.1	Failure mode overview	12
6.2	The probabilistic approach	13
6.3	Failure mode partial safety coefficients	13
7	New failure mode analyses and formulae	15
7.1	Geotechnical failures	15
7.2	Armour layers	15
7.3	Reshaping breakwaters	16
7.4	Scour around roundheads	17
8	Reliability of existing breakwaters	17
9	Acknowledgement	17
10	References	17

1 Introduction

Coastal structures are used in coastal defence schemes with the objective of preventing shoreline erosion and flooding of the hinterland. Other objectives are sheltering of harbour basins and entrances against waves, stabilization of navigation channels at inlets, and protection of water intakes and outfalls. An overview is given in Fig. 1.

Type of structure	Objective	Principal function
Sea dike	Prevent or alleviate flooding by the sea of lowlying land areas.	Separation of shore line from hinterland by a high impermeable structure.
Sea wall	Protect the beach against erosion and alleviate flooding.	Reinforcement of some part of the beach profile.
Groin	Protect the beach against erosion.	Reduction of longshore transport of beach material.
Detached breakwater		Reduction of wave heights in the lee of the breakwater and reduction of longshore transport of beach material.
Reef breakwater		Reduction of wave heights at the shore.
Submerged sill		Retard offshore movement of beach material.
Beach drain		Accumulation of beach material in the drained part of the beach.
Beach nourishment		Artificial infill of beach material to be eroded by waves and currents as compensation for lack of natural supply.
Breakwater		Shelter harbor basins, harbor entrances and water intakes against waves (and currents).
Jetty	Stabilize navigation channels at river mouths and tidal inlets.	Confine streams and tidal flow. Protection against storm water and cross currents.
Training walls	Prevent unwanted sedimentation or erosion. Protect mooring against currents.	Direct natural or man-made current flow by forcing of water movement along the structure.
Storm surge barrier (barrage)	Protect estuaries against storm surge.	Separation of estuary from the sea by movable locks/gates.
Pipeline Outfall	Transport of fluids.	Gravity based stability.
Pile structure	Provide deck space for traffic, pipelines etc. Provide moorings.	Transfer of deck load forces to the sea bed.
Scour (sea bed) protection	Protect coastal structures against instability caused by sea bed scour.	Provision of resistance against erosion caused by waves and current.

Fig. 1. Types and function of coastal structures (prepared for the Coastal Engineering Manual, U.S. Army Corps of Engineers).

In designing structures optimization is wanted, both with respect to function and to economy seen over a structure service life time. Functional design is still very difficult when it involves structure-sediment interactions as for example for groynes in coastal protection schemes. As to optimal design of the structure itself it can be done today for smaller standard structures solely by the use of desk tools, provided that the sea state conditions are known. However, for large and non-standard structures it is necessary to spend quite a lot of money and time on model tests which for some structures include the use of large scale test facilities. The art do not allow conceptual design just based on available formulae and computer programs. The available sets of tools are not of generic nature as they do not provide the freedom of designing coastal structures which deviate significantly from the well proven and documented traditional design concepts.

Despite this not fully satisfactory situation the paper does reflect the significant progress which has been made within the last ten to fifteen years where quite a lot of national and international research projects and special working groups related to coastal structures have been running. Amongst the significant international activities are the European Union MARINE SCIENCE and TECHNOLOGY research program MAST and the Working Groups of PIANC.

The background of the many recent research activities is twofold:

- A series of very serious damages to newly designed major breakwaters appeared, clearly demonstrating large uncertainties in the design tools and even lack of knowledge about important failure modes.
- It became more and more incomprehensible why coastal structures could not be designed with a confidence which matches other civil engineering structures.

The last point involves the fact that only in very few cases the design was based on a rational safety implementation analysis including consideration of major uncertainties, f.ex. on the wave climate estimates.

The paper focuses on safety implementating as well as on results and tools related to the conceptual design of breakwater cross sections. Lay-out design is not discussed because it is too site specific. However, it should not be forgotten that the lay-out is, in most cases, even more important for satisfactory function and economy. Fig. 2 shows examples of the three main types of breakwaters.

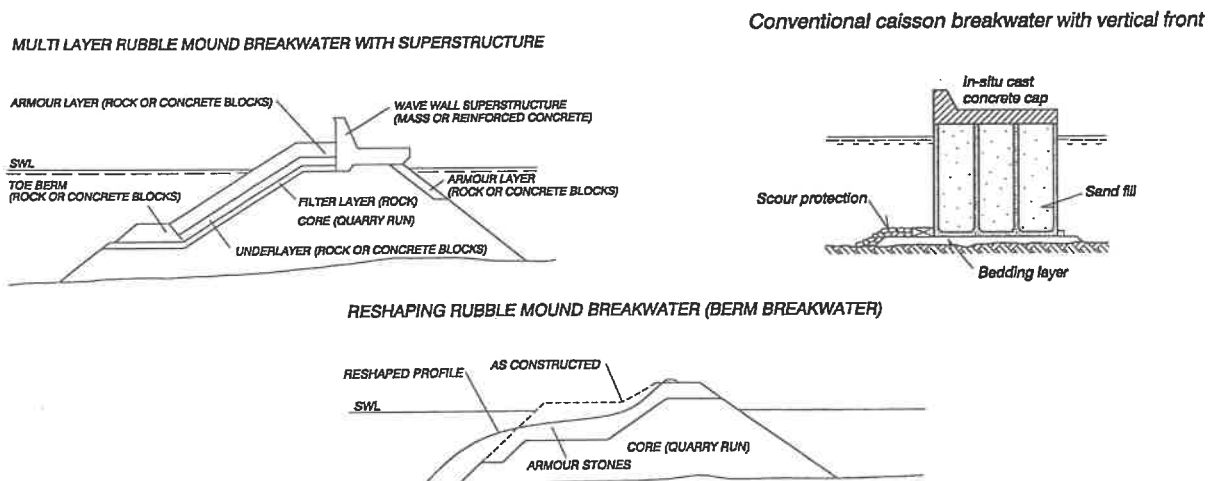


Fig. 2. Main types of breakwaters.

2 Design procedure

- a **Functional requirements and structure life time** are first to be specified. For breakwater cross sections it involves requirements for accessroads, installations, moorings, etc., and related to this also a definition of allowable deformations, wave overtopping, wave transmission, and wave reflection. The last three points constitute the acceptable **hydraulic responses**.
- b **Local long-term and short-term wave/water level statistics** have to be established.
- c **Alternative structure geometries** which meet the functional requirements are sketched.
- d **All possible failure modes** related to the alternatives are identified.
- e **Safety levels** related to the failure modes are defined.
- f **Method of implementation of safety** is selected.
- g **Conceptual design of the alternatives** is performed in which all failure modes are investigated and the overall stability and the stability of structural members are ensured to meet the target safety levels. This includes assessment of the long term durability of the structural parts.
- h **Selection of preferred design**, based on economical optimization.

The contributions from MAST projects and PIANC-working groups are related mainly to items a, d, e, f, and g.

3 Important recent projects

The first large European project on coastal structures was the 1990-92 MAST project:

- (i) **Coastal Structures**. MAST project G 6 – S. Contract 0032, coordinated by HR Wallingford.

This project had an ice-breaker effect in creating strong links between European research groups, and it formed the basis for a series of MAST projects:

- (ii) **Monolithic coastal structures MAS2-CT92-0047**, coordinated by H. Oumeraci, Tech. Univ. of Braunschweig.
- (iii) **Rubble mound breakwater failure modes MAS2-CT92-0042**, coordinated by H.F. Burcharth, Aalborg Univ.
- (iv) **Full-scale dynamic load monitoring of rubble mound breakwaters MAS2-CT92-0023-C**, coordinated by J. De Rouck, Univ. of Ghent.
- (v) **Berm breakwater structures MAS2-CT94-0087**, coordinated by J. Juhl, Danish Hydraulic Institute.
- (vi) **Reflection of waves from natural man-made coastal structures MAS2-CT92-0030-C**, coordinated by M. Losada, Cantabria Univ.

Further the following MAST 3 projects are ongoing more or less as a continuation of two of the above mentioned projects:

- (vii) **Probabilistic design tools for vertical breakwaters** MAS3-CT92-0041, coordinated by H. Oumeraci, Tech. Univ. of Braunschweig.
- (viii) **The optimization of crest level design of sloping coastal structures through prototype monitoring and modelling** MAS3, PL 961158, coordinated by J. De Rouck, Univ. of Ghent.

Another partly EU sponsored project is the combined LIP-MAST2-(MCS)-TAW project:

- (ix) **Wave overtopping and loads on caisson breakwaters under three-dimensional sea states** coordinated by L. Franco Politecnico di Milano, H.F. Burcharth Aalborg Univ., and J.W. van der Meer Delft Hydraulics.

This paper concerns only the effect of non-breaking waves for which reason the following project, sponsored by The Danish Technical Research Council (STVF) was undertaken at Aalborg University:

- (x) **Wave loads and overtopping on caisson breakwaters from three-dimensional breaking waves.**

Like many other European national sponsor organizations STVF also sponsored, through its MARIN TEKNIK programme a number of research projects related to coastal structures. Many of the projects were closely coordinated with the MAST and PIANC activities.

Examples are the following projects:

- (xi) **Wave forces and overtopping of crown walls of rubble mound breakwaters**, J. Pedersen, Aalborg Univ.
- (xii) **Application of reliability in breakwater design**, E. Christiani, Aalborg Univ.
- (xiii) **Scour around breakwater roundheads**, M. Sumer and J. Fredsøe, Technical Univ. of Denmark.

The following two PIANC working group projects have contributed to the development of breakwater design methods by introducing the fully probabilistic approach.

- (xiv) **Analysis of rubble mound breakwaters** PIANC PTC II Working Group 12, chairman J.D. Mettam, Scott Wilson Kirkpatrick.
- (xv) **Breakwaters with vertical and inclined concrete walls** PIANC PTC II Working Group 28, chairman H.F. Burcharth, Aalborg University.

The MAST projects are all very well documented in project reports and workshop proceedings. The PIANC Working Group results are published in the PIANC-Bulletins and in special Working Group reports. The main results of national programmes are published in conference proceedings and/or in journals. A systematic presentation of the MAST projects will not be given here. Reference is made to Oumeraci et. al (1995) in which the MAST 2 projects (ii) - (vi) are discussed.

4 Hydraulic responses

4.1 Run-up

Run-up caused by long-crested head-on waves on most types of rubble mound structures can be predicted quite well. This includes straight slopes and to some extent bermed slopes armoured with rock or concrete armour units (e.g. cubes, Antifer blocks with and without holes, Tetrapods, Dolosse, Accropodes). The information is scattered. Main references are van der Meer (1993) and CUR (1994). Additional references from project (ii) are Berenguer et al. (1994 a and b) and Burcharth et al (1995 b). Most results rely on small scale model tests. Some concern about significant scale effect initiated by the above mentioned project (viii).

4.2 Wave transmission

Wave transmission related to low-crest and submerged rubble structures can be predicted with reasonable accuracy. Main reference is van der Meer (1993). Information on wave transmission over vertical wall structures is given in Goda (1985).

4.3 Wave overtopping

For rubble mound structures without crown walls there is still insufficient information for a more accurate estimation of overtopping in general, see van der Meer (1993), Allsop et al. (1992), and Canel et al. (1992). The latter reference includes the effect of short-crested waves.

For rubble mound breakwaters with crown walls quite a lot of information is available, see f.ex. references in CUR (1994) and van der Meer (1993). The most recent results come from a well documented comprehensive parametric model test study, Pedersen (1996), resulting in a formula for the mean overtopping discharge as function of the breakwater geometry and the sea state. The formula has only one fitting parameter and is valid for head-on long-crested waves.

Overtopping of vertical wall structures has been investigated by Goda (1985) and in a number of recent projects among which are projects (ii), (ix), (x). This includes caisson breakwaters with different crest geometry and with and without perforated front tested in 2-D and 3-D models. The results comprise the effect of oblique short-crested non-breaking waves, Franco et al. (1997), and of breaking (top spilling) waves, Groenbech et al. (1997). The first reference gives, besides the mean discharge, also recommendations of acceptable levels of overtopping. Fig. 3 shows tested cross sections.

The lateral distribution of the overtopping water behind the breakwater front has not been investigated systematically but only for specific cases, see f.ex. Burcharth et al. (1995 a). However, in project (viii) there will be performed a comparative analysis of the distribution between prototype measurements at Zeebrugge and small scale model measurements. This will reveal quantitative information on scale effects.

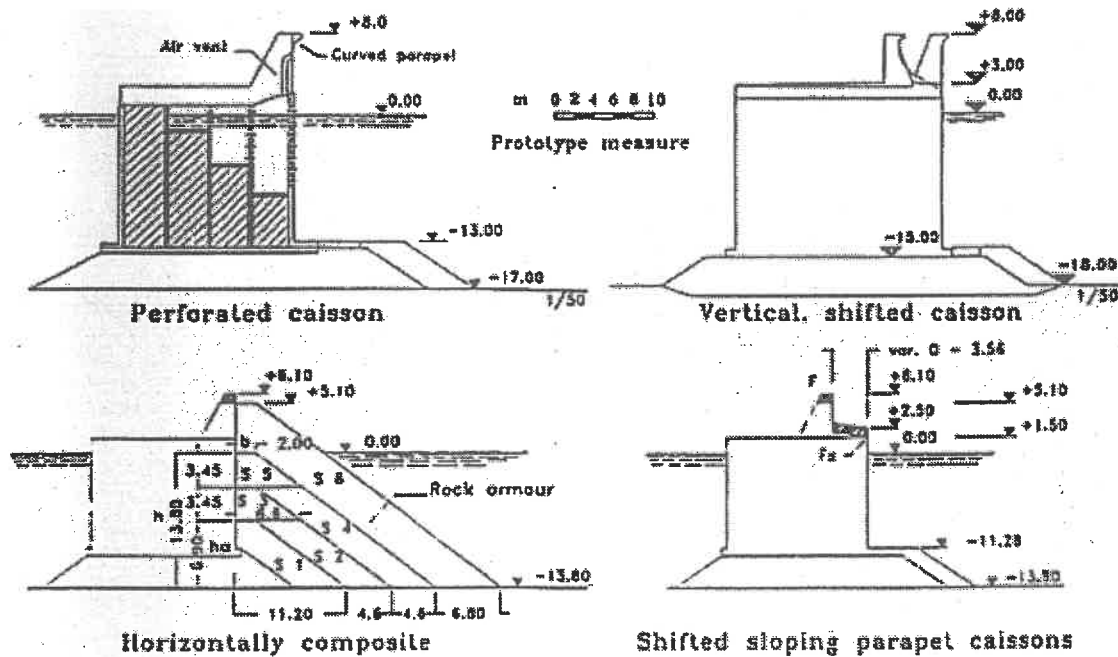


Fig. 3. Cross sections tested in the LIP-MAST 2-TAW project (Franco et al. (1992)).

4.4 Wave reflection

For sloping structures the information is still limited and scattered, but generally it is possible to get some reasonable estimates on the reflection coefficients for head-on long-crested waves, see Allsop et al. (1988), Canel et al. (1992), and CUR (1994). For oblique long-crested waves see Benoit et al. (1994), for detached breakwater field measurements Davidson et al. (1994), and for berm breakwaters Mansard (1991).

For vertical wall structures reflection coefficients for impermeable and permeable fronts were studied in project (ix), Helm-Petersen (1994 and 1995), and for porous (stone-filled) structures at Aalborg University, Helm-Petersen (1996). Both projects included the effect of oblique short-crested waves. Results from 2-D tests performed in project (ii) with perforated screens are given in Allsop et al. (1994).

4.5 Internal porous flow and pore pressure built up

Wave induced non-stationary flow in rubble mound breakwaters and in high mounds and bedding layers under caisson structures as well as in the subsoil is of importance both for the soil mechanics stability of the structures, the soil strength and the uplift pressures on bottom slabs. Very complicated scaling laws and soil strength-dependence on stress level make scale model tests very questionable for which reason numerical modelling is the solution. Partly sponsored by project (i), the problem about scaling of non-stationary flow in coarse stone materials (like quarry rubbles) was solved, partly by experiments, van Gent (1994), Burcharth et al. (1995).

Several numerical models for wave induced flow have been developed in the course of projects (i), (iv), and others, see f.ex. van Gent (1994). The models are not yet entirely based on basic physics but must be calibrated against small scale model results. The latter involves yet unsolved scale effect problems.

Pore pressure built-up under cyclic wave loading is related to porous flow but dealt with experimentally in cyclic loaded triaxial apparatus in order to develop constitutive equations for subsoil materials. Based on experience from offshore platform designs and on extensive advanced laboratory soil tests within project (ii) some guidelines for design of foundation under caisson structures have been presented. The work continues in project (vii) and will probably result in sets of constitutive equations (for characteristic soils) necessary for numerical stability calculations. A comprehensive report on basic mechanics problems related to vertical wall structures is published by the Geotechnical Group (coordinated by M. de Groot, Delft Geotechniques) in the proceedings of project (ii). It contains very useful diagrams for prediction of excess pore pressures in sand foundation under cyclic loading, Andersen (1995).

5 Wave loads and related responses

5.1 Scale and model effects

It is necessary to know the simultaneous load distribution on the surface of the breakwater elements in order to calculate the stability, i.e. the pressure on the front and rear faces as well as uplift pressures on bottom slabs must be known. Because field investigations are extremely expensive and time consuming we are forced to use small scale model experiments. This causes serious scaling problems because the effect of breaking waves do not obey the Froude similarity. This is because compressibility related to the enclosed air bubbles and pockets, and the surface tension effects are not accounted for. Moreover, the size of air bubbles is very different in salt and fresh water, the latter being used in the models. As a result it is uncertain how to convert results involving breaking waves from model to prototype except that the Froude-scaling law gives the upper limit of the forces. The problem has been studied by many researchers and was – for vertical face breakwaters – an important part of project (ii). The research continues in project (vii) which includes several prototype investigations. However, in order to reach more precise conversions it is necessary to know the volume and distribution of the enclosed air. The pulsation period of entrapped air pockets is visible in the force history and can be converted by the use of the Mach-Cauchy scaling law.

Wave induced uplift pressures are affected by the permeability of the foundation soil for which reason viscosity plays an important role in converting from model to prototype. In case of high frequency wave impacts also the compressibility has to be considered. For these reasons the Froude-scaling law cannot be applied. The solution will be development of numerical models which – after proper calibration against results from both scale models and prototypes – can handle this highly transient problem. Both projects (vii) and (viii) deal with this task.

So far has – on the safe side – been used a linear variation of the uplift pressure between the recorded pressures of the edges of the foundation slab, and a Froude scale conversion of the results.

In case of caisson breakwaters not exposed to provoked wave breaking Goda (1985) recommends a certain reduction rule based on prototype experience. Indications about the deviation of the uplift pressures from a linear variation can be found in Losada et al. (1993).

5.2 Wave loads on sloping rubble structures

Wave loadings are treated very differently for sloping rubble structures (like armour layers) and monolithic structures (like caissons and wave walls). In the first case the tradition is to avoid speculations about the wave pressures on the rubble units – simply because of the extremely complicated flowfield of breaking waves on a rough porous slope. For such cases the design is based on formulae expressing directly the response in terms of displacements as function of the sea state, see Chapter 6. The wave loadings are simply put away in a black box. Attempts to measure wave forces on individual blocks have been made in projects (i) and (v), mainly with the objective of getting basic information which can explain the surface profile development of berm (reshaping) breakwaters. Simple numerical models for profile development were also developed, but so far it has not been possible to produce generally applicable models.

5.3 Wave loads on monolithic vertical wall structures

For stability calculation of monolithic structures the wave loading must be known. Although the front face geometry of f.ex. a caisson is very simple, the wave pressures are very complicated functions of the sea state. Fig. 4 illustrates typical force histories.

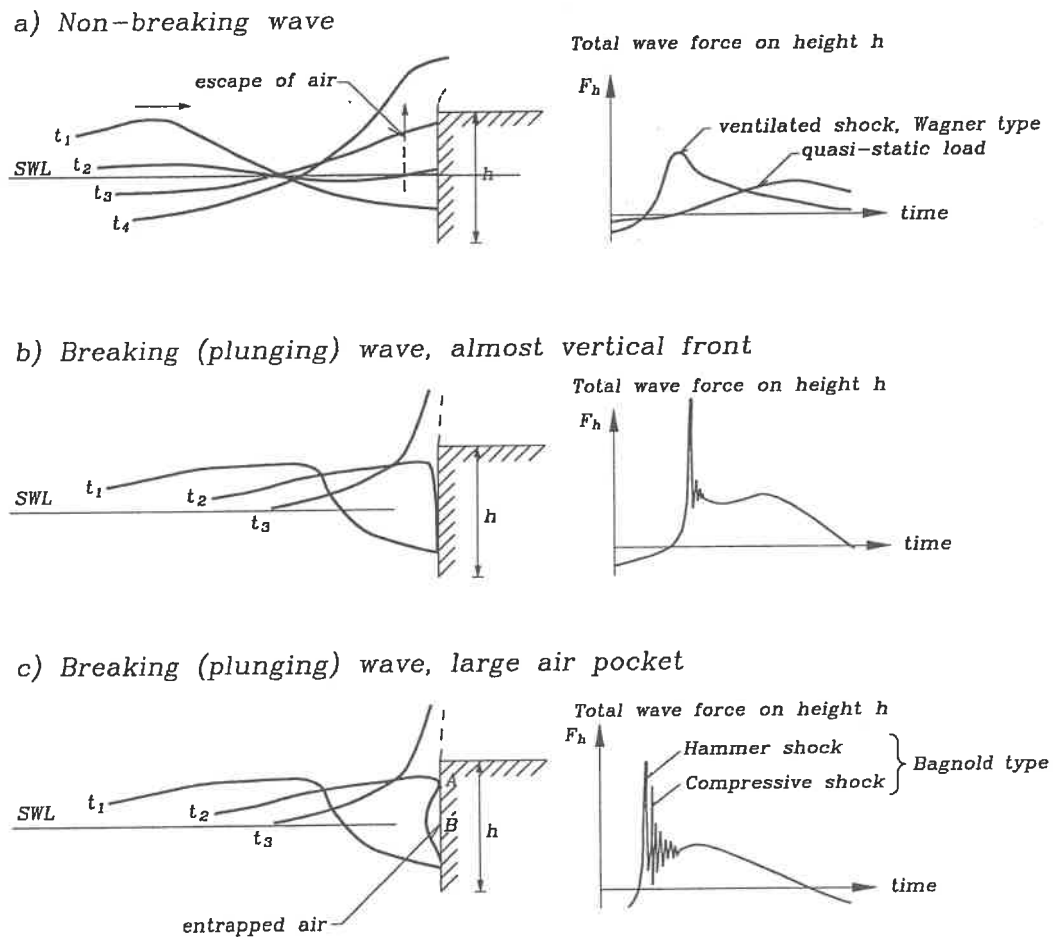


Fig. 4. Illustration of vertical wall wave forces from non-breaking and breaking waves.

The character of the force histories and the pressure distributions have been intensely studied also in large scale facilities at University of Hannover and University of Braunschweig, Oumeraci et al. (1993), and was an important part of project (ii).

Most simple to predict is the loading from non-breaking waves for which case it has been experimentally demonstrated in project (ix) that wave pressures on long structures from oblique short-crested seas, as predicted by Battjes (1982), can be closely estimated by real time calculations, Frigaard et al. (1995).

However, in real storm sea states the waves will break, either by top-spilling as in deep water wave situations, or, in case of shallow water and semi high steep slopes in front of the wall, by plunging. The top-spilling breakers increase the wave load somewhat compared to non-breaking waves and introduce also some higher frequency loadings. It has been demonstrated in project (ii), by comparing with various 2-D model tests at the Danish Hydraulic Institute and Delft Hydraulics, that the Goda formula, which includes the effect of top-spilling wave breaking in real seas, predicts very well the wave loads. The comparison confirmed the deliberately built-in safety margin in the formula. The comparison might however be slightly biased because top-spilling wave breaking in real seas is probably more pronounced than in a wave flume. Project (x) expands the investigations to include the effect of top-spilling breakers on long caisson structures in oblique short-crested seas. Absorption of reflected short-crested waves was used in the project, probably for the first time in a regular testing program. Fig. 5 shows the layout of the model and the position of the wave gauges.

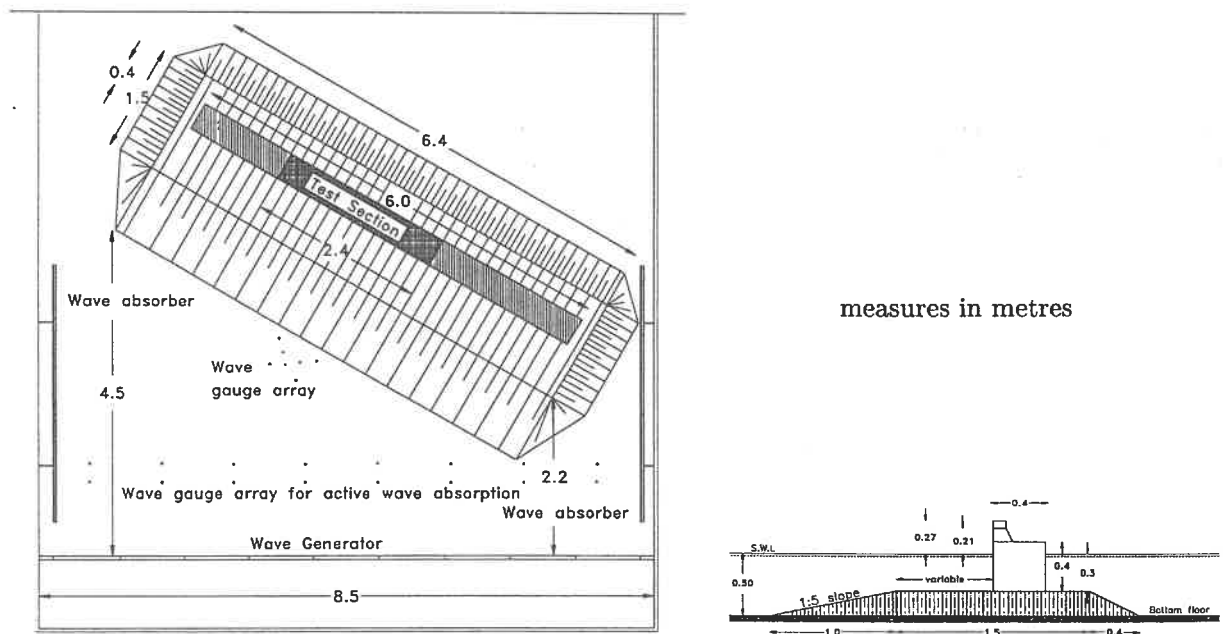


Fig. 5. Test set-up for investigation of wave forces and overtopping in short-crested oblique breaking waves (top spilling). Aalborg University.

Goda (1985) stresses that designs which provoke plunging waves to occur at the structure should be avoided because of the very large impulsive pressures which are generated. Such pressures are responsible for several failures. However, if significant impulsive pressures are to be accounted for, a fully dynamic stability analysis must be performed. This involves the following complications.

- The loadings are extremely difficult to predict due to scale effects, see section 5.1 and due to large sensitivity to the shapes of the waves and the structure geometry. The latter introduces very large scatter.
- The transmission of the loading to the subsoil and the effect on the subsoil characteristics are very complicated.

Solving these problems is part of projects (ii) and (vii). The latter involves 2-D wave load experiments at HR-Wallingford to determine more narrow bands for occurrence of impulsive pressures and the statistics of the loads, Allsop et al. (1996). The dynamic response in terms of deformation of the subsoil has been analysed, Oumeraci et al. (1994), Pedersen (1994 and 1997), Benassai et al. (1997), using linear elastic models for the soil. From this work it can be estimated when it is necessary to use a dynamic analysis. Ibsen et al. (1997) developed a 2-D method based on plasticity for the prediction of permanent soil/structure deformations due to impulsive loadings. Moreover, within project (vii) very interesting prototype experiments with dynamic loading of Italian caissons are performed by University of Bologna. Further, a spring-dashpot model, Kortenhaus et al. (1995), will be tested against the known behaviour of prototype caissons. Generally, progress is made in establishing operational tools for determination of the dynamic wave-structure-soil interactions, see also Sections 4.5 and 5.1. The Geotechnical Group of project (vii) plays a major role in this.

5.4 Wave loads on crown walls

The simultaneous wave induced pressures on the front face and the uplift pressures must be known in order to analyse the crown wall stability. Fig. 6 shows a typical time history pressure distribution on a crown wall.

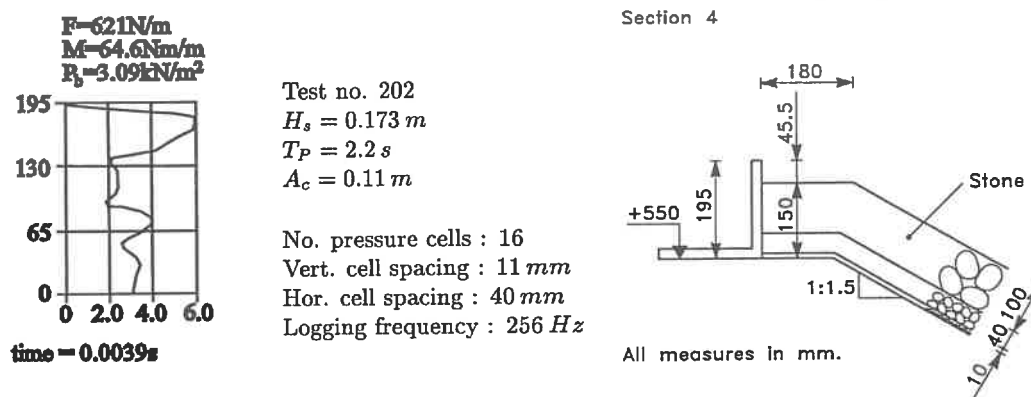


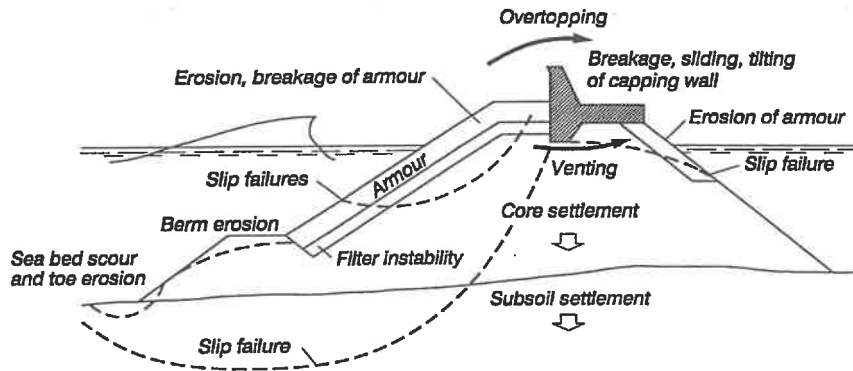
Fig. 6. Example of pressure distribution on crown wall (Pedersen 1996).

A first approach to a realistic model for the pressure distribution over the wave wall front face was presented by Günbak et al. (1983). Pedersen (1996) presented the first systematic parametric model test study of wave forces on crown walls of different heights including influence of water level, berm height and width, slope and armour type. The results comprise the statistics of the horizontal force, the tilting moment and the wall base pressure, thus providing the basis for stability calculations. The uplift pressure distribution is discussed in Section 5.1.

6 Probabilistic failure mode analysis and safety coefficients

6.1 Failure mode overview

Figs. 7 and 8 give an overview of important failure modes related to rubble mound and vertical face monolithic breakwaters. Key references are Ligteringen (1992 and 1997), Oumeraci (1992).



Overview of failure modes for rubble mound breakwaters

Fig. 7. Rubble mound breakwater failure modes.

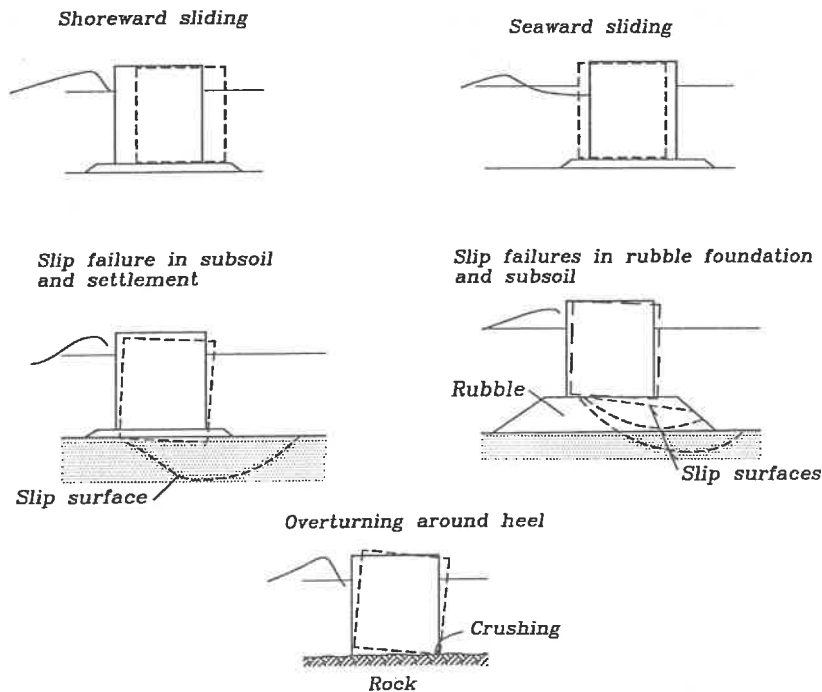


Fig. 8. Important global failure modes for caisson breakwaters.

6.2 The probabilistic approach

The basic principle in reliability analyses is that the probability of damage (usually denoted *failure*) is assessed for each failure mode. On this basis it is possible to estimate the safety or reliability of the whole structure by system analysis.

In each failure mode analysis all load and resistance parameters are treated as stochastic variables. Consequently, it is necessary to introduce the uncertainty of these parameters, e.g. on the sea-state parameters (load) and the soil/strength parameters (resistance). Moreover, the uncertainty on the applied formulae or calculations methods must also be taken into account. The uncertainties on the parameters are given by their probability distributions. As an example is the long term distribution of the max. significant wave heights in storms often given by a Weibull distribution. For most parameters a normal distribution with a certain standard deviation is used. The same holds for uncertainties on formulae. Most often a safety-index method is used for the estimation of the damage probability related to each failure mode, see f.ex. Burcharth (1997).

Related to breakwaters, this approach was first used in a systematic way in the PIANC PTC II Working Group 12, project (xiv), Burcharth (1991), PIANC (1992), and in the MAST 2 project (iii), Soerensen et al. (1995), both for rubble mound structures.

The approach was subsequently used for vertical wall structures in the PIANC PTC II Working Group 28 (project (xv) (to be published ultimo 1997), and it is now a fundamental part of the ongoing MAST 3 project (vii).

6.3 Failure mode partial safety coefficients

The PIANC Working Groups developed on the basis of extensive numerical simulations a system of safety factors for most of the rubble mound breakwater failure modes and for the overall stability failure modes related to caisson breakwaters. The latter is based on static analyses in which wave loads are calculated from the extended Goda formula which includes impulsive pressures, Takahashi et al. (1994). Verification of the use of the coefficients in a fully dynamic analysis will be checked in project (vi) and the system will be extended to include important local structure failure modes for caisson breakwaters.

The PIANC safety factor system is a new and advanced system which provides the safety coefficients corresponding to any wanted safety level (probability of failure) and structure life time, Burcharth (1991), Soerensen et al. (1995). This means that structures, by very simple calculations, can be designed to given safety levels, f.ex. 20% probability of a certain damage within 50 years. Other safety coefficient systems, as f.ex. the Euro Code, do not give coefficients corresponding to prespecified safety levels but only coefficients covering very wide and, for breakwaters, insufficiently specified safety classes. Table 1 contains examples of PIANC safety coefficients. The standard deviations of 0.05 and 0.20 on H_s source data correspond typically to accelerometer buoy recordings and fetch scatter diagram estimates for significant wave heights, respectively, Burcharth (1992).

Table 1. Example of design formulae and related partial safety coefficients γ_Z and γ_H corresponding to various failure probability within T years. (Burcharth 1991, Soerensen et al. 1995 and 1997).

Armour stability (Hudson formula)

$$0 = \frac{1}{\gamma_Z} \hat{\Delta} D_n (K_D \cot \hat{\alpha})^{1/3} - \gamma_H \hat{H}_S^T$$

- $\hat{\Delta}$ central estimate (mean value)
 K_D Damage coefficient
 α slope angle
 D_n (volume of armour unit)^{1/3}
 Δ $\frac{\rho_s}{\rho_w} - 1$, where ρ_s and ρ_w are block and water mass densities
 H_S^T T -years return period value of significant wave height

Failure probability	coefficient of variation on H_S source data			
	0.05		0.20	
P_f	γ_H	γ_Z	γ_H	γ_Z
0.01	1.7	1.04	2.0	1.00
0.05	1.4	1.06	1.6	1.02
0.10	1.3	1.04	1.4	1.06
0.20	1.2	1.02	1.3	1.00
0.40	1.0	1.08	1.1	1.00

Horizontal sliding of caisson on rubble foundation

$$0 = \frac{1}{\gamma_Z} \hat{f} \left[\hat{F}_G - 0.9 \hat{F}_U (\gamma_H \hat{H}_S^T) \right] - 0.9 \hat{F}_H (\gamma_H \hat{H}_S^T)$$

- $\hat{\Delta}$ central estimate (mean value)
 f friction factor
 F_G gravitational force on caisson
 H_S^T T -years return period value of significant wave height
 $F_U (\gamma_H H_S^T)$ Uplift-pressure in which significant wave height is $\gamma_H \hat{H}_S^T$
 $F_H (\gamma_H H_S^T)$ Horizontal wave load in which significant wave height is $\gamma_H \hat{H}_S^T$

Failure probability	coefficient of variation on H_S source data			
	0.05		0.20	
P_f	γ_H	γ_Z	γ_H	γ_Z
0.01	1.4	1.7	1.5	1.7
0.05	1.3	1.4	1.4	1.4
0.10	1.3	1.2	1.4	1.3
0.20	1.2	1.2	1.3	1.2
0.40	1.1	1.0	1.1	1.1

Deep water conditions. Model tests not performed.

7 New failure mode analyses and formulae

7.1 Geotechnical failures

A systematic study of slip surface-rupture zone geotechnical failures related to crown walls and caisson structures is presented in Christiani (1997). Fig. 9 shows examples of the investigated failure modes. The relative importance of the various failure modes is evaluated using probabilistic quasi-static stability analyses on typical prototype structures.

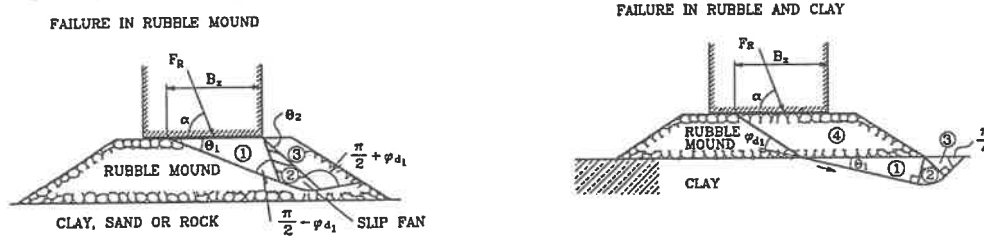


Fig. 9. Examples of geotechnical failure modes (Christiani, 1997).

7.2 Armour layers

Displacement of armour units

References to newer formulae and/or information for estimation of displacement of armour units are:

Rock: Galland (1992), Allsop et al. (1992), van der Meer (1993), CUR (1994), Canel et al. (1992). The latter reference deals with the effect of multidirectional waves.

Accropode: van der Meer (1988), Holtzhausen et al. (1991), Galland (1992), Canel et al. (1992), Kobayashi et al. (1994), Christensen et al. (1995).

Core Loc: Melby et al. (1994), Melby et al. (1997).

Dolosse (includes roundheads and effect of wave walls): Burcharth (1993), Burcharth et al. (1994), Burcharth et al. (1995b).

Tetrapods: van der Meer (1988), Canel et al. (1992), Galland (1992), van Nes (1995).

Cubes: van der Meer (1988), Allsop et al. (1992).

Hollowed cubes and hollowed Antifer cubes include roundheads and effect of wave walls: Galland (1992), Canel et al. (1992), Berenguer et al. (1994a), (1994b), (1995).

Low crest rock breakwaters: Burger (1995), van der Meer et al. (1995).

Rock toe berm-main armour interaction

Project (iii) included a comprehensive experimental study of rock toe berm-main armour interaction in 2-D and 3-D short-crested waves. Conditions for toe failures and the effect on armour stability were identified and a probabilistic model for the interaction was formulated. Lamberti

(1994), Benoit et al. (1996), Donnars et al. (1996), van der Meer et al. (1996), Christiani (1997).

Breakage of slender concrete armour units

Prediction of breakage of slender concrete armour units was for a long period a problem because no formulae for estimation of breakage were available. Recent cooperation within project (iii) between Aalborg University, Techn. Univ. of Delft, Delft Hydraulics, Francius Institute and WES, USA resulted in formulae for a number of broken units. References are:

Dolosse (includes roundheads): Burcharth et al. (1995).

Tetrapods: Burcharth et al. (1995).

In order to estimate the breakage by use of the formulae it is necessary to know the **strength of the concrete in the prototype armour units**. For this reason a field study of in-situ concrete strength in Tetrapods and Dolosse in Italy was undertaken in project (iii), Franco et al. (1995). Average tensile strength varied between 3.5 and 4.3 MPa and the coefficient of variation was app. 20%. WES, Vicksburg, USA has also made in-situ strength studies in the USA, but investigations from more countries are wanted.

Thermal stresses in concrete armour units due to heat of hydration developing during curing can weaken the units significantly, Burcharth (1983).

A field study of reduction of thermal stresses by introducing a hole in cubes is presented in Burcharth (1991).

In project (iii) a systematic study of curing induced thermal stresses in cubes and Tetrapods was performed by the use of numerical calculations, Nooru-Mohamed (1994). Recommendations of how to avoid critical stresses are given in the references.

Deterioration of concrete armour units due to solar stress was as part of project (iii) studied by field investigations in Italy and by numerical calculations, Canarozzi et al. (1995). It was shown that solar stress can be responsible for degradation of the concrete.

There is a potential risk of significant concrete strength reduction due to **fatigue effect** caused by repeated wave loading, Burcharth (1984). A systematic desk study using various fatigue models was undertaken in project (iii), and it was shown that fatigue strength reduction is critical if the in-situ tensile strength of the concrete is less than app. 2.5 MPa, Soerensen et al. (1995).

7.3 Reshaping breakwaters

The so-called berm breakwaters were studied in project (v). Main emphasis was put on profile development and stone transport at trunk and roundhead sections in oblique waves. Recent references are: Lamberti et al. (1994), van der Meer et al. (1995), Hald et al. (1995), Juhl et al. (1996), Alikhani et al. (1996), Hald et al. (1996). Based on these results as well as on earlier results, van der Meer (1988), it is possible to estimate the profile development, the threshold of stone movements, and the amount of stone transport.

7.4 Scour around roundheads

Formulae for scour around cone shaped and circular cylindrical roundheads were developed from experimental studies at the Technical Univ. of Denmark as part of projects (ii) and (iii), Sumer et al. (1997), Fredsøe et al. (1997). Engineering tools for estimation of scour along breakwater trunks are not yet available.

8 Reliability of existing breakwaters

Level 2 reliability analyses of conventional deterministically designed rubble mound and caisson breakwaters were performed within the PIANC PTC II Workings Groups 12 and 28, projects (xiv) and (xv).

Large failure probabilities were found for rubble mound breakwaters; typically corresponding to 40–70% probability of severe damage within a 50 year life time, PIANC (1992), Ligteringen (1992).

For caisson structures designed according to Japanese recommendations, OCDI (1991), the safety level is higher but still very low compared to other civil engineering structures. Burcharth et al. (1995c), Christiani (1997), Ligteringen (1997). Further analyses will be made in project (vii).

9 Acknowledgement

The very fruitful and enjoyable cooperation within MAST-projects and PIANC-working Groups is very much appreciated.

10 References

- Alikhani, A., Tomassicchio, G.R., Juhl, J. (1996). *Berm breakwater trunk exposed to oblique waves*. Proc. 25th Int. Conf. on Coastal Engineering, Orlando, USA.
- Allsop, N.W.H., Franco, C. (1992). *Performance of rubble mound breakwaters: Singular points*. MAST-G6S Coastal Structures, Contract MAST 0032M. Proc. Final Workshop, Lisbon.
- Allsop, N.W.H., McKenna, J.E., Vicinanza, D., Whittaker, T.T.J. (1996). *New design formulae for wave loadings on vertical breakwaters and sea walls*. Proc. 25th Int. Conf. on Coastal Engineering, Orlando, USA.
- Andersen, K.H. (1995). *Excess pore pressure generation in sand under varying cycle shear stress*. Final Proceedings, Monolithic Coastal Structures, MAST 2 Proj. MAS2-CT92-0047.
- Battjes, J.A. (1982). *Effects of short-crestedness on wave loads on long structures*. Applied Ocean Research, Vol 4, No 3.
- Benaissai, E., Calabrese, M., Silvestri, F. (1997). *A parametric study on the dynamic response of vertical breakwaters under impulsive wave loads*. Proc. 1st Workshop MAST Project Probabilistic design tools for vertical breakwaters, MAS3-CT95-0041.
- Benoit, M., Donnars, P. (1996). *Interaction in the stability of main armour and toe-berm for a rubble mound breakwater: An experimental study under both long-crested and short-crested waves*. Final Report of MAST 2 Project MAS2-CT92-0042. Technical Report HE-42/96/002/A. EDF Laboratoire National Hydraulique, France.

- Berenguer, J.M. (1994). *Hollowed cube research: 2-D model tests*. Proceedings of the 2nd Workshop, MAST 2 Proj. MAS2-CT92-0042, Rubble Mound Breakwater Failure Modes, Bressanone, Italy, January 1994.
- Berenguer, J.M. and Baonza, A. (1994). *Design of rubble mound breakwater in Spain using massive concrete blocks*. Proceedings of the 2nd Workshop, MAST 2 Proj. MAS2-CT92-0042, Rubble Mound Breakwater Failure Modes, Bressanone, Italy, January 1994.
- Berenguer, J.M. and Baonza, A. (1994a). *Hollowed cube research: 2-D model tests*. Proceedings of the 3rd Workshop, MAST 2 Proj. MAS2-CT92-0042, Rubble Mound Breakwater Failure Modes, De Voorst, The Netherlands, Nov. 1994.
- Berenguer, J.M. and Baonza, A. (1994b). *Hollowed cube research: 3-D model tests*. Proceedings of the 4th Workshop, MAST 2 Proj. MAS2-CT92-0042, Rubble Mound Breakwater Failure Modes, Aalborg, Denmark, June 1995.
- Berenguer, J.M. and Baonza, A. (1995). *Experiment study on main armour - wave wall interaction*. Proceedings of the final Workshop, MAST 2 Proj. MAS2-CT92-0042, Rubble Mound Breakwater Failure Modes, Sorrento, Italy, Nov. 1995.
- Burcharth, H.F. (1983). *Materials, structural design of armour units*. Proc. Seminar on Rubble Mound Breakwaters. Royal Inst. of Technology, Stockholm, Sweden. Bulletin No TRITA-VBI-120, Ed. Gösta Werner.
- Burcharth, H.F. (1984). *Fatigue in breakwater concrete armour units*. Proc. 19th Int. Conf. on Coastal Engineering, Houston, Texas.
- Burcharth, H.F. (1991). *Analysis of rubble mound breakwaters: Development of a partial coefficient system for the design of rubble mound breakwaters*. Sub-Group F Report of the PIANC PTC II Working Group 12.
- Burcharth, H.F. (1992). *Analysis of rubble mound breakwaters. Uncertainty related to environmental data and estimated extreme events*. Sub-Group B Report of the PIANC PTC II Working Group 12.
- Burcharth, H.F. (1993). *Structural integrity and hydraulic stability of Dolos armour layers*. ISSN 0909-4296 Series Paper No 9. Dept. of Civil Engineering, Aalborg University, Denmark.
- Burcharth, H.F. (1997). *Reliability-based design of coastal structures*. In Advances in Coastal and Ocean Engineering, Vol 3, Ed. Philip L.-F. Liu, World Scientific.
- Burcharth, H.F., Toschi, P.B., Turrio, E., Balestra, T., Noli, A., Franco, L., Betti, A., Mezzedimi, S. (1991). *Bosaso Harbour. A new hot-climate port development*. Proc. 3rd Int. Conf. on Coastal and Port Engineering in Developing Countries, Mombassa, Kenya.
- Burcharth, H.F., Andersen, O.H. (1994). *On the one-dimensional steady and unsteady porous flow equation*. Coastal Engineering, Vol 24 pp 233-257.
- Burcharth, H.F., Liu, Z. (1994). *2-D model tests of Dolos breakwater with superstructure*. Proceedings of the 2nd Workshop, MAST 2 Proj. MAS2-CT92-0042, Bressanone, Italy, January 1994.
- Burcharth, H.F., Jensen, M.S., Liu, Z., van der Meer, J.W., and d'Angremond, K. (1995). *Design formula for Tetrapod breakage*. Proceedings of the 4th Workshop, MAST 2 Proj. MAS2-CT92-0042, Rubble Mound Breakwater Failure Modes, Sorrento, Italy, Nov. 1995.
- Burcharth, H.F., Frigaard, P., Berenguer, J.M., Gonzalez, B., Uzcanga, J., Villanueva, J. (1995a). *Design of the Ciervana breakwater, Bilbao*. Proc. Advances in Coastal Structures and Breakwaters. Institution of Civil Engineers, London, Thomas Telford.
- Burcharth, H.F., Jensen, J.B. and Liu, Z. (1995b). *Design formulae for hydraulic stability and structural integrity of Dolos breakwater round-heads*. Proceedings of the final Workshop, MAST 2 Proj. MAS2-CT92-0042, Rubble Mound Breakwater Failure Modes, Sorrento, Italy, Nov. 1995.

- Burcharth, H.F., Sørensen, J.D., Christiani, E. (1995c). *Application of reliability analysis for optimal design of monolithic vertical wall breakwaters*. Proc. COPEDEC 1995, Rio de Janeiro, Brazil.
- Burger, G. (1995). *Stability of low-crest breakwaters (based on tests by Vidal and van der Meer)*. Final Proceedings MAST 2 project Rubble Mound Breakwater Failure Modes. Contract MAS2-CT92-0042.
- Canel, M., De Graauw, A. (1992). *Rubble Mound breakwater stability with multidirectional waves*. MAST-G6S Coastal Structures, Contract MAST 0032M. Proc. Final Workshop, Lisbon.
- Cannarozzi, A.A., Lamberti, A., Martinelli, L., and Momanyi, F.X. (1995). *Stress analysis of Tetrapods: field survey*. Proceedings of the final Workshop, MAST 2 Proj. MAS2-CT92-0042, Rubble Mound Breakwater Failure Modes, Sorrento, Italy, Nov. 1995.
- Christensen, M. and Burcharth, H.F. (1995). *Hydraulic stability of single layer Dolos and Acropode armour layers*. Proceedings of the final Workshop, MAST 2 Proj. MAS2-CT92-0042, Rubble Mound Breakwater Failure Modes, Sorrento, Italy, Nov. 1995.
- Christiani, E. (1997). *Application of reliability in breakwater design*. Ph.D. thesis. Series paper 14, ISSN-0909-4296. Hydraulics & Coastal Engineering Lab., Dept. of Civil Eng., Aalborg Univer., Denmark.
- CUR (1994). *Manual on the use of rock in hydraulic engineering*. Report 169. Centre for Civil Engineering Research and Codes. The Netherlands.
- Donnars, P., Benoit, M. (1996). *Interaction in the stability of toe-berm and main armour for rubble mound breakwaters: an experimental study*. Proc. 25th Int. Conf. on Coastal Eng., Orlando, USA.
- Franco, C. and Franco, L. (1997). *Wave overtopping over caisson breakwaters: New prediction formulae based on 2-D and 3-D model tests*. Submitted to the ASCE Journal of Waterway, Port, Coastal and Ocean Engineering.
- Franco, L., Noli, A., Girolamo, P.D., and Ercolani, M. (1995). *Concrete strength and durability of prototype Tetrapods and Dolosse: Results of field and laboratory tests*. Proceedings of the final Workshop, MAST 2 Proj. MAS2-CT92-0042, Rubble Mound Breakwater Failure Modes, Sorrento, Italy, Nov. 1995.
- Fredsøe, J., Sumer, M. (1997). *Scour at the round head of a rubble mound breakwater*. Coastal engineering, Vol 29, Nos. 3-4.
- Frigaard, P., Helm-Petersen, J., Christensen, M., Burcharth, H.F. (1995). *Effects of short-crestedness on wave loads on long caissons*. Report of the LIP-MAST-TAW project. Dept. of Civil Eng., Aalborg University. Final Proc. MAST project Monolithic Coastal Structures, MAS2-CT92-0047.
- Galland, J.-C. (1992). *Rubble mound breakwaters stability under oblique waves*. MAST-G6S Coastal Structures, Contract MAST 0032M, Proc. Final Workshop, Lisbon.
- Goda, Y. (1985). *Random seas and design of maritime structures*. University of Tokyo Press.
- Groenbech, J., Burcharth, H.F., Frigaard, P. (1997). *Wave impact on caisson breakwaters situated in multidirectional breaking seas*. Submitted to the ICCE '98, Copenhagen.
- Groenbech, J., Hald, T., Frigaard, P., Burcharth, H.F. (1997). *Wave loading on Caisson Breakwaters in Multidirectional seas*. Proc. XXVII IAHR Congress, San Francisco.
- Günbak, A.R., Ergin, A. (1983). *Damage and repair of Antalya harbour breakwater*. Proc. Conf. on Coastal Structures, Alexandria, Egypt.
- Hald, T., Burcharth, H.F., Frigaard, P. (1995). *Berm breakwaters - hydraulic response of round-heads and trunks exposed to oblique waves*. Proc. Second MAST Days and Euromar Market, Sorrento, Italy.

- Hald, T., Frigaard, P., Burcharth, H.F., Sigurdson, S. (1996). *Berm breakwater design. Influence movements on stone durability*. Proc. Final Workshop, Reykjavik, Iceland. MAST 2 Project MAS2-CT94-0087.
- Helm-Petersen, J. (1994). *Reflection from caissons in multidirectional seas*. Proc. 3rd MCS Workshop, MAS2-CT92-0047, Monolithic Coastal Structures.
- Helm-Petersen, J. (1995). *Laboratory study of wave reflection from caissons*. Final Proc. MAST Project Monolithical Coastal Structures. MAST contract MAS2-CT92-0047.
- Helm-Petersen, J. (1996). *Reflection performance of vertical structures in multidirectional seas*. Proc. 2nd ICOPMAS Conf., Tehran.
- Holtzhausen, A.H., Zwamborn, J.A. (1991). *Stability of Accropode and comparison with Dolosse*. Coastal Engineering, Vol 15, pp 59-86.
- Juhl, J., Alikhani, A., Sloth, P., Archetti, R. (1996). *Roundhead stability of berm breakwater*. Proc. 25th Int. Conf. on Coastal Engineering, Orlando, USA.
- Kobayashi, M., Kaihatsu, S. (1994). *Hydraulic characteristics and field experience of new wave dissipating concrete blocks Accropode*. Proc. 24th Int. Conf. on Coastal Engineering, Kobe, Japan.
- Kortenhaus, A., Oumeraci, H. (1995). *Simple model for permanent displacement of caisson breakwaters under impact loads*. Final Proc. of the MAST Project MAS2-CT92-0047.
- Lamberti, A. (1994). *Preliminary results of main armour - toe berm interaction*. Final Proceedings, MAST 2 Proj. MAS2-CT92-0042, Rubble Mound Breakwater Failure Modes, Sorrento, Italy, Nov. 1995.
- Lamberti, A., Tomasicchio, G.R., Guiducci, F. (1994). *Reshaping breakwaters in deep and shallow water conditions*. Proc. 24th Int. Conf. on Coastal Engineering, Kobe, Japan.
- Ligteringen, H. (1992). *Analysis of rubble mound breakwaters. Investigation of selected cases*. Sub-group E Report of the PIANC PTC II Working Group 12.
- Ligteringen, H. (1997). *Breakwaters with vertical and inclined concrete walls. Analysis of cases*. Sub-Group B Report of the PIANC PTC II Working Group 28. (expected printing ultimo 1997)
- Losada, I.J., Dalrymple, R.A., Losada, M.A. (1993). *Water waves on crown breakwaters*. ASCE J. of Waterway, Port, Coastal and Ocean Eng., Vol 199-4 pp 367-380.
- Melby, J.A., Turk, G.F. (1994). *The CORE-LOC optimized concrete armor*. Proc. 24th Int. Conf. on Coastal Engineering, ASCE, New York pp 1426-1438.
- Melby, J.A., Turk, G.F. (1997). *CORE-LOC concrete armor units*. Technical Report CHL-97-4, USAE Waterways Experiment Station, Vicksburg, MS, USA.
- Nooru-Mohamed, M.B. (1994). *Analysis of temperature stresses in concrete breakwater elements: Hollow cubes and Tetrapods*. Proceedings of the 3rd Workshop, MAST 2 Proj. MAS2-CT92-0042, Rubble Mound Breakwater Failure Modes, De Voorst, The Netherlands, Nov. 1994.
- OCDI (1991). *Technical standards for port and harbour facilities in Japan*. Port and Harbor Research Institute, Ministry of Transport, Japan.
- Oumeraci, H. (1992). *Review and analysis of vertical breakwater failures*. Proc. of the MAST Project Coastal Structures, MAST G6S contract 0032.
- Oumeraci, H., Klammer, P., Partensky, H.-W. (1993). *Classification of breaking wave loads on vertical structures*. ASCE J. Waterways, Port, Coastal and Ocean Eng., Vol 119. No WW4 pp 381-397.
- Oumeraci, H., Burcharth, H.F., De Rouck, J., Juhl, J., Losada, M. (1995). *Coastal Structures. Overview of MAST 2 projects*. Proc. XXVIth IAHR Congress - Hydra 2000. Sept. 1995, London.

- Pedersen, J. (1994). *Dynamic response of rubble mound breakwater crown walls*. Proceedings of the 2nd Workshop, MAST 2 Proj. MAS2-CT92-0042, Rubble Mound Breakwater Failure Modes, Bressanone, Italy, January 1994.
- Pedersen, J. (1996). *Wave forces and overtopping on crown walls of rubble mound breakwaters*. Ph.D. thesis. Series paper 12, ISSN 0909-4296, Hydraulics & Coastal Engineering Lab., Dept. of Civil Engineering, Aalborg University, Denmark.
- Pedersen, J. (1997). *Dynamic response of caisson breakwaters subjected to impulsive wave loading - Design diagrams for static load factors*. Proc. 1st Workshop MAST Project Probabilistic design tools for vertical breakwaters, MAS3-CT95-0041.
- PIANC (1992). *Analysis of Rubble Mound Breakwaters*. Report of Working Group 12 of PTC II. Supplement to PIANC Bulletin 78/79.
- Sloth, P., Juhl, J. (1995). *Individual wave overtopping volumes for a rubble mound breakwater*. Proc. Int. Conf. on Coastal and Port Eng. in Developing Countries. Rio de Janeiro, Brazil.
- Sumer, M., Fredsøe, J. (1997). *Scour at the head of a vertical-wall breakwater*. Coastal Engineering, Vol 29 Nos. 3-4.
- Sørensen, N.B., Burcharth, H.F. and Liu, Z. (1995). *Fatigue of concrete armour units*. Proceedings of the 4th Workshop, MAST 2 Proj. MAS2-CT92-0042, Rubble Mound Breakwater Failure Modes, Aalborg, Denmark, June 1995.
- Sørensen, J.D., Burcharth, H.F., Christiani, E. (1995). *Partial safety factors for rubble mound breakwaters*. Final Proceedings MAST 2 project Rubble Mound Breakwater Failure Modes. Contract MAS2-CT92-0042.
- Sørensen, J.D., Burcharth, H.F. (1997). *Implementation of safety in the design*. Sub-group D Report of the PIANC PTC II Working Group 28 (expected printing ultimo 1997).
- Tokahashi, S., Tanimoto, K., Shimosako, K. (1994). *A proposal of impulsive pressure coefficient for design of composite breakwaters*. Proc. Int. Conf. on Hydro-technical Eng. for Port and Harbour Construction. Port and Harbour Research Inst., Yokosuka, Japan.
- van der Meer, J.W. (1988). *Stability of cubes, Tetrapods and Accropods*. Proc. Conf. Breakwaters '88, Institution of Civil Engineers, London.
- van der Meer, J.W. (1988). *Rock slopes and gravel beaches under wave attack*. Ph.D. thesis Delft University of Technology. Delft Hydraulics Communication 396.
- van der Meer, J.W. (1993). *Conceptual design of rubble mound breakwaters*. Delft Hydraulics publication No 483.
- van der Meer, J.W., Tutuarima, W.H. and Burger, G. (1995). *Influence of rock shape and grading on stability of low-crested structures*. Abstract submitted to the 25th International Conference on Coastal Engineering.
- van der Meer, J.W., Vis, F.C. (1995). *Conceptual design of berm breakwaters*. Int. Conf. on Coastal and Port Engineering in Developing Countries. Rio de Janeiro, Brazil.
- van der Meer, J.W., d'Angremond, K., Gerding, E. (1996). *Toe stability of rubble mound breakwaters*. Proc. Int. Conf. Advances in Coastal Structures and Breakwaters. Institution of Civil Engineers, London.
- van Gent, M.R.A. (1994). *The modelling of wave action on and in coastal structures*. Coastal Engineering, Vol 22, pp 311-339.
- van Gent, M.R.A. (1994). *Permeability measurements for the modelling of wave action on and in porous structures*. Proc. Coastal Dynamics '94 Conference, Barcelona.
- van Nes, C.P. (1995). *Stresses in Tetrapod armour units exposed to wave action*. M.Sc. Thesis, Delft University of Technology, The Netherlands.

A Cofferdam Breakwater in Indonesia - Design and Physical Modelling

by

Arne Hansen, PortConsult A/S
&
Thomas Jensen, Danish Hydraulic Institute (DHI)

Dansk Vandbygningsteknisk Selskabs seminar om
"Nyere metoder til projektering af moler"
Aalborg Universitet den 25 marts 1998

1. INTRODUCTION

This technical note has been prepared for presentation of some design considerations in connection with the detailed design of a breakwater in Indonesia.

The breakwater has been specified by the Client to be constructed as a cellular sheet-piled cofferdam structure. This specification is based on conclusions in studies carried out for the basic design of the marine terminal.

The breakwater, 1420 m of length, shall be constructed in natural water depths from 5.5 to 6.5 m below Land Datum (=High Water Level).

However, removal of substantial soft marine sediments is required for foundation of the breakwater structure on firm layers of natural limestone. The surface of the limestone is located at elevations between approx. -12 m (LD) eastern end and -20 m (LD) western end, according to results of soundings.

The general layout of the marine terminal and the breakwater is shown in Figures 1.1 and 1.2.

2. DESIGN PRINCIPLES

Cellular cofferdams are made up of a series of interconnecting cells. The cells are usually of circular or diaphragm types as shown in Figure 2.1. In the present case the circular type has been adopted.

The cells are constructed from straight web steel sheet piles and filled with granular soils or rock.

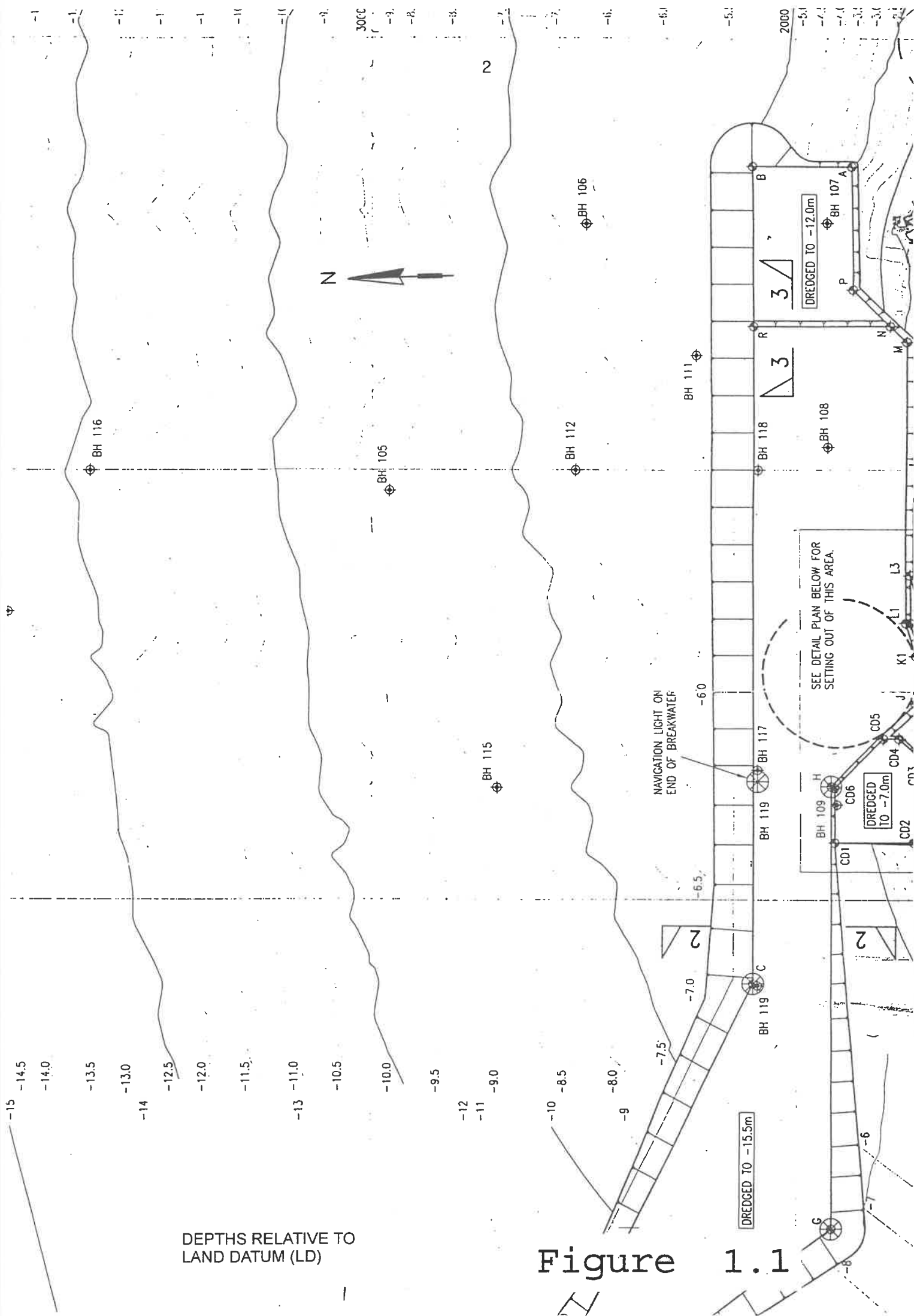
The cells derive their stability against the unbalanced lateral pressures of retained soil, water or incoming waves, from the sand, gravel or rock fill contained within the cells.

In cellular structures no bending moments are developed in the sheet piles and consequently the metal in straight web sections is disposed in a manner which enables the maximum tension to be developed across the profile.

The granular fill within the cells provides stability to the whole structure by resisting shear forces which are set up in the fill when external unbalanced forces are applied. Since the straight web sections themselves are capable of retaining the fill, walings and tie rods are not required.

Investigations of the stability of cellular sheet-piled structures should include consideration of the modes of failure shown in Figure 2.2. In the actual case the tilting due to rotational failure on curved rupture surface at or near the base will be decisive for the design together with the bearing capacity of the subsoil.

When designing a gravity structure like the one in question the main design parameters will be the following:



DEPTHS RELATIVE TO LAND DATUM (LD)

Figure 1.1

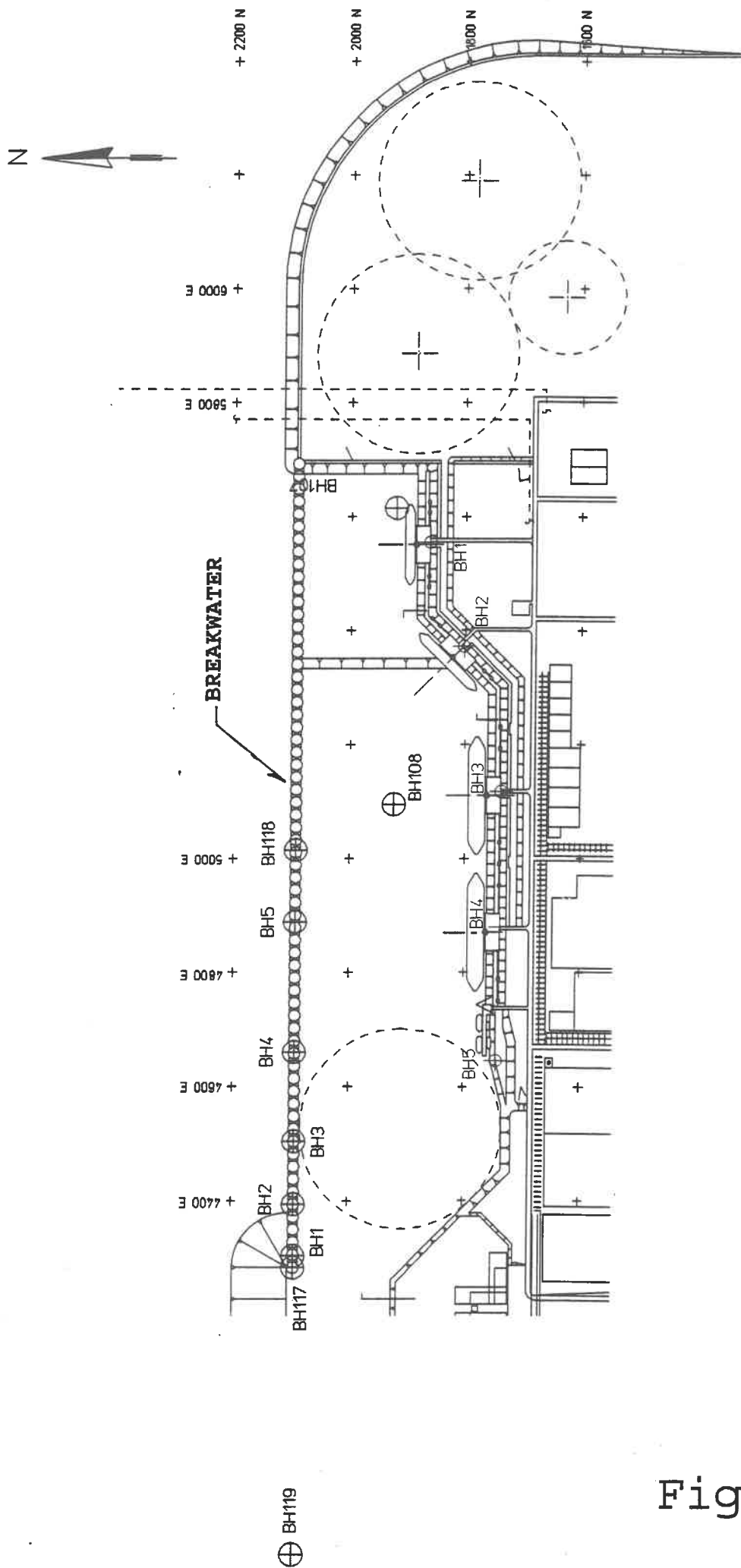


Figure 1.2

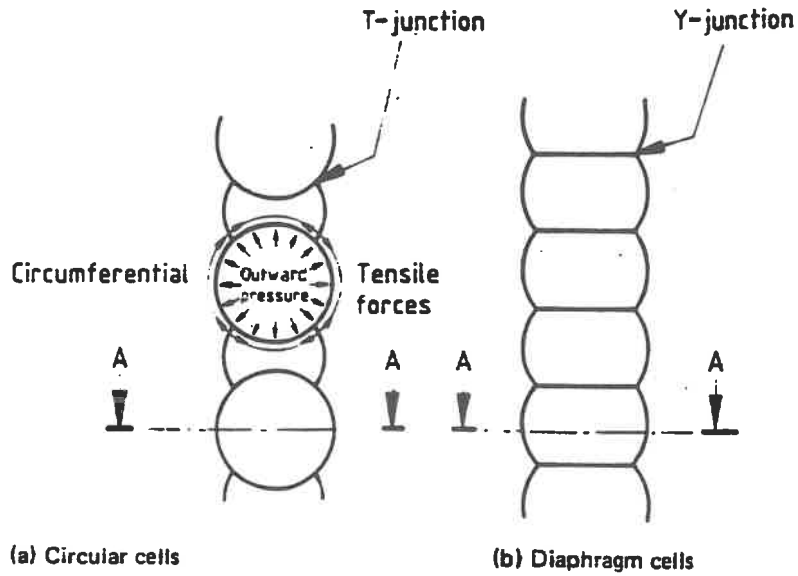


Figure 2.1

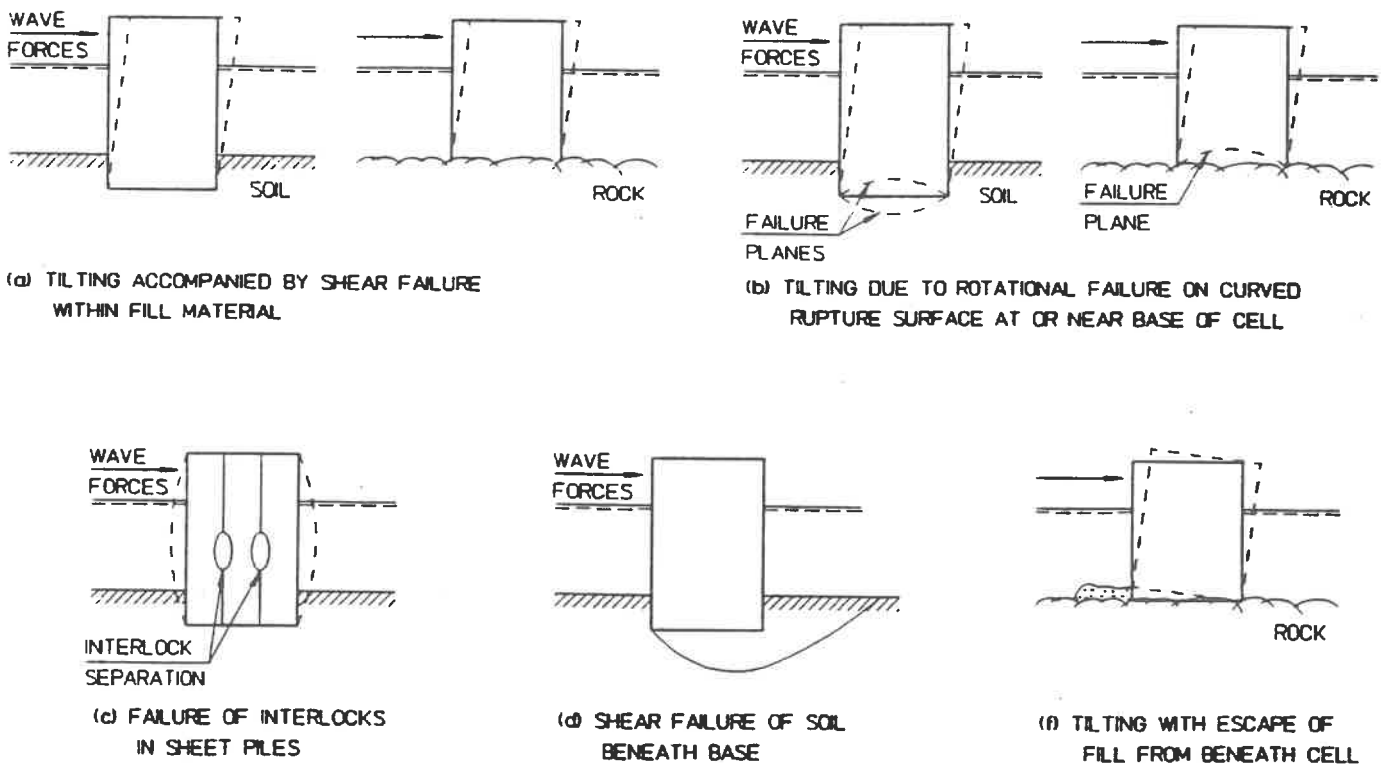


Figure 2.2

- the effective width (w) of the structure
- a high bulk density of the fill material to improve the stability
- a high angle of internal friction to provide internal strength and sliding resistance at the base
- addition of fill on either side of the cells to improve the stabilising forces
- reduction of the wave forces by lowering the seaside front wall
- the driving depth of the sheet piles.

3. DESIGN BASIS

From the Design Basis for the detailed design the following features shall be highlighted (excluding hydrographic conditions, which are covered in Section 4).

- The breakwater shall be substantially constructed within one monsoon period of 9 to 10 months.
- Maintenance programmes shall be implemented for a design life of 50 years.
- Provisions for access on the crest of the breakwater or mooring of vessels along the breakwater are not required.
- Overtopping shall be limited in order not to cause any major wave generation in the harbour basin.
- The breakwater shall be designed to recognised and proven current codes, standards and regulations.
- Earthquake effects shall be considered.

An overview of the soil conditions in the breakwater alignment is given in Figure 3.1.

Following the initial removal of soft sediments, which are acknowledged to be clearly unsuitable for breakwater foundation, the structure will rest on a natural bedrock of limestones.

The basic limestone is described as clastic, moderately weathered, with a submerged density of $6 - 10 \text{ kN/m}^3$ and an internal angle of friction of $\text{min. } 30^\circ$.

4. HYDROGRAPHIC CONDITIONS

The wave climate in the area is governed by the monsoon seasons with westerly and north-westerly waves prevailing during the NW-monsoon season from December through February, and easterly to south-easterly waves prevailing during the SE-monsoon season from April through October. Cyclones and Tsunamis have not been reported in the area.

Based on wave hindcast studies of visually observed wave heights from British Met Office and satellite wave data, the extreme wave conditions corresponding to return periods of 1 year, 10 years and 100 years have been established. The derived extreme wave conditions are shown in Table 4.1.

Table 4.1 Extreme wave conditions

Return period	Significant wave height, H_{m0} (m)	Peak period, T_p (s)
1 year	3.5	10
10 years	4.0	11
100 years	4.5	12

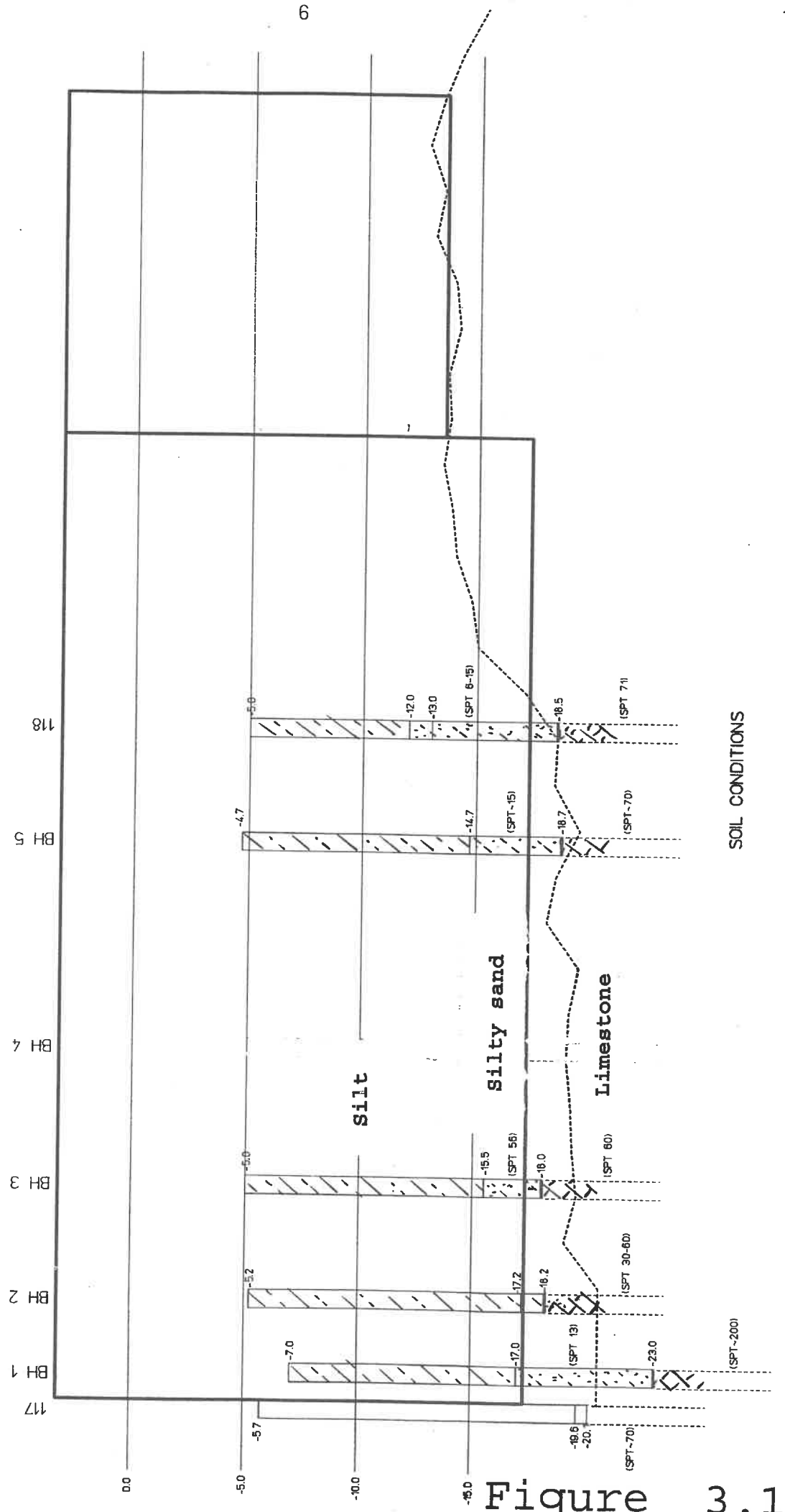


Figure 3.1

The direction of the extreme waves has been conservatively assessed to be perpendicular to the shoreline.

Based on previous studies at the site, the design water level have been established on basis of a 29 days tidal record from the site. The design water levels were based upon the maximum predicted tide for the period 1996 – 2096 plus contributions for seasonal water level variation and storm surge.

The resultant 1 in 100 year design water levels were found to:

- High water : 0.4 m LD = 1.3 m MSL
- Low water : -2.1 m LD = -1.2 m MSL

5. TEST PROGRAMME FOR PHYSICAL MODELLING

To support the detailed design work, physical model tests with the cofferdam breakwater was carried out. The following aspects were investigated:

- The stability of the armour rock on the breakwater crest
- The overtopping of waves
- The wave disturbance behind the breakwater due to overtopping waves
- The wave impact forces on the top and bottom part of the front face of the cofferdam breakwater
- The stability of possible toe (scour) protection on the front of the breakwater

Two different models of the cofferdam breakwater were constructed in the wave flume - one for investigating the top armour stability and wave overtopping and one for investigating the wave impact forces. The models were constructed at a linear scale of 1:40. The test section of the cofferdam breakwater modelled in the wave flume is shown in Figure 5.1. Pictures of the two models are shown in Figures 5.2 and 5.3.

To measure the wave impact forces on the front face, a section covering a circular cell and half of the two adjacent junction cells (ie, a width of 22 m prototype) was separated for force measurements (see Figure 5.3). The section was further divided into a lower cell (up to an elevation of -7 m LD, corresponding to the water depth with backfilled trench) and an upper cell. Each cell was mounted on an electronic strain gauge dynamometer, enabling measurements of the total horizontal and vertical forces as well as the turning moment acting on each cell. On basis of these measurements, the total horizontal force acting on the test section and its corresponding resulting point of action could be derived.

A representative cross section of the seabed bathymetry in front of the breakwater was reproduced in the wave flume. Initially, the bathymetry corresponded to a natural depth of -7 m LD in front of the breakwater, but additional tests were carried out on a modified bathymetry corresponding to a natural depth of -6 m LD.

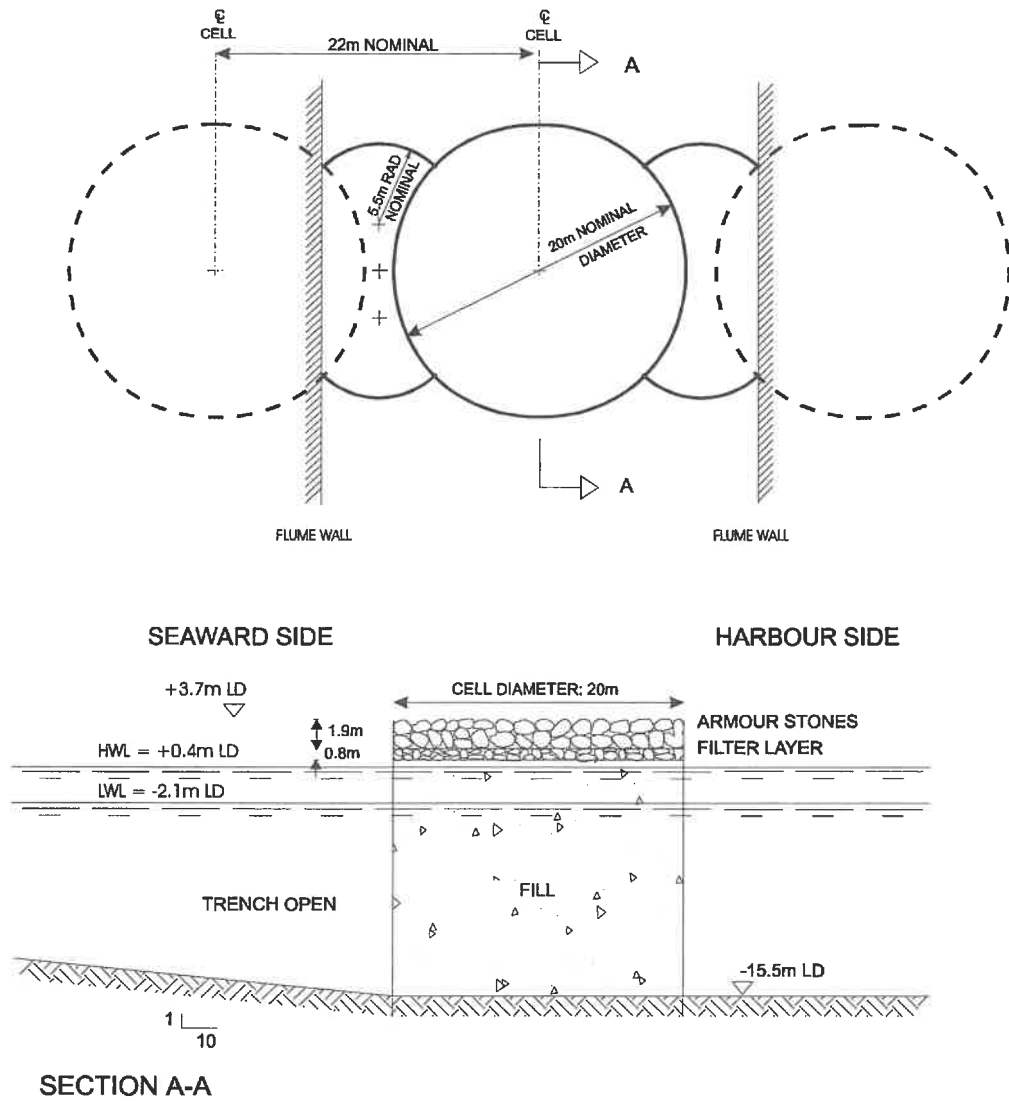


Figure 5.1 Test section of cofferdam breakwater modelled in the wave flume.

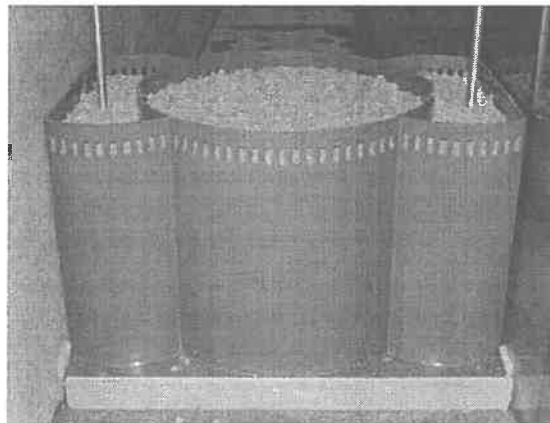


Figure 5.2 Photo of the model used in the armour stability and overtopping tests (the top armour layer has not yet been installed).

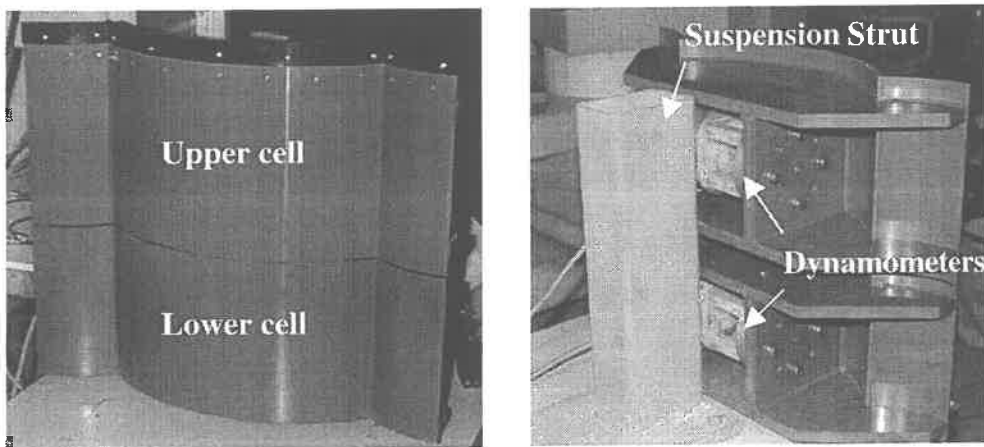
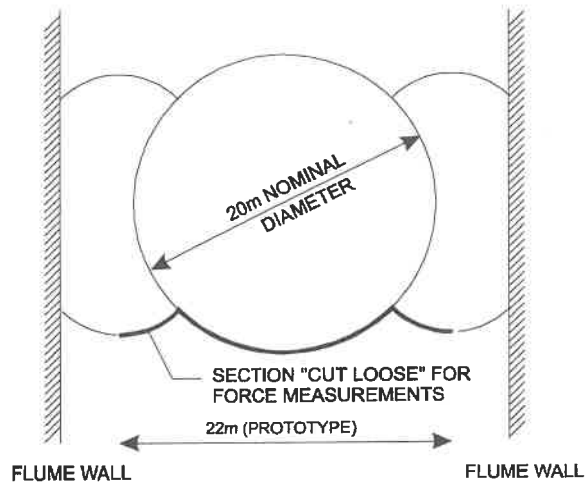


Figure 5.3 Model section applied for wave impact force measurements and photos of the wave impact force model.

Initially, a breakwater layout with a 20 m primary cell diameter and a crest elevation of 3.7 m LD was tested for the following three configurations of the seabed in front of the breakwater:

- Dredged trench in front of the breakwater left open
- Dredged trench in front of the breakwater backfilled
- Dredged trench left open, but with a toe protection in front of the breakwater in order to prevent scouring

The tested layouts are sketched in Figure 5.4.

In order to reduce the wave impact force on the front face of the breakwater, a layout with a lowered crest elevation of 2.7 m LD (as opposed to 3.7 m LD) was also tested. The seabed configuration in front of the breakwater for this layout featured the toe protection.

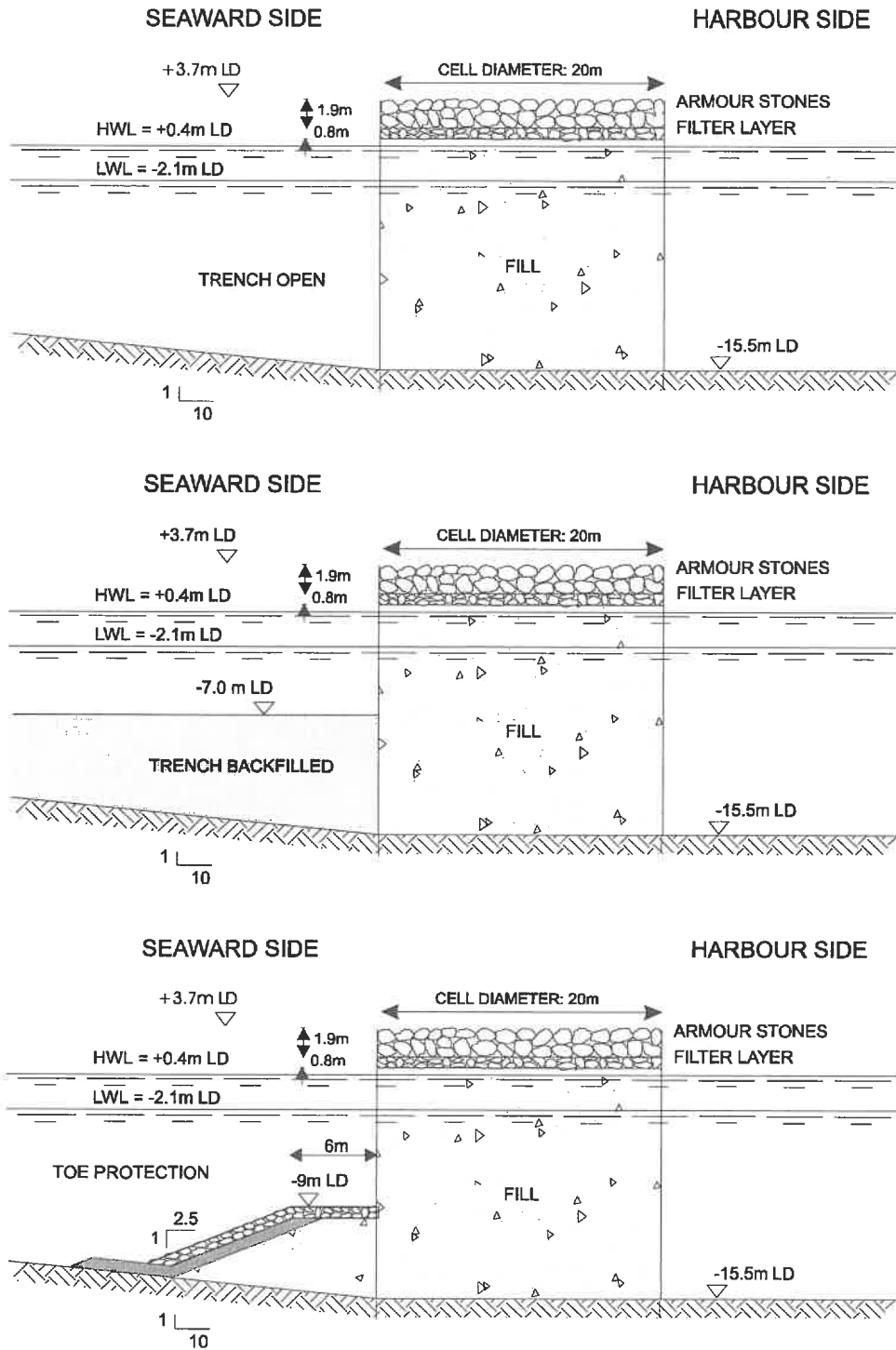


Figure 5.4 The three breakwater layouts tested initially (levels relative to LD).

For investigation of the stability of the top armour layer, two different armour stone configurations were tested; one with armour stones corresponding to $M_{50}=1650 \text{ kg}^*$, and one with armour stones corresponding to $M_{50}=2300 \text{ kg}$ combined with stones up to 3000 kg ($M_{50}=2800 \text{ kg}$) in the critical section (ie, the front section) of the armour layer. In both cases, the stones corresponded to a prototype rock density of 2600 kg/m^3 . Gradation curves for the three applied stone gradations are shown in Figure 5.5.

* M_{50} is armour stone mass given by 50 % on the mass distribution curve.

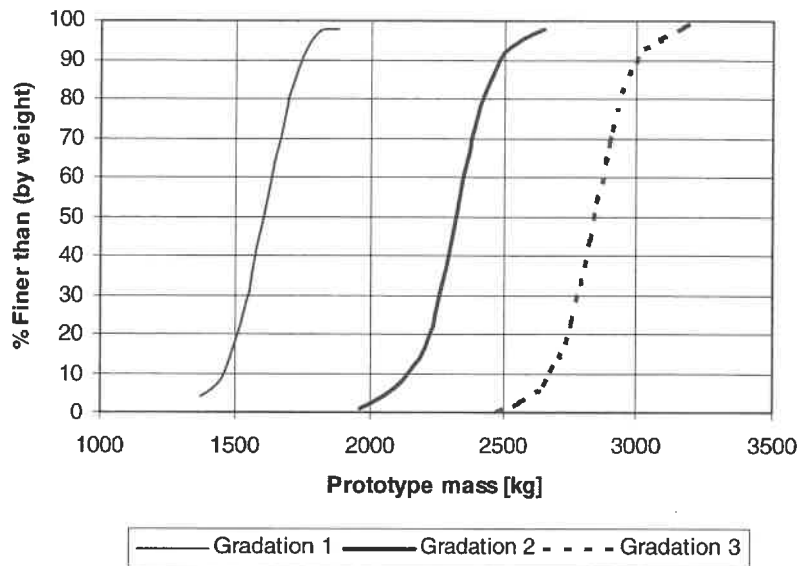


Figure 5.5 The three stone gradations applied in the physical modelling of top armour stability.

For investigation of top armour stability, the tests were carried out in test series composed of the three wave conditions presented in Table 4.1 plus one wave condition with a recurrence period of more than 100 years ($H_{m0}=5.0$ m and $T_p=13$ s) in order to assess the reserve stability of the top armour.

All tests were carried out with long-crested irregular waves of JONSWAP type. The incident waves in the test were determined by reflection analysis and the wave generation was performed with active absorption in order to avoid re-reflections of waves from the wave paddle.

The duration of each sea state was five hours (prototype) in the top armour stability and overtopping tests. In the wave impact force tests, the duration of each sea state corresponded to approximately 1000 waves.

Since the highest possible water level will impose the most severe wave impact on the breakwater, the majority of the tests were carried out at the 100 year high water level (HWL) of 0.4 m LD. However, the stability of the toe protection in front of the breakwater was confirmed at the 100-year low water level (LWL) of -2.1 m LD.

6. RESULTS OF PHYSICAL MODELLING

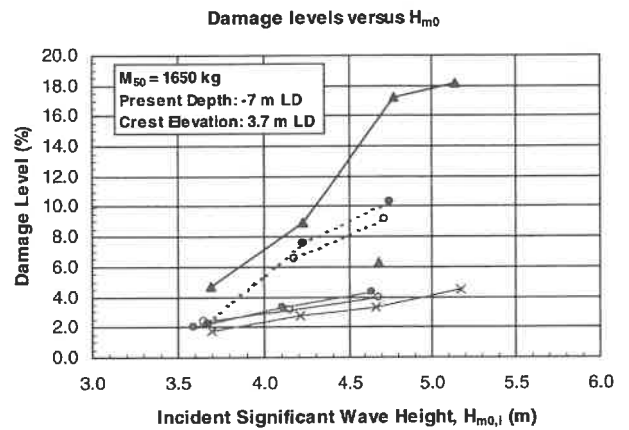
The damage to the top armour layer was observed by counting the number of displaced stones during a test. The amount of overtopping was measured by collecting overtopping water in a tray behind the breakwater and the wave disturbance due to overtopping waves was measured at distances of 20 m and 40 m behind the breakwater.

As regards both armour stability and overtopping, significantly different results were obtained depending on the trench configuration in front of the breakwater. The most severe wave impact on the breakwater was obtained for the layout with backfilled trench and the least severe wave impact for the layout with open trench.

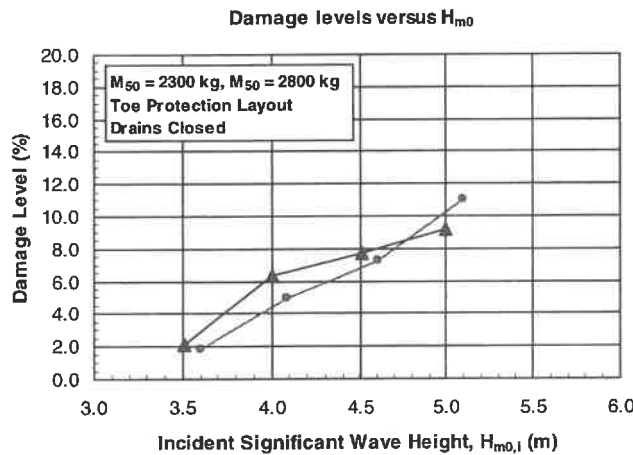
The reason for the different wave impacts in the three layouts is the different wave transformation in front of the breakwater occurring for open trench, backfilled trench or toe protection.

Top Armour Stability

With the armour stones corresponding to $M_{50}=1650$ kg, the accumulated damage level in the 100-year condition reached almost 18 per cent in case of open trench, and four to five per cent with open trench. For the layout with toe protection, the accumulated damage level in the 100-year condition was approximately ten per cent. The results as regards armour stability are shown in Figure 6.1.



- x— Test Series A1a (Drains open, Trench open)
- o— Test Series A1b (Drains open, Trench open)
- ▲ Test Series A1b (WL=0.65 m LD, Drains open, Trench open)
- Test Series A1c (Drains closed, Trench open)
- ▲— Test Series A2 (Drains closed, Trench backfilled)
- ...●... Test Series A3 (Drains closed, Toe protection)
- ...o... Test Series A4 (Drains open, Toe protection)



- Test Series A5 (Present Depth: -7 m LD, Crest Elevation: 3.7 m LD)
- ▲— Test Series A6 (Present Depth: -6 m LD, Crest Elevation: 2.7 m LD)

Figure 6.1 Accumulated damage levels versus incident significant wave height.

As expected, the damage levels for the armour configuration with stones corresponding to $M_{50}=2300$ kg and the critical section of the armour layer reinforced with larger stones ($M_{50}=2800$ kg) were smaller than with $M_{50}=1650$ kg. For comparison, the accumulated damage level in the 100-year condition was approximately eight per cent for a crest elevation of 3.7 m LD and a natural water depth of -7 m LD. Lowering the crest elevation to 2.7 m LD and with a natural water depth of -6 m LD, the accumulated damage level in the 100-year condition was slightly lower, ie in the order of seven per cent.

The acceptable damage levels of the top armour layer must be defined on basis of the possibilities and willingness for repairing possible damage. The overall stability and functionality of the breakwater will not be threatened by a damaged top armour layer unless stones are displaced out of the cells en masse. This was not the case in any of the tests.

Stability of Toe Protection

The stability of possible toe protection on the front of the breakwater was investigated at both the 100-year high water level (HWL) and at the 100-year low water level (LWL). The armour stones used for toe protection corresponded to $M_{50}=125$ kg (with a gradation ranging from 50 kg to 200 kg) and a prototype rock density of 2600 kg/m³.

Exposing the toe protection to several 100-year wave conditions combined with both HWL and LWL only lead to insignificant damage to the toe protection. On the basis of this it was concluded that the tested toe protection was adequately stable.

Overtopping

The mean overtopping discharge for open trench, a natural water depth of -7 m LD and a crest elevation of 3.7 m LD was found at approximately 1 l/s/m (litres per second per metre breakwater width) in the 100-year condition. In the 1-year condition, the mean overtopping discharge was in the order of 0.2 l/s/m for an open trench and ten times higher for the backfilled trench. Comparing these amounts to the amount of overtopping discharge generally regarded as dangerous to persons (0.05 l/s/m according to /1/), they seem rather high. However, the observed amounts are not considered a problem unless pathways, berths, building, etc, are constructed on or closely behind the breakwater.

As regards the wave disturbance in the harbour, it is believed that this will be dominated by the waves entering the harbour entrance and that the contribution from overtopping waves will not be critical for the large vessels.

Wave Impact Forces

As mentioned previously, the resulting horizontal wave impact forces on a 22 m wide section of the breakwater front face (ie, covering a circular cell and half of the two adjacent junction cells) was measured using electronic strain gauge dynamometers. The forces were measured separately on the lower (from -15.5 m LD up to -7 m LD) and upper (from -7 m LD and upwards) parts of the breakwater front.

The force measurements enabled determination of the resulting horizontal wave impact force (F_x) on both the upper and lower cell parts as well as its point of action. Figure 6.2 shows an example of the the point of action of the horizontal wave impact force versus its magnitude.

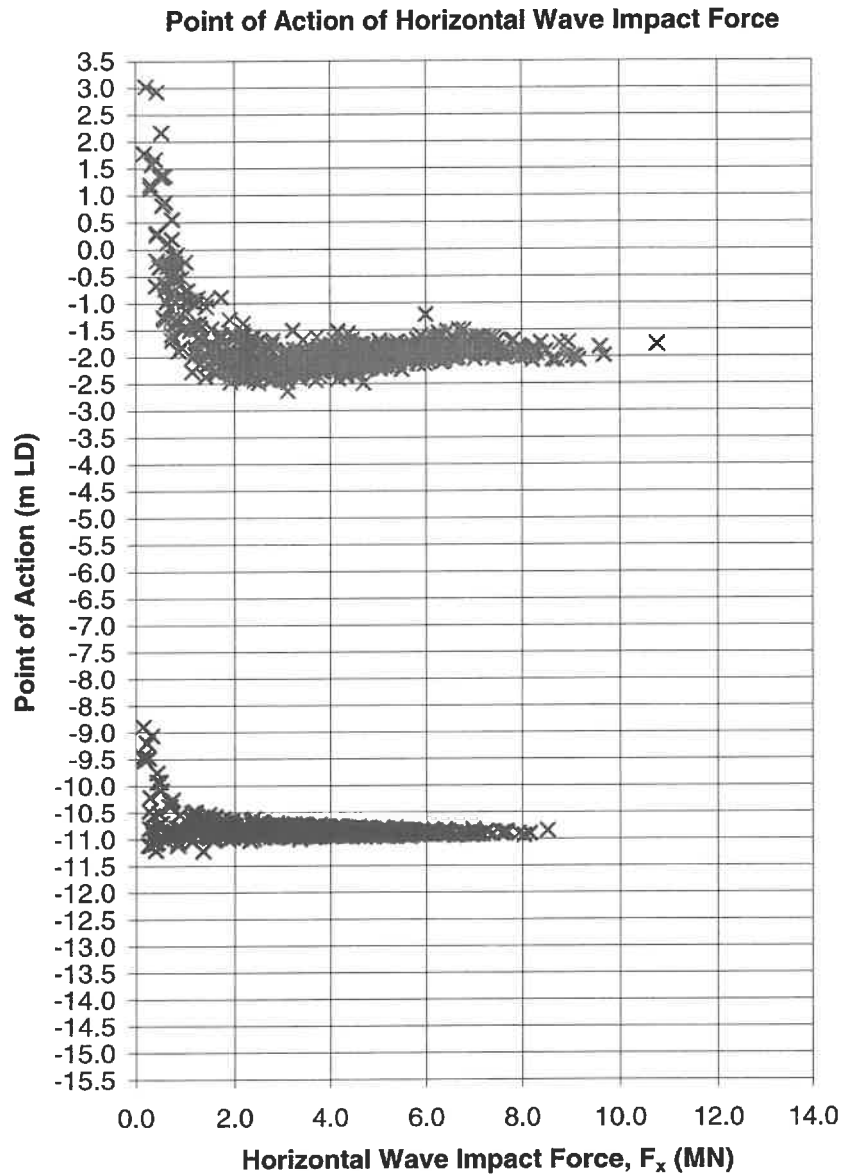


Figure 6.2 Point of action of horizontal wave impact force versus its magnitude. 100 year wave condition with toe protection. Natural depth: -7 m LD, Crest elevation: 3.7 m LD.

On basis of the measurements, a statistical estimate of the maximum horizontal wave force within 1000 waves ($F_{x,0.1\%}$) was derived for each individual test. Figure 6.3 shows the estimated $F_{x,0.1\%}$ versus the incident significant wave height $H_{m0,i}$ for both the upper and lower cell.

As expected from the results of the top armour stability and overtopping tests, the highest wave forces were associated with the layout with backfilled trench.

Furthermore, it is seen from Figure 6.3 that the wave impact forces are reduced when the natural depth is -6 m LD instead of -7 m LD. Lowering the crest elevation of the breakwater from 3.7 m LD to 2.7 m LD also leads to a reduction of the wave impact forces. However, the reduction was only observed on the upper cell.

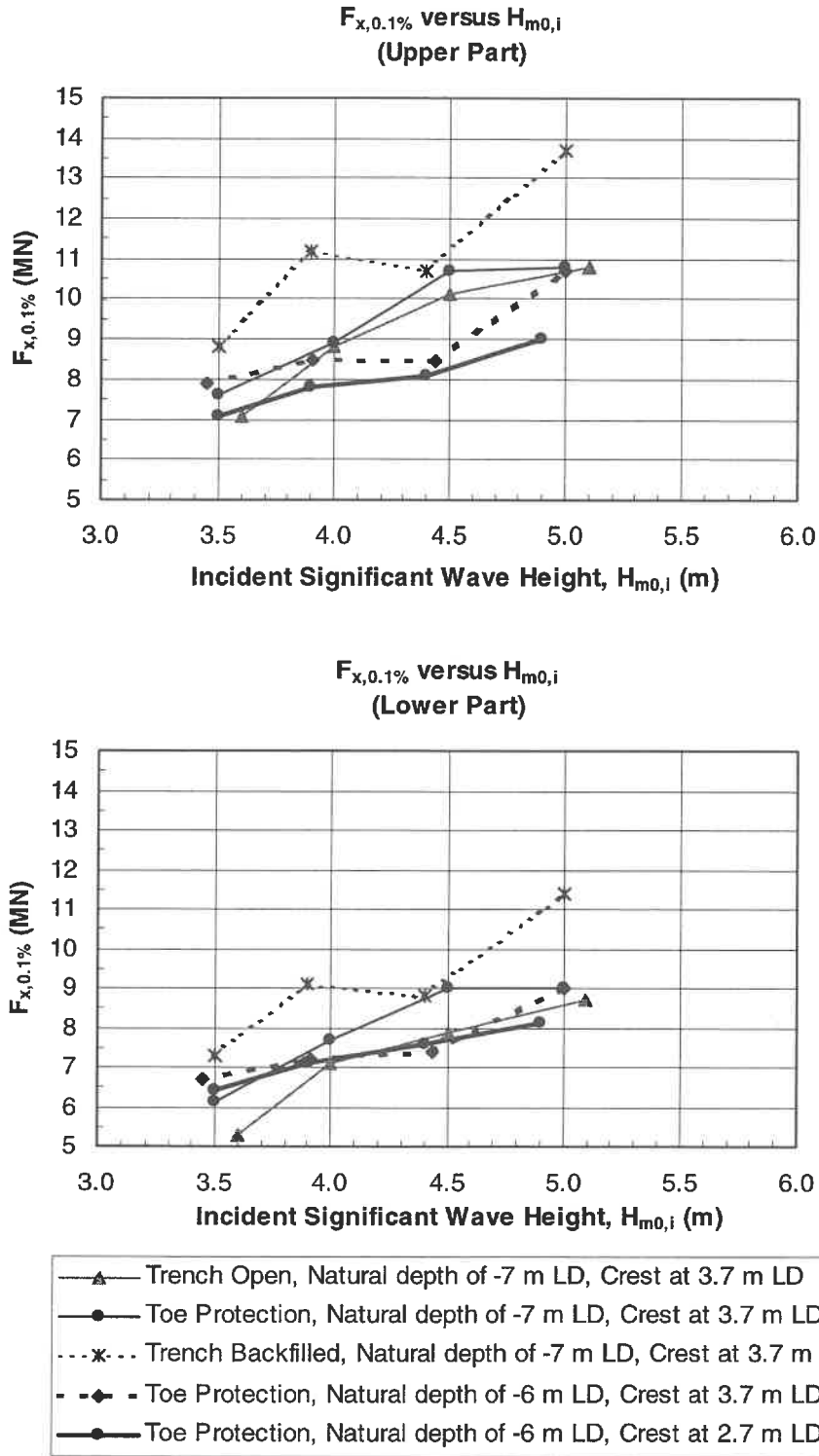


Figure 6.3 Estimated maximum horizontal wave force within 1000 waves ($F_{x,0.1\%}$) versus the incident significant wave height $H_{m0,i}$ (Resulting force on a 22 m wide section of the breakwater front face).

As regards the resulting point of action of the resulting wave impact force, it was identified (see Figure 6.2) that the largest forces on the lower cell strike at level -10.9 m LD and that the largest wave forces on the upper cell strike at levels -1.9 m LD and -2.2 m LD for crest elevations of 3.7 m LD and 2.7 m LD, respectively.

Thus, together with the reduction of the wave impact force on the upper cell for the lowered crest of 2.7 m LD, the resulting point of action of the force is lowered by 0.3 m.

7. RECOMMENDED DESIGN

On basis of the results from the physical model tests and in consideration of the Client's interests a recommended design for the cofferdam breakwater was determined. The recommended design is shown in Figure 7.1 (Western End).

Applying partial safety factors to load components as well as to the internal angle of friction of the fill material in the cells in accordance with the Design Basis a resulting stability factor, f , has been calculated (ratio of stabilising moment to tilting moment).

For a cell diameter of 20 m along the entire breakwater stability factors of 1.05 to 1.2 are achieved.

The bearing capacity of the foundation base has been checked for the combined base load of the vertical weight of the breakwater and extreme horizontal wave loads as deducted from the model tests. Partial safety factors have been applied in accordance with the Design Basis.

In the deep section (Western End) a small berm is required to ensure the necessary bearing capacity of the base.

8. ROCK MATERIALS IN CELLS

According to the basic design the top protection of the fill in the cells against wave overtopping should be provided by two layers of artificial concrete units (antifer cubes of 2.5 tonnes unit weight).

Since limestone rock is available in the project site vicinity, the potential use of limestone has been analysed as part of the detailed design.

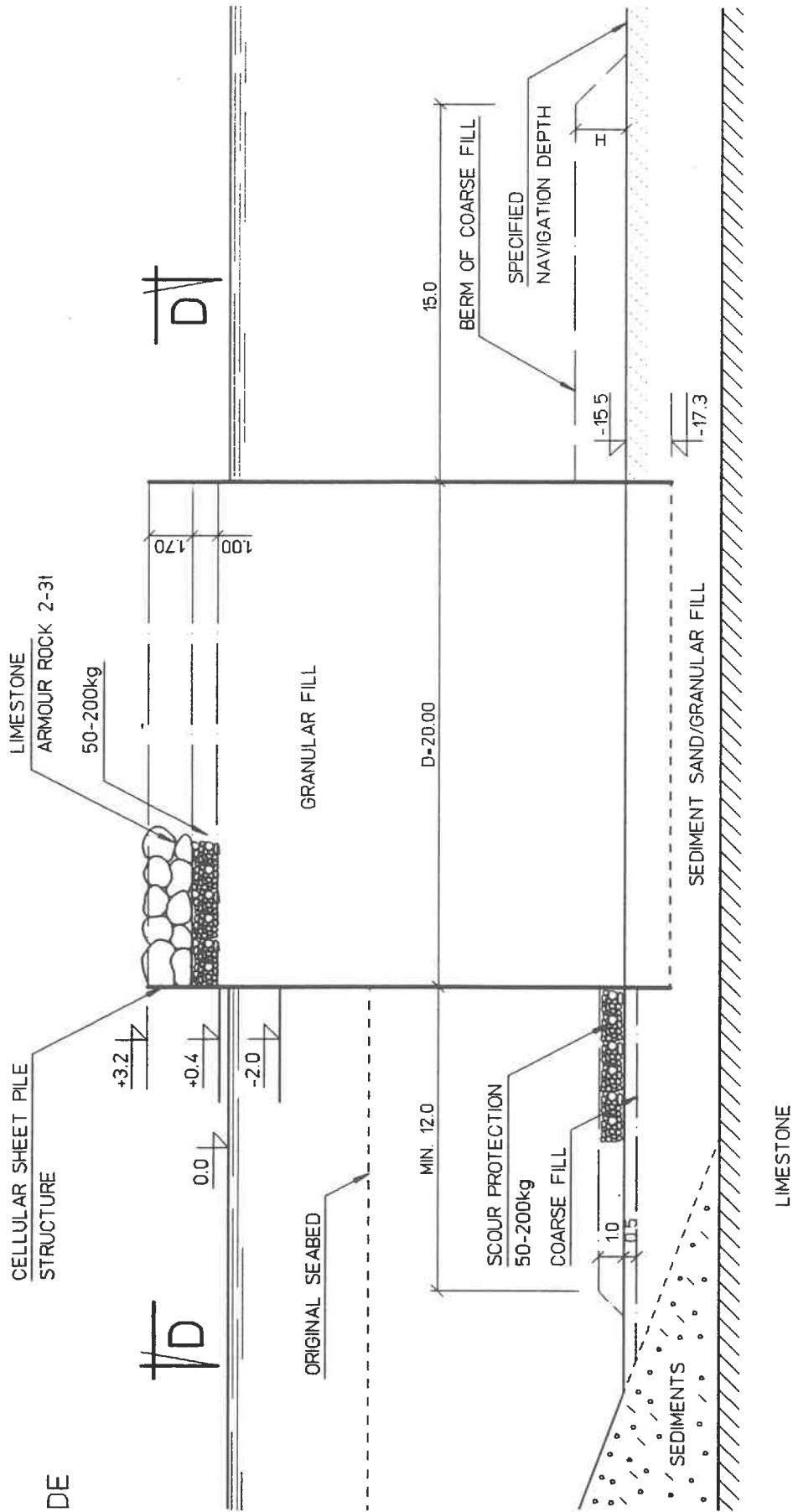
In a local quarry the upper 2 to 3 m of hard caprock is put aside in connection with the production of CaCO_3 for industrial use.

A test programme has been recommended and carried out with the following results:

- bulk density ~ 27 kN/m³
- water absorption ~ 3.0 %
- compressive strength ~ 160 kg/cm²
- sulphate soundness ~ 3 %

On a scale of 'Excellent/Good/Marginal/Poor' the reported results on density and physical soundness are assessed to be 'good' whereas the mechanical properties are only 'marginal'.

Considering the fact that the proposed specific use of armour blocks is limited to the top of the cells and consequently only exposed to wave impacts during extreme sea states it is concluded that the tested limestone can be used as top layer in the cells.



SECTION B-B, 1:250

Figure 7.1

9. **FILL MATERIALS**

Granular fill is required as back fill in the breakwater cells when installed and in the bedding layer for the cells on top of the limestone bedrock which falls below the foundation level on the westerly section of the breakwater.

The fill materials are expected to be produced from dredging of limestone in the future harbour basin using cutter suction equipment.

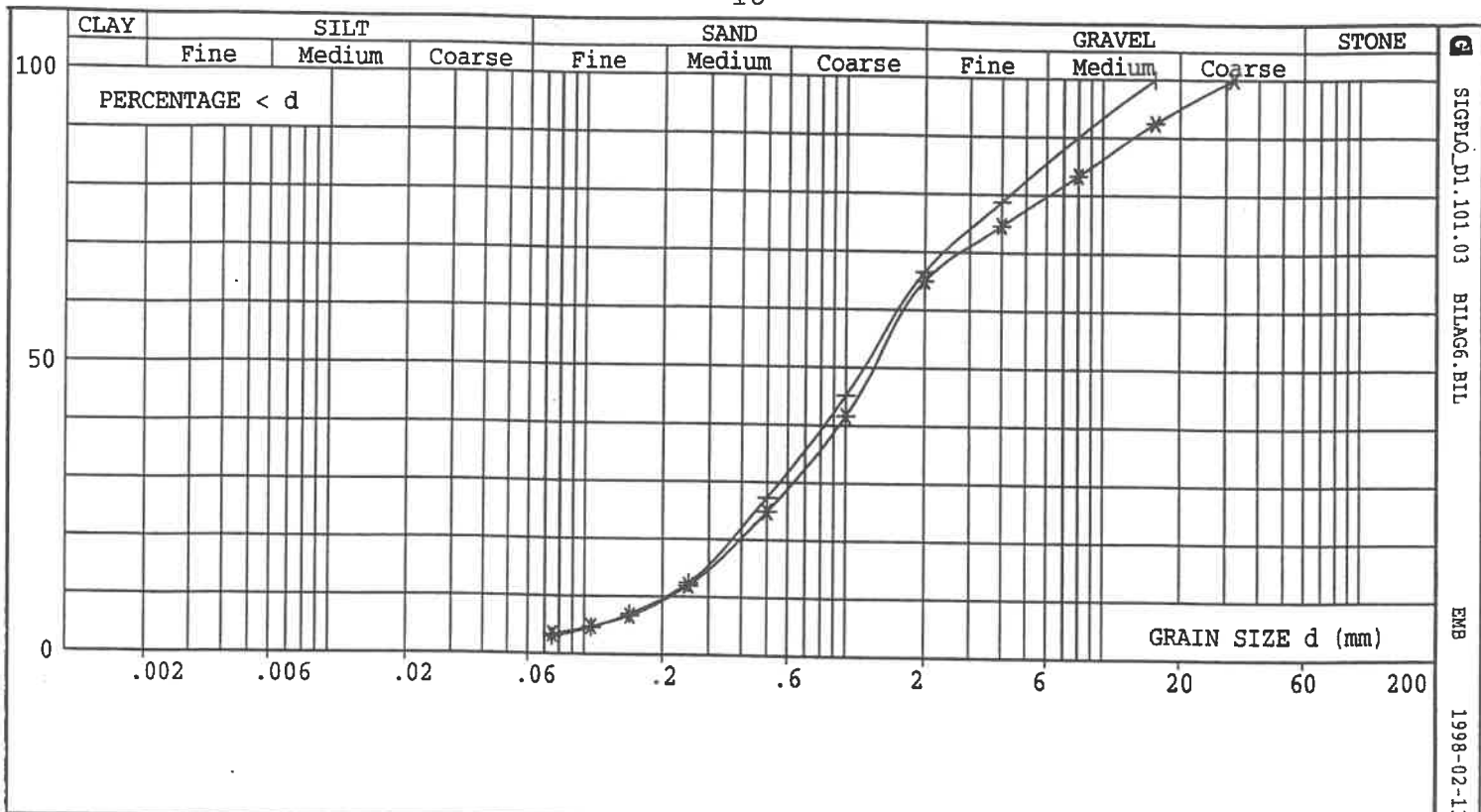
By proper sedimentation of dredge materials in the flushing water a substantial part of the fines can be separated from the sand/gravel fractions.

In Figure 9.1 test results from a sample of fill already produced is shown.

However, the analysis of the fill materials for compliance with requirements to density, internal friction, liquefaction potential have not yet been finalised.

10. **REFERENCES**

- /1/ CIRIA/CUR, 1991. *Manual on the use of rock in coastal and shoreline engineering*. Construction Industry Research and Information Association (CIRIA), Special Publication 83. Centre for Civil Engineering Research and Codes (CUR), Report 154.



Lab. No.	6	6.1 (after cons.)	
Sign	*	*	+
Loose layering, emax, dry	1.505	-	-
Loose layering, emax, wet	1.500	-	-
For small equipment emax	-	1.387	
For small equipment emin	-	0.970	
W _{nat} (%)	12.9	28.4	

Consolidation curve

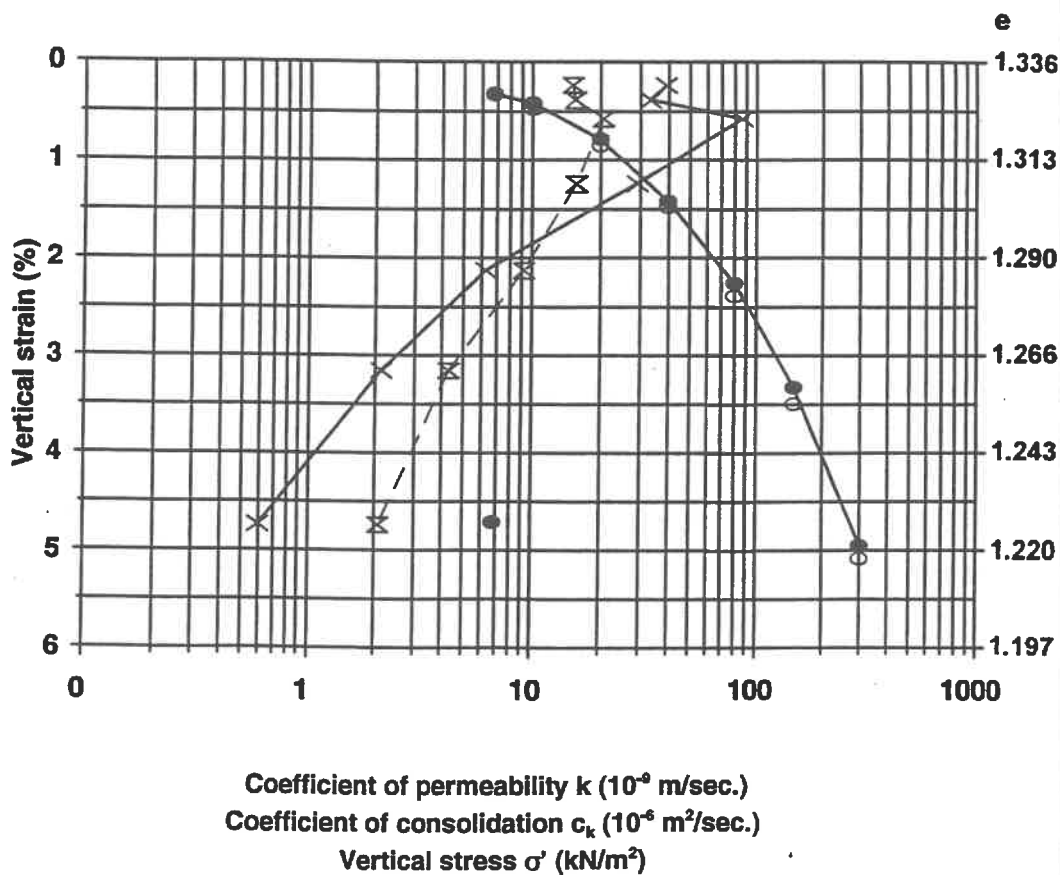


Figure 9.1



Rock Armoured Single Layer Rubble Mound Breakwaters in Norway

by

T. Hald, Aalborg University

A. Tørum, SINTEF NHL

T. Holm-Karlsen, Norwegian Coast Directorate

Dansk Vandbygningsteknisk Selskabs seminar om
"Nyere metoder til projektering af moler"
Aalborg Universitet, den 25. marts 1998

Rock Armoured Single Layer Rubble Mound Breakwaters in Norway

T. HALD ¹, A. TØRUM ² and T. HOLM-KARLSEN ³

¹ Hydraulics and Coastal Engineering Laboratory, Aalborg University, Denmark

² SINTEF Civil and Environmental Eng., Dep. of Coastal and Ocean Engineering, Norway

³ Norwegian Coast Directorate, Oslo, Norway

1. INTRODUCTION

Along the Norwegian coastline more than 600 breakwaters have been build since 1866. Some of these breakwaters are located on severely exposed locations with significant wave heights up to 6.5 m. The present value of these breakwaters is estimated to approximately 4.000 mio. NKr. The far most build breakwater type is the socalled single layer rubble mound breakwater utilizing only one layer of rock in the armour layer. This type of breakwater has developed from the time when heavy equipment was not easily available and the armour layer was constructed by tipping the stones from the breakwater crest.

Obviously the use of one layer rock in the armour layer requires fewer blocks than the traditional two-layer rubble mound breakwater. Despite the fact that heavier blocks are required for the single layer breakwater there is normally a better balance in quarry yields between large armour blocks and the smaller fractions used in the core for the single layer than for the two-layer breakwater.

The use of one layer rock in the armour layer is in most countries not allowed because of apparant weaknesses in the construction. However, the Norwegian experience with respect to low maintenance cost is fairly good. The total maintenance budget is normally 2 – 4 mio. NKr. per year and in extreme winters the maintenance budget may occasionally raise to approximately 15 mio. NKr, c.f. Holm-Karlsen and Tørum (1998).

Thus, regarding both construction and maintenance the single layer breakwater has been considered to be a cost effective structure in Norway.

There have been several investigations on the stability of site specific single layer breakwaters, e.g. for Søvær Fishing Port, Bratteland and Tørum (1971) and for Berlevaag Harbour, Kjellstrup (1977). However, despite the frequent use of the single layer design only little systematic investigations of the stability have been conducted until now. During the winter/spring 1997 a series of physical model tests have been conducted at SINTEF NHL with focus put on the hydraulic performance of the single layer rubble mound breakwater armour layer (Hald and Tørum (1997)). The present paper describes the results of these tests.

1.1. Construction of a single layer breakwater

Many of the older breakwaters in Norway were designed and built before any good knowledge of wave climate and on breakwater hydraulics was available, i.e. before the sixties. Thus experience and subsequent trial-and-error procedures were used.

Traditionally, the armour layer was constructed by tipping the armour stones from the breakwater crest from rail wagons or trucks. This dumping of the stones has to some extent been an art and the result depended also on the skills of the constructor. If an armour stone did not come into its right position it was necessary to use dynamite to blow it away before any new stones were placed. During the construction it was aimed at placing the stones orderly with the longest side almost perpendicular to the filter layer and the smallest area facing the waves, but often the result was a random placement. In order to make the stones roll in position the slope needed to be fairly steep and typical breakwaters were constructed with a slope of 1:1.25 to 1:1.5.

The period of construction was frequently over several years with longer breaks during winter and autumn due to hard weather. The winter storms have settled the unfinished breakwater incurred small damages to it. Possible damages were subsequently repaired during the following construction period and the net result was an improved stability of the finished breakwater.

In some cases today backhoes have been used to place the stones orderly in the armour layer. This method can only be applied from a level of approximately 2 m below LWL because of the limited range of the backhoe. Below this level the armour stones are placed traditionally by tipping from crest. This calls for special attention paid to the lower part in order to secure a safe foundation for the orderly placed upper part. Recently some of the newer build breakwaters built this way have suffered heavy damage.

1.2. Årviksand breakwater

Fig. 1 shows the single layer breakwater at Årviksand Fishing Port, Arnøya, in the northern Norway. The harbour is located on an open coast facing the Norwegian Sea. The estimated 100-year significant wave height in 20 m water depth is approximately 6.5 m and the corresponding peak period 14 s. Daily tidal variations are approximately 3.0 m. The maximum water depth at the breakwater head is approximately 10 m, c.f. Tørum et al. (1990).

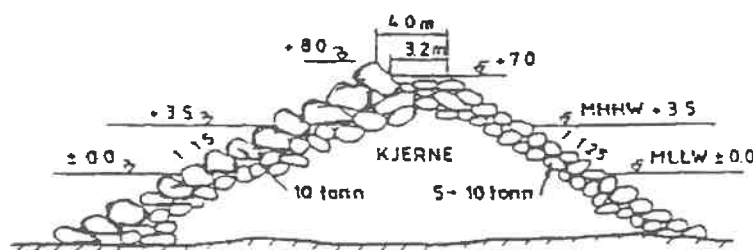


Figure 1: Cross section of Årviksand old breakwater.

The breakwater head suffered severe damage during a storm in January 1964 and suffered further damage during the winter 1964/1965. The breakwater was repaired by casting a monolithic concrete core above HWL on top of the broken breakwater. Succeedingly, the armour layer was placed by tipping stones from the crest on a slope of 1:1.5.

From 41 armour stones above SWL the length L , the width B and the thickness T , corresponding to a stone fitting a box with the dimensions $L \times B \times T$, were measured (Tørum et

al. (1990)). Based on an estimated form factor of the individual stones of 40%, see Tab. 1, the average weight was estimated to $W_{50} = 11.7 \text{ t}$ and the fraction $\frac{W_{85}}{W_{15}} = 2.5$. The density of the used stones was 2.8 t/m^3 . In Fig. 2 the weight distribution and the shape characteristics are shown.

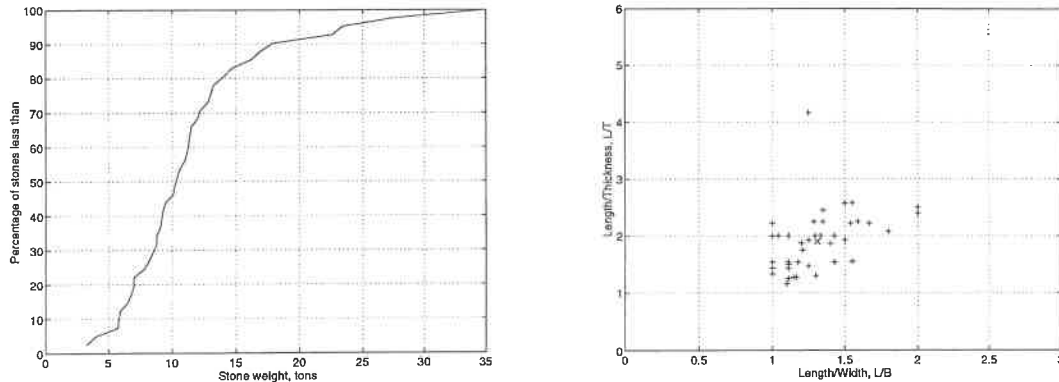


Figure 2: Characteristics of armour stones used at Årviksand.

2. MODEL TEST SETUP

Based on investigations of cross sectional parameters and armour stone characteristics of the Svartnes, Årviksand and Sørvær breakwaters a 3D scale model of 1:30 – 1:40 has been designed. Characteristics of the armour stones are given in Tab. 1.

Armour layer	W_{50}	ρ_m [g/cm ³]	$\frac{W_{85}}{W_{15}}$ [-]	L_{50} [mm]	B_{50} [mm]	T_{50} [mm]	$\frac{W_{50}}{\rho_m T B L}$ [-]
Årviksand	11.7 t	2.8	1.3	-	-	-	0.40
Sørvær	22.0 t	-	1.7	-	-	-	-
Svartnes	18.0 t	-	1.6	-	-	-	-
Stone type A	152 g	2.7	1.8	80.5	54.1	33.3	0.40
Stone type B	306 g	2.7	1.9	96.2	67.5	42.0	0.41

Table 1: Armour stone characteristics.

The breakwater scale model was composed of a core with stones of 4–8 mm, a toe of 118 g stones, a filter layer of 6.4 g stones and a superstructure. The filter layer stone size has been designed according CIRIA–CUR (1991) and with a thickness of 50 mm corresponding to 3–4 stone diameters. On the filter layer the armour layer was constructed with a constant slope of 1:1.5. Two types of armour stones with different weight but similar gradings and shape characteristics were used, see Tab. 1, type A and B. The toe has been designed to withstand the most severe waves in order to avoid reconstruction after every test. In Fig. 3 the model cross section is shown.

The model was installed on a slope of 1:30 in a 54 m long and 5 m wide basin approximately

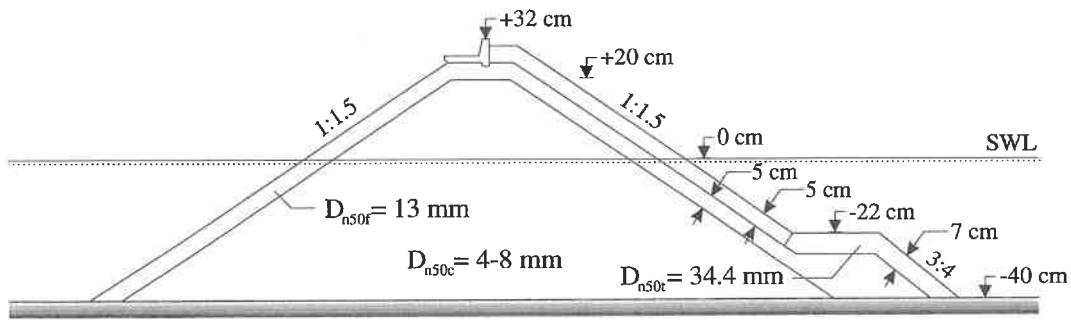


Figure 3: Model test cross section.

25 m from the wave generator, see Fig. 4. The breakwater head was constructed by rotating the cross section for the trunk 180° around a vertical axis through the centerline of the model. Opposite the wave generator waves were absorbed on a parabolic shaped beach. To damp eventual cross modes perforated steel boxes were installed along both basin walls behind the breakwater model and in the gap between the model and the wall.

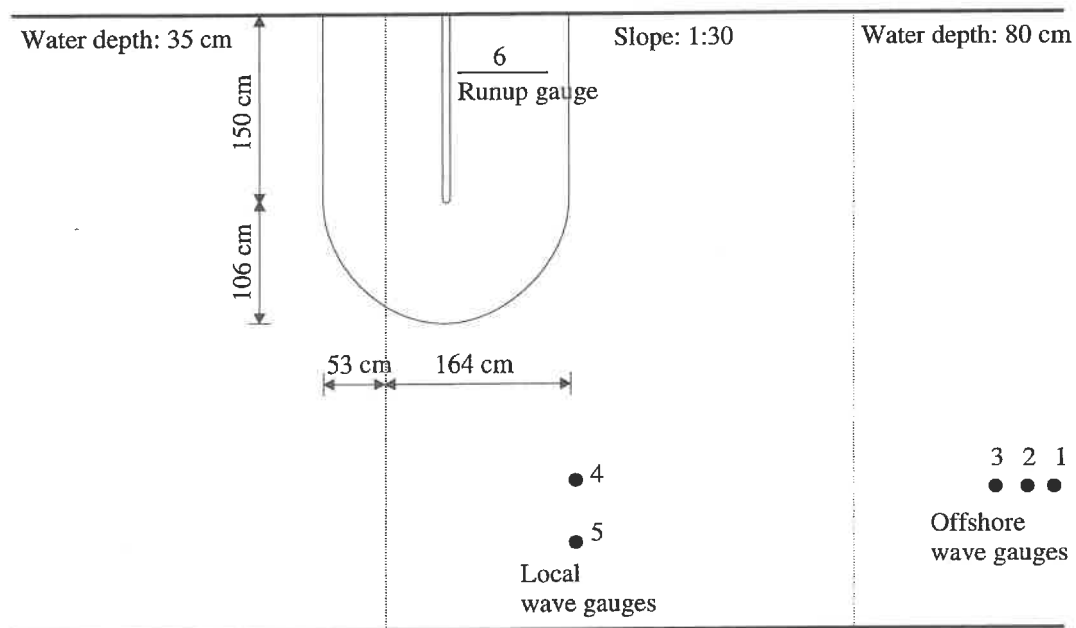


Figure 4: Model test layout.

Five resistance type wave gauges were used to measure the incident wave, see Fig. 4. Three gauges were placed offshore on a constant water depth of 0.8 m and two gauges were placed in the gap between the breakwater model and the basin wall on a water depth of 0.4 m corresponding the the water depth at the toe. To measure the up- and downrush a resistance type gauge was placed on the slope. The sampling frequency was kept constant at 20.0 Hz.

3. STABILITY OF ARMOUR LAYER

3.1. Damage registration

The damage was registered by counting the accumulated number of moved stones N_m and by measuring the average eroded area A_e after each sea state run. The stones included in N_m were defined as the stones moved more than one D_{n50} from their original position and the stones that does not have a stabilizing effect. With respect to the average eroded area profiles were measured by laser for every 10 cm over the width of the breakwater. On the trunk 10 profiles, corresponding to a measurable width of 1.0 m, were averaged to obtain the average profile $\bar{z}_i(x)$. The vertical difference between two individual profiles was calculated so erosion becomes negative, i.e.

$$\Delta\bar{z}(x) = \bar{z}_{i+1}(x) - \bar{z}_i(x) \quad (1)$$

Followingly, the average eroded area was calculated by integration of negative values of $\Delta\bar{z}(x)$ between the toe and the breakwater crest.

$$A_e = \int_{x_{toe}}^{x_{crest}} (\bar{z}_{i+1}(x) - \bar{z}_i(x)) dx \quad (2)$$

The damage level S was then calculated by

$$S = \frac{A_e}{D_{n50}^2} \quad (3)$$

Physically S can be interpreted as the number of squares with the length D_{n50} that fits into the average eroded area.

As a comparison between the two damage measures, the equivalent number of stones moved N_{mS} corresponding to the measured damage level S was calculated.

$$N_{mS} = \frac{S N D_{n50}}{l(1-n)} \quad (4)$$

where

- l : Length of measureable part of trunk section, i.e. 1.0 m
- n : Porosity of armour layer, $n = 0.4$

For small degrees of damage the counting method is considered the most reliable since the profiling also includes settling while profiling is considered better for larger degrees of damage when counting is more difficult.

Corresponding to the accumulated number of moved stones after each sea state the procentage damage $N_{\%D}$ and N_d that represents the number of stones moved in a down-slope row with the diameter D_{n50} were calculated.

3.2. Test programme

The tests were performed according to the test programme in Tab. 2

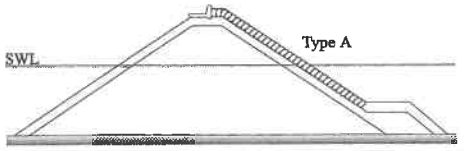
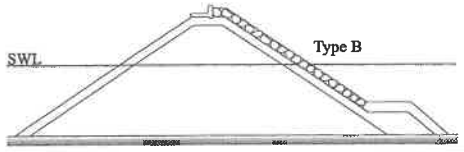
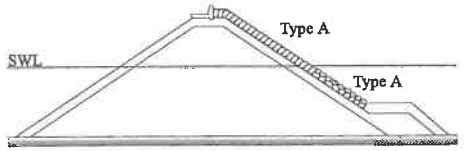
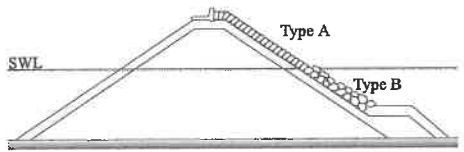
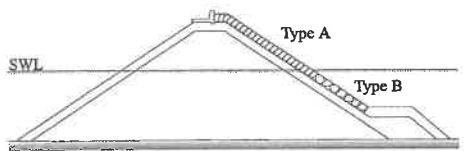
Test identifier	Test runs	s_m	Armour layer characteristics	Cross section
A	3	3%	1-layer orderly, stone type A	
	3	5%		
B	3	3%	1-layer randomly, stone type B	
	3	5%		
Ca	1	5%	1-layer orderly above level -7 cm stone type A 2-layer randomly below level -7 cm stone type A	
Cb	3	5%	1-layer orderly above SWL stone type A 2-layer randomly below SWL stone type B	
D	3	3%	1-layer orderly above level -7 cm stone type A 1-layer randomly below level -7 cm stone type B	

Table 2: Test programme for stability investigations.

In each test the steepness s_m was kept constant and the wave height was increased by 1.5 cm until failure was reached. The waves were generated according to a JONSWAP spectrum with $\gamma = 3.0$. Each sea state was run for approximately 2000 waves.

Due to the stochastic nature of the waves and the constructed model all tests were repeated up to 3 times in order to provide some statistical sound data.

3.3. Stability of orderly placed stones

The damage begins above SWL by displacement of single stones from the armour layer followed by down-slope rolling of the stones. When the wave height increases the damage develops by displacement of more and more stones from the armour layer. As the stones are moved from the armour layer the remaining stones in the armour layer begin to turn downwards. In some cases the armour stones are hindered from turning by a high degree of interlocking and support from neighbouring stones. When sufficient stones have been displaced or turned downwards the high degree of support decreases and failure is inevitable.

In more quantitative terms the damage development for orderly placed stones on the trunk is shown in Fig. 5 the for the wave steepness of 3% and the wave steepness of 5%, respectively.

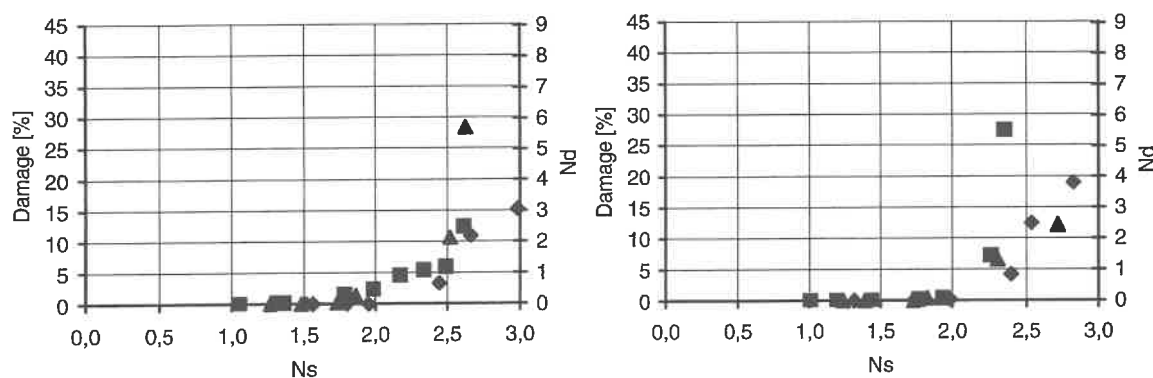


Figure 5: Damage development for orderly placed stones on trunk, $s_m = 3\%$ (left) and $s_m = 5\%$ (right).

From Fig. 5 only little spreading between repeated tests and no or only little influence of wave steepness is observed. Furthermore, the damage develops slowly. Considering a damage level of 5% the stability number is approximately 2.3 which corresponds to a stability coefficient K_D in the Hudson formulae of 8.1.

3.4. Stability of randomly placed stones

For a randomly placed armour layer the damage begins around SWL as a result of large settlements of the armour layer below water level. In single tests a long transverse fissure just above SWL with a width of 2–4 cm was observed. An increase in wave height resulted in displacement of more and more stones in the area around SWL.

In Fig. 6 the damage development for randomly placed stones on the trunk is shown for the wave steepness of 3% and the wave steepness of 5%, respectively.

From Fig. 6 only little spreading between repeated tests and only little influence of wave steepness is observed. Opposite the orderly placed armour layer the damage development for the randomly placed armour layer is very rapid. Considering a damage level of 5% the stability number is approximately 1.05 for a steepness of 3% and 1.1 for a steepness of 5% which corresponds to a stability coefficient K_D in the Hudson formulae of 0.8 and 0.9, respectively.

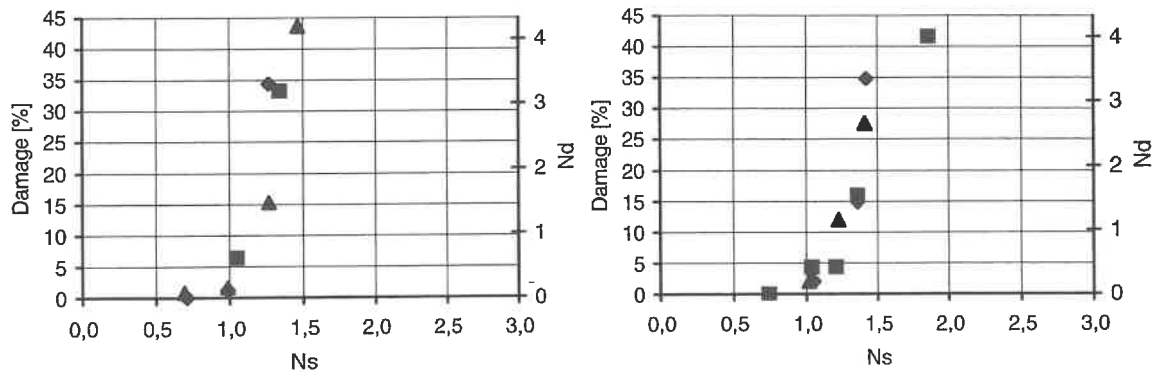


Figure 6: Damage development for randomly placed stones on trunk, $s_m = 3\%$ (left) and $s_m = 5\%$ (right).

3.5. Stability of armour with combined placement methods

Fig. 7–8 depicts the damage development for the tests with orderly placed armour stones on top of an armour layer constructed by randomly placed stones. For a more complete description of the combined placement methods it is referred to Tab. 2.

In Fig. 7 the damage development for the construction type Ca (left) and Cb (right) is shown for a wave steepness of 5%.

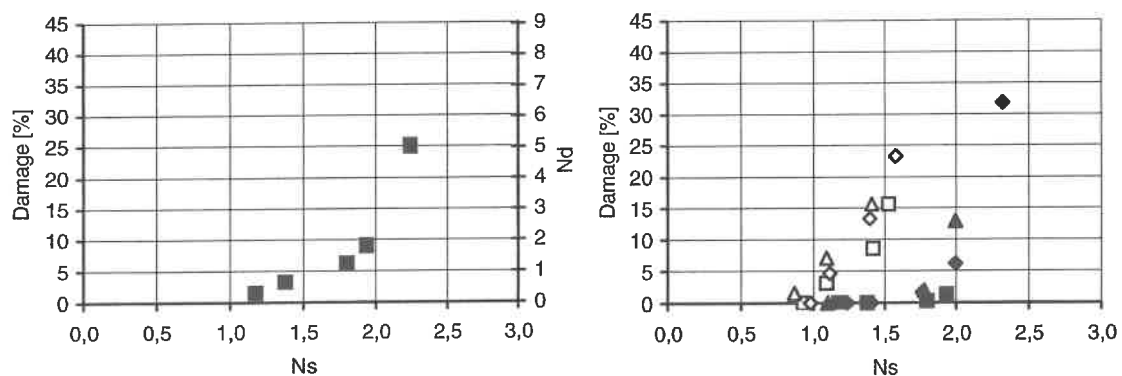


Figure 7: Damage development for combined placement methods, type Ca (left) and Cb (right), closed = stone type A, open = stone type B.

For the construction type Ca the stone type A have been used in both the orderly and in the randomly placed armour layer. In Fig. 7 (left) a slow damage development is seen. However, this is not a true picture of the behaviour since only stones in the lower randomly placed armour layer are moved up till a certain damage level. Above this level the orderly placed part starts to slide. At a damage level of 5% the stability number is 1.6 corresponding to a stability coefficient of 2.7.

For the construction type Cb the stone type B have replaced stones type A in the randomly placed lower part of the armour layer in type Ca. The damage development for type Cb is shown in Fig. 7 (right). Compared to the Ca-type the behaviour of the armour layer is

similar: Almost same slow damage development of the lower randomly placed armour layer followed by a rapid damage development of the upper orderly placed armour layer. At a damage level of 5% the stability number is 1.2 corresponding to a stability coefficient of 1.2. This level is significantly lower than for type Ca since the transition between the two methods of placement is at a higher level, see Tab. 2.

In Fig. 8 the damage development for the construction method D is shown for a wave steepness of 3%.

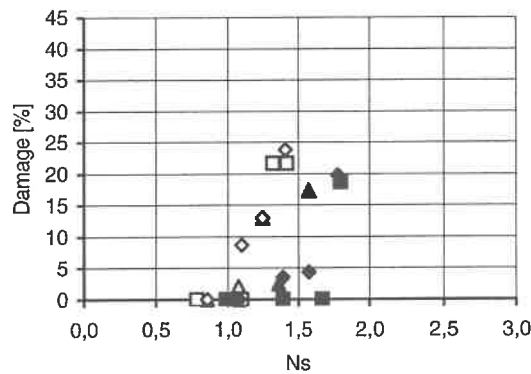


Figure 8: Damage development for combined placement method, type D, closed = stone type A, open = stone type B.

The construction method D differs from the C-types by the use of only one layer of stones in the randomly placed lower part of the armour layer and when comparing the way damage develops a more rapid damage development for the randomly placed part and a more slowly developed damage for the orderly placed part is observed. This is due to the larger settlements related to the single layer randomly placed armour layer. Corresponding to 5% damage the stability number is more or less similar with the Cb-type.

3.6. Overall stability performance

The stability performance of the placement methods A–D is summarized in Tab. 3 in terms of stability number and coefficient corresponding to 5% and 10% damage.

Method	5% damage level		10% damage level	
	N_s	K_D	N_s	K_D
A	2.3	8.1	2.5	10.4
B	1.1	0.9	1.2	1.2
Ca	1.6	2.7	2.0	5.3
Cb	1.2	1.2	1.4	1.8
D	1.1	0.9	1.2	1.2

Table 3: Stability performance of placement methods A–D.

4. WAVE INDUCED FORCES

4.1. Wave force registration

For measuring forces a single stone was selected and a reprint was made in coated plastic foam and succedingly mounted on a load transducer able to measure two force directions. The load transducer was designed and manufactured by MARINTEK A/S, SINTEF. The principle of the transducer is measuring shear strain in different cross sections enabling measurements of the force both parallel and normal to the slope. To avoid any contact with neighbouring stones a chicken wire was wrapped around the mounted stone with a distance of approximately 1 cm.

The load transducer with mounted stone was placed in four positions over the slope as shown in Fig. 9. Also the definition of force directions is shown. Before positioning, the load transducer was calibrated in dry conditions up to 500 g.

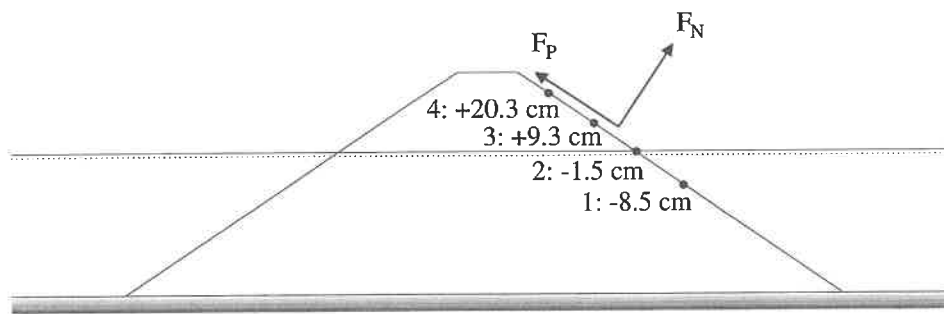


Figure 9: Position of load transducer and positive direction of forces.

Both tests with regular waves and irregular waves were conducted with the transducer positioned in all four positions. For regular waves a wave steepness of 3% and of 5% was tested by increasing the wave height in three steps: 9.0 cm, 12.0 cm and 15.0 cm. For irregular waves the wave height was kept constant at 13.5 cm for both steepnesses. Forces were sampled at 500.0 Hz and subsequently lowpass filtered with a cutoff frequency of 250.0 Hz for regular waves, and at sampled 40.0 Hz and subsequently lowpass filtered with a cutoff frequency of 20.0 Hz for irregular waves.

In the measured force time series maxima and minima peaks have been determined by zero-crossing analyses of the time derivative of the measured force time series. In order to determine only independent peaks, registered peaks within a desired filterwidth are sorted out leaving only one peak within one wave period.

4.2. Wave force characteristics

Measured force characteristics are shown in Fig. 10–11. Generally, force characteristics are invariante with varying wave height why only $H = 15$ cm is presented.

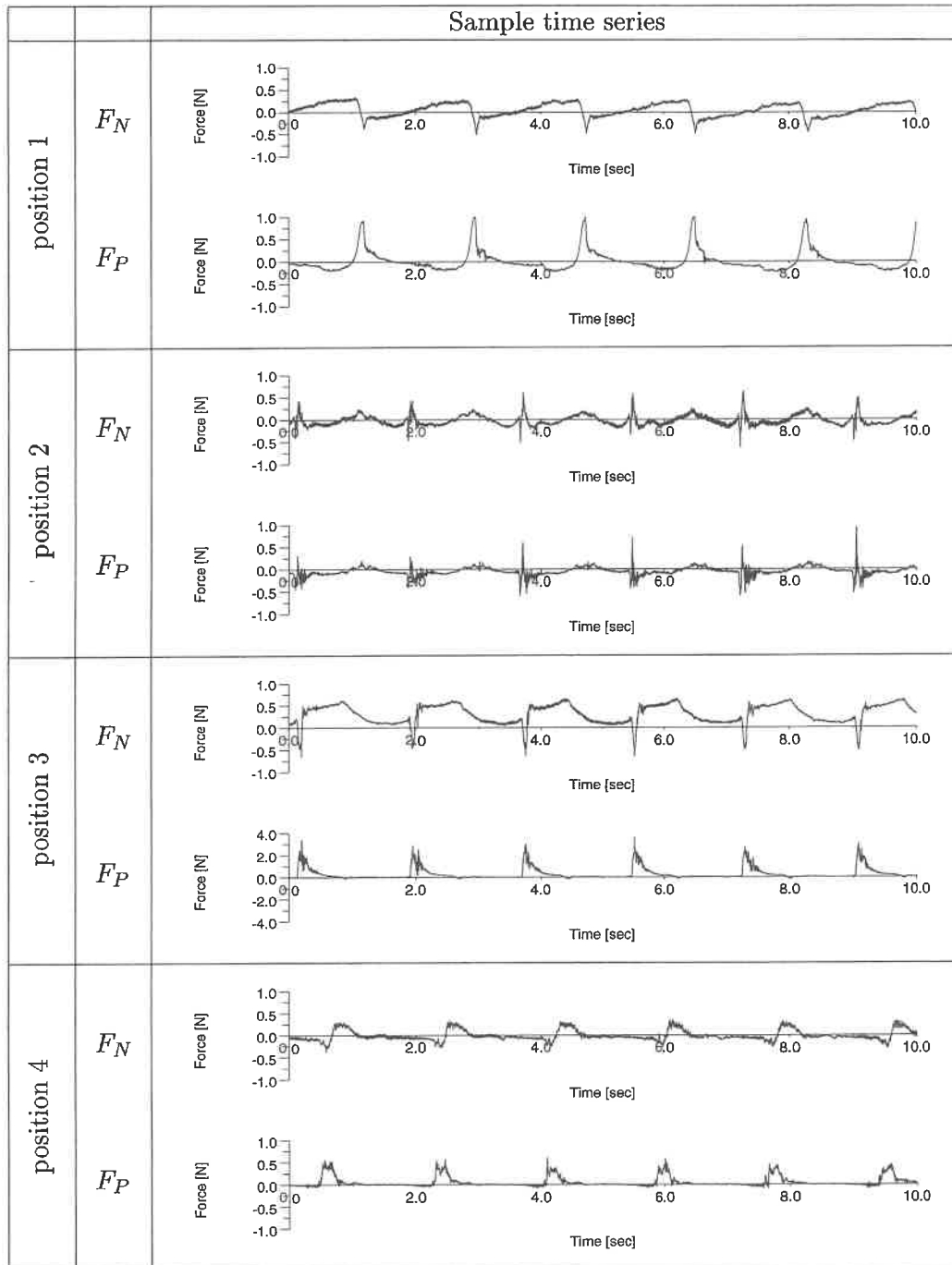


Figure 10: Sample normal and parallel force time series for $s_m = 3\%$, $H = 15$ cm.

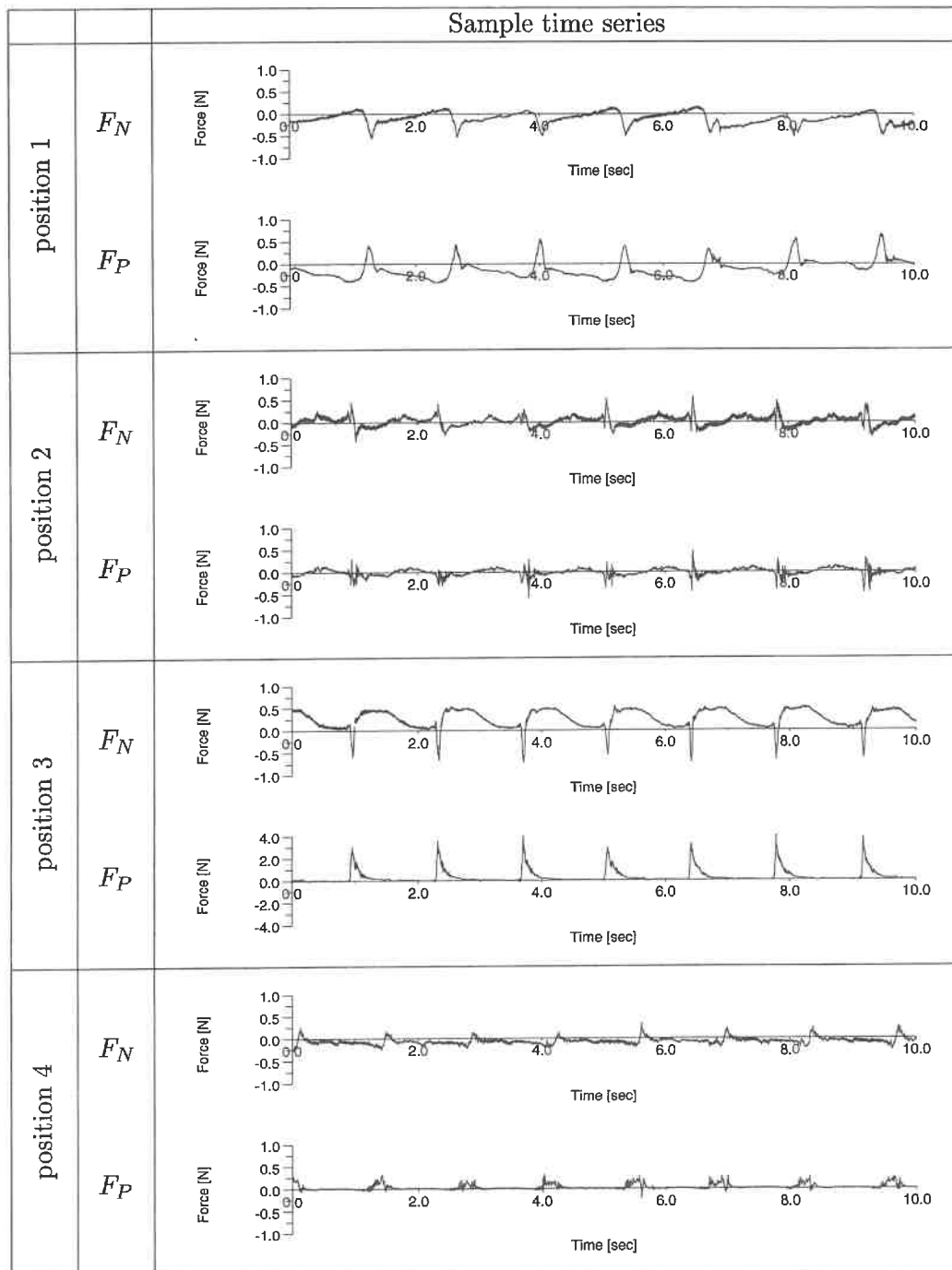


Figure 11: Sample normal and parallel force time series for $s_m = 5\%$, $H = 15$ cm.

Comparing Fig. 10 and 11 somewhat larger forces are observed for a steepness of 3%. Also notice that the largest forces occur 10 cm below and 10 cm above SWL (in position 1 and 3) despite that the waves break directly upon the stone positioned in SWL (in position 2).

4.3. Regular wave induced forces

To illustrate how the total force and corresponding direction varies down the slope all combinations of normal and parallel force within one test are plotted in a (x,y) -coordinate system – a so-called hodograph. As the total force varies in each direction, the average force within intervals of 5° was calculated. In Fig. 12 hodographs for each position and each combination of wave height and period are shown.

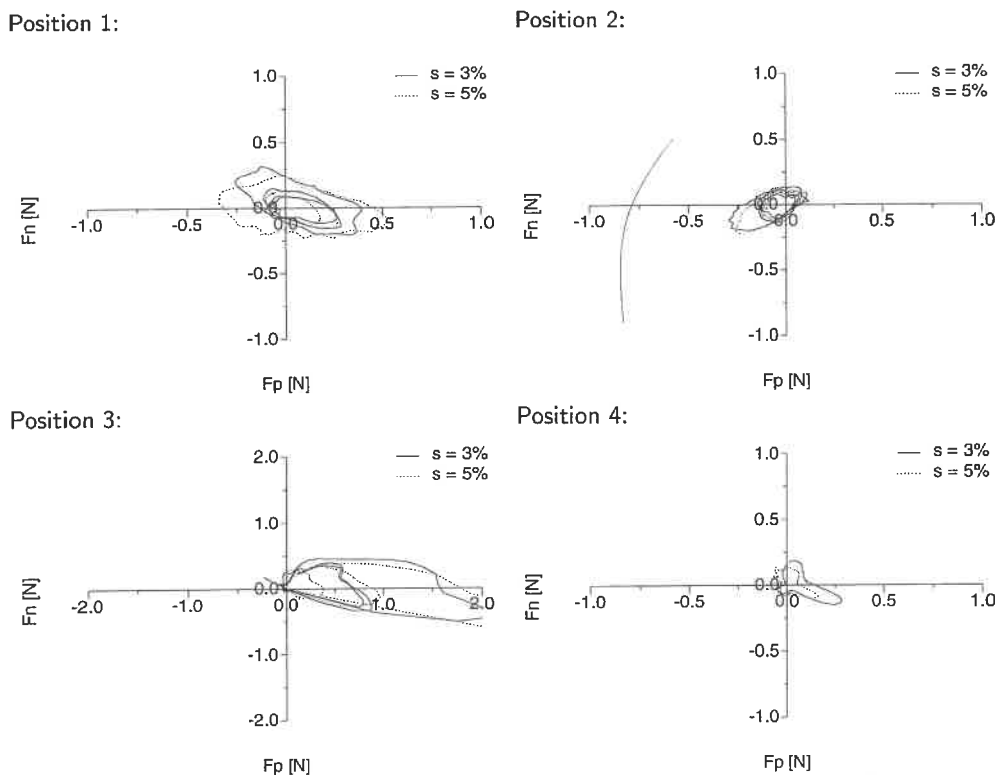


Figure 12: Hodographs at position 1–4 for regular waves based on F_m .

Generally, the shape of each hodograph for all combinations of wave height and period within each position is very similar, c.f. Fig. 12. The largest forces occur below and above SWL in position 1 and 3. In position 1 the dominating forces are either directed outwards and down-slope or inwards and up-slope. In position 2 the forces are smaller and of more or less the same magnitude in all directions. Further up-slope in position 3 the largest forces occur in up slope direction and mainly parallel to the slope. In position 4 the force is of the same character as in position 3 but only smaller.

The most interesting forces are the destabilizing forces in outward directions and in order to get an impression of the vertical distribution along the slope three outward directions are selected: 45° down-slope, 90° slope normal and 45° up-slope, see Fig. 13.

Considering Fig. 13 it is observed that each position except 0.25 times the water depth above SWL, i.e. position 3, the force magnitude is of the same order of magnitude for all directions. In position 3 the force increases as the direction becomes more upward directed.

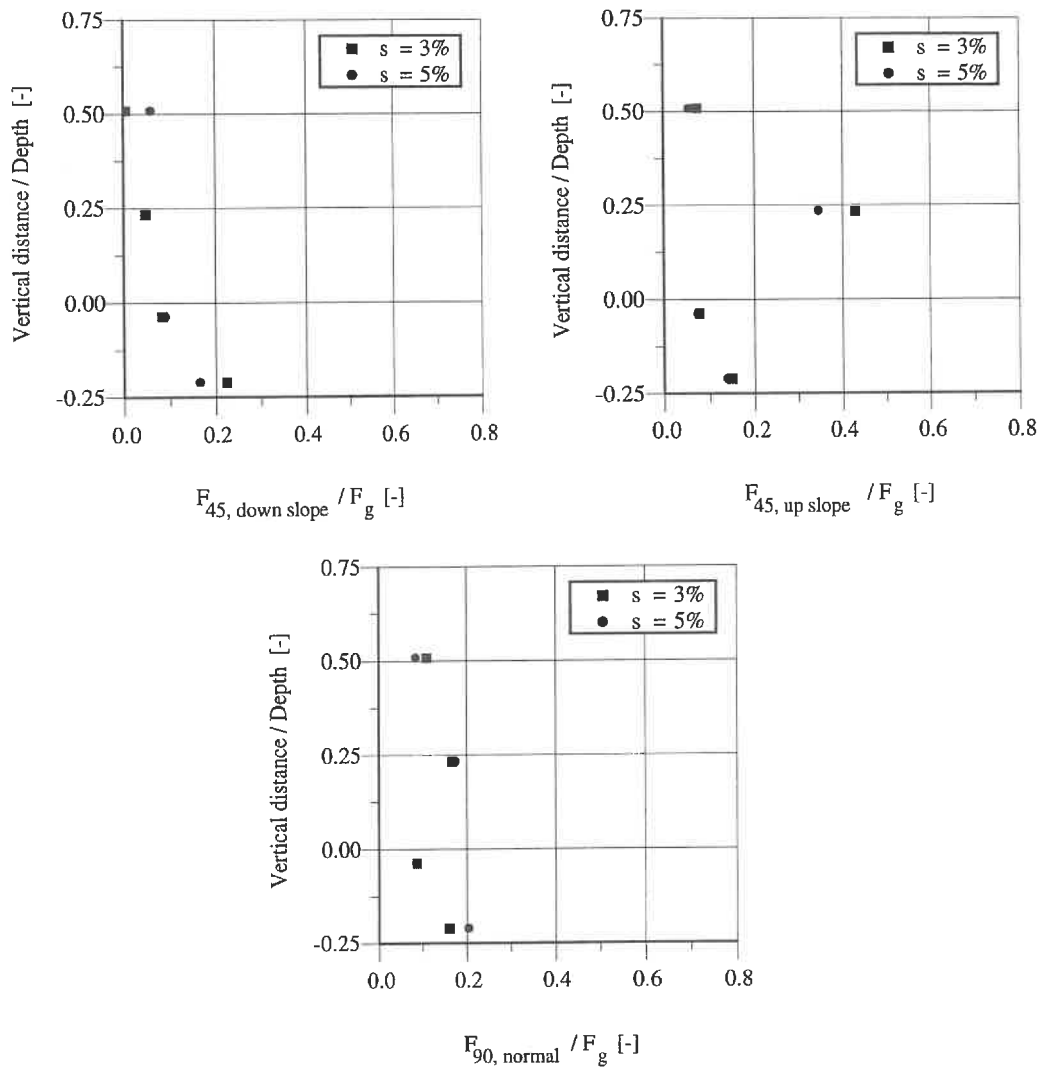


Figure 13: Vertical distribution of outward directed mean force F_m based on regular wave tests, $H = 15$ cm.

4.4. Irregular wave induced forces

Regarding irregular wave induced forces the same characteristics as for regular waves are observed within each individual wave cycle. As for the regular wave tests force hodographs are plotted for the four positions, but opposite the regular wave tests the average force is no longer of interest since only a fraction of the waves are large enough to induce forces able to remove stones from the armour layer. Therefore the average of the highest 1/250 of the force peaks is used as a representative parameter. This parameter is termed $F_{1/250}$. Of course it could be argued that another fraction such as 1/50 should be used but the same conclusions are reached with this parameter as with $F_{1/250}$. In Fig. 14 the force hodographs in all four positions are depicted.

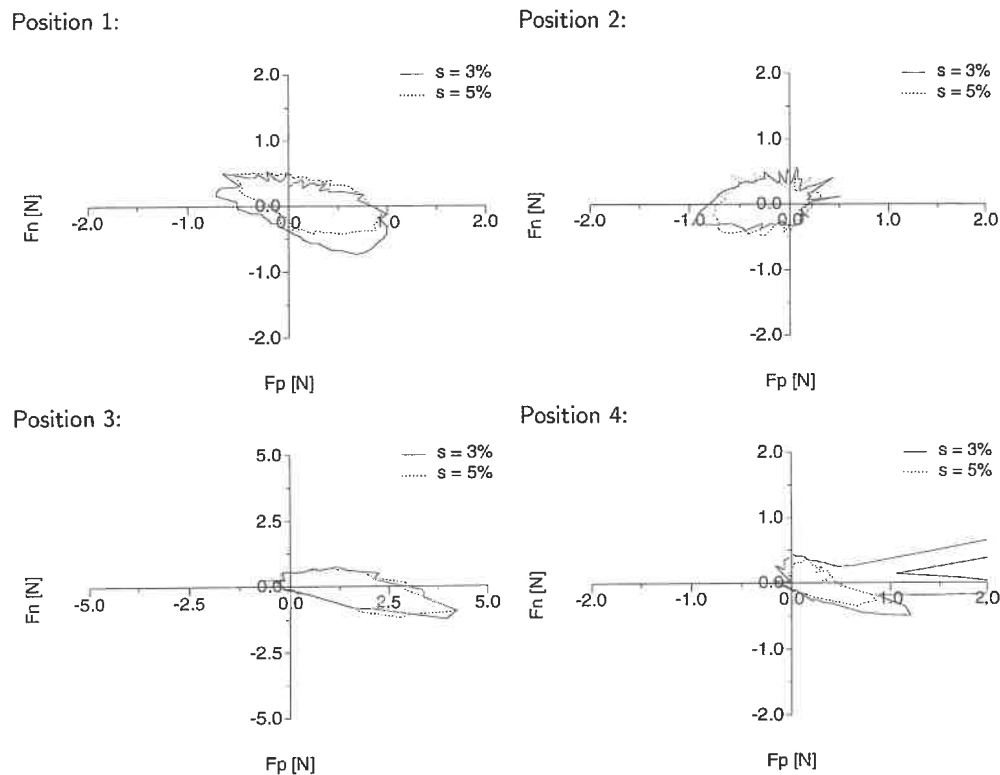


Figure 14: Hodographs at position 1-4 for irregular waves based on $F_{\frac{1}{250}}$.

The shape of the hodographs presented in Fig. 14 corresponds very well with the hodographs obtained with regular waves and the same conclusions apply. Regarding the vertical distribution of the total force acting away from the slope the distributions are presented in Fig. 15.

The displayed forces are somewhat higher than the regular wave induced forces but still it is observed that the largest forces occur approximately one fourth water depth above and one fourth water depth below SWL.

4.5. Comparison with stability

Comparing video recordings from the model tests it is observed that for the randomly placed stones, damage is initiated below SWL. However, for the orderly placed stones damage is initiated above SWL.

Relating the stability observations to the force measurements it is interesting to see that only in the case of random placements, the downward directed force is able to remove the individual stones from their original position. This downward directed force is not sufficient to remove any stones when placed orderly because of the higher degree of interlocking and support from neighbouring stones. In this case high normal forces are required to remove any stone. These forces are present above SWL in position 3.

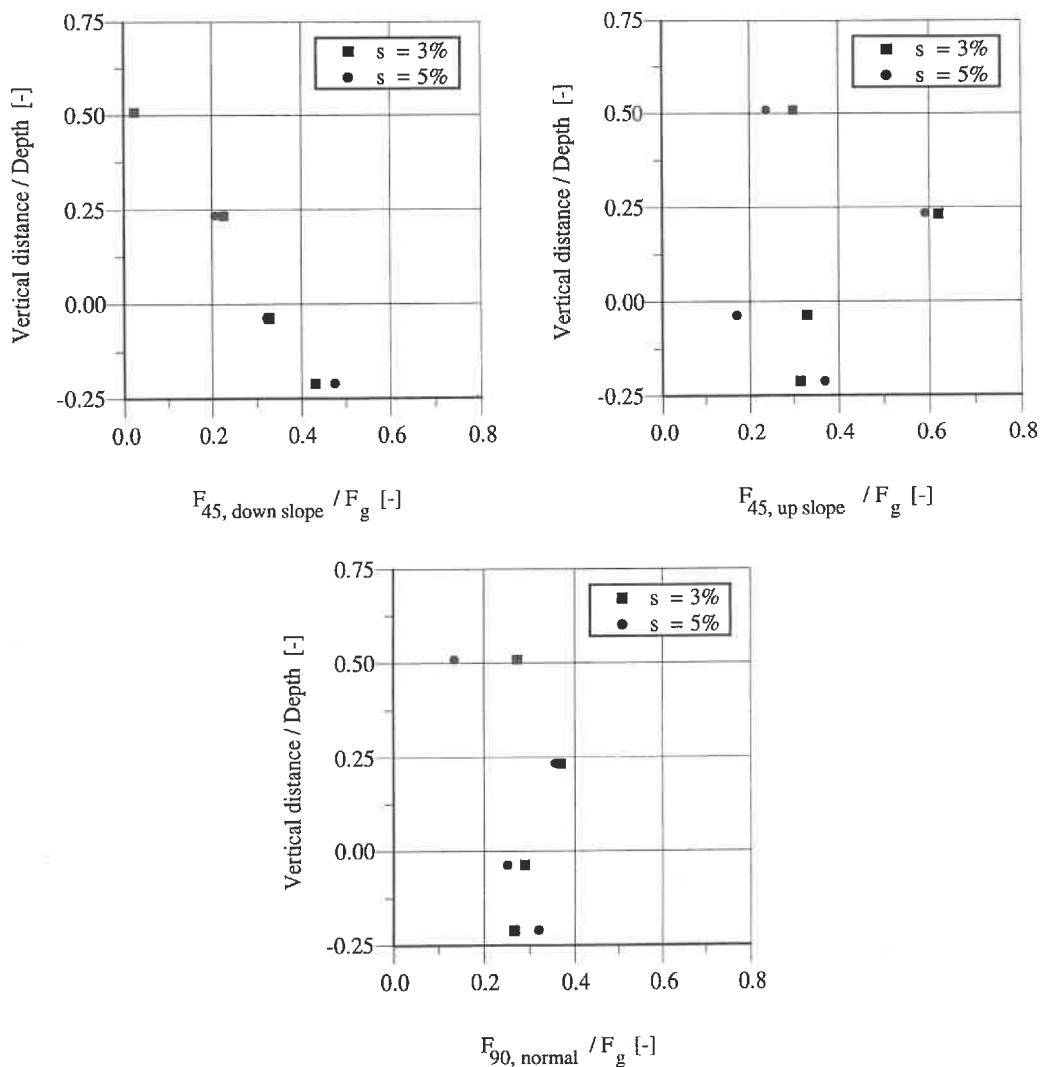


Figure 15: Vertical distribution of outward directed peak force $F_{\frac{1}{250}}$ based on irregular wave tests, $H_s = 13.5$ cm.

5. CONCLUSIONS

The stability of different types of single layer rubble mound breakwaters have been investigated in a scale model for two characteristic wave steepnesses. The scale model and the sea states correspond to typical Norwegian breakwaters in scale 1:30 to 1:40 and typical prevailing storm situations in the Norwegian Sea.

Different methods of placing the armour stones in the armour layer have been investigated, see Tab. 2 and the stability performance is presented in Tab. 3. The highest degree of stability is obtained by placing the stones orderly. This placement method doubles the stability in terms of the Hudson-type stability coefficient compared to the conventional random placement method in two layers. Placing the stones randomly in one layer a very low stability of one third to one fourth of the stability obtained by the conventional method is found. Generally, no influence of steepness was observed.

With respect to the wave induced forces on single armour stones the normal and the parallel force have been measured in 4 positions over the slope. Both tests with regular and irregular waves have been conducted with two wave steepnesses. Large destabilizing forces were identified both above and below SWL. The influence of wave period little as was the case for the stability tests whereas the influence of wave height was significant in some cases, especially in the positions above and below SWL.

ACKNOWLEDGEMENTS

The work is jointly supported by the Danish Technical Research Council under the frame programme Marin Teknik 2 and the Norwegian Coast Directorate.

REFERENCES

- Bratteland, E., Tørum, A., *Stability tests on a rubble mound breakwater head in regular and irregular waves. Sørvær fishing port, Norway*, In: Proc. from the 1st Int. Conf. on Port and Ocean Engineering under Arctic Conditions, Trondheim, Norway, 1971.
- CIRIA/CUR, *Manual on the use of rock in coastal and shoreline engineering*, Published jointly by the Construction Industry Research and Information Association in the UK and the Centre for Civil Engineering Research, Codes and Specifications in the Netherlands, 1991.
- Hald, T., Tørum, A., *Stability investigations of single layer rubble mound breakwaters* (in Danish), SINTEF NHL report STF22 A97252, 1997.
- Holm-Karlsen, T., Tørum, A., *Single layer quarry stone rubble mound breakwaters, The Norwegian practice and experience*, Abstract for 29th Int. Navigation Congress of PIANC, The Netherlands, 1998.
- Kjelstrup, Sv., *Berlevaag Harbour on the Norwegian Arctic Coast*, In: Proc. from the 4th Int. Conf. on Polar and Ocean Engineering under Arctic Conditions, Memorial University at St. Johns, New Foundland, 1977.
- Tørum, A., *Reliability of Norwegian breakwaters* (in Norwegian), SINTEF NHL report STF60 F93057, 1993.
- Tørum, A., Mathiesen, M., Vold, S., *Årviksand harbour, Wave penetration and breakwater stability* (in Norwegian), SINTEF NHL report STF60 F90057, 1990.

An Accropode Breakwater in Beirut

by

Mogens Hebsgaard, Danish Hydraulic Institute (DHI)

&

Peer F. Smed, Rambøll

Dansk Vandbygningsteknisk Selskabs seminar om
"Nyere metoder til projektering af moler"
Aalborg Universitet den 25 marts 1998

An Accropode[®] Breakwater in Beirut

M Hebsgaard¹, P F Smed²

1 Introduction

As part of its ongoing extension and rehabilitation, Port of Beirut intends to create an up-to-date container terminal and a new quay to accommodate container ships of 3rd and 4th generation.

In this process, RAMBØLL was selected as consultant by the Port of Beirut to carry out a detailed study where the following aspects were considered:

- optimisation of the layout of Quay 16 (600 m length, 15.5 m depth) and a new detached breakwater (600 m, -26 m depth)
- confirmation of the chosen layout by mathematical modelling of wave penetration
- computer simulation of ship manoeuvring (performed by Danish Maritime Institute as subcontractor)
- model tests of wave disturbance and breakwater stability (performed by Danish Hydraulic Institute as subcontractor)
- preliminary and detailed design of Quay 16 and the detached breakwater
- assessment of sedimentation risks
- requirements for dredging
- preparation of tender documents in accordance with the FIDIC conditions
- assistance to bid evaluation

On basis of the preliminary design and later decisions, detailed design was carried out for:

- a layout of a 600 m long Quay 16 allowing a 280 m length for Quay 15, of which 30 m should be designed as Quay 16 and included in the tender package
- a steel sheet pile quay structure
- a breakwater cross-section with Accropodes[®], and this cross-section has been tested in model tests in laboratory at Danish Hydraulic Institute

¹ Danish Hydraulic Institute, Agern Allé 5, DK-2970 Hørsholm, Denmark – Tel: +45 45 179 100, Fax: +45 45 179 200

² Rambøll Consulting engineers, Olof Palmes Allé 22, DK-8200 Århus N, Denmark – Tel: +45 89 44 77 00, Fax: +45 89 44 76 25

Total construction costs of the Quay 16 and the detached breakwater was estimated to approximately 50 mill \$.

Engineering works for an extension of approximately 300 m of the existing breakwater and construction of Quay 15 is going on today. These works are scheduled to be finished at the end of 1998.

Quay 16 and the detached breakwater are scheduled to be built in two phases, in which Phase I covers the 600 m quay length and the 600 m breakwater length. The engineering works for these constructions is scheduled to be finished at the beginning of 2000.

Fig 1.1 shows the position of Port of Beirut and Fig 1.2 shows the existing port layout and the extended port layout.

2 Natural Design Conditions

2.1 Bathymetry

Water depths at the site of the detached breakwater are in the range of 20-25 m.

2.2 Hydrographic Conditions

Wave Conditions

Significant wave heights, H_s , according to probable storm return periods to be applied for the design of the detached breakwater are given in Table 2.1.

Table 2.1 H_s versus return period for wave direction interval $N335^\circ-N15^\circ$ (to be applied for the design of the detached breakwater)

Return period, R	H_s (m)
5 years	4.8
20 years	5.8
50 years	6.5
100 years	7.0

The maximum values for the peak period, T_p , probably are as follows:

- $T_p = 15.5$ s for $R = 10$ years
- $T_p = 16.5$ s for $R = 50$ years
- $T_p = 17$ s for $R = 100$ years

Lower peak period values may be taken into consideration, particularly for the N sector where $9 \text{ sec} < T_p < 14 \text{ sec}$ may be considered.

Water Levels

The tides in Beirut are of the semi-diurnal type. This means that there are two low waters and two high waters per day with a total range of:

- 0.20m during neap tides
- 0.40m during spring tides

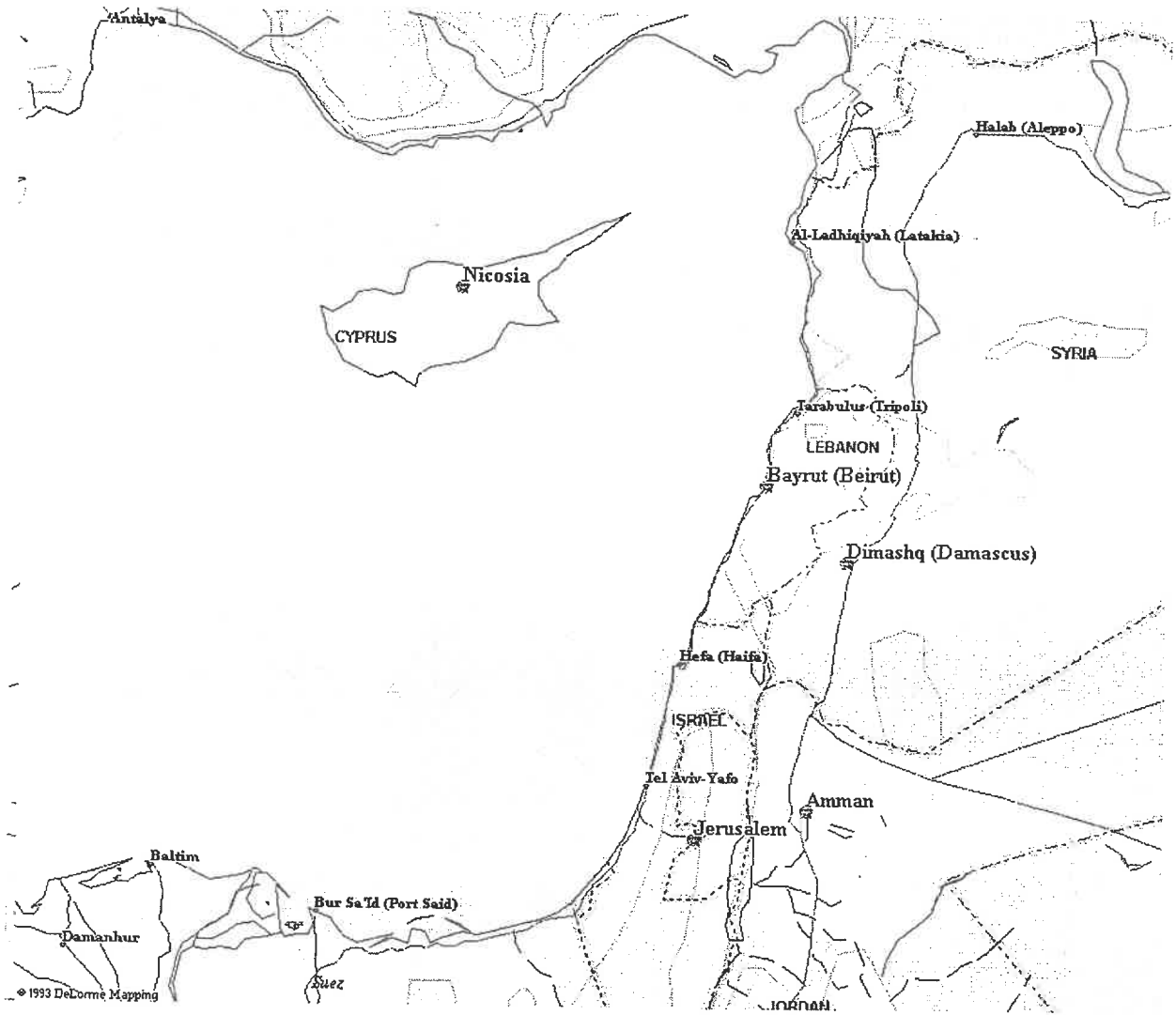


Fig 1.1
Position and
plan of Port
of Beirut.

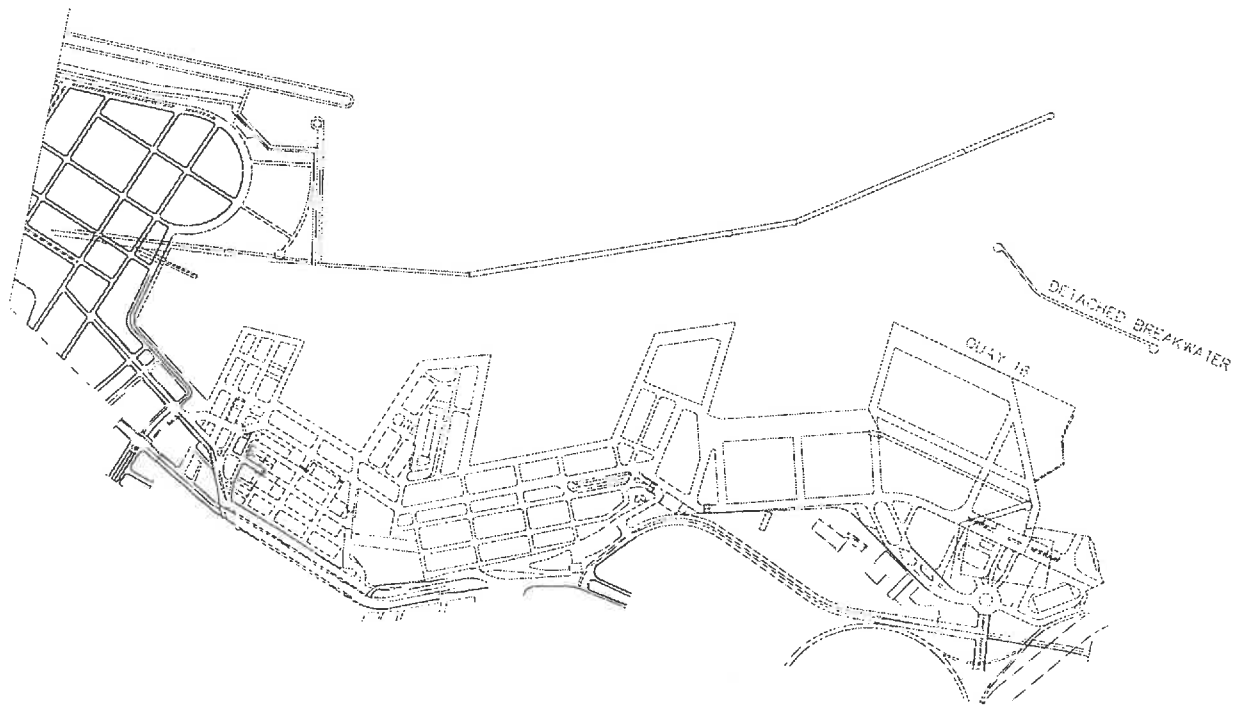
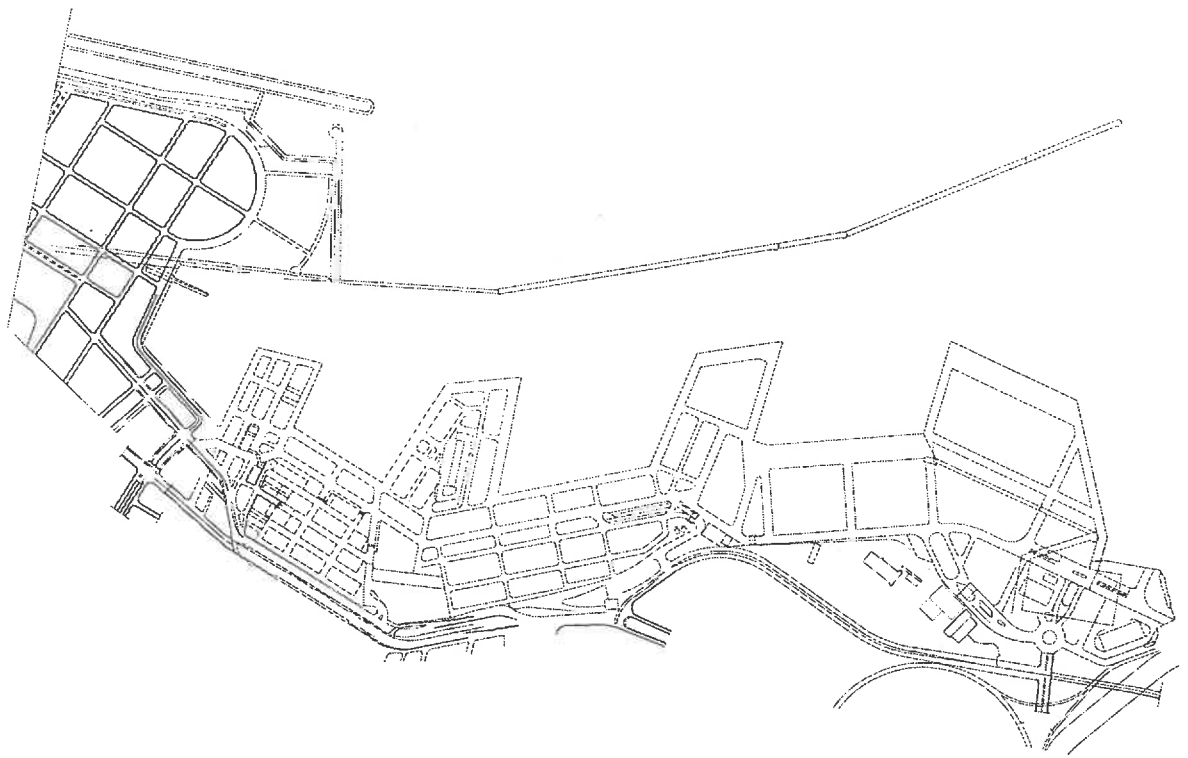


Fig 1.2 Above: Existing port layout. Below: Extended port layout

The mean sea level (MSL) coincides with the vertical datum NGL (Nivellement Général du Liban, used for onshore and non-maritime charts). Hence, the lowest astronomic tide level (LAT) is -0.40 m NGL.

The extreme sea levels resulting from the combined effects of the astronomical tide, winds and atmospheric pressure are -0.45 m and +0.85 m relative to MSL.

2.3 Soil Conditions

For the detached breakwater, results of few borings are available. Some are located about 150 m from the centreline of the proposed detached breakwater and indicate 5-8 m very soft silty clay overlaying up to 4 m medium dense to dense sand and finally rock. Other borings indicate 1.5-4 m soft clay, silty sand or sandy clay, overlaying medium to dense silty sand. The very soft clay has a very low bearing capacity and will have to be exchanged with sand.

3 Breakwater Design

3.1 Introduction

Initially, an evaluation of type of detached breakwater was performed. Either a conventional multi-layer rubble mound breakwater or a caisson-based breakwater was examined. Several aspects were considered, among others topics like economy, construction design, related engineering works, wave disturbance. Based on the evaluation, it was decided to consider a conventional rubble mound breakwater for future investigations.

Accropodes[®] were at an early stage in the design process selected for the armour layer. This selection was based on economical considerations taking into account the following items:

- only one layer of Accropodes[®] is required
- a large slope of 1:1.33 can be applied, useful at large water depths
- a large KD factor (=15) can be used in Hudson stability formula, useful to minimise weight requirements
- the on-going extension of the existing breakwater was performed by use of Accropodes[®], hence tradition was maintained and acceptance from the Port of Beirut was easily obtained

3.2 General Information on the Accropode[®] Technique

The French consulting company, Sogréah, has developed and perfected a system of artificial block armouring used to protect river and maritime structures against waves and currents, as well as a special process to manufacture the armouring blocks using moulds.

This protective system and the manufacturing process are protected in France by patent No 79-03774, issued on 14 June 1982.

The commercial name for the artificial armouring blocks is 'Accropode[®]', a distinctive trademark, which was registered internationally under No 446 953 on 5 March 1979.

The Port of Beirut has directly from Sogréah obtained the right to use the Accropode[®] technique for this particular project.

3.3 Breakwater Layout Proposed by RAMBØLL

Based on generally accepted formulas (Hudson, etc), recommendations from Sogréah and notices of the existing breakwater design, RAMBØLL made a design for the detached breakwater. Following aspects were considered:

- a design wave height, $H_{s,50}=6.5$ m, with a direction of NNW to NNE
- an average water depth of 22.5 m
- the detached breakwater will be less exposed to waves less than the existing breakwater
- maximum application of the exchange of the very soft clay with sand below the breakwater
- no roads or footpath on top of the breakwater
- for design conditions, relatively high overtopping and wave agitation behind the breakwater can be accepted

Fig 3.1 shows the proposed breakwater trunk section. This section was tested at Danish Hydraulic Institute.

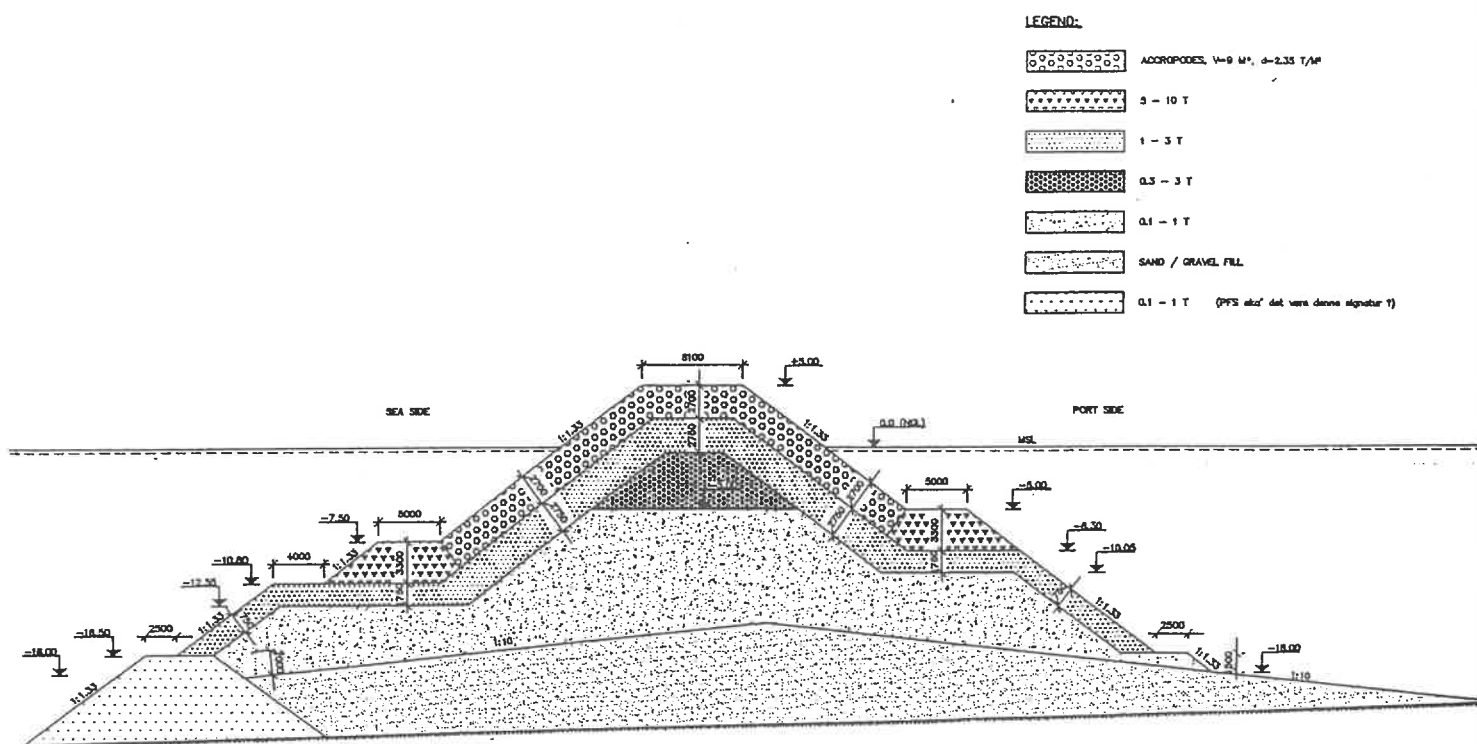


Fig 3.1 Proposed breakwater trunk section

4 Beirut, Hydraulic Model Tests

4.1 Introduction

Hydraulic model tests to determine the stability of the new detached breakwater were carried out at the Danish Hydraulic Institute.

The tests comprised both 2D (wave flume) and 3D (wave basin) tests.

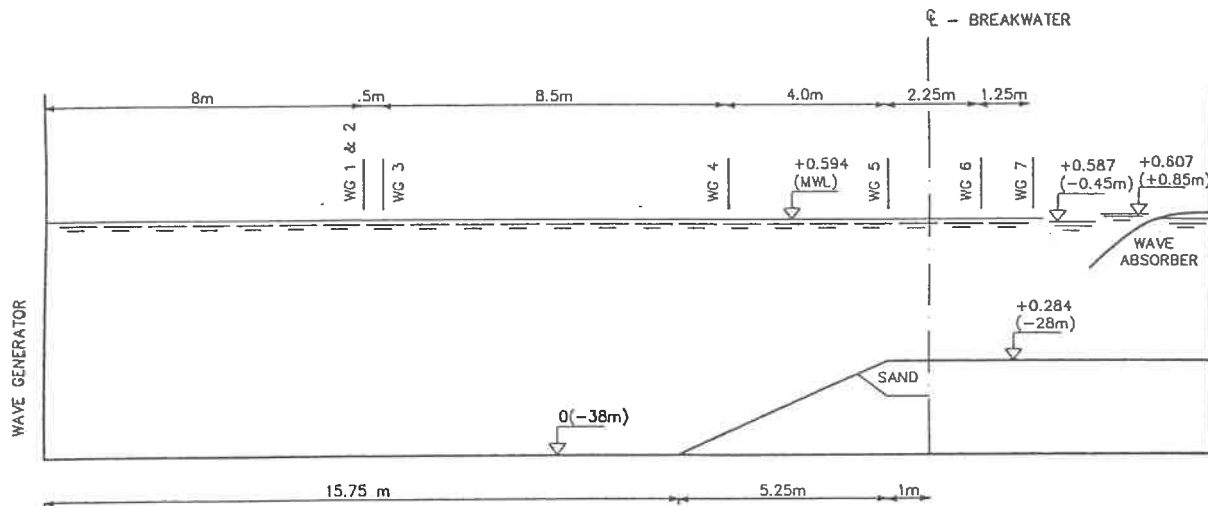
4.2 2D Stability Model Tests (Flume Tests)

The model tests were carried out with a trunk section of the breakwater. In addition to the stability tests, the model was also used for measurements of wave overtopping.

Model Set-up

The 2D physical model was constructed at a length scale of 1:64 in a 0.6 m wide flume. The seabed was constructed as a fixed bed. The breakwater profile was constructed on a layer of fine sand in order to obtain a qualitative impression on the interaction between the toe protection and the seabed. The longitudinal section of the flume is shown in Fig 4.1.

The rock material and artificial model blocks were reproduced in the model according to Froude's model law.



NOTE:
 WG 1 < POSITION OF WAVE GAUGE 1
 THE DISTANCE BETWEEN WAVE GAUGE 1 AND 2 IS 5cm
 ALL MEASURES IS IN THE MODEL VALUES IN () REFER TO PROTOTYPE

Fig 4.1 Model set-up, wave flume

Test Procedures

Measurements and Observations

The following measurements and observations were made:

Wave measurements

The incoming wave conditions were measured at wave gauges positioned in front of the wave generators in deep water. The incoming and reflected wave conditions were separated.

Breakwater stability

The damage and movements of blocks and rocks in the armour layer (seaside, rear side and crest), the berm layer, the toe protection, etc, were registered visually during and after each test run.

Measurement of overtopping

The overtopping amount was measured by means of a tray placed behind the breakwater section. Furthermore, the wave conditions behind the breakwater were measured at two locations.

Test Programme

Stability tests

The stability tests were carried out in two test series. The first test series comprised nine individual tests, each with duration of five hours in nature. The tests were carried out with wave conditions ranging from return periods of one year to 50 years. Furthermore, tests with wave heights up to 20 per cent higher than design were carried out to investigate the reserve stability of the structure. The second test series were carried out with a profile which was adjusted on basis of the results from the first test series. This test series included eight tests.

The investigated profiles are shown in Fig 4.2. During the stability tests, the wave conditions behind the breakwater were measured.

Generally, the test series were carried out with mean water level, but the tests series also included tests with high and low water level.

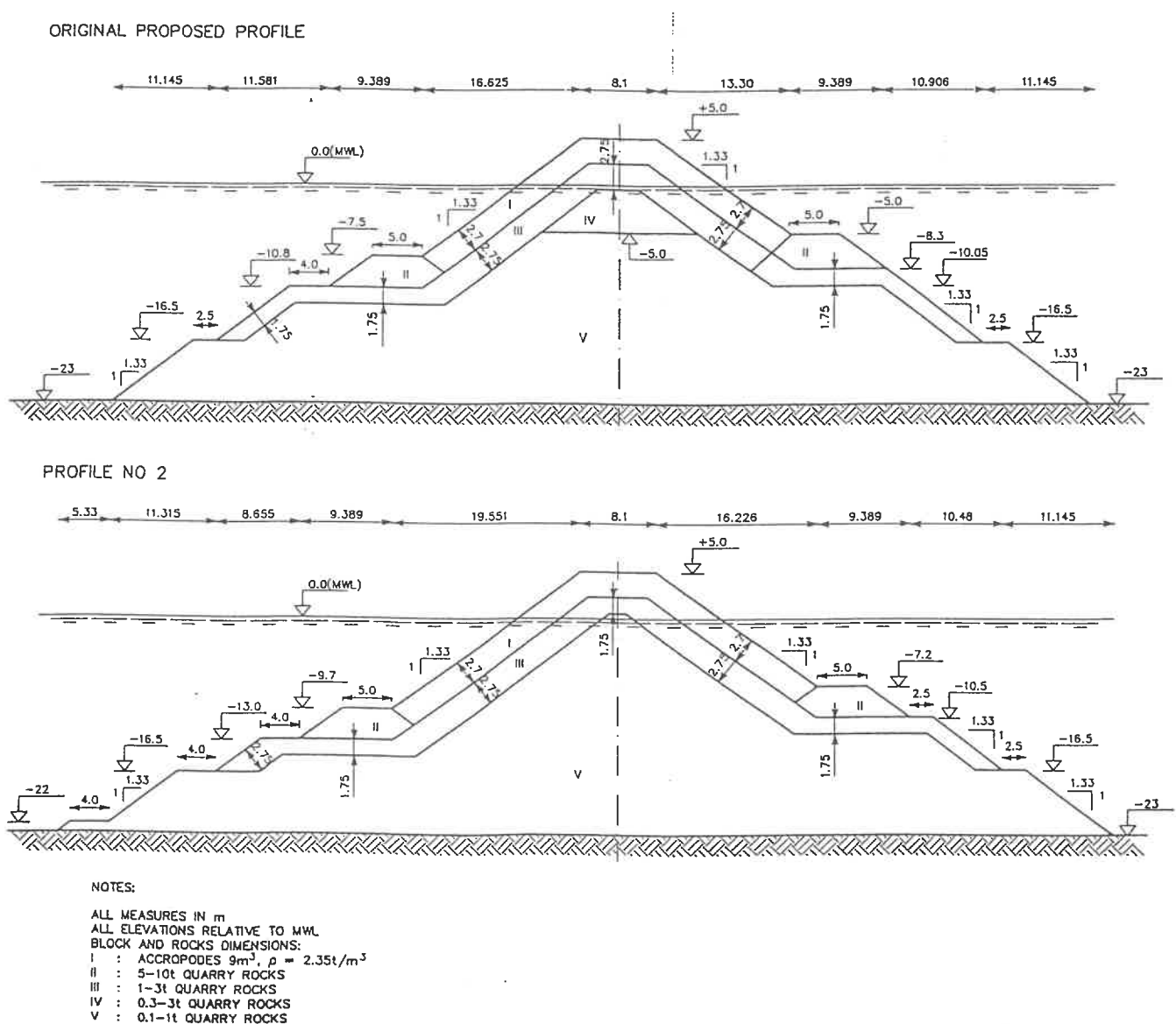


Fig 4.2 Profiles investigated in the flume tests

Overtopping tests

Each overtopping test had duration corresponding to one hour in nature.

Test Results, Stability Tests

Stability Tests - Test Series 1

The tests with the proposed profiles showed that the stability of the individual elements of the breakwater was:

Main armour layer

The main armour layer of Accropode[®] units of 9 m³ covered the seaside from the berm level, the crest and the harbour side down to level -5 m.

During the test series, the blocks in the upper layer at the sea and harbour side settled, meaning that the porosity of the layer was reduced. This caused the porosity of the layer at the crest to increase. Apart from the movements the blocks experienced due to the settlements, the blocks were generally stable up to the design wave conditions. One unit was damaged (displaced out of the layer) during the test with wave height 12 per cent higher than design, and the entire seaside Accropode[®] layer failed during the test with wave height 20 per cent higher than design.

Seaside berm and toe protection

The berm suffered major damage during the test series. About 100 rocks in the berm were damaged, ie displaced more than one rock dimension, after the test with the design wave height. Most of the rocks were displaced out of the layer, either upwards or downwards. These damages were so severe that at the end of the test series, the upper layer of the berm was eroded, and it is estimated that this was the main reason for the failure of the Accropode[®] layer.

Large relocations of the lower parts of the profile took place during the tests. The layer of filter material at the lower berm was penetrated leaving the core material directly exposed. The lower part of the profile was smoothed out resulting in a slope of approximately 1:2.2 from the Accropode[®] layer down to the seabed (see Fig 4.3).

Berm, harbour side

Relatively large damage took place to the rear side berm. After the tests with the design wave conditions, approximately 50 rocks were displaced out of the berm, and 25 per cent of the upper layer rocks were damaged.

Conclusions – Stability Tests - Test series 1

The overall conclusion, which could be drawn on basis of the test series, was that the Accropodes[®] were sufficiently stable, but too large damage took place at the seaside and rear side berm. Generally, the lower part of the seaside of the profile suffered too large damage.

Stability Tests, Test Series 2

Before test series 2, the following adjustments were made to the originally proposed profile:

- the seaside berms were lowered by 2.2 m
- the thickness of the filter layer in the lower berm was increased
- the rear side berm was lowered by 2.2 m

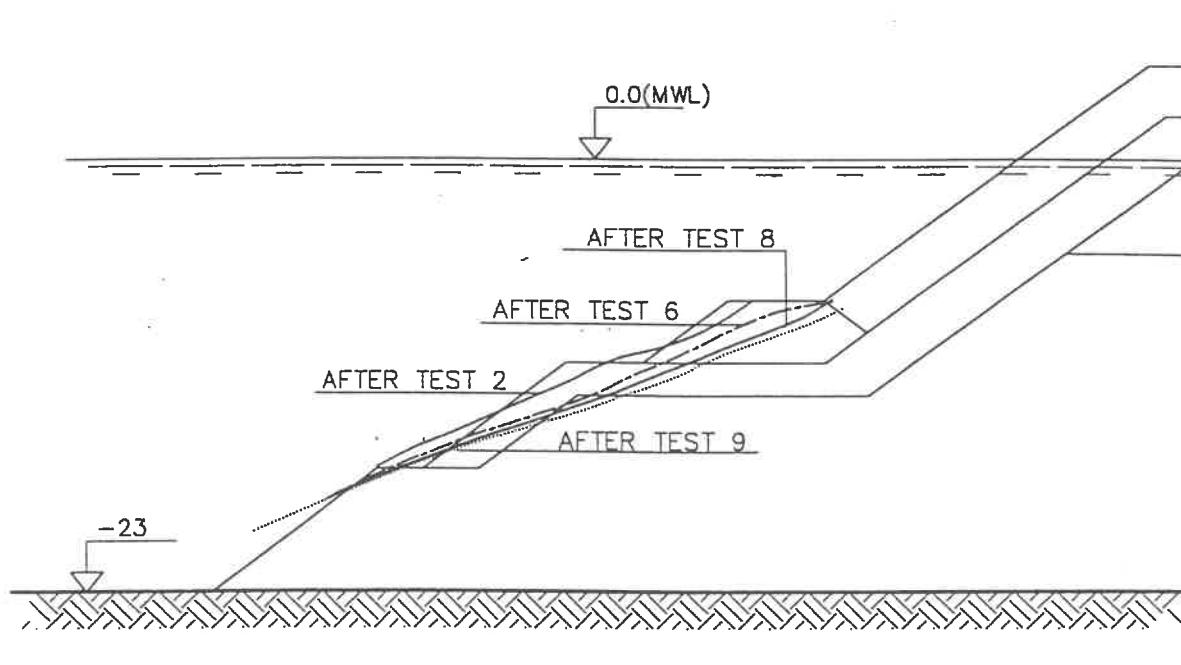


Fig 4.3 Development of the lower part of the profile during the test series.

The results of the tests in this series are described in the following.

Main armour

The settlements of the block layer at the seaside and at the rear side seen in test series 1 were also seen in test series 2. However, no damage took place to the seaside armour layer until the test with design wave height and high water level where one unit was displaced to the seabed. During the tests with larger wave heights than the design conditions, at least five units were rocking, but no further damage took place.

Seaside berm and toe protection

The lowering of the seaside berm resulted in an increase of the stability of this part of the structure. However, as it was seen in the first test series, the lower part of the profile was smoothed out during the tests. After the test series, the berm width was reduced to 2-3 m, a relative large number of berm and filter rocks were displaced to the Accropode[®] layer, and a large number of berm rocks were displaced to the lower parts of the profile. From the berm level to the seabed, a slope of approximately 1:2.3 was developed through the tests.

Berm, harbour side

The berm of 5-10 t rocks on the harbour side was smoothed out during the tests. Approximately 25 rocks were damaged during the test series, but the rocks were only displaced to the lower berm and will thus still participate to stabilise the structure.

Conclusions – Stability Tests - Tests series 2

The stability of the Accropode[®] layer was adequate. The lower part of the seaside profile proved to give a sufficient basis for the Accropodes[®]. However, it should be noted that the width of the berm was reduced significantly and that a relatively large number of rocks were displaced to the Accropode[®] layer.

The stability of the rear side was acceptable.

Recommendations

As a result of both test series 1 and 2, the following recommendations on the profile with regard to stability are made:

- the Accropode[®] unit size (9 m³) is adequate
- the width of the seaside berm is recommended increased to minimum 7.5 m
- the rock size in the seaside berm with the top at level -9.7 m is recommended increased to 8-12 t. Alternatively, a further lowering of the 5-10 t berm in the order of 1 m is recommended. This will limit the number of rocks being displaced to the armour layer
- the rear side is recommended unchanged (relative to test series 2)

Test Results - Overtopping Tests

Overtopping amounts were measured for wave conditions ranging from $H_s=3$ m to $H_s=6.5$ m. This means that a $H_s/\Delta h$ ratio ranging from 0.6 to 1.3 was investigated. Δh is the vertical distance from still water level to crest level.

The results showed overtopping intensities from 2×10^{-6} m³/m/s ($H_s/\Delta h=0.6$) to 0.3 m³/m/s. As no installation will be present behind the breakwater, no criterion for maximum overtopping has been defined, however.

Wave conditions behind the breakwater

During all stability tests, the wave heights were measured behind the breakwater at distances of 80 and 160 m behind the crest. The results showed the following relation between the maximum wave height behind the breakwater and the incoming wave height (results from test series 1 and 2):

Table 4.1 Maximum wave height behind the breakwater as function of the incoming wave conditions, $WL=\pm 0.0$ m.

Incoming wave conditions [H_s (cm); T_p (s)]	Maximum wave height (m)	
	80 m behind the crest	160 m behind the crest
[3.0; 15.5]	1.0	0.10
[4.9; 15.5]	2.6-2.8	1.9-2.1
[6.15; 16]	3.7-4.3	3.4-3.5
[6.5; 16.5]	4.3-4.7	3.9-4.4
[6.5; 13.5]	3.5-4.3	3.7-4.0

This means that wave conditions with incoming wave heights up to $H_s \sim 3$ m will not disturb significantly the wave conditions at the berth due to overtopping, while incoming waves with $H_s=4.9$ m or higher may cause a significant disturbance at the berth.

Table 4.1 shows the maximum wave height of the individual wave created by overtopping.

4.3 3D Stability Model Tests (Basin Tests)

The model tests were carried out with the eastern head of the Detached Breakwater. Furthermore, a short section of the adjacent trunk was constructed in order to describe the stability conditions for the transition area.

Model Set-up

The 3D physical model was constructed at a length scale of 1:63 in a 30 m by 30 m wave basin. The seabed was constructed as a fixed bed.

Test Procedures

Measurements and Observations

The following measurements and observations were made:

Wave measurements

The wave conditions were measured by six wave gauges positioned in the area off the breakwater.

The wave period referred to is the peak wave period, T_p , of the incoming waves.

Breakwater stability

The damage and movements of blocks in the armour layer and rocks in the berm layer and the toe protection were registered during and after each test run.

Test Programme

The stability tests were carried out in five test series containing one or more tests. The investigated profiles are shown in Figs 4.4 and 4.5. Each test had duration of five hours in nature. The tests were carried out with wave conditions ranging from return periods of one year to 50 years.

Generally, the test series were carried out with mean water level, but the test series also included tests with high water level.

Test Results

Test Series 4, Proposed Profile (Fig 4.4)

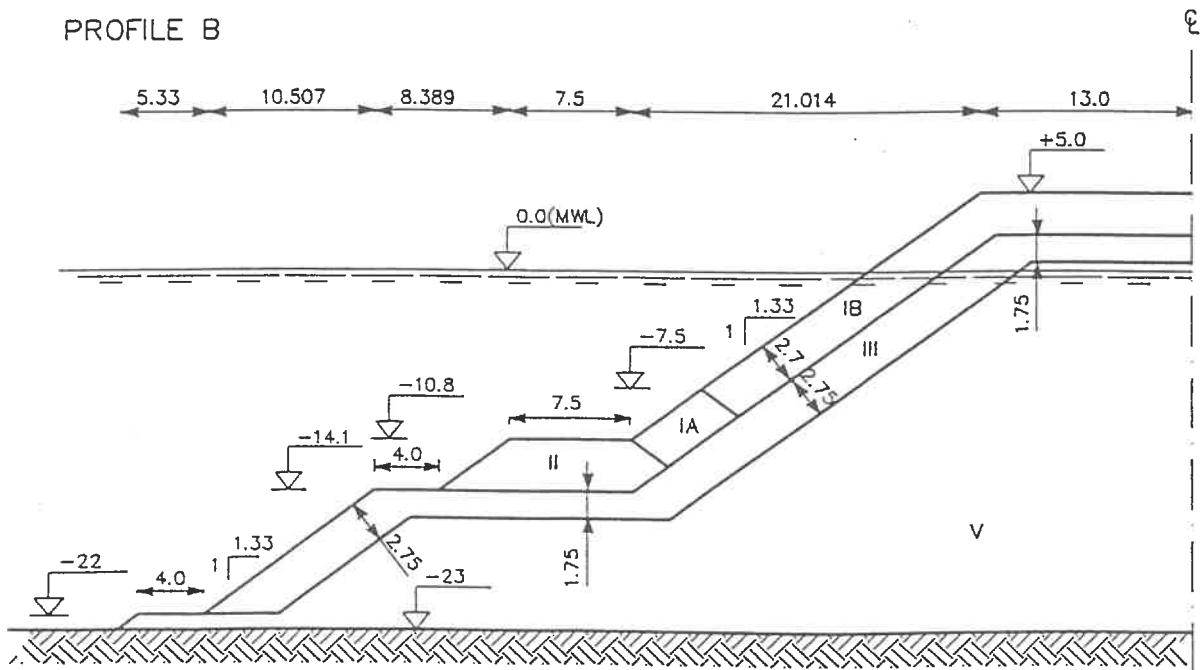
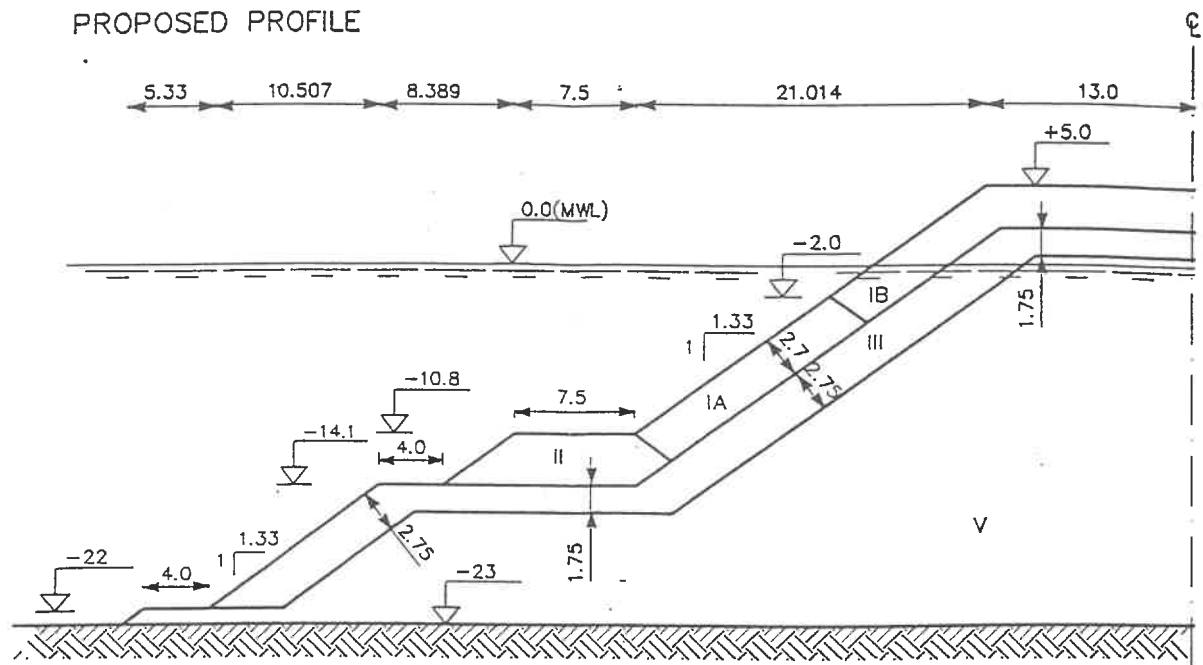
The test series was carried out with a structure where 9 m³ blocks were used as armour. From the seaside berm level (-10.8 m relative to MWL) and up to a level of -2 m, a block density of 2.35 t/m³ was used, and from -2 m to the crest, a block density of 2.55 t/m³ was used. The crest level was at +5 m.

The test series contained one test, which was stopped after four hours due to very large damage to the breakwater head. The test conditions related to an average return period of five years.

Test Series 5, Profile B (Fig 4.4)

Test series 5 was carried out principally with the same profile as the previous test series 4, but the transition zone between the high and normal density units was lowered from -2.0 m to -7.5 m.

This test series was initiated with a low wave height in order to ensure that initial settling in the layer took place gently. During the next test with $H_s=4.7$ m, minor displacements took place at the berm, but no Accropodes[®] were displaced. However, settlements took place in the layer as a pre-warning of the damage which took place just a few minutes into the subsequent test with $H_s=6.0$ m. The stability of the structure was thus not acceptable.



NOTES:

- ALL MEASURES IN m
 ALL ELEVATIONS RELATIVE TO MWL
 BLOCK AND ROCKS DIMENSIONS:
 IA : ACCROPODES 9m^3 , $\rho = 2.35\text{t/m}^3$
 IB : ACCROPODES 9m^3 , $\rho = 2.55\text{t/m}^3$
 II : 5-10t QUARRY ROCKS
 III : 1-3t QUARRY ROCKS
 V : 0.1-1t QUARRY ROCKS

Fig 4.4 Profiles investigated in the basin tests (proposed profile and profile B)

Test Series 6, Profile C (Fig 4.5)

The profile investigated in this test series was identical to the one tested in test series 5, but with a crest elevation of +7.2 m relative to MWL. The crest level was raised as it was estimated that the overtopping contributed to the damage development.

The test series contained the same tests as series 5. During the test with $H_s=6$ m, serious damage took place to the Accropode[®] layer. The damage developed, however, due to the high crest elevation much more slowly than in test series 5.

Test Series 7, Profile D (Fig 4.5)

As a consequence of the large damage taking place during test series 4-6, the size of the Accropodes[®] was increased to 16 m^3 with normal density (2.35 t/m^3). The crest level was increased to +7.5 m.

The test series contained 12 tests with wave directions N, NNW and NNE. No repair work to the breakwater head was made during the test series.

The tests were carried out with wave heights of 4 m to 6.6 m, where $H_s=6.6$ m represents the design wave height.

The tests showed that minor settlements and movements in the armour layer took place for wave heights up to $H_s \cong 6$ m. During the tests with a significant wave height of 6.6 m, larger settlements and relocations took place in the layer, though without damaging the breakwater during the first hours of testing. However, it was observed that this wave height caused serious fractures in the layer at a sector of the breakwater head. This means that the structure contains a very limited residual stability.

The damage to the berm was generally very limited, except at a position determined by the wave direction. The damage area is located at $160\text{-}170^\circ$ (see Fig 4.6). The damage, however, was considered acceptable, as the support of the Accropodes[®] was unaffected.

Test Series 8, Profile D (Fig 4.5)

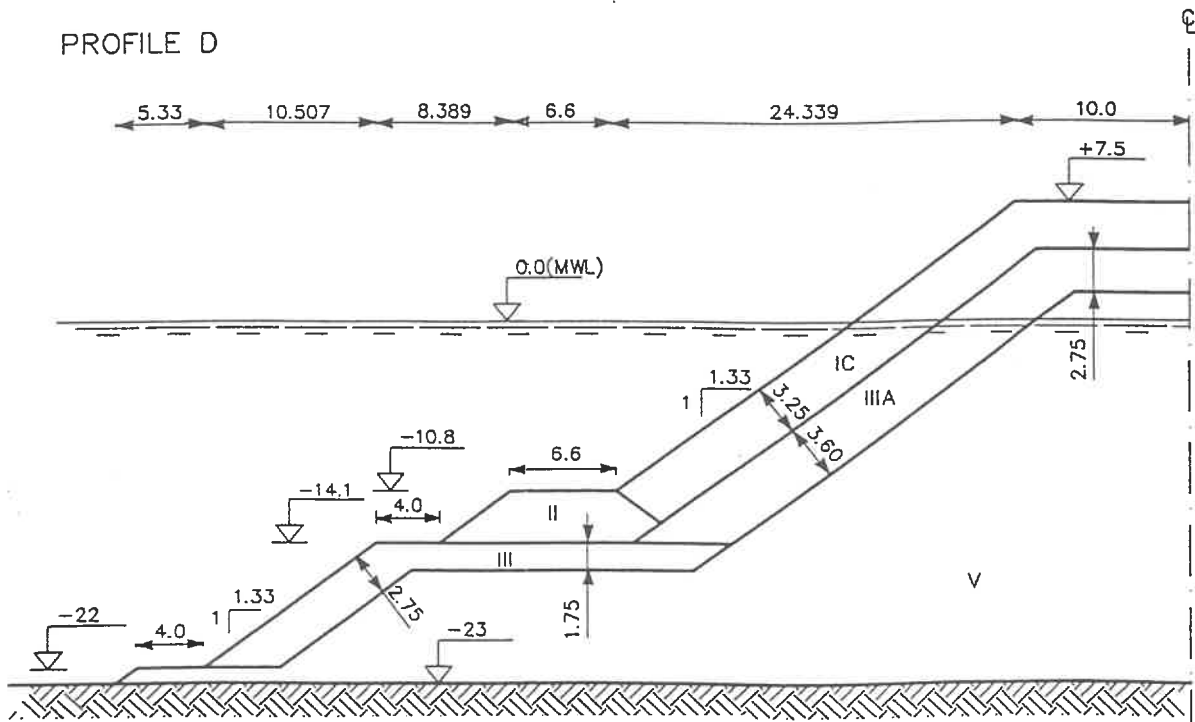
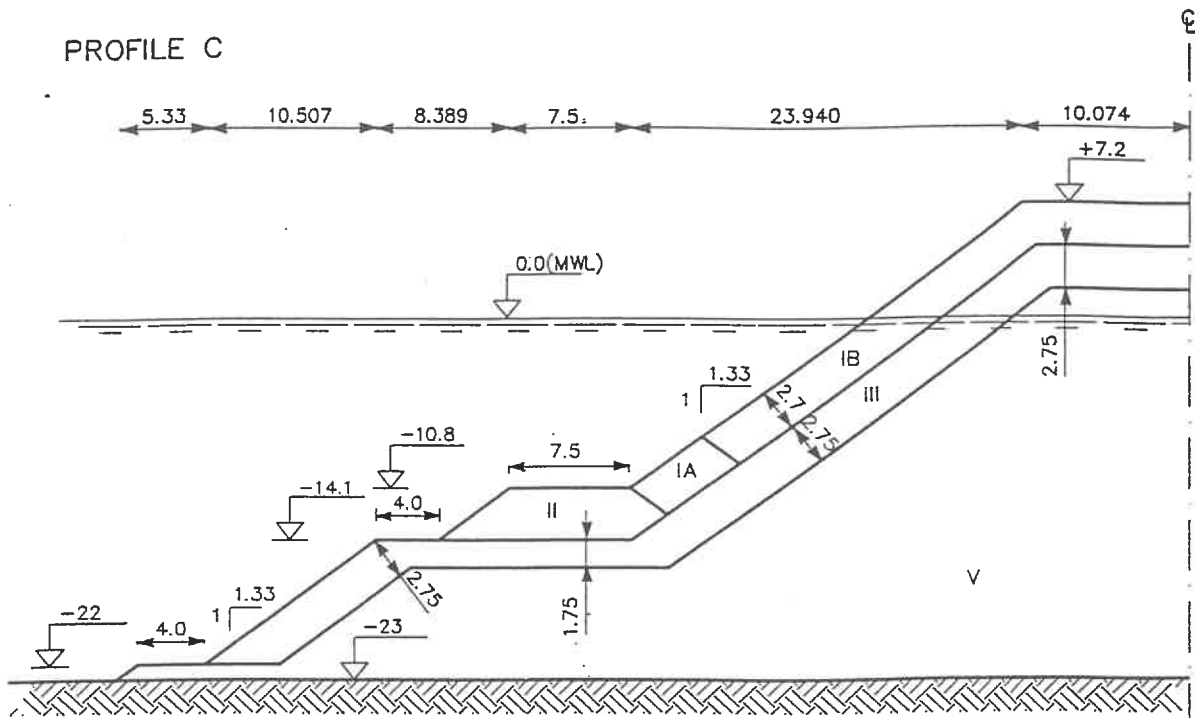
As a consequence of the limited residual stability of the structure concluded from the results of the previous test series, it was decided to carry out a test series with reduced (and more realistic) wave periods. This was done to investigate whether a larger safety margin against serious damage to the roundhead could be documented.

The test series was carried out with wave direction N. The results of the tests showed that the structure was able to withstand two five-hour tests with wave condition corresponding to the design conditions. However, settlements and small displacements took place within the layer. These settlements were so large that an additional design storm will most likely cause large damage. The conclusions of this test series were thus similar to test series 7.

Conclusions

The following conclusions can be drawn from the 3D model tests:

- None of the 16 m^3 Accropodes[®] with normal density (2.35 t/m^3) were displaced more than one block dimension during two five-hour tests with the design wave heights. Settlements and small relocations in the layer weakened, however, this structure in a way that large and unacceptable damage took place during a subsequent test with the design or larger wave height. In view of the difficulties which are envisaged to be associated with a proper reconstruction of a damaged breakwater head, it is concluded that the residual stability of the breakwater head will not be sufficient.



NOTES:

- ALL MEASURES IN m
 ALL ELEVATIONS RELATIVE TO MWL
 BLOCK AND ROCKS DIMENSIONS:
- IA : ACCROPODES 9m^3 , $\rho = 2.35\text{t/m}^3$
 - IB : ACCROPODES 9m^3 , $\rho = 2.55\text{t/m}^3$
 - IC : ACCROPODES 16m^3 , $\rho = 2.35\text{t/m}^3$
 - II : 5-10t QUARRY ROCKS
 - III : 1-3t QUARRY ROCKS
 - IIIA : 2-5t QUARRY ROCKS
 - V : 0.1-1t QUARRY ROCKS

Fig 4.5 Profiles investigated in the basin tests (profiles C and D)

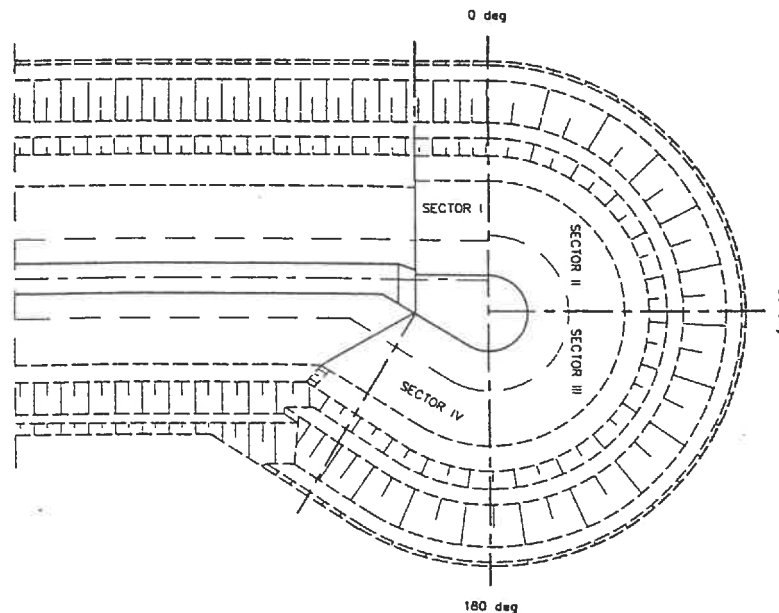


Fig 4.6 Definitions of sectors at the breakwater head

- The tests carried out with the seriously damaged structure showed that the damaged structure most likely will be able to resist a storm with wave heights up to about 6 m without being totally destroyed.
- Based on the tests both with the undamaged and the damaged structure, it is estimated that a significant wave height slightly less than the design wave height is the wave height for which the settlements in the armour layer become so large that a subsequent impact by a wave height close to or higher than the design wave height will cause serious damage. These conclusions are based on the results of test series 7 and 8.
- The berm was sufficiently stable at the roundhead with only minor damage, except at one position which is determined by the wave direction. The damage was concentrated at 160-170°.

Recommendations

Based on the test results, it was estimated that sufficient stability conditions can be achieved using 16 m³ Accropodes[®] by increasing their density from 2.35 t/m³ to 2.55 t/m³. Hence, 16 m³ Accropodes[®] with a density of 2.55 t/m³ or more were recommended for the breakwater roundhead in the sector 70-180°. This sector was recommended considering the possible wave direction interval in which the waves may reach the structure without reduction due to diffraction around the existing main breakwater head. The direction interval considered is 340-15°N. On other sectors, Accropodes[®] of 16 m³ with a density of 2.35 t/m³ are recommended.

4.4 Additional Tests, 3D Tests

After the test series described above, three additional test series were carried out in order to determine whether a dense packing as described by Sogréah would improve the stability conditions. According to Sogréah, the packing may be performed in two ways, as described in Fig 4.7 below.

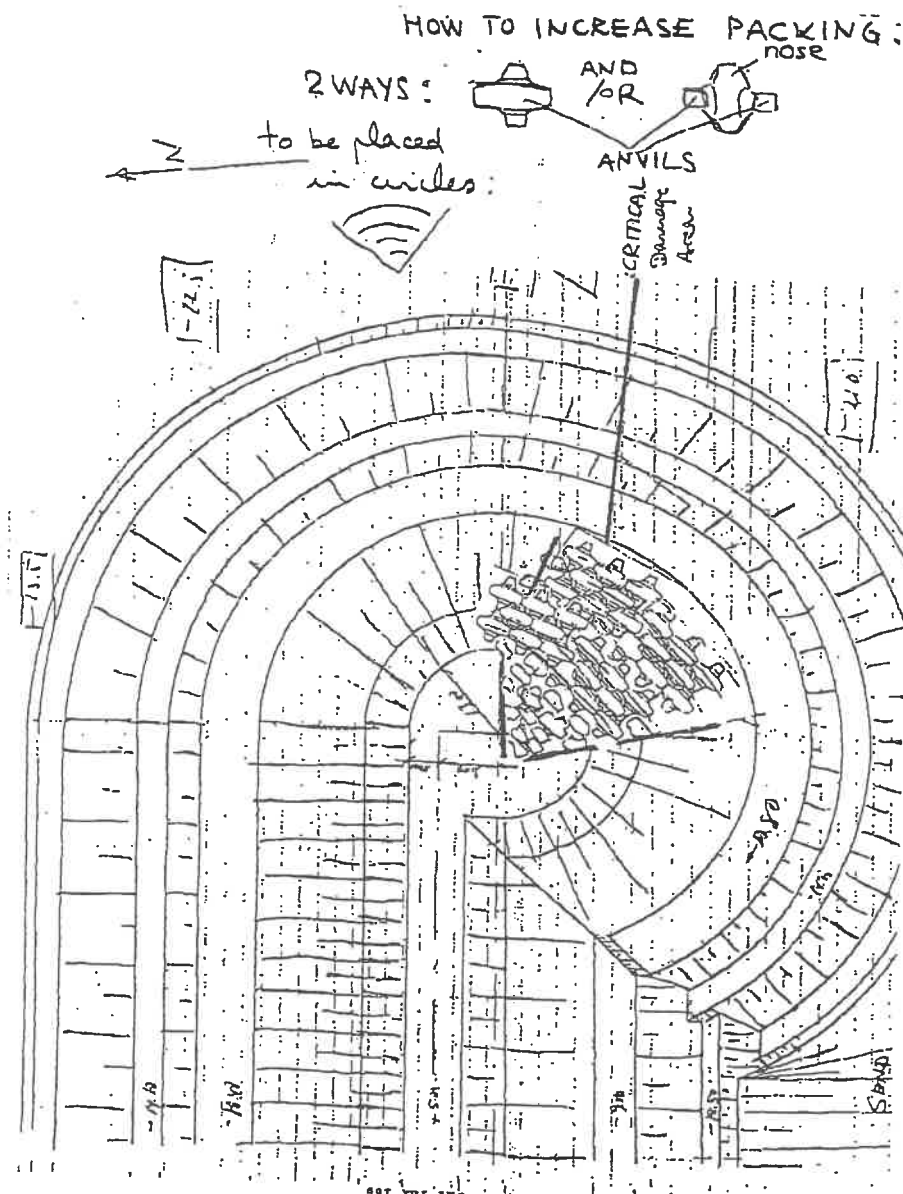


Fig 4.7 Sketch showing increased packing density

Both methods were investigated and the tests showed that the increasing packing gave much better stability of the layer at the critical sectors of the breakwater head.



Danish Hydraulic Institute

Berm Breakwaters

Dansk Vandbygningsteknisk Selskabs seminar om
"Nyere metoder til projektering af moler"
Aalborg Universitet d. 25 marts 1998

BERM BREAKWATERS

*Peter Sloth*¹

Abstract

This note on Berm Breakwaters is prepared in connection with the seminar on breakwaters held by the Danish Society of Hydraulic Engineering at Aalborg University on 25 March 1998. The basis for the note is mainly Juhl and Jensen (1995) and the Final Report from the MAST II research project on Berm Breakwaters (1997).

The note describes the features of berm breakwaters including advantages and drawbacks in comparison to traditional rubble mound structures. A review of selected practical experience with eight berm breakwaters is described in terms of typical cross-sections and key parameters.

Finally, a description of the most recent research on berm breakwaters is given.

Introduction

Berm Breakwater

In principle, two different types of rubble mound breakwaters exist, ie conventional rubble mound breakwaters with or without a crown wall and berm breakwaters. The main armour layer of a conventional rubble mound breakwater is designed for limited damage (statically stable), whereas for a berm breakwater the berm reshapes into a flatter and more stable profile. The more stable reshaped profile of a berm breakwater is the basic idea of the S-shaped breakwater, which initially is built with a flatter statically stable slope around still water level. In **Figure 1**, typical cross-sections of the three mentioned types of rubble mound breakwaters are shown. Further, a number of hybrids of conventional and berm breakwaters exist, eg conventional rubble mound breakwaters with a small berm or increased armour layer thickness.

Berm breakwaters have unconsciously been known since the middle of the nineteenth century, but increasing attention has been paid to this type of breakwater during the last 10 to 15 years. Many of the early breakwater structures were constructed by simply dumping quarried stones, which were available at the site, into the sea. Material was placed until a stable breakwater profile was reached, and after severe damage repair was carried out by simply adding more stone material.

¹ *Danish Hydraulic Institute, Agern Allé 5, DK-2970 Hørsholm, Denmark – Tel: +45 45 179 100, Fax: +45 45 179 200*

In literature, various synonyms have been used for a berm breakwater, ie dynamically stable breakwater, unconventional breakwater, reshaping breakwater, naturally armouring breakwater and mass armoured breakwater. However, it is important to distinguish between berm breakwaters, which reshape into a statically stable profile or dynamically stable profile.

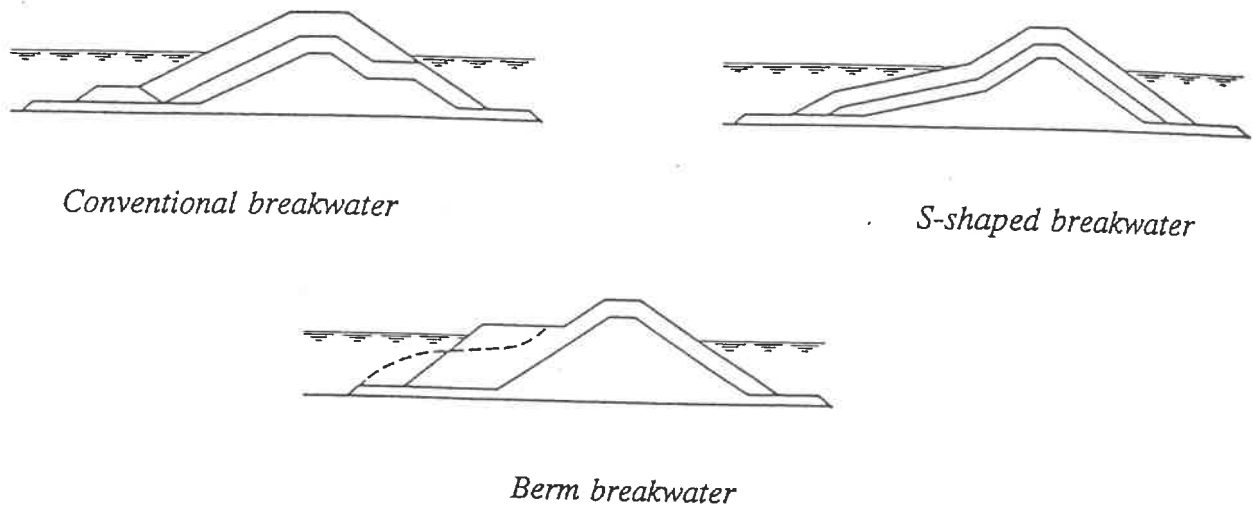


Figure 1 Typical cross-sections of three types of rubble mound breakwaters.

A berm breakwater is a rubble mound breakwater with a berm above still water on the seaward side. During exposure to wave action of certain intensity, the berm reshapes until eventually an equilibrium profile of the stones on the seaward face is reached. For each wave height, there is thus an equilibrium profile corresponding to this wave height. Just below the water level the reshaped profile has typically a slope of about 1:5. In front of this flat slope, stones are deposited with a steeper slope approaching the natural angle of repose. Wave energy is dissipated in the mass of stones in the flat slope resulting in reduced wave run-up above still water level where the natural equilibrium slope is steeper.

Berm breakwaters can be designed to be in either static or dynamic equilibrium in the long-term. For a dynamically stable berm breakwater the stones are allowed to move somewhat but with the average profile being in equilibrium. In order to ensure long-term stability, berm breakwaters should reshape into a statically stable profile where movements are only occurring in very severe and rare conditions. This requirement is due to the fact that frequent stone movements could result in abrasion and fracturing or displacement of stones finally resulting in degradation of the breakwater.

Longshore Transport

A berm breakwater trunk section exposed to oblique waves has to be designed with stones larger than a certain critical size in order to avoid continued movements of stones in the wave direction (longshore transport) which would eventually endanger the breakwater.

Singular Points

Singular points are of special interest for berm breakwaters, eg bends and roundheads. Stone displacements occurring at singular points result in stones being moved in the wave direction and the structure is consequently weakened. A point of special concern is whether, and under which

conditions, a singular point of a berm breakwater may develop in a way that in the long-term will lead to structural failure. For a permanent structure, such features are normally undesirable as it would require maintenance from time to time in order to ensure the long-term stability.

Rock Size

The average armour rock size needed in a berm breakwater structure is smaller than in a traditional rubble mound structure. This is due to the flatter final slope of the seaward face on which the breaking wave plunges and dissipates energy, and the higher proportion of wave energy dissipated within the porous mound (reducing the hydrodynamic forces acting on the individual stones). Further, wave action causes consolidation of the breakwater and nesting of the stones, which increase the stability. Typically stones with a weight two to ten times smaller can be used for construction of the berm compared to the main armour layer of a conventional breakwater.

Especially when a quarry is available near the construction site and it is not possible to produce a sufficient quantity of large armour stones for a conventional rubble mound breakwater, a berm breakwater can be a feasible solution. Berm breakwaters are presently being considered for more and more applications worldwide, and several berm breakwaters are or have already been constructed. Berm breakwaters can normally be constructed with only two stone gradations as indicated in **Figure 1**. Proper design of berm breakwaters might lead to utilisation of almost 100 per cent of the quarry yield.

Construction Method

The smaller stones to be used for berm breakwaters have also an influence on the construction method and equipment to be used. The core can be constructed by end tipping trucks or dumping by barges, whereas the berm can be constructed by cranes with stone grabs, end tipping trucks or excavators. Generally lighter and less specialised construction equipment can be used compared to construction of conventional breakwaters. Even if the construction tolerances are wider for berm breakwaters than for conventional rubble mound breakwaters, fulfilment of the specifications to the stone material (mean weight, gradation, geometrical shape, quality, content of fines, etc), construction method and breakwater profiles is strictly required.

Breakwater Examples

Berm breakwaters have been designed and model tests have been performed for many projects, of which some have actually been constructed to date. This section describes eight examples of constructed berm breakwaters. In three cases, the profile development has been measured in prototype. In the following, H_s is the significant wave height, Δ is the relative stone density, $D_{n50} = (W_{50}/\rho_s)^{1/3}$ is the nominal diameter, W_{50} is the median weight, and ρ_s is the stone density.

Norwegian Experience

Two berm breakwaters have been constructed in Norway; one in Årviksand and one in Rennesøy. In order to reduce construction costs, both projects included a structural variant to the typical berm breakwater profile. These structural variants are further discussed in the following.

Årviksand

The berm breakwater constructed in Årviksand in northern Norway is an extension of a breakwater for a fishing port. In the design, a significant wave height of $H_s=6.5$ m and a water level of +3.6 m have been used.

Through model tests, it was found economical to use larger stones for the rear side of the breakwater to protect against wave overtopping rather than increasing the crest elevation or extending the berm width. The disadvantage of this solution is an additional stone class to be handled in the quarry. A typical profile of the trunk section including a strengthened rear side is shown in **Figure 2**. Armour stones with a median weight of 4.4 t was used for the berm, which results in a stability parameter of $H_s/\Delta D_{n50}=3.4$. The breakwater head was also constructed of stones with an average weight of 4.4 t, but the upper part was armoured with 8 to 14 t stones and the top elevation of the berm increased from +3.6 m to +4.5 m, as shown in **Figure 3**.

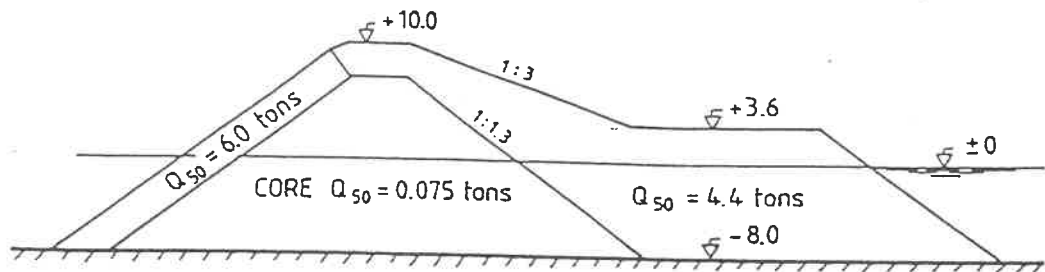


Figure 2 Extension of breakwater at Årviksand, profile of breakwater trunk section (Figure from Tørum et al (1990)). All measures are in metres.

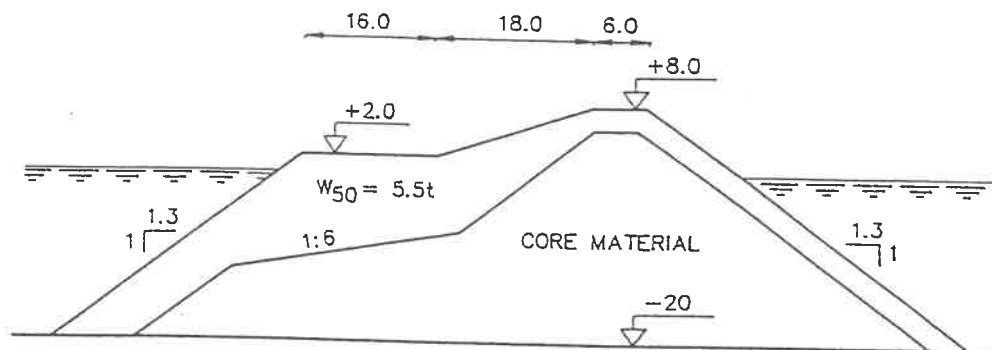


Figure 3 Extension of breakwater at Årviksand, profile of breakwater head, (Figure from Tørum et al (1990)). All measures are in metres.

After construction the armour profile has been monitored and new monitoring will be made after major storms in which reshaping of the breakwater has occurred. Fifty of the armour stones have been marked and it is the plan to track their movements after reshaping has taken place. The monitoring of the berm breakwater in Årviksand and similar monitoring of the breakwater in Rennesøy will give valuable prototype experience on profile development.

Rennesøy

A new ferry terminal has been constructed on Rennesøy with a berm breakwater protecting the harbour facilities (Espedal and Lothe (1994)). From an economical point of view, it was desirable to extend the core (0-1.5 t stones) into the berm to make better use of the quarry yield. Based on results from model tests, the profile shown in **Figure 4** was selected for the most exposed parts of the trunk, whereas the roundhead was designed with larger stones on the top of the berm and without extension of the core into the berm. In the design, a significant wave height of approximately $H_s=7.0$ m was used and the stability parameter for the trunk section has accordingly been assessed to $H_s/\Delta D_{n50}=3.3$.

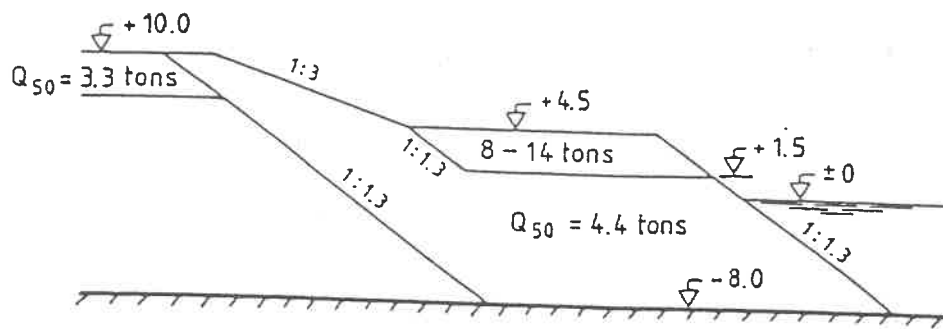


Figure 4 Typical cross-section for berm breakwater on Rennesøy. All measures are in metres.

This structural variant may in many cases be economical due to substitution of berm stones by cheaper core material. The disadvantage of this substitution is lower energy dissipation in the porous berm material and therefore reduced stability of the berm stones.

The berm was constructed using an excavator with a hydraulic hand. One by one, the quarry stones were dropped or thrown to the right position in the breakwater. Special attention was paid to quality control during construction in order to ensure the long-term stability of the berm breakwater. Examples of the established demands are (see Espedal and Lothe (1994)):

- Not accept stones with a mass less than 1.0 t for the berm, whereas no upper restriction was given.
- All stones for the berm were weighed, and control of the mean weight was made for samples of 200 t.
- The quarry stones should be clean and have no fissures, and restrictions to the shape were made in order to avoid flat stones (the height to width ratio should not exceed 3:1).
- For each 30,000 m³ of stone material, it was checked that the density at least was 2.7 t/m³.
- The core material was specified to range from 0 to 1.5 t, but no topsoil, clay, silt or sand was allowed.
- Continuous surveying of the breakwater was made during construction in order to ensure the correct geometry of all parts of the breakwater (including the transition from one to another stone class). Permission to continue construction was given when it was proven that the given demands to acceptable geometrical deviations were fulfilled.

Icelandic Experience

Since 1983, seventeen rubble mound structures of the berm type have been constructed in Iceland. Ten of these were new structures, whereas the others were reinforcements or repairs of existing breakwaters in the form of additional protection on the seaside of old caisson breakwaters or modifications of existing conventional breakwaters. Presently, four berm breakwaters are planned or under construction in Iceland.

The main problem facing construction of rubble mound breakwaters in Iceland is the poor quality of the stones (basalt) and the often-associated lack of sufficiently large armour stones. This can be exemplified by results from an inspection of a rubble mound structure built in 1968-69 in one of the most exposed locations in Iceland (Vopnafjörður). The armour layer of the breakwater was originally constructed from stones of 10 to 15 t. An inspection showed that

abrasion and splitting of stones had caused deterioration of the breakwater. Weathering took place above the water level, and the estimated loss in diameter was 0.5 to 1.0 cm per year in a 20-year period. This corresponds to a weight loss of 1.8 to 3.4 t for a 10 t stone. This severe problem with abrasion and splitting of stones in Iceland is normally treated by using stones with reduced size in the model tests.

Sigurdarson and Viggooson (1994) mention that a high utilisation of quarried rocks can be achieved by construction of berm breakwaters, and that this is of great importance in Iceland where shortage of sufficiently large armour stones is a problem. The berm breakwaters in Iceland often consist of several stone classes, with the largest stones used for singular points and as a protecting layer on the berm and crest. The sorting of quarry stones is only increased marginally as all stones are weighed as part of the handling in the quarry. The application of the largest stones for the most exposed parts of the berm breakwaters makes the profiles more stable and/or results in a high utilisation of the quarry output. This means that it is of great importance to obtain knowledge of the distribution of the quarry yield in an early stage of the design phase.

In addition to the normally stated advantages of berm breakwaters, two other factors are mentioned by Viggooson (1990): Local contractors with no special experience in marine work can be used as the construction can be made with available land based equipment and the tolerances for placement of stones are eased. Shortage of funds often makes it necessary to extend the construction period over two summers with a stop in the winter season (experience in Iceland indicates that a partially completed berm breakwater functions well through the storms of one winter, and repairs are much easier than for a conventional breakwater).

Sigurdarson and Viggooson (1994) state that a comprehensive quality assurance programme is necessary during the construction of berm breakwaters to ensure that the armour stones fulfil the requirements of quality and durability. They propose that a quality assurance programme include:

- grading, weight requirements, specific gravity, and water absorption compatible with the design criteria
- visible inspection for defects, joints, aspect ratio and colour index

Bakkafjordur

The first berm breakwater in Iceland was built in 1983-84 at Bakkafjordur. The 50-year design wave condition is $H_s=4.8$ m and $T_p=12.0$ s for a design water level of +2.5 m. The berm consists of stones in the range from 2.0 to 6.0 t with an average weight of 3.0 t. The stability parameter has been calculated at $H_s/\Delta D_{n50}=2.9$. A typical cross-section of the constructed berm breakwater is shown in **Figure 5** together with comparisons of prototype measurements and results from model tests. Reasonable agreement was found between the profile developments in model and prototype. The possible rounding and breakage of the available poor quality stones was included in the model study by testing with reduced stone size. In nature, some deterioration of stones has been observed at the breakwater head.

Keflavik (Helguvik)

The berm breakwater project at Keflavik was described by Baird (1987). A typical cross-section of the breakwater is shown in **Figure 6**. The 50-year design wave condition is $H_s=5.8$ m and $T_p=9.6$ s with an angle of incidence equal to 45° , and a corresponding design water level of +5.0 m. The berm consists of 1.7 to 7.0 t stones with an average weight of 3.2 to 4.2 t, and the

stability parameter has been calculated at $H_s/\Delta D_{n50}=3.2-3.5$. In the model tests, smaller stones were used in order to take into account possible deterioration of the stones.

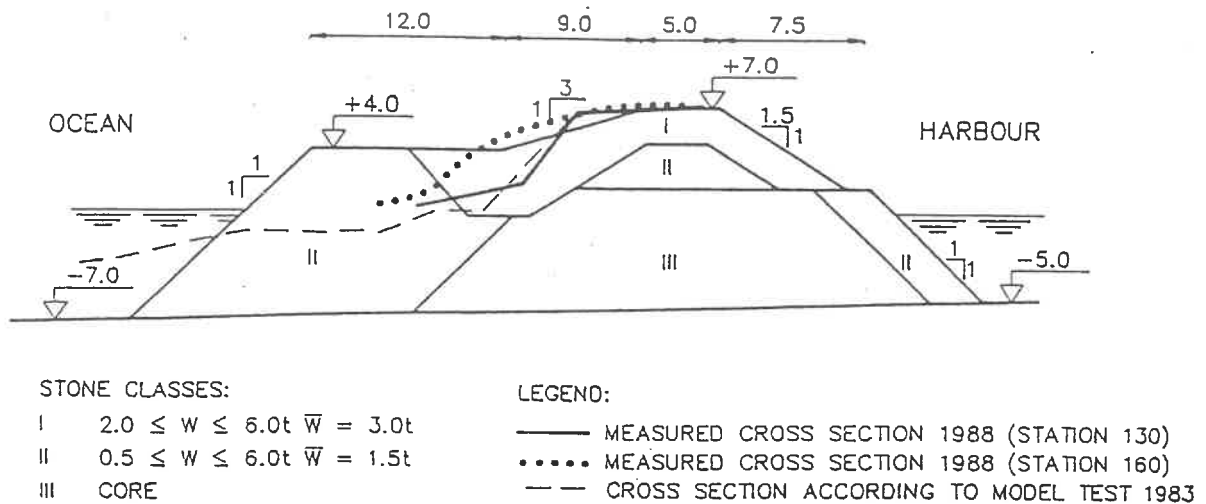


Figure 5 Measurements of profile reshaping of berm breakwater at Bakkajordur (based on figures from Viggoisson (1990)). All measures are in metres.

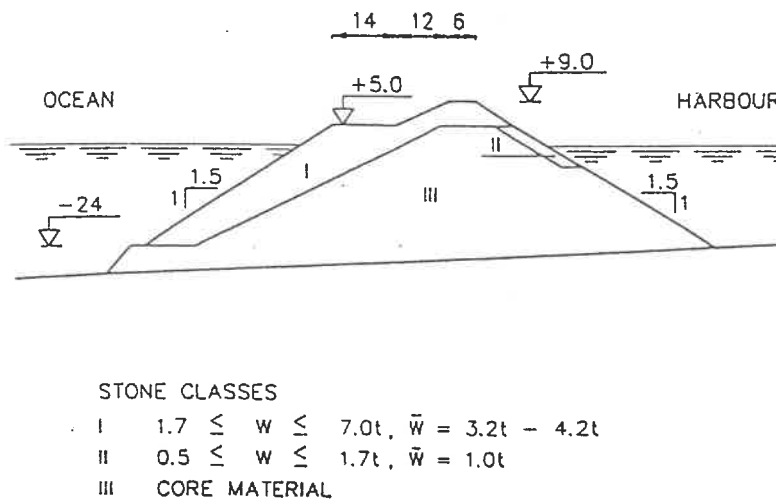
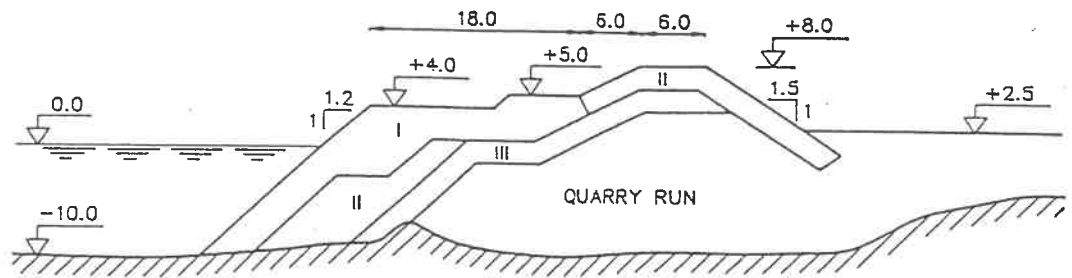


Figure 6 Cross-section of a berm breakwater at Keflavik. (Based on figure from Baird (1987)). All measures are in metres.

Skopun, Faroe Islands

Presently, a berm type breakwater is being constructed in Skopun with the aim of reducing the wave overtopping at the existing harbour and for protection of reclamation. The design conditions corresponding to a return period of 50 years are $H_s=5.8$ m and $T_p=18$ s. The design water level is about +1.0 m. A typical cross-section of the berm breakwater consisting of several stone gradations is shown in **Figure 7**. The small berm is constructed of stones ranging from 5.5 to 12.5 t, with an average stone weight of about 8.3 t. With a stone density of 2.65 t/m³, the stability parameter has been calculated at $H_s/\Delta D_{n50}=2.5$. Three-dimensional model tests have been carried out as part of the design, and the reshaped profile of the most exposed section of the breakwater is shown in **Figure 8**.



STONE CLASSES:
 I QUARRY STONES $W = 5.5 - 12.5t$, $\bar{W} = 8.3t$
 II QUARRY STONES $W = 2.5 - 5.5t$, $\bar{W} = 3.7t$
 III QUARRY STONES $W = 0.3 - 2.5t$

Figure 7 Typical profile for Skopun harbour. All measures are in metres.

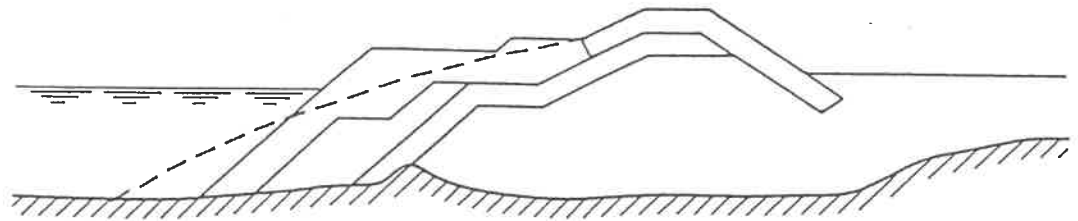
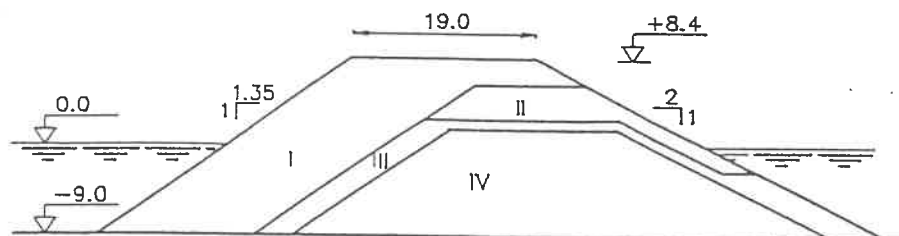


Figure 8 Reshaped profile after exposure to the design wave conditions (results from model tests). All measures are in metres.

Hay Point, Australia

For protection of a tug boat harbour, a berm breakwater has been model tested and constructed as described by Bremner et al (1987). Numerical wave modelling has revealed a 100-year significant wave height of $H_s=5.0$ m and a corresponding peak period of $T_p=7$ s, and a design water level of +4.5 m. The stones used for the berm had a weight of 4.0 to 7.0 t with an estimated average weight of 5.3 t. Applying a stone density of 2.65 t/m³, the stability parameter can be assessed at $H_s/\Delta D_{n50}=2.5$. A typical profile of the designed berm breakwater is shown in Figure 9.



STONE CLASSES:
 I ARMOUR STONES 4-7t
 II ARMOUR STONES 1-2t
 III FILTER STONES 0.25-2t
 IV CORE MATERIAL

Figure 9 Typical cross-section for a berm breakwater at Hay Point. (Based on figure from Bremner et al (1987)). All measures are in metres.

St George, Alaska, USA

A berm breakwater project on St George Island has been described by Gilman (1987). The concept profile for this breakwater was developed through model tests performed at the Danish Hydraulic Institute. The design wave condition is $H_s=10.4$ m offshore (and about 6.4 m in front of the breakwater) and $T_p=18.0$ s. The harbour layout is shown in **Figure 10**, and a typical cross-section of the roundhead in **Figure 11**. The berm for the breakwater roundhead had a top elevation of 16 feet (4.9 m) and a width of 61 feet (18.6 m), and the berm for the trunk section had a top elevation of 12 feet (3.7 m) and a width of 55 feet (16.8 m). The berm of both the trunk and roundhead was constructed of stones with a weight from 1.5 to 9.0 t. The average stone weight is about 4.8 t, and the stability parameter is calculated at $H_s/\Delta D_{n50}=3.3$.

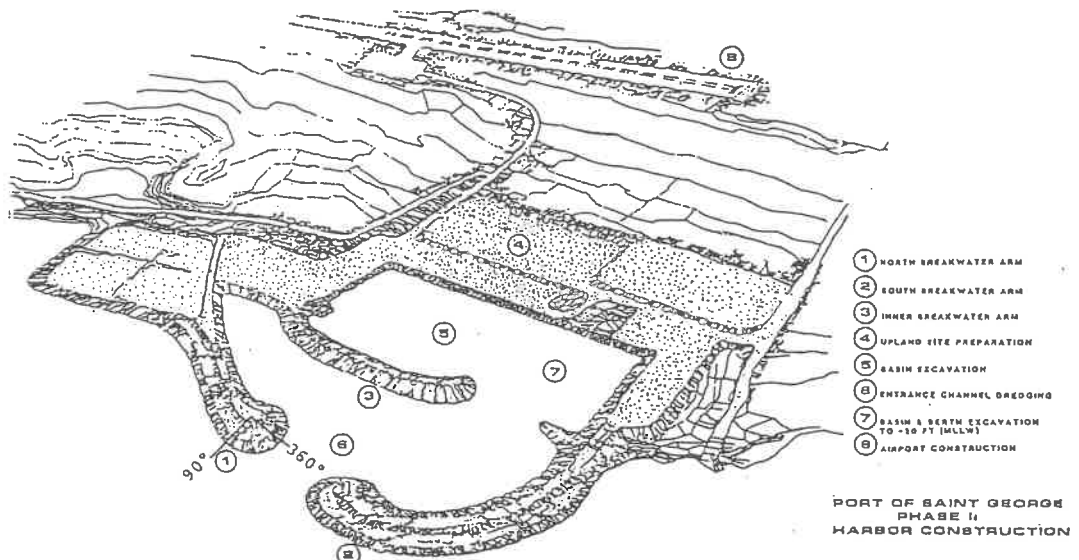


Figure 10 Harbour layout for St George. (Figure from Gilman (1987)).

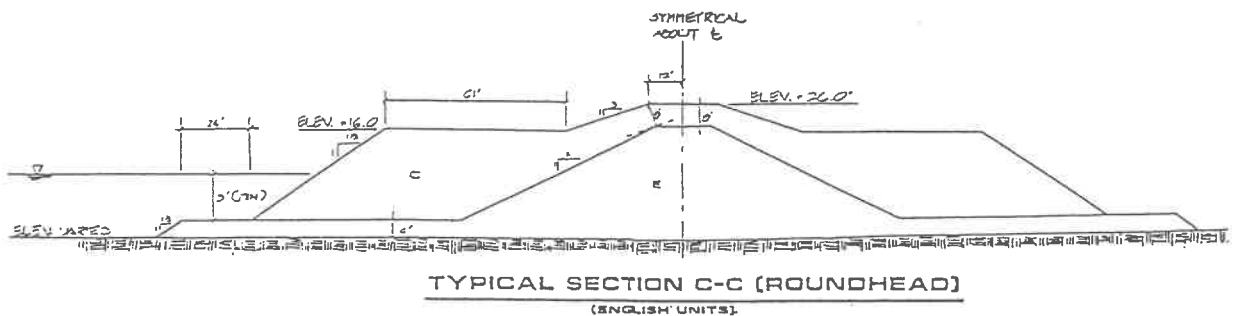


Figure 11 Typical cross-section of berm breakwater roundhead for St George. (Figure from Gilman (1987)). All measures are in feet.

Before completion of the breakwater, construction was shut down in late 1986 with the North breakwater roundhead only half completed (30 ft of the horizontal berm was constructed, none of which rose above elevation +12 ft). During the winter of 1986-87, storms occurred which approached the design storm in intensity. Surveys of the breakwater profiles were made before and after the winter storms, showing only minor changes in the profiles. This indicates that the incomplete berm breakwater performed well during these severe wave conditions (see Gilman (1987)).

Racine, Wisconsin, USA

The implementation and performance of a berm breakwater design at Racine, Western shore of Lake Michigan, have been described by Montgomery et al (1987). The design conditions, corresponding to a return period of 20 years, are a significant wave height of $H_s=4.4$ m, a significant wave period of $T_s=10.0$ s and a water level of +1.4 m relative to low water datum. The water depth in front of the breakwater is 6-8 m and a typical cross-section is shown in **Figure 12**. The width of the berm is 12.2 m at the trunk and 15.2 m at the roundhead. Stones with a weight in the range 0.14 to 3.6 t have been used, which with an average weight of 0.82 t gives a stability parameter of $H_s/\Delta D_{n50}=4.1$.

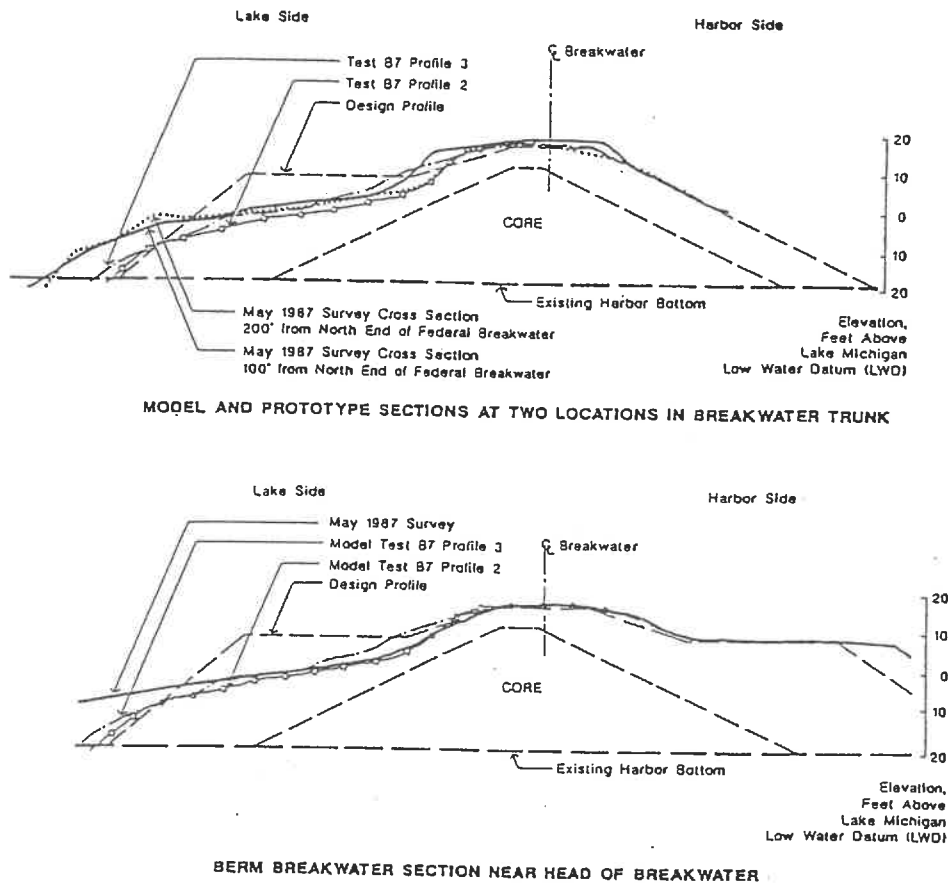


Figure 12 Comparison of model tests and prototype measurements. (Figures from Montgomery et al (1987)). All measures are in feet.

After construction, the berm breakwater was levelled and found to be in good agreement with the design. The breakwater was completed in the autumn of 1986 and was in February and March 1987 exposed to two major storms, which approximated the design conditions. A description of the breakwater performance is summarised below (see Montgomery et al (1987)).

Visual, underwater and survey assessments of the berm breakwater were performed after the March storm with the following main observations:

- the berm was reshaped so that it was generally below water along the trunk section, whereas parts of the roundhead were less reshaped
- small rounded cobbles (diameter of 15 to 45 cm) were observed at the water line, indicating breakage of some of the berm stones

- some of the berm stones had moved towards the crest
- the reshaped berm had a typical slope between 1:6 to 1:10
- no evidence of substantial overtopping was observed as the rear side appeared unaffected

A subsequent survey was conducted and indicated that despite the fairly dramatic change in the above-water appearance, the berm breakwater appeared to have behaved similarly to the model tests with respect to berm reshaping. Survey cross-sections and profiles from the modelling study are presented in Figure 12. A fine agreement was found between the reshaped profiles measured during model testing and in prototype.

Summary of Breakwater Examples

A summary of selected geometrical, wave and stone size data for the presented breakwaters is listed in **Table 1**.

Table 1 Summary of the data for the described examples of constructed berm breakwaters.

Location	h^* (m)	R_c^{**} (m)	H_s (s)	T_p (s)	W (t)	W_{50} (t)	D_{n50} (m)	$H_s/\Delta D_{n50}$	R_c/H_s
Árvíksand	11.6	6.4	6.5	~14.0	-	4.4	1.18	3.4	0.98
Rennesøy	-	-	7.0	-	-	5.5	1.28	3.3	-
Bakkafjörður	10.5	4.5	4.8	12.0	2.0-6.0	3.0	1.05	2.9	0.94
Keflavík	29.0	4.0	5.8	9.6	1.7-7.0	3.2-4.2	1.07-1.17	3.2-3.5	0.69
Skopun	11.0	7.0	5.8	18.0	5.5-12.5	8.3	1.46	2.5	1.20
Hay Point	13.5	3.9	5.0	7.0	4.0-7.0	5.3	1.26	2.5	0.78
St George	8.2	6.4	6.4	18.0	1.5-9.0	4.8	1.22	3.3	1.00
Racine	9.8	3.5	4.4	~10.6	0.14-3.6	0.82	0.68	4.1	0.80

Note: * h is the water depth in front of the structure in the design situation

** R_c is the freeboard, ie the vertical distance from the actual water level to the crest

The listed parameters should be regarded with caution as some of the data are uncertain. For example, is it rarely indicated in the literature if the wave heights refer to offshore or nearshore conditions?

The practical experience with the berm breakwaters described in the present paper shows that the dimensionless stability parameter, $H_s/\Delta D_{n50}$, is in the range from 2.5 to 4.1. The Icelandic experience from 15 berm breakwaters shows a stability parameter in the range from 2.4 to 3.2 for breakwater trunk sections and in the range of 1.7 to 2.4 for breakwater roundheads where traditionally the largest quarry stones were applied. These values of the stability parameter are in the lower end of the classification of breakwaters made by Van der Meer (1988) quoting: $H_s/\Delta D_{n50}=3-6$ for berm breakwaters and S-shaped profiles.

The ratio between the freeboard and the significant wave height, R_c/H_s , varies between 0.7 and 1.2, which is smaller than for conventional rubble mound breakwaters as the porous berm reduces wave run-up and overtopping. This range of dimensionless crest free board is found to agree well with results from a series of model tests carried out for studying the rear side stability of berm breakwaters (Andersen, Juhl and Sloth, 1992).

Recent Research on Berm Breakwaters

Introduction

A research project on berm breakwater structures was carried out with the overall objective of arriving at a better design basis. Eight European organisations from Denmark, The Netherlands, United Kingdom, Norway, Italy and Iceland participated in the joint research project co-sponsored by the European Commission under the second research and development programme on Marine Science and Technology, MAST II. Studies were made for understanding the physics of berm breakwaters, profile development, problems related to practical engineering applications and three-dimensional (3D) effects. A combination of theoretical work, physical model tests and numerical modelling was used in the project.

A summary of the main results of the research project is presented here including numerical modelling of the flow on and in berm breakwaters and of the berm reshaping, parameter analysis, study of the influence of permeability and stone gradation, results of model tests with scour protection, and analysis of 3D model tests carried out in both deep and shallow water for studying the roundhead and trunk stability.

3D Model Tests

The major task within the research project was the 3D model tests for studying the stability of the breakwater roundhead and adjacent trunk section. Deepwater tests were carried out at Danish Hydraulic Institute and shallow water tests at SINTEF NHL. Model tests for studying the influence of storm duration, short-crested waves and rock shape on berm reshaping and longshore transport were made at Aalborg University.

Deep Water Tests, Roundhead

For berm breakwaters as compared with traditional rubble mound breakwaters, special measures have to be taken for the breakwater roundhead. If stone displacements occur on a roundhead, the stones will be moved in the wave direction and loose most of their stabilising effect.

A total of six test series were carried out in a wave basin at Danish Hydraulic Institute for studying the development of berm breakwater roundheads, see **Figure 13**. Five wave incidence angles were tested together with two wave steepnesses. All tests were carried out with irregular long-crested waves, and each test series consisted of five tests for reshaping of the breakwater ($H_0=2.0, 2.5, 3.0, 3.5$ and 4.0).

The berm breakwater was constructed with two stone classes, ie one for core and scour protection and one for berm, crest and rear side protection as shown in **Figure 14**.

The measurements included a total of 38 profiles along the breakwater which were subsequently interpolated into a 3D representation of the breakwater. This formed the basis for detailed calculations on the profile development, recession of the berm, eroded and deposited volumes and transport of stones in arbitrary sections of the breakwater.

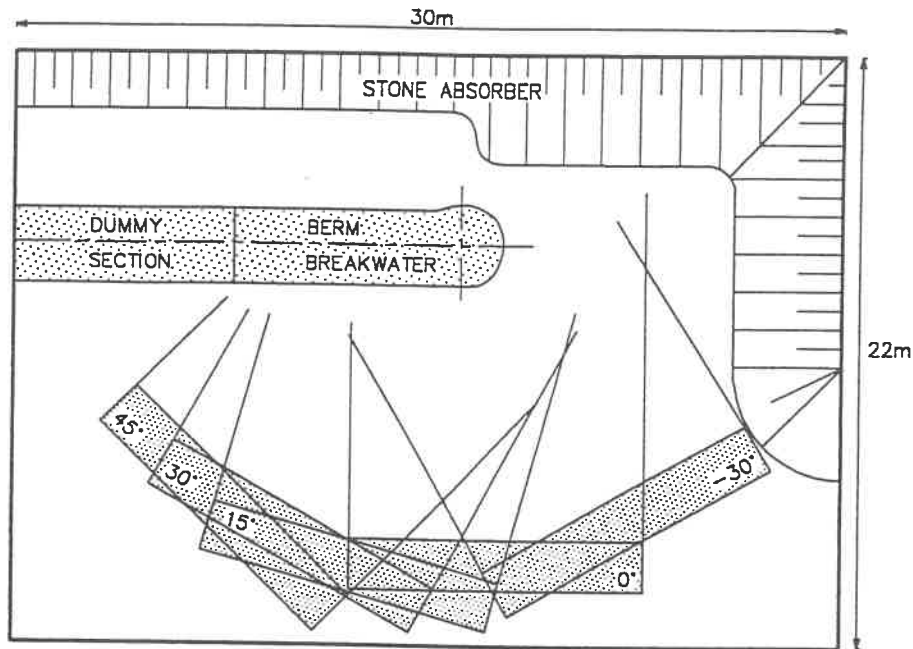


Figure 13 Model plan, including positions of the wave generators.

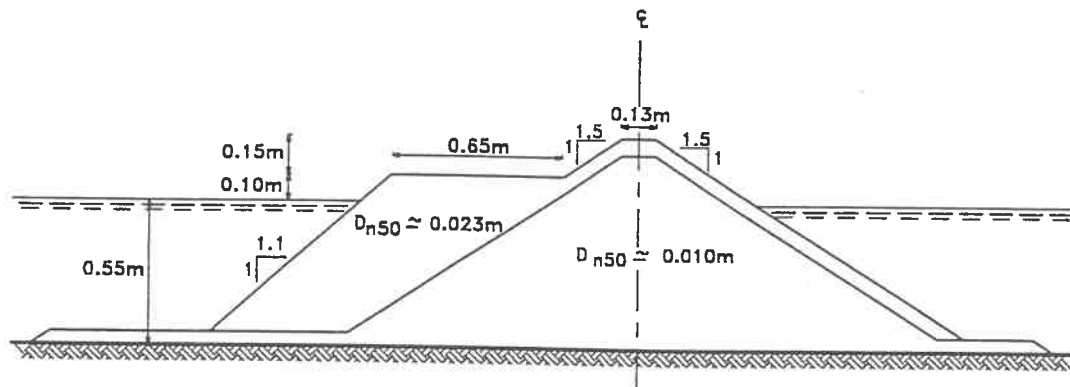


Figure 14 Cross-section of the initial profile for the trunk. The roundhead was made by rotating the profile around the centreline.

Recession

Plotting the recession measured after $H_0=4.0$ for all wave directions as function of the relative angle, see Figure 15, shows that the recession pattern follows the wave direction, and that maximum recession occurs at an area directly exposed to the waves. It is found that the maximum recession on the head occurs for wave direction 0° , where the recession reaches the initial berm width for H_0 between 3.5 and 4.

Comparing the maximum recession found at the head with the recession on the trunk, see Figure 16, it is found that only in the case with wave direction 45° the maximum recession on the head is equal to or less than the recession on the trunk section. In the case with wave direction -30° , the recession on the head is up to 75 per cent higher than for the trunk section. For head on waves, the maximum recession on the head is 50 per cent higher than the recession on the trunk.

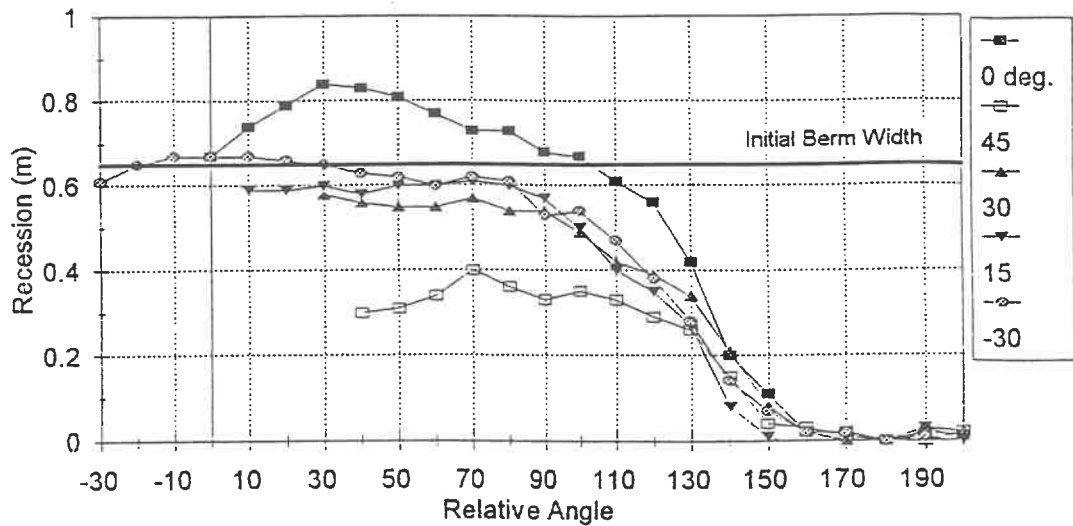


Figure 15 Recession. All wave directions. After $H_o=4.0$, $S_m=0.05$.

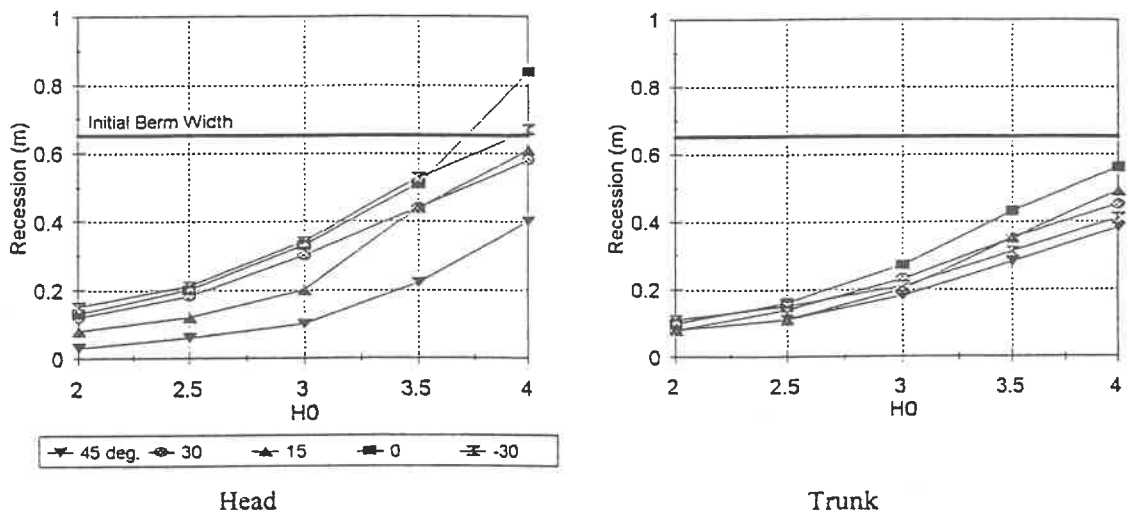


Figure 16 Maximum recession on head, respectively trunk

When analysing the maximum recession as function of the wave direction, it can be seen that the maximum recession on the head is increased by a factor of up to 2 comparing the results for wave directions 45° and 0° , whereas the recession on the trunk is increased by a factor of about 1.4. The recession on the head is thus more sensitive to changes in the wave direction than the recession on the trunk.

The influence of the wave steepness was investigated for wave direction -30° . The results showed a strong influence by the wave steepness, as the maximum recession on the head for $S_m=0.03$ was almost twice the recession found for $S_m=0.05$. On the trunk, the influence was less pronounced. Analysis showed that a good agreement between the two data sets ($S_m=0.03$, respectively 0.05) was obtained when plotting the recession as function of $H_o T_o$, especially for the trunk section. T_o is given by $T_o = T_m \sqrt{g / D_{n,50}}$.

Erosion and Deposition

Figure 17 presents the erosion and deposition pattern around the breakwater head, after $H_o=4.0$ for all wave directions as function of the relative angle, again showing that the reshaping pattern follows the wave direction closely. A pronounced deposition area at the rear of the roundhead and a relative wide area of erosion are found. The reshaping of the head accelerates for $H_o T_o > 80-100$.

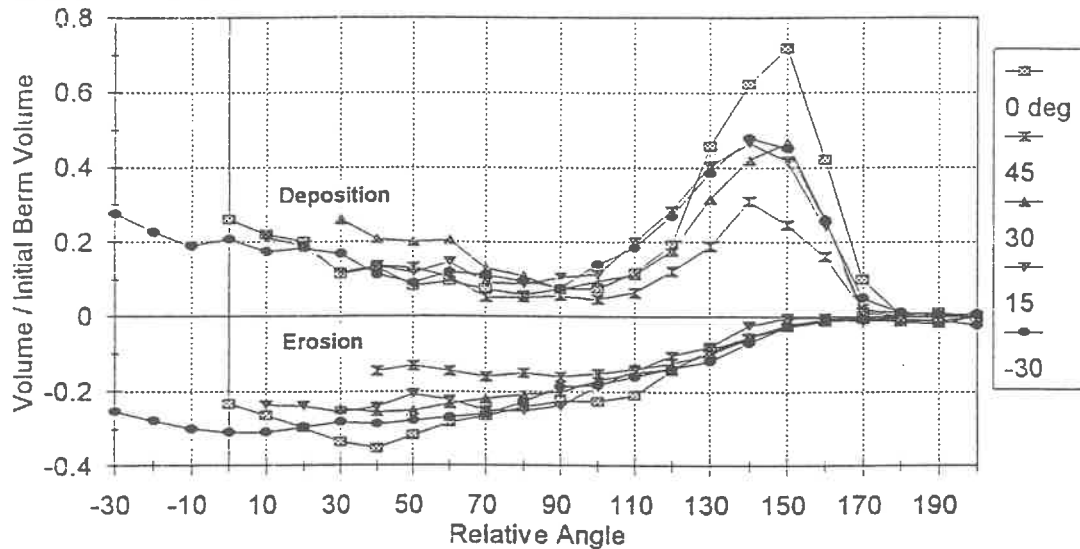


Figure 17 Erosion and deposition after $H_o=4.0$. All wave directions.

Stone Transport

In Figure 18, the stone transport for $H_o=4.0$ is plotted for all wave directions as function of the relative angle, showing that the maximum transport takes place at the sections $110^\circ-130^\circ$ relative to the wave direction. The maximum stone transport on the head occurs with head on waves (0°) being up to three to four times higher than for wave direction 45° .

Trunk Section

A berm breakwater trunk section exposed to head-on waves can hardly be destroyed unless it is damaged by overtopping waves, whereas for oblique waves the stones can move along the breakwater. A study was made to describe the influence of wave obliquity on the profile shape, on the initiation of longshore transport and on the longshore transport rate at the trunk section both during and after the profile reshaping, see Alikhani et al (1996).

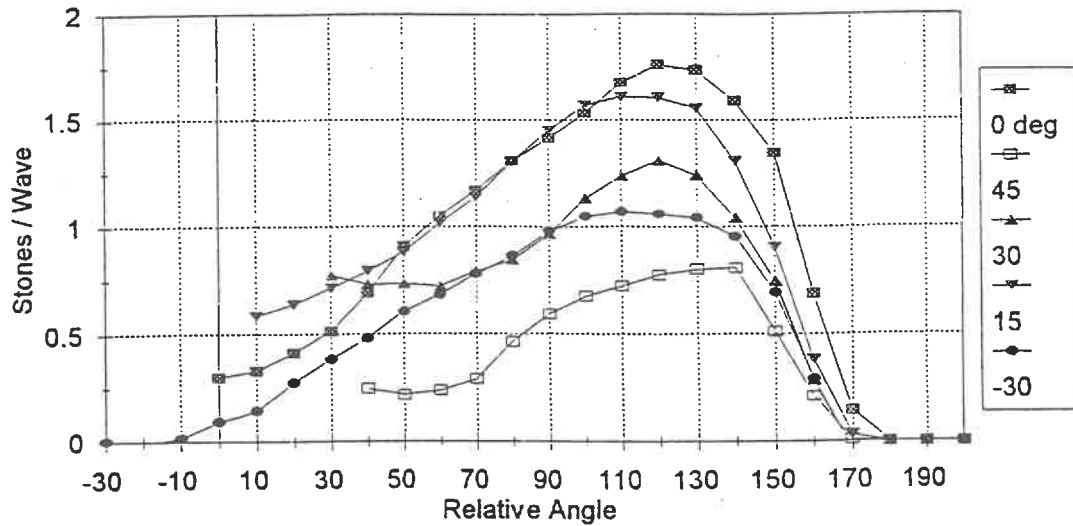


Figure 18 Stone transport for $H_o=4.0$. All wave directions.

Model testing of a trunk section exposed to oblique waves was carried out at the Danish Hydraulic Institute together with the model tests for studying roundhead stability. Basin tests were made at Aalborg University for studying the influence of storm duration and of short-crested waves. Assessment of the stone movements was made based on visual observations and photos taken after each test run. Observations were made both during the reshaping process involving a large number of stone movements and after the reshaping. In order to facilitate observations of the threshold conditions and the longshore transport rate, all the berm stones in a 1.0 m and 0.6 m, respectively for the two test series, wide section of the trunk were painted.

Threshold of Stone Movement

In general, the model tests showed that the largest transport distance occurs for an angle of wave attack, β , of 45° with a decreasing tendency for smaller and larger angles. It was found that the threshold values for longshore transport can be expressed as $H_o T_{op} > 50 / \sqrt{(\sin 2\beta)}$ during the reshaping phase, and $H_o T_{op} > 75 / \sqrt{(\sin 2\beta)}$ after the re-shaping phase.

Longshore Transport

An equation for calculation of the longshore transport rate under oblique wave attack was established considering that the longshore component of the incident wave energy is one of the most important parameters:

$$S = 0.8 \cdot 10^{-6} \sqrt{\cos \beta} \left(H_o T_{op} \sqrt{\sin 2\beta} - 75 \right)^2$$

The equation is calibrated to give the maximum longshore transport for a wave angle of 45° and zero transport for head-on waves and waves propagating parallel to the breakwater axis. A graphical presentation of the longshore transport rate after reshaping found from the tests made at Danish Hydraulic Institute is shown in **Figure 19** together with the derived equation. The test results and the equation show comparable relationships of the wave conditions and angle of wave attack.

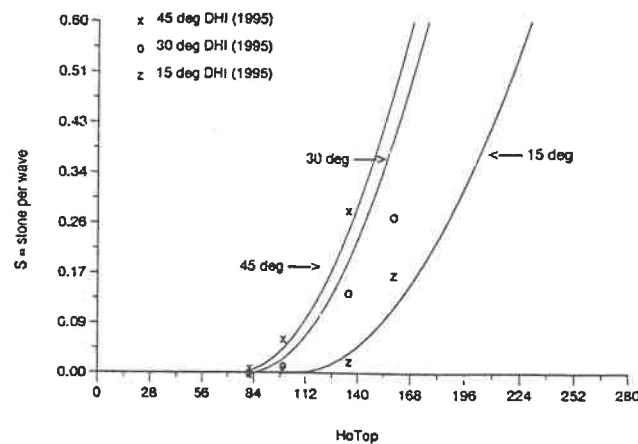


Figure 19 Longshore transport, in the form of stones per wave, S , as function of $H_o T_{op}$.

Tests with directional waves have shown that the longshore transport is much lower than for long-crested waves. For example for $s=10$, where s is a parameter that controls the angular distribution in the cosine power spreading function, the longshore transport was $\frac{1}{4}$ of the case for long-crested waves (wave angle 60° and $H_o=4.0$).

Long duration tests with registration of the number of moved stones after each 1,000 waves showed that the transport rate decreases in an exponential way with increasing number of waves.

Influence of Stone Shape

A series of wave basin tests were made with a berm breakwater trunk for studying the influence of stone shape on longshore transport, see Frigaard et al (1996). All tests were run with an angle of wave attack of 30° , and the breakwater was built as a homogeneous structure. Four type of stone shapes were used, ie rounded, normal, flat and mixed stones. All four types followed the same gradation curve and had a nominal diameter of $D_{n,50}=17.9$ mm.

Longshore transport was initiated for a stability number, N_s , of approximately 3.0, and it was found that the transport for the flat stones was three to five times higher than for the rounded stones and the transport for the normal stones being in between these. Any measurable differences in the reshaped profiles with different stone types were not observed in the tests.

Numerical Modelling

Numerical modelling of the flow on and inside permeable structures and of the reshaping of berm breakwaters was made by 1D and 2D numerical models. The 1D numerical model developed by Delft University of Technology can after some additional verification of the reshaping part be regarded as an engineering tool, whereas the other models at the moment are research tools which have to be developed further in order to be applicable for normal engineering services.

1D Numerical Model

Wave interaction with permeable coastal structures, with the emphasis on berm breakwaters, was studied by Delft University of Technology (Gent (1995) and Gent (1996)). Physical processes involved in the hydraulic and structural response of berm breakwaters under wave attack were examined, and a predictive numerical model for wave interaction with berm breakwaters developed. Special attention was given to berm breakwaters that reshape under heavy storm conditions by redistributing the stones in the seaward profile. The reshaping of such dynamic structures was modelled numerically.

The reshaping process of dynamic seaward slopes as a result of hydrodynamic loadings was studied. Van der Meer (1992) performed many model tests to study the stability of the seaward slope of berm breakwaters. The results were summarised in empirical relations determined by for instance wave height, wave period, stone diameter, number of waves and initial slope. The relations are valid for a wide range of parameters. However, it can be useful to study the reshaping process in a more detailed way. This can be done by modelling the reshaping process numerically by using hydrodynamic properties such as velocities and accelerations, ultimately leading to a more general applicable method and a complementary design tool.

A new approach to simulate the reshaping process as a result of the hydrodynamic loadings is presented. The initiation of movement is based on a Morison-type of equation including drag, inertia and lift forces. The new position of unstable stones is determined using the hydrodynamic forces which vary in time and space. The new position of the moved stones is immediately incorporated in the wave model. Verification and sensitivity analyses showed that the model can provide rather accurate results for quite some practical cases. **Figure 20** shows a comparison with prototype measurements described by Montgomery et al (1987).

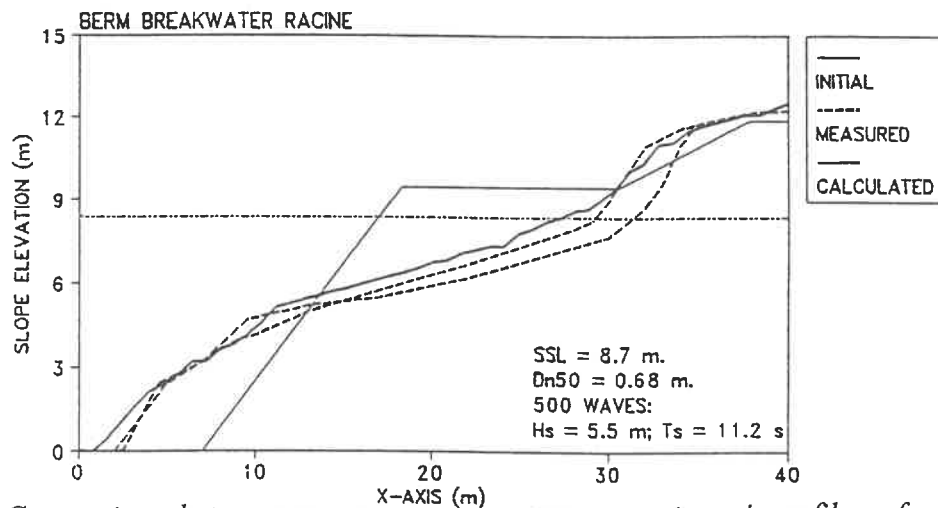


Figure 20 Comparison between measured and computed reshaped profiles of a prototype berm breakwater.

Several computations were made to show the dependencies on the reshaped profiles of wave height, wave period, stone diameter and initial slope. **Figure 21** shows that the affected reshaped profile becomes longer for longer wave periods. This was also observed in the experiments by van der Meer (1992). Also the influence of the size of the stones is represented as detected in physical model tests, see **Figure 22**. Similar conclusions can be drawn for variations of the wave height and of the initial slope.

A set of physical model tests were run at Delft University of Technology and used for additional validations of the numerical modelling of the wave interaction with berm breakwaters.

The numerical reshaping model was extended by Delft Hydraulics to include the effects of stone gradation.

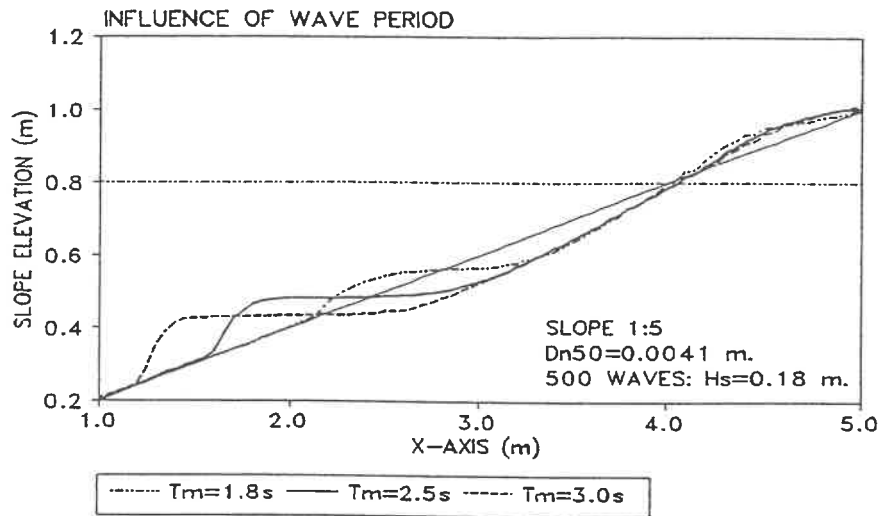


Figure 21 Influence of wave period on calculated profiles

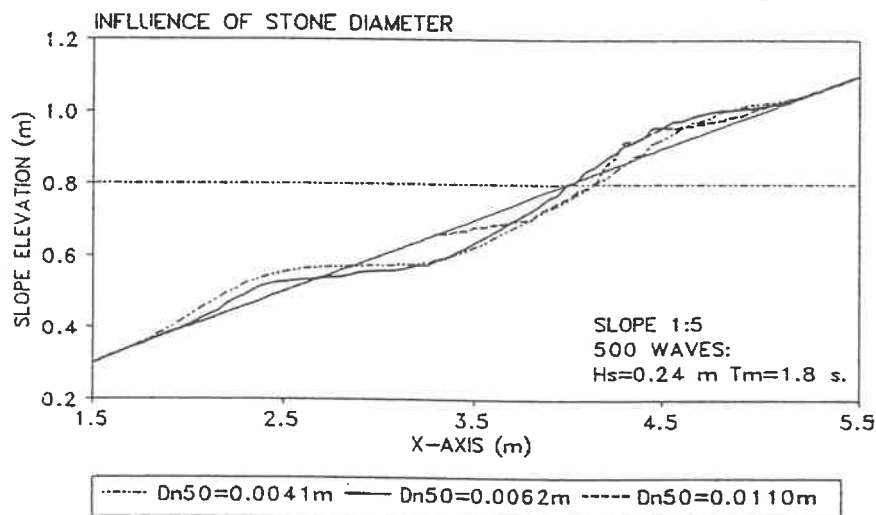


Figure 22 Influence of stone diameter on calculated profiles

Parameter Analysis

In order to develop a set of parameters to describe the berm profile development due to wave attack, a database with results from about 550 model tests was established by the University of Bologna.

All the information regarding the 2D and 3D tests are reported in a database organised as follows:

- reference to the source of data
- reference to the initial profile
- id number of the test
- structural parameters related to the rock: D_{n50} , D_{n15}/D_{n85} , Δ
- parameters related to waves: H_s , $H_{2\%}$, H_0 , T_m , $H_0 T_0$, s_m and the shoaling coefficient
- number of waves
- parameters related to the cross-section: crest freeboard, berm width, angle of structure slope, and depth in front of structure
- parameters characterising the profile after each wave attack

The berm breakwater profiles were schematised by using the six parameters previously established by van der Meer (1992), all of which are related to the local origin placed at the intersection between the initial profile and the water level (l_r , h_c , l_c , h_s , l_s , $tg\beta$).

All the wave heights were transferred to the water depth in front of the structure using the formula of Goda. Previous analysis by Lamberti et al (1994) showed that $H_{2\%}$ was the best value for the design, rather than H_s , so the non-dimensional parameters related to the waves (H_0 , $H_0 T_0$, s_m) were re-arranged with $H_{2\%}$.

In order to examine the relationship among a set of six correlated variables (profile parameters), it was useful to transform the original set of variables into a new set of non-correlated variables called principal components. The technique for finding this transformation is called Principal Component Analysis. The usual objective of the analysis is to see if the first few components account for most of the variation in the original data and thus can be used in describing the phenomena without any significant loss of information and bringing the highest simplification compatible.

The first component found from the available set of data is highly and positively correlated to the five lengths describing the profile, and represents the general erosion process and is a function of the intensity of the wave attack. The second component is highly correlated to the slope of the step and is a function mainly of the depth at the toe. The third, which describes, together with the second, the difference in the two parts of the active profile, above and under the SWL, is a function of the initial slope and of the intensity of the wave attack. The first component describes 69 per cent of the variance, and the first with the second and the third describe 95 per cent of the variance. The conclusion of the factor analysis is that the variables describing the phenomena can be reduced to three components.

The three components are a function of the number and the intensity of the waves (H_0 and s_m), of the water depth and of the initial slope of the berm. When the three components are evaluated, it is possible to estimate the six parameters describing the evolution of the profile through an inverse transformation. Knowing the parameters, the reshaped profiles can be reconstructed with respect to the conservation of volume during the wave attacks.

The reshaping of the breakwater based on the PCA was compared with experimental profiles from the 3D model tests run at Danish Hydraulic Institute in 1995, see Juhl et al (1996). The test programme carried out was a sequence of six wave attacks with increasing intensity (from

$H_0=1.5$ to $H_0=4.0$, $s_m=0.05$). The profiles were compared also with the predictive method based on the equations derived by van der Meer (1992), see **Figure 23**.

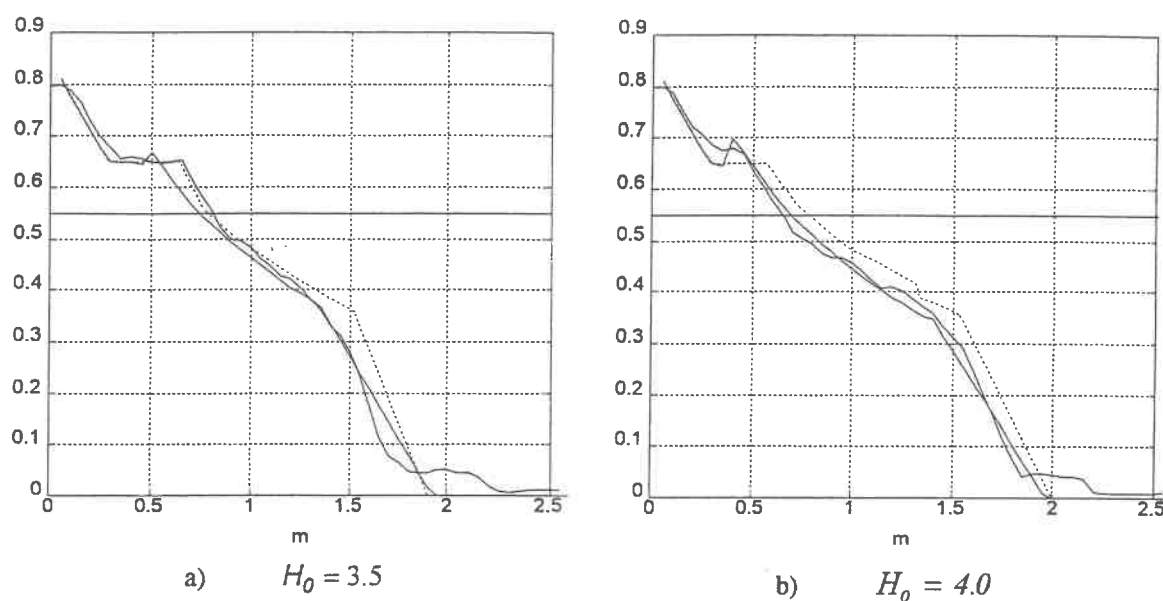


Figure 23 Results from parameter analysis compared to results from model tests (curve including breakwater toe) and the predictive method of van der Meer (dashed line).

The output from the principal component analysis is satisfactory for initial berm reshaping occurring for small wave heights and when significant reshaping takes place for large wave heights. In cases in which the berm still exists and is wide, the proposed method does not properly describe the dependence of the shape of the initial profile and thus overestimates the reshaping for modest wave attack.

Influence of Berm Permeability and Stone Gradation

The influence of permeability and stone gradation on the reshaping and wave overtopping of berm breakwaters was studied by flume model tests at the Danish Hydraulic Institute, see Juhl (1997). Another aspect studied was the difference in reshaping comparing a traditional berm breakwater constructed of two stone classes and a more stable Icelandic type of berm breakwater with the largest stones used as an armour layer covering a part of or the entire berm.

A total of twelve series of model tests were carried out in a wave flume covering studies of the effect of two stone gradations, three permeabilities, two crest and berm elevations, three berm breakwater solutions based on the Icelandic experience, and two wave steepnesses.

The profiles used in the 12 test series are shown in **Figure 24**. The water depth in front of the berm was 0.25 m for all tests. Test series 1 to 8 were carried out for comparing the reshaping of a berm breakwater constructed of two stone classes with the reshaping of a more stable Icelandic type of berm breakwater with the largest stones armouring the berm. Test series 1 to 4 were made with relatively high-crested breakwaters not allowing wave overtopping.

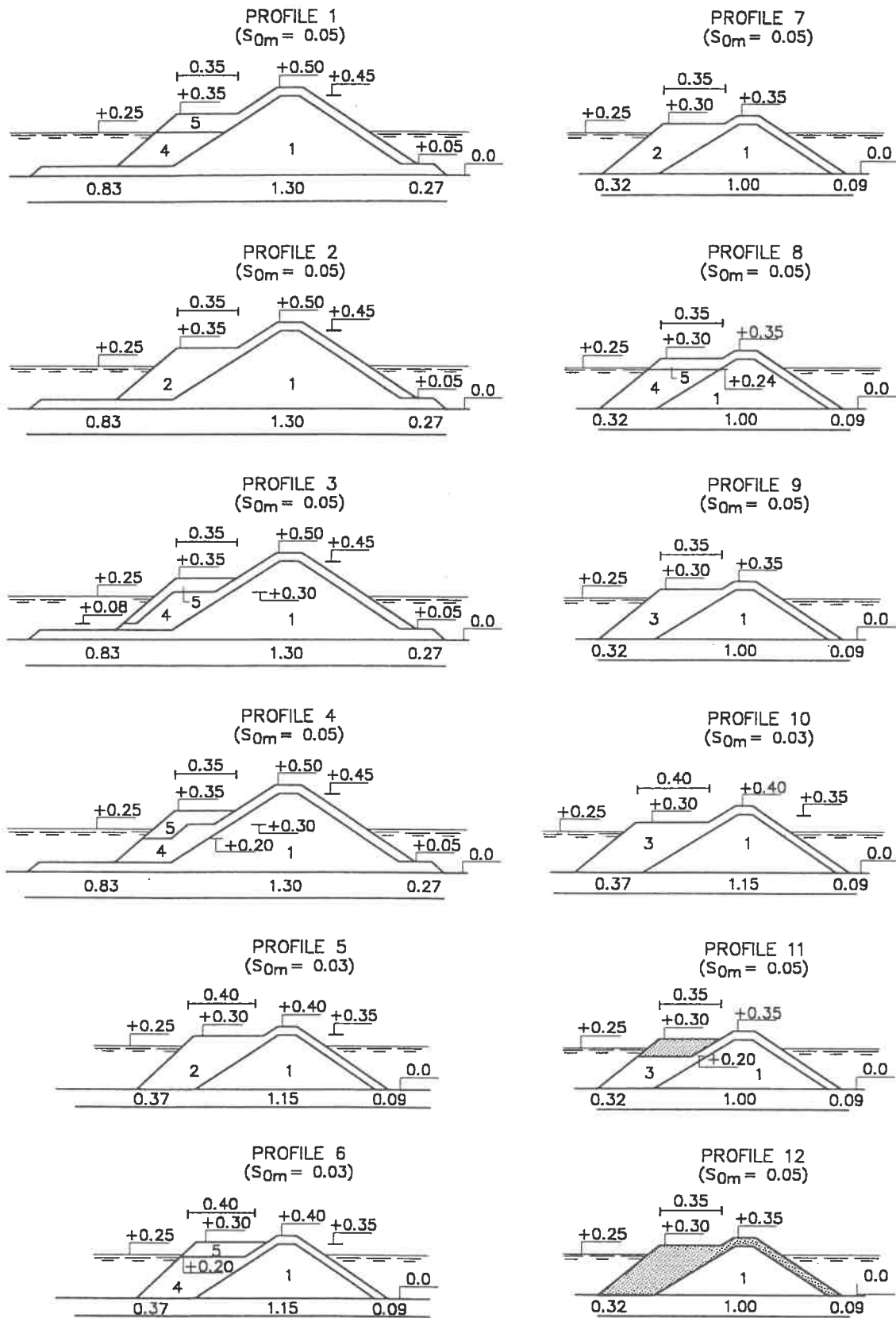


Figure 24 Tested berm breakwater profiles.

Three alternative berm breakwaters of the Icelandic type were tested and compared to tests for a berm breakwater consisting of two stone classes (reference profile). For the subsequent test series, the Icelandic type studied was a profile similar to profile 1. Test series 5 to 8 were made with more low-crested breakwaters with the crest elevation and berm width adjusted to the difference in wave steepness ($S_{om}=0.03$ and 0.05). Test series 9 and 10 were made for studying the influence of stone gradation, and test series 11 and 12 for studying the influence of permeability (25 per cent of fines added to the berm material).

The berm breakwaters were constructed of two or three stone classes, ie one for the core and scour protection and one or two for the berm, crest and rear side protection. The reference case is a berm breakwater constructed of two stone classes, a relative wide stone gradation for the berm, $D_{n,85}/D_{n,15}=1.80$ (stone class 2) and a core (stone class 1). In testing of the Icelandic type of berm breakwaters, the berm stones were separated into two classes, the lower fraction to be used for the berm (stone class 4) and the higher fraction to be used as an armour layer (stone class 5). Stone class 3 was a more narrow stone gradation with $D_{n,85}/D_{n,15}=1.40$.

Influence of Introducing an Armour Layer (Icelandic Type)

Three alternative Icelandic type berm breakwater profiles were tested and compared to tests with a traditional berm breakwater profile consisting of two stone classes (test series 1 to 4). **Figure 25** shows the reshaped profiles after testing with $H_o=4.0$. All three Icelandic type breakwaters showed significant less erosion volume and berm recession compared to the traditional berm breakwater. The profile resulting in the smallest erosion volume and berm recession was profile 3 (an armour layer at the top and at the front of the berm) followed by profile 4 (armour layer placed as a hammer head), whereas profile 1 (armour at the top of the berm) showed a little less effect, but has an advantage in construction.

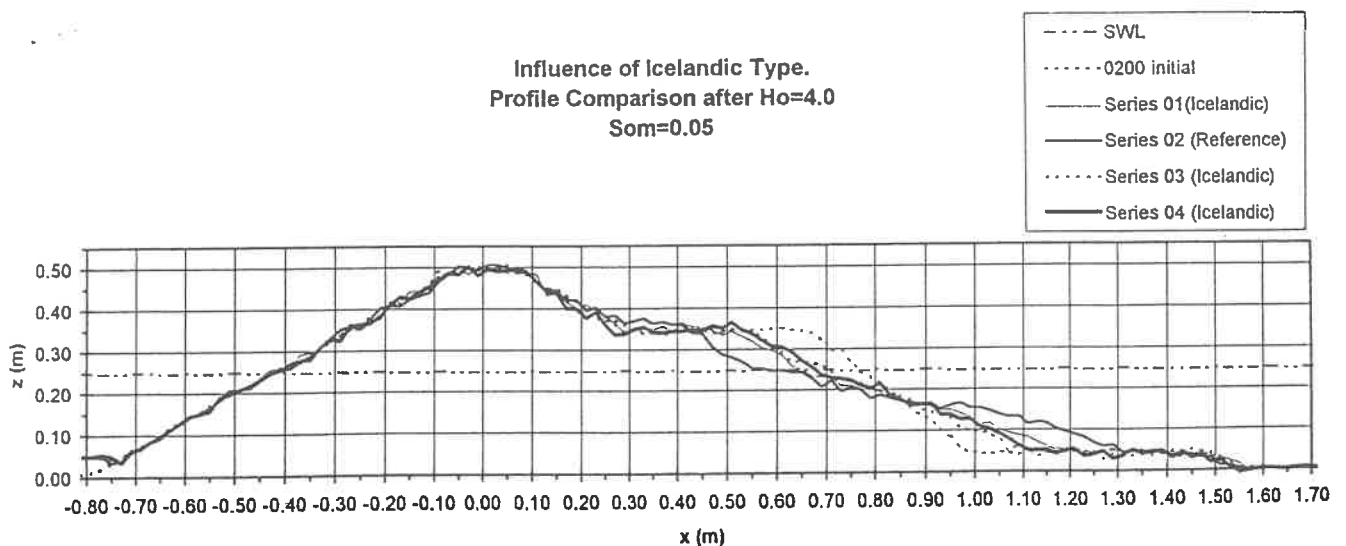


Figure 25 *Berm reshaping for a traditional berm breakwater and three alternative Icelandic type of berm breakwaters.*

Also the other tests made for studying the influence of an armour layer showed a reduction in the erosion volume and recession of the berm. The increased stability implies that the overall dimensions can be reduced.

An increase in the berm freeboard is associated with an increased berm volume and was found to result in less recession of the berm.

Influence of Stone Gradation

Model tests were carried out with two stone gradations, a wide stone gradation having $D_{n,85}/D_{n,15}=1.80$ (test series 5 and 7) and a more narrow having $D_{n,85}/D_{n,15}=1.40$ (test series 9 and 10). Results of test series 7 and 9 are presented in **Figure 26**. It is found that the wider stone gradation resulted in larger erosion volume and berm recession. Also the rear side stability is less for the wider stone gradation. In a wide stone gradation, the smaller stones will partly fill the voids between the larger stones resulting in a reduced permeability, which for the considered stone gradations are expected to cause increased erosion volume and berm recession due to decreased energy dissipation in the berm.

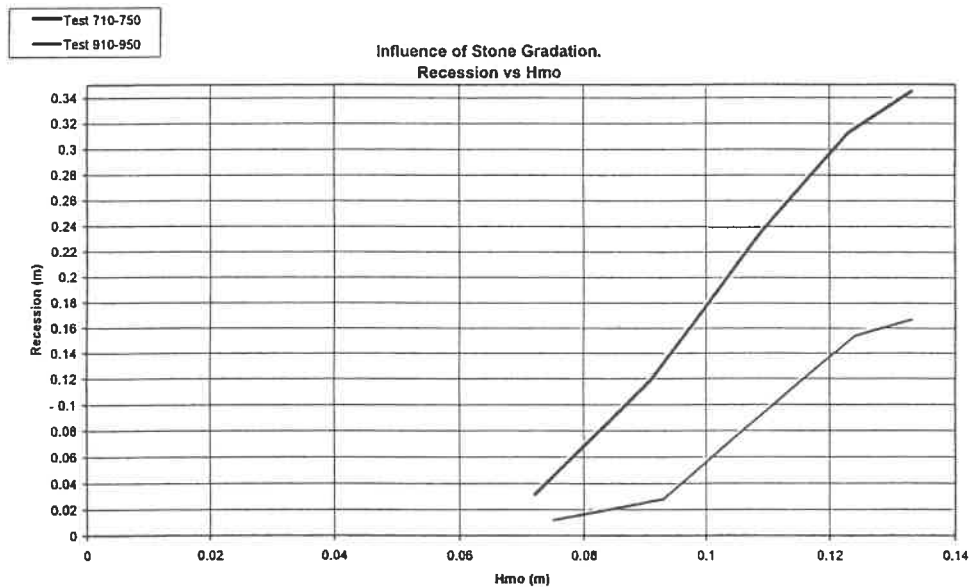


Figure 26 Influence of stone gradation on berm recession for a wave steepness of $S_{om}=0.05$.

Influence of Permeability

Wave run-up and overtopping conditions are significantly influenced by the presence of fine material in the berm material reducing the permeability and thus the energy dissipation, which is one of the main features of berm breakwaters. The influence of the permeability was studied in two test series with finer material added either to the top of the berm or to the entire berm constructed of stones with the narrow gradation, $D_{n,85}/D_{n,15}=1.40$. An increase in the erosion volume and berm recession was observed by adding the finer material to the top of the berm (test series 11). Adding finer material to the entire berm (test series 12) lead to a further increase in the erosion volume and berm recession, which exceeded the berm width. Further, a significant increase in overtopping was found, resulting in severe damage to both crest and rear side. **Figure 27** shows the influence on the berm recession by reducing the permeability of the berm.

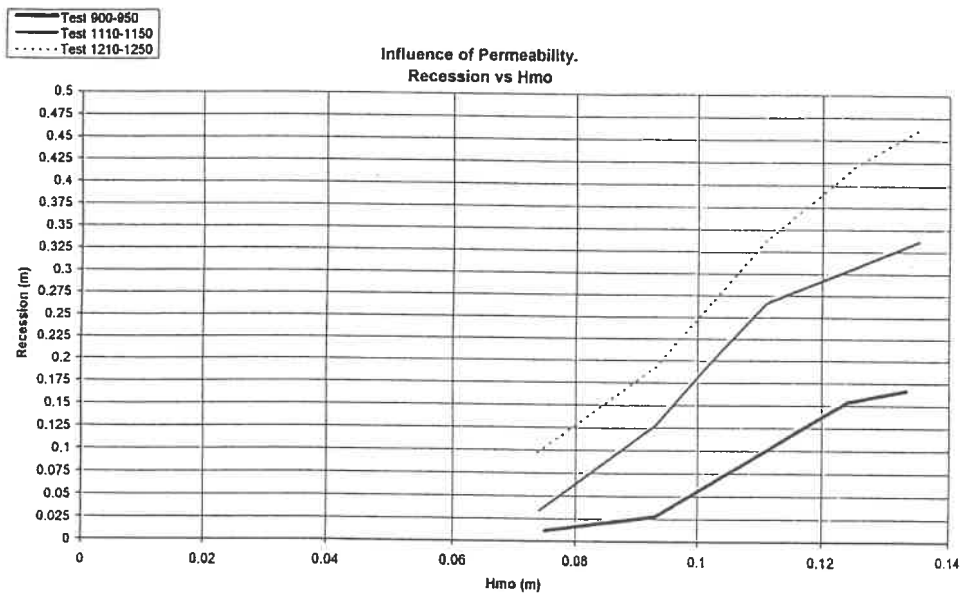


Figure 27 Influence of permeability on berm recession.

Scour Protection

Local scour can occur at a breakwater constructed on a sandy seabed and may endanger the overall stability due to sliding of the main armour layer if the toe and scour protection is failing. The scouring pattern is a function of the water depth, wave conditions, sediment characteristics, and breakwater configuration and reflection characteristics as described by Arneborg et al (1996). A simultaneous current flow at the breakwater will significantly influence the scouring.

Scouring in front of a berm breakwater constructed without a sufficient scour protection layer may result in berm stones to be moved into the scour hole, which will lead to further reshaping of the protecting berm. Physical 2D model tests were made for qualitatively studying the scour development in front of a berm breakwater. A total of four test series were carried out in order to study the influence on the scouring and breakwater performance of varying wave steepness and of two types of scour protections, see Juhl and Archetti (1997).

A summary of the findings is presented below:

- The scouring was found to increase by decreasing the wave steepness from 0.05 to 0.03. A significant increase in the extent of the scour hole was found by decreasing the wave steepness from 0.03 to 0.02.
- Subsidence of berm stones into the sandy seabed was found for the profiles without a scour protection layer.
- Introduction of a scour protection layer moved the scour hole out in front of this and no subsidence of berm stones into the sandy seabed was found. Consequently, the reshaping of the berm and thus also the berm recession were reduced.

- During reshaping of the scour protection material placed as an extension of the berm, some of this finer material was mixed into the berm material. The resulting reduced permeability led to increased wave run-up and overtopping.

Acknowledgements

The research project on Berm Breakwater Structures was co-sponsored by the European Commission under the second research and development programme on Marine Science and Technology, MAST II (contract MAS2-CT94-0087).

References

- Alikhani, A; Tomasicchio, GR; Juhl, J (1996): *Berm breakwater trunk exposed to oblique waves*. Proceedings of XXV Conference on Coastal Engineering, Orlando, USA.
- Andersen, OH; Juhl, J; and Sloth, P (1992): *Rear side stability of berm breakwaters*. Proceedings of the International Conference on Coastal Engineering, Venice, Italy.
- Arneborg, L; Asp Hansen, E; Juhl, J (1996): *Modelling of local scour in front of vertical breakwaters*. Submitted to Coastal Engineering.
- Espedal, G; and Lothe, A (1994): *The Mortavika breakwater - a harbour exposed to severe weather*. Proceedings of the Conference 'Straight crossings' in Ålesund, Norway.
- Frigaard, P; Sand Jensen, M; Hald, T (1996): *Berm breakwater design - influence of rock shape* (not published).
- Gent, MRA van (1995): *Wave interaction with permeable coastal structures*. PhD thesis, Delft University of Technology, ISBN 90-407-1182-8, Delft University Press.
- Gent, MRA van (1995): *Wave interaction with berm breakwaters*. Journal of Waterway, Port, Coastal and Ocean Engineering, Vol 121, No 5, pp 229-238, ASCE, New York.
- Gent, MRA van (1996): *Numerical modelling of wave interaction with dynamically stable structures*. Proceedings of the International Conference on Coastal Engineering, Orlando, USA (in press).
- Juhl, J (1997): *Influence of permeability and stone gradation* (not published).
- Juhl, J; Alikhani, A; Sloth, P; Archetti, R (1996): *'Roundhead stability of berm breakwater'*. Proceedings of the XXV Conference on Coastal Engineering, Orlando, USA.
- Juhl, J; and Archetti, R (1997): *Stability of toe protection and scour protection* (not published).
- Juhl, J; and Jensen, OJ (1995): *Features of berm breakwaters and practical experiences*. Proceedings of the Fourth International Conference on Coastal and Port Engineering in Developing Countries (COPEDEC IV), Rio de Janeiro, Brazil.
- Kobayashi, N and Wurjanto, A (1990): *Numerical model for waves in rough permeable slopes*, Journal of Coastal Research, S17, Spring 1990, pp 149-166.

Lamberti, A; Tomasicchio, GR; and Guiducci, F (1994): *Reshaping breakwaters in deep and shallow water conditions*. Proceedings of the International Conference on Coastal Engineering, Kobe, Japan.

Lissev, N; and Tørum, A (1996): *Influence on the core configuration on the stability of berm breakwaters*. Proceedings of the XXV Conference on Coastal Engineering, Orlando, USA.

Meer, JW van der (1992): *Stability of the seaward slope of berm breakwaters*. Journal of Coastal Engineers, 16 (1992), pp 205-234.

Meer, JW van der; and Veldman, JJ (1992): *Singular points at berm breakwaters: scale effects, rear, roundhead and longshore transport*. Journal of Coastal Engineers, 17 (1992), pp 153-171.

Montgomery, RJ; Hofmeister, GJ; and Baird, WF (1987): *Implementation and performance of berm breakwater design at Racine*. Seminar on Berm Breakwaters: Unconventional Rubble-Mound Berm Breakwaters, Ottawa, Canada.

Sigurdarson, S; and Viggosson, G. (1994): *Berm breakwaters in Iceland, practical experiences*. Hydro-Port'94, International Conference on Hydro-Technical Engineering for Port and Harbour Construction, Japan.

Sigurdarsson, S; Viggosson, G; Benediktsson, S; and Smarason, OB (1995): *Berm breakwaters and quarry investigations in Iceland*. Proceedings of the Fourth International Conference on Coastal and Port Engineering in Developing Countries (COPEDEC IV), Rio de Janeiro, Brazil.

Tørum, A (1994): *Wave-induced forces on armour unit on berm breakwaters*. Journal of Waterway, Port, Coastal, and Ocean Engineering, Vol 120, No 3.

Tørum, A; Mathiesen, M; Vold, S; Bjørdal, S; and Næss, S (1990): *Årviksand fishing port breakwater extension*. Proceedings of the 27th PIANC Congress, Osaka, Japan.

Westeren, K; and Tørum, A (1996): *Irregular wave induced forces on armour units on berm breakwaters*.



Wave Loading and Overtopping on Vertical wall breakwaters in Multidirectional Breaking Seas

by

KOFOED J. P., GRØNBECH J., HALD T.,
BURCHARTH H. F. and FRIGAARD P.
Hydraulics and Coastal Engineering Laboratory
Dept. of Civil Engineering, Aalborg University, Denmark

Dansk Vandbygningsteknisk Selskabs seminar om
"Nyere metoder til projektering af moler"
Aalborg Universitet, den 25. marts 1998

ABSTRACT

The present paper concerns the results and findings of a physical study on wave impacts on vertical caisson breakwaters situated in irregular, multidirectional breaking seas. The study has taken place as part of the framework programme "Dynamics of Structures" financially supported by the Danish Technical Research Council, during the period of January 97 to December 97. The tests were carried out in the 3D wave basin at the Hydraulics and Coastal Engineering Laboratory, Aalborg University. The objective of the study was to assess the effects of wave obliquity and multidirectionality on the wave induced loading and overtopping on caisson breakwaters situated in breaking seas. Regarding the wave forces only minor differences between breaking and non breaking waves in deep water were observed, and it was found that the prediction formula of Goda also seems to apply well for multidirectionally breaking waves at deep water. The study on wave overtopping showed that the 3D wave overtopping formula suggested by Franco et al., 1995b, predicts the wave overtopping reasonable well for both non breaking and breaking waves at deep water.

1. INTRODUCTION

Attention has been addressed to the effects of wave obliquity and multidirectionality on wave loads and wave overtopping on vertical caisson breakwaters situated in non-breaking seas. Within the joint European (MAST-LIP-TAW) research project, a 3D model investigation was carried out at Delft Hydraulics to assess these effects. The results have been published by several researchers, among them Franco et al., 1995a and Franco et al., 1995b. Several researchers have investigated the effects of wave breaking and impact forces on vertical structures in the past, and it is still generally acknowledged that the impact loading of vertical structures is the main damage source, see Oumeraci et al., 1995. The research work on impact forces has mainly been based on 2D breaking waves. So far, no attention has been paid to the effects of wave obliquity and multidirectionality on the wave loads and wave overtopping on caisson breakwaters placed in deep water breaking seas. The effects of wave obliquity and multidirectionality on the wave loads were investigated by measuring the wave induced pressure at 50 locations on a 6.0 meter wide caisson breakwater model, enabling determination of the horizontal force in one section as well as the lateral distribution of the horizontal force. The results and findings on the effects on the lateral distribution of the horizontal force are not included in this paper, but is published in the test report Results of Caisson Breakwater Tests in Multidirectional Breaking Seas. The present paper intends to stress the effects of wave obliquity and multidirectionality on the horizontal force in one vertical section.

The wave overtopping was measured on a 1.0 meter wide section of the caisson breakwater model, and the findings regarding the effects of wave obliquity and multidirectionality of the waves are presented in terms of the mean average overtopping discharge.

2. EXPERIMENTAL SETUP

The caisson breakwater model was constructed in plywood and as the wave induced uplift pressures at the caisson bottom was not considered in the study the caisson was placed on a smooth concrete berm. The cross section of the model is seen in Figure 1, and as it appears a crest element is placed on the top of the model in order to enabling a variation of the crest height. The size of the model does not refer to any particular prototype structure. However, a Froude scaling of 1:20 - 1:25 seems appropriate for this type of structures. In order to generate a sea state representing breaking waves in deep water in front of the caisson model, the berm was constructed with a relatively short 1:5 slope as seen in Figure 1.

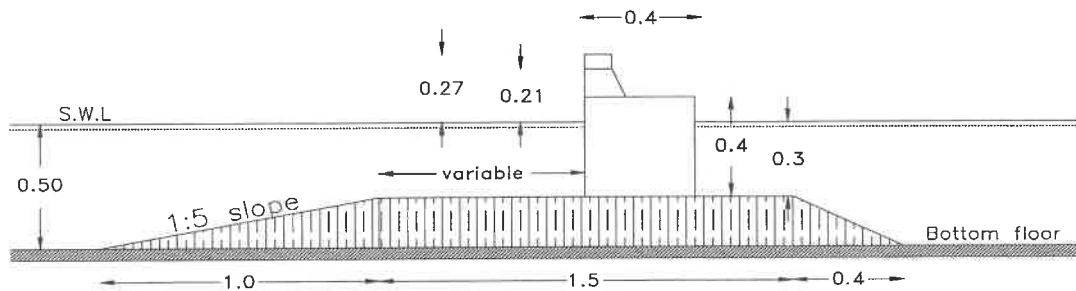


Figure 1 - Cross section of caisson model(s).

For harbor type structures situated at deep water, the percentage of breaking waves in a storm event depends on the structure location and at the wave climate at this location. However, for this study it is decided to keep the number of breaking waves at about 5 to 10 per cent of the total number of waves. Using the numerical wave transformation model "MildSim", developed at the Hydraulics & Coastal Engineering Laboratory at Aalborg University, tests with 2D irregular waves with a significant wave height of 0.18 m and a peak period at 1.2 s showed that about 6 to 7 per cent of the waves are breaking.

Due to the wave diffraction processes around the two ends of the breakwater, the sea states in the vicinity of the ends would be disturbed during the tests. Therefore, since the lateral distribution of the horizontal force was to be considered in this study, it was important that the sea state in front of the test section not was influenced by the diffraction at the two ends. The numerical wave transformation tests showed, depending on the wave obliquity, that the sea state at the two ends was disturbed at a distance corresponding to approximately 1-1.5 times the wavelength. Therefore, to take into account the disturbance from the diffraction processes, and to obtain a width of the test section corresponding to one wavelength, the total width of the model should be about 6 meter.

The experiments were carried out in the 3D deep water wave basin at the Hydraulics & Coastal Engineering Laboratory, Aalborg University. The wave basin is capable of generating irregular multidirectional waves. A plan view of the wave basin and the caisson model is seen in Figure 2.

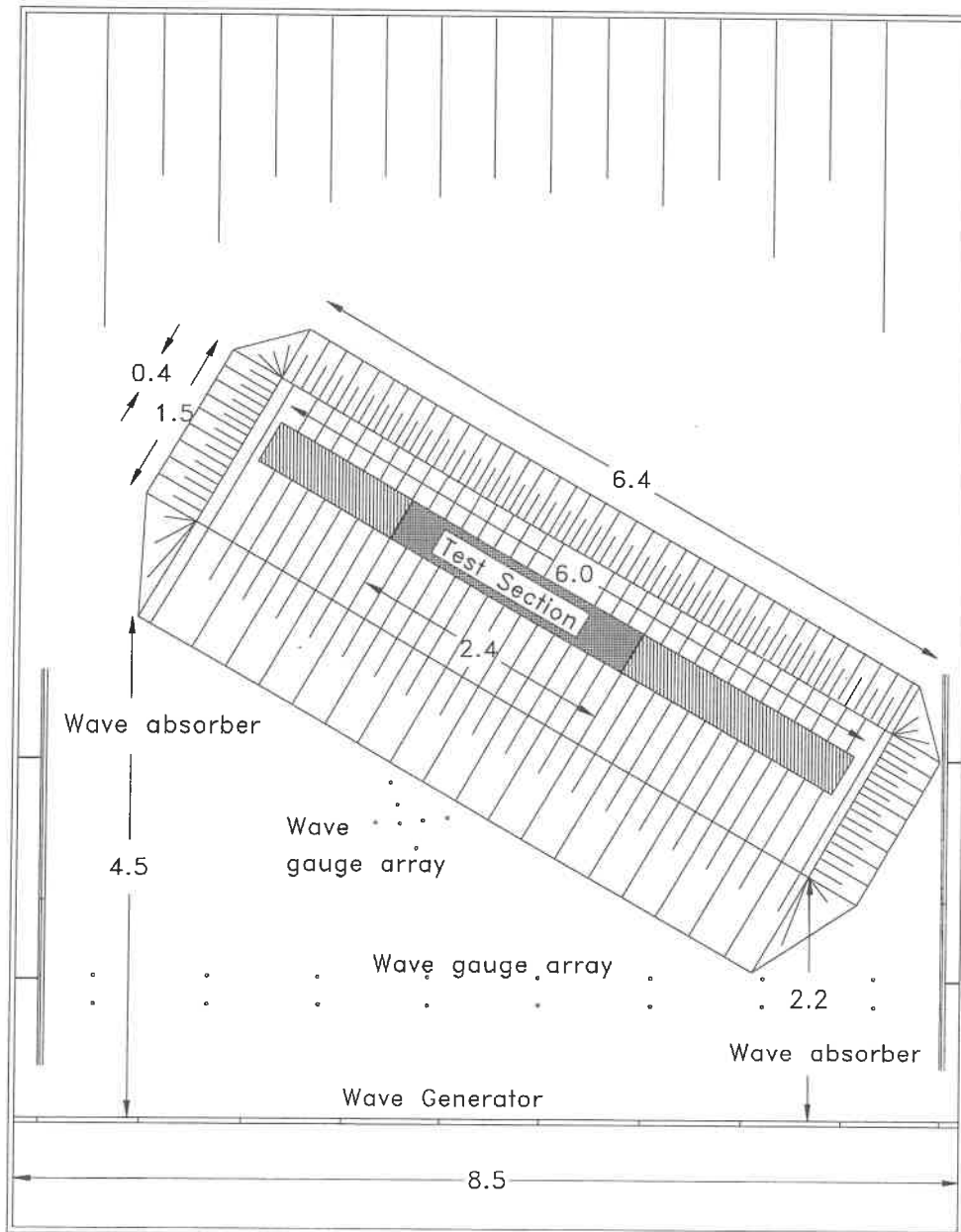


Figure 2 - Plan view of the 3D wave basin layout. Measures in meters.

Although the amount of wave energy passing through the gabs between the caissons and the side walls of the basin is small compared with the reflected wave energy, the rear end of the basin is equipped with a spending beach constructed of gravel material. Along the side walls of the basin, vertical steel absorbers are placed to damp any cross modal activity occurring during the tests. Due to limitations in the wave generation, the obliquity of the generated waves should be kept less than 30° , and therefore the model was placed under 60° with the wave paddles of the wave generator, as seen in Figure 2. Due to the high reflection from the caissons, a three dimensional active wave absorption system is applied to avoid too much re-reflected wave energy

in front of the caissons. The active absorption system operates on-line by digital filtering of surface elevations measured in 16 individual positions in the wave field in front of the wave paddles, as seen in Figure 2. The wave absorption system is in its complete form outlined in Hald and Frigaard, 1997. In front of the model the wave field is measured by an array of 7 wave gauges, see Figure 2. The wave gauges are placed at deep water, i.e. in front of the 1:5 slope, which is about 1.5 meter, seaward the model. The incident wave field was estimated based on the Bayesian Directional spectrum estimation Method (BDM). Furthermore, the caisson has been instrumented with two wave gauges on the front. Thus, by assuming full reflection, and therefore neglecting that some water is overtopping, the water height can also be estimated at the structure.

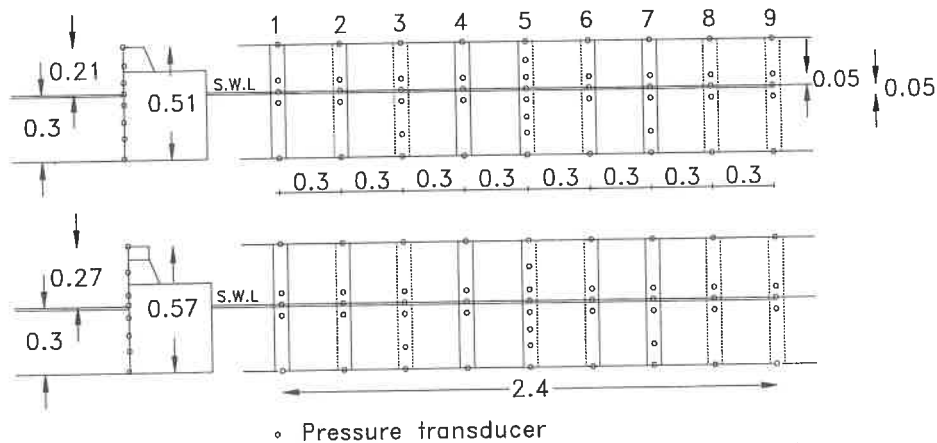


Figure 3 - Instrumentation of the caisson model. Measures in meters.

The wave pressures were measured by a set of 50 pressure transducers placed as shown in Figure 3. The position of the pressure transducers enables the study of the vertical distribution of the horizontal pressure in different sections along the caisson model. By means of these vertical distributions of the horizontal pressures, the lateral distribution of the horizontal forces can be studied, and not only the lateral distribution of the horizontal pressures. This is important due to the unknown correlation between the lateral distribution of the horizontal pressure and the lateral distribution of the horizontal force.

Sideways, the pressure transducers are placed within a distance of 0.3 m enabling the study of the vertical distribution of the horizontal pressure in 9 sections along the 2.4 meter wide test section. A row of pressure transducers is placed at still water level. Furthermore, a row of transducers is placed 5 cm above and 5 cm below the still water level.

The wave overtopping measurements concern the determination of the mean discharge of a test sequence, the number of wave overtopping events and finally the determination of the water volume in each of the individual overtopping events. In this study, the wave overtopping is determined by recording the water level in a water tank, in which all the overtopping water is collected. The collected overtopping water corresponds to a width of 1.0 m of the test section. The amount of water collected in

the tank is determined by recording the water level in the tank during the tests. The water level is measured by a set of two wave gauges placed in the water tank. Due to the irregularity of the waves, the amount of overtopping water varies from wave to wave, and in order to obtain reasonable increments of the water level in the tank even for the smallest wave overtopping events, the cross section area of the tank must be kept relatively small.

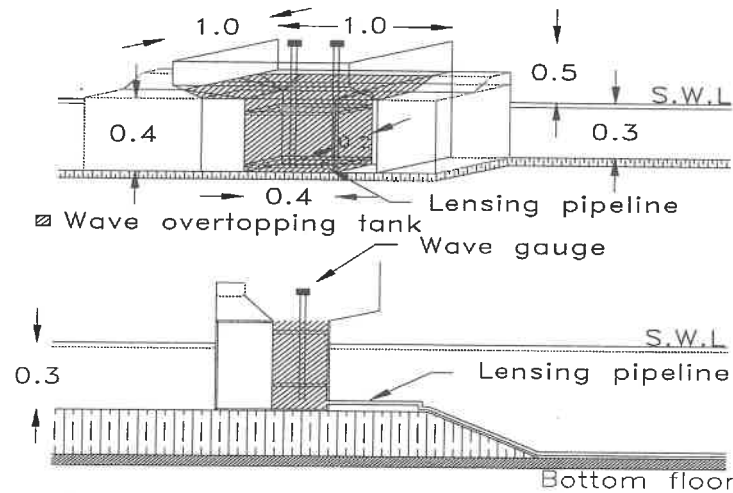


Figure 4 - Wave overtopping measuring device. Measures in meters.

3. TEST CONDITIONS

As the main objective of the study was to assess the effect of wave obliquity and multidirectionality the changes on test conditions were mainly the incident mean direction of the waves and the directional spreading of the waves, i.e. the energy distribution around the mean direction of the waves. The mean direction or the incident angle of wave attack was varied from 0° (head on waves) to 50° for some of the tests. A cosine squared ($\cos^{2s}(\theta/2)$) spreading function with fixed s -values of 10 and 29 was used in the tests, which corresponds to standard deviations of 25° and 15° , respectively. See Frigaard et al., 1997. The incident target significant wave height was fixed at 0.16 m for the non breaking waves and 0.18 m for the breaking waves. A JONSWAP wave spectrum with a peak enhancement factor of 3.3 and a peak period of 1.2 sec was applied in all the tests, giving a steepness at 0.07 for non breaking waves and 0.08 for breaking waves. To obtain an adequately statistically validity of the test results, rather long test series were performed with no test series having less than 1800 waves. In table 1, the various target parameters of the test series are shown.

Wave spectrum	JONSWAP, $\gamma = 3.3$
Peak period, T_p	1.2 sec
Significant wave height	0.16 m to 0.18 m
Crest freeboard, R_c	0.21 and 0.27
Water depth, h_d	0.3 m
Angle of wave attack, θ	$0^\circ, 15^\circ, 30^\circ, 45^\circ, (60^\circ)$
Type of spreading	Cosine squared, with $s=10$ and $s=29$

Table 1 - Wave parameters.

Regarding this paper, the results are all based on the test cases listed below and with a crest freeboard of 0.27.

- 3D non breaking waves, $H_s = 0.16$ m, $\sigma = 15^\circ$, $\theta = 0^\circ$ to 40°
- 3D non breaking waves, $H_s = 0.16$ m, $\sigma = 25^\circ$, $\theta = 0^\circ$ to 40°
- 3D breaking waves, $H_s = 0.18$ m, $\sigma = 15^\circ$, $\theta = 0^\circ$ to 48°
- 3D breaking waves, $H_s = 0.18$ m, $\sigma = 25^\circ$, $\theta = 0^\circ$ to 40°

4. WAVE FORCE ANALYSIS

The horizontal wave forces are determined by a linear integration of the measured pressure time series. The horizontal forces presented below are all based on the pressure measurements of section 5, see Figure 3, where 8 pressure measurement positions are used representation of the vertical distribution of the horizontal pressure. In Figure 5, a plot of the measured horizontal pressures are shown along with the calculated force time series. The plot shows 10 sec of the test series with head on breaking waves and a spreading corresponding to $\sigma = 25^\circ$.

The pressure time series are sampled at 800 Hz, and only the maximum peaks within one wave period are used for the determination of the probability distribution of the horizontal forces.

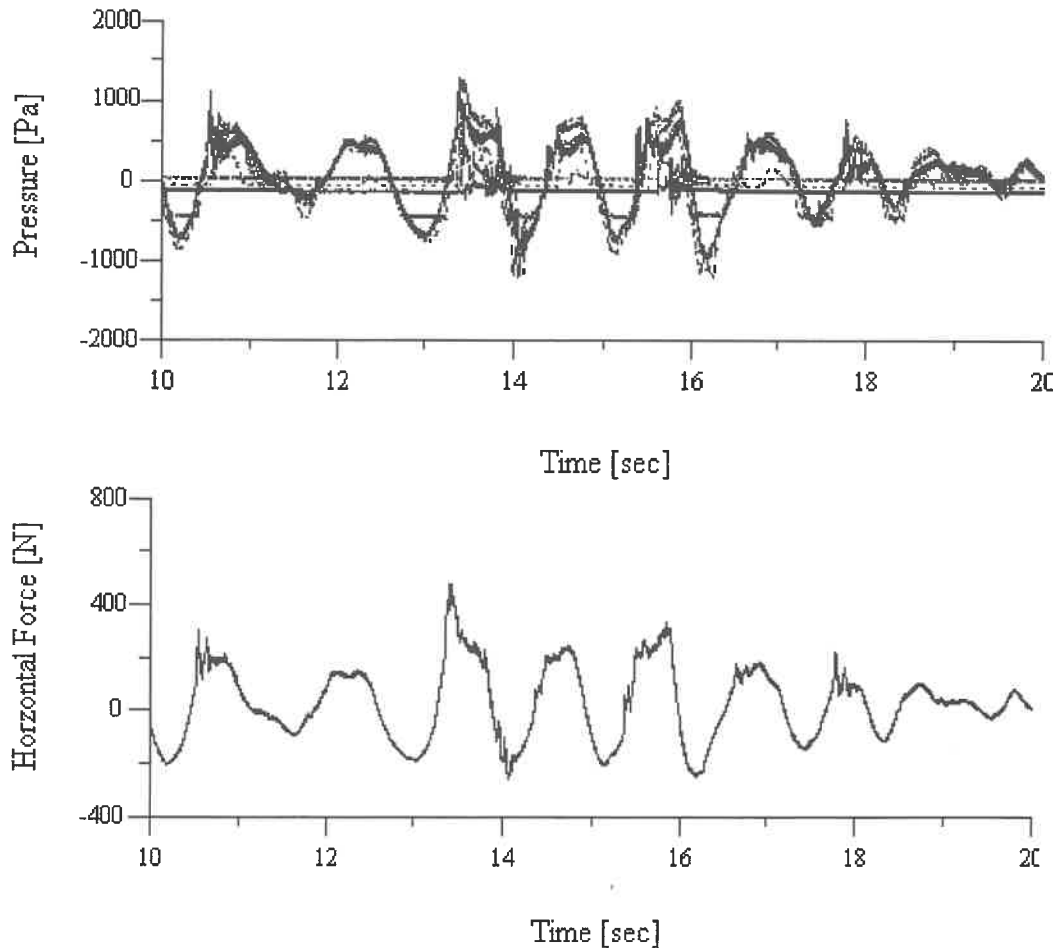


Figure 5 - Pressure record with corresponding force time series.

In the evaluation of the forces determined in the performed tests the wave pressure formulae developed by Goda (see Goda, 1974) are used as a reference. The formulae are based on model tests in head-on waves, but have been modified on the basis of work by Tanimoto, 1976, to include also oblique waves. The formulae also include the effect of breaking waves to the extent of normal accidental (not provoked by a steep sea bed or structural configurations) wave breaking. In Figure 6 the definition sketch for the Goda formulae is shown.

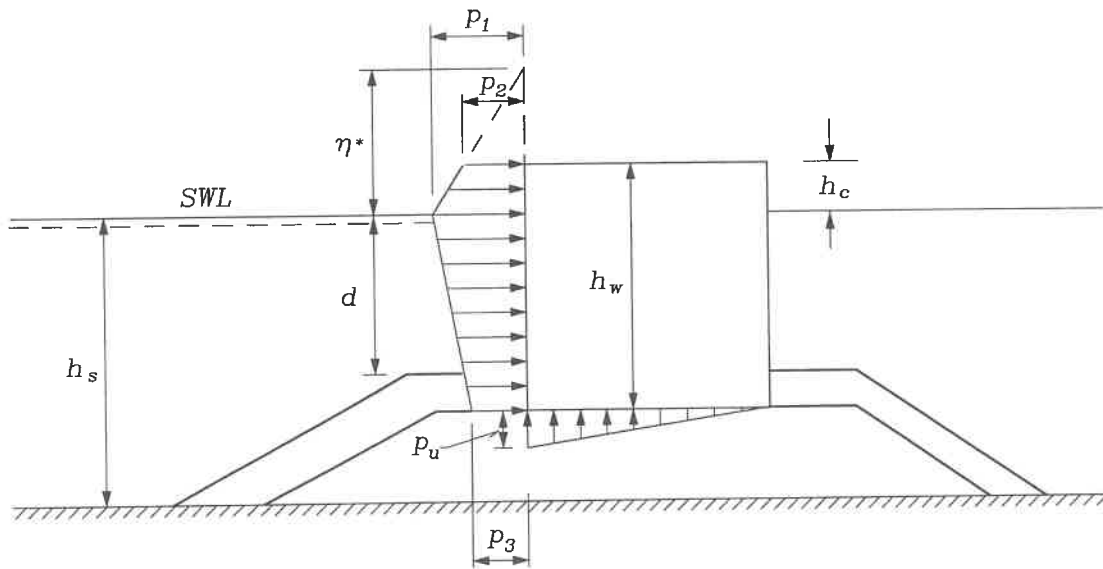


Figure 6 – Definition sketch for the Goda formula for wave induced pressure under a wave crest.

According to Goda the wave induced pressures can be calculated by use of the following expressions:

$$\eta^* = 0.75(1 + \cos\beta)H_{\text{design}}$$

$$p_1 = 0.5(1 + \cos\beta)(\alpha_1 + \alpha_2 \cos^2 \beta) \rho_w g H_{\text{design}}$$

$$p_1 = \begin{cases} \left(1 - \frac{h_c}{\eta^*}\right) & \text{for } \eta^* > h_c \\ 0 & \text{for } \eta^* \leq h_c \end{cases}$$

$$p_3 = \alpha_3 p_1$$

Where

β angle of incidence of waves (angle between wave crest and front of structure)

H_{design} design wave height defined as the highest wave in the design sea state at a location just in front of the breakwater. If seaward of a surf zone a value of $1.8 H_s$ might be used corresponding to the 0.1 % exceedence value for Rayleigh distributed wave heights. If within a surf zone at a distance $5 H_s$ seaward the structure.

L wave length corresponding to the significant wave period $T_s \approx 1.1 T_m$, where T_m is the average period.

$$\alpha_1 = 0.6 + \frac{1}{2} \left[\frac{4\pi h_s / L}{\sinh(4\pi h_s / L)} \right]^2$$

$$\alpha_2 = \text{the smaller of } \frac{h_b - d}{3h_b} \left(\frac{H_{\text{design}}}{d} \right) \text{ and } \frac{2d}{H_{\text{design}}}$$

$$\alpha_3 = 1 - \frac{h_w - h_c}{h_s} \left[1 - \frac{1}{\cosh(2\pi h_s / L)} \right]$$

h_b water depth at a distance of $5 H_S$ seaward of the breakwater front wall.

By integration of the pressure over the vertical wall the horizontal wave force F_{Goda} is found.

In order to compare the test results with the F_{Goda} found from the prediction formula of Goda, the statistical force parameter $F_{1/250}$ is calculated from each of the force time series. Due to the applied number of waves this force is calculated as an average value of the 7 largest forces found by the analysis of the force time series. In order to compare the results of the tests with non breaking waves with the tests with breaking waves, the calculated $F_{1/250}$ forces are normalized by the predicted Goda force corresponding to the actual wave obliquity and wave height measured by the wave gauges placed at deep water. Such normalization is however not unambiguous because due to shoaling the waves at the model structure are quite different from the recorded waves at deep water, whereas this was not the case in the tests of Goda. For this reason, alternative normalization is presented in Section 6 of this paper.

The results of the normalization based on the recorded non shoaling waves are shown in Figure 7. Deeper interpretation of the results should not be done because of the normalization as discussed above. However, if this is disregarded it can be seen that the formula of Goda seems to apply well for both the non breaking as well as the breaking waves. Most of the calculated forces are seen to deviate less than 10% from the Goda predicted forces. Apparently, the Goda formula applies best in case of waves within the range of 0 to 35 degrees. However, the pronounced scatter for waves with larger obliquity than 35 degrees could also be due to the relative error of these forces.

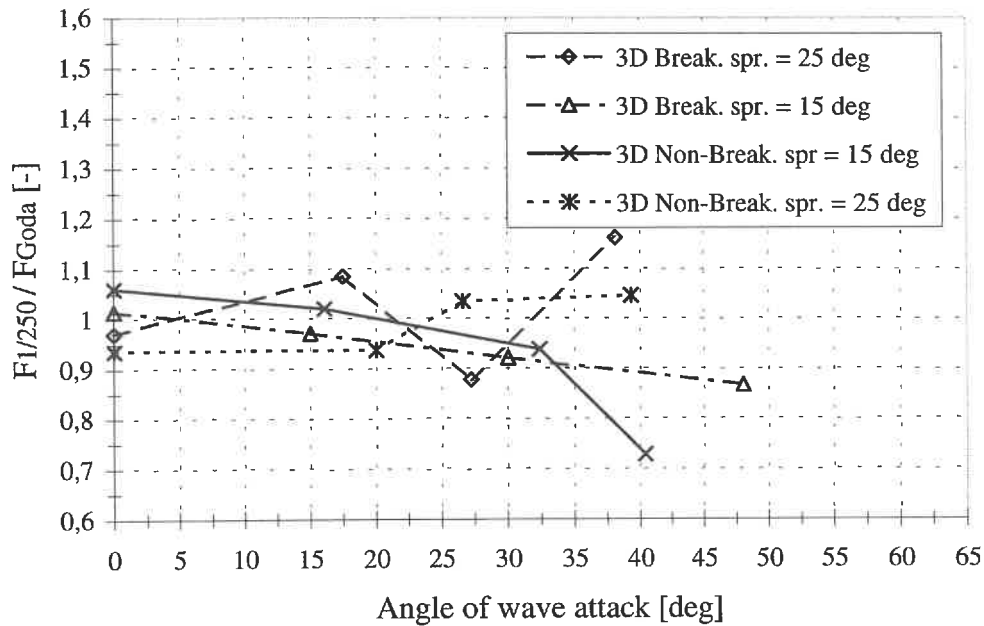


Figure 7 - Comparison with Goda predicted forces based on recorded non shoaling waves at a distance from the structure.

Franco et al. 1995a found for non breaking waves that the forces predicted by the formula of Goda, which does not take into account the multidirectionality of the waves, should be reduced with about 10%. This trend is, however, not seen in the results of this study.

One would expect the breaking waves to produce higher forces than the non breaking waves due to the impact forces. This is also seen if the shoaling waves at the structure are used as reference waves instead of the non shoaling waves, cf. Section 6.

5. WAVE OVERTOPPING ANALYSIS

For each test series, the wave overtopping was determined by recording the water level in the overtopping tank. The water levels were measured by a set of two wave gauges during the tests, and each of the overtopping events were recorded as an increase in water level. In Figure 8

the measured overtopping rate is shown for the test with head on non breaking waves, and a spreading corresponding to $\sigma = 25^\circ$. The total amount of water collected in the water tank during a complete time series is determined by calculating the water volume of each of the individual overtopping events.

The non dimensional mean overtopping discharge is defined as:

$$Q = \frac{q}{\sqrt{gH_s^3}}$$

where

- q is the average wave overtopping discharge per meter structure length.
- H_s is the significant wave height.
- g is the gravity acceleration.

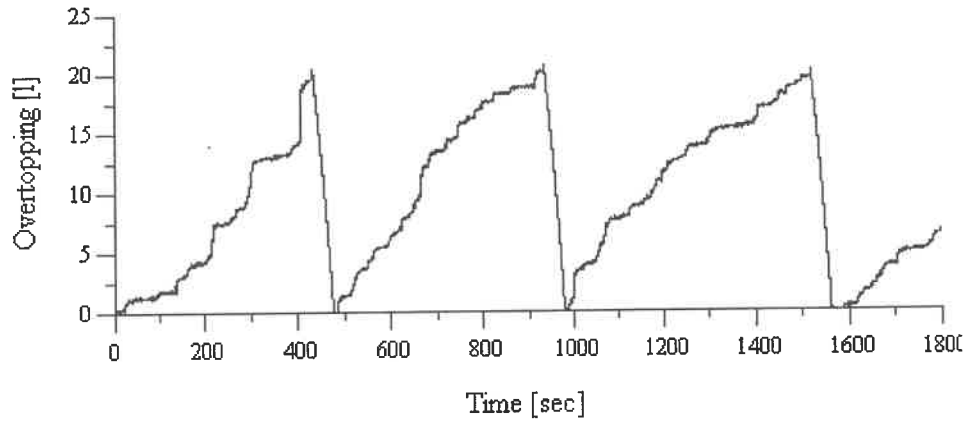


Figure 9 - Recorded wave overtopping time series.

The basic assumption, confirmed by many researchers, is that the main parameters influencing the wave overtopping performance, i.e. the significant wave height, the crest height and the average wave overtopping discharge are related through an exponential function as:

$$Q = ae^{\left(-b \frac{R_c}{H_s}\right)}$$

Based on more than 80 hydraulic model tests performed in the directional wave basin at Delft Hydraulics, Franco et al., 1995b, suggested the use of a = 0.082 and b = 3.0 for plain vertical structures exposed to head on waves. To take into account the effects of wave obliquity and multidirectionality a reduction factor was introduced to the non dimensional expression.

$$Q_p = ae^{\left(\frac{-b R_c}{\gamma H_s}\right)}$$

Through best fit regression analysis Franco et al., 1995b suggested the following relation between γ and the wave obliquity for multidirectional waves.

$$\begin{aligned} \gamma &= 0.83 && \text{for } 0^\circ \leq \theta \leq 20^\circ \\ \gamma &= 0.83 \cos(20^\circ - \theta) && \text{for } \theta \geq 20^\circ \end{aligned}$$

In Figure 9 the results of the 4 test cases are shown. The wave overtopping is expressed in terms of the measured average overtopping discharge Q_m normalized by the predicted average wave overtopping discharge Q_p .

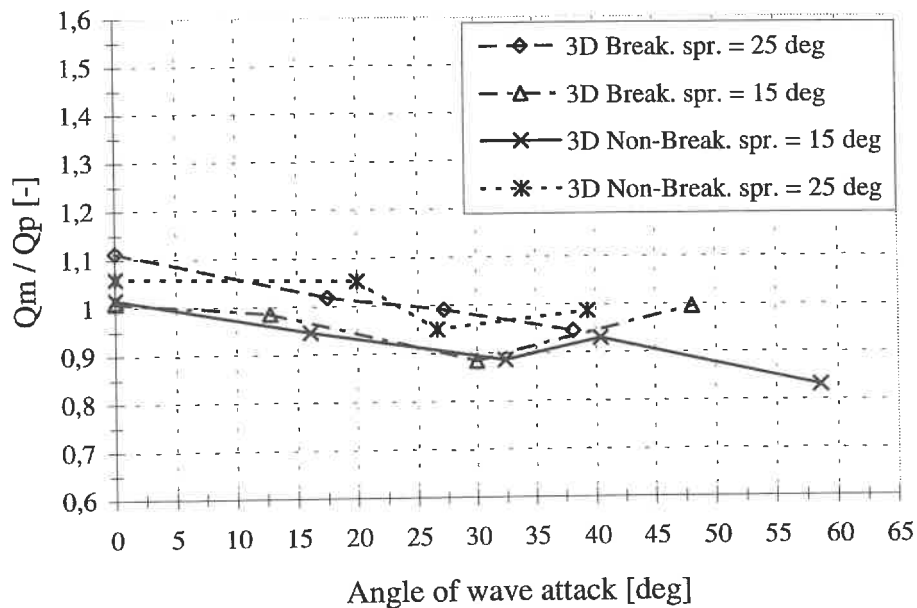


Figure 9 - Comparison of measured and predicted wave overtopping based on non shoaling waves at a distance from the structure.

As it appears, the suggested prediction formula of Franco et al., 1995b seems to apply well with most of the compared data deviating less than 10%. It is, however, observed that for angles of wave attack smaller than approximately 20° , the predicted wave overtopping tends to be smaller than the measured wave overtopping, whereas, the wave overtopping seems to be over predicted for angles of wave attack larger than approximately 20° .

Comparing the results of non breaking waves to the results of breaking waves, it is seen, that no apparent difference exist, indicating that in terms of 3D waves, it is not necessary to distinguish breaking waves from non breaking waves. However, it was visually observed during the tests with breaking waves that the breaking process causes a significant increase in spray, which of course should be considered in the prototype case.

6. RESULTS BASED ON WAVE HEIGHTS AT THE STRUCTURE

As described in Section 2 it is the sloping bottom in front of the caisson that introduces the wave breaking in the breaking waves test series. This means that the wave height in these tests varies as the waves approaches the caisson. Thus, the wave heights determined by the BDM analysis of the waves measured at the deep water is not the wave heights of the breaking waves as they reach the caisson. This wave height at the structure is very difficult to estimate, due to the high amount of reflection. But by using the wave gauges placed on the front of the caisson, the wave height at the structure has been estimated. Using these wave heights Figures 7 and 9 will change into the plots shown in Figure 10 and Figure 11.

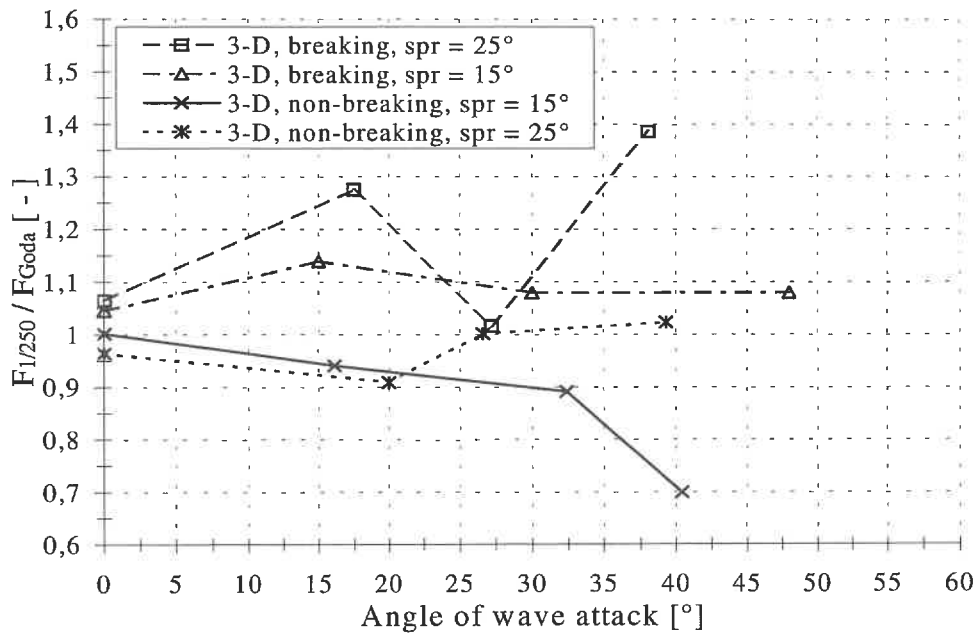


Figure 10 – Comparison with Goda predicted forces (wave heights at the structure).

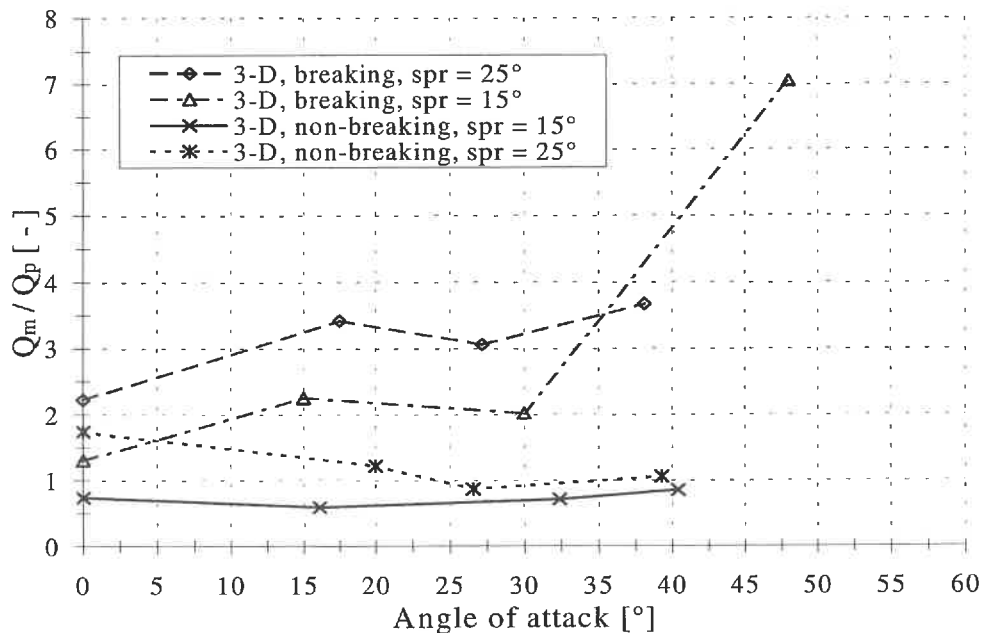


Figure 11 – Comparison of measured and predicted wave overtopping (wave heights at the structure).

The new plots show more scatter than the previous plots due to the poorer estimation of wave heights. As expected the breaking waves loose more energy on the slope than the non breaking waves, and the normalized forces and overtopping rates are therefore increased for the breaking waves compared to the previous plots, while the

rates for the non breaking waves are relatively unaltered. These results seem more logic than those presented in Figure 7.

7. CONCLUSION

Regarding the effects of wave obliquity and multidirectionality on wave loading and wave overtopping on caisson breakwaters only minor differences were observed between breaking and non breaking waves when the results were normalized with deep water wave heights. In the case where the forces were normalized with wave heights at the structure larger wave force rates were observed for the breaking waves.

Despite the observed amount of spray during the tests, the measured overtopping rates for breaking waves seem to agree well with the prediction formula for 3D non breaking waves given by Franco et al., 1995b as long as the deep water wave heights were used. Using the wave heights at the structure results in significantly larger overtopping rates for the breaking waves, than predicted by the overtopping formula by Franco for non breaking waves. The rates for the non breaking waves were better predicted by the Franco formula.

8. ACKNOWLEDGEMENTS

This work has been carried out with support from the frame work programme *Dynamics of Structures* of the *Danish Technical Research Council*.

8. REFERENCES

- Battjes, J. A. and Jansen, J. P. F. M. (1978). *Energy loss and set-up due to breaking of random waves*, Proceedings of the 16th International Conference on Coastal Engineering, Hamburg.
- Hald, T. and Frigaard, P. (1997). *Alternative Method for Active Absorption in Multidirectional Waves*. IAHR seminar on Multidirectional Waves and their Interaction with Structures, 27th IAHR Congress, San Francisco, 10-15 August 1997.
- Franco, C., Franco, L., Passoni, G., Restano, C., van der Meer, J.W. (1995a). *The effect of wave obliquity and short-crestedness on the horizontal and uplift forces on caisson breakwaters*. Final proceedings, MAST II, (MAS2-CT92-0047), MCS-Project: Monolithic (Vertical) Coastal Structures, Paper 4.8, 22 pp.
- Franco, C., Franco, L., Restano, C., van der Meer, J.W. (1995b). *The effect of wave obliquity and short-crestedness on the overtopping rate and volume distribution on caisson breakwaters*. Final proceedings, MAST II, (MAS2-CT92-0047), MCS-Project: Monolithic (Vertical) Coastal Structures, Paper 4.9, 37 pp.
- Frigaard, P., Helm-Petersen, J., Klopman, G., Stansberg, C. T., Benoit, M., Briggs M. J., Miles, M., Santas, J., Schäffer, H.A., Hawkes, P.J. (1997). Grønbech J., Hald, T. and Frigaard, P., Burcharth H. F. (1997). *Wave Loading and Overtopping on Caisson Breakwaters in Multidirectional Breaking Seas*. IAHR seminar on Multi-directional

Waves and their Interaction with Structures, 27th IAHR Congress, San Francisco, 10-15 August 1997.

Goda, Y., 1974. *A new method of wave pressure calculation for the design of composite breakwater*. Proc. 14th Int. Conf. Coastal Eng., Copenhagen, Denmark.

IAHR List of Sea State Parameters. IAHR seminar on Multidirectional Waves and their Interaction with Structures, 27th IAHR Congress, San Francisco, 10-15 August 1997.

Oumeraci, H., Hewson, P., Juhl, J. and van der Meer, J.W. (1995). MCS-Project: *Multi-Disciplinary Research on Monolithic Coastal Structures*, Final proceedings, MAST II, (MAS2-CT92-0047), MCS-project: Monolithic (Vertical) Coastal Structures. Papers Task 1-2.

Results of Caisson Breakwater Tests in Multidirectional Breaking Seas (Internal Laboratory Test Report). Hydraulics and Coastal Engineering Laboratory, Dept. of Civil Engineering, Aalborg University, Denmark, December 1997.

Tanimoto, K., 1976. *Wave forces on a composite-type breakwater*. Proc. 1976 Annual Res. Present. of Port and Harbour Research Institute, Japan (in Japanese).



Stability of Reshaping Breakwaters with Special Reference to Stone Durability

Dansk Vandbygningsteknisk Selskabs seminar om
"Nyere metoder til projektering af moler"
Aalborg Universitet, den 25. marts 1998

Stability of Reshaping Breakwaters with Special Reference to Stone Durability

P. Frigaard ¹, T. Hald ¹, H.F. Burcharth ¹, Sigurdur Sigurdarson ²,

1 Introduction

Traditionally, conventional rubble mound breakwaters are designed with stable armour units, and consequently, very large stones or even artificial armour units are required. Reshaping breakwater designs allow reshaping of the seaward slope thus involving stone movements. Ultimately, dependent on the degree of safety in the design, this reshaping process might end up in a stable profile where no changes in the cross sections occur even though stone movements are allowed.

Unfortunately, large movements of the protecting stones during the structural lifetime in combination with high stone velocities inherently cause some breakage and abrasion of the individual stones and thereby also reduced stability. In order to avoid excessive abrasion a high stone quality is demanded or larger stones must be applied when constructed. To allow the designer to account for abrasion and armour stone breakage due to the stone motion a description of the overall wave climate during the structural lifetime must be derived involving knowledge of transport rates, movement patterns, stone velocities and stone quality.

The main objective of the paper is to describe a tool enabling calculation of the anticipated armour stone movements. Also tensile stresses occur, as a result of stone against stone impact are discussed in order to make a more close connection between wave climate, stone movements and abrasion/breakage. Finally, a comparison to selected prototype structures is made to compare the armour stone movement model with visual profile observations of existing breakwaters.

¹Hydraulics & Coastal Engineering Laboratory, Aalborg University, Sohngaardsholmsvej 57,
DK-9000 Aalborg, Denmark, tel + 45 98158522, fax +45 98142555

²Icelandic Harbour Authority, Vesturvör, 2200 Kópavogur, Iceland

2 Longshore Transport Rate

Motion of stones along the active profile occurs when even slightly oblique waves attack the breakwater. This longshore motion has been evaluated in model tests performed by Burcharth and Frigaard (1988) and by van der Meer and Veldman (1992). Longshore transport was measured by observing the movements of stones layed out in coloured bands over the profile. To calculate the steady state transport the number of stones per wave passing a specific cross section at each sea state was divided by the number of waves. This ratio is termed the longshore transport rate S_x .

In Figure 1 the measured longshore transport rate is plotted against the mobility index $H_o T_{op} = \frac{H_o}{\Delta D_{n50}} T_p \sqrt{\frac{g}{D_{n50}}}$. The longshore transport rate seems to be described quite well by a power function as originally proposed by Vrijling (1991). The best fit of the power function to the data is:

$$S_x = 85 \cdot 10^{-6} (H_o T_{op} - 105)^2 \quad (1)$$

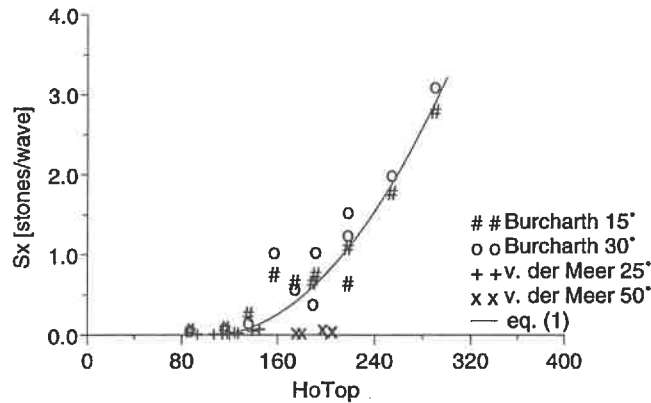


Figure 1: Longshore transport rate for reshaping breakwaters.

One might argue if the model in eq. (1) is too simple because of the absence of obliquity. The model can however, easily be adjusted to include the angle of incidence θ as discussed by Alikhani et al. (1996). Though the effect of obliquity is small.

Another aspect of the transport model is the obvious sensitivity to the onset of motion. From the model it is seen that sea states slightly above those corresponding to the onset of motion result in significant transport due the rapid increase of the power function. The latter comparison with prototype breakwaters outlines this sensitivity.

3 Longshore Distribution of Transported Material

To characterize the motion of the individual stones on the breakwater several video recordings from the model tests performed by Burcharth and Frigaard (1988) have

been reanalysed thoroughly.

The main conclusion based on the analysis of the video recordings was a typical zigzag motion pattern as shown in Figure 2. The typical upward motion of the stone follows

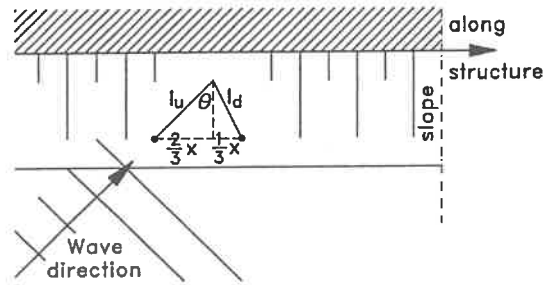


Figure 2: Typical pattern for single stone motion.

the wave direction θ whereas the downward motion is more controlled by gravity and an angle of half the angle of incidence seems more appropriate, see Figure 2. From Figure 2 the total travelled longshore distance can be calculated, assuming the upward and downward distances orthogonal to the structure in average are equal

$$l = l_u + l_d = \frac{2x}{3 \sin(\theta)} + \frac{x}{3 \sin(\frac{1}{2}\theta)} \quad (2)$$

To quantify the travelled longshore distance x the longshore distribution of the transported material has been derived from the same tests. The longshore distribution was derived from recordings of the number of stones positioned in 5 cm wide bands over the profile along the entire length of breakwater. From these recordings the number of stones per m, the position of the individual stones and the mean stone movements are calculated. Figure 3 shows an example from a single longshore transport test.

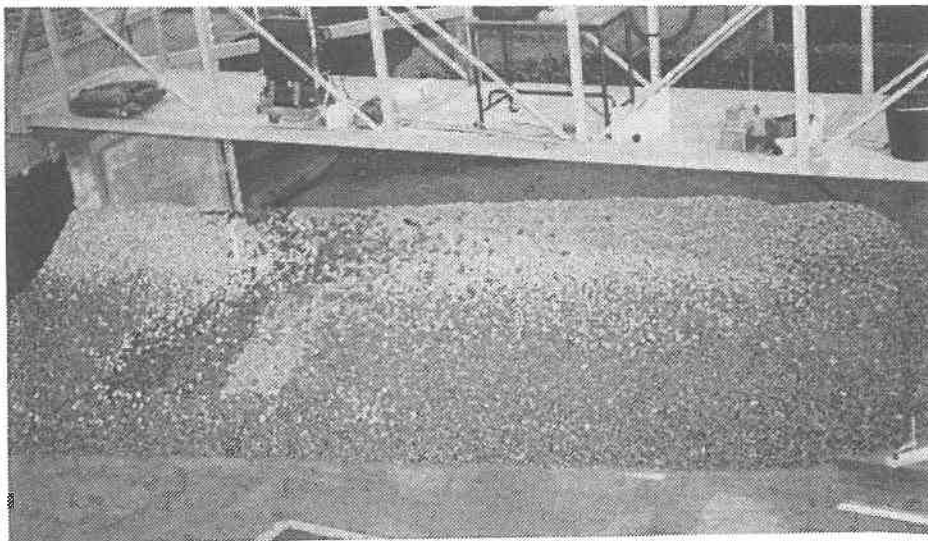


Figure 3: Example of the longshore distribution of transported material.

In Figure 4 the longshore distribution is shown for all 22 tested wave conditions. As abscissa the travelled longshore distance x is normalized by the mean travelled distance \bar{x} and as ordinate the stone distribution along the structure $s(x)$ (unit: stones/m per wave) is normalized by multiplying with $\frac{\bar{x}}{S_x}$.

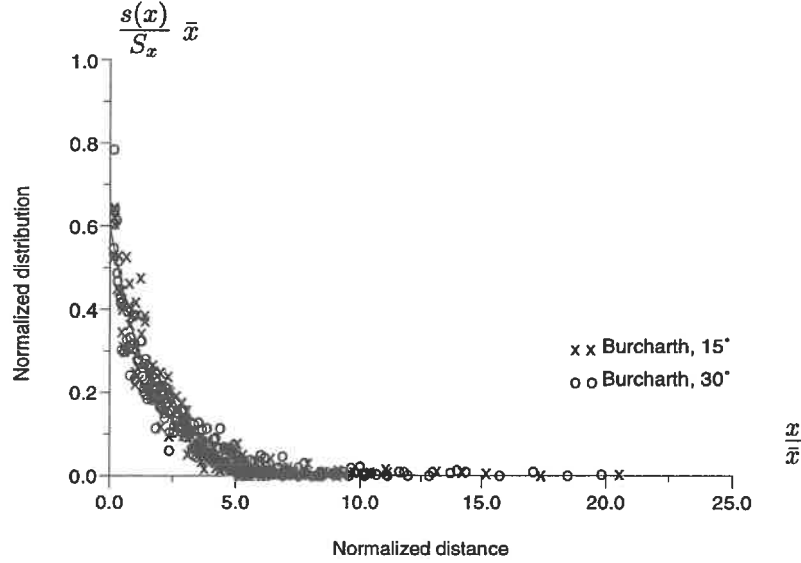


Figure 4: Longshore distribution of transported material.

From Figure 4 an excellent uniformity of the distribution curves for different wave climates and different angles of incidence is seen. Hence, a general exponential function can be fitted to the entire data set

$$s(x) = 0.6 \exp\left(-0.6 \frac{x}{\bar{x}}\right) \frac{S_x}{\bar{x}} \quad (3)$$

In Figure 5 the mean stone movement is plotted against the mobility index for all 22 tested wave climates.

The mean stone movement is described by

$$\bar{x} = 5.3 \cdot 10^{-3} D_{n50} (H_o T_{op} - 105) \sin^{0.8}(2\theta) \quad (4)$$

or by inserting the longshore transport model eq. (1).

$$\bar{x} = 0.6 D_{n50} \sqrt{S_x} \sin^{0.8}(2\theta) \quad (5)$$

Inserting the mean travelled distance in the expression for l , eq. (3) gives the average distance moved per wave. Knowing the wave height/period scatter diagram describing the storm history for a specific area, it is possible to calculate the accumulated average distance moved by each single storm during the structural lifetime simply based on the easy accessible parameters, H_s , T_p , θ , number of waves and D_{n50} .

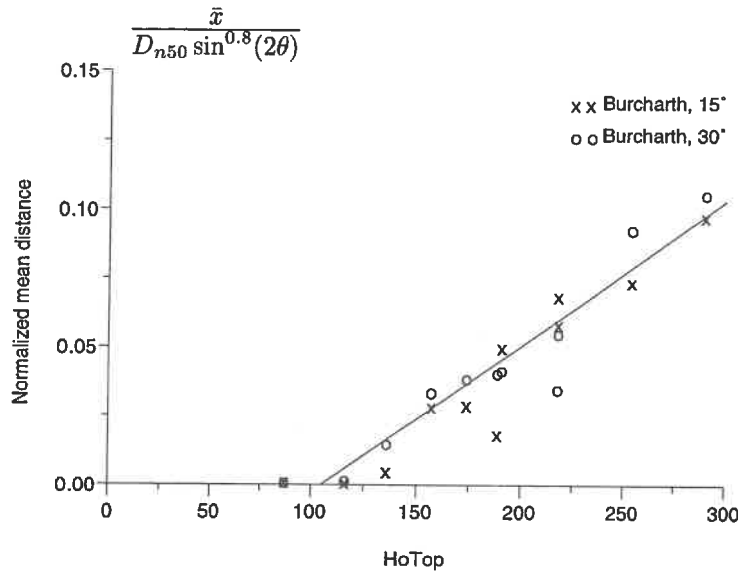


Figure 5: Mean stone movement versus the mobility index.

4 Impact Stresses in Armour Stones

A more close description than the stone motion connecting abrasion and breakage is to consider the tension stresses as a result of armour stones impacting armour stones during movements. This impact results in a shock wave propagating through the stone which is reflected at the edge structure resulting in a reverse propagating tensile stress wave. In case the tensile stress is too high the stone may crack depending on the stone quality.

In Figure 6 an idealized static model of a stone impact is sketched where the impacted stone remains at rest after impact. This is modelled by giving the stone infinity mass and zero velocity.

Applying Hertz' law to the system in Figure 6 results in the following equation

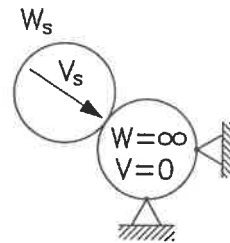


Figure 6: Static model

$$\sigma_{max} \propto \left(\frac{V_s^4}{D_{n50}} \right)^{0.2} E \quad (6)$$

where:

- W_s = Stone weight
- V_s = Stone velocity
- D_{n50} = Nominal stone diameter
- E = Young's Modulus

Generally, eq. (6) describes the stresses with reason: a high velocity yields high stresses, a small diameter signifies large curvature and thus larger impact stresses because of the smaller contact area, and finally the elasticity of the stone is described by Young's Modulus. Another aspect is that by simple Froude scaling larger stones gain larger stresses.

From the previously described tests typical stone velocities during both run-up and run-down were investigated by video. A typical stone velocity during run-down equals the wave run-down velocity whereas the typical stone velocity during run-up is approximately 50-70% of the wave run-up velocity.

Several attempts to assess the run-up and run-down velocities have been made showing that the maximum expected velocity can be well described by H_s and $\xi = g(\alpha, H_s, T_p)$. The overall maximum velocity is expected to be in the order of $1.5\sqrt{gH_s}$, e.g. Sawaragi, (1995).

From the above considerations it seems that the impact stresses can be described by the same easy accessible parameters as the movement model. The model still needs verification and calibration to physical model tests as well as prototype measurements. More work has to be done into these subjects.

5 Comparison with Prototype Breakwaters

For prototype comparison four sites are investigated with wave and structural characteristics given in the two tables 1 and 2. The accumulated travelled mean distance have been calculated followingly:

- Calculation of longshore transport rate from eq. (1) for each storm.
- Calculation of mean position moved from eq. (5) for each storm.
- Calculation of total travelled distance from eq. (3) for each storm.
- Summation of total travelled distance during lifetime.

Regarding

1. Caldera, Costa Rica: Estimated stone movements are rather small indicating little stone movements during lifetime. Observations show little profile changes but some broken stones. This might be due to the very poor quality of the stones.
2. St. Paul, Alaska: Vast stone movements are estimated. Total damage of the breakwater was observed.
3. Racine, Wisconsin: Long travelled distance is estimated. Severe breakage and large profile changes were observed.

4. Bolungarvik, Iceland: Little stone motions were estimated. Little profile changes observed.

It seems that the calculated distance corresponds very well to what might have happened. Though, it is clear that actual damage depends on both the travelled distance and the quality of the stones. In all, the comparison indicates that there is reason in relating breakwater damage to the armour stone motion.

6 Conclusions

A model enabling calculation of the accumulated travelled stone distance is given based on the easy accessible parameters such as H_s , T_p , θ , number of waves and D_{n50} . Furthermore, a short discussion focusing on the structural integrity is given. It is argued that the anticipated maximum tensile impact stresses can be evaluated by the same easily accessible parameters, though more work need to be done into this subject.

A comparison with selected prototype structures is presented showing that there is reason in relating breakwater damage to the armour stone motion. The comparison also signifies that only little transport should be allowed in order to avoid severe damage.

In areas where sufficiently large armour stones can be difficult to get, the stone quality is often poor. Even little stone transport or stone motion will in these cases result in breakage and abrasion of the armour stones. In practice it is difficult to avoid the abrasion and breakage of the armour stones and thus little transport should be allowed. The best possible design of the berm breakwater with maximum utilization of the quarry when possible is suggested by Sigurdarson et al. (1995). The aim is to minimize stone movements and make a more or less statically stable structure with little expected movements during the lifetime if suitable quarries are found in the vicinity. Still if stone movements occur on the berm breakwater no abrupt failure occur. By the berm concept up to 100% of the quarry yield can be used. This design approach have been used videly in Iceland with succes, see Sigurdarson and Viggosson (1994).

7 Acknowledgement

The work carried out is partly sponsored by the Danish Technical Research Council and partly by the Commission of the European Community under the MAST II Berm Breakwater Structure project, contract no. MAS2-CT94-0087.

8 References

- Alikhani, A., Tomasicchio, R. and Juhl, J., *Berm Breakwater Trunk Exposed to Oblique Waves*, to be published in Proc. 25th ICCE, Orlando, USA, 1996.
- Burcharth, H.F., Frigaard, P., *On 3-Dimensional Stability of Reshaping Breakwaters*, Proc. 21th ICCE, Malaga, Spain, 1988.
- CIRIA/CUR, *Manual on the Use of Rock in Coastal and Shoreline Engineering*, Published jointly by the Construction Industry Research and Information Association in the UK and the Centre for Civil Engineering Research, Codes and Specifications in the Netherlands, 1991.
- Lamberti, A., Tomasicchio, G.R., *Stone Mobility and Abrasion on Reshaping Breakwaters* to be published in Coastal Engineering, 1996.
- van der Meer, J.W., Veldman, J., *Singular Points at Berm Breakwaters: Scale Effects, Rear, Round Head and Longshore Transport*, Coastal Engineering, Vol. 17, Nos. 3,4, August 1992.
- Vrijling, J.K., Smit, E.S.P. and Swart, P.F., *Berm Breakwater Design; the Longshore Transport Case: a Probabilistic Approach*, ICE, Proc. Coastal Structures and Breakwaters, London, 1991.
- Sawaragi, T., *Coastal Engineering – Waves, Beaches, Wave-Structure Interactions*, Developments in Geotechnical Engineering, 78, Elsevier Science B.V., 1995.
- Sigurdarson, S., Viggosson, G., *Berm Breakwaters in Iceland, Practical Experiences*, Proc. Int. Conf. on Hydro-Technical Engineering for Port and Harbour Construction, Yokosuka, Japan, October 1994.
- Sigurdarson, S., Viggosson, G., Benediktsson, S., Samarason, O. B. *Berm Breakwaters and Quarry Investigations in Iceland*, Proc. 4th Int. Conf. on Coastal & Port Engineering in Developing Countries, Rio de Janeiro, Brazil, September 1995.

Location	W_{50} [t]	ρ [t/m ³]	storm	duration [waves]	H_s [m]	T_p [sec]	Θ [deg]	H_0	$H_0 T_{op}$	S [stones/wave]	l_i [m]
Caldera, Costa Rica	5.0	2.40	21.09.78	3000	3.65	18.7	50	2.1	109.5	$1.7 \cdot 10^{-3}$	155
	5.0	2.40	21.05.81	3000	3.55	17.9	50	2.1	101.2	0	0
	5.0	2.40	18.07.83	3000	3.47	17.1	50	2.0	95.2	0	0
	5.0	2.40	18.06.78	3000	3.30	17.5	50	1.9	92.6	0	0
St. Paul, Alaska	1.5	2.77	13.11.84	1900	5.34	31.0	15	3.8	417.1	8.3	7886
	1.5	2.77	07.12.84	4000	5.34	15.0	15	3.8	201.8	0.8	5155
Racine, Wisconsin	0.82	2.61	08.03.87	2500	4.4	11.2	15	4.15	176.6	0.4	1984
Bolungarvik, Iceland	6.0	2.85	27.10.95	3000	6.0	15	10	2.65	109.9	$2.0 \cdot 10^{-3}$	338

Table 1: Experienced wave conditions and structural parameters for selected prototype structures.

Location	St. type/ shape	W_{50} [t]	ρ [t/m ³]	$\frac{W_{50}}{W_{15}}$	$H_{0,max}$	$H_0 T_{Op,max}$	S_{max} [st./wave]	$\sum l_i$ [m]	Visual profile observations
Caldera, Costa Rica	Sand stone/ Rough angular	5.0	2.40	1.5	2.1	110	$1.7 \cdot 10^{-3}$	155	app. 5-10% broken stones, severe abrasion little profile changes and longshore transport. total damage, 150 m recession of breakwater head.
St. Paul, Alaska	Crushed stone	1.5	2.77	3.0	3.8	417.1	8.3	13041	severe breakage of armour stones, large profile changes and longshore transport.
Racine, Wisconsin	Crushed limestone	0.82	2.61	2.5	4.15	176.6	0.4	1984	no armour stone breakage, little profile changes, no longshore transport.
Bolungarvik, Iceland	Quarry stone/ Rough angular	6.0	2.85	2.5	2.65	109.9	$2.0 \cdot 10^{-3}$	338	

Table 2: Comparison of experienced wave conditions, structural parameters and profile observations for selected prototype structures.

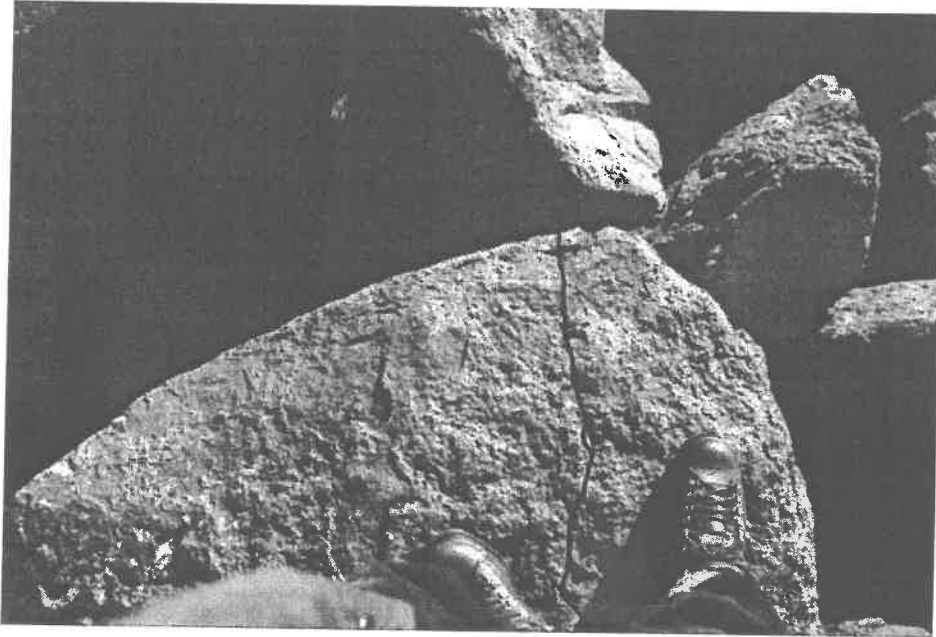


Photo from Icelandic berm breakwater



Photo from Norwegian berm breakwater



Design Formulae for Breakage of Unreinforced Dolosse and Tetrapods

by

Hans F. Burcharth and Zhou Liu

Department of Civil Engineering
Aalborg University

Dansk Vandbygningsteknisk Selskabs Seminar om
"Nyere metode til projektering af moler"
Aalborg Universitet, den 25. marts 1998

Design formulae for breakage of unreinforced Dolosse and Tetrapods

Hans F. Burcharth¹ Zhou Liu²

Abstract

The slender, complex types of armour units, such as Tetrapods and Dolosse are widely used for rubble mound breakwaters. Many of the recent failures of such structures were caused by unforeseen early breakage of the units, thus revealing an imbalance between the strength (structural integrity) of the units and the hydraulic stability (resistance to displacements) of the armour layers. Breakage is caused by stresses from static, pulsating and impact loads. Impact load generated stresses are difficult to investigate due to non-linear scaling laws. The paper describes a method by which impact loads on slender armour units can be studied by load-cell technique. In order to make the application of the results easier, a dimensional empirical formula is produced by the multi-parameter linear fitting on the data base corresponding to the conventional design of Dolosse and Tetrapods. Moreover, the paper presents Dolos design diagrams for the prediction of both breakage and hydraulic stability.

Introduction

The slender complex types of armour units, such as Tetrapods and Dolosse are widely used. Breakage of the armour units has caused many of the recent breakwater failures. Thus there is a need for studying stresses in the units.

Due to the stochastic nature of the wave loads, the complex shape of the armour units and their random placement, the problem cannot be dealt with on a deterministic basis, but must be handled as a probabilistic problem.

Consequently, a very large number of situations must be investigated. This can be performed at reasonable costs only by small scale experiments. Stresses in small scale armour units are studied by the use of load-cells inserted in the units.

¹Prof. of Marine Civil Engineering, Aalborg University, Denmark.

²Research Engineer, Ph.D. Aalborg University, Denmark.

Load-cell technique involves a number of complications. The installation of the load-cell makes the material properties of the unit different from those of the homogeneous prototype units and consequently the impact responses, which depend on the elastic behaviours of the bodies, cannot be directly reproduced in model tests. Besides this, the responses of the instrumented units could involve dynamic amplification effects. Moreover, the ultra short duration of solid body impact loads and the wave slamming necessitates high frequency sampling which results in data storage capacity problem. The frequencies of the impact stresses are in the order of 800-1500 Hz for the applied model units.

The paper first discusses the scale law for the impact stress in the armour units and presents results of impact calibration of the load-cell instrumented Tetrapods and Dolosse. In order to make the application of the results easier, a dimensional empirical formula is produced by the multi-parameter linear fitting on the data base corresponding to the conventional design of Dolosse and Tetrapods. Moreover, the paper presents Dolos design diagrams for the prediction of both breakage and hydraulic stability.

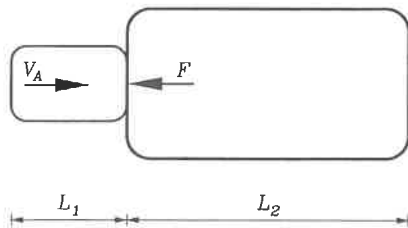
Duration of impacts

When two solid bodies collide the impact force and the related stresses will depend on the duration of the impact, i.e. the time of contact, τ . Due to the non-linear material properties of concrete and to the complex shape of slender armour units it is not possible to establish a formula by which τ can be quantified. However, it is sufficient for the present research to formulate a qualitative expression for τ . In the following are discussed two realistic models for estimation of τ . It is shown that for geometrically similar systems and constant Poisson's ratio it is reasonable to assume

$$\tau \sim L \sqrt{\frac{\rho_A}{E_A}} \quad (1)$$

where \sim means proportional to.

Case 1. Impacting blunt bodies of identical linear elastic material.



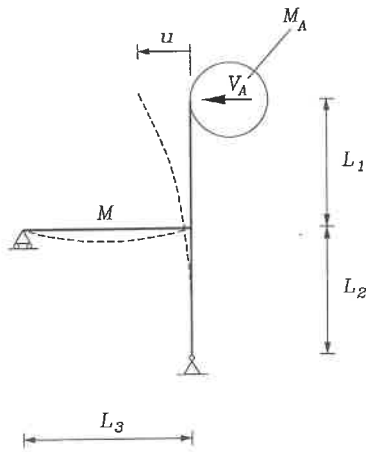
L_1 and L_2 are proportional to the characteristic length L of the system.

It is assumed that the impact generates mainly one-dimensional compression

longitudinal shock waves which travel with the rod wave speed, $C = \sqrt{E_A/\rho_A}$, the distances L_1 and L_2 to the free edges, where they are reflected as tension waves. The two bodies will loose contact at the first return of a tension wave to the impact surface. Consequently, because $L_1 < L_2$

$$\tau = \frac{2L_1}{C} = \frac{2L_1}{\sqrt{\frac{E_A}{\rho_A}}} \quad \text{or} \quad \tau \sim L\sqrt{\frac{\rho_A}{E_A}}$$

Case 2. Slender body impacted by blunt body of identical linear elastic material.



$$L_1 \sim L_2 \sim L_3 \sim L$$

$$M \sim M_A \sim \rho_A L^3$$

The impacting blunt body of mass M_A hits the slender structure of mass $M \sim M_A$ with impact velocity V_A by which a vibration mainly caused by bending and shear is initiated. It is assumed that the maximum value of τ corresponds to contact between the two bodies during approximately one half period T of the first mode of vibration for the slender body.

If it is assumed that the slender structure has a linear response corresponding to transverse impacts on free and simply supported beams then the system corresponds in principle to a mass-spring system with spring stiffness

$$k \sim \frac{E_A I}{L^3} \quad (2)$$

where $I \sim L^4$ is the moment of inertia.

The deflection time defined as one half period of the first mode of vibration is

$$\tau \simeq \frac{T}{2} \simeq \sqrt{\frac{M_A + M_o}{k}} \quad (3)$$

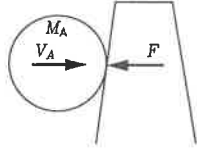
where $M_o \sim M \sim M_A \sim \rho_A L^3$ is the modal mass of the slender body.

From eqs (2) and (3) is then obtained eq (1). This conclusion was already presented in Burcharth (1984).

Scaling law for impact stresses of armour units

Case 1. Scale law in case of free fall impinging body

Geometrical similarity and constant coefficient of restitution are assumed



$$\begin{aligned} V_A &\sim \sqrt{2g L} \\ M_A &\sim \rho_A L^3 \end{aligned} \quad (4)$$

The momentum equation reads

$$F \tau = M_A \Delta V_A \sim M_A V_A \quad (5)$$

where τ is the duration of the impact and ΔV is the velocity difference of the impinging body before and after the collision. $\Delta V \sim V_A$ is due to the assumed constant coefficient of restitution.

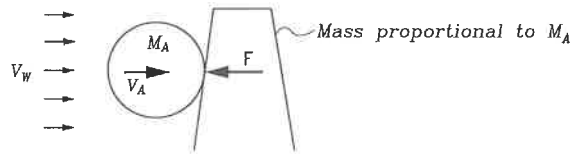
Inserting eqs (1) and (4) in eq (5) yields

$$F \sim \frac{\rho_A L^3 (g L)^{0.5} E_A^{0.5}}{L \rho_A^{0.5}} = \rho_A^{0.5} E_A^{0.5} g^{0.5} L^{2.5}$$

Introducing $\lambda = \frac{\text{model value}}{\text{prototype value}}$ we obtain

$$\lambda_{\sigma_{Impact}} = (\lambda_{\rho_A} \lambda_{E_A} \lambda_L \lambda_g)^{0.5} \quad (6)$$

Case 2. Scale law of impinging body affected only by flow forces



V_A is found from Newton's equation

$$F_W = M_A \frac{dV_A}{dt} \quad (7)$$

$$V_A = \frac{F_W}{M_A} t = \frac{F_W}{\rho_A L^3} t \quad (8)$$

where F_w is the flow force on the impinging body.
By the use of eqs (1), (5) and (8) is obtained

$$F \sim \frac{\rho_A L^3 F_W t E_A^{0.5}}{\rho_A L^3 L \rho_A^{0.5}} = \rho_A^{-0.5} L^{-1} F_W t E_A^{0.5}$$

$$\lambda_{\sigma_{Impact}} = \lambda_{\rho_A}^{-0.5} \lambda_L^{-3} \lambda_{F_W} \lambda_t \lambda_{E_A}^{0.5} \quad (9)$$

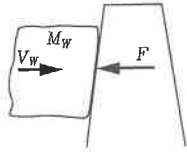
Because in the Froude model, $\lambda_{F_W} = \lambda_{\rho_W} \lambda_L^3$ and $\lambda_t = \lambda_L^{0.5}$, then

$$\lambda_{\sigma_{Impact}} = \lambda_{\rho_A}^{-0.5} \lambda_{\rho_W} \lambda_{E_A}^{0.5} \lambda_L^{0.5} \quad (10)$$

The variation in F_w due to viscous effects is neglected. This, however, introduces some unknown bias, the size of which depends on the Reynolds number range.

Case 3. Collision between impinging water (slamming) and a solid body.

The air-cushioning effect is neglected because it is unlikely that air-pockets will be entrapped due to the limited size and rounded shape of the elements.



$$V_W \sim \sqrt{g L}$$

$$M_W \sim \rho_W L^3 \quad (11)$$

τ is assumed given by (1) because the solid body stress wave is reflected from a free surface of the armour unit long time before reflection from a free surface of the wave (travel distance $\simeq H_s >$ dimension of armour unit; shock wave speed is smaller in water than in concrete) and the deflection time will be shorter than the transverse time of the elastic wave in the water.

From the momentum equation

$$F \tau = M_W \Delta V_W \sim M_W V_W \quad (12)$$

and eqs (1) and (8) is obtained

$$F \sim \frac{\rho_W L^3 g^{0.5} L^{0.5} E_A^{0.5}}{L \rho_A^{0.5}} = \rho_A^{-0.5} \rho_W E_A^{0.5} L^{2.5} g^{0.5}$$

and consequently

$$\lambda_{\sigma_{Impact}} = \lambda_{\rho_A}^{-0.5} \lambda_{\rho_W} \lambda_{E_A}^{0.5} \lambda_L^{0.5} \lambda_g^{0.5} \quad (13)$$

The difference between the above three scaling laws eqs (6), (10) and (13) is related to the scales of the densities only, because generally

$$\lambda_{\rho_A} \neq \lambda_{\rho_A}^{-0.5} \lambda_{\rho_W} \quad (14)$$

As long as the model is made of approximately the same concrete as the prototype, eq (6) can be chosen as the scaling law for the impact stresses, as it introduces less than 1% error for $0.97 \leq \lambda_{\rho_A} \leq 1.00$ and $0.98 \leq \lambda_{\rho_W} \leq 1.00$.

Apparent elasticity of the units with load-cell

The scaling law for the impact stresses of armour units is related to the elasticity of the material. Unfortunately, the insertion of the load-cell destroys the homogeneity of the material. This means that the impact stresses recorded in the small scale model tests cannot be scaled up to prototypes by the use of eq (6) valid only for homogeneous materials. Fig.1 shows the 200 g Dolos and 280 g Tetrapod with the load-cells.

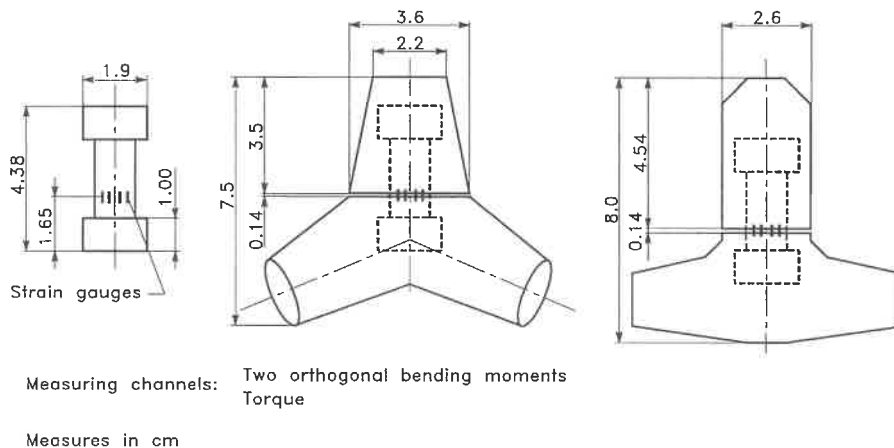


Fig.1. 200 g Dolos and 280 g Tetrapod with the load-cells.

However, by comparison of small scale impact test results for Dolosse and Tetrapods with results of the similar large scale impact tests (Burcharth, 1980, Bürger et al. 1990), it is possible to obtain an apparent elasticity for the small scale units. The apparent elasticity is then used for the interpretation of the impact signals recorded in the hydraulic flume tests.

The impact calibration results of the small scale Dolosse with load-cell have been published in Burcharth et al.(1990). The results of impact calibration of the Tetrapods are given in Fig.2. For the applied pendulum test set-up the reference is made to Bürger et al.(1990).

A way of checking the apparent elasticity is to compare the impact duration of the small load-cell mounted units with those of the various large size units, cf. eq (1). Fig.3 shows the ratio of dimensionless stress of various sizes of Dolosse using the apparent elasticity of the 200 g Dolos. Even though there is a big scatter, it can be seen that most ratios are around the value of 1, thus confirming the value of the apparent elasticity.

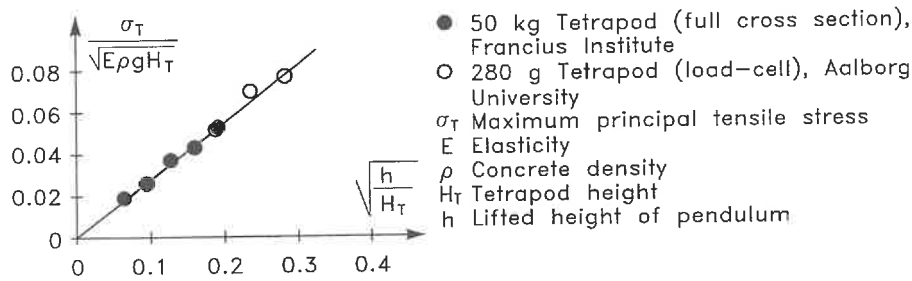


Fig. 2. Comparison of pendulum test results of the large scale Tetrapod with surface mounted strain gauges and the small scale Tetrapod with load-cell. Apparent elasticity $E = 4799 \text{ MPa}$.

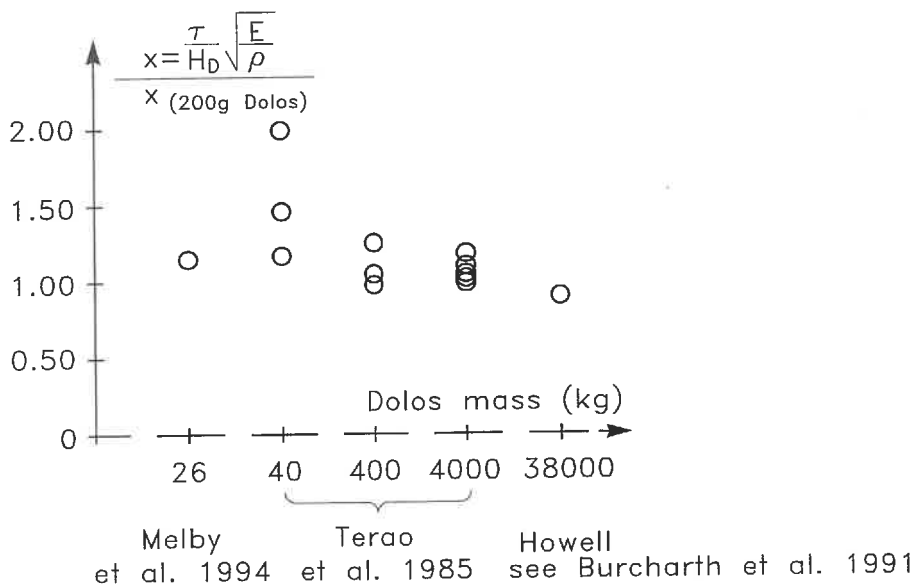


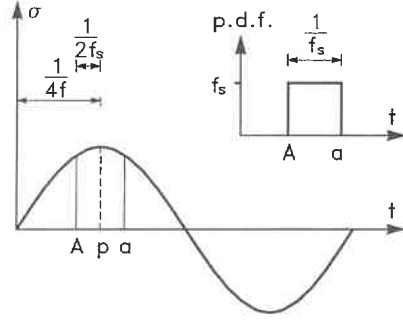
Fig. 3. Ratios of the dimensionless impact duration of large scale Dolosse against 200 g Dolos with load-cell. Apparent elasticity $E = 3500 \text{ MPa}$.

Sampling frequency

The ultra short duration of solid body impact loads and wave slamming requires

a very high sampling frequency. The following analysis gives the underestimation of the stress corresponding to a certain sampling frequency.

Suppose the stress signal is recorded at frequency f_s and the stress signal is sinusoidal with the maximum stress σ_p and the frequency f .



$$\sigma = \sigma_p \sin(2\pi f t) \quad (15)$$

Fig. 4. Sinusoidal stress signal.

The most unfavourable case is when the two adjacent sampling points, A and a , are symmetrically located around the center of the peak p . For this case the sampled maximum stress σ_A is

$$\sigma_A = \sigma_p \sin(2\pi f t_A) = \sigma_p \sin\left(2\pi f \left(\frac{1}{4f} - \frac{1}{2f_s}\right)\right) \quad (16)$$

and the maximum relative error is

$$\frac{\sigma_p - \sigma_A}{\sigma_p} = 1 - \sin\left(\pi\left(\frac{1}{2} - \frac{f}{f_s}\right)\right) \quad (17)$$

On the other hand, if the sampling points are uniformly distributed along the length $(A-a)$, the average of the sampled maximum stress is

$$\begin{aligned} \bar{\sigma} &= \int_{t_A}^{t_a} \sigma_p \sin(2\pi f t) f_s dt \\ &= \frac{\sigma_p f_s}{2\pi f} \left(\cos\pi\left(\frac{1}{2} - \frac{f}{f_s}\right) - \cos\pi\left(\frac{1}{2} + \frac{f}{f_s}\right) \right) \end{aligned} \quad (18)$$

and the average relative error is

$$\frac{\sigma_p - \bar{\sigma}}{\sigma_p} = 1 - \frac{1}{2\pi} \frac{f_s}{f} \left(\cos\pi\left(\frac{1}{2} - \frac{f}{f_s}\right) - \cos\pi\left(\frac{1}{2} + \frac{f}{f_s}\right) \right) \quad (19)$$

The maximum relative error and the average relative error are depicted in Fig.5. However, the actual impact signals are not sinusoidal, cf. Fig.6. In order to check the influence of the sampling frequency a series of Dolos pendulum tests with different sampling frequencies have been performed. The results are depicted in Fig.6. It can be seen that the sinusoidal results hold also for the actual impact signal when the offset for $f_s = 10000 \text{ Hz}$ is considered.

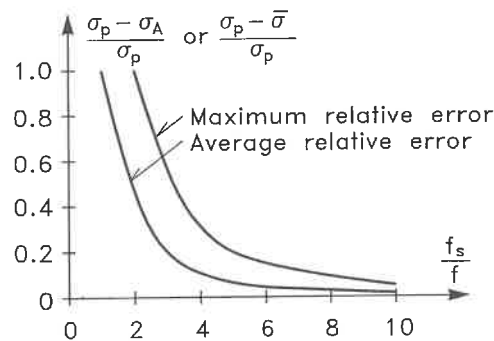


Fig. 5. Maximum relative error and average relative error due to the limited sample frequency.

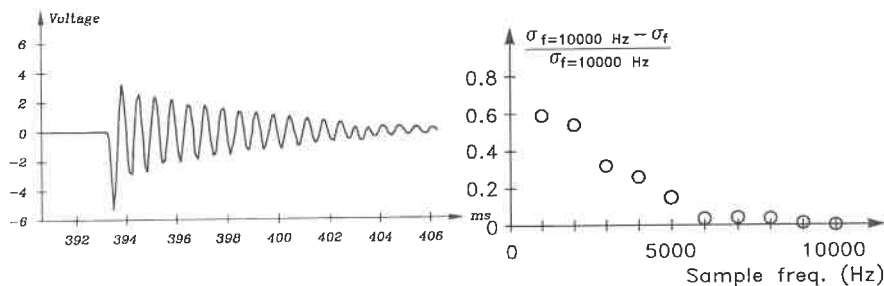


Fig. 6. Example of the impact signals of the 200 g load-cell instrumented concrete Dolosse ($f = 1500 \text{ Hz}$) and the relative error of the Dolos pendulum test results as function of the sampling frequency.

In the Dolos hydraulic model test, the applied sampling frequency is $f_s = 6000 \text{ Hz}$ and the damped natural frequency of the instrumented Dolosse $f = 1500 \text{ Hz}$. On average the sampled maximum impact stress is underestimated by 10% due to the limited sampling frequency. Therefore, in the data processing all sampled maximum impact stresses were increased by 10% .

Check for the dynamic amplification by wave slamming

It is well-known that resonance occurs when the frequency of the load is close to the natural frequency of the system. The installation of the load-cell into the model Dolos makes its natural frequency smaller, cf. eq (1). In order to check if the reduced natural frequency of the Dolosse is close to the wave slamming frequency, and hence introduces dynamic amplification, the frequency of the wave slamming on the Dolos armour layer was recorded by a pressure transducer installed in the stem of the Dolos. The pressure transducer did in all tests face the breaking waves. The results are given in Fig.7, showing the highest frequency of the wave slamming on the Dolos armour to be 330 Hz, far away from the natural frequency of 1500 Hz for the Dolosse with the load-cells. Consequently, no dynamic amplification are present in the model tests.

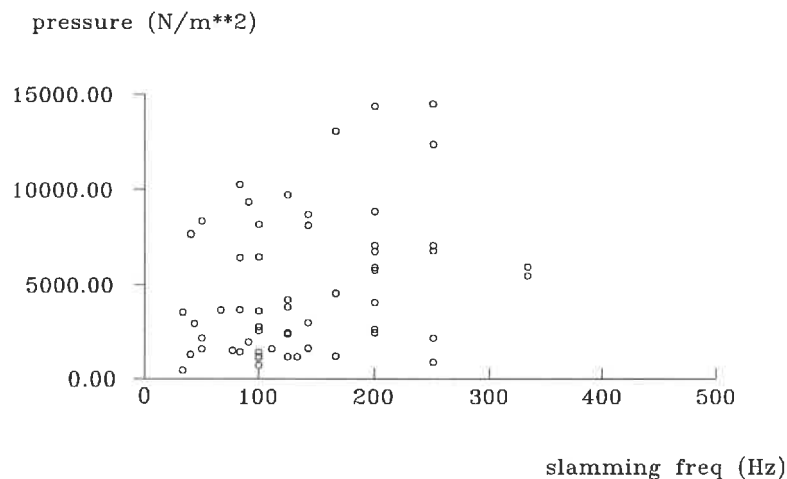


Fig. 7. Recorded frequencies of the wave slamming on the Dolos armour units.

Brief description of experiments

The detailed description of the model tests of the trunk of the Dolos breakwater, the round-head of the Dolos breakwater and the trunk of the Tetrapod breakwater has been given in Burcharth et al. (1992), Burcharth et al. (1995) and d'Angremond et al. (1994), respectively. Table 1 gives an outline of the test conditions.

Table 1. Summary of the hydraulic model tests

	Dolos trunk	Dolos round-head	Tetrapod trunk
Breakwater slope α	1.5	1.5	1.5
Foreshore	1:20	horizontal	1:50
Water depth at toe (cm)	23	50	30 and 50
Mass of units (kg)	0.187	0.187	0.290
Concrete density (ton s/m^2)	2.3	2.3	2.3
Spectral peak period T_p (s)	1.5-3	1.5-2.5	1.3-2.8
Significant wave height H_s (cm)	5.7-17.7	5-13	8.8-27.3
Surf similarity parameter $\xi = (H_s/L_p)^{-0.5} \tan \alpha$	3-7.5	3.8-7.5	2.7-4.1

In the tests with the trunk of Dolos breakwaters, three types of dolos waist-to-height ratios were applied, namely 0.325, 0.37 and 0.42, while in the round-head tests, only the waist-to-height ratio of 0.37 was applied.

Only head-on waves are applied in the round-head tests.

Distribution of stresses over the slope

The distribution of σ_T over the slope is of interest in order to identify the potential areas for armour breakage.

Fig. 8 shows typical distributions given by the 2% exceedence values of σ_T for each of the six instrumented Dolos positions for 10 t and 50 t Dolos of waist ratios 0.325 and 0.42 exposed to wave action levels, $N_S = \frac{H_{m_o}^t}{\Delta D_n} = 0.9, 1.8$ and 2.6.

The following conclusions can be drawn from the analyses of a large number of distributions of maximum σ_T over the slope:

- The contribution of the impact stress to the maximum principal tensile stress σ_T is small for $N_S \leq 2.0$.
- The contribution from the impact stress to σ_T is small in the bottom layer.
- The contribution from the impact stress to σ_T is very significant in the top layer.
- Breakage will in most cases start in the top layer in the zone just below SWL. This zone is more vulnerable to breakage than the zone above SWL.

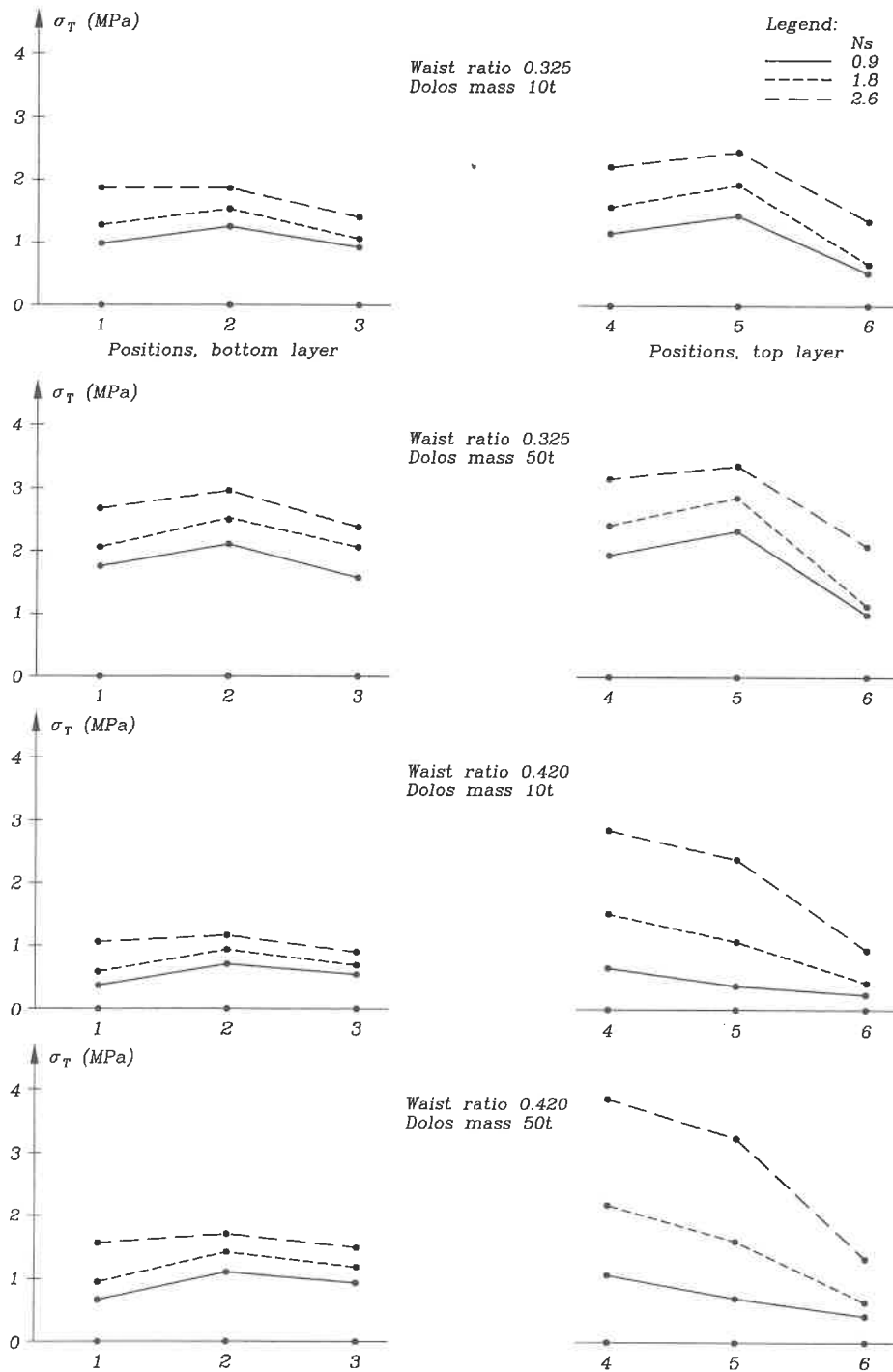


Fig. 8. Distribution of σ_T over the slope, Dolos positions 1 to 6, cf. Fig. 8. 2% stress exceedence probability level.

Design diagramme

In the analysis of breakage it is only the maximum value of σ_T in each instrumented Dolos within a test run which is of interest. Repeated short test runs of 100-300 waves were used because most movements take place in the beginning of each test.

The results are given in the design diagrams, one of which is shown in Fig.9. For the complete set of the design diagrams reference is made to Burcharth (1993). The concrete tensile strength in the diagrams is the one corresponding to static load. However, the diagrams take into account the dynamic amplification of the strength when impacts are involved.

Design formulae for breakage of unreinforced Dolosse and Tetrapods

The variables involved in unit breakage are the unit mass M , the concrete properties (density ρ_A , elasticity E and tensile strength S), the sea state (water depth d , significant wave height H_s and peak wave period T_p) and the breakwater geometry parameters (slope, armour unit placement and packing density).

In the hydraulic model tests, a certain breakwater geometry parameters have been applied, cf. the description of the experiment. Further the influence of water depth and wave period could not be identified within the tested range. The parameters to be considered are therefore: M , ρ_A , E , S and H_s .

Because of the different scaling laws for the non-impact and impact stresses, various nondimensional form of the formula produces a poor fitting. In stead of trying nondimensional empirical formula, it is decided to present simple dimensional formulae, covering the usual design situations. The formula for relative breakage takes the form

$$B = C_0 M^{C_1} S^{C_2} H_s^{C_3} \quad (20)$$

where	B	relative breakage
	M	unit mass in ton
	S	concrete strength in MPa
	H_s	significant wave height in meter
	C_0, C_1, C_2, C_3	fitted parameters

The density and static elasticity of the concrete material assumed to be 2.3 ton/m³ and 30000 MPa, respectively.

The least square method of multi parameter linear fitting is applied to fit the

obtained data sets to eq (20). The fitted parameters are listed in Table 2. The fittings are shown in Fig.10.

Table 2. Fitted parameters for the breakage formula

	waist ratio	Variational Coef. of C_0	C_0	C_1	C_2	C_3
Trunk of Dolosse	0.325	0.188	0.00973	-0.749	-2.58	4.143
	0.37	0.200	0.00546	-0.782	-1.22	3.147
	0.42	0.176	0.01306	-0.507	-1.74	2.871
Round-head of Dolosse	0.37	0.075	0.025	-0.65	-0.66	2.42
Trunk of Tetrapods		0.25	0.00393	-0.79	-2.73	3.84

- Legend:
- Hydraulic stability limit ($N_z=1000$, $\varphi=0.74$, $\Delta=1.29$) corresponding to relative number of displaced units D .
 - Tensile strength limit corresponding to relative number of broken Dolosse B
 - H_{mo}^t Significant wave height in front of breakwater
 - r Dolos waist ratio
 - S Concrete tensile strength
 - B Relative number of broken Dolosse
 - D Relative number of displaced Dolosse

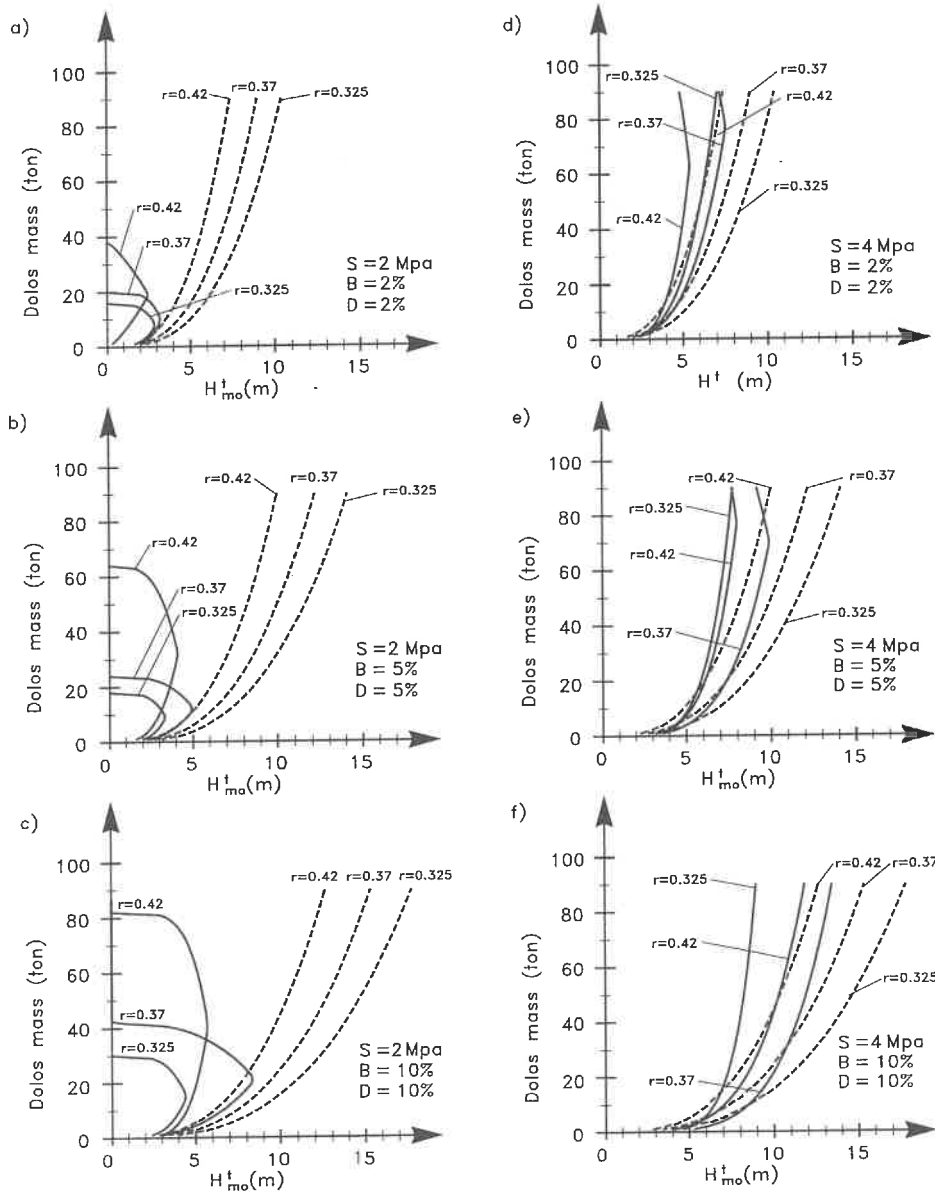


Fig. 9. Design diagrams for structural integrity and hydraulic stability of Dolos armour. Reference area $SWL \pm 6.5D_n$.

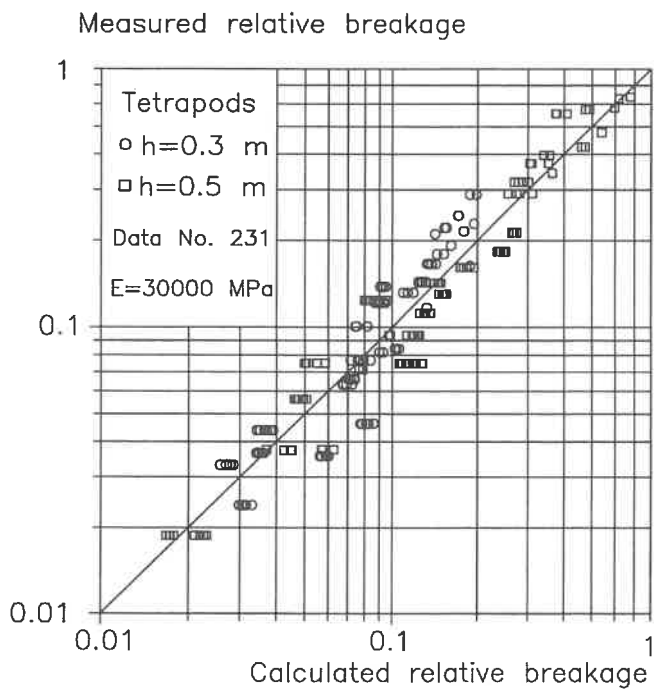
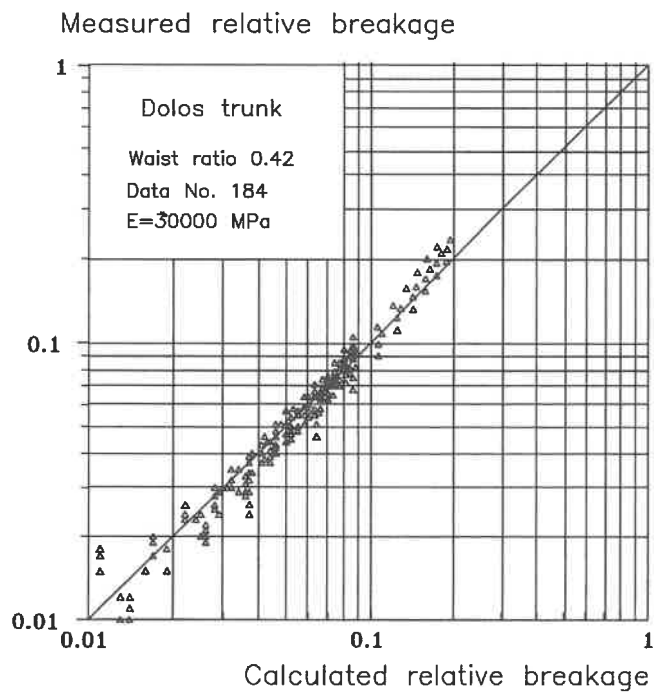


Fig.10. Fitting of the breakage formula.

Verification of formula

The design formulae have been checked against observed behaviour of prototype Dolos breakwaters and good agreement was found, cf. Table 3.

Table 3. Observed and predicted damage of some Dolos breakwaters.

	Crescent City USA	Richards Bay SA	Sines POR
H_s (m)	10.7 ⁽¹⁾	5 ⁽²⁾	9 ⁽³⁾
slope	1:4	1:2	1:1.5
Dolos mass (ton)	38	20	42
Waist ratio	0.32	0.33	0.35
Dolos packing density	0.85	1	0.83
Concrete density (kg/m^3)	2500	2350	2400
Elasticity (MPa) ⁽⁴⁾	30,000	30,000	30,000
Tensile strength (MPa) ⁽⁴⁾	3	3	3
Reported displacement	7.3%		
Reported breakage	19.7%		
Reported displacement+breakage ⁽⁵⁾	26.8%	4%	collapse
Predicted displacement	3.6%	0.6%	3.6 %
Predicted breakage by the diagrammes ⁽⁶⁾	> 10%	5%	> 10%
Predicted breakage by the formulae ⁽⁷⁾	> 68%	4.8%	> 31%

(1) depth limited in front of breakwater

(2) in front of breakwater

(3) offshore \approx in front of breakwater

(4) estimated values

(5) broken and displaced unit is counted only once

(6) design diagramme for Dolos breakage is given in Burcharth (1993)

A better verification is certainly wanted, but it has been very difficult to find Dolos breakwaters where the breakage has been carefully monitored. Also, breakage could be due to less careful placement during construction and bad concrete quality.

Acknowledgements

The load-cells applied in this study were kindly made available by CERC, USA. The project was partly sponsored by the Commission of the European Community under the Marine Science And Technology Research Program (MAST II), and partly sponsored by the Danish Technical Research Council under the MARIN TEKNIK Research Program.

References

- Burcharth, H.F. (1981). Full-scale dynamic testing of Dolosse to destruction. *Coastal Engineering*, 4 (1981).
- Burcharth, H.F. (1984). Fatigue in breakwater armour units. Proceedings of the 19th International Conference on Coastal Engineering, Houston, Texas, 1984.
- Burcharth, H.F. and Liu, Z.(1990). A general discussion of problems related to the determination of concrete armour unit stresses inclusive specific results related to static and dynamic stresses in Dolosse. Proc. Seminar on Structural Response of Armour Units. CERC, Vicksburg, MISS, USA.
- Burcharth, H.F., Howell, G.L. and Liu, Z.(1991). On the determination of concrete armour unit stresses including specific results related to Dolosse. *Coastal Engineering*, 15 (1991), pp 107-165.
- Burcharth, H.F. and Liu, Z. (1992). Design of Dolos armour units. Proceedings of the 23rd International Conference on Coastal Engineering. Venice. Italy.
- Burcharth, H.F. (1993). Structural integrity and hydraulic stability of Dolos armour layers. Series Paper 9, published by the Department of Civil Engineering, Aalborg University, Denmark, 1993
- Bürger, W.W., Oumeraci, H., Partenscky, H.W. (1990). Impact strain investigations on tetrapods results of dry and hydraulic tests. ASCE Proc. Seminar Stresses in Concrete Armor Units.
- Melby, J.A. and Turk, G.F. (1994). Scale and modeling effects in concrete armor experiments. Coastal Dynamics'94, Barcelona, Spain.
- Terao, T., Terauchi, K., Ushida, S., Shiraishi, N., Kobayashi, K. and Gahara, H. (1985). Prototype testing of Dolosse to destruction. Proc. Workshop on Measurement and Analysis of Structural Response in Concrete Armor Units. U.S. Army Corps of Engineers, CERC, WES, Vicksburg, MISS., USA.

Scour at the head of a vertical-wall breakwater

Dansk Vandbygningsteknisk Selskabs seminar om
"Nyere metoder til projektering af moler"
Aalborg Universitet, den 25. marts 1998

Scour at the head of a vertical-wall breakwater

B.M. Sumer, J. Fredsøe

Department of Hydrodynamics and Water Resources (ISVA), Technical University of Denmark, 2800 Lyngby, Denmark

Received 18 December 1995; accepted 13 May 1996

Abstract

This paper presents the results of an experimental investigation on the near-bed flow patterns, the bed shear stress amplification and scour around the head of a vertical-wall breakwater, using regular waves. The Keulegan–Carpenter number (KC), based on the diameter of the breakwater head, is found to be the major parameter that governs the flow and the equilibrium scour depth. Basic flow structures are identified as function of KC. The scour depth is found to increase with increasing the Keulegan–Carpenter number. The necessary extent of the conventional stone protection is studied. An empirical formula is worked out for the width of the protection layer as function of KC. Also, the effects of head shape, the angle of attack and the presence of a co-directional current are investigated. The results indicate that the scour depth is increased considerably in the presence of a current. Likewise, the scour depth is increased when the head shape is changed from a round shape to a sharp-edged one. It is found that the angle of attack is also an influencing factor as regards the scour depth.

Keywords: Breakwaters; Currents; Sand; Scour; Waves

1. Introduction

Analysis of breakwater failures (see the recent review by Oumeraci, 1994a) has proven that more basic knowledge on scouring around breakwaters needs to be accommodated in the preparation of design guidelines.

Scour in front of a vertical-wall breakwater in the two-dimensional case where the waves attack at right angle to the breakwater has been investigated by De Best et al. (1971), Xie (1981, 1985), Irie and Nadaoka (1984) and Hughes and Fowler (1991). The key mechanism in this case is the action of standing waves, leading to a steady streaming pattern in the vertical plane, which presumably results in a distinct scour and

deposition pattern in front of the breakwater in the form of an alternating scour and deposition areas lying parallel to the breakwater (as described in a recent review paper by Oumeraci, 1994b).

The mechanism regarding the scour around the head of a vertical-wall breakwater may be different from the aforementioned two-dimensional case. In this three-dimensional situation, separation vortices forming at the lee side of the breakwater may play an important role with regard to the scour processes, as will be demonstrated later in the paper. Also, the so-called horse-shoe vortex, a spiral type of vortex which forms in front of the breakwater due to rotation in the approaching flow, may be important in the case when the wave climate is extremely severe or when there is a current component perpendicular to the breakwater. Although much effort has been put in the study of the previously-mentioned two-dimensional scour, no detailed study of the three-dimensional scour at the head of a vertical-wall breakwater is yet available.

Recently, large amount of knowledge has accumulated in the area of scour around offshore and coastal structures such as piles where the scouring action of the separation vortices are the key element behind the scour processes (Herbich et al., 1984; Sumer et al., 1992). There are similarities between the scour process around a pile and that around the head of a breakwater. In both cases, the major flow structures which cause scour are the vortices, either in the form of lee-wake vortices or in the form of a horse-shoe vortex or both, depending on the actual flow environment. The two cases differ, however, in several aspects. The lee-wake vortices in the case of pile form at the two side edges of the structure and interact with each other quite strongly, which may lead to vortex shedding. Likewise, the horse-shoe vortex is influenced rather strongly with the small width of the pile. Whereas, in the case of breakwater, the lee-wake vortex forms at the tip of the breakwater, and there is only one vortex forming in each half cycle of the waves, as will be described in greater detail later in the paper. Regarding the horse-shoe vortex, this is affected heavily by the extremely large length of the breakwater. These considerations imply that the resulting scour process in the case of breakwater will be different from that around piles.

The purpose of the present study is to extend the aforementioned investigation on scour around piles to the study of scour around the head of a vertical-wall breakwater. (An earlier version of this work has been presented at the Conference on Hydro-Technical Engineering for Port and Harbor Construction held in Yokosuka, Japan in 1994 (see Gökçe et al., 1994).

It may be noted that an accompanying paper (Fredsøe and Sumer, 1997) presents the results of a parallel work on scour around the head of a *rubble-mound* breakwater.

2. Experimental set-up and procedure

2.1. Flow-visualization experiments

The purpose of these experiments was to get an understanding of the near-bed flow around the head of a vertical-wall breakwater.

The experiments were conducted in a wave flume 0.6 m in width, 0.8 m in depth and

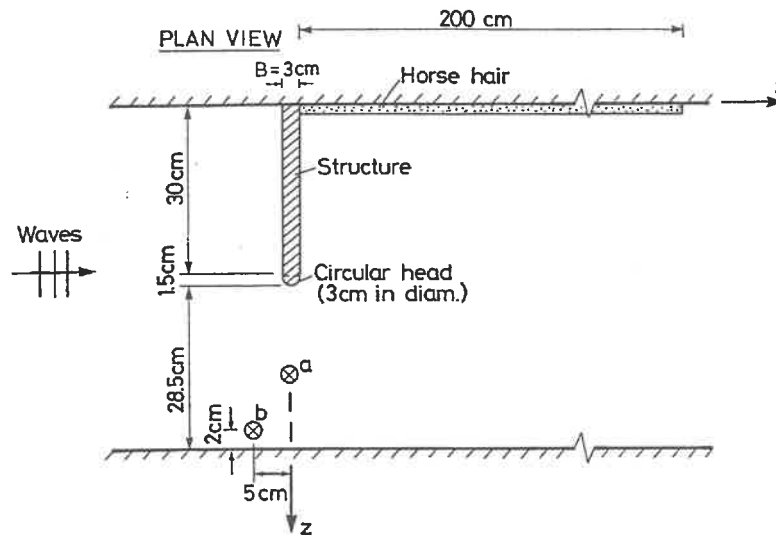


Fig. 1. Test set-up for the flow-visualization experiments. (a) location of the underwater mini camera for video recording, approx. 10 cm away from the bed. (b) location of velocity measurements.

26.5 m in length, using regular waves. The experimental set-up is depicted in Fig. 1. The model structure, located at 13.5 m distance from the wave generator, was a smooth-surface wall, 31.5 cm in length, 3 cm in width and 61 cm in height with a circular head.

The hydrogen-bubble technique was used in the experiments. Two bubble wires (30-cm-long and 0.050-mm-diameter copper wires) were stretched in the transverse (z) direction at a vertical distance $y = 3$ mm from the bottom; one at the upstream side and the other at the downstream side of the model structure, the wires being at distances 1 cm from the side-walls of the model. The lowermost 2 cm portion of the model was made from a transparent material through which the light was spread out.

An underwater pen-size mini camera was used for video recording of the flow processes. It was positioned at an angle to the bottom so that the near-bed flow patterns, visualized by the hydrogen bubbles around and in front of the model structure, can be viewed. The flow processes were videotaped for the Keulegan–Carpenter number range from practically $KC = 0$ to 15 where KC was incremented by 0.5 between $KC = 0.5$ and 6, by 1 between $KC = 6$ and 10 and by 5 between $KC = 10$ and 15. Here, KC number is defined by

$$KC = \frac{U_m T}{B} \quad (1)$$

in which U_m is the maximum value of the undisturbed *orbital* velocity of water particles at the bed at the section where the structure is placed, T is the wave period and B is the diameter of the head of the structure, see Fig. 1. The velocities were measured by a DANTEC Laser Doppler Anemometer (LDA). As seen from Fig. 1, the point at which the velocity measurements were made was located at $y = 1$ cm away from the bed and at a distance of 5 cm upstream of the structure (Fig. 1). (Experimental constraints necessitated this 5 cm offset in the position of the velocity-measurement point). Also, velocity profile measurements were made at $y = 2$ cm from the bed along the transverse

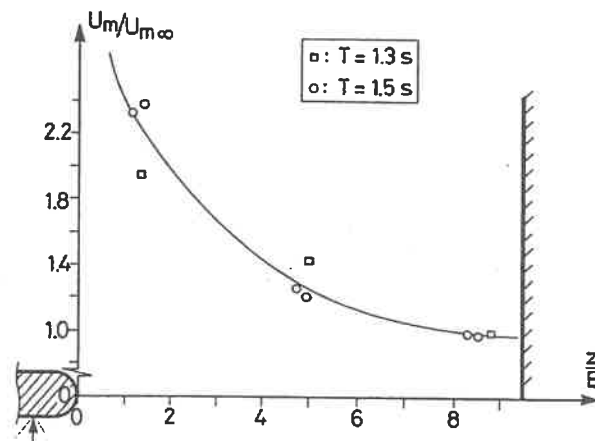


Fig. 2. Velocity distribution over the space between the breakwater and the side wall of the test channel at a distance of $y = 2$ cm from the bottom in the flow visualization study.

direction over the space between the head of the structure and the opposing side wall of the flume (Fig. 2). The figure shows that the velocity attains a constant value (namely the $U_{m\infty}$ value) for large z distances. So, no blockage effect was present.

In addition to pure-wave experiments, a few runs were conducted where a co-directional current with 0.1 m/s velocity was superimposed on waves.

The test conditions are summarized in Table 1.

Table 1

Flow visualization experiments. The mean water depth in the tests was maintained at 40 cm

Test No.	T (sec)	U_m (m/s)	$KC = U_m T / B$	$Re = U_m B / \nu$	U_c (m/s)
V1	1.0	0.015	0.5	450	—
V2	1.0	0.030	1.0	900	—
V3	1.3	0.035	1.5	1050	—
V4	1.3	0.045	2.0	1350	—
V5	1.3	0.055	2.5	1700	—
V6	1.5	0.06	3.0	1800	—
V7	1.5	0.07	3.5	2100	—
V8	1.5	0.08	4.0	2400	—
V9	1.5	0.09	4.5	2700	—
V10	1.5	0.10	5.0	3000	—
V11	1.5	0.11	6.0	3300	—
V12	1.7	0.12	7.0	3600	—
V13	1.7	0.14	8.0	4200	—
V14	1.7	0.16	9.0	4800	—
V15	1.7	0.18	10	5400	—
V16	1.7	0.26	15	7800	—
V17	0.8	0.056	1.5	—	0.1
V18	1.5	0.10	5	—	0.1
V19	1.7	0.15	8.5	—	0.1

Table 2

Bed shear stress experiments. The mean water depth in the experiments was 40 cm

Test No.	T (sec)	U_m (m/s)	$KC = U_m T / B$	$Re = U_m B / \nu$
1	1.3	0.028	1	840
2	2.1	0.12	8	3600

2.2. Bed shear–stress experiments

These experiments were carried out in the same flume as in the flow-visualization experiments. The breakwater was the same as that used in the flow-visualization tests. The bed shear stress was measured with a flush-mounted “Dantec 55R46 spec” hot-film probe, a specially designed two-component hot-film probe, which enabled the bed shear stress to be measured as a vector quantity in time dependent flows. The details as regards the working principle, the in-situ calibration of the probe and the other pertinent information are given in Sumer et al., 1993a).

Test conditions regarding the bed shear–stress experiments are given in Table 2.

2.3. Scour experiments

These experiments were carried out in a large wave flume, 4 m in width, 1 m in depth and 28 m in length. The experimental set-up is illustrated in Fig. 3. The mean water

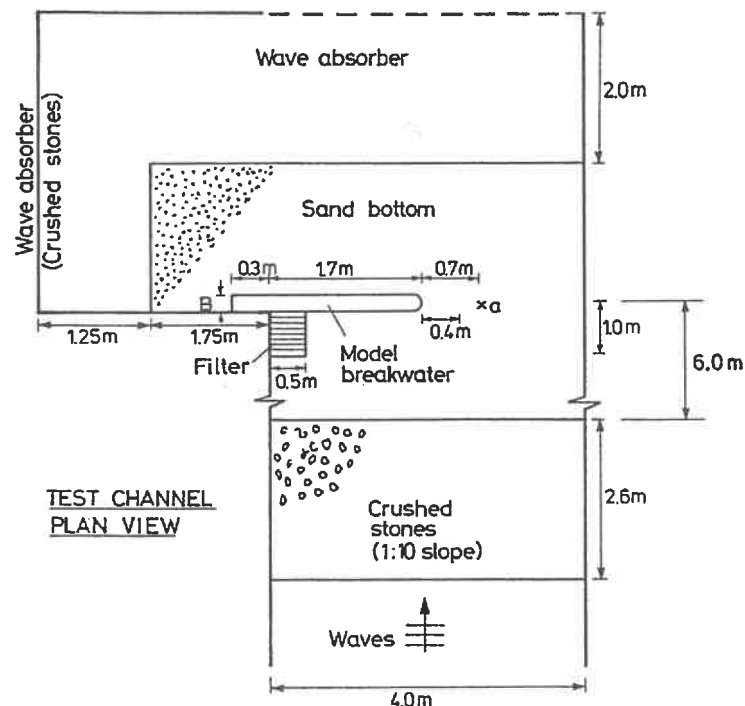


Fig. 3. Test set-up for scour experiments. Point a: location of underwater mini camera.

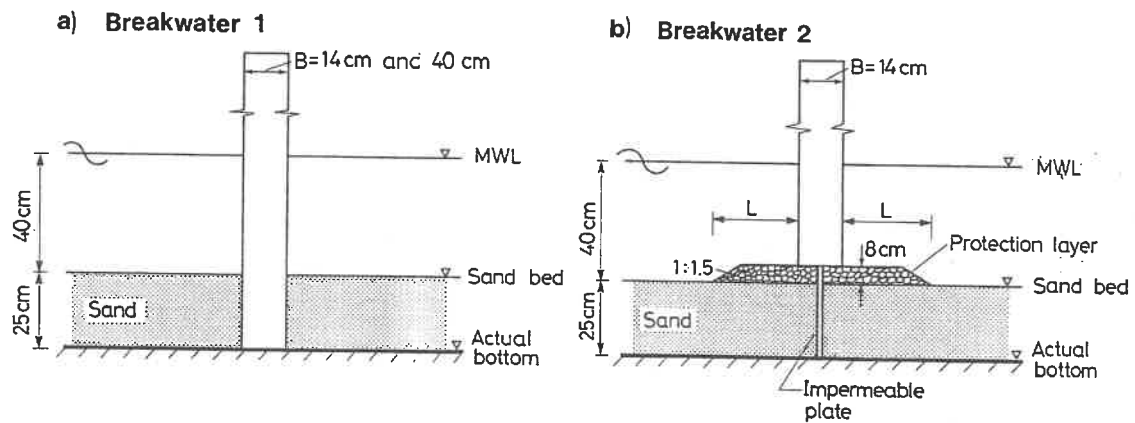


Fig. 4. Cross-section of the model set-ups.

depth in most of the experiments was held constant at 40 cm. Regular waves were used in the experiments. In the parallel work referred to earlier (Fredsoe and Sumer, 1997, where the rubble-mound-breakwater scour was investigated), irregular waves were used;

Table 3
Scour tests with pure waves. Breakwater 1

Test No.	B (cm)	T (s)	U_m (m/s)	θ	$KC = \frac{U_m T}{B}$	$Re = \frac{U_m B}{\nu}$	S (cm)	S/B	x_s/B	z_s/B	z'_s/B
1	14	1.5	0.22	0.12	2.5	2.9×10^4	1.2	0.092	—	—	—
2	14	1.7	0.11	0.08	1.4	2.4×10^4	0.7	0.054	—	—	—
3	14	1.7	0.15	0.10	2.0	2.0×10^4	1.0	0.077	—	—	—
4	14	1.7	0.175	0.11	2.3	2.3×10^4	1.2	0.092	—	—	—
5	14	1.7	0.185	0.11	2.4	2.4×10^4	1.5	0.115	—	—	—
6	14	1.7	0.195	0.11	2.6	2.5×10^4	2.0	0.154	—	—	—
7	14	1.7	0.22	0.11	2.9	2.9×10^4	2.2	0.169	—	—	—
8	14	2.0	0.22	0.11	3.4	2.9×10^4	2.1	0.162	—	—	—
9	14	2.0	0.22	0.11	3.4	2.9×10^4	1.9	0.146	—	—	—
10	14	2.0	0.275	0.12	4.2	3.6×10^4	3.2	0.246	—	—	—
11	14	2.0	0.29	0.12	4.5	3.8×10^4	3.3	0.25	—	—	—
12	14	3.0	0.22	0.09	5.1	2.9×10^4	3.0	0.231	—	—	—
13	14	3.0	0.30	0.10	6.9	3.9×10^4	4.0	0.308	—	—	—
14	14	3.0	0.38	0.11	8.8	4.9×10^4	4.7	0.362	—	—	—
15	14	3.0	0.45	0.11	10.4	5.9×10^4	6.2	0.477	—	—	—
16	14	1.7	11.5	0.07	1.39	1.6×10^4	0.6	0.043	1.00	0.86	0.50
17	14	1.7	21.3	0.16	2.59	3.0×10^4	2.0	0.143	2.4	1.8	1.00
18	14	3.0	23.9	0.19	5.12	3.3×10^4	3.5	0.250	3.21	2.64	2.00
19	14	3.0	28.6	0.24	6.14	4.0×10^4	3.9	0.279	3.21	3.21	2.21
20	14	4.0	23.4	0.18	6.67	3.2×10^4	4.4	0.314	4.64	3.36	1.71
21	40	1.7	11.4	0.06	0.5	4.5×10^4	0.0	0.000	0.00	0.00	0.00
22	40	1.7	21.2	0.16	0.9	8.5×10^4	0.7	0.018	0.65	0.55	0.40
23	40	3.0	18.1	0.12	1.4	7.2×10^4	1.0	0.025	1.05	0.98	0.70
24	40	3.0	23.9	0.19	1.8	9.5×10^4	1.5	0.038	1.30	1.25	0.78
25	40	3.0	29.0	0.24	2.2	1.1×10^5	3.7	0.093	1.45	1.68	0.95
26	40	4.0	24.0	0.19	2.4	1.0×10^5	3.3	0.083	1.75	1.75	0.95

Table 4
Scour tests with sharp-edged-head breakwater. Pure waves. Breakwater 1 ($B = 14$ cm)

Test No.	T (s)	U_m (cm/s)	θ	$KC = U_m T / B$	$Re = U_m B / \nu$	S (cm)	S/B
1	1.7	11.9	0.06	1.44	1.7×10^4	1.6	0.114
2	1.7	21.2	0.16	2.57	2.0×10^4	3.5	0.250
3	3.0	18.2	0.12	3.90	2.5×10^4	4.4	0.311
4	3.0	23.9	0.19	5.11	3.3×10^4	7.9	0.561
5	3.0	28.0	0.23	6.01	3.9×10^4	8.9	0.632
6	4.0	23.6	0.19	6.73	3.2×10^4	10.9	0.775

this was to avoid large bed undulations in the long-duration, $O(10)$ – $O(40)$ hrs, tests. However, that was not a problem in the present case, because the test durations were in the order of magnitude of half an hour or shorter, and therefore no large bed undulations emerged during the tests.

Two kinds of model structures were used: Breakwater 1 and Breakwater 2. In the case of Breakwater 1, the model structure was placed in a sand bed without protection, as sketched in Fig. 4a. The structure was a box, 2 m in length and 1.2 m in height with impermeable walls and with a circular round head, the diameter of the head, B , being $B = 14$ cm in most of the experiments and $B = 40$ cm in a few cases. The length of the structure exposed to the flow was 1.7 m in most of the cases (Fig. 3). The structure extended down to the actual bottom of the flume in the vertical section (Fig. 4a).

In the case of Breakwater 2, the previously mentioned box was used as the main part of the breakwater. However, in this case, the box was placed on a protection layer (Fig. 4b); thus, the set-up as such, simulated an actual, vertical wall breakwater with its conventional bedding layer and stone protection. One important aspect regarding this latter set-up is that an impermeable plate was implemented (Fig. 4b), along the length of the protection layer, to avoid the undermining of the structure due to piping. For the protection layer, crushed stones the size of approximately $d_{50} = 2$ cm were used. The experiments were conducted for three different values of the width of the protection layer, namely $L = 10$ cm, 20 cm and 50 cm.

The sand used as the bed material had d_{50} equal to 0.17 mm with $d_{84}/d_{16} = 0.67$. Scour process around the head of the structure was continuously monitored with the

Table 5
Supplementary scour tests with rough-surface breakwater. Pure waves. Breakwater 1 ($B = 16$ cm, including the roughness). Roughness was achieved by gluing crushed stones the size of about 1 cm

Test No.	T (s)	U_m (cm/s)	θ	$KC = U_m T / B$	$Re = U_m B / \nu$	S (cm)	S/B
1	1.7	12.0	0.06	1.5	1.7×10^4	0.7	0.04
2	1.7	21.1	0.15	2.6	3.0×10^4	2.1	0.13
3	3.0	17.9	0.12	3.9	2.5×10^4	3.0	0.19
4	3.0	23.6	0.19	5.1	3.3×10^4	3.2	0.20
5	3.0	28.0	0.23	6.0	3.9×10^4	5.0	0.31
6	4.0	23.4	0.18	6.7	3.3×10^4	5.0	0.31

Table 6

Scour tests at angles of attack different from 90°. Pure waves. Breakwater 1 ($B = 14$ cm)

Test No.	T (s)	ϕ (°)	U_m (cm/s)	θ	$KC = U_m T / B$	$Re = U_m B / \nu$	S (cm)	S/B
1	1.8	60	15.3	0.05	2.0	2.1×10^4	1.6	0.11
2	2.3	60	17.8	0.06	3.0	2.4×10^4	3.2	0.23
3	2.7	60	20.8	0.08	4.0	2.9×10^4	2.6	0.19
4	3.0	60	23.8	0.09	5.1	3.3×10^4	4.6	0.33
5	3.8	60	22.1	0.08	5.9	3.0×10^4	5.7	0.41
6	3.8	60	22.1	0.08	5.9	3.0×10^4	5.8	0.41
7	3.8	60	22.8	0.09	6.1	3.2×10^4	6.3	0.45
8	4.0	60	24.8	0.10	7.1	3.5×10^4	7.8	0.56
9	4.5	60	25.0	0.10	8.0	3.5×10^4	6.8	0.49
10	4.8	60	26.7	0.11	9.1	3.7×10^4	7.9	0.56
11	4.8	60	28.1	0.12	9.5	3.9×10^4	8.6	0.61
12	6.0	60	23.1	0.09	10.0	3.2×10^4	6.3	0.45
13	4.8	60	29.8	0.13	10.0	4.2×10^4	9.2	0.66
14	5.3	60	28.1	0.12	10.6	3.9×10^4	5.1	0.36
15	5.3	60	29.4	0.13	11.0	4.1×10^4	5.3	0.38
16	6.0	60	25.5	0.10	11.0	3.5×10^4	6.7	0.48
17	1.8	120	15.5	0.05	2.0	2.2×10^4	5.0	0.04
18	2.7	120	20.0	0.07	3.9	2.8×10^4	1.2	0.09
19	3.0	120	23.8	0.09	5.1	3.3×10^4	0.8	0.06
20	3.0	120	28.0	0.12	6.0	3.9×10^4	1.2	0.09

previously mentioned underwater mini video camera. Velocity measurements were made by a LDA instrument and a bi-directional propeller to determine the velocity amplitude U_m . These velocity measurements indicated that no blockage effect existed.

Table 7

Scour tests with pure waves. Tests with Breakwater 2 (with a protection layer, L being the width of the protection layer)

Test No.	L (cm)	L/B	T (s)	U_m (m/s)	θ	$KC = U_m T / B$	$Re = U_m B / \nu$	S (cm)	S/B
1	10	0.71	1.7	0.116	0.07	1.4	1.6×10^4	0.0	0
2	10	0.71	1.7	0.219	0.16	2.7	3.1×10^4	0.4	0.029
3	10	0.71	3.0	0.233	0.17	5.0	3.3×10^4	2.8	0.200
4	10	0.71	3.0	0.277	0.22	6.0	3.9×10^4	2.2	0.157
5	10	0.71	4.0	0.246	0.20	7.0	3.4×10^4	5.3	0.379
6	20	1.4	1.7	0.118	0.06	1.4	1.7×10^4	0.2	0.014
7	20	1.4	1.7	0.215	0.16	2.6	3.0×10^4	0.7	0.050
8	20	1.4	3.0	0.239	0.19	5.1	3.3×10^4	1.4	0.100
9	20	1.4	3.0	0.297	0.24	6.4	4.0×10^4	1.5	0.107
10	20	1.4	4.0	0.252	0.20	7.2	3.5×10^4	2.6	0.186
11	50	3.6	1.7	0.121	0.06	1.5	1.7×10^4	0.0	0
12	50	3.6	1.7	0.211	0.15	2.6	3.0×10^4	0.6	0.043
13	50	3.6	3.0	0.240	0.19	5.1	3.4×10^4	0.1	0.007
14	50	3.6	3.0	0.255	0.21	5.5	3.6×10^4	0.7	0.050
15	50	3.6	4.0	0.240	0.19	6.9	3.4×10^4	0.0	0

Table 8

Scour tests with combined waves and currents. Breakwater 1. Tests were run for only 30 minutes

Test No.	T (s)	U_m (m/s)	θ	KC	$Re = U_m B / \nu$	U_c (m/s)	S (cm)	S/B	$\frac{U_c}{U_c + U_m}$
1	1.7	0.11	0.08	1.4	1.4×10^4	0.10	8.5	0.65	0.47
2	1.7	0.15	0.10	2.0	2.0×10^4	0.10	9.0	0.69	0.40
3	1.7	0.195	0.11	2.6	2.5×10^4	0.10	9.0	0.69	0.34
4	3.0	0.30	0.10	6.9	3.9×10^4	0.10	13.0	1.00	0.25

The test conditions are summarized in Tables 3–8 where θ is the Shields parameter defined by

$$\theta = \frac{U_{fm}^2}{g(s-1)d_{50}} \quad (2)$$

in which g is the acceleration due to gravity, $s =$ the relative density of sediment ($= \rho_s / \rho$ in which ρ is the density of water and ρ_s is that of sediment), $U_{fm} =$ the maximum value of the undisturbed bed shear velocity,

$$U_{fm} = \sqrt{\frac{f_w}{2}} U_m \quad (3)$$

in which f_w is the wave friction coefficient. This has in the present study been calculated by the method of Fredsøe (1984).

As is seen from the tables, the experiments were conducted under live-bed conditions, namely for $\theta > \theta_{cr}$ in which θ_{cr} is the critical value of the Shields parameter for the initiation of sediment motion at the bed.

In the experiments, the upper boundary of the KC range was kept rather large, namely $KC = O(10)$, whereas in practice KC can hardly exceed the value of $KC = 4-5$. However, experimenting with large KC numbers helped illustrate the trends better with regard to the variation of various quantities with respect to the KC number.

3. Flow regimes

Fig. 5 summarizes the flow regimes observed in the present flow-visualization experiments.

There are three kinds of flow regimes: (1) the unseparated-flow regime — the creeping flow ($KC \leq 1$), (2) the separated flow regime with a lee-wake vortex formation behind the structure ($1 \leq KC \leq 12$), and (3) the separated flow regime with a lee-wake vortex formation behind the structure and a horse-shoe vortex formation in front of it ($KC \geq 12$).

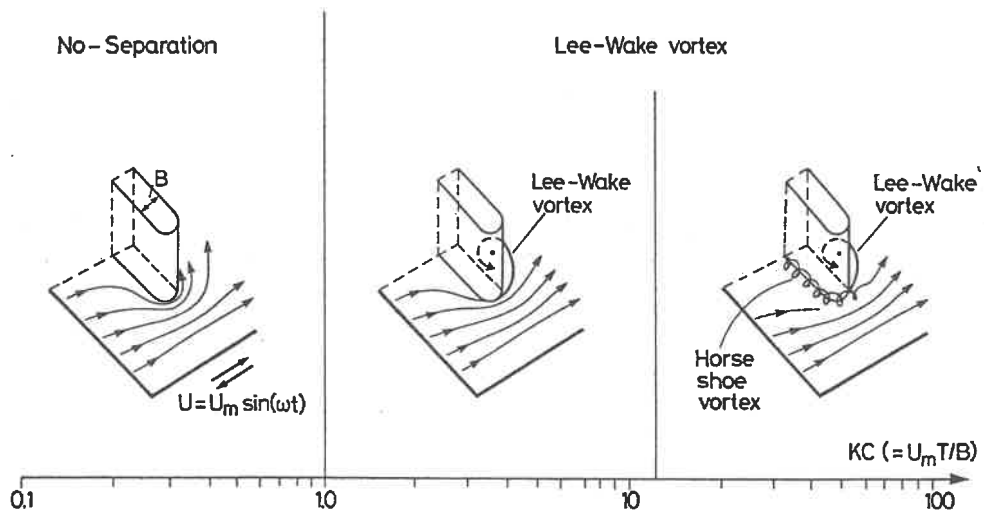


Fig. 5. Near-bed flow regimes around the head of a vertical-wall breakwater.

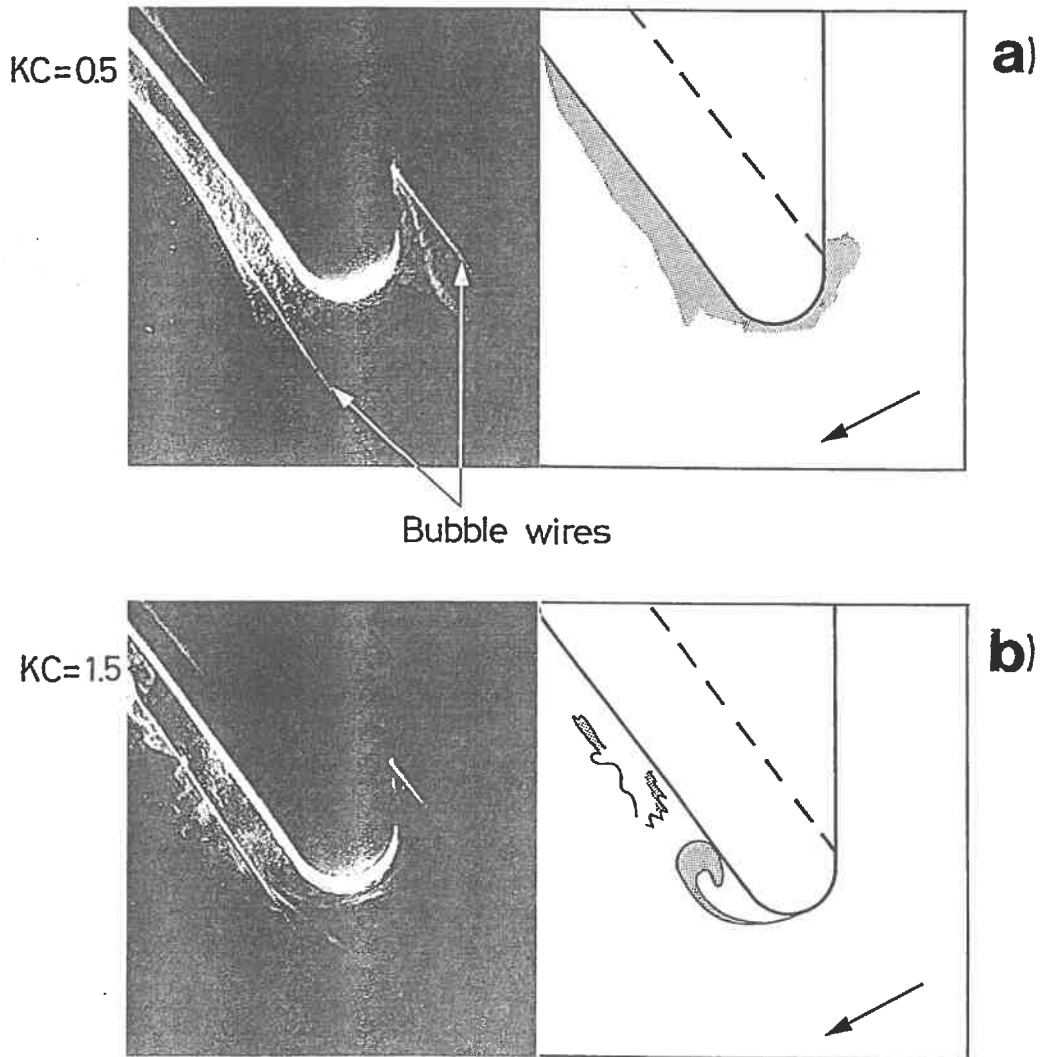


Fig. 6. Video frames. (a) No separation. (b) Separation.

3.1. The unseparated-flow regime ($KC \leq 1$)

The flow does not separate for KC below approximately unity (Fig. 5). Fig. 6 depicts two video frames, one with $KC = 0.5$ and the other with $KC = 1.5$, corresponding to approximately the same instant in the phase space. While there is no separation in the former case, the separation clearly occurs in the latter situation.

The preceding finding agrees rather well with the corresponding result in the case of flow around a circular cylinder (Sarpkaya (1986); Sarpkaya's results show that, for the same Reynolds number as in the present tests, namely $Re \cong 10^3$ (Table 1), the unseparated-flow regime in the case of cylinder terminates at $KC = 1.1$ (cf. $KC = 1$ in Fig. 5).

3.2. Separated-flow regime with no horse shoe vortex ($1 \leq KC \leq 12$)

In this flow regime, a lee-wake vortex forms behind the structure in every half period (Fig. 5).

The present flow-visualization experiments reveal that the way in which this vortex forms and further develops basically does not vary with the KC number. (Fig. 7 depicts a sequence of sketches, illustrating the evolution of the flow picture around the structure during the course of approximately one half period of the motion. Note that $\omega t = 0$ corresponds to the instant where the wave crest passes the section at which the structure

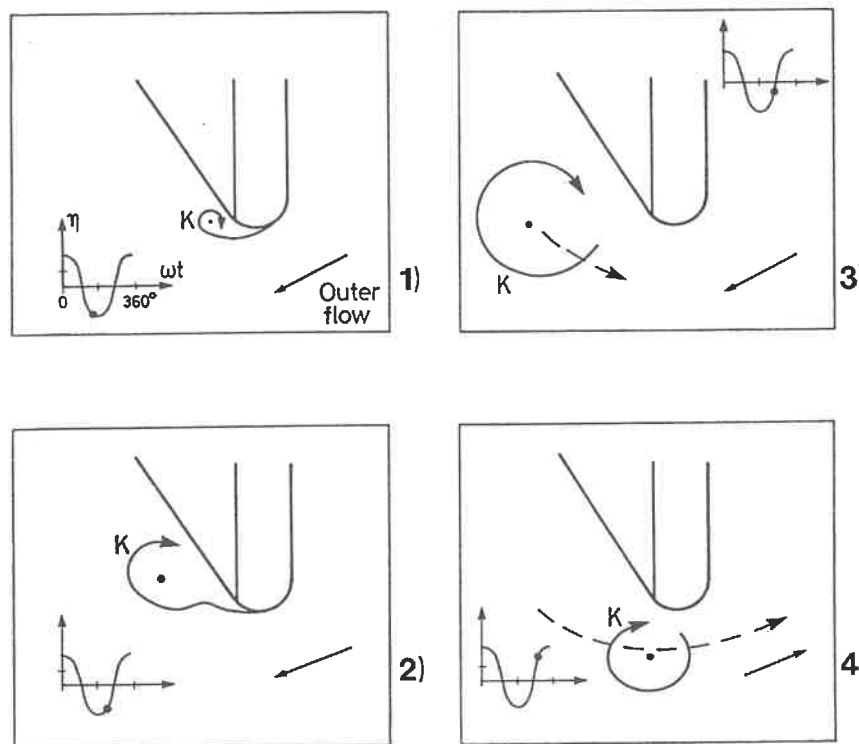


Fig. 7. Development of flow around the head of breakwater $KC = 8$. η : the surface elevation recorded at the section where the breakwater is placed. Frame 1: Lee-wake vortex forms. Frame 2: It grows in size. Frames 3 and 4: It is eventually washed around the structure.

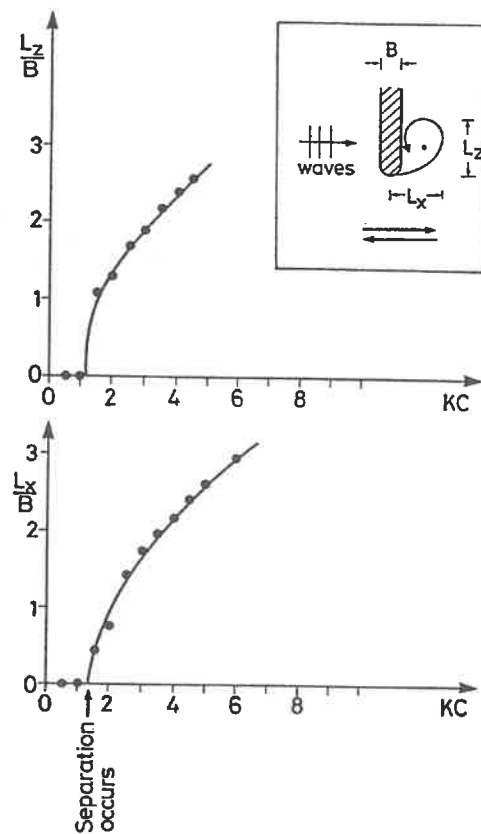


Fig. 8. Dimensions of lee-wake vortex.

is placed.) Yet, the video recordings reveal that the phase variation of the development of the flow patterns as well as the dimensions of the flow structures are strongly dependent on the KC number. Fig. 8 presents the data regarding the plan-view extent of the lee-wake vortex normalized by the diameter of the structure head plotted as function of the KC number. As seen, the larger the KC number, the larger of the lee-wake vortex.

3.3. Separated-flow regime with a horse-shoe vortex ($KC \geq 12$)

When KC is increased further, a point is reached (namely at $KC \cong 12$) where, in addition to the lee-wake vortex, a spiral-shape vortex begins to form in front of the structure as sketched in Fig. 9a. This vortex is similar to the horse-shoe vortex in front of a vertical cylinder (Fig. 9b). The latter is known to play an important role in scour around bridge piers and vertical piles (Breusers et al., 1977; Sumer et al., 1992). As is known, the horse-shoe vortex is formed at the seabed because of the rotation in the incoming flow velocity. In waves, this rotation is formed in the wave boundary layer (Fig. 9). However, the horseshoe vortex is insignificant when the wave boundary layer is thin (Sumer et al., 1992).

As stated above, the present observations indicate that a horse-shoe vortex first emerges in front of the structure when $KC \geq 12$. The observations further indicate that this occurs over a very brief period of time during the course of one half period of the motion. Considering the extremely small values of KC number experienced in real-life

situations ($KC = O(1)$), it may be argued that this flow regime is of no practical significance with regard to scour problems encountered in practice.

Finally, it should be noted that the present visualization study indicated that the horse-shoe vortex existed even in the case of $KC = 1.5$ when a co-directional current (Tests V17–V19) is superimposed on waves.

3.4. Scale effects regarding flow regimes

Clearly, when real-life dimensions are considered, some changes may be expected in the values of the critical KC numbers separating the three different flow regimes summarized in Fig. 5.

As for the first critical KC number, namely the KC number beyond which separation occurs, we may deduce from Sarpkaya's (1986) results referred to in Section 3.1 that, for very large structures where Re number is extremely large and the surface of the structure is rather rough, the flow would remain unseparated for $KC \leq 2$. We may therefore anticipate that the curves in Fig. 9 may shift slightly to the right, suggesting that the normalized size of the lee-wake vortices would be slightly smaller in the field for the same KC number.

Regarding the second critical KC number, namely the KC number at which the horse-shoe vortex begins to emerge, this is related to the boundary-layer thickness (Sumer et al. (1992)). In the present flow-visualization experiments, the wave boundary layer was in laminar regime, and the undisturbed boundary layer thickness δ was estimated to be $\delta/\ell = O(0.005)$ (Jensen et al. (1989)) in which ℓ is the length of the model breakwater. In the field, this ratio is even smaller, meaning that the horse-shoe vortex can emerge for values of KC which are even larger than the value indicated in

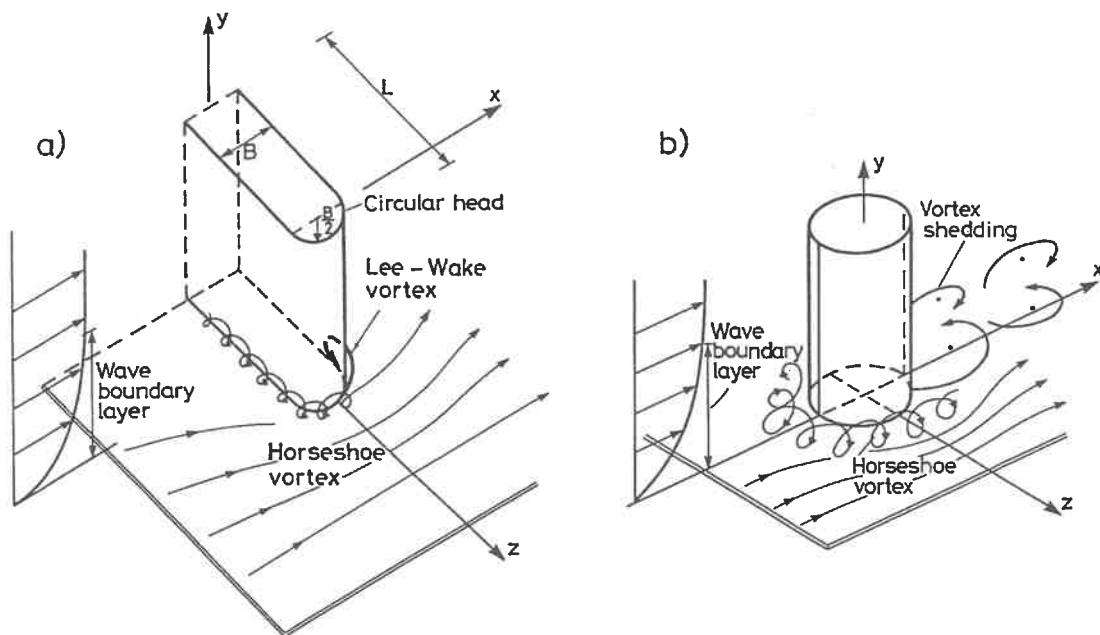
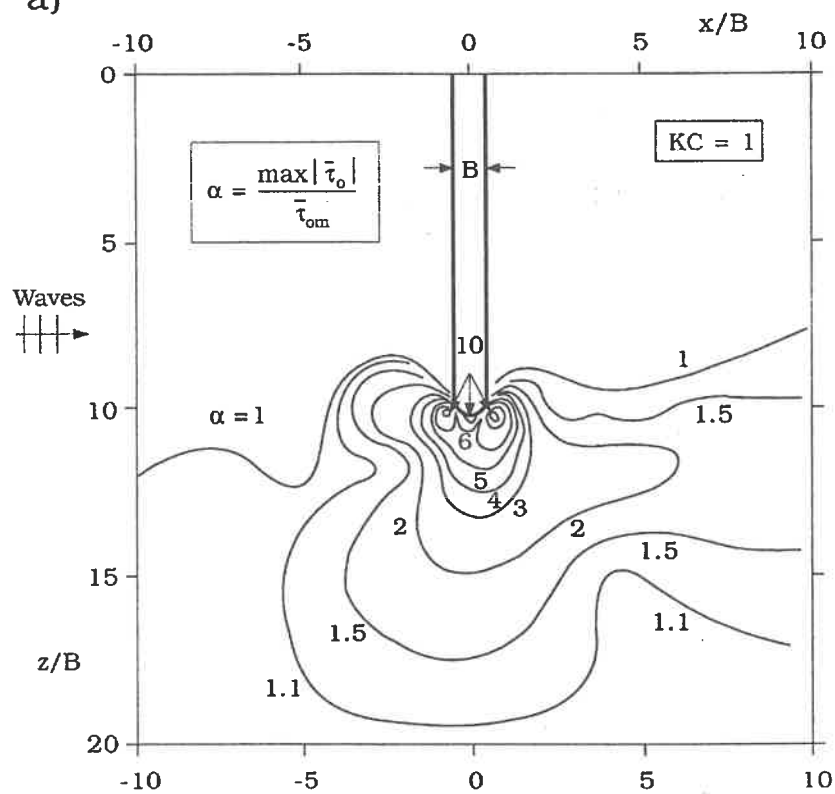


Fig. 9. Flow pattern. (a) Vertical-wall breakwater. (b) Vertical cylinder.

a)



b)

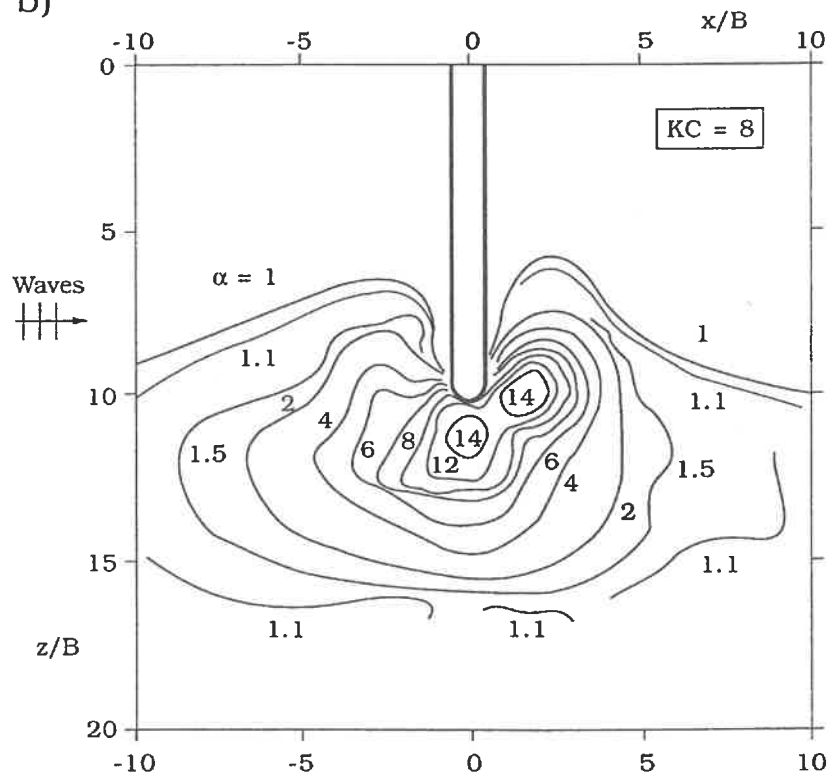


Fig. 5, $KC \geq 12$. As already pointed out, such high KC numbers can not occur in the field, therefore the corresponding flow regime would have no practical significance with regard to the scour processes.

4. Results of bed-shear-stress measurements

Fig. 10 illustrates the distribution of the bed shear stress around the head of the breakwater for the tested KC numbers. Here α is the amplification defined by

$$\alpha = \frac{\max|\bar{\tau}_0|}{\bar{\tau}_{0m}} \quad (4)$$

in which $\bar{\tau}_0$ = the mean bed shear stress in the presence of the breakwater and $\bar{\tau}_{0m}$ = the maximum value of the undisturbed mean bed shear stress. As seen, the amplification in the bed shear stress near the structure can be as high as $\alpha = O(10)$. This is consistent with the velocity measurements undertaken in the scour experiments: for $KC = 2.8$, the amplification in the velocity measured near the tip of the breakwater was found to be 3, indicating that an α value in the order of magnitude of 10 must have been experienced in the actual scour experiments.

Fig. 10 further illustrates that the concentration of the bed shear stress takes place in a small area in the neighbourhood of the head of the breakwater. Amplifications larger than 4, for example, occur within a distance of only $(2-3)B$ from the tip of the breakwater for $KC = 1$, while this area is a little larger, namely $(4-5)B$, for $KC = 8$. However, at a distance from the tip of the breakwater of about $(8-10)B$, α reduces to its undisturbed value. It may be noted that the slight asymmetry in the contour plots in Fig. 10 is due to the asymmetry in waves.

Fig. 11a and Fig. 11b give vector plots of the bed shear stress at certain phase values over approximately one half period of waves.

While Fig. 11a indicates no formation of lee-wake vortex ($KC = 1$), Fig. 11b reveals that the lee-wake vortex begins to form at approximately $\omega t = -30^\circ$ and grows in size with increasing ωt . This observation agrees with the results of the flow visualization study (Figs. 5–7).

Fig. 11b shows that the bed shear stress underneath the lee-wake vortex could be rather large, apparently in the same order of magnitude as that caused by the contraction of the streamlines near the tip of the breakwater.

5. Results of scour experiments

Fig. 12 illustrates the scour holes in two cases corresponding to the equilibrium stage, one with no protection layer and the other with a protection layer (Test 12 in Table 3 and Test 9 in Table 7, respectively). As is seen, the maximum scour depth occurs at the

Fig. 10. Amplification in the bed shear stress.

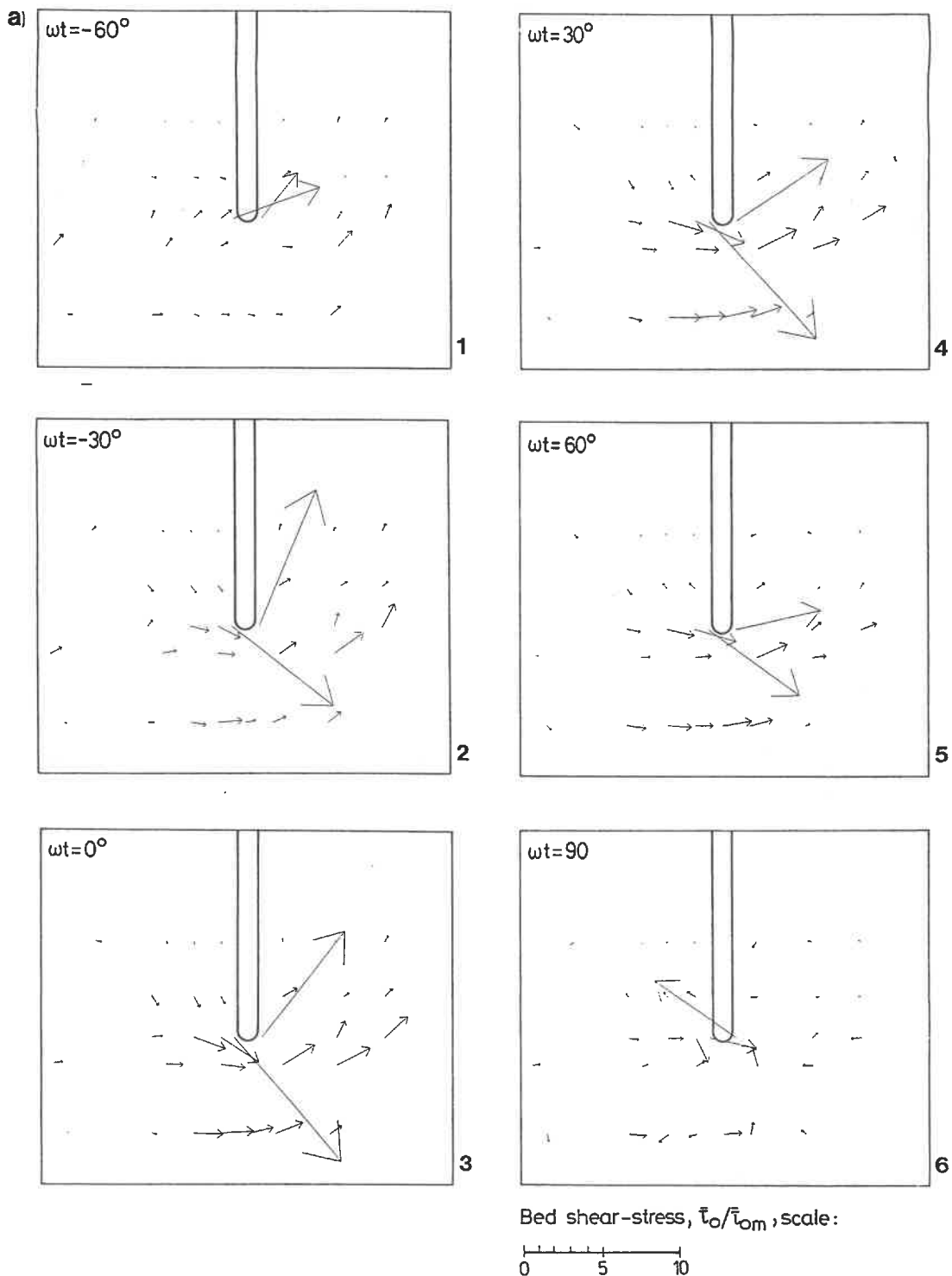


Fig. 11. (a) Time development of bed shear stress. $KC = 1$. The phase $\omega t = 0^\circ$ corresponding to the wave crest. (b) Time development of bed shear stress. $KC = 8$. The phase $\omega t = 0^\circ$ corresponding to the wave crest.

tip of the breakwater or very close to it. Fig. 13, on the other hand, illustrates how the maximum scour depth develops with time. As seen, the maximum scour depth attains its equilibrium stage through a transition period.

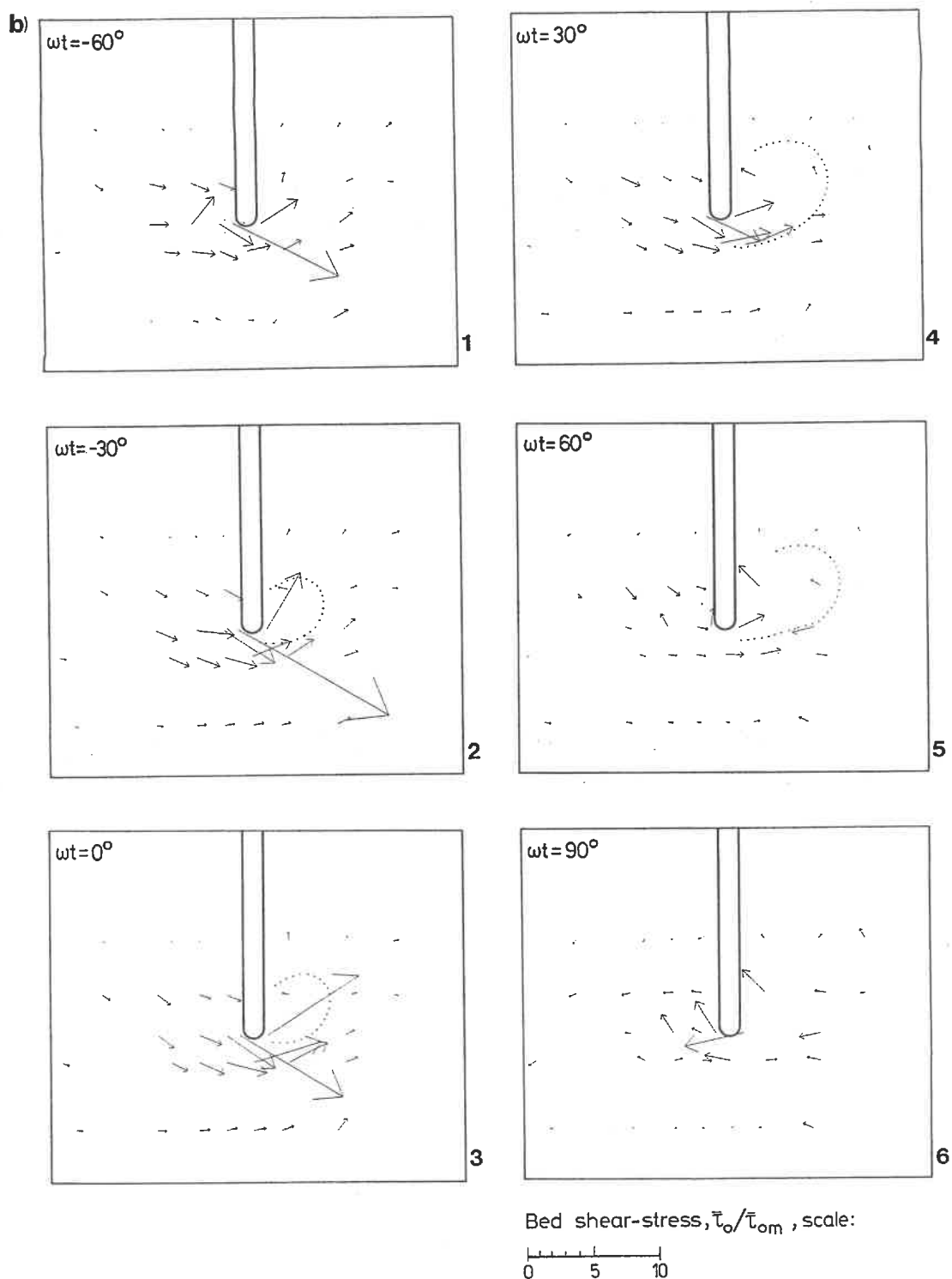


Fig. 11 (continued).

Fig. 13 indicates that the time needed for a substantial scour to occur is $O(10 \text{ min})$, or alternatively $O(200 \text{ waves})$. This is in contrast to the much larger times needed for 2-D scour, namely $O(10^4 \text{ waves})$, Fig. 27 in Xie (1981). The reason for this behaviour is that

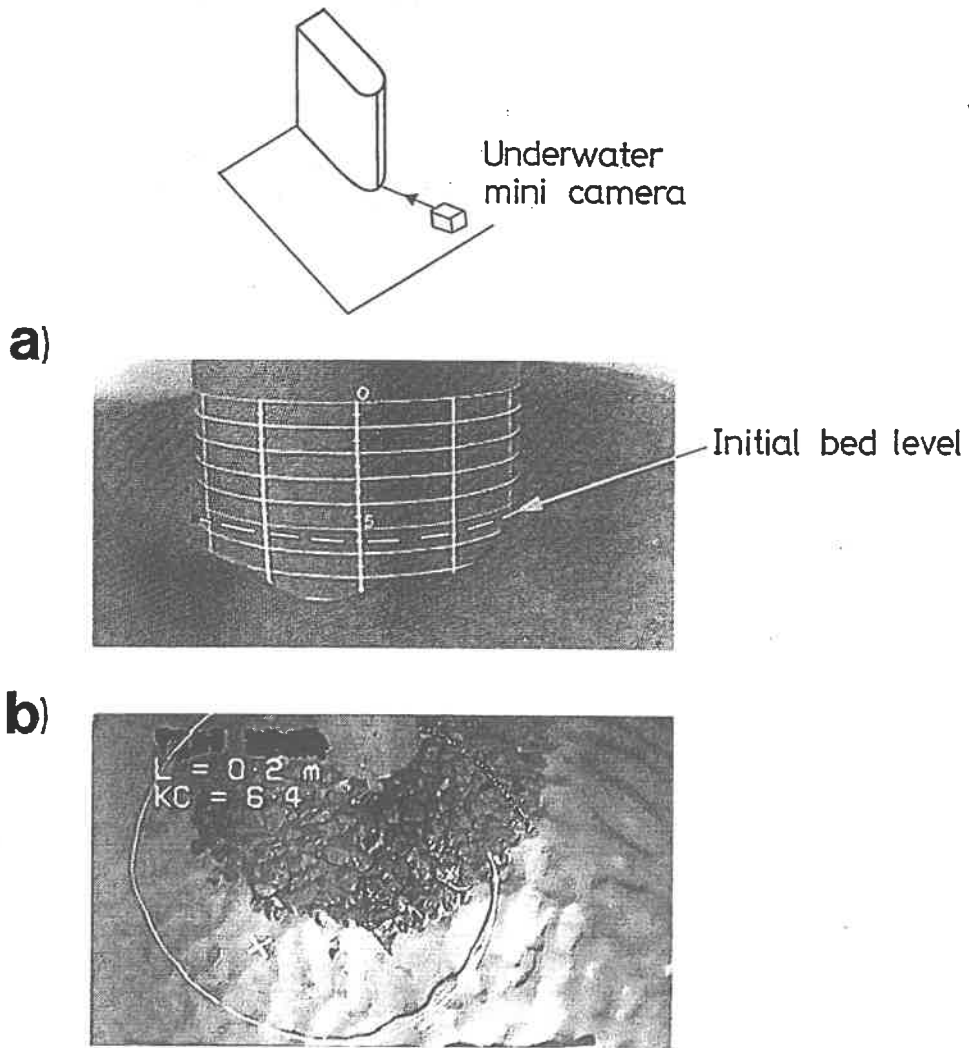


Fig. 12. Scour picture as viewed from “a” in Fig. 3. (a) Breakwater 1 (Test 12, Table 3). (b) Breakwater 2 (Test 9, Table 7), Cross sign indicates the point where the scour depth is maximum.

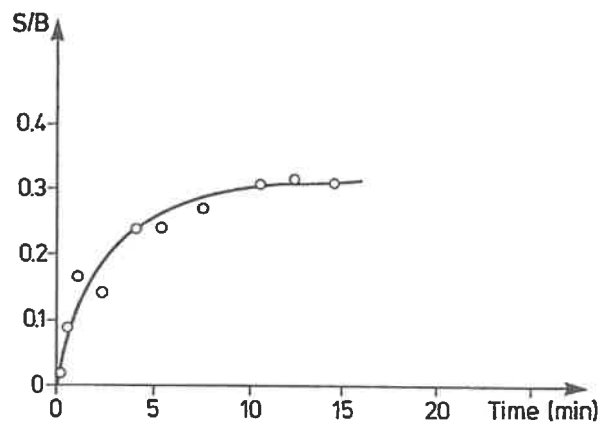


Fig. 13. Scour-depth development. Test 13, Table 3.

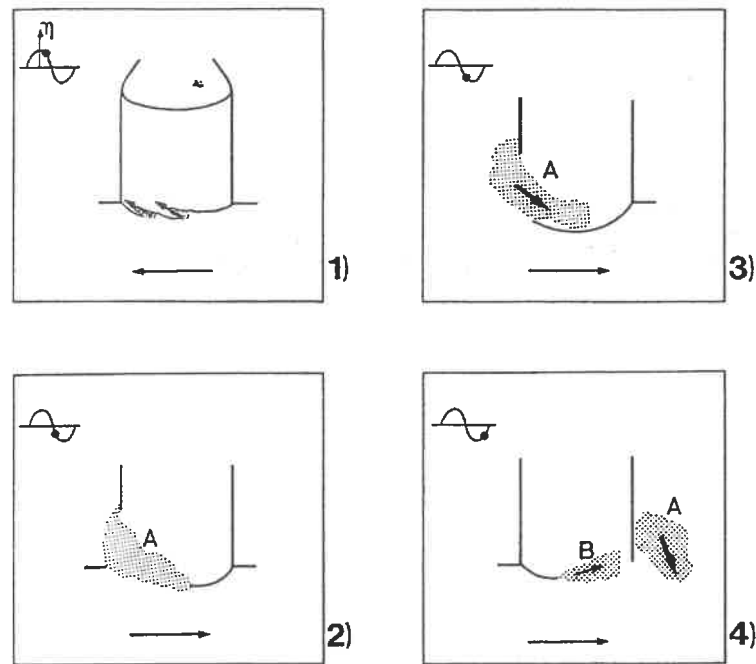


Fig. 14. Sequence of video frames illustrating the way in which scour occurs. The small sketches on the upper left corner of each frame shows the water surface elevation at the section where the breakwater is located.

the mechanism for the present head-scour is entirely different from that of 2-D trunk scour; in the present case, the scour is mainly due to the lee-wake vortices (as will be seen later in the section), while the scour in the 2-D case is due to the steady streaming (Section 1). The latter is known to be a very slow process, as is demonstrated by Fredsøe and Sumer (1997) in conjunction with the scour around the head of a rubble-mound breakwater. It may be noted that the present time scales are consistent with those observed for the case of vertical piles (Sumer et al., 1993b) where the mechanism behind the scour is similar to the present case, namely the scour is induced by the effect of vortices.

Fig. 14 schematically illustrates the way in which the scour develops around the structure. The bed at the head of the structure is eroded by the high-speed flow (A in Frame 1), and the eroded sediment is swept into the lee-wake vortex where the sediment grains are lifted up into the upper portion of the lee-wake vortex (A in Frame 2). As this vortex is washed around the structure by the flow reversal (Vortex K, Fig. 7), the sediment trapped in the vortex is carried by this vortex (A in Frame 3) and eventually deposited away from the structure (A in Frame 4). Clearly, the erosion in Frame 1 and further transport of sand illustrated in Frame 2 are related to the large amplification in the bed shear stress (Figs. 10 and 11). In the next half cycle, the process repeats itself; this time, the flow structure B (Frame 4), plays the same role as A in the previous half cycle.

Since the formation and the development of the lee-wake vortex is primarily governed by the KC number (Figs. 5 and 8), it might be expected that the resulting scour, too, is mainly governed by this parameter.

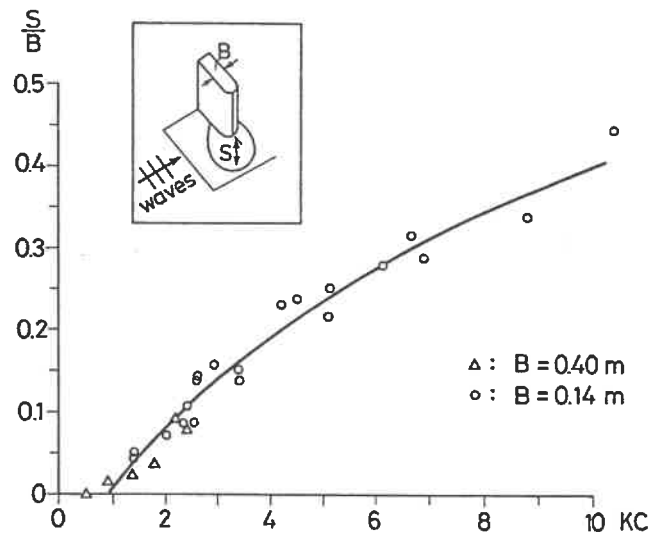


Fig. 15. Normalized equilibrium scour depth as function of KC, at the head of breakwater with no protection layer. Breakwater 1 experiments. Solid curve: Eq. (5). Live bed ($\theta > \theta_{cr}$).

The importance of the KC number in scour problems such as the scour below pipelines and that around vertical piles has been demonstrated previously (Sumer and Fredsøe, 1990 and Sumer et al., 1992, respectively). Gökçe and Günbak's (1991) experimental study, and Hansen's (1992) numerical study have later confirmed the relation between the scour depth and the KC number obtained in Sumer and Fredsøe (1990) in conjunction with scour below pipelines.

Fig. 15 depicts the present maximum scour-depth data obtained for Breakwater 1, plotted as function of KC number. S , the maximum (equilibrium) scour depth, is normalized by B , the diameter of the head. As is seen, the correlation is remarkable.

First of all, the scour depth is practically nil for the values of KC number below approximately unity. This is due to the non-separated flow regime observed for such KC numbers (Fig. 5). It is interesting to note that the amplification in the bed shear stress for such small KC numbers is still rather large (Fig. 10a and Fig. 11a), although the scour is nil. Clearly, this highly amplified oscillatory flow at the tip of the breakwater stirs up the sediment and brings it into suspension. This suspended sediment is then driven by the flow back and forth around the head. However, in the absence of a convection mechanism (a mechanism such as that described in Fig. 14) the sediment will not be carried away from the structure, and the net scour around the head of the breakwater will presumably be zero. (It may be noted, however, that some slight scour may occur even in the absence of a convection mechanism, due to turbulent diffusion.)

Second, the scour depth increases with increasing KC number. This increase is due to the increased extension of the lee wake with the KC number (Fig. 8).

Third, although limited to a narrow range of KC number, namely $0 < KC < 2.5$, the results obtained for two different sizes of breakwaters ($B = 0.14$ and $B = 0.40$ m) collapse on a single curve. The latter indicates that the results are apparently free of scale effects. Also, it further indicates small-scale ripples present in the tests are not an essential factor in the scour process, although the B value for the large model is a factor

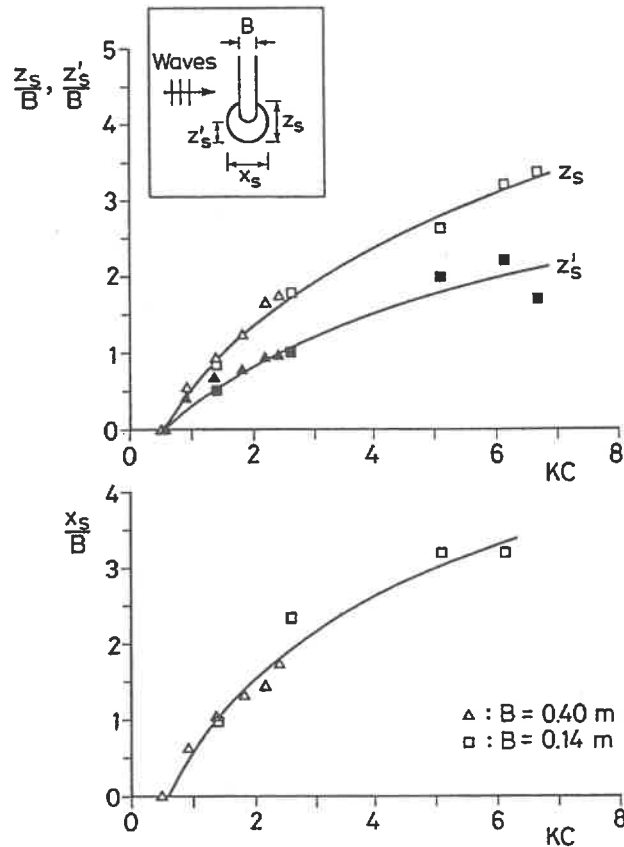


Fig. 16. Plan-view extent of equilibrium scour hole as function of KC at the head of breakwater with no protection layer. Breakwater 1 experiments. Live bed ($\theta > \theta_{cr}$).

of 3 larger than that for the small model. This is because the bed shear stress is so large near the tip of the breakwater that the ripples are washed away in this area. Therefore, they are not an influencing factor in the scour process. A general discussion on the scale effects can be found in the review paper by Oumeraci (1994b).

Finally, the scour-depth-versus-KC relationship in Fig. 15 can be represented by the following empirical expression

$$\frac{S}{B} = 0.5C[1 - \exp\{-0.175(KC - 1)\}] \tag{5}$$

in which C is an uncertainty factor with a mean value of 1 and a standard deviation of $\sigma_C = 0.6$.

Fig. 16 gives the data regarding the plan-view extent of the scour hole. Here, too, the correlation between the dimensions of scour hole and the KC number is remarkable. Furthermore, comparison of Figs. 8 and 16 indicates that the plan-view dimensions of scour hole agree with those of the lee-wake vortices.

To study the sensitivity of the results to the water depth, additional tests were carried out with two different water depths, namely $h = 25$ cm and 50 cm. These tests indicated that the results were practically the same as in the main experiments where $h = 40$ cm.

Likewise, a similar sensitivity study was carried out with regard to the length, ℓ , of

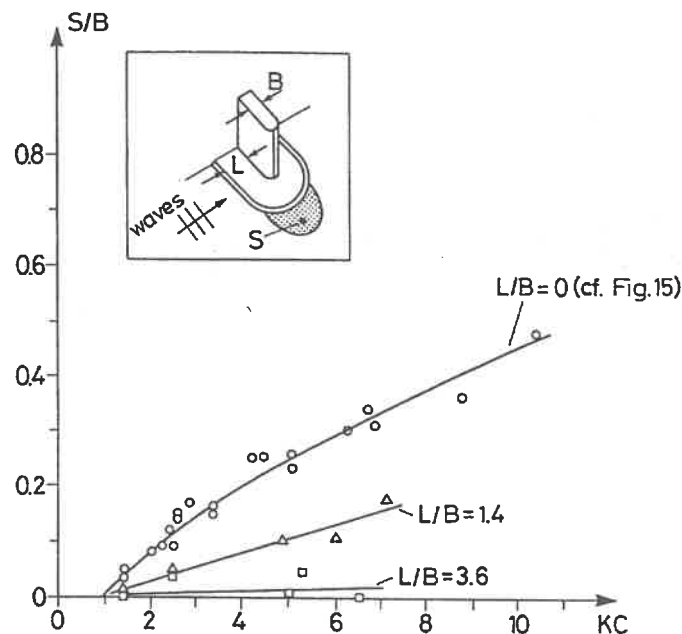


Fig. 17. Normalized scour depth, S/B , at the head of breakwater with a protection layer. $L/B = 0$ data: Breakwater 1 with $B = 14$ cm (from Fig. 15). The rest of the data: Breakwater 2. Live bed ($\theta > \theta_{cr}$).

the breakwater model exposed to the flow: additional tests were undertaken with two different model lengths $\ell = 140$ cm and $\ell = 200$ cm. These experiments, gave practically the same results as in the case of the main experiments with $\ell = 170$ cm.

Although the present findings indicate that the scour is practically nil for $KC \leq 1$, a slight erosion–deposition pattern may appear in the field due to the secondary, steady streaming mechanism. The latter mechanism is described in Fredsøe and Sumer (1997) in the accompanying paper in relation to scour at the head of a rubble-mound breakwater.

5.1. Effect of a protection layer

Fig. 17 presents the scour data obtained for Breakwater 2 (the breakwater with a protection layer) together with the data presented in Fig. 15 ($L/B = 0$ situation). The data corresponding to $L/B = 0.71$ ($L = 10$ cm, see Table 7) are not shown in the figure, to keep the figure relatively simple. The scour depths measured for this value of L are mainly below those measured for $L/D = 0$ (cf. Tables 3 and 7). Fig. 17 clearly indicates that the larger the width of the protection layer, the smaller the scour depth. In fact, for $L/B = 3.6$, the scour is practically eliminated for the tested range of KC .

To see the effect of the height of the protection layer, a sensitivity study was undertaken. In this study, the Breakwater 2 tests were repeated for a protection layer with zero height (i.e., the surface of the protection layer is flush with the surface of the sand bed). These tests indicated that the results were insensitive to the height of the protection layer. This result is not entirely unexpected, since the key point here is to protect the sand bed against the action of the lee-wake vortices. As long as the plan-view

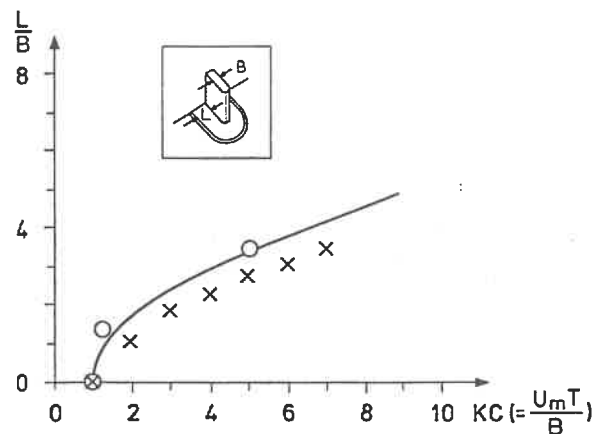


Fig. 18. The width of protection layer necessary for scour protection at the head of a vertical-wall breakwater. Solid line: Eq. (6). Crosses: the average size of lee-wake vortices. Circles: from Fig. 17 corresponding to $S/B \leq 0.01$.

extent of the protection layer is maintained larger than the size of the area affected by the vortices (regardless of the height of the protection layer), the bed will be protected.

Fig. 18 displays the required width of the protection layer as function of the KC number, based on the scour data in Fig. 17, corresponding to $S/B \leq 0.01$. (The resulting protection-layer width is not extremely sensitive to the particular choice of the limiting value, namely 0.01. However, the chosen value does imply that the allowed scour is of no practical significance). The data related to the lee-wake vortex-dimensions are also plotted in Fig. 17 for comparison. The figure reveals that the area of the bed which is exposed to the action of the lee-wake vortex must be covered. The width of the protection layer may be expressed by the following empirical expression

$$\frac{L}{B} = 1.75(KC - 1)^{0.5} \quad (6)$$

Using the linear wave theory, the preceding equation can be written in the following alternative form

$$L = 1.75B \left[\frac{\pi H}{B \sinh(kh)} - 1 \right]^{0.5} \quad (7)$$

in which H is the wave height and k is the wave number. (It may be noted that, for the 2-D scour in the trunk section, Xie (1985, Section 5) reports that there is essentially no scour over a distance of $\lambda/2$ from the breakwater, when L is taken as $3\lambda/8$ in which λ is the wave length.)

Regarding the use of the preceding expressions in the design work, Eqs. (6) and (7), caution must be exercised when there are other effects such as the head shape, the presence of current and the angle of attack. The influence of these effects on scour will be described in the following sub-sections.

Also, it must be remembered that the preceding equations have been obtained, using regular waves, and also with no significant steady-streaming effect (the latter led to

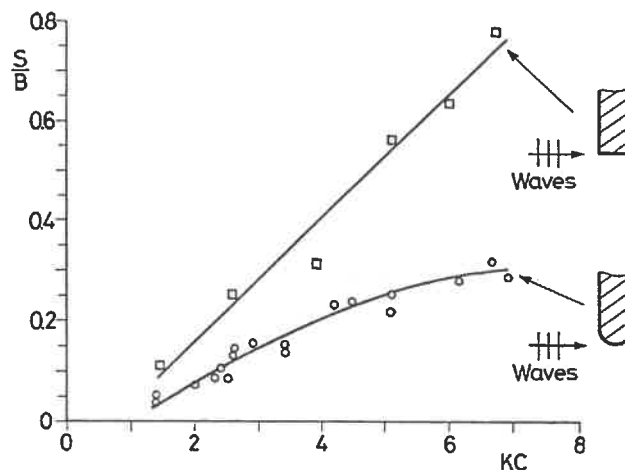


Fig. 19. Effect of the shape of breakwater head on equilibrium scour depth.

considerably shorter test durations, as has been pointed out at the beginning of this section in relation to Fig. 13).

It may be noted that when the protection layer is designed in the way as described above, the maximum value of the Keulegan–Carpenter number based on the *total* width of the protection layer (i.e., $2L + B$) will be smaller than $O(1)$ in most of the practical cases. This ensures that no scour will occur in the sand bed around the protection layer itself (Fig. 15).

5.2. Effect of head shape

Fig. 19 illustrates the effect of head shape on the scour depth. The round-head results are taken from Fig. 15. It is clear that the scour hole is deeper in the case of sharp-edged-head breakwater than in the case of round-head breakwater. This may be attributed to the increase in the size of lee-wake vortices in the case of sharp-edged head, although the tests revealed that the plan-view extents of the scour holes were practically the same as in the case of round-head breakwater. The latter suggests that, although the size of the lee-wake vortex may differ in the studied two cases, their trajectories during the flow reversals (where the vortices are washed around the structure, Fig. 14) may not be extremely different, resulting in practically the same plan-view extents of the scour holes. The aforementioned trajectories are not extremely different because they are, to a first approximation, governed by the KC number rather than the head shape.

5.3. Effect of angle of attack

Fig. 20 depicts the results of the tests with two different values of the angle of attack, namely $\phi = 60^\circ$ and 120° together with those presented in Fig. 15. As seen, the angle of attack is also an influencing parameter. The results show that the scour depth is slightly larger when $\phi = 60^\circ$ while it is smaller when $\phi = 120^\circ$ than the values experienced in

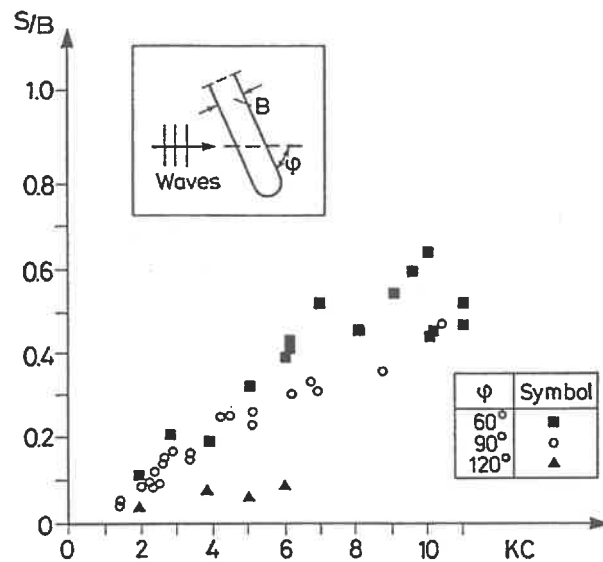


Fig. 20. Effect of angle of attack on scour depth.

the case of $\phi = 90^\circ$. The results for $\phi = 60^\circ$ and 120° do not collapse although these ϕ values are symmetric with respect to $\phi = 90^\circ$. This is due to asymmetry in the waves; the asymmetry between the crest and the trough may lead to different scour depths for the two symmetric angles of attack. This is because the plan-view extension of the lee-vortex in the crest half period is larger for $\phi = 60^\circ$ than for $\phi = 120^\circ$. As a matter of fact, the vortex size decreases with increasing ϕ . This explains why the scour depth is slightly smaller for $\phi = 90^\circ$ than that for $\phi = 60^\circ$ (Fig. 20).

5.4. Effect of superimposed currents

A few experiments have been conducted to see the effect of the presence of a current on the scour depth (Table 8). The current in the tests was in the same direction as the wave propagation. Each test was conducted for only 30 minutes. This was due to the limited sand-layer thickness in the experiments. Therefore the results regarding the scour depth indicated in Table 8 do not represent the equilibrium values. The data in Table 8 are plotted in Fig. 21 along with the corresponding pure-waves scour data indicated in Table 3.

Also plotted in Fig. 21 is the equilibrium scour depth calculated from the empirical relationship given by Liu et al. (1961) (the dashed asymptotic line), namely

$$\frac{S}{h} = c \left(\frac{\ell}{h} \right)^{0.4} \left(\frac{U_c}{\sqrt{gh}} \right)^{0.33} \quad (8)$$

for the case of a groin exposed to a steady current. Here ℓ is the length of the groin and c is a constant which can be taken as 2.15, as recommended by Liu et al. (1961), when the groin terminates at a vertical wall and also when it has a vertical wall on the upstream side. The plotted value is the one which was found for the experimental conditions adopted in the present combined waves and current tests (namely, U_c (the

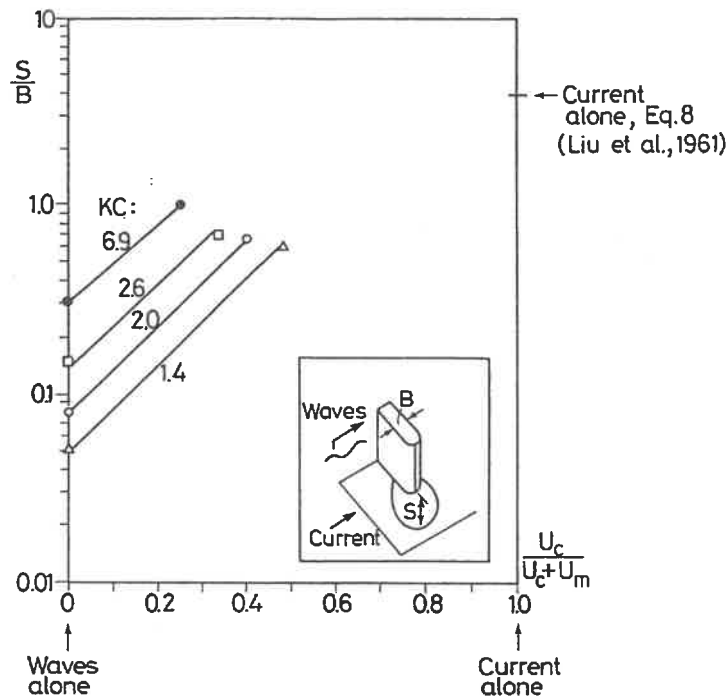


Fig. 21. Effect of current on scour in combined co-directional waves and current. Live bed ($\theta > \theta_{cr}$). Data points: Present experiments. Dashed line: Calculated from Eq. (8) (see the text for details).

depth-averaged current velocity) = 10 cm/s, $h = 40$ cm, $B = 14$ cm and $\ell = 170$ cm). No current-alone test was carried out in the present experiments, as the thickness of the sand layer was too small (Fig. 4) to accommodate the anticipated scour depth, a depth in the order of magnitude of 50–60 cm.

From the figure, it is seen that the presence of a steady current causes the scour depth to increase considerably. The increase in the scour depth may be attributed partly (1) to the formation of horse-shoe vortex in front of the structure (Fig. 9a) revealed by the present hydrogen-bubble flow-visualization tests made in the presence of a slight current, partly (2) to an increase in the effective KC number in the half period where the wave-induced flow is in the same direction as the current, and partly (3) to the presence of the current itself by which the eroded material is transported away from the structure in the downstream direction.

It may be noted that the video recording of the scour process made in these tests revealed very clearly the presence of a highly strong horse vortex, which is visualized by the sand.

The latter may be an important element in the scour process in the case of extremely small KC numbers. While the net scour around the structure is zero for very small KC numbers ($KC \leq 1$) in the case of pure waves (Fig. 15), substantial scour may occur due to the presence of even a small current, as suggested by Fig. 21. The examined combination of waves and current may be relevant in relation to the scour occurring at the head of a jetty.

Finally, it should be noted that further caution must be taken when Eq. (6) (or, alternatively, Eq. (7)) is used in the design work in the case of presence of a current,

since the scour depth in this case will be larger, and therefore larger extents of the bed area around the structure head may need to be protected.

5.5. Scale effects

In the case of pure waves, the scour process is related directly to the formation and further development of the lee-wake vortex. Therefore the scale effect on the scour must be felt through the scale effect related to the formation and the development of the lee-wake vortex itself. The latter has been discussed in Section 3.4, and it was concluded that the non-dimensional extents of the lee-wake vortices in the field, namely L_x/B and L_y/B in Fig. 8, may be slightly smaller than those observed in the small-scale laboratory experiments. This suggests that the scour in the field may be slightly smaller than that predicted by the diagram in Figs. 15 and 17.

To see the effect of roughness discussed in Section 3.4 on the end results, some scour tests were carried out with Breakwater 1 ($B = 14$ cm) with its surface covered by crushed stones the size of about 1 cm. The results of these tests are plotted in Fig. 22 together with those obtained for the smooth-surface breakwater model (Fig. 15). The width of the breakwater, B , was taken 16 cm in the case of roughened breakwater when plotting the normalized scour depth. Although a slight decrease in the scour depth was expected according to the argument put forward in the preceding paragraph when the surface is rough, the results in Fig. 22 indicate that this is not the case. This may be due to small Re numbers, $Re = O(10^4)$ in the laboratory tests.

In the case of combined waves and current, on the other hand, the major factors are (1) the formation of a horse-shoe vortex in front of the structure and (2) the mere presence of the current itself (so that the sediment can be carried away from the structure), as discussed in the preceding paragraphs. Item (1) is practically unaffected by the scale effect, as long as a current boundary layer exists. Therefore the results depicted in Fig. 21 might be expected to be unaffected by the change in the scale.

The preceding paragraphs discuss the possible scale effects in relation to the scour processes around the head of the breakwater. The scale effects in conjunction with scour

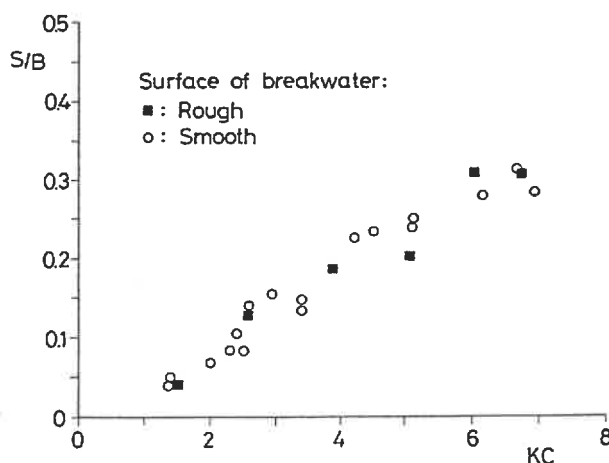


Fig. 22. Effect of surface roughness of breakwater on scour depth.

around piles have been discussed in Sumer et al. (1992) and Sumer et al. (1993b). Oumeraci (1994b), on the other hand, discusses the scale effects with particular emphasize on the 2-D scour in front of a vertical-wall breakwater.

6. Conclusions

(1) Three kinds of flow regimes are identified for flow around the circular-head of a vertical-wall breakwater exposed to waves: (a) the unseparated-flow regime, which is observed for $KC \leq 1$ where KC is the Keulegan–Carpenter number based on the diameter of the breakwater head, B ; (b) the separated flow regime with no horse-shoe-vortex formation in front of the breakwater observed for $1 \leq KC \leq 12$; and finally (c) the separated flow regime with a horse-shoe-vortex formation in front of the breakwater. This flow regime is observed when $KC \geq 12$.

(2) Scour around the head of such a structure is governed by the KC number. The maximum scour depth, S , is found to be practically nil when $KC \leq 1$. (A slight scour-and-deposition pattern, induced by the steady streaming around the head may exist, however.) For $KC \geq 1$, the normalized scour depth S/B increases with increasing KC number.

(3) The scour may be prevented by employing a conventional stone protection. The width of the protection layer may be selected according to the empirical expression given in Eq. (6) (or, alternatively, Eq. (7). Caution must be exercised, however, when there exist other effects such as the head shape, the presence of a current and the angle of attack.

(4) The head shape is found to be an important factor. The maximum scour depth may increase by a factor of 2 when the head is changed from a round head to a sharp-edged one.

(5) Likewise, the angle of attack is also an influencing factor.

(6) The effect of the presence of co-directional current on the scour depth is found to be extremely important. The results indicate that, given the KC number, the scour depth increases considerably even with a slight current.

The present results are applicable only for non-cohesive sediment.

7. Notation

B	Diameter (or width) of the head of the breakwater.
c	Constant in the empirical formula given in Eq. (8).
C	Constant in the empirical formula given in Eq. (5).
d	Sand grain size taken equal to d_{50} .
f_w	Wave friction coefficient.
g	Acceleration due to gravity.
h	Water depth at the structure head.
KC	Keulegan–Carpenter number (Eq. (1)).
l	Length of breakwater.

L	Width of protection layer from the side of the breakwater to the sand-bed end.
$L_{x,z}$	x - and z -dimensions of lee-wake vortex, respectively.
Re	Reynolds number based on U_m and B , $Re = U_m B / \nu$.
s	Relative density of sand grains, $s = \rho_s / \rho$.
S	Maximum scour depth.
T	Wave period.
U_c	Depth-averaged current velocity.
U_m	Maximum value of the undisturbed <i>orbital</i> velocity at the sea bottom.
U_{fm}	Maximum value of bed friction velocity.
x	Coordinate axis in the direction (in the horizontal plane) perpendicular to the breakwater.
y	Vertical coordinate axis.
z	Coordinate axis in the direction of breakwater.
x_s, z_s	x - and z -dimensions of scour hole.
z'_s	z -dimension of scour hole measured from the tip of breakwater.
α	Amplification in bed shear stress (Eq. (4)).
θ	Shields parameter (Eq. (2)).
ν	Kinematic viscosity of water.
τ_0	Bottom shear stress.
ϕ	Angle of attack of waves.

Acknowledgements

This work was undertaken as part of the “MAST II Monolithic (Vertical) Coastal Structures” research programme. It was funded jointly by the Commission of the European Communities, Directorate General for Science, Research and Development, under MAST contract No. MAS2-CT92-0047 and by the Danish Technical Research Council (STVF) under the programme “Marine Technique”.

Dr. K. Tunç Gökçe took part in the flow visualization tests. The scour tests were carried out partly by Dr. Gökçe and partly by Mr. Søren Bo Hansen, M.Sc., and Dr. Niels Christiansen was involved in the bed shear stress measurements.

References

- Breusers, H.N.C., Nicollet, G. and Shen, H.W., 1977. Local scour around cylindrical piers. *J. Hydraul. Res.*, 15(3): 211–252.
- De Best, A., Bijker, E.W. and Wichers, J.E.W., 1971. Scouring of sand bed in front of a vertical breakwater. In: *Proc. Conf. on Port and Ocean Eng. under Arctic Conditions*, NTH, Trondheim, pp. 1077–1086.
- Fredsøe, J., 1984. Turbulent boundary layers in wave-current motion. *J. Hydraul. Eng. ASCE*, 110(HY8): 1103–1120.
- Fredsøe, J. and Sumer, B.M., 1997. Scour at the round head of a rubble-mound breakwater. *Coastal Eng.*, 29: 231–262.
- Gökçe, T. and Günbak, A.R., 1991. Self-burial and stimulated self-burial of pipelines by waves. In: *Proc. of the First (1991) International Offshore and Polar Engineering Conf.*, Edinburgh, Vol. 2, pp. 308–314.

- Gökçe, T., Sumer, B.M. and Fredsøe, J., 1994. Scour around the head of a vertical-wall breakwater. In: Proc. International Conf. on Hydro-Technical Engineering for Port and Harbor Construction, Yokosuka, pp. 1097–1116.
- Hansen, E.A., 1992. Scour below pipelines and cables: A simple model. In: Proceedings of 11th Offshore Mechanics and Arctic Engineering Conference (OMAE 92), Vol. 5A, Pipeline Technology, ASME, pp. 133–138.
- Herbich, J.B., Schiller, R.E., Jr., Watanabe, R.K. and Dunlap, W.A., 1984. Sea Floor Scour — Design Guidelines for Ocean Founded Structures (Ocean Engineering 4). Marcel Dekker, New York, NY, pp. 203–210.
- Hughes, S.A. and Fowler, J.E., 1991. Wave-induced scour prediction at vertical walls. In: Proc. Conf. Coastal Sediments '91, ASCE, pp. 1886–1899.
- Irie, I. and Nadaoka, K., 1984. Laboratory reproduction of seabed scour in front of breakwaters. In: Proc. 19th ICCE, Houston, TX. ASCE, pp. 1715–1731.
- Jensen, B.L., Sumer, B.M. and Fredsøe, J., 1989. Turbulent oscillatory boundary layers at high Reynolds numbers. *J. Fluid Mech.*, 206: 265–297.
- Liu, H.K., Chang, F.M. and Skinner, M.M., 1961. Effect of bridge constriction on scour and backwater. Civ. Eng. Section, Colorado State Univ., Fort Collins, Colorado, Report No. CER60HKL22, Prepared for Bureau of Public Roads under Contract CPR11-5480, February, 1961. The report is obtainable from ISVA.
- Oumeraci, H., 1994a. Review and analysis of vertical breakwater failures — lessons learned. In: H. Oumeraci, J. van der Meer and L. Franco (Editors), *Vertical Breakwaters*. *Coastal Eng.*, 22: 3–29.
- Oumeraci, H., 1994b. Scour in front of vertical breakwaters — Review of problems. In: Proc. International Workshop on Wave Barriers in Deep Water, Port and Harbour Research Institute, Yokosuka, pp. 281–307.
- Sarpkaya, T., 1986. Force on a circular cylinder in viscous oscillatory flow at low Keulegan–Carpenter numbers. *J. Fluid Mech.*, 165: 61–71.
- Sumer, B.M. and Fredsøe, J., 1990. Scour below pipelines in waves. *J. Waterw. Port Coastal Ocean Eng.* ASCE, 116(3): 307–323.
- Sumer, B.M., Fredsøe, J. and Christiansen, N., 1992. Scour around vertical pile in waves. *Am. Soc. Civ. Eng. J. Waterw. Port Coastal Ocean Eng.*, 118(1): 15–31.
- Sumer, B.M., Arnskov, M.M., Christiansen, N. and Jørgensen, F.E., 1993a. Two-component hot-film probe for measurements of wall shear stress. *Exp. Fluids*, 15: 380–384.
- Sumer, B.M., Christiansen, N. and Fredsøe, J., 1993b. Influence of cross-section on wave scour around piles. *Am. Soc. Civ. Eng. J. Waterw. Port Coastal Ocean Eng.*, 119(5): 477–495.
- Xie, S.L., 1981. Scouring patterns in front of vertical breakwaters and their influence on the stability of the foundations of the breakwaters. Report, Dept. of Civil Eng., Delft University of Technology, 61 pp.
- Xie, S.L., 1985. Scouring patterns in front of vertical breakwaters. *Acta Oceanologica Sinica*, 4(1): 153–164.

Scour at the round head of a rubble-mound breakwater

Dansk Vandbygningsteknisk Selskabs seminar om
"Nyere metoder til projektering af moler"
Aalborg Universitet, den 25. marts 1998

Scour at the round head of a rubble-mound breakwater

J. Fredsøe, B.M. Sumer

Department of Hydrodynamics and Water Resources (ISVA); Technical University of Denmark, 2800 Lyngby, Denmark

Received 18 December 1995; accepted 13 May 1996

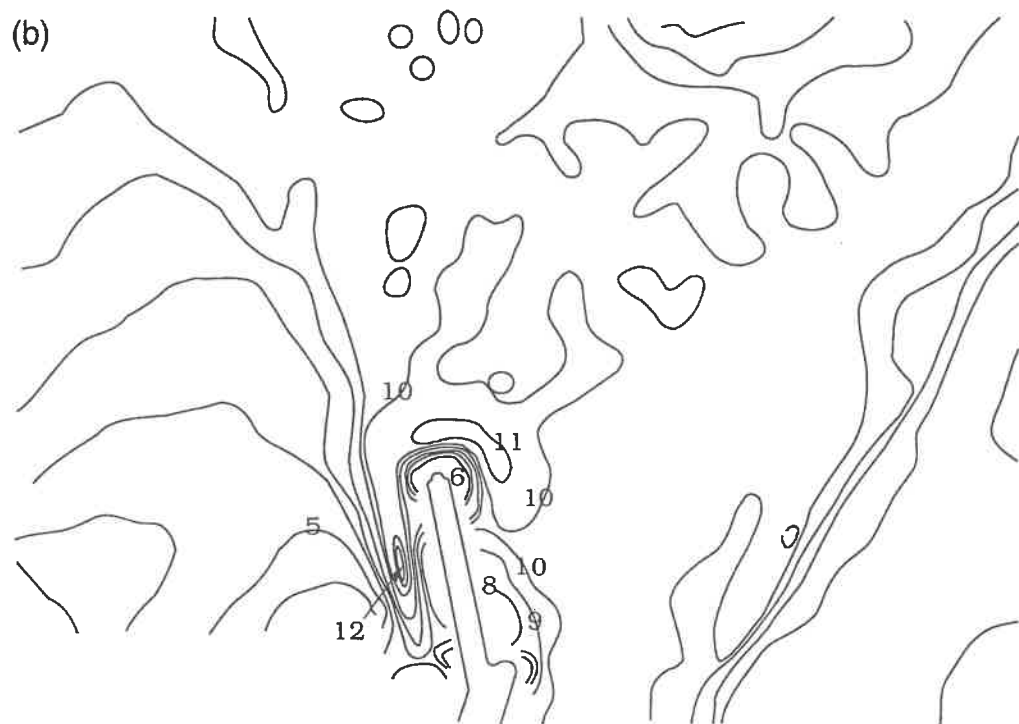
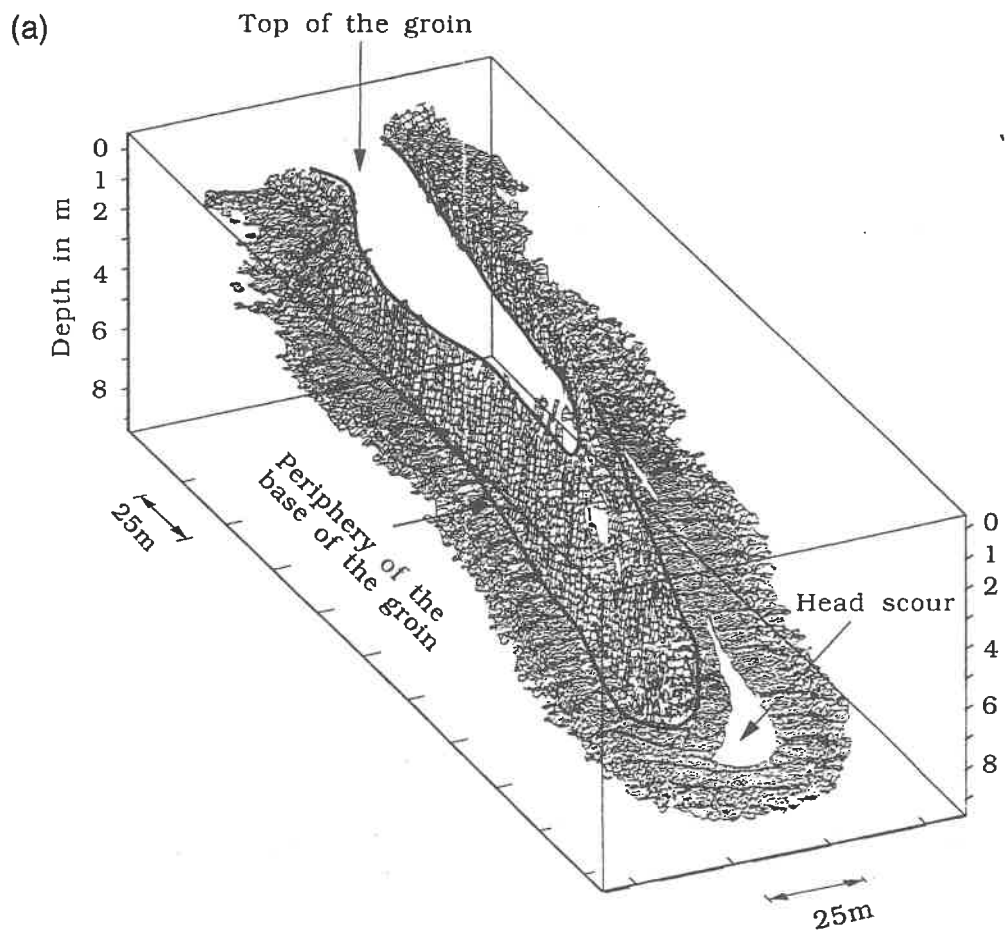
Abstract

This study complements the investigation on scour around the head of a breakwater, reported in the companion paper where the case of vertical-wall breakwater was considered. The present study deals with the case of rubble-mound breakwater. Two key mechanisms with regard to the scour processes around the round head of the breakwater are identified. One is the steady streaming occurring around the head in plan view. This generates a scour hole in front of the breakwater. The second one is the plunging breaker which occurs locally at the breakwater head. This generates a scour hole at the lee-side of the breakwater. The Keulegan–Carpenter number based on the base diameter of the breakwater head appears to be the main governing parameter regarding the streaming-induced scour, while a parameter, namely $T_p \sqrt{gH_s} / h$, involving the peak wave period, T_p , the significant wave height, H_s , the water depth, h , and the acceleration due to gravity, g , appears to be the main governing parameter regarding the breaker-induced scour. The scour depth increases with increasing values of these parameters. The conventional stone protection is investigated in the study. An empirical formula is developed for the extent of the protection layer.

Keywords: breakwaters; currents; sand; scour; waves

1. Introduction

The occurrence of scour around rubble-mound breakwaters is one of the failure modes of these structures (see, for example, Lillycrop and Hughes, 1993). Scour may be experienced (1) along the trunk section of the breakwater and (2) around the head of the structure. Basically, the scour causes toe failure and therefore slumping of the structure's armour layer into the generated scour hole, presumably leading to the instability of the structure.



Scour along the trunk section and its associated scour protection in the two-dimensional case where the waves attack at right angle to the breakwater have been studied by Sawaragi and Kawasaki (1960), Hales (1980), Eckert (1983) and Markle (1989). A recent review of the subject is given by Fowler (1993). The key mechanism of scour in this case is the steady streaming in the vertical plane caused by the action of partially standing waves in front of the breakwater, similar to the case of vertical-wall breakwater (see Introduction section in Sumer and Fredsøe, 1997, hereafter referred to as SF). The difference between the vertical-wall breakwater case and the rubble-mound breakwater case lies in the reflection coefficient associated with the rubble-mound structure; scour decreases with decreasing reflection coefficient.

Regarding the scour occurring around the head of the rubble-mound breakwater, this three-dimensional scour may be caused by mechanisms which are different from that experienced in the previously mentioned two-dimensional case. Lillycrop and Hughes' (1993) recent report on scour hole problems experienced by the U.S. Army Corps of Engineers gives quite a substantial amount of field data, revealing scour hole formations around rubble-mound structure heads. Fig. 1 displays two field measurements from the Danish West Coast; Fig. 1a presents a three-dimensional picture of a scour formation monitored near the head of a groin, Groin No. 57, located in Thyborøn, while Fig. 1b presents a contour plot of bed topography monitored near the head of the Hirtshals harbour breakwater. Although the precise environmental conditions which generated these scour formations are not known, the general pattern of scour displayed in Fig. 1 resembles rather well that observed in the present laboratory investigation, as will be seen later in the paper.

In SF, scour around the head of a vertical-wall breakwater was investigated. It was found that the major mechanism behind this scour is the formation of lee-wake vortices in each half period of the waves; sediment swept into these vortices is carried by these flow structures and eventually deposited away from the head of the breakwater, resulting in a net scour around the breakwater head. The study showed that the Keulegan–Carpenter number, KC , based on the diameter of the breakwater head, B , is the main governing parameter with regard to the formation of lee-wake vortices and the resulting scour process.

In the case of rubble-mound breakwater, however, the range of the KC number, defined by

$$KC = \frac{U_m T_p}{B} \quad (1)$$

is practically from nil to $O(1)$, meaning that no lee-wake vortices would form in this case, as will be demonstrated in the present paper. (Here, U_m is the maximum value of the undisturbed orbital velocity at the sea bottom, T_p the wave period, and B the base

Fig. 1. (a) Three-dimensional illustration of scour formation monitored near the head of Groin No. 57, located in Thyborøn on the Danish West Coast (by courtesy of John Jensen, Danish Coastal Authority). (b) Contour plot of bed topography near the head of the Hirtshals harbour breakwater, on the Danish West Coast. Numerical figures indicate the depth in metres (by courtesy of Hans Kjær, State Ports Authority, Denmark).

diameter of the round head.) This means that the scour around the head in the present rubble-mound breakwater case is caused by mechanisms different from that caused by the lee-wake vortex.

The purpose of the present study is to make a detailed investigation of scour around the round head of a rubble-mound breakwater. It turns out that two effects, namely (1) the wave-induced steady streaming around the head and (2) the occurrence of a local, plunging breaker at the head, are mainly responsible for the scour processes in the present case.

Some of the earlier results of this investigation have been presented at the 1994 Coastal Engineering Conference (Sumer et al., 1994).

2. Experimental set-up and procedure

2.1. Flow-visualization experiments

The purpose of these experiments was to study the formation and the development of lee-wake vortices around the head of the rubble-mound breakwater.

The experiments were conducted in the same wave flume as that used in SF. The experimental set-up is depicted in Fig. 2. The lay-out of the breakwater was the same as in SF (see Fig. 1 in SF). The side slope of the breakwater was chosen to be 1 : 1, a slope value somewhat larger than that normally encountered in practice. The hydrogen-bubble technique was used in the experiments. The details regarding the experimental technique and all the other pertinent information are given in SF.

2.2. Bed shear-stress experiments

These experiments were carried out in the same wave flume as in the flow visualization experiments. The breakwater was the same as that used in the flow visualization experiments (Fig. 1). The details regarding the experimental technique are given in SF.

2.3. Scour experiments

These experiments were conducted in the same “large” flume as described in SF. The mean water depth was maintained constant at $h = 40$ cm. Fig. 3 displays the plan view of the experimental set-up, while Fig. 4 displays the cross-sections of the breakwater models used in the experiments.

The breakwater has a side slope of 1 : 1.5. Side slopes smaller than this value was avoided to minimize the blockage effect. Velocity measurements were made by a bi-directional micro propeller. These measurement indicated that practically no blockage effect occurred in the tests.

To reduce the reflection from the side wall adjacent to the breakwater, an absorbing mat of 2 cm thickness was fixed to the wall (Fig. 3). Also, to prevent extensive scour (induced by the standing waves) at the corner area where the breakwater meets the wall,

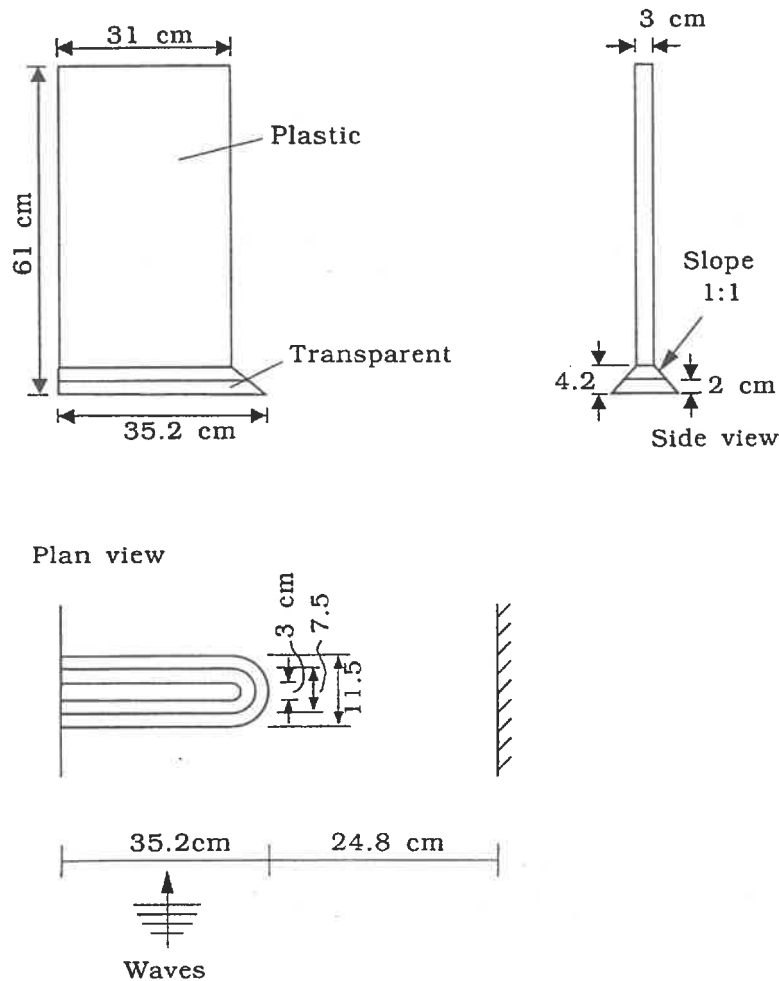


Fig. 2. Test set-up used for the flow visualization and bed shear stress experiments.

a layer of crushed stones was laid on the bed in this area (Fig. 3). This was important in the present case because of the very long duration of the tests ($O(10-40 \text{ hrs})$ in the laboratory tests). Note that the scour occurring in the corner area did not pose any major problem in the case of vertical breakwater reported in SF because of the considerably short test periods ($O(10 \text{ min})$) during which the corner scour propagated very little along the length of the breakwater towards the breakwater head.

The breakwater was made from steel profiles; a truss structure, made from steel profiles, was covered with metal sheets. The surface of the breakwater was hydraulically smooth. It extended down to the actual bottom of the flume (Fig. 4a). In one test (Test 4 in Table 1), the breakwater had the same side slope and a slightly larger width, namely $B = 2.4 \text{ m}$. The breakwater used in this particular test was built in a different fashion; large concrete blocks were used to form the main body of the structure, and then the surface of the structure was covered by sand bags to give the final form of the breakwater. This was the very first test made in the study. However, this model structure was later abandoned because the structure showed tendencies not to remain completely intact after several hours test time.

Table 1
Test conditions

Test No.	Diameter of the round head B [m]	Width of protection layer L [m]	L/B	Wave period (peak period) T_p [s]	Significant wave height H_s [m]	Max. undisturbed flow velocity (measured) U_m [m/s]	Max. shear velocity U_{fm} [m/s]	Shields parameter θ	Structure Reynolds number Re	Keulegan-Carpenter number KC	Dimensionless plunging breaker parameter $\frac{T_p \sqrt{gH_s}}{h}$
(1)	(2)	(3)	(4)	(5)	(6)	(7)	(8)	(9)	(10)	(11)	(12)
1	2.25	-	-	1.4	0.139	0.157	0.013	0.035	3.5×10^5	0.1	4.1
2	2.25	-	-	2.3	0.176	0.158	0.012	0.05	3.5×10^5	0.16	7.6
3	2.25	-	-	2.9	0.145	0.205	0.015	0.072	4.6×10^5	0.27	8.7
4	2.4	-	-	4.76	-	0.198	0.014	0.062	4.4×10^5	0.41	-
5	2.25	-	-	5.6	0.161	0.21	0.014	0.064	4.7×10^5	0.52	18.0
6	2.25	0.5	0.22	2.9	0.145	0.205	0.015	0.072	4.6×10^5	0.27	8.7
7	2.25	0.5	0.22	5.6	0.161	0.21	0.014	0.064	4.7×10^5	0.52	18.0
8	2.25	1	0.44	2.9	0.145	0.205	0.015	0.072	4.6×10^5	0.27	8.7
9	2.25	1	0.44	5.6	0.161	0.21	0.014	0.064	4.7×10^5	0.52	18.0

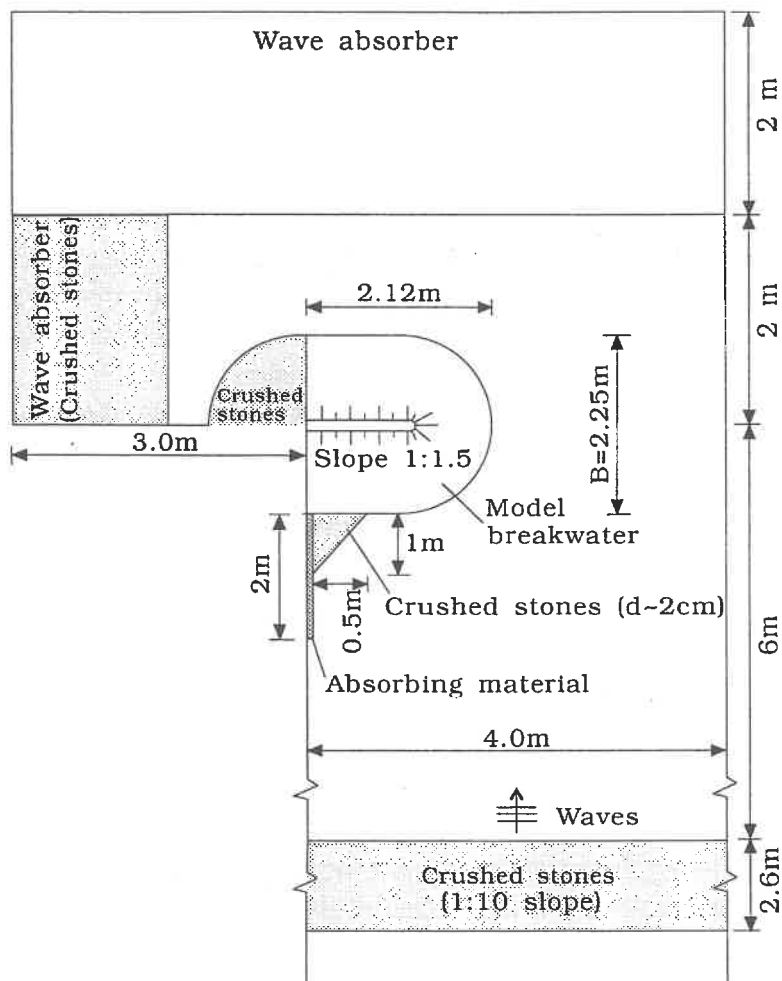


Fig. 3. Test set-up used for the scour experiments.

To study the effect of a scour-protection layer, a layer of crushed stones the size of approximately $d_{50} = 2$ cm was laid on the bed around the breakwater (Fig. 4b), and some of the main scour tests were repeated for this test set-up.

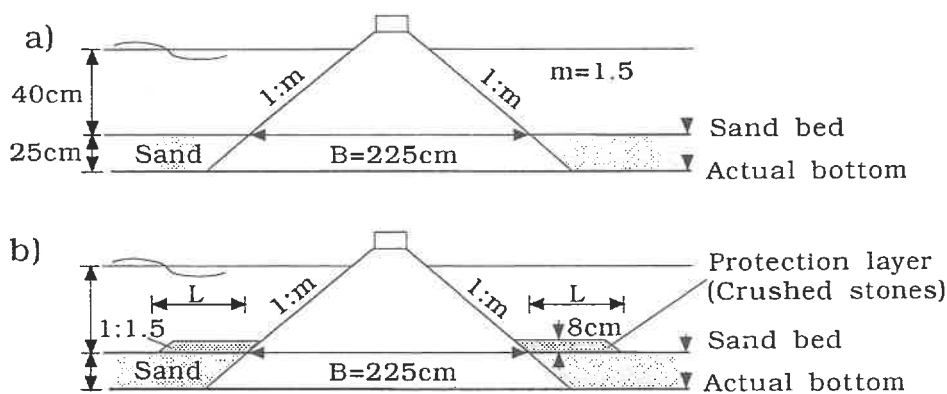


Fig. 4. Cross-sections of the breakwater model in actual scour experiments (a), and in the experiments where the scour protection layer was tested (b). Note that B is 2.4 m in Test 4.

The sand used in the experiments has a d_{50} of 0.19 mm, with $d_{84}/d_{16} = 0.67$. The bed topography around the breakwater head was measured manually with a meter stick (with a sharpened point end). This was achieved over a bed area extending about 2 m in the transverse direction from the tip of the breakwater and about 1.5 m in the offshore direction and 1 m in the inshore direction from the breakwater. The accuracy of the measurements was within ± 1 mm. The measurements were taken every 2 hrs. During the measurements, waves were stopped. In addition to these measurements, the scour and deposition process was monitored in a few cases by two underwater mini video cameras, one placed in front of the breakwater and the other at a location halfway between the front and the back sides of the breakwater.

Unlike the scour experiments reported in SF, irregular waves were used in the present experiments. This was to avoid large bed undulations which emerge under large-amplitude regular waves in long-duration, O(10)–O(40) hrs, tests. The waves were recorded by wave gages. A measured in-situ water elevation spectrum for the North Sea storm conditions was used as the control spectrum to generate wave generator displacement signals. This spectrum is well described by the JONSWAP wave spectrum, as was shown in a previous study (Kozakiewicz et al. (1994)).

The test conditions are summarized in Table 1. In the table, T_p is the wave period corresponding to the peak frequency of the wave spectrum, H_s is the measured significant wave height, U_m is the maximum undisturbed orbital velocity at the bed obtained from $U_m = \sqrt{2} \sigma_U$ in which σ_U is the standard deviation of the undisturbed orbital velocity measured at 5 cm above the bed (the plan-view location of the measurement point being 10 cm from the side wall and 85 cm in the offshore direction from the axis of the breakwater). Furthermore, in Table 1, θ is the Shields parameter defined by

$$\theta = \frac{U_{fm}^2}{g(s-1)d_{50}} \quad (2)$$

in which s is the specific gravity of sediment grains, d_{50} is the mean grain size and U_{fm} is the maximum value of the bed shear velocity,

$$U_{fm} = \sqrt{\frac{f_w}{2}} U_m \quad (3)$$

The wave friction factor, f_w , is calculated from Fredsøe (1984). The Reynolds number, Re , in the table is defined by

$$Re = \frac{U_m B}{\nu} \quad (4)$$

in which ν is the kinematic viscosity of the water.

Note that all the tests were carried out under live bed conditions, namely $\theta > \theta_{cr}$, as seen from the table, in which θ_{cr} is the critical value of the Shields parameter, corresponding to the initiation of motion of sediment at the bed.

2.4. Particle-tracking experiments

These experiments were carried out in the same flume as the scour experiments. The purpose of these experiments was to get a quantitative picture of the near-bed steady streaming pattern around the breakwater head induced by the waves. To this end, a plastic ball of 2 cm diameter was used as a tracer. The diameter of the ball was chosen relatively large to make it possible to trace the trajectory of the ball by video. The weight of the ball was adjusted so that the fall velocity was about 2 cm/s. This ensured that the ball travelled near the bed.

In the tests, the ball was released from different positions in plan view, and its trajectories were videotaped by a camera placed above the flume, covering a viewing area extending about 2 m from the tip of the breakwater in the transverse direction, about 1.5 m in the offshore direction and about 0.8 m in the inshore direction from the breakwater. Three tests were made; one was rather extensive (under the same test conditions as in Test 4) and the other two were supplementary tests (under the same test conditions as Tests 2 and 5).

3. Effects causing scour

Scour around the head of a rubble-mound breakwater may be caused by the effects such as the steady streaming induced by waves, the plunging breaker occurring at the head just behind the tip of the breakwater, the contraction of streamlines and the action of lee-wake vortices.

3.1. The steady streaming

Fig. 5 depicts the results of the particle tracking experiments described in Section 2.4. The figure shows that there is a steady streaming near the bed in the neighbourhood of the breakwater head. The particles released in the region marked M end up at locations outside this region. Similar behaviour has been observed also in the previously-mentioned supplementary particle-tracking tests.

It is known from the oscillatory-boundary-layer research that, in the non-uniform boundary layers, the period-averaged velocity becomes different from zero, presumably resulting in a steady streaming. Longuet-Higgins (1957) predicted the streaming under sinusoidal waves due to the non-uniformity of the wave boundary layer caused by the spatial changes of the orbital velocities. The streaming in the present case, displayed in Fig. 5, is also caused by the non-uniform wave boundary layer; however, the non-uniformity of the boundary layer in the present case is due to the strong convergent–divergent geometry in plan view of the flow environment. This phenomenon has earlier been treated experimentally in a convergent–divergent channel in an oscillating water tunnel by Sumer et al. (1993).

The picture displayed in Fig. 5 suggests that the sediment stirred up by waves and brought into suspension will be transported by this steady streaming near the bed, from Area M and deposited on the bed over Areas N, Q and R. This would eventually result

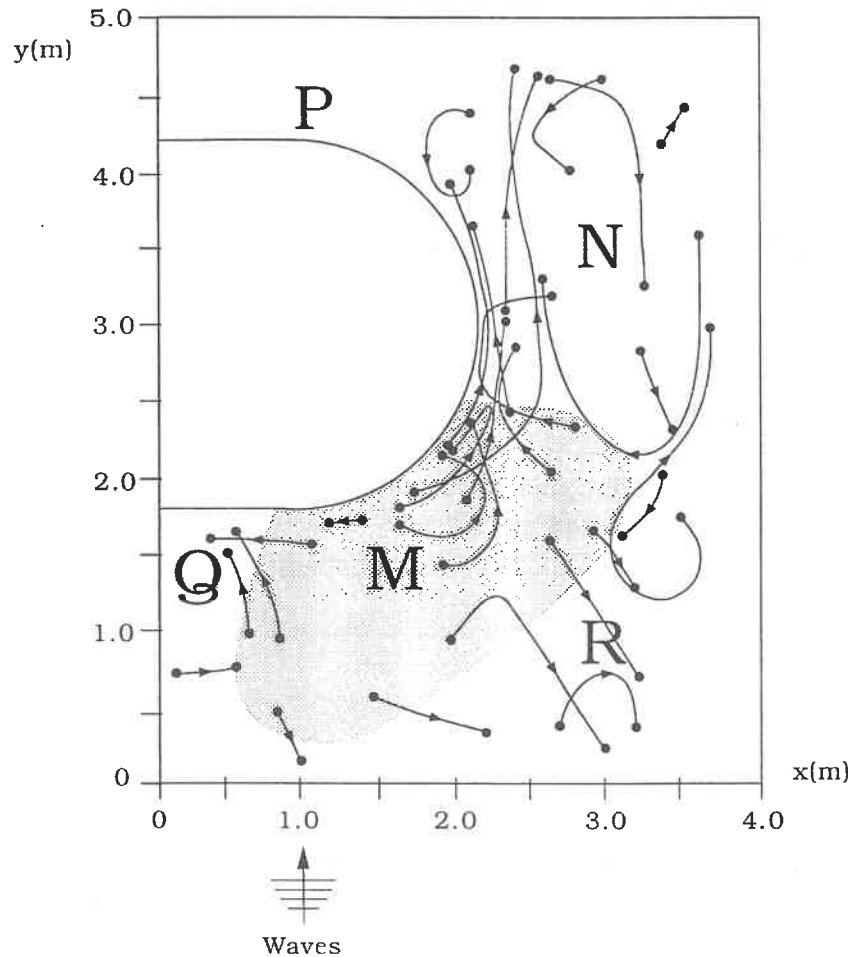


Fig. 5. Particle trajectories and major scour and deposition areas. Test 4. M: Scour (induced by the steady streaming); P: Scour (induced by the plunging breaker); and N, Q, R: Deposition (induced by the steady streaming).

in the formation of a scour hole in front of the breakwater head (basically, over the area M in Fig. 5). The present scour experiments revealed this, as will be shown later in the paper.

Area P in Fig. 5 is the location where the plunging-breaker-induced scour hole develops, as will be described in the next sub-section.

3.2. The plunging breaker

When the waves are sufficiently large, plunging breakers may occur on the head of the breakwater, as illustrated schematically in Fig. 6. The latter figure displays the time evolution of such a breaker, obtained from a video recording made in the present study (an underwater mini video camera was used to record the part of the process which occurs below the free surface).

Unlike the familiar two-dimensional plunging breaker, the breaker in the present case is three-dimensional, and it generates a round jet, as sketched in Frame 3 in Fig. 6. The visual observations revealed that this jet impinges on the bed and mobilizes the sand

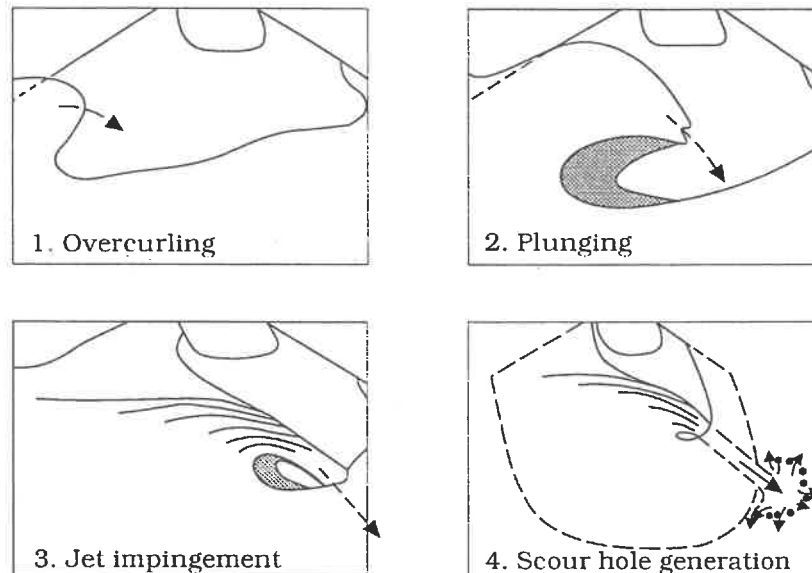


Fig. 6. Sequence of sketches illustrating the development of 3-D plunging breaker at the head of breakwater.

grains there, leading to a scour hole (Frame 4, Fig. 6). The generated scour hole is located at the lee-side of the breakwater at the junction between the head and the trunk sections (marked P in Fig. 5), as will be seen later.

In a supplementary test, the breaker was prevented from occurring by placing a vertical plate, perpendicular to the incoming waves, at the tip of the breakwater head where the plate extended from the top of the breakwater right down to the surface of the breakwater, submerged about half-way through the water depth. This test revealed that no scour occurred, showing that the scour occurring at this location is only caused by the breaker.

The previously mentioned visual observations further indicated that the way in which the scour is generated is quite similar to that observed in the case of a round vertical (or inclined) submerged jet described in Breusers and Raudkivi (1991) (p. 103).

Finally, it may be noted that the scour induced by the plunging-breaker effect may not occur if the breakwater is a composite type breakwater where caissons are placed on a rubble-mound foundation.

3.3. The lee-wake vortex

Fig. 7 presents the results of the flow visualization study made with the rubble-mound breakwater model. The figure includes also the results obtained in the case of vertical-wall breakwater described in SF. The quantities L_x and L_y are dimensions of the lee-wake vortex, as sketched in the Fig. 7.

The results show that the lee-wake vortex first comes into existence when the KC number is larger than unity, the same critical value of the KC number obtained for the vertical wall breakwater case (see SF). The figure further shows that the influence of the side slope is felt only after the KC number reaches the value of about 1.5–2. The net effect of the side slope is to decrease the dimensions of the lee-wake vortex, as indicated by Fig. 7. Considering the real-life side slopes, namely, slope angles of a factor of 2

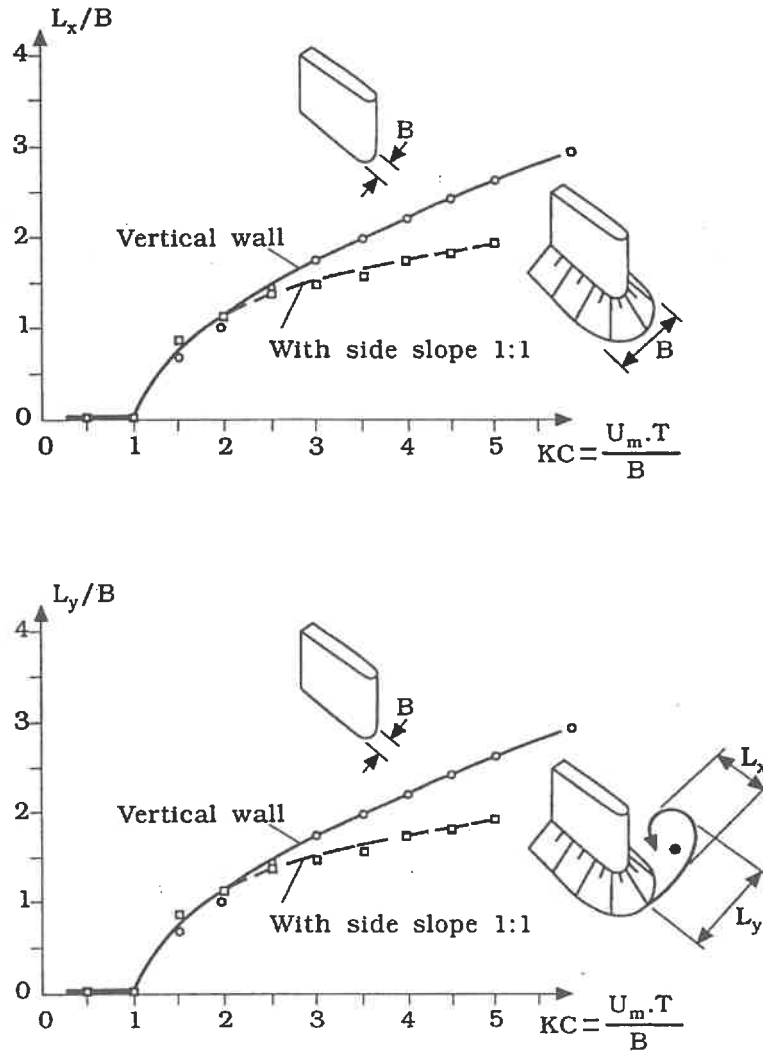


Fig. 7. Plan-view dimensions of lee-wake vortex.

smaller than the tested one, the previously mentioned effect would be even more pronounced.

However, when the real-life dimensions of a breakwater are considered, it will be seen that the KC number is always below unity, as mentioned earlier. Hence, normally, no lee-wake vortex would be formed in a real-life situation, and therefore it may be concluded that the lee-wake vortex should not be of any practical significance with regard to scour problems encountered in practice.

3.4. Contraction of streamlines

Fig. 8 displays the results of the bed shear stress measurements. The quantity α is the amplification in the bed shear stress defined by

$$\alpha = \frac{\max|\vec{\tau}_0|}{\tau_{0m}} \quad (5)$$

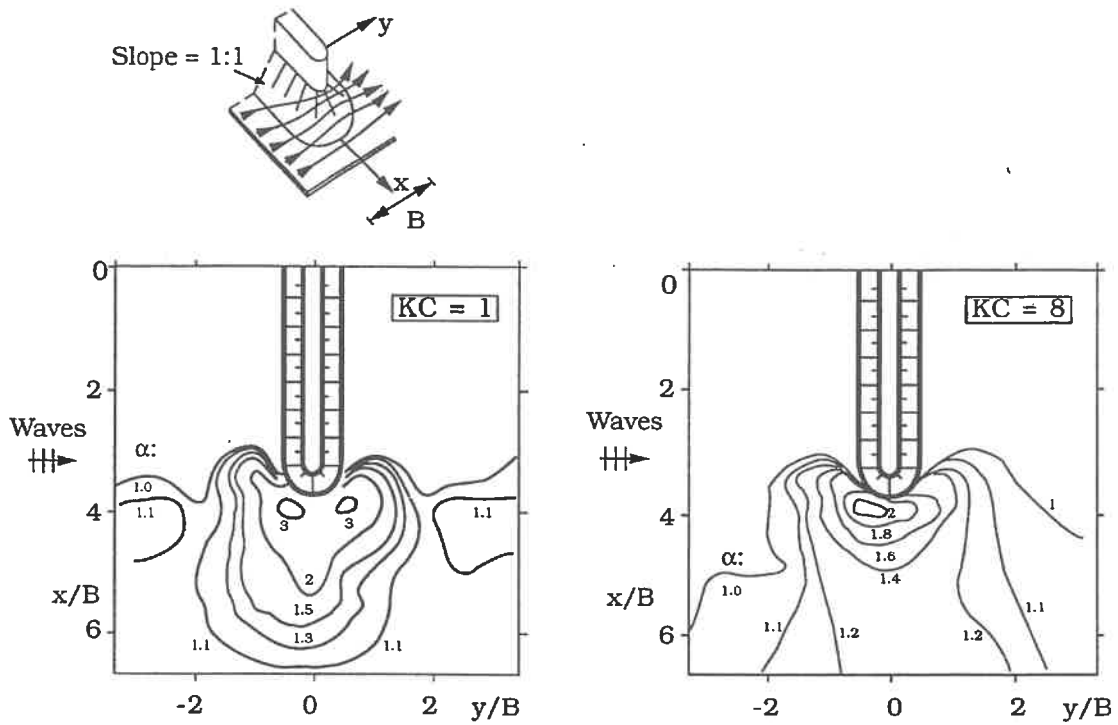


Fig. 8. Contour plot of the amplification in the bed shear stress.

in which $\max|\vec{\tau}_0|$ is the maximum value of the magnitude of the bed shear stress vector. In contrast to the case of vertical breakwater, the amplification in the present case is not very extensive; while α is $O(10)$ in the case of vertical-wall breakwater (see Fig. 10 in SF), it is a factor of 4 smaller for $KC = 1$ and a factor of 7 smaller for $KC = 8$ in the case of rubble-mound breakwater (cf. Fig. 8 of the present paper and Fig. 10 in SF). This large reduction in α is simply due to the geometry of the rubble-mound structure; quite a substantial amount of water will be diverted over the sloping wall of the breakwater at the head, therefore much less contraction of streamlines will take place at the bed near the tip of the structure, and hence the amplification in the bed shear stress will not be drastically large in the present case. Yet, the amplification in the order of magnitude of 2–3 around the head will be sufficiently large to help develop the streaming-induced scour process fairly quickly.

4. Results of the scour experiments

Fig. 9 and Fig. 10 illustrate how the scour and deposition develop with time. As seen, the scour and deposition processes attain their states of equilibrium through a transition period.

Fig. 11 presents a three-dimensional picture of the bed topography around the head of the breakwater in Test 2 in the equilibrium stage, after 18 hrs test time. Area M represents the streaming-induced scour hole, while Areas N and Q represent the streaming-induced deposition areas. Area P represents the scour hole induced by the plunging breaker (cf. Fig. 5).

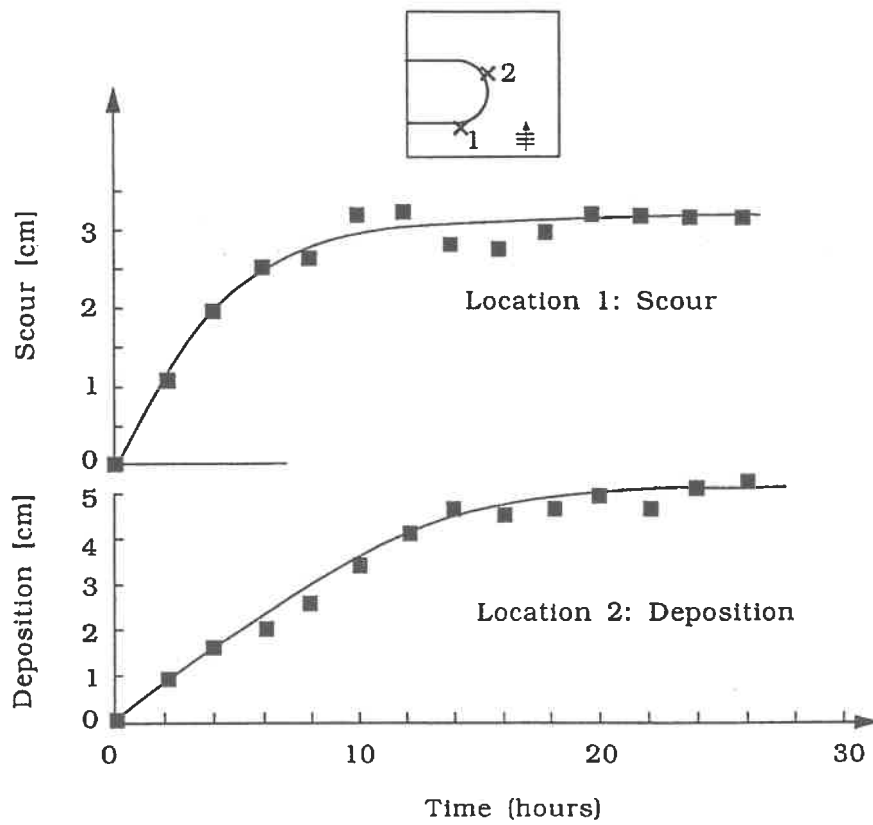


Fig. 9. Time development of scour and deposition induced by the steady streaming. Test 3.

Fig. 12A–E depicts the contour plots of the equilibrium-stage bed topographies obtained in Tests 1–5. All the diagrams reveal the scour and deposition pattern displayed in Fig. 11.

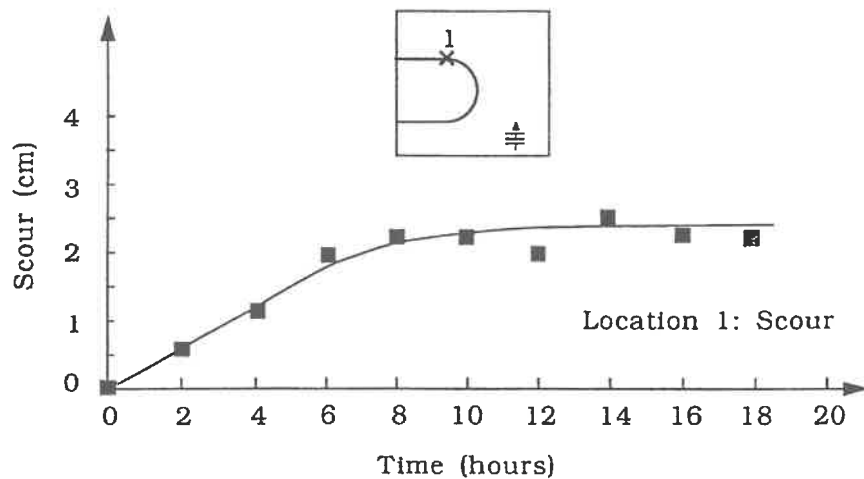


Fig. 10. Time development of scour induced by the plunging breaker. Test 2.

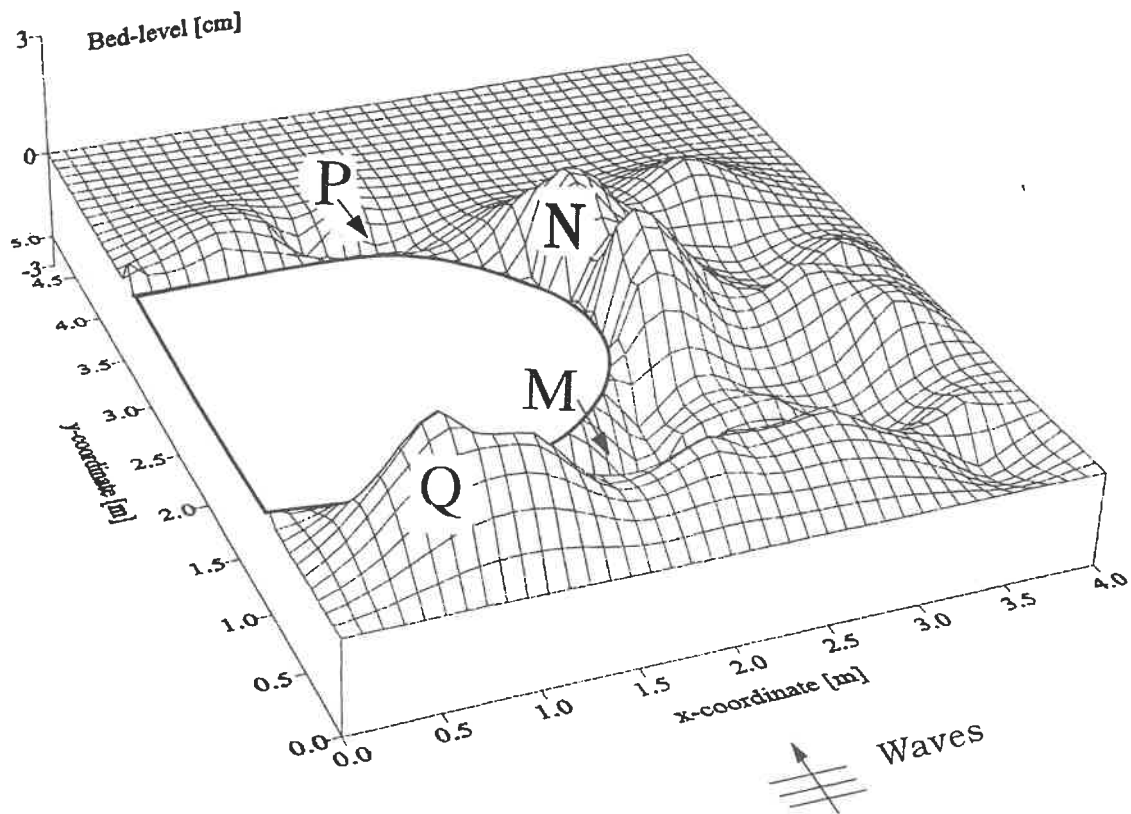


Fig. 11. Three-dimensional plot of the measured equilibrium bed topography. Test 2.

4.1. The streaming-induced scour and deposition

The steady streaming around the head of the breakwater depends on the following quantities: the maximum value of the undisturbed orbital velocity at the bed, U_m , the wave period, T_p , the base diameter of the breakwater head, B , the bed roughness (characterized by the grain diameter, d), the kinematic viscosity, ν , and the side slope of the breakwater, m . From dimensional analysis, the scour and deposition characteristics can be found to depend on the following parameters

$$S/B = f(KC, \theta, m, a/d, Re) \quad (6a)$$

$$D/B = g(KC, \theta, m, a/d, Re) \quad (6b)$$

in which a is the amplitude of the undisturbed orbital motion at the bed. Given the breakwater and the sediment, the scour and deposition characteristics will vary only with the Keulegan–Carpenter number, KC , and the Shields parameter, θ . When the live-bed scour ($\theta > \theta_{cr}$) is considered, however, the influence of θ is not very important and may be ignored to a first approximation, therefore the scour and deposition characteristics in this case will vary only with the KC number.

Fig. 13 illustrates the variation of maximum scour depth with the KC number. Likewise, Fig. 14 gives a similar illustration for the maximum depth of deposition occurring at the inshore side of the breakwater head (Location N in Fig. 11). (Note that

the locations of maximum scour and deposition depths will be discussed later in the paper).

Fig. 13 includes also one field result taken from Lillycrop and Hughes (1993); see Table 2. This table includes the field results reported in the aforementioned publication

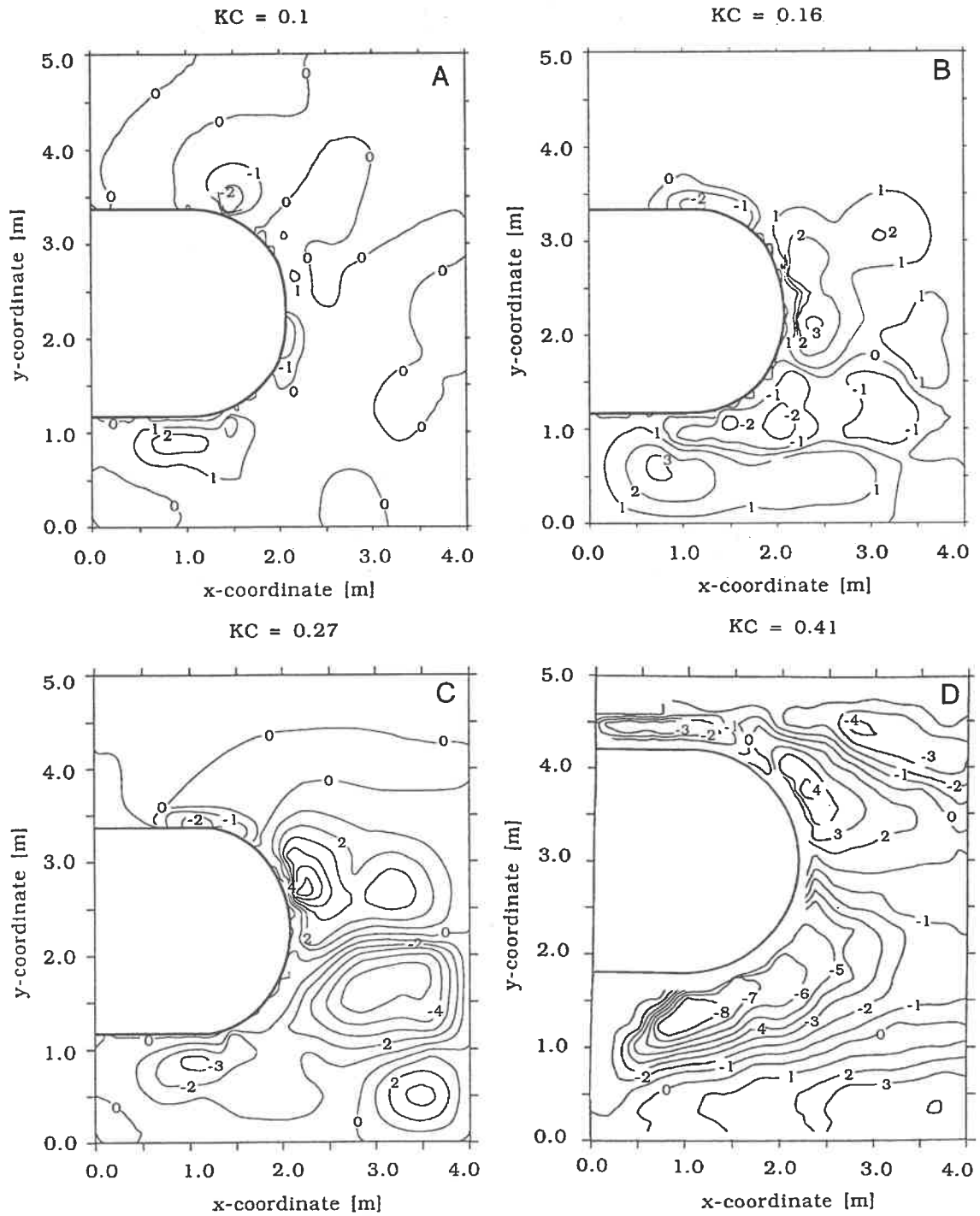


Fig. 12. Contour plot of the measured equilibrium bed topography. (A) Test 1, (B) Test 2, (C) Test 3, (D) Test 4, (E) Test 5.

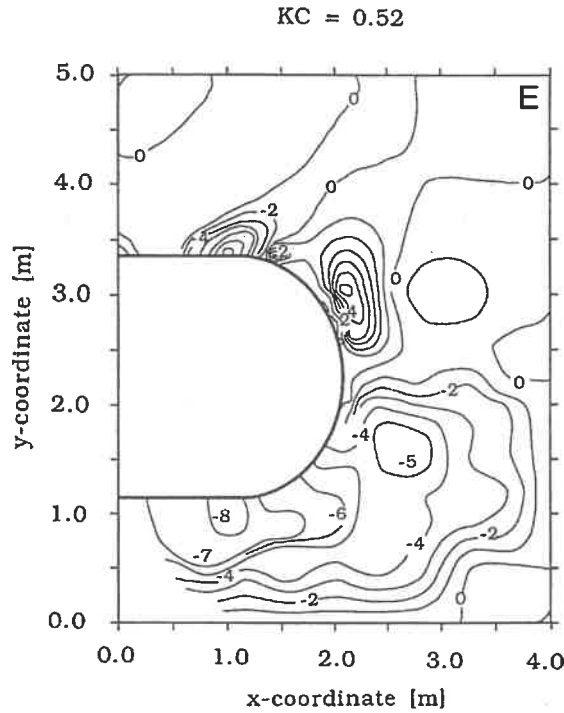


Fig. 12 (continued).

with regard to scour at breakwater/jetty heads where the contributing process is waves only. The quantity U_m is calculated from the linear wave theory where the wave height is taken as

$$H = 2(\sqrt{2} \sigma_\eta) = 2[\sqrt{2} (H_s/4)] = H_s/\sqrt{2} \tag{7}$$

in which σ_η is the standard deviation of surface elevation.

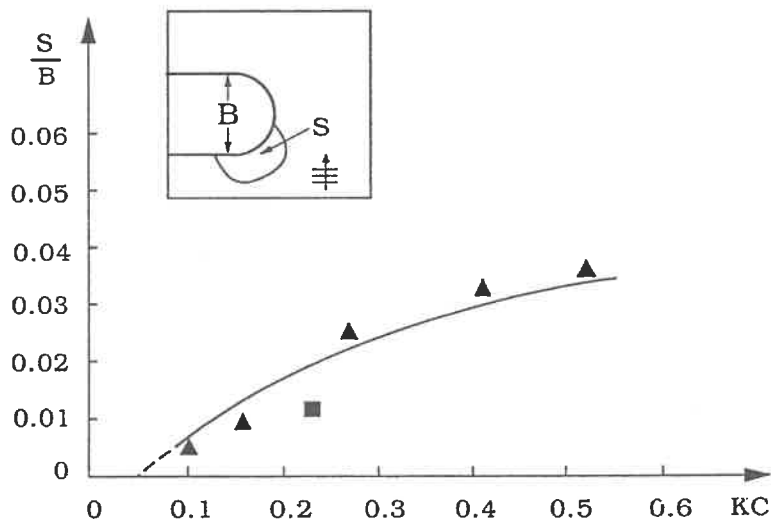


Fig. 13. Maximum depth of scour hole in front of the breakwater. Scour induced by the steady streaming. Triangles: Present data, Tests 1–5. Square: Field data (Cattaraugus, NY, USA; see Table 2) taken from Lillycrop and Hughes (1993). Solid line: Eq. (8).

Table 2
Scour holes generated by waves reported in Lillycrop and Hughes (1993). In addition to those listed in this table, the latter authors report scour holes at the head of south jetty in Yaquina Bay (Oregon), at the head of West breakwater in Irondequoit Bay, NY, and at the heads of Lake Michigan Harbour breakwaters

Project name	Type of jetty or breakwater	Side slope	Diameter of round head B (m)	Adjacent water depth h (m)	Significant wave height H_s (m)	Wave height used to calculate max. orbital velocity H (m)	Wave period T_p (s)	Maximum undisturbed orbital velocity U_m (m/s)	Keulegan-Carpenter number KC	Plunging breaker parameter $\frac{T_p \sqrt{g H_s}}{h}$	Bottom material	Depth of front-side scour at the head S (m)	Depth of lee-side scour at the head S (m)	Contributing process
(1) Morro Bay, CA; North jetty	Rubble	~ 1:2	67	6.1	5.3	3.8	10–15 ^a	2.2–2.3	0.33–0.52	11.8–17.7		(13)	(14)	Pure waves
Columbia River entrance, Oregon; North jetty	Rubble	1:2	~ 70	7.6							Medium sand		17	Pure waves
Cattaraugus Harbor, NY; South breakwater	Rubble	1:2	50	3.0	2.35	1.7	8.3	1.4	0.23	13.3	Sand, gravel	0.6	1.2	Pure waves

^a T_p is assumed to be 10–15 s, since no wave period was reported in the original reference.

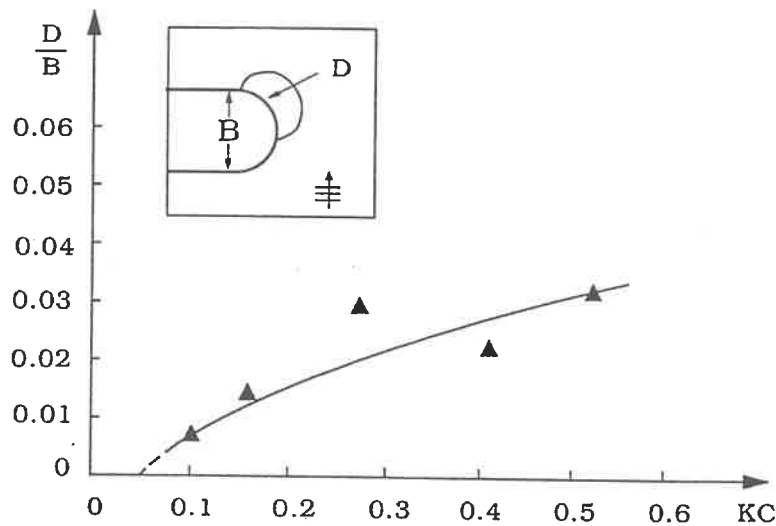


Fig. 14. Maximum depth of deposition induced by the steady streaming. Tests 1–5. Solid line: Eq. (9).

First of all, the diagrams in Figs. 13 and 14 show that the scour and deposition depths correlate with the KC number rather well. The larger the KC number, the larger the scour and deposition depths. This is simply because of the increasing magnitude of the streaming with increasing KC number.

Second, the field result depicted in Fig. 13 appears to be consistent with the present results despite the large differences in dimensions of the structures and also in wave characteristics; the width of the breakwater is a factor of 20 larger, the wave height is a factor of 15 larger and the wave period is a factor of 3–4 larger in the field. The latter suggests that the Re number and a/d dependence indicated in Eqs. (6a) and (6b) is not very important, as the Re number is a factor of 200 and a/d a factor of 20–30 larger in the field study than in the laboratory tests.

Finally, the S/B versus KC and D/B versus KC relationships in Figs. 13 and 14 can be approximated by the following empirical expressions:

$$S/B = 0.04C_1[1 - \exp\{-4(KC - 0.05)\}] \quad (8)$$

$$D/B = 0.04C_1[1 - \exp\{-3.5(KC - 0.05)\}] \quad (9)$$

in which C_1 is an uncertainty factor with a mean value of 1 which has a standard deviation of $\sigma_{C_1} = 0.2$ based on the data shown in Figs. 13 and 14.

4.2. Scour induced by the plunging breaker

By analogy to the scour by a submerged vertical jet (Breusers and Raudkivi, 1991, p. 103), it can be seen that the scour induced by the plunging breaker is mainly governed by the following features of the breaker: (1) the velocity of the jet generated by the breaker (at the point where the jet enters into the main body of the water), (2) the size of the jet (again, at the point of entrance), and (3) the water depth. The first two features depend on the following parameters: the wave height at breaking, taken as H_s (= the significant wave height) in the present analysis; the wave period, T_p ; the water depth, h ;

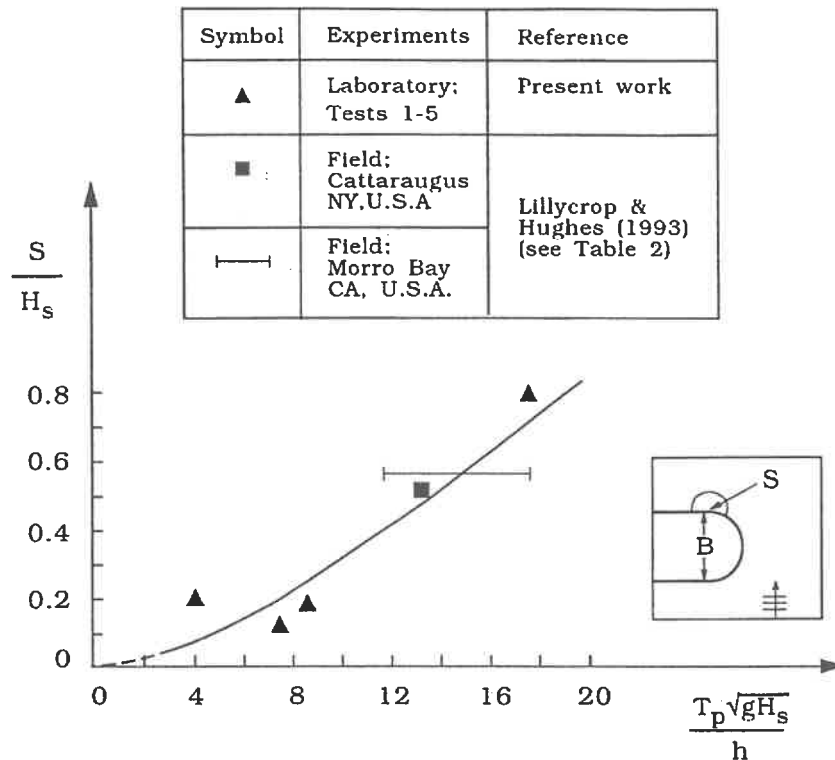


Fig. 15. Maximum depth of scour hole at the lee-side of the breakwater. Scour induced by the plunging breaker. Solid line: Eq. (11).

the side slope of the breakwater, m ; and the acceleration due to gravity, g . From dimensional analysis (considering the sediment properties as well), the scour can then be found to depend on the following non-dimensional parameters

$$S/H_s = f\left(T_p\sqrt{gH_s}/h, \theta, m\right) \quad (10)$$

Given the breakwater and the sediment, and for a live-bed scour ($\theta > \theta_{cr}$), the scour will depend only on the non-dimensional parameter $T_p\sqrt{gH_s}/h$.

Fig. 15 displays the variation of maximum scour depth with this parameter. The figure includes also two field results (see Table 2): for the case of Morro-Bay field study, no wave period was given in the original reference; the wave period is taken as 10–15 s in this case, to calculate the parameter $T_p\sqrt{gH_s}/h$. The standard deviation sign in the figure represents this latter interval.

The figure shows that the scour depth normalized by H_s correlates with the parameter $T_p\sqrt{gH_s}/h$ rather well. The data point corresponding to the smallest value of the latter parameter may be subject to some experimental uncertainty due to the rather small scour depths experienced in this case. The figure shows that the larger the value of the parameter $T_p\sqrt{gH_s}/h$, the larger the scour depth. This is expected, however. The numerator, $T_p\sqrt{gH_s}$, actually characterizes the amount of water in the plunging breaker entering into the main body of the water. Clearly, the scour must be directly proportional to this quantity. Regarding the denominator, h , on the other hand, the submerged jet has a penetration distance. If h is large compared with the aforementioned penetration

distance, practically no scour would occur. Obviously, the smaller the water depth, the larger the scour. Hence, from the preceding arguments, the scour depth should increase with increasing $T_p\sqrt{gH_s}/h$.

Fig. 15 shows that the field data and the present results agree remarkably well despite the large differences in the breakwater dimensions and in the wave conditions. Similar to the observation made in the case of streaming-induced scour (Section 4.1), this agreement suggests that the scale effects are apparently not very important. However, it should be emphasized that, due to the limited size of the data, the preceding results may not be conclusive. The scale effects in conjunction with scour problems in general, and scour in front of a vertical-wall breakwater in particular, have been discussed in detail in a recent review paper by Oumeraci (1994).

The relationship between the normalized scour depth and the parameter $T_p\sqrt{gH_s}/h$ in Fig. 15b can be approximated by the following simple expression

$$S/H_s = 0.01C_2\left(T_p\sqrt{gH_s}/h\right)^{1.5} \quad (11)$$

in which C_2 is an uncertainty factor with a mean value of 1 and a standard deviation of $\sigma_{C_2} = 0.34$.

Finally, it is interesting to note the following point regarding the effect of the Shields parameter. As will be described in Section 5, some tests were made to study the effect of a protection layer. Crushed stones were used as the protection material, as described earlier (Fig. 4b). The undisturbed Shields parameter corresponding to this material is a factor of 100 smaller than the actual bed material (Section 2.3). Even then, scour occurred at the location where the breaker jet impinged on the protection layer. Apparently, the maximum scour depth experienced in the protection layer was not drastically different (only 30% smaller) from that experienced with the sand bed. This reveals that the influence of the Shields parameter is not very important, as expected. As for the damage occurred to the protection layer, we shall return to this issue in Section 5.

4.3. Plan-view extent of scour and deposition areas

Fig. 16 depicts the plan-view extents of the scour and deposition areas. The dimensions of the areas of scour and deposition induced by the streaming are normalized with B and plotted as a function of the KC number (Fig. 16a,b), in the same way as in Fig. 13 and Fig. 14, while those of the scour area associated with the plunging breaker are plotted as a function of the parameter $T_p\sqrt{gH_s}/h$ (Fig. 16c), as in Fig. 15.

First, Fig. 16a and b together with Figs. 13 and 14 suggest that the streaming-induced scour is more extensive than the deposition occurring at the head of the breakwater. This is expected, however, because the scoured material is transported not only to Area N (Fig. 16), but also to Areas Q and R (Fig. 5) where the deposition takes place, as mentioned earlier.

Second, Fig. 16a shows that the dimensions of the scouring area increase with increasing KC number. This may be attributed to the increase of the magnitude of the streaming with increasing KC number, as mentioned previously in conjunction with the scour-depth variation with KC (Fig. 13).

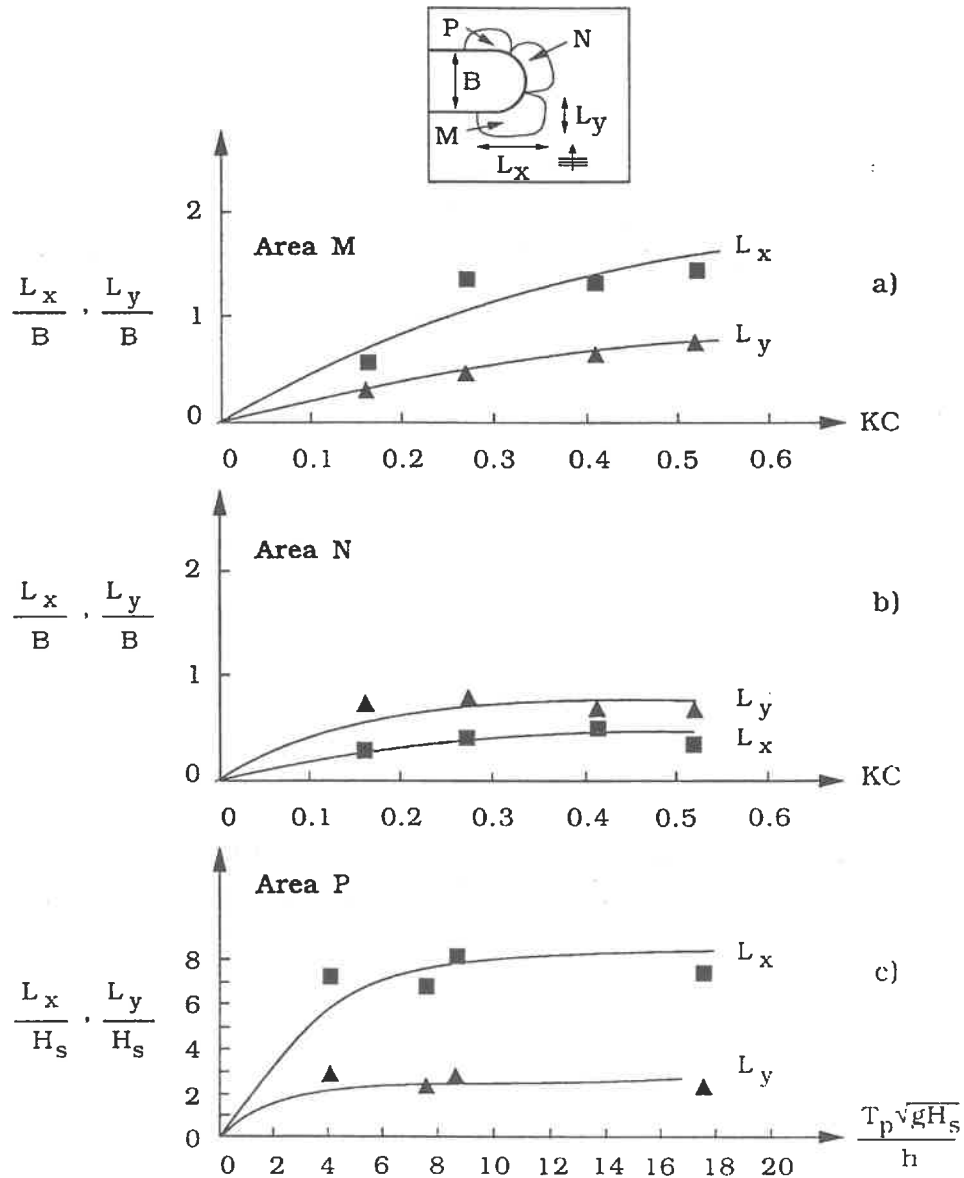


Fig. 16. Plan view extent of scour and deposition areas around the head of breakwater. Area M and Area N: areas of scour and deposition, respectively, induced by the streaming. Area P: scour induced by the plunging breaker.

Third, Fig. 16b shows a similar behaviour; however, the increase of deposition area with the KC number is rather weak. Apparently, the dependence of the extent of the deposition area on the KC number is overshadowed by the tremendous decrease in the streaming velocity due to the strong divergent geometry of the flow environment in this region.

Fourth, Fig. 16c indicates that, for the range of the present tests, the normalized dimensions of the scour area associated with the plunging breaker seem to be weakly dependent on the parameter $T_p \sqrt{gH_s} / h$, although the wave period in the experiments changed over a relatively wide range (Table 1). No clear explanation has been found for this behaviour.

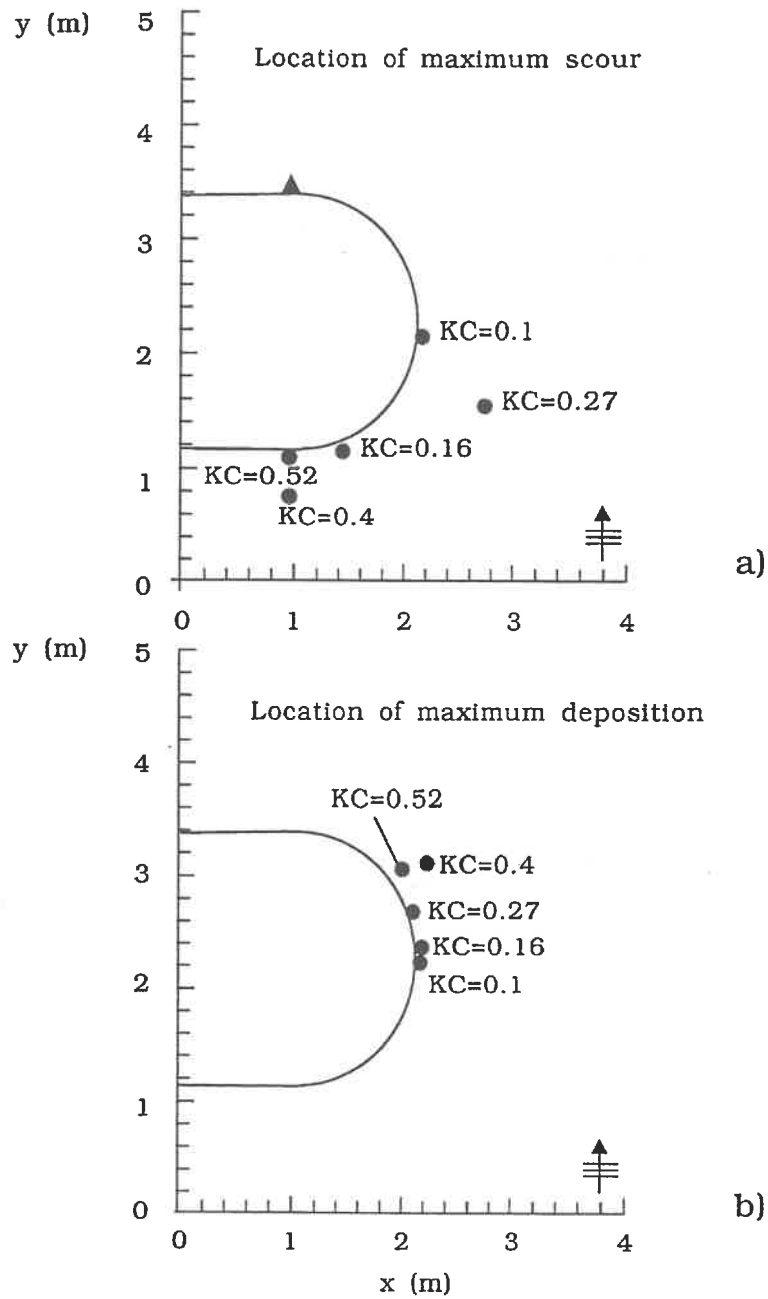


Fig. 17. Location of maximum scour and deposition. Circles: scour and deposition induced by the streaming. Triangle: scour induced by the plunging breaker.

Fig. 17 displays the locations of maximum scour and maximum deposition points. Regarding the streaming-induced scour and deposition (the circle symbols in the figure), Fig. 17a shows that the location of maximum scour moves along the periphery of the base of the breakwater towards the offshore direction, while that of maximum deposition moves in the opposite direction. This is related to the increasing extension of the area of streaming with the KC number. As for the plunging-breaker induced scour (the triangle symbol in the figure), Fig. 17a shows that the location of maximum scour remains

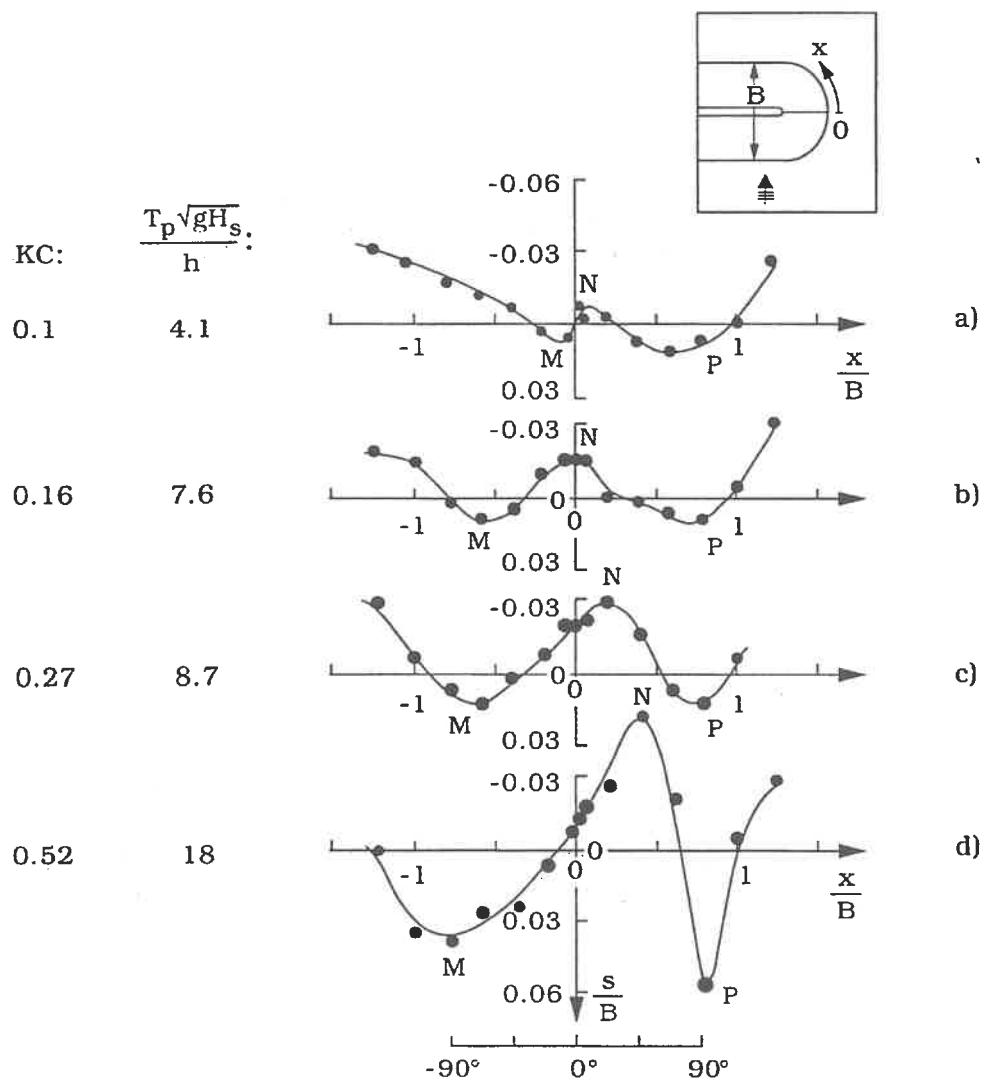


Fig. 18. Depth of scour and deposition at the periphery of the base of the breakwater. (a) Test 1, (b) Test 2, (c) Test 3, (d) Test 5.

unchanged, at the point where the head section meets the trunk section, regardless of the value of the parameter $T_p \sqrt{gH_s} / h$. This is, however, with one exception; namely, the maximum scour point appeared to be at slightly offshore side (at about 20°) in Test 1 where the parameter $T_p \sqrt{gH_s} / h$ takes its smallest value, namely 4.1.

4.4. Scour-deposition at the periphery of the base of the breakwater head

Fig. 18 depicts the scour and deposition along the periphery of the base of the breakwater head for the present tests. Test 4 was not included in the figure because the base of the breakwater head was not well defined due to the model material used in this test (Section 2.3), to cover the breakwater surface. The streaming-induced scour is marked M, the streaming-induced deposition is marked N and the breaker-induced scour is marked P. The picture displayed in this figure is much the same as that presented in

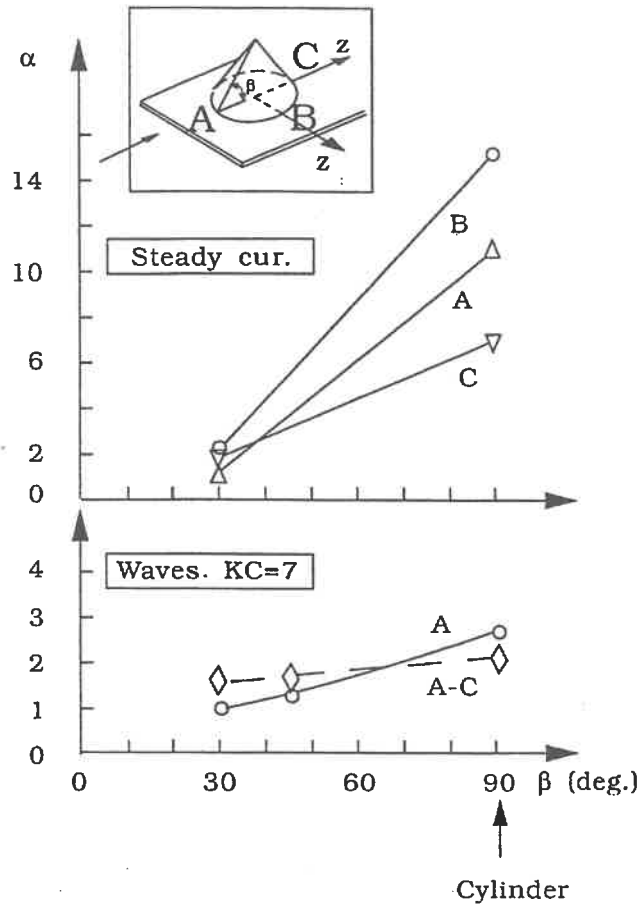


Fig. 19. Influence of the side slope on the amplification in the bed shear stress. The case of cone-shaped structure.

the preceding paragraphs (Figs. 13–17). As seen, the live bed conditions ($\theta > \theta_{cr}$) prevail in these tests, too.

4.5. Influence of the side slope on scour

The experimental constraints due to the finite width of the wave flumes did not allow us to study the influence of the side slope directly. However, supplementary experiments have been carried out, employing a structure with a very simple geometry, namely a cone-shaped structure, to assess how the results would be affected when the side slope was changed. Two kinds of side slopes were tested, 30° and 45°, and two kinds of experiments were conducted, the bed shear stress measurements and the scour experiments. Regarding the bed shear stress measurements, cones with $D = 9$ cm base diameter were used in the same flume as that described in Section 2.2. To facilitate comparison, a circular cylinder with the same diameter was also tested. Regarding the scour experiments, the test conditions are given in Table 3.

Fig. 19 depicts the results related to the bed shear stress measurements. As seen, the net effect of decreasing the side-slope steepness, m , is to decrease the amplification in

Table 3
Test conditions for scour experiments carried out with cone-shaped structure

Side slope, β	Mean sand size, d_{50} (mm)	Diameter of cone, D (mm)	Water depth, h (cm)	Wave period, T_p (peak period) (s)	Maximum flow velocity U_m (cm/s)	Maximum friction velocity (cm/s)	Shields parameter θ	Keulegan-Carpenter number KC	Structure Reynolds number Re
30°	0.16	860	53	—	33	1.6	0.1	∞ (steady c.)	3×10^5
30°	0.16	860	43	2.5	36	2.5	0.25	1	3×10^5
45°	0.16	880	53	—	33	1.6	0.1	∞ (steady c.)	3×10^5
45°	0.16	880	50	2.5	34	2.4	0.2	1	3×10^5

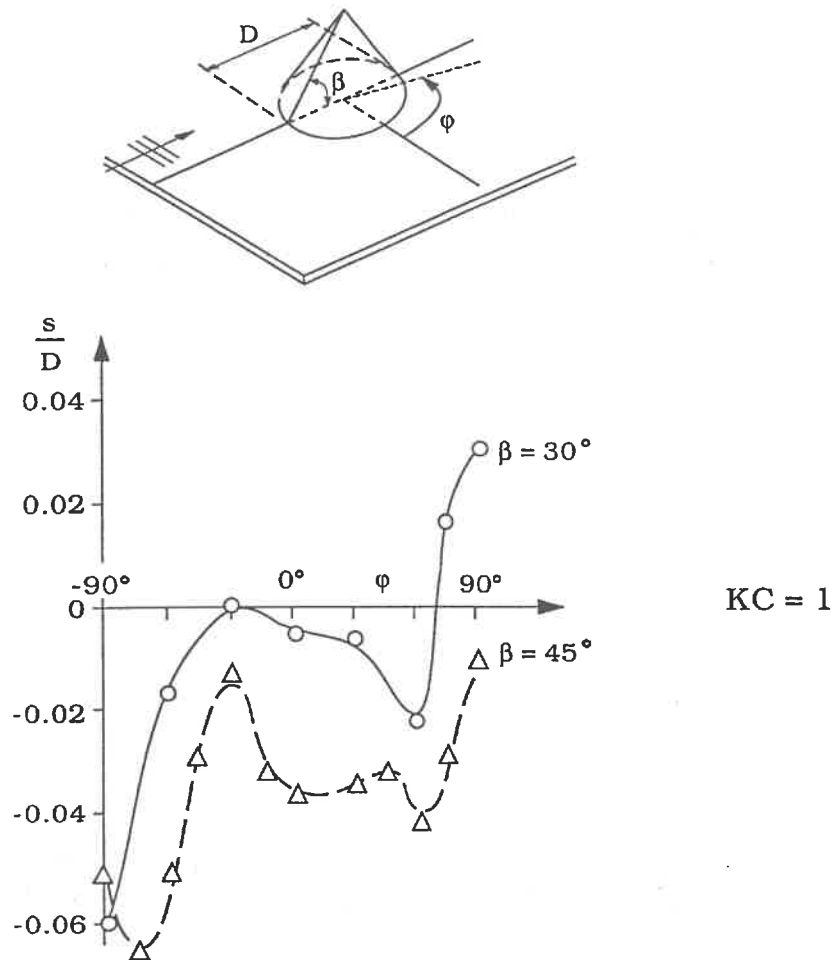


Fig. 20. Depth of scour around the periphery of cone-shaped structure. Influence of side slope. $KC = 1$.

the bed shear stress, as expected. Water will be diverted over the structure in larger and larger quantities with decreasing m , leading to smaller and smaller contraction of the streamlines over the bed near the structure, and therefore to smaller and smaller bed shear stresses. The consequence of the preceding result as regards the scour process is that smaller amount of sediment will be put into suspension when the side slope is decreased. This, in combination with the fact that the streaming itself will decrease with decreasing side-slope steepness, means that smaller streaming-induced scour will occur with decreasing side-slope steepness.

Fig. 20 presents the results of the scour experiments. First of all, the scour and deposition pattern (which is similar to that observed for the breakwater case) reveals the presence of the streaming-induced scour and deposition process in the cone case, too. Second, it is seen that the scour decreases with decreasing side slope, as expected; a decrease in the side-slope angle from 45° to 30° leads to a decrease in the scour depth by as much as a factor of 2.

The side slope in the present breakwater experiments (Section 2.3) was 1:1.5. The range of side slope encountered in practice is from about 1:1.3 to 1:2, depending on the material used for the rubble mound breakwater, or alternatively, on the armour layer in

the case of multi-layer rubble mound breakwaters (1:2 for the rock cubes, while 1:(4/3) for the accropode material). When side slopes different from the tested slope, 1:1.5, are considered, the scour induced by the streaming mechanism may be assessed, to a first approximation, using Figs. 12 and 17 where the scour figures may be increased or decreased depending on the slope, using Fig. 19. However, it must be stressed that this increase or decrease will not be very extensive, considering the rather narrow range of side slopes encountered in practice.

As for the breaker-induced scour, the experimental constraints in the present investigation did not allow us to study the precise influence of the side slope on this scour. However, considering, again, the range of side slopes encountered in practice, the scour depth for slope values different from 1:1.5 will not be radically different from that depicted in Figs. 15 and 18.

4.6. Influence of surface roughness of the breakwater

The present findings were obtained from the tests where the surface of the breakwater was impermeable and relatively smooth. For a rubble-mound breakwater the surface roughness may be considerably larger. This larger roughness must be expected to reduce the strength of the plunging breaker on the rear side as well as the streaming pattern in the front. For these reasons, the present results for the scour depths must be considered as conservative estimates.

5. Effect of protection layer

Some of the tests were repeated with the test set-up where a protection layer was placed on the bed around the head of the breakwater, as described earlier (Fig. 4b). The tests were performed with two different values of the width of the protection layer (see Table 1). Widths larger than 1 m were avoided due to the limited space between the tip of the protection layer and the side wall of the flume.

Fig. 21 presents the results of these experiments. The results regarding the case of $L/B = 0$ are taken from Fig. 13. The figure indicates that, for a complete scour protection, the total area of the bed exposed to the scour must be covered by the protection layer, cf. the dimension L_y in Fig. 16a with L in Fig. 21 obtained when S/B is extrapolated to 0.

Fig. 22 gives the width of the protection layer required (1) for a complete scour protection, $S/B = 0$ (here, the previously mentioned extrapolated values are used); and (2) for a scour protection where a scour of 1% of the diameter B , $S/B = 0.01$, is allowed. (Regarding the latter limit, namely 0.01, it gives an allowable scour depth of $O(0.2 \text{ m})$ for $B = O(20 \text{ m})$, which is reasonable. However, for larger values of B , caution must be exercised, since the corresponding scour depths can be rather large). The relationships between L/D and the KC number in Fig. 22 can be approximated by the following expression:

$$L/B = A_1 KC \quad (12)$$

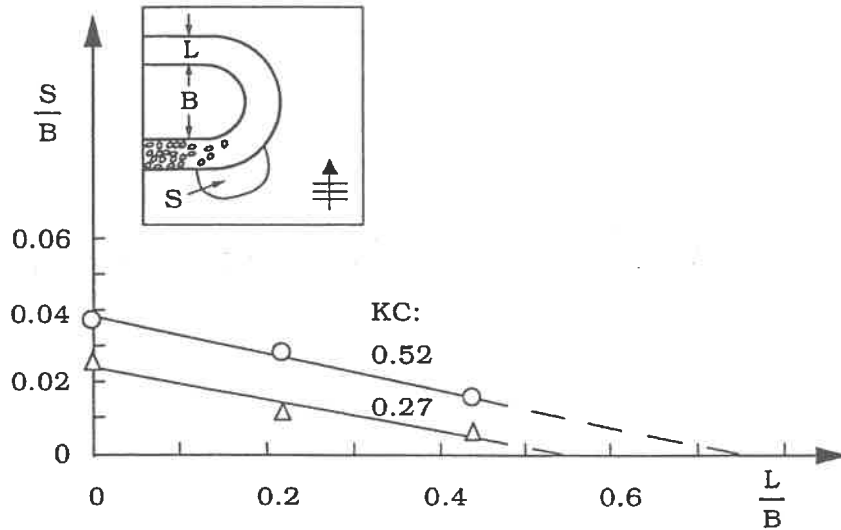


Fig. 21. Maximum depth of scour in front of the breakwater head as function of the width of the protection layer. Tests 3, 5, 6–9.

in which $A_1 = 1.5$ for a complete scour protection (i.e. $S/B = 0$) and $A_1 = 1.1$ for $S/B = 0.01$. Using Eq. (1), adopting the linear wave theory, and recalling $H = H_s/\sqrt{2}$ (Eq. (7)), the preceding equation can be written in the following form

$$L = AH_s/\sinh(kh) \tag{13}$$

in which k is the wave number and A is

$$A = 3.3 \text{ for a complete scour protection} \tag{14}$$

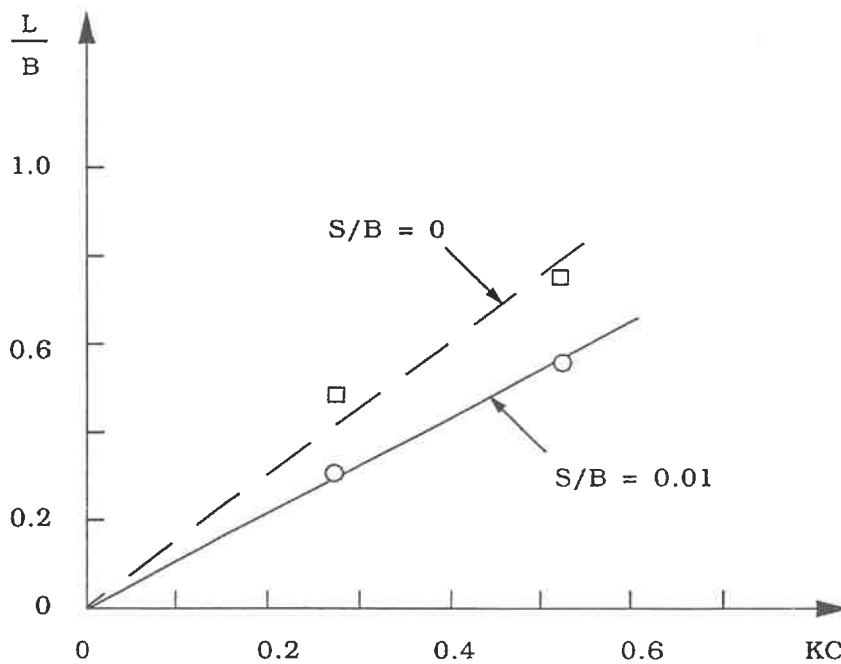


Fig. 22. The width of the protection layer, corresponding to (1) a complete scour protection and (2) to a protection work where a scour of $S/B < 0.01$ is allowed. Data from the previous plot.

or

$$A = 2.4 \quad \text{for } S/B = 0.01 \quad (15)$$

This is to protect the breakwater against the scour induced by the streaming. The present scour-protection tests showed that the implemented widths of the protection layer (even the smallest one) was able to protect the sand bed completely against the breaker-induced scour. However, it must be pointed out that, in these tests, scour (damage) occurred in the protection layer itself, as mentioned earlier, despite the extremely small values of the Shields parameter, θ , corresponding to the protection material (θ was a factor of 100 smaller than that of the sand bed). This issue was not investigated further in the present study.

6. Conclusions

(1) There are two mechanisms which cause scour around the round head of a rubble-mound breakwater: (a) the steady streaming which occurs above the bed, around the head of the breakwater; and (b) the plunging breaker which occurs at the head of the breakwater.

(2) Regarding the former mechanism, the net effect is that a scour hole is formed in front of the breakwater head and adjacent to it. This scour is mainly governed by the Keulegan–Carpenter number, KC , based on the base diameter of the breakwater head. The larger the value of KC , the larger the scour.

(3) Regarding the plunging breaker-induced scour, the scour hole produced by this effect is located at the lee side of the breakwater head. This scour is governed by a parameter involving the wave period, the wave height, the water depth and the acceleration due to gravity, namely $T_p/\sqrt{gH_s}/h$. The larger the value of this parameter, the larger the scour depth.

(4) The previously mentioned steady streaming also produces a deposition. The area where this deposition occurs is located between the front-side scour hole and the lee-side scour hole.

(5) The location of the maximum depth of the lee-side scour is approximately constant, at the junction between the head and trunk sections at the lee side. The location of the maximum depth of front-side scour and that of deposition are dependent on the KC number.

(6) Scour can be prevented by a conventional stone protection layer. The width of the protection layer may be selected according to the empirical formulae given in Eqs. (13)–(15).

7. Notation

- a : Amplitude of undisturbed orbital motion at the bed.
 B : Base diameter of the breakwater head.
 d : Sediment size taken as d_{50} .

- D : Deposition depth.
 D_{cone} : Base diameter of cone-shaped structure.
 f_w : Wave friction coefficient.
 g : Acceleration due to gravity.
 h : Water depth at the structure head.
 H : Wave height.
 H_s : Significant wave height.
 k : Wave number, $2\pi/\lambda$.
 KC : Keulegan–Carpenter number based on the base diameter of the round head.
 L : Width of protection layer.
 m : Side slope.
 Re : Reynolds number based on U_m and B , $Re = U_m B / \nu$.
 s : Relative density of sediment grains, $s = \rho_s / \rho$.
 t : Time.
 T_p : Wave period, corresponding to the peak frequency.
 U_m : Maximum value of the undisturbed *orbital* velocity at the bed.
 U_{fm} : Maximum value of the undisturbed bed shear stress velocity
 α : Amplification in the bed shear stress, $\alpha = \max|\vec{\tau}_0|/\tau_{0m}$
 θ : Shields parameter, Eq. (2).
 θ_{cr} : Critical value of Shields parameter for the initiation of motion at the bed.
 σ_η : Standard deviation of surface elevation.
 ν : Kinematic viscosity.
 τ_0 : Bed shear stress.
 τ_{0m} : Maximum value of undisturbed bed shear stress.

Acknowledgements

This work was undertaken as part of the “MAST II Rubble Mound Breakwater Failure Modes” research programme. It was funded jointly by the Danish Technical Research Council (STVF) under the programme “Marine Technique” and by the Commission of the European Communities, Directorate General for Science, Research and Development, under MAST contract No. MAS2-CT92-0042.

Dr. Niels Christiansen was involved in the bed shear stress measurements. Mr. Søren B. Hansen, M.Sc., was involved in the flow visualization experiments and some of the scour experiments. Most of the scour experiments were performed by Ms. Trine B. Bojsen, M.Sc.

The 3-D illustration of the monitored scour formation displayed in Fig. 1a was provided to the authors by Mr. John Jensen of the Danish Coast Authority, and Fig. 1b by Mr. Hans Kjær of the State Ports Authority, Denmark.

References

- Breusers, H.N.C. and Raudkivi, A.J., 1991. Scouring. I.A.H.R. Hydraulic Structures Design Manual 2, A.A. Balkema, Rotterdam.

- Eckert, J.W., 1983. Design of toe protection for coastal structures. In: Coastal Structures 83. A Specialty Conference on the Design, Construction Maintenance and Performance of Port and Coastal Structures. Proceedings. Arlington, VA, pp. 331–341.
- Fowler, J.E., 1992. Scour Problems and Methods for Prediction of Maximum Scour at Vertical Seawalls. Technical Report CERC 92-16, US Army Engineer Waterways Experiment Station, Coastal Engineering Research Center, Vicksburg, MS.
- Fredsøe, J., 1984. Turbulent boundary layer in wave-current motion. *J. Hydraul. Eng. ASCE*, 110: 1103–1120.
- Hales, L.Z., 1980. Erosion Control of Scour During Construction: Report 2, Literature Survey of Theoretical, Experimental and Prototype Investigations, Technical Report HL-80-3, US Army Engineer Waterways Experiment Station, Vicksburg, MS.
- Kozakiewicz, A., Sumer, B.M., and Fredsøe, J., 1994. Cross-flow vibration of cylinder in irregular oscillatory flow. *J. Waterw. Port Coastal Ocean Eng. ASCE*, 120(6): 515–534.
- Lillycrop, W.J. and Hughes, S.A., 1993. Scour Hole Problems Experienced by the Corps of Engineers; Data presentation and summary. Miscellaneous papers. CERC-93-2, US Army Engineer Waterways Experiment Station, Coastal Engineering Research Center, Vicksburg, MS.
- Longuet-Higgins, M.S., 1957. The mechanics of the boundary-layer near the bottom in a progressive wave. Appendix to R.C.H. Russell and J.C.C. Osorio, An experimental investigation of drift profiles in a closed channel. In: Proc. 6th Int. Conf. Coastal Engineering, Miami, FL, pp. 184–193.
- Markle, D.G., 1989. Stability of Toe Berm Armour Stone and Toe Buttrressing Stone on Rubble-Mound Breakwater and Jetties. Technical Report REMR-CO-12, US Army Engineer Waterways Experiment Station, Vicksburg, MS.
- Oumeraci, H., 1994. Scour in front of vertical breakwaters — review of problems. In: Proc. International Workshop on Wave Barriers in Deep Water, Port and Harbour Research Institute, Yokosuka, pp. 281–307.
- Sawaragi, T., and Kawasaki, Y., 1960. Experimental study on behaviours of scouring at the toe of sea dikes by waves. In: Proceedings of the 4th Japanese Coastal Engineering Conference, Japan Society of Civil Engineers, pp. 1–12.
- Sumer, B.M., Laursen, T. and Fredsøe, J., 1993. Wave boundary layers in a convergent tunnel. *Coastal Eng.*, 20: 317–342.
- Sumer, B.B., Fredsøe, J., Christiansen, N. and Hansen, S.B., 1994. Bed shear stress and scour around coastal structures. In: Proc. 24th International Conference on Coastal Engineering, Kobe, Vol. 2, pp. 1595–1609.
- Sumer, B.M. and Fredsøe, J., 1997. Scour at the head of a vertical-wall breakwater. *Coastal Eng.*, 29: 201–230.

WAVE FORCES AND OVERTOPPING OF RUBBLE MOUND BREAKWATER CROWN WALLS

JAN PEDERSEN, M.Sc, Ph.D.

Aalborg University, Dept. of Civil Engineering, Sohngårdsholmsvej 57, DK-9000 Aalborg
RAMBØLL, Frodesgade 125A, DK-6700 Esbjerg

WAVE FORCES AND OVERTOPPING OF RUBBLE MOUND BREAKWATER CROWN WALLS

Abstract

This paper presents the main results from a large parametric laboratory study including a total 373 long-duration model tests. The study addresses both the wave forces imposed on the breakwater crown wall as well as the performance of the structure in reducing the wave overtopping. The testing programme includes variations of the sea state parameters and of the geometrical configuration of the breakwater and crown wall. Basic relations between forces/overtopping and the varied parameters are examined and design equations for estimation of impact forces and overtopping discharges are proposed.

1 Introduction

Wave forces on a crown wall structure exposed to irregular waves are of a stochastic and hence very complicated nature. The imposed loads on a wall depend on both the characteristics of the waves and the geometry, including permeability and roughness, of the seaward face of the breakwater.

In order to improve the knowledge of how breakwater crown walls perform under random wave attack an extensive test programme was set up. Wave loading exerted on the vertical front face of the crown walls as well as the amount of water overtopping the structures were measured. A total of 373 tests were performed. Each test had a duration corresponding to 5000 waves or more in order to quantify the low probabilistic wave force estimates, e.g. the 0.1% fractile of the horizontal wave force, with reasonable accuracy.

2 Model tests description

All tests were performed in a 1.6 *m* wide and 26 *m* long wave flume located at Aalborg Hydraulics and Coastal Engineering Laboratory, Aalborg University.

A breakwater model test section of 1.0 *m* width, delimited by wave guidance walls, was installed in the middle of the flume as far away from the wave generator as possible. Behind the breakwater a gravel beach with a 1:5 slope was laid out. This setup, shown in figure 1, was chosen in order to limit wave reflections in the flume.

The wall structure itself was constructed from 6 *mm* thick aluminium plates which were mounted onto the wave guidance walls. The aluminium structure was further strengthened by means of four triangular stiffener plates. Water levels varied between 0.51 *m* and 0.59 *m*. The base of the crown wall was in all tests located at level +0.55 *m* and the crest of the

armour berm at level $+0.70\text{ m}$. In front of the breakwater an array of 3 wave gauges was placed in order to analyse the wave field with respect to incident and reflected waves.

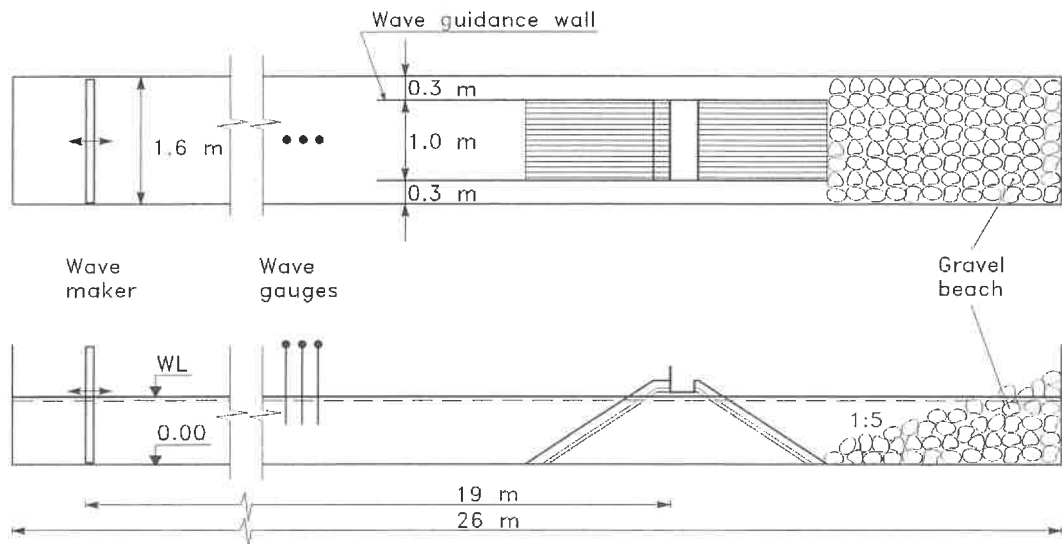


Figure 1: Outline of breakwater setup in wave flume

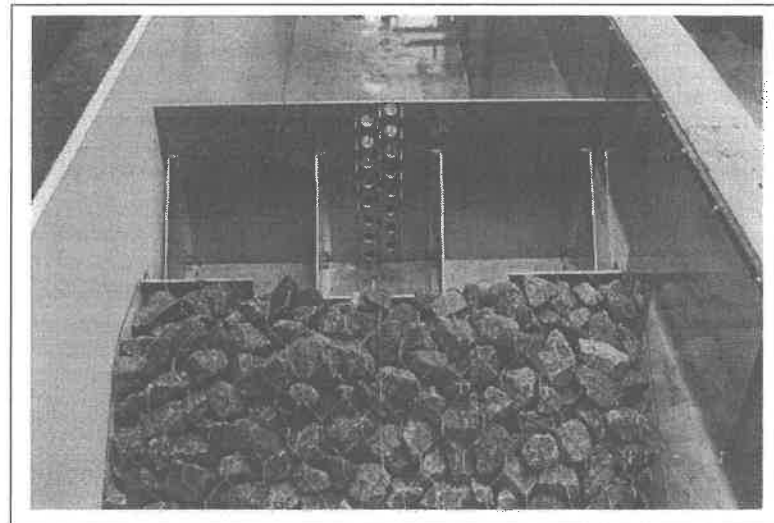


Figure 2: Crown wall seen from the lee-side.

2.1 Investigated parameters

In the following a brief listing of the investigated parameters is given. Figure 3 sketches all the relevant parameters with the exception of the sea state parameters.

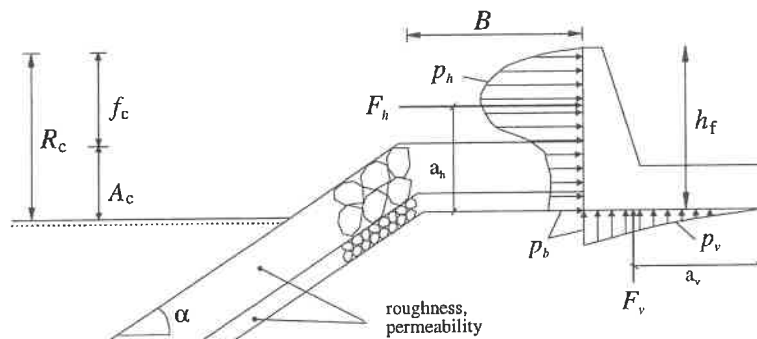


Figure 3: Definition of parameters and pressures.
Redrawn from Burcharth (1993)

Since waves were generated from a predefined spectrum the spectral estimates H_s and T_p were chosen as representatives of the wave field. In table 1 the investigated parameters and their respective variational ranges are given.

Table 1: Investigated parameters and their variations.

Parameter	Range	Ratio	Range
H_s	0.10 m – 0.18 m	ξ_m	1.1 – 5.1
T_p	1.20 s – 2.20 s	H_s/A_c	0.5 – 1.7
h	0.51 m – 0.59 m	R_c/A_c	1 – 2.6
armour	random: rock, Dolos, cubes smooth: cubes	A_c/B	0.3 – 1.1
h_f	0.15 m – 0.33 m	$\cot \alpha$	1.5 – 3.5
A_c	0.11 m – 0.19 m		
R_c	0.11 m – 0.37 m		
B	0.18 m – 0.36 m		
$\cot \alpha$	1.5 – 3.5		

The above variations were chosen in order to cover the most common structural variations observed in prototype structures. Tests with the highest wall ($h_f = 0.33$ m) are in that sense unrealistic, but were performed in order to assess the total momentum in the waves.

2.2 Investigated cross sections

For all the tested breakwater configurations the core was constructed of relative coarse sand ($d_{n,50} \approx 2\text{ mm}$). Between the core and the inner filter layer (10 mm thick and $d_{n,50} = 5\text{ mm}$) a geotextile was placed to prevent out-washing of the core material. The second filter layer had a thickness of 40 mm and consisted of stones with a nominal diameter of $d_{n,50} = 12\text{ mm}$. Finally a 100 mm thick armour layer with different units in different tests was placed. To ensure the armour remained stable under all wave conditions a thin chicken wire was placed on top of the layer – see figure 2.

Figure 4 illustrates the principal structure of the breakwater cross section.

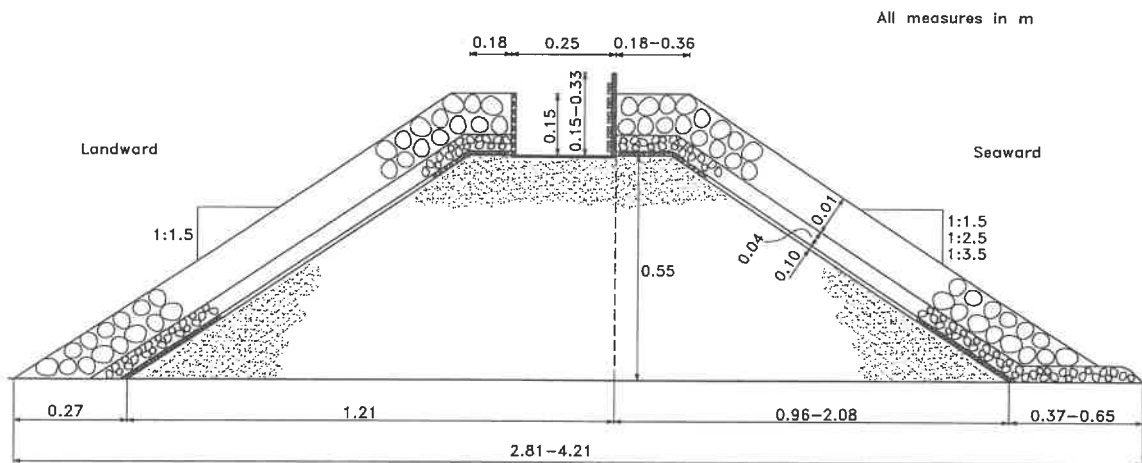


Figure 4: Sketch of breakwater cross section with overall measures of geometrical variations.

In order to examine the influence from the parameters given in table 1 the 12 different breakwater cross sections outlined in figure 5 were tested. Most of the tests were carried out on the cross sections 1–4 where the influence of the parameters H_s , T_p , h_f , R_c and A_c was investigated. Cross sections 2, 5, 6 and 7 were used to assess the influence of the armour crest width B . The slope angle α was studied by comparing cross sections 2, 8 and 9 and finally the influence of the applied type of armour (roughness/permeability) was investigated with the sections 8, 10, 11 and 12.

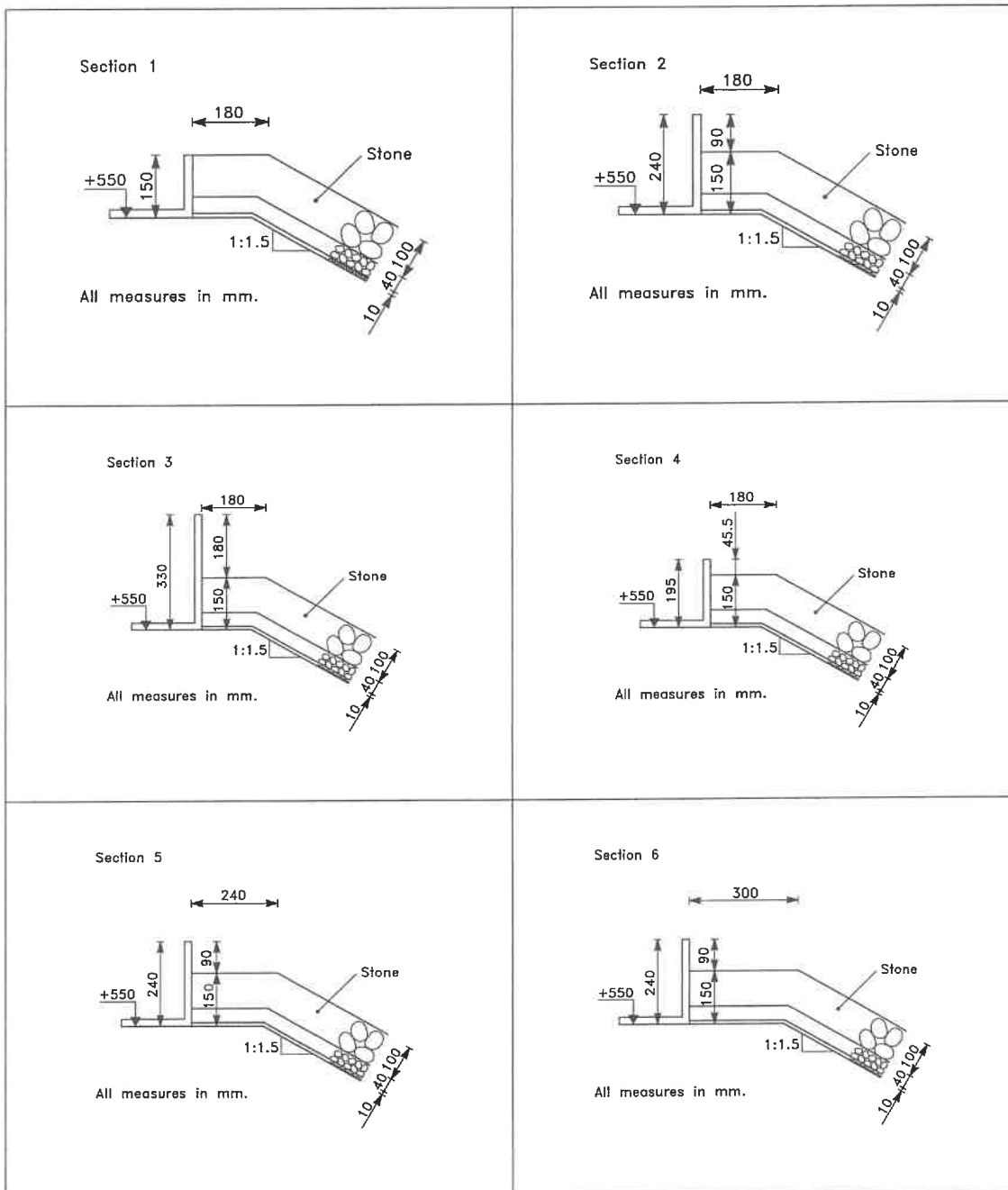


Figure 5: Cross sections 1 - 6

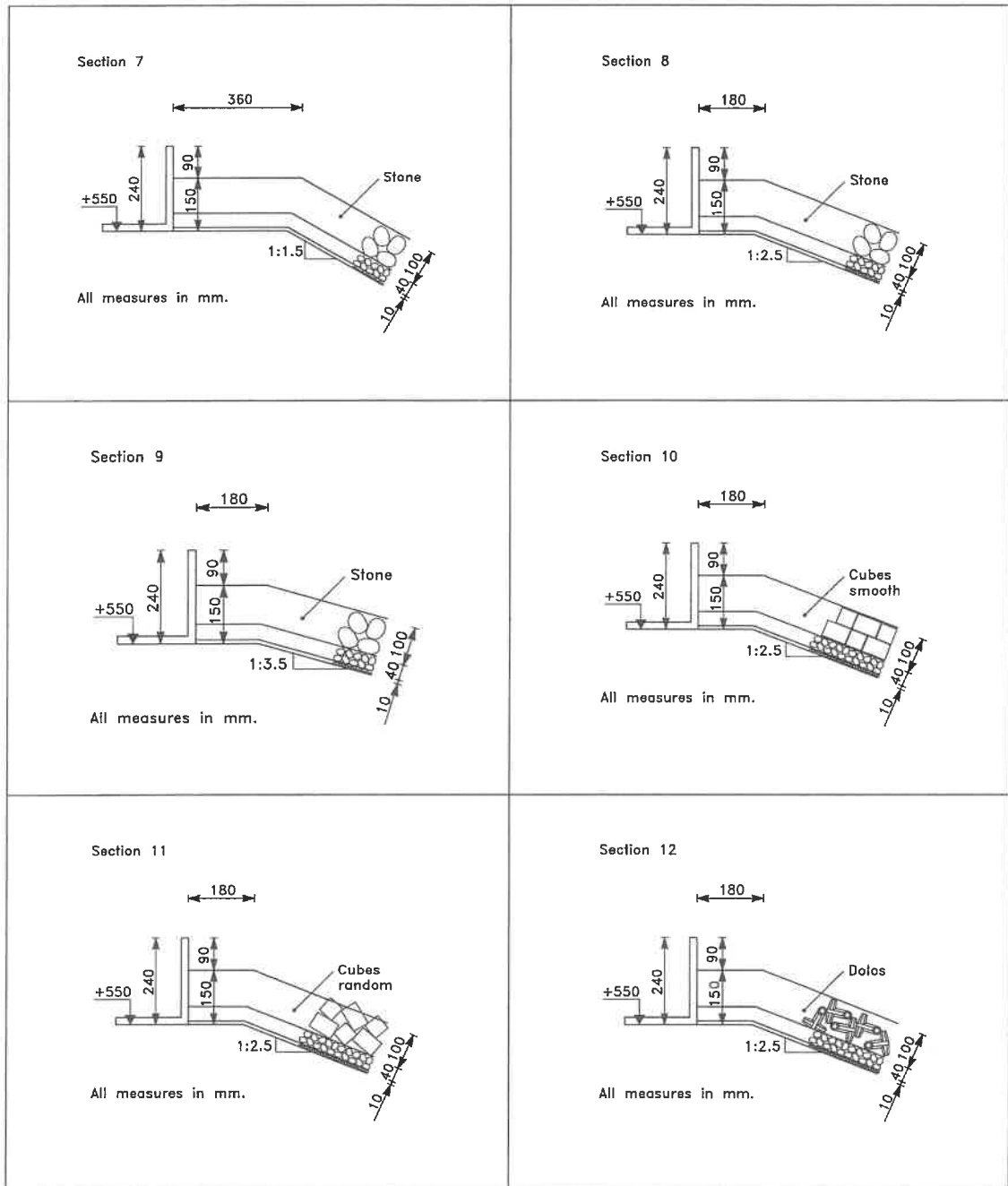


Fig. 5 continued: Cross sections 7 - 12

The four investigated wall heights - cross sections 1-4 - are shown in figure 6.

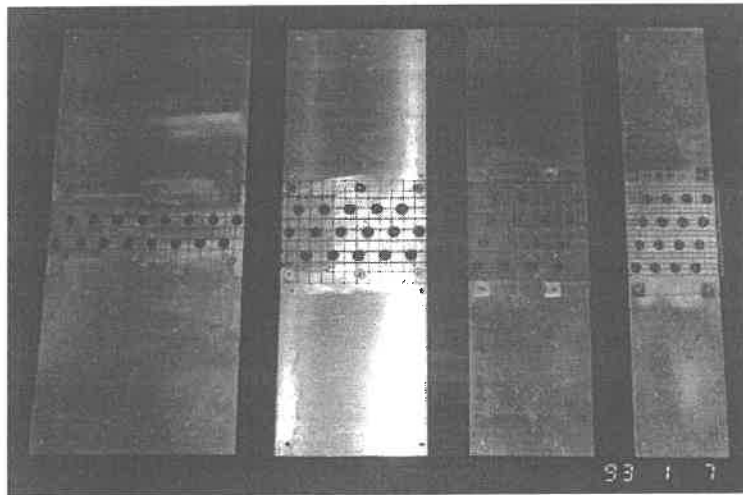


Figure 6: Photography of the 4 used walls.

2.3 Pressure measurements

Initial tests with a wall section suspended in a dynamometer showed that this type of setup introduced several errors in the measurements of forces exerted on the crown walls. The problems were caused by the wide frequency range that must be covered by the force table, without introducing dynamic amplification, in order to measure both short duration impact forces as well as hydrostatic forces having a duration in the order of the wave period. In practice it turned out to be impossible to construct a dynamometer sufficiently rigid (high natural frequency) to avoid dynamic errors and at the same time have a measurable output from the system. Hence it was decided to measure the wave forces by means of pressure transducers.

To avoid disturbances in the pressure field on the wall, the pressure cells were built into the walls and aligned with the vertical face. The sensors should preferably have a smooth surface and a quite large diameter to smoothen out local pressure transients. With these constraints in mind the Phillips P13-OEM pressure transducer with a diaphragm diameter of 18 mm were chosen. The 16 sensors have an operational pressure range between 0 and 4 bar (0-40 kN/m^2) which is around 5-10 times the maximum pressures expected in the model tests.

Figure 7 shows 2 pressure cells mounted with a water proof chasing and 8 other cells mounted into one of the walls.

All pressures were measured relative to atmospheric pressure. The dynamic response of the sensors was not tested other than visually verifying that the transducers responded to short duration impact loadings. The transducers were powered from a signal amplifier and the sensor output was amplified by a factor of 1000. The amplifier was checked to be linear up

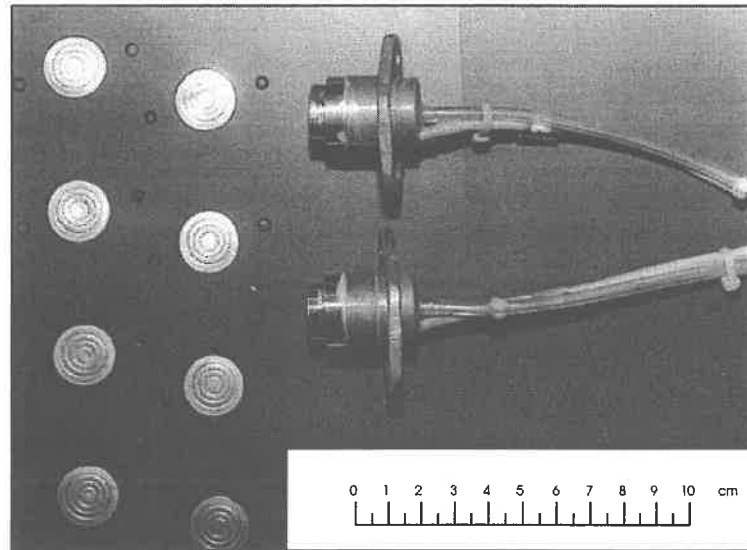


Figure 7: Phillips P13-OEM pressure transducers.

to 0.5 kHz . Prior to the experiments it was verified that the pressure transducers did not suffer from temperature drift and nonlinearity. The sensors were calibrated at least twice each week and showed very little variation through the entire testing period.

Initial tests showed that a sampling rate of 256 Hz was sufficient in order to avoid losing resolution in the signals. In some of the tests with the lowest wall, where rapid pressure rises do not occur since the wall is fully protected by the armour stones, a sampling rate of 128 Hz was used. A voltage regulator was used to feed all electronic devices in order to minimise voltage gradient effects in the measurements. With the regulator in circuit it was not necessary to filter the pressure signals. Due to the large amount of data the pressure signals were instantly transformed to resultant wave forces and only the pressure distributions for the 3 largest wave impacts in each test serie were stored.

2.4 Overtopping measurements

Overtopping measurements were conducted by measuring the amount of water falling into a $0.6 \text{ m} \times 0.8 \text{ m}$ tray mounted on the rear side of the crown wall. Only green water overtopping was measured as the wind field could not be simulated in the laboratory.

From the tray the water was pumped back into the wave flume through a flow meter which should be manually recorded. Since many of the tests were run as batch jobs during nights the recordings of the flow meter were done by means of computer controlled camera which

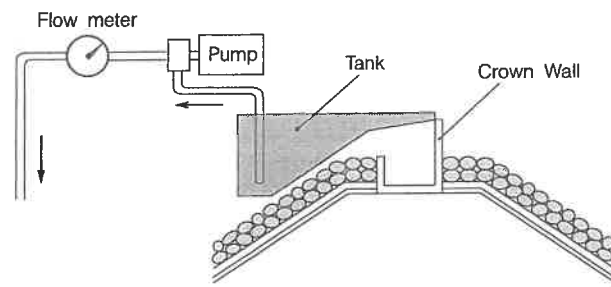


Figure 8: Sketch of setup for wave overtopping measurements.

was triggered to take a picture after each run. Unfortunately, this remote registration did not work properly in all the tests resulting in lack of overtopping measurements in some of the series.

Only the mean overtopping quantity from each test was measured.

3 Wave pressures and derived force components

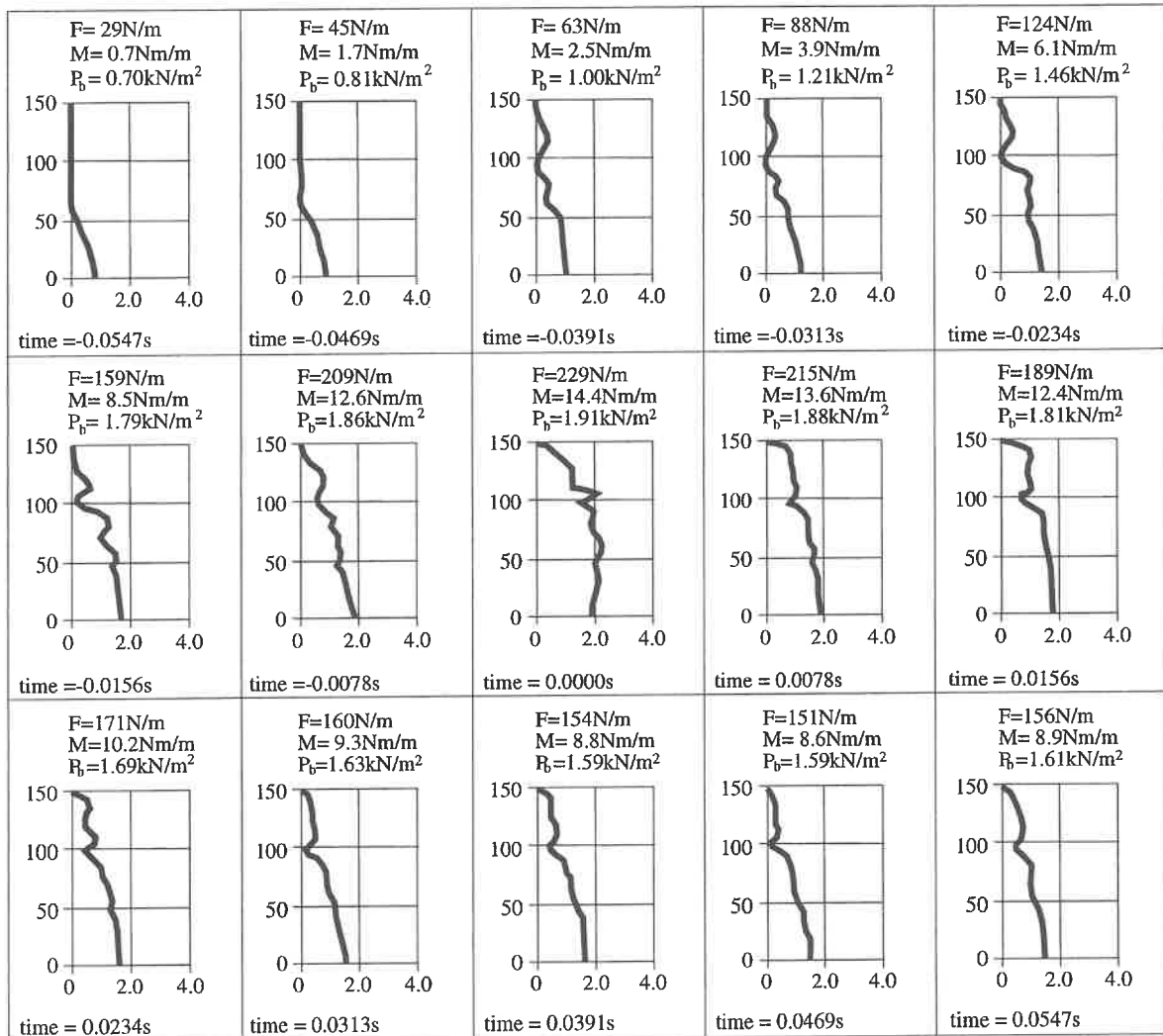
In the following the results obtained from the performed model tests will be presented. As the measurements were performed by measuring the pressures exerted on the front face of the wall informations on both spatial and temporal pressure distributions have been obtained as well as information of the resulting forces imposed on the wall.

3.1 Spatial pressure distributions

Depending on the wave climate and the geometry of the actual cross section the spatial distribution of wave induced pressure on the wall face develops differently. In figures 9 and 10 evolutions of wave pressure are shown for identical wave conditions for 2 of the 4 crown wall heights used. In the figures the maximum wave loading occurs at time $t = 0.000$ s. The figures are representative of typical developments of maximum pressure on the respective cross sections.

For a crown wall fully protected by the armour units in front of it (figure 9) the pressure rise is relatively gentle and an almost even pressure distribution at the time of maximum loading is observed.

Crown walls with an upper unprotected wall part are subject to high impact pressures in the region just above the armour crest berm. A typical evolution of wave pressure on these type of high structures is illustrated in figure 10. Initially ($t < -0.027$ s) no wave pressures act on the wall face. In less than 0.006 s the pressures rise from 0 to approximately 6 kN/m^2 in a narrow region immediately above the armour crest. Within the next 0.03 s the high-pressure impact zone is widened and an increase in more slowly varying pressures on the lower protected part of the wall as the water starts to penetrate into the voids in the armour is observed. At time $t \approx 0$ s the maximum load on the wall is reached. The distribution of pressure is characterised by a high pressure intensity on the upper part and an almost even distribution of half or less the intensity on the lower unprotected part.



Test no. 89
 $H_s = 0.182\text{ m}$
 $T_p = 2.2\text{ s}$
 $A_c = 0.15\text{ m}$

No. pressure cells : 16
 Vert. cell spacing : 8.5 mm
 Hor. cell spacing : 40 mm
 Logging frequency : 128 Hz

Section 1

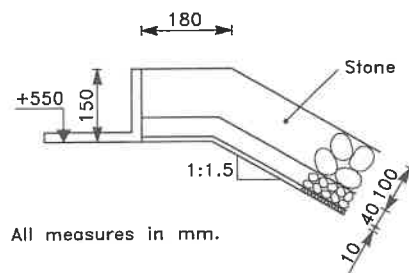
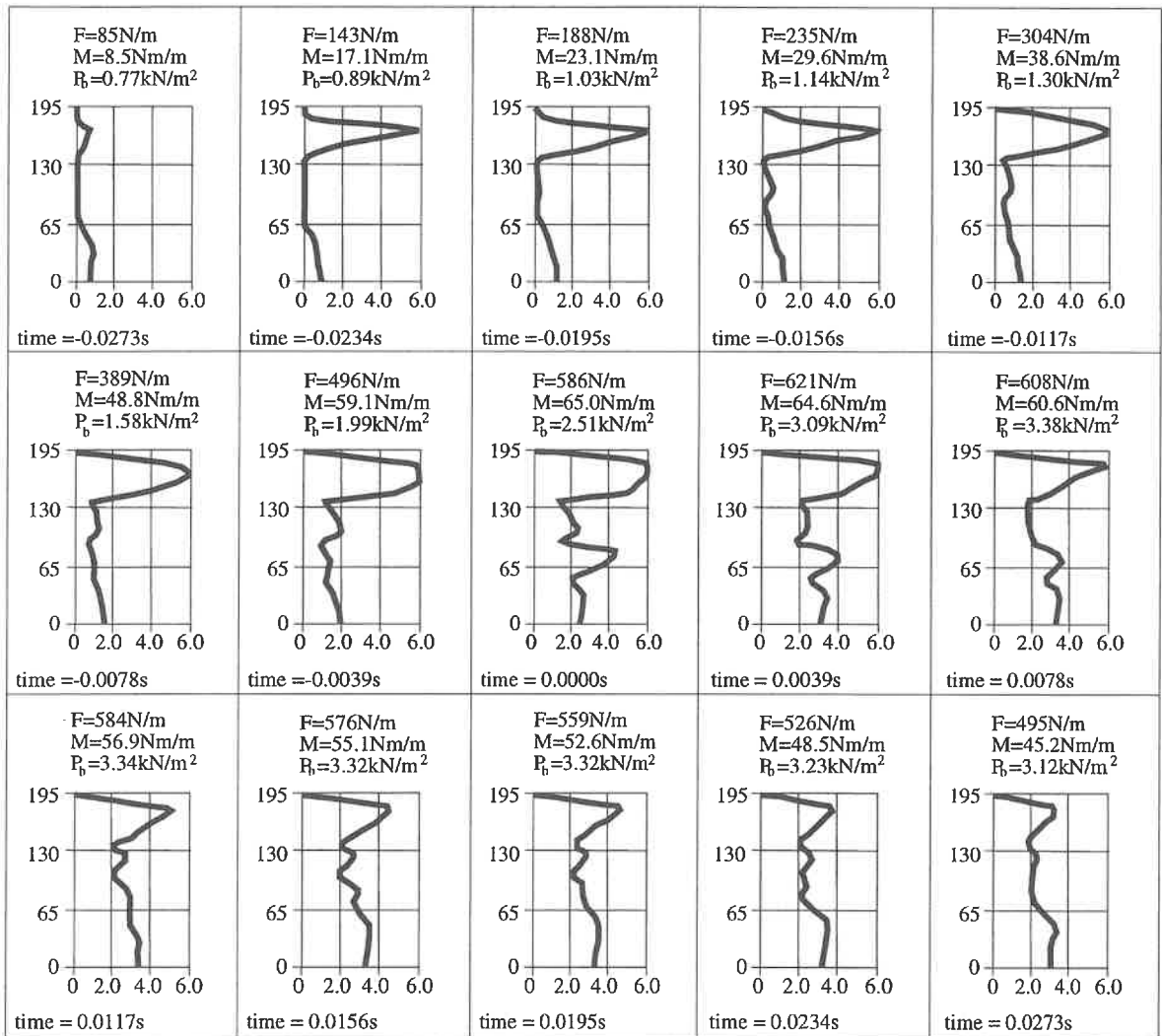


Figure 9: Typical maximum pressure distribution on low crown wall.



Test no. 202
 $H_s = 0.173 \text{ m}$
 $T_p = 2.2 \text{ s}$
 $A_c = 0.11 \text{ m}$

No. pressure cells : 16
 Vert. cell spacing : 11 mm
 Hor. cell spacing : 40 mm
 Logging frequency : 256 Hz

Section 4

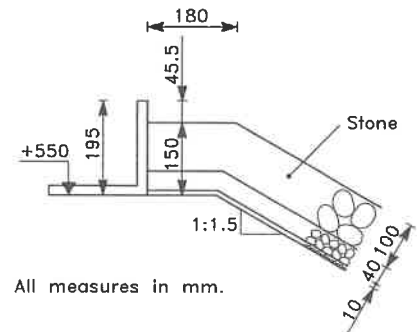
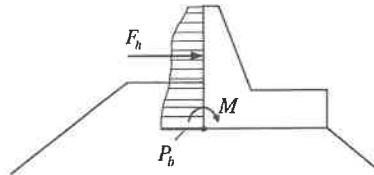


Figure 10: Typical maximum pressure distribution on crown wall with unprotected upper part.

3.2 Wave force components

Since the amount of data from the pressure sensors is enormous – approximately 50Mb disc storage per test – the pressure recordings are transformed to the following 3 resultant wave force components by numerical spatial integration over the wall height :

- Horizontal wave force F_h
- Overturning moment M
- Wall base pressure P_b .



The pressure P_b at the base of the wall is stored since this component can be used to assess the uplift force acting beneath the base slab of the structure.

Calculations of the overturning moments are solely based upon the wave pressures acting on the vertical wall face, i.e. contributions from uplift pressures are not included.

Time series of P_b and F_h are not filtered or smoothed in any way. The overturning moment M is smoothed by averaging the sum of the value at each time step and its neighbouring values. Examples of time series of the three force components are shown in figures 11 – 12 for different load situations.

Figure 11 illustrates a typical lapse of time during a wave attack on the lowest wall type which is fully protected against impact forces by the armour stones in front of the wall. In all tests with this wall configuration relatively smooth force component time series without a distinct peak around the time of maximum load were observed. Also it was noticed that the peak values of the 3 components occurred simultaneously in the majority of the test series. Rise times, i.e. the time from zero loading to maximum loading were typically in the range $0.1 \text{ s} < t_{rise} < 0.2 \text{ s}$.

Figure 12 shows the force time series for the maximum force record in a test with the highest wall configuration. The loads are clearly defined by a single peak and all 3 force components reach their maximum values at the same time. This type of force development is registered for the majority of the impacting waves on high crown walls.

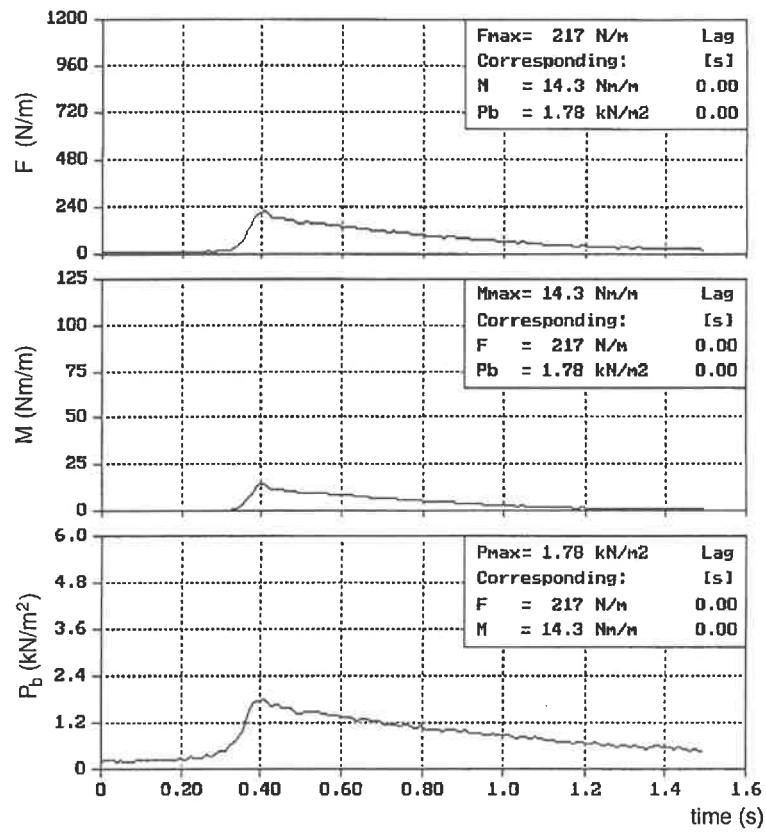


Figure 11: Example of typical force time series on the lowest protected wall.

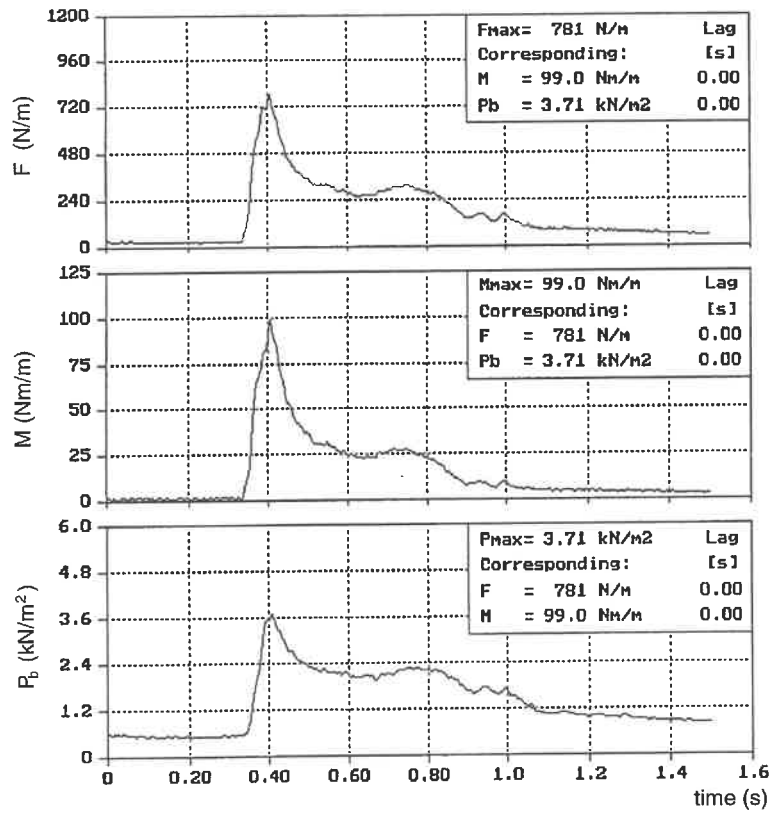


Figure 12: Example of typical force time series on highest wall.

In an extensive study concerning wave loading on caisson breakwaters Bagnold (1939) found that the horizontal wave force imposed on such structures typically had a lapse of time as shown in figure 13. This observation was later verified by Oumeraci and Kortenhuis (1992) and Marinski and Oumeraci (1992) in a very comprehensive study involving both wave force assessment and stability evaluations of caisson breakwaters. The same principal shape of the wave force evolution was found in the present study. Hence the time evolution of the horizontal wave force component can be described by the peak force ($F_{h,peak}$), the more slowly varying (semi-static) part of the impact ($F_{h,static}$) and the two periods t_{rise} and t_{decay} .

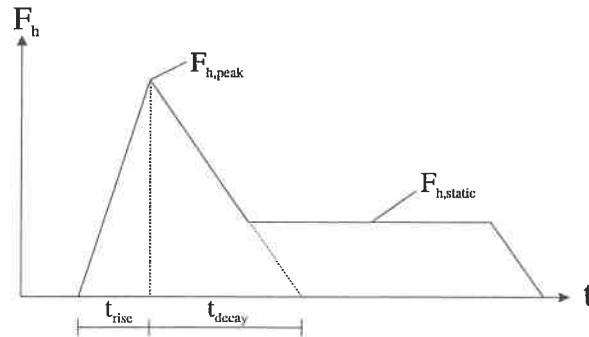


Figure 13: Schematised wave force evolution.

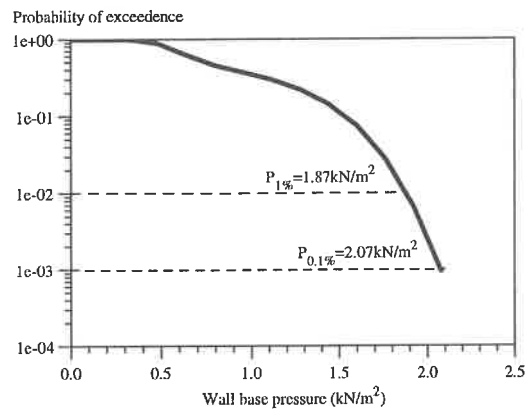
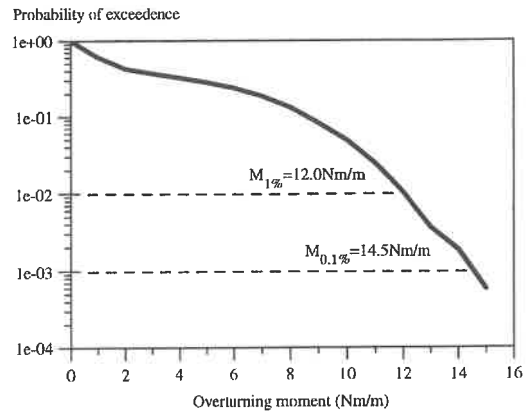
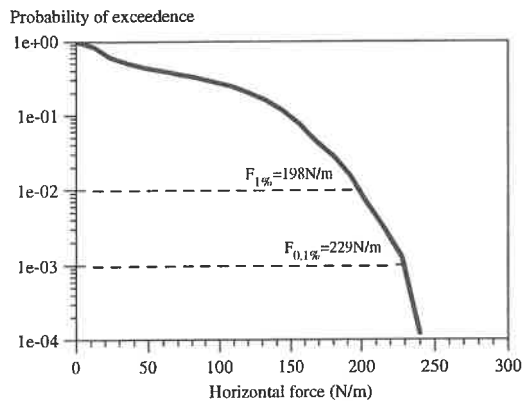
The rise times t_{rise} were, for all the configurations with an upper unprotected wall part (cross sections 2–12 in figure 5) and exposed to waves sufficiently large to impact on this part, found to lie in the range $0.01\text{ s} < t_{rise} < 0.1\text{ s}$. For wave conditions where only the lower protected wall part was loaded the rise times were similar to those found for cross section 1, i.e. $0.1\text{ s} < t_{rise} < 0.2\text{ s}$. For the high walls the decay time is typically within the range $0.1\text{ s} < t_{decay} < 0.25\text{ s}$ whereas for the lowest wall type the decay of the force components is in the order of the wave period.

3.3 Force distributions and statistical force estimates

Examples of distribution curves for the three force components are given in figures 14 – 15 for the lowest and highest wall types respectively and for almost identical wave conditions. It is noticeable how the distribution curves turn out to be straight lines in the logarithmic (\log_{10}) probability plots for the highest crown wall where hardly any overtopping occurs. A study of figure 14 representing the lowest crown wall shows that this linearity does not exist due to the excessive wave overtopping taking place on this configuration.

For further analyses two statistical estimates of each force component were extracted :

- the 1% force fractile, i.e. the force which in average is exceeded by 1% of the waves.
- the 0.1% force fractile, i.e. the force which in average is exceeded by only 0.1% of the waves.



Test no. 89
 Cross section 1
 $H_s = 0.182 \text{ m}$
 $T_p = 2.2 \text{ s}$
 $A_c = 0.15 \text{ m}$
 Excessive overtopping

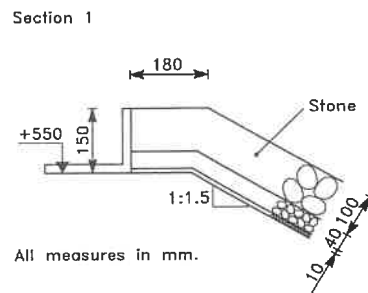
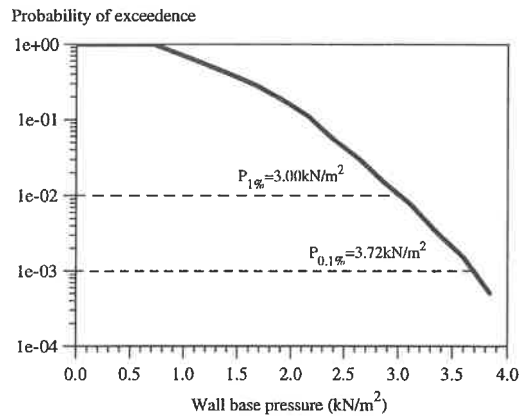
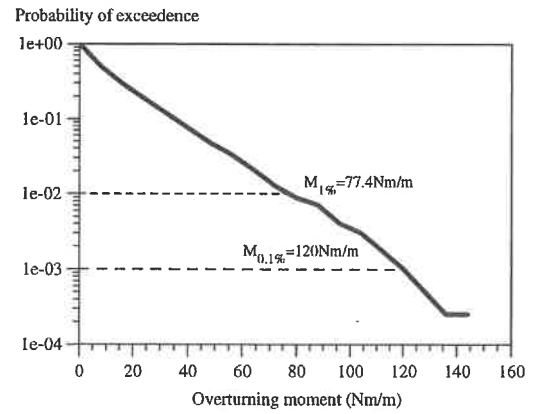
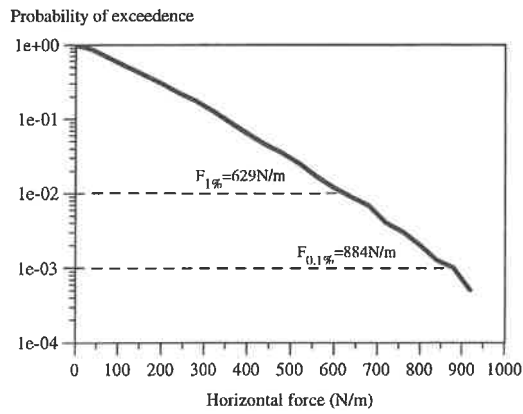


Figure 14: Examples of force distributions with lowest crown wall where excessive overtopping took place.



Test no. 166
 Cross section 3
 $H_s = 0.183 \text{ m}$
 $T_p = 2.2 \text{ s}$
 $A_c = 0.11 \text{ m}$
 $Q_m = 52 \cdot 10^{-6} \text{ m}^3/\text{m}/\text{s}$

Section 3

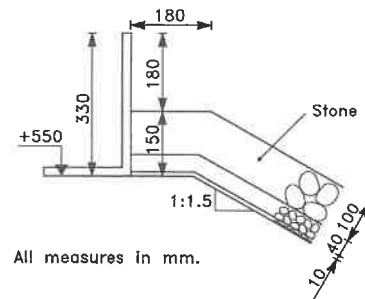


Figure 15: Examples of force distributions from test with highest crown wall with very moderate overtopping.

3.4 Correlation between force component estimates

In figures 16 and 17 $M_{0.1\%}$ vs. $F_{h,0.1\%}$ and $P_{b,0.1\%}$ vs. $F_{h,0.1\%}$ are plotted respectively for all 373 test series.

A very strong almost linear relationship between $F_{h,0.1\%}$ and $M_{0.1\%}$ is observed. Compared to this the correlation between P_b and the other two force components is not as pronounced. For small wave loadings the correlation between $P_{b,0.1\%}$ and $F_{h,0.1\%}$ is quite high but for higher load intensities rather large discrepancies are observed.

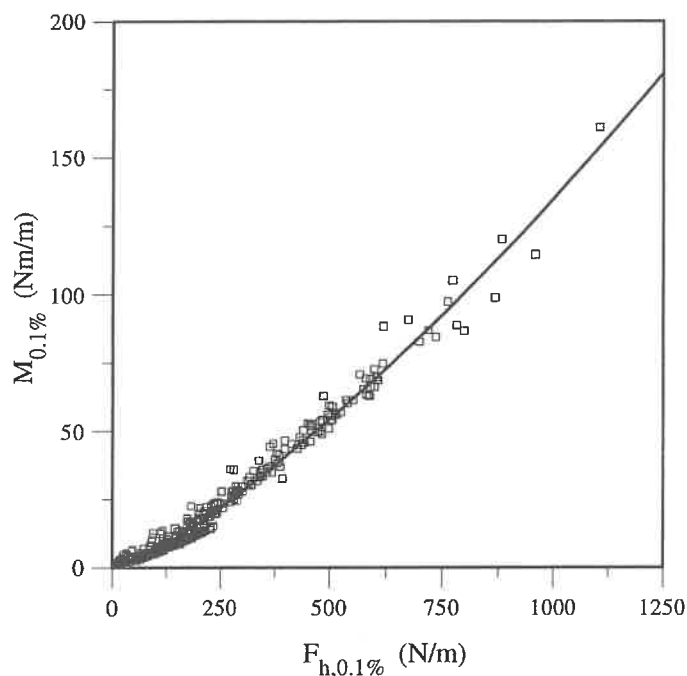


Figure 16: $M_{0.1\%}$ plotted vs. $F_{h,0.1\%}$.

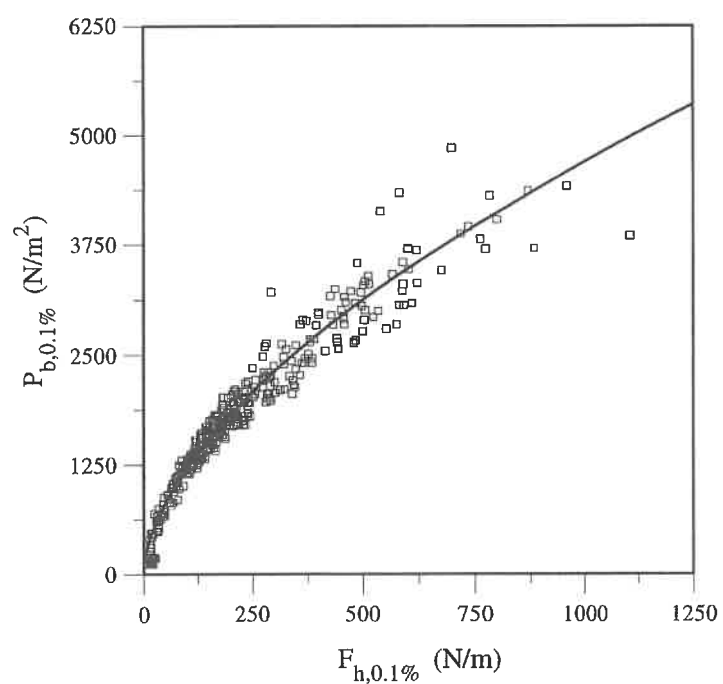


Figure 17: $P_{b,0.1\%}$ plotted vs. $F_{h,0.1\%}$.

4 Parametric investigation

In the following an outline of the influence of the different investigated parameters on the horizontal wave force $F_{h,0.1\%}$ will be given. The influence of the investigated parameters in relation to the two other force components (M and P_b) is reflected by the correlation between these and F_h as given in figures 16 – 17.

Influence of wave height

As representative of wave height the incident significant wave height (H_s) measured just in front of the breakwater is used. As found in earlier studies (eg. Jensen (1984) and Hamilton and Hall (1992)) a pronounced linear dependency between the horizontal wave force $F_{h,0.1\%}$ and H_s is observed as long as massive green water overtopping does not occur. Figure 18 shows the results from measurements on cross section 3 for a fixed wave period and four levels of the armour berm crest (A_c).

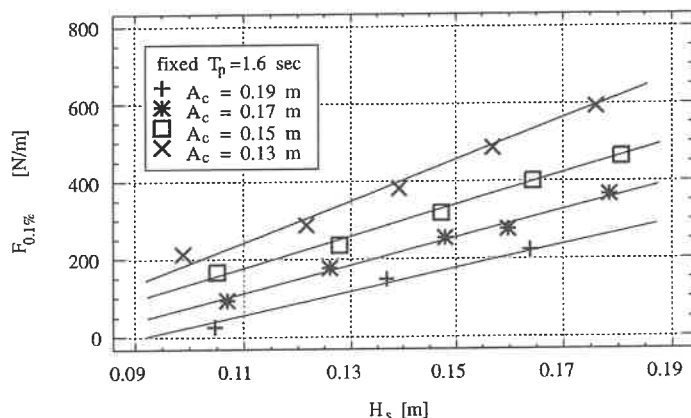


Figure 18: $F_{h,0.1\%}$ plotted against H_s .

Figure 19 also shows $F_{h,0.1\%}$ plotted against the significant wave height but for four different wall heights. The results originate from tests with cross sections 1 to 4. For the applied conditions ($T_p = 1.4$ s and $A_c = 0.15$ m) the two highest walls are not significantly overtopped for any of the examined wave heights and a clear linear dependence is seen. For the two lowest walls ($h_f = 0.15$ m and 0.195 m) a clear reduction in wave force rate is experienced. On the lowest of the four investigated walls a maximum value of imposed wave force has been reached corresponding to approximately twice the hydrostatic pressure that would be found if the water table was located at the wall crest.

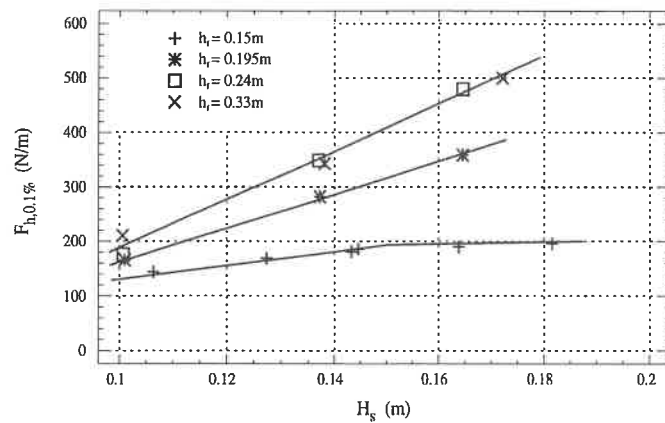


Figure 19: $F_{h,0.1\%}$ plotted against H_s for 4 different wall heights.

Influence of wave period/length

Like the wave height also the wave period shows a pronounced effect on F_h . Since all wave conditions can be classified as intermediate or shallow water conditions a similar influence can be expected using a local wave length e.g. L_p which is plotted against $F_{h,0.1\%}$ in figure 20.

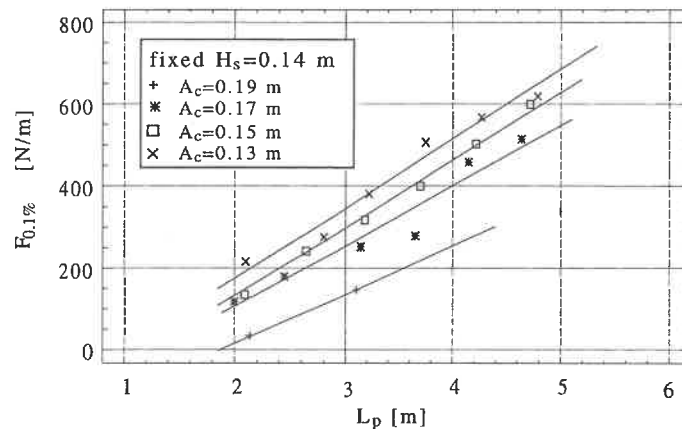


Figure 20: $F_{h,0.1\%}$ plotted against L_p .

Far more scatter around the fitted lines is seen when compared to the similar figures illustrating the influence of the wave height. Though it can be concluded that the imposed wave force almost increases linearly with increasing wave length. Naturally the constraints concerning massive green water overtopping also applies to the influence of wave length/period.

Influence of armour crest freeboard

Jensen (1984) found a linear relation between the inverse of the armour crest freeboard (A_c) and the horizontal wave force. Figure 21 showing $F_{h,0.1\%}$ plotted against the dimensionless wave height/freeboard ratio $\frac{H_s}{A_c}$ clearly confirms Jensen's findings.

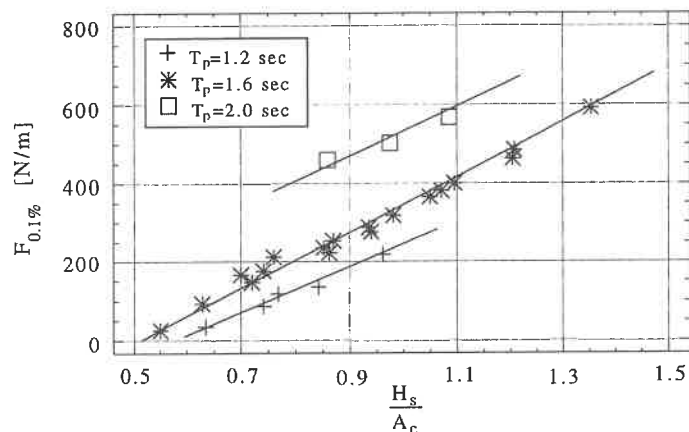


Figure 21: $F_{h,0.1\%}$ plotted against the dimensionless wave height - armour freeboard ratio H_s/A_c .

Influence of slope angle

As expected the imposed wave loading on the crown wall decreases with decreasing slope angle (flatter slope). In figure 22 $F_{h,0.1\%}$ is plotted against the inverse of $\cot \alpha$. The figure clearly shows that a linear dependency between F_h and $\frac{1}{\cot \alpha}$ exists.

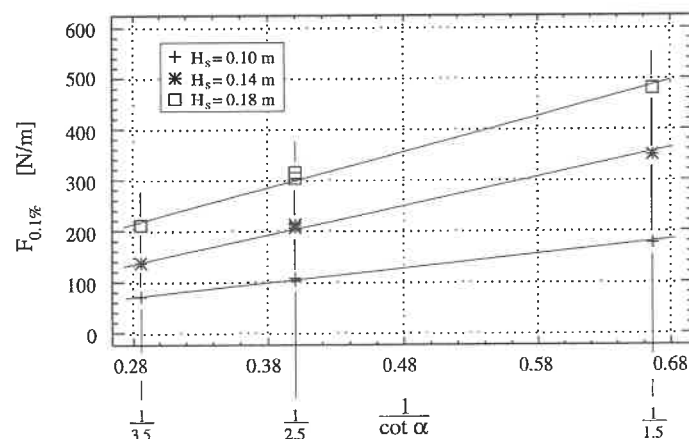


Figure 22: $F_{h,0.1\%}$ plotted against $\frac{1}{\cot \alpha}$.

4.1 Influence of armour layer type

In order to examine the influence of roughness/permeability of the armour layer, identical test runs were performed with four types of armour :

- Concrete cubes placed in a regular pattern creating a very smooth upper surface and a very low layer permeability. See cross section 10, figure 5.
- Random placed concrete cubes. See cross section 11, figure 5.
- Random placed rock armour. See cross section 2, figure 5.
- Random placed Dolos units. See cross section 12, figure 5.

Figure 23 shows that the wave loading on the crown wall is practically identical for the three randomly placed armour types (rocks, cubes and Dolos units) whereas the wave forces measured on the cross section with concrete cubes placed in a regular pattern are nearly twice those obtained for the randomly placed armour configurations.

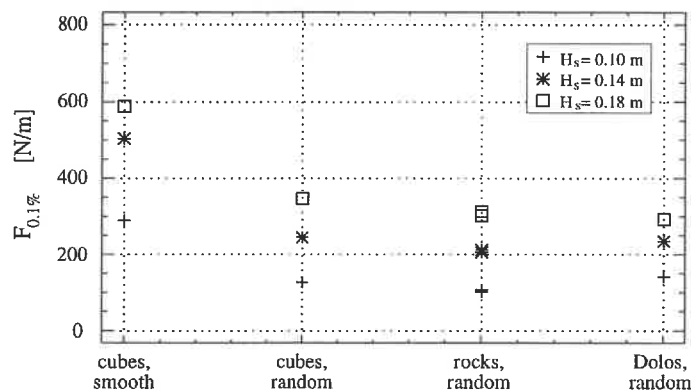


Figure 23: $F_{h,0.1\%}$ plotted against the four investigated armour layer types.

Influence of crown wall height

The influence of the wall height (h_f) on the wave loading is highly complex, which is illustrated by figure 24 where h_f is plotted against $F_{h,0.1\%}$ for a constant value of $H_s/A_c = 1.27$ and for three wave periods. The measurements used in the figure originate from tests with cross sections 1 to 4 only. All large waves were breaking on the rubble slope (plunging waves).

On the right hand side of the grey overtopping threshold line hardly any overtopping was registered in the respective tests, hence all wave energy is imposed on the crown wall face. Increasing the wall height beyond this threshold does not affect the wave loading on the wall. On the left hand side of the threshold line excessive wave overtopping takes place and the wall height has an important influence on wave loading. The fitted curves in this region indicate that F_h is proportional to h_f^2 .

In figure 25 a plot similar to figure 24 but for a lower value of the ratio H_s/A_c is shown. For wave periods of 1.2 s and 1.6 s the same trends as found above are registered, i.e. increase in wave force for increasing wave period and a clear threshold for when further increase in wall height does not influence the wave loading. The curve for a wave period of $T_p = 2.2$ s deviates from this pattern as the measured forces are lower than those for $T_p = 1.6$ s and also the threshold point is located at a much lower wall height than should be expected. The only possible explanation for these deviations is that the wave steepness for this wave period is very low and that the waves do not break on the slope (surging waves).

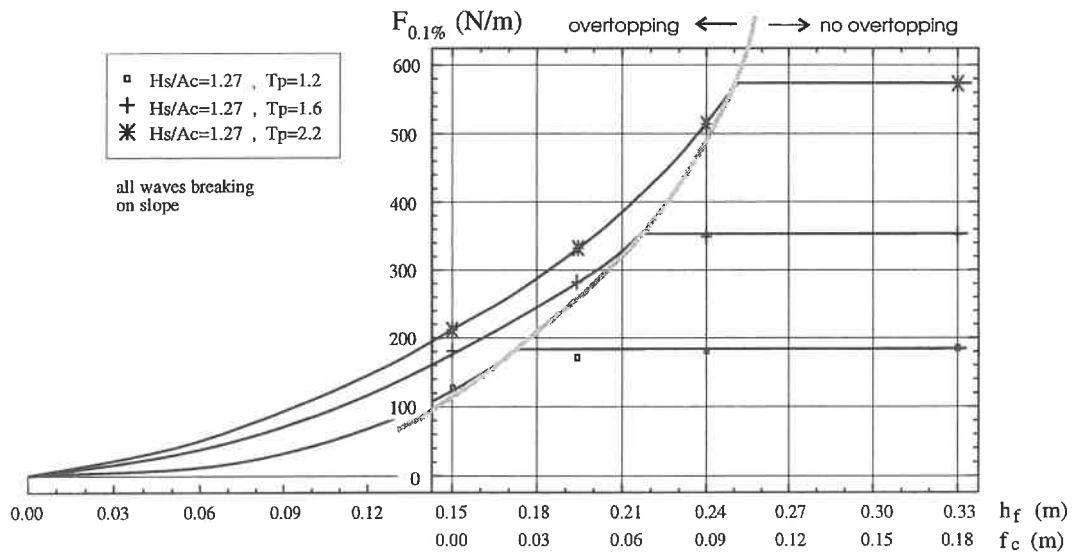


Figure 24: $F_{h,0.1\%}$ plotted against the crown wall height h_f for a constant ratio of $H_s/A_c = 1.27$.

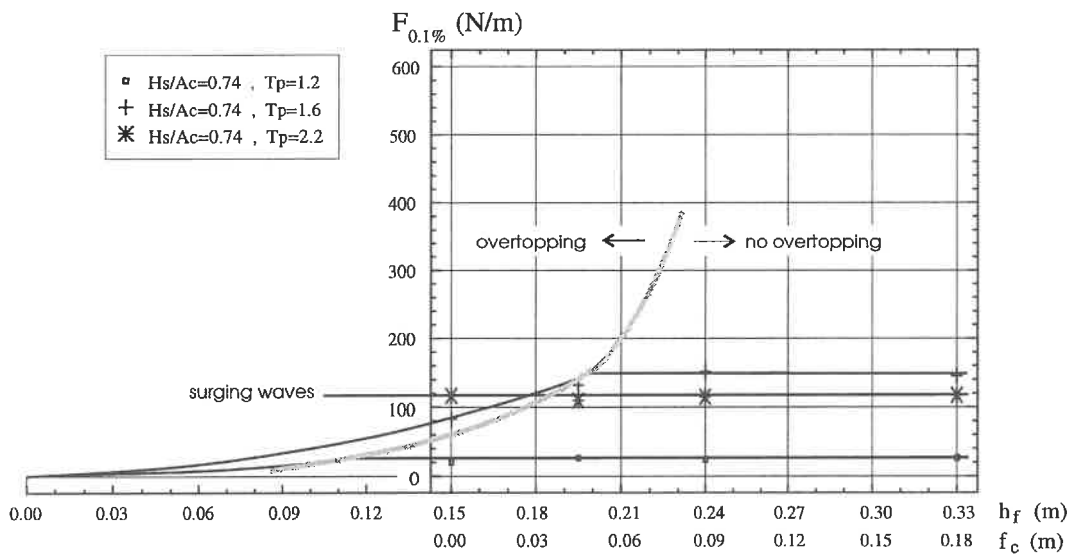


Figure 25: $F_{h,0.1\%}$ plotted against the crown wall height h_f for a constant ratio of $H_s/A_c = 0.74$.

Influence of armour berm width

The influence of the armour crest width is illustrated in figure 26 indicating that the width of the armour crest berm has only a slight influence on the crown wall loading. Unfortunately, all tests with varying berm widths were performed with a crown wall height of 0.24 m, which caused quite some overtopping especially for the smaller berm widths making it difficult to draw any definite conclusions concerning the influence of berm width. Though it is noticeable that the wave forces obtained for $B = 0.24\text{ m}$ under severe wave conditions are larger than those obtained for $B = 0.18\text{ m}$. A similar phenomenon was reported by Bradbury et al. (1988). The phenomenon may be explained by considering the path of the uprushing water. Assuming the path to be parabolic the width of the berm will determine the vertical level of the contact point between the water tongue and the wall and hence, if severe overtopping takes place, reduce the wave force. Extending the berm width beyond 0.24 m ($4 \times d_{n,50}$) the expected decrease in wave loading is observed.

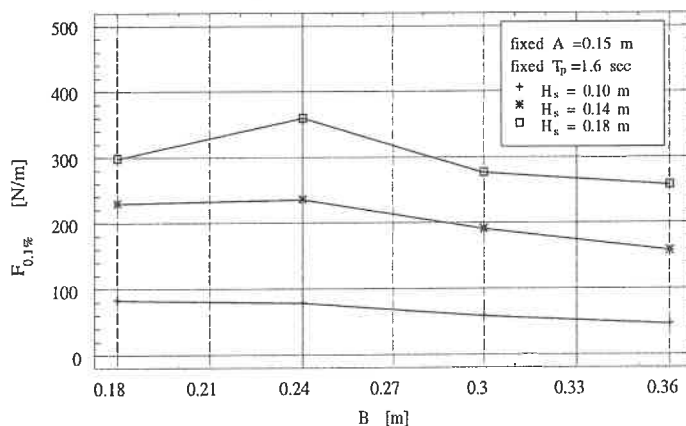


Figure 26: $F_{h,0.1\%}$ plotted against the armour crest berm width B .

Resume of parametric investigation

A brief summary concerning the influence of the different investigated parameters on the horizontal wave force is outlined.

Wave height

A linear dependency of the wave height is observed as long as massive green water overtopping does not occur. When green water overtopping commences the linear relation is no longer valid and the imposed wave force tends to approach an asymptotic value which for the lowest of the four tested walls, being fully protected by the armour in front of it, can be determined as twice the wave force calculated assuming a hydrostatic pressure distribution from the water table level at the wall crest.

Wave period/length

A pronounced increase in wave force is registered for increasing wave period/length. The relation between the local peak wave length L_p and F_h can be assumed to be linear.

Armour crest freeboard

A clear linear dependency between $\frac{1}{A_c}$ and F_h is found.

Front slope angle

A clear linear dependency between $\frac{1}{\cot \alpha}$ and F_h is found.

Armour type

The three tested randomly placed armour types - rocks, cubes and Dolos units - yield almost identical values for the horizontal force. Cubes placed in a regular pattern forming a smooth surface on the front slope results in wave forces up to twice as high as for the randomly placed armour types.

Crown wall height

For mild wave conditions where none of the four investigated walls are severely overtopped the actual height of the wall does not have any influence on the imposed wave load. For overtopped walls the wave forces are proportional to the square of the wall height.

Armour crest berm width

The influence of the width of the armour crest berm on the horizontal wave force is ambiguous. By increasing the berm width from 0.18 m to 0.24 m (from 3 to 4 $d_{n,50}$) a small increase in wave load is observed. Widening the berm beyond 0.24 m causes the wave forces to decrease.

5 Wave force design formulae

Two different ways of establishing a design methodology have been proposed by Jensen (1984) and by Günbak and Ergin (1983).

The method by Jensen where the wave force is made dimensionless by dividing with selected parameters and relating this ratio to the dimensionless wave height ratio H_s/A_c and 2 empirical constants is too simple to cover all the different parameters influencing the wave force exerted on a crown wall. Hence, if a method similar to Jensens was to be adopted it would be necessary to calibrate the two empirical coefficients to each breakwater configuration. Although the method is usable it is not preferable due to its non-versatility when designing breakwater configurations different from those calibrated.

The other possibility is to use a method similar to the one proposed by Günbak and Ergin (1983) where the wave force is calculated from an assumed wall face pressure distribution which is related to the wave run-up. In their work Günbak and Ergin assumed the pressure distribution on the vertical wall face to be the sum of an impact contribution and a contribution from the hydrostatic head. The use of the run-up height incorporates many of the features concerning the influence of slope inclination, wave height and wave period observed in the tests. This method also takes into account the reducing effect of severe overtopping over low walls, an aspect which the method proposed by Jensen cannot include.

In the following a design method for assessing the total horizontal wave force imposed on the wall face will be given. The method is largely based on the same assumptions about run-up and distribution of pressures as made by Günbak and Ergin (1983).

5.1 Assumed pressure distribution

Analyses of the results from the present study indicate that for all wall types and cross section configurations the maximum wave forces, i.e. the 0.1% force estimates, are governed by wave impact pressures and that pressure contributions from the hydrostatic head are so small that they can be ignored. Hence the pressures on the wall face can be assumed to have a spatial distribution similar to the one outlined in figure 27.a).

It is assumed that the magnitude of the impact pressure p_m can be determined as the stagnation pressure corresponding to the up-rush velocity v_0 at the edge of the armour crest, i.e. that the water hitting the wall face with a direction perpendicular to the face has a velocity of v_0 .

Having calculated the run-up level (R_u) and assuming no energy loss due to friction or dissipation between the armour crest level (A_c) and the run-up level the velocity v_0 can be calculated as :

$$v_0 = \sqrt{2g(R_u - A_c)} \quad (1)$$

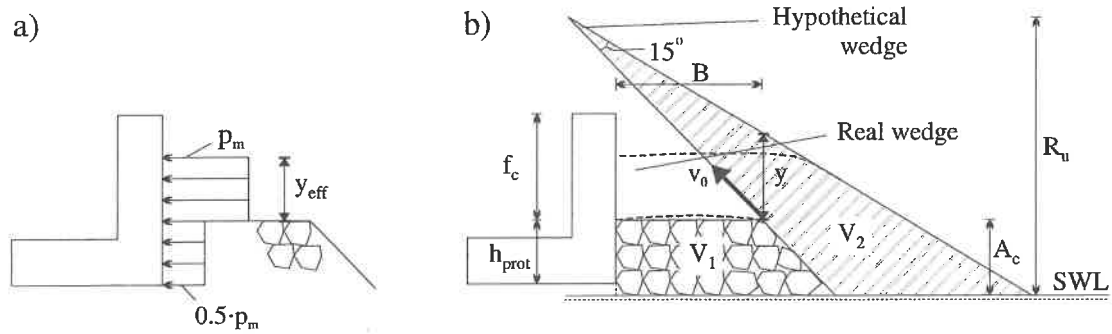


Figure 27: a) Assumed pressure distribution on crown wall.
b) Outline of run-up wedge and design parameters.

The resulting stagnation pressure p_m is then given by :

$$p_m = g\rho_w \frac{v_0^2}{2g} = g\rho_w (R_u - A_c) \quad (2)$$

Van der Meer (1988) measured run-up levels on several configurations of armoured rubble slopes. He found that the run-up level could be described by the surf similarity parameter (CIRIA/CUR 1991) :

$$\frac{R_{ux}}{H_s} = a \cdot \xi_m \quad \text{for } \xi_m < 1.5 \quad (3)$$

$$\frac{R_{ux}}{H_s} = b \cdot \xi_m^c \quad \text{for } \xi_m > 1.5 \quad (4)$$

For very permeable structures the run-up is limited to a maximum of :

$$\frac{R_{ux}}{H_s} = d \quad (5)$$

where $\xi_m = \tan \alpha / \sqrt{H_s / L_{0m}}$ and L_{0m} is the deep water wave length corresponding to the mean wave period.

Values for the coefficients a , b , c and d are given for different exceedence levels (x) in table 2

It must be remembered that the run-up values are calculated from tests with infinitely long slopes where, in the case of a permeable rough slope, a large amount of energy loss occur between level A_c and level R_u . Hence the calculated values of v_0 are too small. This error is partly balanced by disregarding the effect of entrained air in the uprushing water which would reduce the impact loading. With these implications in mind it is obvious that the calculated stagnation pressures are not fully correct. On the other hand the calculation of p_m serves as a valuable starting point in the assessment of the wave loading.

Table 2: Coefficients for calculation of run-up levels

Run-up level x %	coefficients			
	a	b	c	d
0.1	1.12	1.34	0.55	2.58
1	1.01	1.24	0.48	2.15
2	0.96	1.17	0.46	1.97
5	0.86	1.05	0.44	1.68
10	0.77	0.94	0.42	1.45

Günbak and Ergin (1983) assumed that the impact zone height on the wall face equals the wedge thickness y at the edge of the armour crest. By comparing the calculated wedge thicknesses y assuming a wedge angle of 15° with the actual observed impact zones on the upper unprotected wall part it was found that that the calculated values were approximately twice the measured. Hence the effective impact zone height y_{eff} is defined as :

$$y_{\text{eff}} = \min \left[\frac{y}{2} ; f_c \right] \quad (6)$$

For negative values of $\frac{y}{2}$ ($R_{u,0.1\%} < A_c$) a value of $y_{\text{eff}} = 0$ should be used.

Applying the assumed pressure distribution in figure 27.a) the following two intermediate force contributions on the upper unprotected and lower protected wall part respectively can be calculated:

$$F_{hu} = p_m \cdot y_{\text{eff}} \quad (7)$$

$$F_{hl} = \frac{1}{2} p_m \cdot h_{\text{prot}} \quad (8)$$

where h_{prot} is the height of the protected part of the wall face, c.f. figure 27.b).

As previously mentioned the above forces are not fully correct due to the incorrect assessment of the up-rush velocity v_0 and the assumption about pressure distribution on the lower and upper wall part. Also the influence of the armour crest berm width is not included.

5.2 Design equation for horizontal wave force

In order to obtain an expression for the total horizontal wave force imposed on the crown wall face equations (7) and (8) will be analysed with respect to the influence of the different basic parameters, i.e. wave height, wave length etc.

Assuming a rough permeable slope, $\xi_m > 1.5$ and that the crown wall is not totally inundated ($y_{\text{eff}} < f_c$) equation (7) can be written :

$$F_{hu,0.1\%} = p_m \cdot y_{\text{eff}} = \rho_w g (R_{u,0.1\%} - A_c) \cdot a R_{u,0.1\%} \quad (9)$$

where a is a constant denoting that y_{eff} is proportional to R_u .

Depending on the relative magnitudes of F_{hu} and F_{hl} the influence on the total horizontal force F_h from the different parameters will vary. Assuming the two contributions to be nearly equal the resulting horizontal force :

$$F_{h,0.1\%} = a (b \cdot F_{hu,0.1\%} + F_{hl,0.1\%}) \quad (10)$$

a and b being empirical coefficients, will be proportional to :

$$F_{h,0.1\%} \propto H_s^{1.45} \left(\frac{1}{\cot \alpha} \right)^{1.1} L_{0m}^{0.55} - A_c H_s^{0.73} \left(\frac{1}{\cot \alpha} \right)^{0.55} L_{0m}^{0.27} + H_s^{0.73} \left(\frac{1}{\cot \alpha} \right)^{0.55} L_{0m}^{0.27} h_{prot} - A_c h_{prot} \quad (11)$$

Comparing equation (11) with the observations concerning the parametric influence outlined in section 4 it is seen that the linear influence of H_s and $\frac{1}{\cot \alpha}$ is approximately present in equation (11) whereas the observed linear dependence of wave length is not adequately described in the above expression where L_{0m} enters in a power between 0.27 and 0.55. Also equation (11) totally lacks information about the influence from the armour crest berm width B .

In order to compensate for the underestimated influence of wave length and the missing incorporation of the armour crest berm width the ratio $\sqrt{L_{0m}/B}$ is used as a correction term in equation (10) which then can be written :

$$F_{h,0.1\%} = a \cdot \sqrt{\frac{L_{0m}}{B}} (b \cdot F_{hu,0.1\%} + F_{hl,0.1\%}) \quad (12)$$

When the predicted forces by equation (12) for optimised values of a and b were compared to the measurements it turned out that the wave forces on the lower protected wall part were overestimated for the mildest wave conditions where the run-up level hardly exceeded the level of the armour crest. In order to compensate this the two volumes V_1 and V_2 outlined in figure 27.b) are used. For situations where $V_2 < V_1$ the wave forces on the lower wall part must be corrected with the ratio $\frac{V_2}{V_1}$. The resulting expression is then given by :

$$F_{h,0.1\%} = a \cdot \sqrt{\frac{L_{0m}}{B}} \cdot (b \cdot F_{hu,0.1\%} + \mathbf{V} \cdot F_{hl,0.1\%}) \quad (13)$$

$$\mathbf{V} = \begin{cases} \frac{V_2}{V_1} & \text{for } V_2 < V_1 \\ 1 & \text{for } V_2 \geq V_1 \end{cases}$$

Equation (13) was fitted to the measured values $F_{h,0.1\%}$ in the 373 test series and best estimates of the coefficients a and b were found to be :

$$\begin{aligned} a &= 0.21 & \sigma_a &= 0.02 \\ b &= 1.6 & \sigma_b &= 0.1 \end{aligned}$$

where σ denotes the standard deviation of a and b assuming that the two values are random Gaussian distributed variables. The final design equation then reads :

$$F_{h,0.1\%} = 0.21 \cdot \sqrt{\frac{L_{0m}}{B}} \cdot (1.6 \cdot F_{hu,0.1\%} + \mathbf{V} \cdot F_{hl,0.1\%}) \quad (14)$$

$$\mathbf{V} = \begin{cases} \frac{V_2}{V_1} & \text{for } V_2 < V_1 \\ 1 & \text{for } V_2 \geq V_1 \end{cases}$$

The wave forces predicted by equation (14) are plotted in figure 28 against the corresponding measured values. The figure shows a good agreement between the developed semi-empirical model given by equation (14) and the measured forces. In this context it must be emphasized that figure 28 comprises all the 12 tested breakwater/crown wall configurations given in figure 5.

The validity of equation (14) is limited to the parametric ranges given in table 3.

Table 3: Parameter ranges for equation (14).

Parameter	Range
ζ_m	1.1 – 4.2
H_s/A_c	0.5 – 1.5
R_c/A_c	1 – 2.6
A_c/B	0.3 – 1.1
$\cot \alpha$	1.5 – 3.5

In figures 29 and 30 the developed design equation is plotted against measured values of $F_{h,0.1\%}$ for two different breakwaters tested by Jensen (1984) – figures 5.9.h and 5.9.i in Jensen (1984) and termed breakwater X and Y respectively in the following.

For the X breakwater equation (14) is seen to predict the lowest wave forces ($F_{h,0.1\%} < 2000 \text{ kN/m}$) quite well whereas large errors on the unsafe side are experienced for the larger forces. For the lowest well predicted forces the ratio $\frac{H_s}{A_c}$ is in the range 0.76 – 1.5 which is within the range covered by equation (14). For the larger forces ($F_{h,0.1\%} > 2000 \text{ kN/m}$) the ratio ranges between 1.5 and 2.5 which is outside the range covered by the developed design equation. It has not been tried to develop equation (14) further in order to include the extreme conditions tested by Jensen (1984).

Figure 30 shows the predicted versus the by Jensen (1984) measured values of $F_{h,0.1\%}$ on the Y breakwater. In contrast to figure 29 equation (14) is in this case overpredicting the imposed wave forces. Again the deviations can be explained by studying the parametric ranges. Where equation (14) was fitted primarily to situations with plunging/collapsing breaking waves ($\xi_m < 4$) the measurements in figure 30 are obtained for surging wave conditions only ($4.8 < \xi_p < 7.1$). Again it has not been tried to incorporate such extreme conditions into the developed design model.

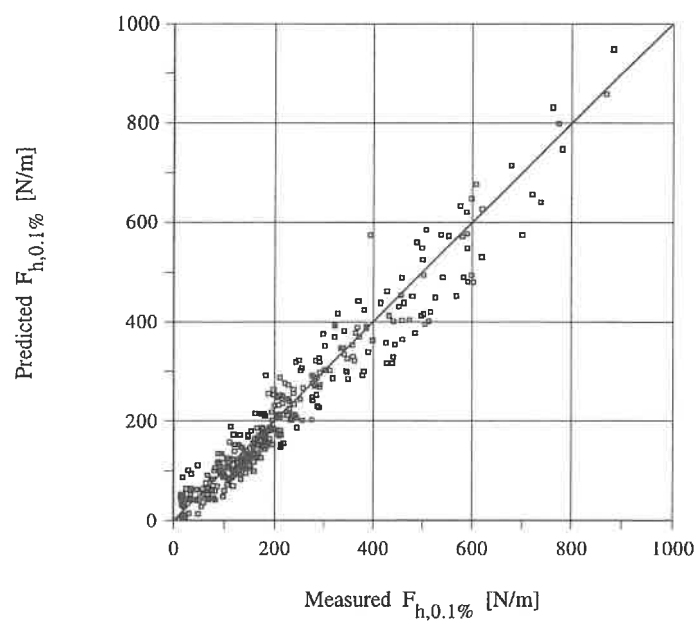


Figure 28: Fitted model versus measured values of $F_{h,0.1\%}$

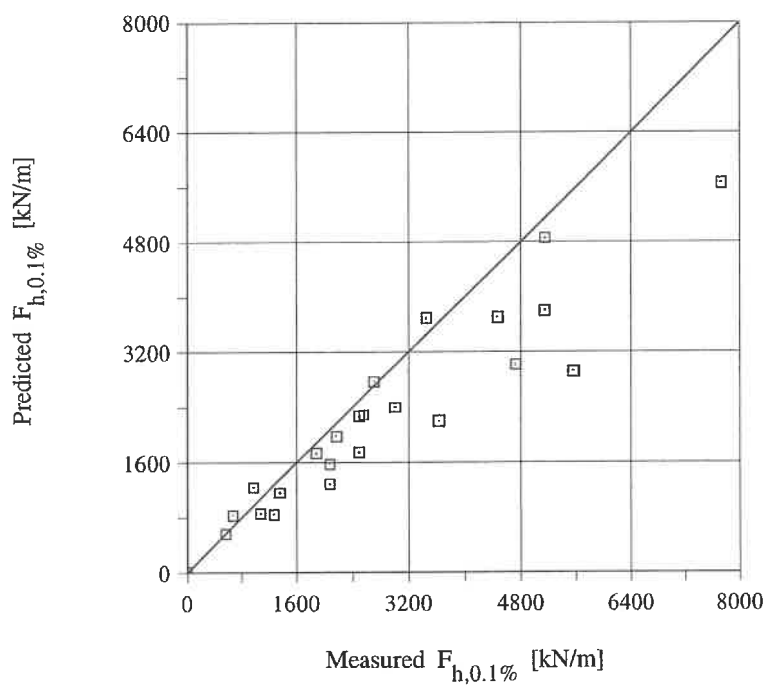


Figure 29: Fitted model versus measured values of $F_{h,0.1\%}$ for the X breakwater tested by (Jensen 1984).

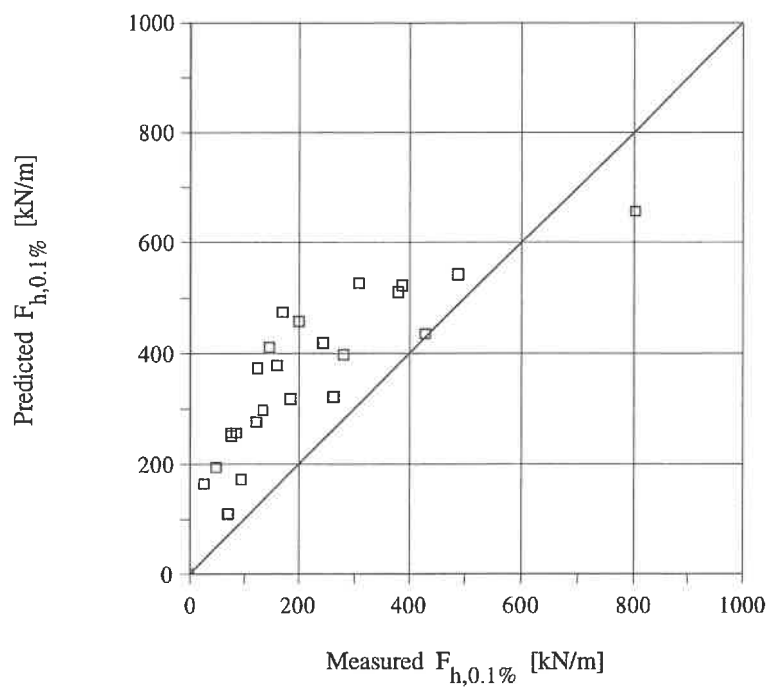


Figure 30: Fitted model versus measured values of $F_{h,0.1\%}$ for the Y breakwater tested by (Jensen 1984).

In a design situation some safety is normally wanted. In equation (15) the ratio $\frac{V_1}{V_2}$ is omitted and a value of $a = 0.23$ is used giving a safety margin corresponding to approximately one standard deviation :

$$F_{h,0.1\%} = 0.23 \cdot \sqrt{\frac{L_{0m}}{B}} \cdot (1.6 \cdot F_{hu,0.1\%} + F_{hl,0.1\%}) \quad (15)$$

Equation (15) is plotted against the measured forces in figure 31.

..

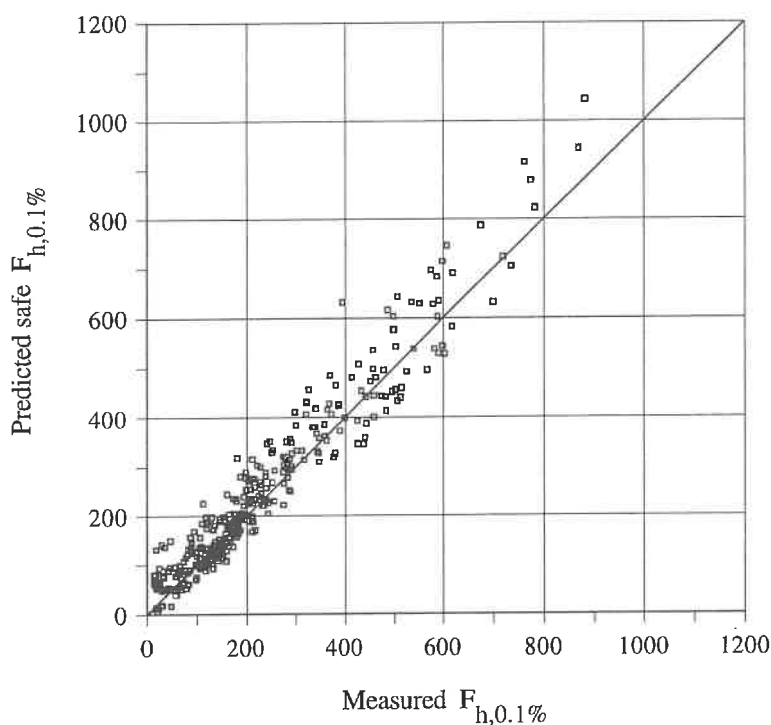


Figure 31: Fitted safe design model versus measured values of $F_{h,0.1\%}$

Expressions similar to the design equations for the 0.1% fractile could be made for other significance levels, e.g. the 1% force fractile, but since the structure must be designed according to the maximum wave loading during a storm situation, typically having a duration corresponding to approximately 1000 waves, only the 0.1% fractile have been considered.

5.3 Design equation for overturning moment

With the almost perfect linear correlation between F_h and M – c.f. figure 16 – it is obvious that the overturning moment can be expressed by means of F_h . From analysis of the data the following design equation for the overturning moment was derived :

$$M_{0.1\%} = 0.55 \cdot (h_{prot} + y_{eff}) \cdot F_{h,0.1\%} \quad (16)$$

with a standard deviation of approximately $\sigma(0.55) = 0.07$.

The fit of equation (16) is shown in figure 32 where the predicted values of $M_{0.1\%}$ is plotted against the measured values. As for the horizontal wave force the correlation between the developed design equation and the measurements is good. The calculated values of $M_{0.1\%}$ are obtained for the central estimate of $F_{h,0.1\%}$ given in equation (14).

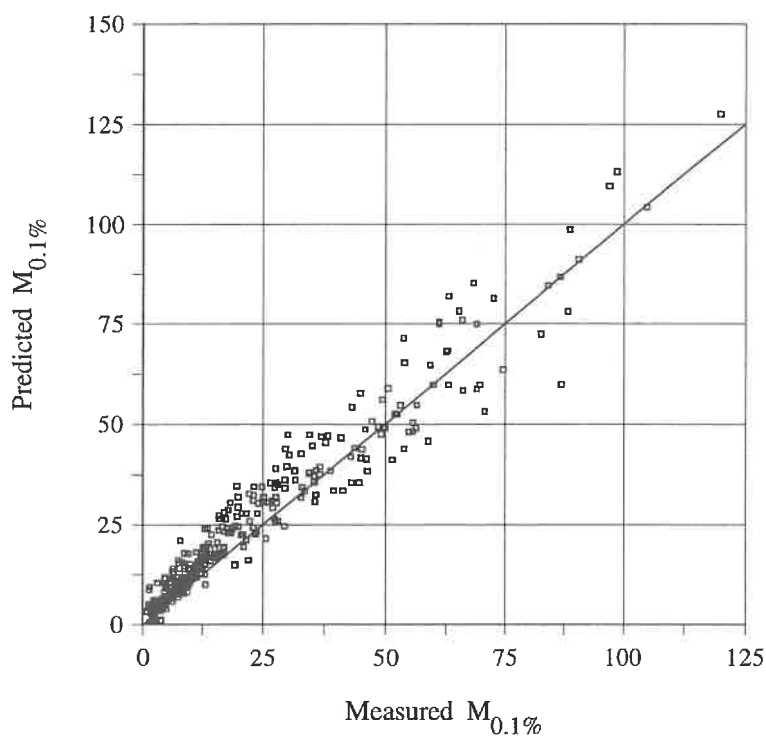


Figure 32: Fitted model for overturning moment $M_{0.1\%}$ plotted against measured values of $M_{0.1\%}$

5.4 Design equation for base pressure

The rather poor correlation between the wall base pressure P_b and the other two force components as outlined in figure 17 complicates the establishment of a reliable design equation for the base pressure. A very simple but rather unsafe estimate is provided by the following expression :

$$P_{b,0.1\%} = 1 \cdot V p_m \quad (17)$$

with a standard deviation of approximately $\sigma(1) = 0.3$. The estimated pressures are plotted against the corresponding measured values in figure 33.

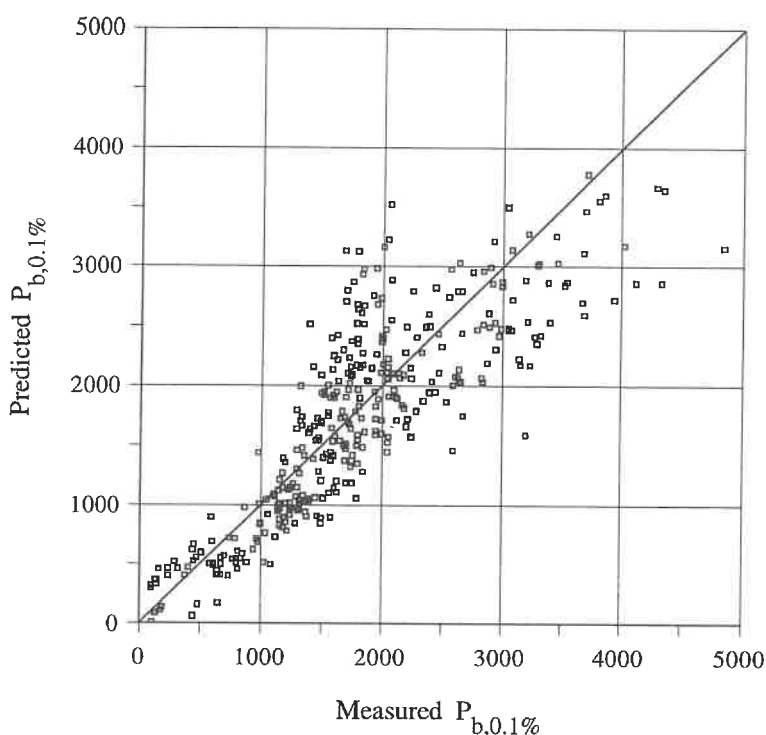


Figure 33: Fitted model for wall base pressure $P_{b,0.1\%}$ plotted against measured values of $P_{b,0.1\%}$

It is obvious from figure 33 that the values predicted by equation (17) are quite uncertain and therefore only should be used with great care for predicting the lift force acting beneath the wall base. On the other hand it must be remembered when judging the validity of equation (17) that the measured maximum pressures are not necessarily occurring at the same time as the maxima of the other force components which inevitably will give some deviations.

5.5 Summary of wave force design equations

In the following a short summary of the developed design method for assessing the wave loading on a crown wall structure will be given. In order to enhance the understanding figure 27 is redrawn below.

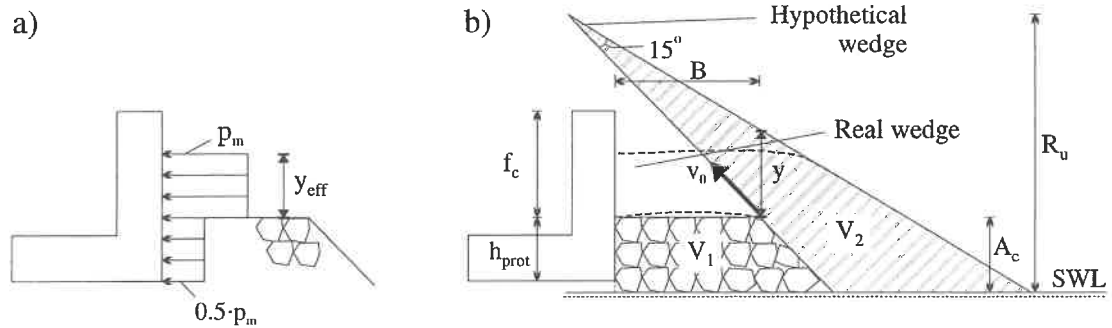


Figure 34: a) Assumed pressure distribution on crown wall.
b) Outline of run-up wedge and design parameters.

The first step in the calculation of the wave loading is to calculate the run-up level $R_{u,0.1\%}$. For rough porous slopes where the model tests showed that it was not necessary to distinguish between the different randomly placed units (rocks, cubes and Dolos) the run-up level can be calculated as:

$$\frac{R_{u,0.1\%}}{H_s} = 1.12 \cdot \xi_m \quad \text{for } \xi_m \leq 1.5 \quad (18)$$

$$\frac{R_{u,0.1\%}}{H_s} = 1.34 \cdot \xi_m^{0.55} \quad \text{for } \xi_m > 1.5 \quad (19)$$

where $\xi_m = \tan \alpha / \sqrt{H_s / L_{0m}}$, L_{0m} being the deep water wave length corresponding to the mean wave period.

For smooth *impermeable* slopes Van der Meer and Stam (1992) proposed a relationship of a form similar to equation (18) describing the $R_{u,2\%}$ level. This expression was calibrated to the present measurements where the breakwater is not impermeable and the following equation for calculating $R_{u,0.1\%}$ was found :

$$R_{u,0.1\%} = 0.9 \cdot R_{u,2\%} \quad (20)$$

$$\frac{R_{u,2\%}}{H_s} = 1.5 \cdot \xi_p \quad \text{with a maximum of } \frac{R_{u,2\%}}{H_s} = 3.2 \quad (21)$$

where $\xi_p = \tan \alpha / \sqrt{H_s / L_{0p}}$, L_{0p} being the deep water wave length corresponding to the spectral peak wave period.

Having calculated the run-up level the run-up wedge is now assumed to have a wedge angle of $\theta = 15^\circ$. The wedge thickness (y) at the crest of the armour berm can be calculated as :

$$y = \frac{R_{u,0.1\%} - A_c}{\sin \alpha} \cdot \frac{\sin 15^\circ}{\cos(\alpha - 15^\circ)} \quad (22)$$

and secondly the effective impact zone height (y_{eff}) is given by:

$$y_{\text{eff}} = \min \left[\frac{y}{2} ; f_c \right] \quad (23)$$

where f_c is the height of the unprotected wall face. For negative values of $\frac{y}{2}$ ($R_{u,0.1\%} < A_c$) a value of $y_{\text{eff}} = 0$ is used.

The next step is to calculate the stagnation pressure p_m from the impacting water :

$$p_m = g \rho_w (R_{u,0.1\%} - A_c) \quad (24)$$

For small run-up values the two volumes V_1 and V_2 must be determined. The design equations corresponding to the central estimates for each of the 3 wave load components $F_{h,0.1\%}$, $M_{0.1\%}$ and $P_{b,0.1\%}$ finally read :

$$F_{h,0.1\%} = 0.21 \sqrt{\frac{L_{0m}}{B}} \left(1.6 p_m \cdot y_{\text{eff}} + \mathbf{V} \cdot \frac{p_m}{2} \cdot h_{\text{prot}} \right) \quad (25)$$

$$M_{0.1\%} = 0.55 \cdot (h_{\text{prot}} + y_{\text{eff}}) \cdot F_{h,0.1\%} \quad (26)$$

$$P_{b,0.1\%} = 1 \cdot \mathbf{V} p_m \quad (27)$$

$$\mathbf{V} = \begin{cases} \frac{V_2}{V_1} & \text{for } V_2 < V_1 \\ 1 & \text{for } V_2 \geq V_1 \end{cases}$$

$$\sigma(0.21) = 0.02$$

$$\sigma(1.6) = 0.1$$

$$\sigma(0.55) = 0.07$$

$$\sigma(1) = 0.3$$

The above expressions can be applied to structures/waves conditions satisfying the variational limits given below :

Table 4: Parameter ranges for design equations.

Parameter	Range
ζ_m	1.1 - 4.2
H_s/A_c	0.5 - 1.5
R_c/A_c	1 - 2.6
A_c/B	0.3 - 1.1
$\cot \alpha$	1.5 - 3.5

6 Wave overtopping

Existing design formulae for prediction of overtopping discharges generally suffer from lack of versatility in the sense that they contain one or more coefficients which must be calibrated for the actual breakwater/crown geometry. The following chapter contains a description of the main findings from the parametric investigation as well as a proposal for a new and more versatile design formula for the mean overtopping discharge.

6.1 Parametric investigation

In the following an outline of the influence of the various investigated parameters on the mean overtopping rate Q_m will be given. Main emphasis will be paid to tests with the lowest of the four used crown wall configurations where the amount of wave overtopping is most pronounced. For small overtopping rates the uncertainty on the measurements is relatively large due to the importance of the few largest waves and their succession contributing to the majority of the overtopping discharge.

Influence of wave period

During the investigation of the influence of the wave period/length on the mean overtopping discharge a perfectly linear relationship between Q_m and the ratio $\frac{L_{0m}^2}{T_m}$ ($= c_m L_{0m}$) was found. Figure 35 shows Q_m plotted against $\frac{L_{0m}^2}{T_m}$ for three different values of wall crest freeboard (R_c). From this relationship a dimensionless mean discharge Q_m^* can be defined :

$$Q_m^* = \frac{Q_m T_m}{L_{0m}^2} \quad (28)$$

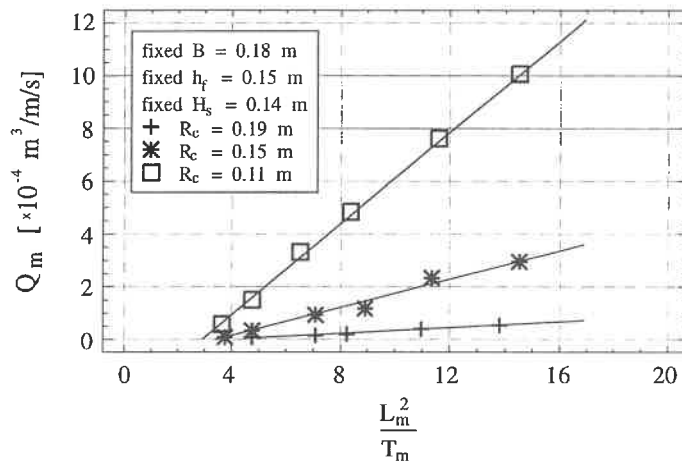


Figure 35: Q_m plotted against $\frac{L_{0m}^2}{T_m}$. Fixed values of : $H_s = 0.14$ m , $B = 0.18$ m , $\cot \alpha = 1.5$, rock slope.

Influence of wave height

In figure 36 Q_m is plotted against the significant wave height H_s for five different values of wall crest freeboard (R_c). The figure clearly shows that the amount of overtopping increases rapidly with increasing wave height. The best fit of the curves yields that Q_m approximately is proportional to H_s^5 which corresponds quite well to the findings by both Owen (1980) and Bradbury et al. (1988).

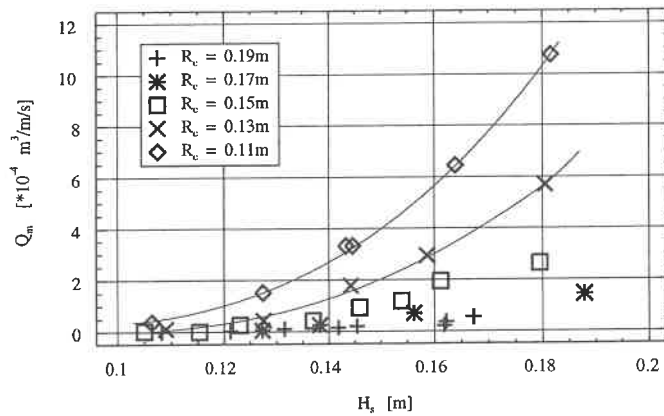


Figure 36: Q_m plotted against H_s . Fixed values of : $T_p = 1.6s$, $\cot \alpha = 1.5$, $B = 0.18m$, rock slope.

Influence of wall crest freeboard

Like H_s the wall crest freeboard R_c also has a major influence on the discharge. In figure 37 Q_m is plotted against $\frac{1}{R_c}$ for three different significant wave heights. The fitted lines suggest Q_m to be proportional to R_c^{-4} .

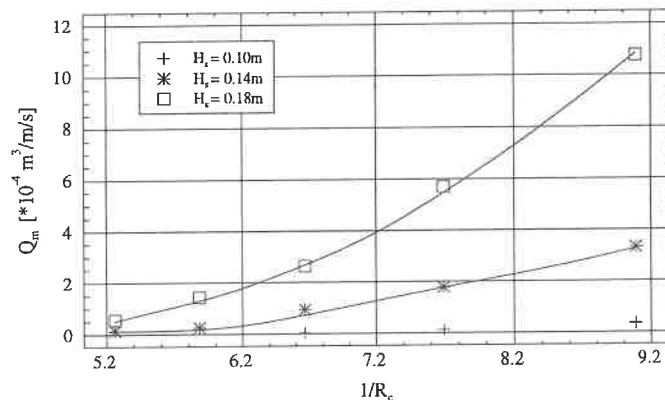


Figure 37: Q_m plotted against $\frac{1}{R_c}$. Fixed values of $T_p = 2.2s$, $B = 0.15m$, $\cot \alpha = 1.5$, rock slope

Influence of slope angle

The perfectly linear relationship between $\frac{1}{\cot \alpha}$ and F_h as found in the parametric investigation on wave forces is also observed between $\frac{1}{\cot \alpha}$ and Q_m . Figure 38 shows Q_m plotted against $\frac{1}{\cot \alpha}$ for three values of H_s .

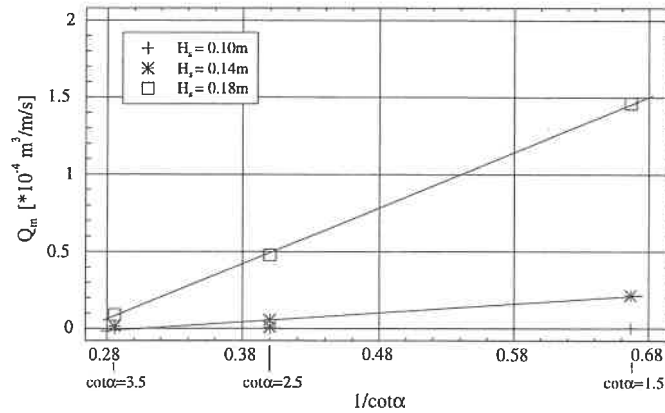


Figure 38: Q_m plotted against $\cot \alpha$. Fixed values of : $R_c = 0.24\text{m}$, $T_p = 1.6\text{s}$, $B = 0.18\text{m}$, rock slope

Influence of armour crest berm width

A reduction in overtopping discharge is observed when the armour berm width is increased although the reduction is not as pronounced as for other parameters. Figure 39 shows that Q_m is approximately proportional to $1/B$.

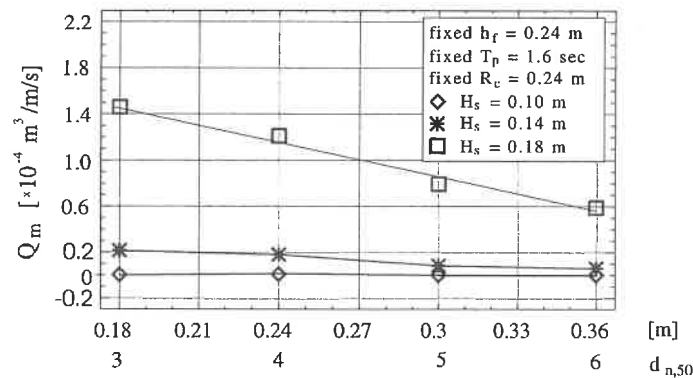


Figure 39: Q_m plotted against B . Fixed values of : $R_c = 0.24\text{m}$, $T_p = 1.6\text{s}$, $\cot \alpha = 1.5$, rock slope

Influence of armour layer type

As in the study of wave forces wave the overtopping measurements were performed on four different types of armour layers. The measurements from the tests with cubic blocks placed in a regular pattern (smooth face) were unfortunately not recorded by the camera setup. From visual observations overtopping rates of at least a magnitude larger than observed for the rougher armour types were estimated.

In figure 40 an example of the obtained results from the three layers with randomly placed armour units is shown. The amount of overtopping is largest for the cube layer followed by the Dolos and rock layers.

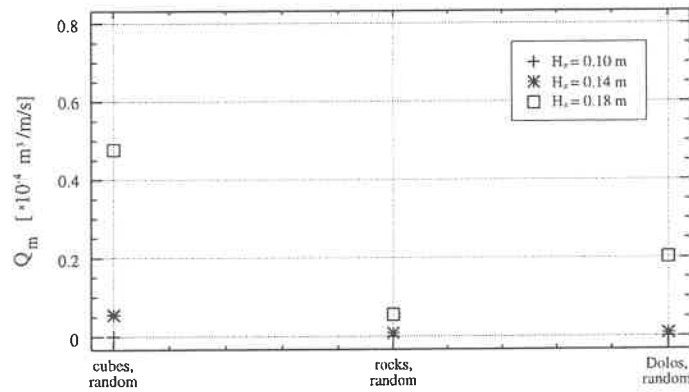


Figure 40: Armour types plotted against Q_m . Fixed values of :
 $R_c = 0.24m$, $T_p = 2.2s$, $\cot \alpha = 2.5$, rock slope

6.2 Design equation for overtopping discharge

From the parametric study the following functionality between the defined dimensionless discharge Q_m^* and the investigated parameters can be extracted :

$$Q_m^* = \frac{Q_m T_m}{L_{0m}^2} \propto f(H_s^5, R_c^{-4}, \cot \alpha^{-1}, B^{-1}) \cdot f(\text{armour}) \quad (29)$$

Arranging the right hand side of equation (29) to obtain a non-dimensional expression yields :

$$Q_m^* = \frac{Q_m T_m}{L_{0m}^2} = a \cdot \frac{H_s^5}{R_c^4 B \cot \alpha} \cdot f(\text{armour}) \quad (30)$$

where a is a dimensionless constant.

By closer examinations of equation (30) it turned out that overtopping discharges on structures with $f_c > 0$ (unprotected upper part) were underestimated. This of course has to do with the detailed geometry of the breakwater crest which is not adequately described by the wall crest freeboard R_c alone – a point which was also pointed out by Bradbury et al. (1988).

Further analyses revealed that by multiplying the correction term $\frac{R_c}{A_c}$ to the right hand side of equation (30) the observed disagreements were minimised :

$$Q_m^* = a \cdot \frac{H_s^5}{R_c^4 B \cot \alpha} \cdot \frac{R_c}{A_c} \cdot f(\text{armour}) \quad (31)$$

$$\Downarrow$$

$$Q_m^* = a \cdot \frac{H_s^5}{R_c^3 A_c B \cot \alpha} \cdot f(\text{armour}) \quad (32)$$

Since the majority of the tests have been performed with rock armoured slopes this configuration will be used as a default case and a value of $f(\text{armour type}) = 1$ will be applied. Assuming a in equation (32) to be random Gaussian distributed variable a best fit of the coefficient was obtained from the measurements with rock slope configurations :

$$a = 3.2 \cdot 10^{-5}, \sigma_a = 0.3 \cdot 10^{-5}$$

The resulting design equation for rock armoured structures can then be written :

$$Q_m^* = \frac{Q_m T_m}{L_{0m}^2} = 3.2 \cdot 10^{-5} \frac{H_s^5}{R_c^3 A_c B \cot \alpha} \cdot f(\text{armour}) \quad (33)$$

where $f(\text{armour}) = 1$

In figure 41 Q_m^* is plotted against the right hand side in equation (33). The plot shows a good correlation between the measured and the estimated values. Table 5 lists the valid parametric ranges for equation (33).

Table 5: Parameter ranges for equation (33).

Parameter	Range
ξ_m	1.1 - 5.1
H_s/A_c	0.5 - 1.7
R_c/A_c	1 - 2.6
A_c/B	0.3 - 1.1
$\cot \alpha$	1.5 - 3.5

As the fit of the coefficient a in equation (32) has been performed in a linear scale of Q_m the very large overtopping discharges for the lowest crown walls are dominating the fitted value. For small discharges analyses have revealed that equation (33) slightly overestimate the actual measured overtopping quantities.

Finally the values of $f(\text{armour})$ for the two other investigated armour layer types have been determined. Referring to equation (33) the following values are obtained as a best fit to the measurements :

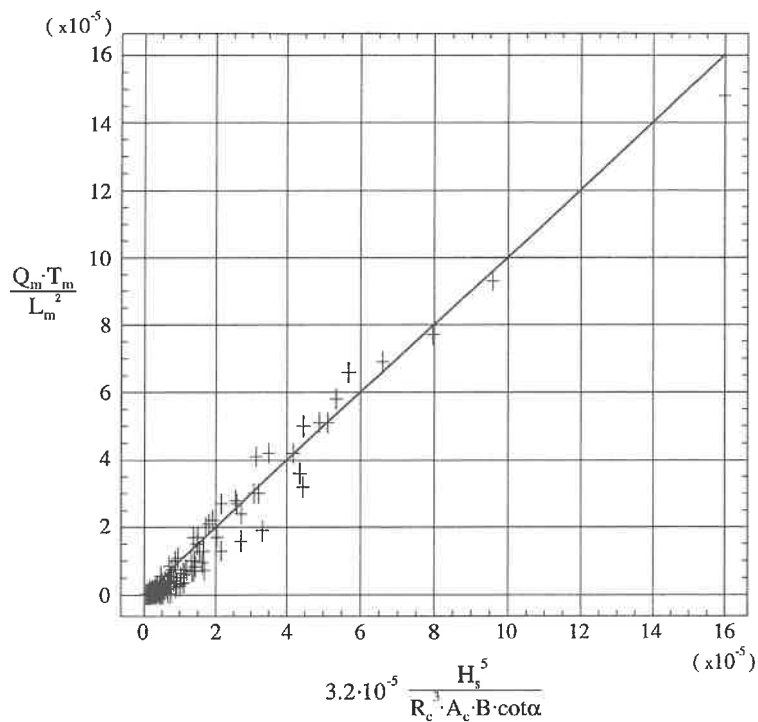


Figure 41: Measured mean overtopping discharges plotted against equation (33).

Armour type	$f(\text{armour})$
Rock	1
Dolos	1
Cubes	3

The results for Dolos and cube armour are very insecure as rather few tests with these configurations were performed and as overtopping discharges were quite small in these tests.

7 Conclusions

A new design method for assessing the wave loading on crown wall structures is presented. The method is applicable to a wide range of structure geometries and sea states.

Further verification of the method is required preferably in a larger scale as the importance of eventual scale effects and air entrainment remains unsolved.

Further unsolved is the assessment of uplift pressures beneath the base of the structure which has not been dealt with in the present study.

A new design formula for assessing the mean overtopping discharge over crown wall structures has also been developed. This new approach is more versatile than existing design formulae as it does not require a calibration of one or more coefficients depending on the breakwater/crown geometry.

Acknowledgements

The present paper is an extract of the Ph.D. thesis "Wave Forces and Overtopping on Crown Walls of Rubble Mound Breakwaters - An Experimental Study" which was elaborated at Aalborg University under a grant from the Danish Technical Research Council in connection with the frame work programme *Marin Teknik, 1989-1992*.

Sincere appreciation is given to the sponsoring council and all the staff in the Department of Civil Engineering and Coastal Laboratory at Aalborg University.

References

- Bagnold, R. A. (1939). Interim report on wave-pressure research. *Journal of Inst. Civil Engineers Vol. 12*, 202 - 226.
- Bradbury, A. P., N. W. H. Allsop, and R. V. Stevens (1988). Hydraulic performance of breakwater crown walls. Technical Report SR 146, Hydraulics Research, Wallingford, UK.
- Burcharth, H. F. (1993). The design of breakwaters. Internal report, Aalborg University.
- CIRIA/CUR (1991). *Manual on the use of rock in coastal and shoreline engineering*. The Netherlands. CUR, London, UK: CIRIA.
- Günbak, A. R. and A. Ergin (1983). Damage and repair of antalya harbour breakwater. In *Proc. Conference on Coastal Structures, Alexandria, Egypt*.
- Hamilton, D. G. and K. R. Hall (1992). Preliminary analysis of the stability of rubble mound breakwater crown walls. In *Proc. 23rd International Conference on Coastal Engineering, Venice, Italy*. Publ. by American Society of Civil Engineers.
- Jensen, O. J. (1984). *A monograph on rubble mound breakwaters*. Danish Hydraulic Institute, Hørsholm, Denmark.
- Marinski, J. G. and H. Oumeraci (1992). Dynamic response of vertical structures to breaking wave forces - review of the CIS design experience. In *Proc. 23rd International*

Conference on Coastal Engineering, Venice, Italy, pp. 1357 – 1370. Publ. by American Society of Civil Engineers.

Oumeraci, H. and A. Kortenhaus (1992). Analysis of the dynamic response of caisson breakwaters. MAST G6-S, Project 2 report, Franzius Institute, University of Hannover.

Owen, M. W. (1980). Design of seawalls allowing for wave overtopping. Technical Report EX 924, Hydraulics Research, Wallingford, UK.

Van der Meer, J. W. (1988). *Rock Slopes and Gravel Beaches under Wave Attack*. Doctoral Thesis, Delft Technical University.

Van der Meer, J. W. and C. J. M. Stam (1992). Wave runup on smooth and rock slopes of coastal structures. *of Waterway, Port, Coastal and Ocean Engineering Vol. 118, No. 5*.



Reliability-based Design of Coastal Structures

by

BURCHARTH H. F.

Hydraulics and Coastal Engineering Laboratory
Dept. of Civil Engineering, Aalborg University, Denmark

Dansk Vandbygningsteknisk Selskabs seminar om
"Nyere metoder til projektering af moler"
Aalborg Universitet, den 25. marts 1998

RELIABILITY-BASED DESIGN OF COASTAL STRUCTURES

HANS F. BURCHARTH

*Department of Civil Engineering
Aalborg University, Denmark*

Contents

Foreword	2
1 Introduction	3
2 Failure modes and failure functions	3
2.1 Rubble mound breakwaters	4
2.2 Vertical wall monolithic breakwaters	6
2.2.1 Sliding	6
2.2.2 Foundation failure in rubble and clay	7
2.2.3 Foundation failure in the rubble mound	10
2.2.4 Formula for the wave loads	11
3 Single failure mode probability analysis	13
3.1 Level III methods	13
3.2 Level II methods	15
3.2.1 Linear failure functions of normal-distributed random variables	15
3.2.2 Non-linear failure functions of normal-distributed random variables	18
3.2.3 Non-linear failure functions containing non-normal distributed random variables	26
3.2.4 Time-variant random variables	36
4 Failure probability analysis of failure mode systems	40
5 Uncertainties related to parameters determining the reliability of the structure	47
5.1 Uncertainty related to failure mode formulae	47
5.2 Uncertainty related to environmental parameters	47
5.3 Uncertainty related to structural parameters	51
6 Introduction of a partial coefficient system for implementation of a given reliability in the design	51
6.1 Introduction to partial coefficients	51
6.2 Overall concept of the proposed partial coefficient system	53
6.3 Method of determining the partial coefficient	54
6.4 Breakwater types and failure modes	54

6.5	Partial coefficient system format for single failure modes	55
6.6	Format for multi failure modes	56
6.7	Investigated ranges of parameter variations	57
6.8	Example of design equations and recommended values of k_α and k_β	60
6.9	Examples of the use of the partial coefficient system	62
6.10	Conclusions	65
7	Acknowledgement	66
8	References	66

Foreword

The objective of this paper is to introduce the application of reliability theory for conceptual design and evaluation of coastal structures. It is without the scope to discuss the validity and quality of the various design formulae available for coastal structures. The contents of the paper is a combination of material presented in the following references: Burcharth, H.F. (1992) Reliability evaluation of a structure at sea. Proceedings of the Short Course on Design and Reliability of Coastal Structures. Venice, Scuola di S. Giovanni Evangelista, 1992. 23rd International Conference on Coastal Engineering. Burcharth, H.F. (1993) Design of Breakwaters. Aalborg University. Department of Civil Engineering. Aalborg, Denmark. Burcharth, H.F., Dalsgaard Sørensen, J., Christiani, E. (1995) Application for reliability analysis for optimal design of monolithic vertical wall breakwaters. Proceedings Conference of Port and Coastal Engineering in developing countries. Rio de Janeiro, Brazil, 1995.

1 Introduction

Conventional design practice for coastal structures is deterministic in nature and is based on the concept of a design load, which should not exceed the resistance (carrying capacity) of the structure. The design load is usually defined on a probabilistic basis as a characteristic value of the load, e.g. the expectation (mean) value of the 100-year return period event, however, often without consideration of the involved uncertainties. The resistance is in most cases defined in terms of the load which causes a certain design impact or damage to the structure and is not given as an ultimate force or deformation. This is because most of the available design formulae only give the relationship between wave characteristics and structural response, e.g. in terms of run-up, overtopping, armour layer damage etc. An example is the Hudson formula for armour layer stability. Almost all such design formulae are semi-empirical being based mainly on central fitting to model test results. The often considerable scatter in test results is not considered in general because the formulae normally express only the mean values. Consequently, the applied characteristic value of the resistance is then the mean value and not a lower fractile as is usually the case in other civil engineering fields. The only contribution to a safety margin in the design is then the one inherent in the choice of the return period for the design load.

It is now more common to choose the return period with due consideration of the encounter probability, i.e. the probability that the design load value is exceeded during the structure lifetime. This is an important step towards a consistent probabilistic approach.

A safety factor or a conventional partial coefficient (as given in some national standards) might be applied too, in which cases the methods are classified as Level I (deterministic/quasi probabilistic) methods. However, such approaches do not allow the determination of the reliability (or the failure probability) of the design, and consequently it is neither possible to optimize, nor to avoid over-design of a structure. In order to overcome this problem more advanced probabilistic methods must be applied where the uncertainties (the stochastic properties) of the involved loading and strength variables are considered. Methods where the actual distribution functions for the variables are taken into account are denoted Level III methods. Level II methods comprise a number of methods in which a transformation of the generally correlated and non-normally distributed variables into uncorrelated and standard normal distributed variables is performed and reliability indices are used as measures of the structural reliability. Both Level II and III methods are discussed in the following. Described is also an advanced partial coefficient system which takes into account the stochastic properties of the variables and makes it possible to design to a specific failure probability level.

2 Failure modes and failure functions

Evaluation of structural safety is always related to the structural response as defined by the failure modes. Neglect of an important failure mode will bias the estimation of the safety of the structure. In the following is presented typical failure functions representing

three important types of failure modes, namely:

- Hydraulic instability of rubble mound armour (illustrated by a main armour layer of a rubble mound breakwater).
- Sliding of a monolithic structure on a soil (illustrated by sliding of a vertical wall caisson on a rubble foundation).
- Bearing capacity failure of soils (illustrated by soil mechanics failure of a vertical wall caisson placed on a rubble foundation and clay subsoil).

2.1 Rubble mound breakwaters

Fig. 1 illustrates the failure modes for a conventional rubble mound breakwater with a capping wall.

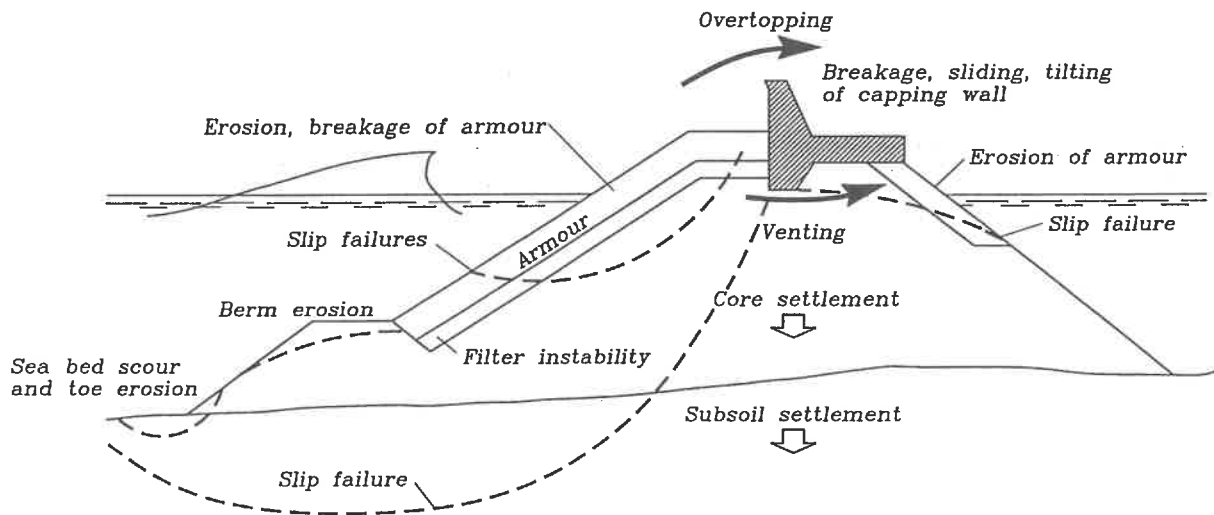


FIG. 1. Failure modes for a rubble mound breakwater.

Each failure mode must be described by a formula and the interaction (correlation) between the failure modes must be known. As an illustrative example let us consider only one failure mode, "hydraulic stability of the main armour layer", described by the Hudson formula

$$D_n^3 = \frac{H_s^3}{K_D \Delta^3 \cot \alpha} \quad (1)$$

where D_n^3 is the block volume, $\Delta = \frac{\rho_s}{\rho_w} - 1$, where $\frac{\rho_s}{\rho_w}$ is the ratio of the block and water densities, α is the slope angle, H_s is the significant wave height and K_D is the coefficient

signifying the degree of damage (movements of the blocks).

The formula can be split into load variables X_i^{load} and resistance variables, X_i^{res} . Whether a parameter is a load or a resistance parameter can be seen from the failure function. If a larger value results in a safer structure it is a resistance parameter and if a larger value results in a less safe structure it is a load parameter.

According to this definition one specific parameter can in one formula act as a load parameter while in another it can act as a resistance parameter. An example is the wave steepness in the van der Meer formulae for rock armour stability, which is a load parameter in the case of surging waves but a resistance parameter in the case of plunging waves. The only load variable in eq. (1) is H_s , while the others are resistance variables.

Eq. (1) is formulated as a *failure function*, also called performance function or limit state function

$$g = A \cdot \Delta \cdot D_n (K_D \cot \alpha)^{1/3} - H_s \begin{cases} < 0 & \text{failure} \\ = 0 & \text{limit state (failure)} \\ > 0 & \text{no failure (safe region)} \end{cases} \quad (2)$$

All the involved parameters are regarded as stochastic variables, X_i , except K_D , which signifies the *failure*, i.e. a specific damage level chosen by the designer. The factor A in eq. (2) is also a stochastic variable signifying the uncertainty of the formula. In this case the mean value of A is 1:0.

In general eq. (2) is formulated as

$$g = R - S \quad (3)$$

where R stands for resistance and S for loading. Usually R and S are functions of many random variables, i.e.

$$R = R(X_1^{res}, X_2^{res}, \dots, X_m^{res}) \quad \text{and} \quad S = S(X_{m+1}^{load}, \dots, X_n^{load}) \quad \text{or} \quad g = g(\bar{X})$$

The limit state is given by

$$g = 0 \quad (4)$$

which is denoted the *limit state equation* and defines the so-called *failure surface* which separates the safe region from the failure region.

In principle R is a variable representing the variations in resistance between nominally identical structures, whereas S represents the maximum load effects within a period of time, say successive T years. The distributions of R and S are both assumed independent of time. The *probability of failure* P_f during any reference period of duration T years is then given by

$$P_f = Prob [g \leq 0] \quad (5)$$

The reliability \mathcal{R} is defined as

$$\mathcal{R} = 1 - P_f \quad (6)$$

2.2 Vertical wall monolithic breakwaters

Vertical wall breakwaters can be constructed in a number of different ways. The most common types are shown in Fig. 2, namely one type where the caisson is placed on a thin bedding layer and one type where the caisson is placed on a rubble mound. The caisson is regarded a monolithic in the present analysis.

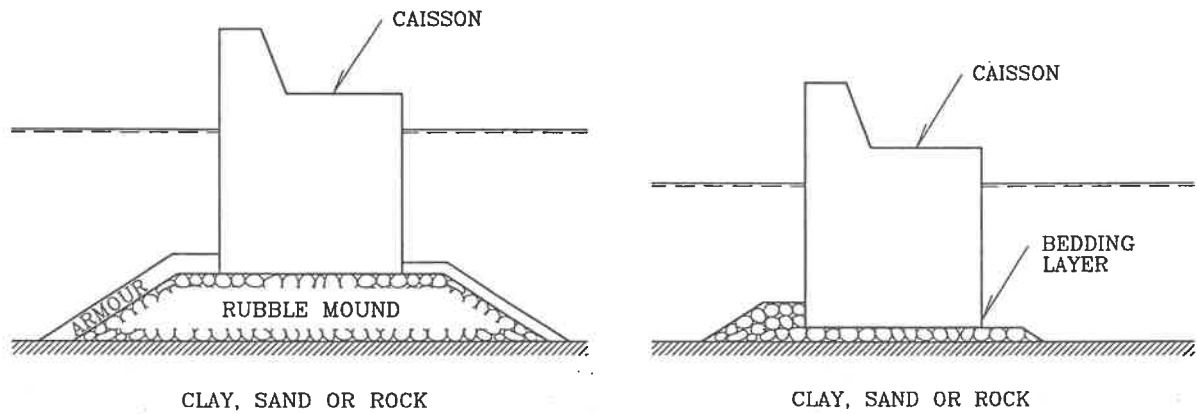


FIG. 2. Monolithic vertical wall structure on high rubble foundation and on bedding layer.

Some important overall stability failure modes for this type of breakwaters are sliding and failure of the foundation. Sliding failure, foundation failure in the rubble mound and foundation failure in clay subsoil, will be discussed in the following. Despite non-stationarity and possible dynamic effects the presented examples are treated as static load cases in order to keep the calculations simple.

2.2.1 Sliding

Sliding, i.e. horizontal displacement of the caisson, can occur as a slip either at the interface between the caisson concrete base plate and the rubble material, or entirely in the rubble material.

Corresponding to the first mentioned case stability against sliding exists when the ratio of the resultant horizontal force, F_H , to the resultant vertical force is equal to or less than $\tan \xi$, i.e.

$$F_H \leq (F_G - F_U) \tan \xi \quad (7)$$

where F_G is the weight of the caisson reduced for buoyancy, F_U is the wave induced uplift force on the base plate and ξ is the angle of friction between the concrete base plate and

the rubble mound or the bedding layer. Reference is given to Takayama (1992) for values of $\tan \xi$.

If the sliding failure takes place entirely in the rubble material, e.g. in the bedding layer, then ξ must be substituted by the effective angle of friction φ' of the material, and the angle of dilatation must be considered. The most critical of the two cases should be considered in the design.

The corresponding failure function is

$$g = (F_G - F_U) \tan \varphi' - F_H \quad \left\{ \begin{array}{l} < 0 \text{ failure} \\ = 0 \text{ limit state} \\ > 0 \text{ no failure} \end{array} \right. \quad (8)$$

F_H and F_U are in this paper calculated by the use of the Goda formula (Goda, 1985), cf. Section 2.2.4.

The resultant of the forces F_H , F_G and F_U is indicated in Fig. 3 as F_R .

2.2.2 Foundation failure in rubble and clay

A kinematic admissible solution for the rupture configuration in the soil is chosen, and the principle of equating internal and external work is used in order to estimate the bearing capacity of the soil. Application of a kinematic admissible solution is in principle on the unsafe side if it is not at the same time a static solution. However, if the rupture is realistic it is known that the method of calculation provides solutions close to the true one. In order to simplify the calculations it might be assumed that the friction force vector along a slip surface in the rubble is normal to the displacement vector (normality condition which implies zero work). This is the case if the effective angle of friction φ' is set equal to the angle of dilatation ψ . However, because for quarry run rubble φ' is somewhat larger than ψ (typical values are 44° and 16° , respectively) a reduced value of φ' given as $\varphi_d = \tan^{-1} \left(\frac{\sin \varphi \cos \psi}{1 - \sin \varphi \sin \psi} \right)$, (Hansen, 1979), is used in order not to bias the safety too much ($\varphi_d \simeq 40^\circ$). Both φ' og ψ are dependent on the stress level for which reason either reasonable mean values must be used, or calculations must be performed on increments.

Three dimensional effects are not included in the derivation of the zone rupture mechanism. The plane failure mode is shown in Fig. 3. Note that it is assumed that tensile stresses cannot occur under the caisson base plate. Also note that because the caisson is a stiff body the rupture shown is not fully kinematic admissible. Actually, the intersection point A should be at the corner of the caisson, and the slip surface A-B is not necessarily a straight line. However, the rupture configuration is a close approximation as can be demonstrated by comparison with results of finite element analyses.

$$W_2 = \delta \left(\theta + \frac{\pi}{4} \right) \int_0^{B_z \cdot \sin \theta} c_u(l) dl \quad (12)$$

$$W_3 = \delta \int_0^{B_z \cdot \sin \theta} c_u(l) dl \quad (13)$$

where c_u is the undrained shear strength of the clay, B_z is the width of the first stiff zone, and l is a coordinate along the rupture boundary BCDE.

$$W_4 = \delta R_1 \int_0^{R_1} \int_0^{\theta + \frac{\pi}{4}} c_u(a, \theta) d\theta da \quad (14)$$

where δ is the displacement of the top point in the Prandtl zone, $R_1 = B_z \sin \theta$, a is a vertical coordinate, and θ is defined in Fig. 3.

In the equilibrium at limit state conditions $W_I = W_E$. Thus the bearing capacity of the foundation can now be determined from the equation

$$0 = W_I - (F_G + F_{G_4}) \sin \theta - F_H \cos \theta \quad (15)$$

where θ is determined by minimizing the ratio W_I/W_E .

The undrained shear strength of the clay is modelled as a log-Gaussian stochastic field $\{c_u(x, z)\}$, see e.g. Keaveny et al. (1989) and Andersen et al. (1992). If only uncertainty related to c_u is considered and the correlation lengths for $\{c_u(x, z)\}$ are small compared to the integration intervals it follows from the central limit theorem that the total internal work can be approximated by a normal distributed stochastic variable W_I with mean value μ_{W_I} and standard deviation σ_{W_I} . The failure function is written

$$g_{clay} = \mu_{W_I} + u_W \sigma_{W_I} - W_E = \sum_{i=1}^4 E[W_{Ri}] + u_W \cdot \left(\sum_{i=1}^4 \sum_{j=1}^4 Cov[W_{Ri}, W_{Rj}] \right)^{\frac{1}{2}} - W_E \quad (16)$$

where u_W is a realization of a normal distributed stochastic variable U_W with mean 0 and unit standard deviation.

Further, as exemplification of the elements in eq. (16), the mean value of W_4 is

$$E[W_4] = \delta R_1 \int_0^{R_1} \int_0^{\theta + \frac{\pi}{4}} E[c_u(a, \theta)] d\theta da \quad (17)$$

where $E[c_u(a, \theta)]$ is the expected value of c_u at the position described by (a, θ) , and the variance of W_4 is

$$Var[W_4] = \delta^2 R_1^2 \int_0^{R_1} \int_0^{\theta + \frac{\pi}{4}} \int_0^{R_1} \int_0^{\theta + \frac{\pi}{4}} Cov[c_u(a_1, \theta_1), c_u(a_2, \theta_2)] d\theta_2 da_2 d\theta_1 da_1 \quad (18)$$

where $Cov[c_u(a_1, \theta_1), c_u(a_2, \theta_2)]$ is the covariance function of c_u at the positions corresponding to (a_1, θ_1) and (a_2, θ_2) .

external forces.

$$0 = -F_H \frac{\cos(\theta_1 - \varphi_d)}{\cos \varphi_d} - (F_G - F_U) \frac{\sin(\theta_1 - \varphi_d)}{\cos \varphi_d} - W_1 + W_2 + W_3 \quad (22)$$

where θ_1 and θ_2 are unknown angles to be determined by minimizing the ratio between the stabilizing work and the driving work.

The failure function for failure in the rubble mound is then

$$g = -F_H \frac{\cos(\theta_1 - \varphi_d)}{\cos \varphi_d} - (F_G - F_U) \frac{\sin(\theta_1 - \varphi_d)}{\cos \varphi_d} - W_1 + W_2 + W_3 \quad (23)$$

2.2.4 Formula for the wave loads

Wave pressure formulae have been developed by Goda et al. (1972) and Goda (1974) for the case of a conventional vertical front where wave breaking on the wall is not enhanced by a steep sea bed or by structural configurations. The formulae are based on model tests in head-on waves but were expanded to cover also oblique waves on the basis of work by Tanimoto et al. (1976). The formulae include the effect of breaking waves to the extent of normal accidental (non-provoked) wave breaking. The formulae are currently used in the Japanese standards. Fig. 5 shows the related definition sketch for the wave induced pressure under a wave crest.

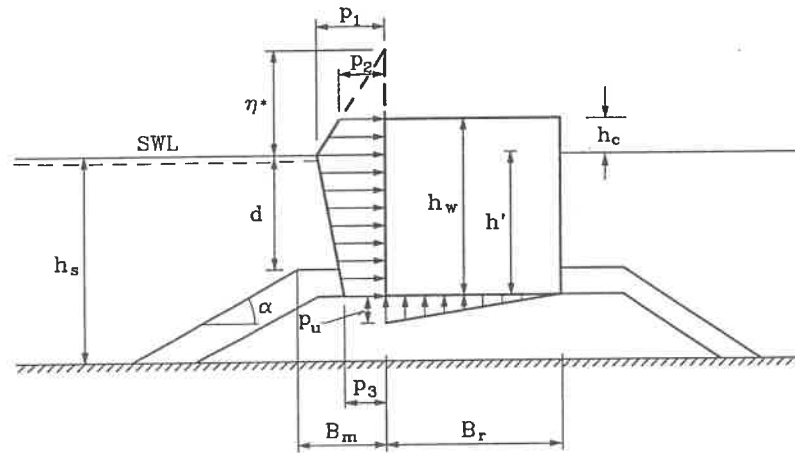


FIG. 5. Definition sketch for the Goda formula for wave induced pressure under a wave crest.

$$\eta^* = 0.75(1 + \cos\beta) H_{design} \quad (24)$$

$$p_1 = 0.5(1 + \cos\beta)(\alpha_1 + \alpha_2 \cos^2\beta) \rho_w g H_{design} \quad (25)$$

$$p_2 = \begin{cases} \left(1 - \frac{h_c}{\eta^*}\right) p_1 & \text{for } \eta^* > h_c \\ 0 & \text{for } \eta^* \leq h_c \end{cases} \quad (26)$$

$$p_3 = \alpha_3 p_1 \quad (27)$$

where

β angle of incidence of waves (angle between wave crest and front of structure)

H_{design} design wave height defined as the highest wave in the design sea state at a location just in front of the breakwater. If seaward of a surf zone Goda recommends a value of $1.8 H_s$ to be used corresponding to $H_{1/250}$, i.e. the average of the 250 largest waves. If within a surf zone H_{design} is recommended to be taken as the highest of the random breaking waves at a distance $5H_s$ seaward of the structure.

L wave length corresponding to that of the significant wave $T_s \simeq 1.1T_m$, where T_m is the average period.

$$\alpha_1 = 0.6 + \frac{1}{2} \left[\frac{4\pi h_s/L}{\sinh(4\pi h_s/L)} \right]^2 \quad (28)$$

$$\alpha_2 = \text{the smallest of } \frac{h_b - d}{3h_b} \left(\frac{H_{design}}{d} \right)^2 \text{ and } \frac{2d}{H_{design}} \quad (29)$$

$$\alpha_3 = 1 - \frac{h_w - h_c}{h_s} \left[1 - \frac{1}{\cosh(2\pi h_s/L)} \right] \quad (30)$$

h_b water depth at a distance of $5H_s$ seaward of the breakwater front wall.

Although the wave induced uplift pressure, p_u , at the front edge of the base plate is equal to p_3 it is suggested by Goda to use a somewhat reduced value

$$p_u = \frac{1}{2} (1 + \cos\beta) \alpha_1 \alpha_3 \rho_w g H_{design} \quad (31)$$

This is because analyses of the behaviour of Japanese breakwaters revealed that the use of $p_u = p_3$ together with an assumed triangular distribution of the uplift pressure gave too conservative results compared to prototype conditions.

3 Single failure mode probability analysis

3.1 Level III methods

A simple method – in principle – of estimation of P_f is the Monte Carlo method where a very large number of realisations x of the variables X are simulated. P_f is then approximated by the proportion of the simulations where $g \leq 0$.

The reliability of the method depends of course on a realistic assessment of the distribution functions for the variables X and their correlations.

Given $f_{\bar{X}}$ as the joint probability density function (jpdf) of the vector $\bar{X} = (X_1, X_2, \dots, X_n)$ then eq. (5) can be expressed by

$$P_f = \int_{R \leq S} f_{\bar{X}}(\bar{x}) d\bar{x} \quad (32)$$

Note that the symbol x is used for values of the random variable X .

If only two variables R and S are considered then eq. (32) reduces to

$$P_f = \int_{R \leq S} f_{(R,S)}(r, s) dr ds \quad (33)$$

which can be illustrated as shown in Fig. 6. If more than two variables are involved it is not possible to describe the jpdf as a surface but requires an imaginary multi-dimensional description.

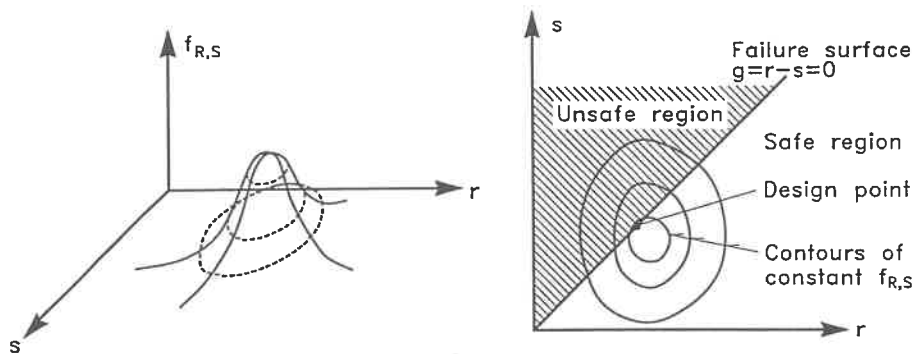


FIG. 6. Illustration of the two-dimensional joint probability density function for loading and strength.

Fig. 6 also shows the so-called *design point* which is the design point on failure surface where the joint probability density function attains the maximum value, i.e. the most probable point of failure.

Unfortunately, the jpdf is seldom known. However, the variables can often be assumed independent (non-correlated) in which case eq. (32) is given by the n -fold integral

$$P_f = \int \int \int \dots \int_{R \leq S} f_{X_1}(x_1) \dots f_{X_n}(x_n) dx_1 \dots dx_n \quad (34)$$

where f_{X_i} are the marginal probability density function of the variables X_i . The amount of calculations involved in the multi-dimensional integration eq. (34) is enormous if the number of variables, n , is larger than say 5.

If only two variables are considered, say R and S , then eq. (34) simplifies to

$$P_f = \int \int_{R \leq S} f_R(r) f_S(s) dr ds \quad (35)$$

which by partial integration can be reduced to a single integral

$$P_f = \int_0^{\infty} F_R(x) f_S(x) dx \quad (36)$$

where F_R is the cumulative distribution function for R . Formally the lower integration limit should be $-\infty$ but is replaced by 0 since, in general, negative strength is not meaningful.

Eq. (36) can be explained as the product of the probabilities of two independent events, namely the probability that S lies in the range $x, x+dx$ (i.e. $f_S(x)dx$) and the probability that $R \leq x$ (i.e. $F_R(x)$), cf. Fig. 7.

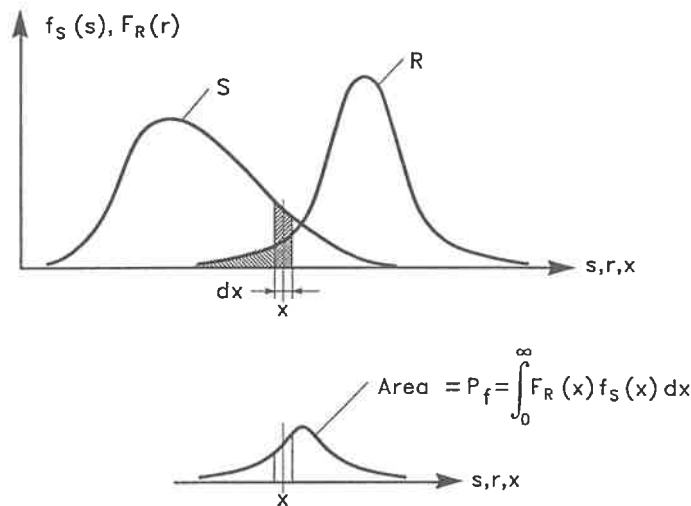


FIG. 7. Illustration of failure probability in case of two independent variables, S and R .

3.2 Level II methods

3.2.1 Linear failure functions of normal-distributed random variables

In the following is given a short introduction to calculations at level II. For a more detailed description see Hallam et al. (1977) and Thoft-Christensen and Baker (1982). Only the so-called *first-order reliability method* (FORM) where the failure surface is approximated by a tangent hyperplane at some point will be discussed. A more accurate method is the *second-order reliability method* (SORM) which uses a quadratic approximation to the failure surface.

Assume the loading $S(x)$ and the resistance $R(x)$ for a single failure mode to be statistically independent and with density functions as illustrated in Fig. 7. The failure function is given by eq. (3) and the probability of failure by eq. (35) or eq. (36).

However, these functions are in many cases not known but might be estimated only by their mean values and standard deviations. If we assume S and R to be independent normally distributed variables with known means and standard deviations, then the linear failure function $g = R - S$ is normally distributed with mean value,

$$\mu_g = \mu_R - \mu_S \quad (37)$$

and

$$\text{standard deviation, } \sigma_g = (\sigma_R^2 + \sigma_S^2)^{0.5} \quad (38)$$

The quantity $(g - \mu_g) / \sigma_g$ will be unit standard normal and consequently

$$P_f = \text{prob} [g \leq 0] = \int_{-\infty}^0 f_g(x) dx = \Phi \left(\frac{0 - \mu_g}{\sigma_g} \right) = \Phi(-\beta) \quad (39)$$

where

$$\beta = \frac{\mu_g}{\sigma_g} \quad (40)$$

is a measure of the probability of failure and is denoted the *reliability index* (Cornell 1969), cf. Fig. 8 for illustration of β . Note that β is the inverse of the coefficient of variation and is the distance in terms of number of standard deviations from the most probable value of g (in this case the mean) to the failure surface, $g = 0$.

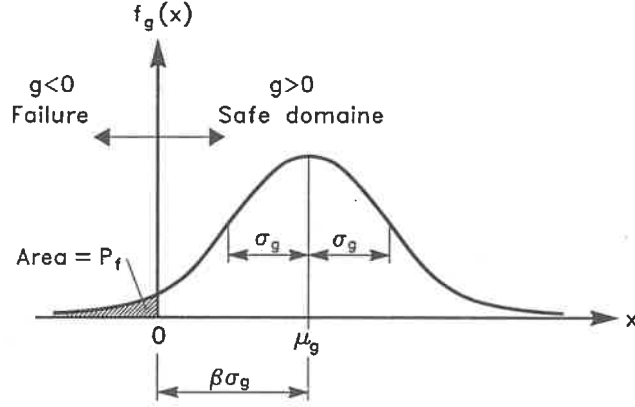


FIG. 8. Illustration of the reliability index.

Some corresponding values of β and P_f are given in Table 1.

Table 1. Corresponding values of β and P_f .

β	$P_f = \Phi(-\beta)$
0.0	0.50
0.5	0.31
1.0	0.16
1.5	0.067
2.0	0.023
3.0	0.0013
4.0	$0.32 \cdot 10^{-4}$
5.0	$0.29 \cdot 10^{-6}$

If R and S are normally distributed and “correlated” then eq. (39) still holds but σ_g is given by

$$\sigma_g = (\sigma_R^2 + \sigma_S^2 + 2\rho_{RS} \sigma_R \sigma_S)^{0.5} \quad (41)$$

where ρ_{RS} is the *correlation coefficient*

$$\rho_{RS} = \frac{C_{ov}[R, S]}{\sigma_R \sigma_S} = \frac{E[(R - \mu_R)(S - \mu_S)]}{\sigma_R \sigma_S} \quad (42)$$

R and S are said to be *uncorrelated* if $\rho_{RS} = 0$.

In general, if the failure function $g = g(\bar{X})$ is a *linear* function of the normally distributed basic variables X_1, X_2, \dots, X_n , i.e.

$$g = a_0 + a_1 X_1 + a_2 X_2 + \dots + a_n X_n \quad (43)$$

then $\beta = \frac{\mu_g}{\sigma_g}$ and P_f can be found from eq. (39) using

$$\mu_g = a_0 + a_1\mu_1 + a_2\mu_2 + \dots + a_n\mu_n \quad (44)$$

and

$$\sigma_g^2 = a_1^2\sigma_1^2 + \dots + a_n^2\sigma_n^2 + \sum_{i=1}^n \sum_{\substack{j=1 \\ j \neq i}}^n \rho_{ij} a_i a_j \sigma_i \sigma_j \quad (45)$$

where ρ_{ij} expresses the correlation coefficient between any pair of variables, cf. eq. (42).

Besides the illustration of β in Fig. 8 a simple geometrical interpretation of β can be given in case of a linear failure function $g = R - S$ of the independent variables R and S by a transformation into a *normalized coordinate system* of the random variables $R' = (R - \mu_R)/\sigma_R$ and $S' = (S - \mu_S)/\sigma_S$, cf. Fig. 9.

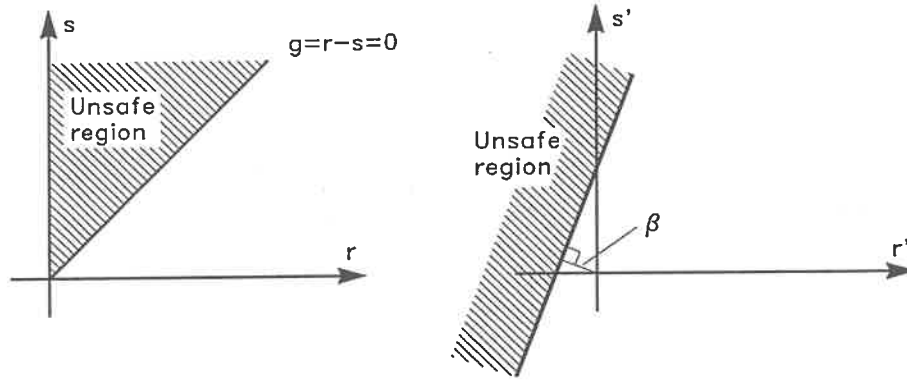


FIG. 9. Illustration of β in normalized coordinate system.

With these variables the failure surface $g = 0$ is linear and given by

$$R'\sigma_R - S'\sigma_S + \mu_R - \mu_S = 0 \quad (46)$$

By geometrical considerations it can be shown that the shortest distance from the origin to this linear failure surface is equal to

$$\beta = \frac{\mu_g}{\sigma_g} = \frac{\mu_R - \mu_S}{(\sigma_R^2 + \sigma_S^2)^{0.5}}$$

in which eqs. (37) and (38) are used.

3.2.2 Non-linear failure functions of normal-distributed random variables

If the failure function $g = g(\bar{X})$ is *non-linear* then approximate values for μ_g and σ_g can be obtained by using a *linearized failure function*.

Linearization is generally performed by Taylor-series expansion about some point retaining only the linear terms. If the expansion is performed around the mean values $(X_1, \dots, X_n) = \mu_1, \dots, \mu_n$ then

$$g \simeq g(\mu_1, \dots, \mu_n) + \sum_{i=1}^n \frac{\partial g}{\partial X_i} (X_i - \mu_i) , \quad (47)$$

where $\partial g / \partial X_i$ is evaluated at (μ_1, \dots, μ_n) . The approximate values of μ_g and σ_g are then

$$\mu_g \simeq g(\mu_1, \dots, \mu_n) \quad (48)$$

$$\sigma_g^2 \simeq \sum_{i=1}^n \sum_{j=1}^n \frac{\partial g}{\partial X_i} \frac{\partial g}{\partial X_j} Cov[X_i, X_j] \quad (49)$$

If the random variables \bar{X} are "uncorrelated", i.e. $\rho_{X_i X_j} = 0$, then eq. (49) reduces to

$$\sigma_g^2 \simeq \sum_{i=1}^n \left(\frac{\partial g}{\partial X_i} \sigma_{X_i} \right)^2 \quad (50)$$

because $Cov[X_i, X_i] = \sigma_{X_i}^2$ and $Cov[X_i, X_j] = 0$ for all i and j , $i \neq j$.

When linearization is performed around the expected mean values the method is often called a *first-order mean value approach* (FMA).

The values of μ_g and σ_g , and thereby also the value of β , depend on the choice of linearization point. Moreover, the value of β defined by eq. (40) will change when different but equivalent non-linear failure functions are used. For example an equivalent failure function to eq. (2) would be

$$g = A^3 \Delta^3 D_n^3 K_D \cot \alpha - H_s^3 \quad (51)$$

which expresses the Hudson formula as does eq. (2), but will result in different β -values.

In order to overcome these problems a transformation of the basic variables $\bar{X} = (X_1, X_2, \dots, X_n)$ into a new set of normalized variables $\bar{Z} = (Z_1, Z_2, \dots, Z_n)$ is per-

formed. For *uncorrelated* normal distributed basic variables \bar{X} the transformation is

$$Z_i = \frac{X_i - \mu_{X_i}}{\sigma_{X_i}} \quad (52)$$

in which case $\mu_{Z_i} = 0$ and $\sigma_{Z_i} = 1$. By this linear transformation the *failure surface* $g = 0$ in the x -coordinate system is mapped into a failure surface in the z -coordinate system which also divides the space into a safe region and a failure region, cf. Fig. 10.

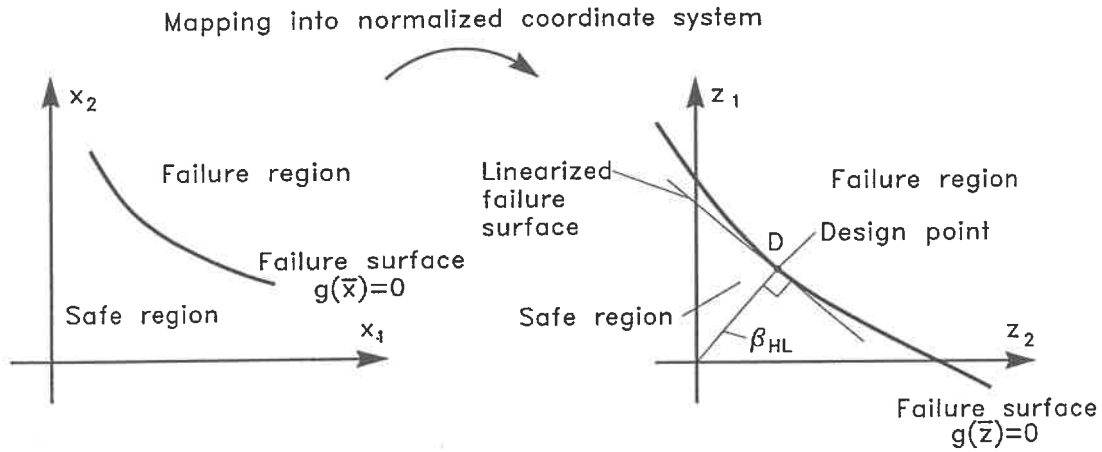


FIG. 10. Definition of the Hasofer and Lind reliability index, β_{HL} .

Fig. 10 introduces the Hasofer and Lind reliability index β_{HL} which is defined as the distance from origo to the nearest point, D , of the *failure surface* in the z -coordinate system. This point is called the *design point*. The coordinates of the design point in the original x -coordinate system are the most probable values of the variables \bar{X} at failure. β_{HL} can be formulated as

$$\beta_{HL} = \min_{g(\bar{z})=0} \left(\sum_{i=1}^n z_i^2 \right)^{0.5} \quad (53)$$

The special feature of β_{HL} as opposed to β is that β_{HL} is related to the failure "surface" $g(\bar{z}) = 0$ which is invariant to the failure function because equivalent failure functions result in the same failure surface.

The two reliability indices β and β_{HL} will coincide when the failure surfaces are linear, cf. Figs. 9 and 10. Obviously, this will also be the case if non-linear failure functions are linearized by Taylor Series expansion around the design point.

Linearization around the design point instead of mean values is therefore very much to be preferred, also because the design point is the most probable point of failure, cf. Fig. 6.

Linearization around mean values can lead to quite erroneous results but due to the simplicity of the method it might be used to get a first order-of-magnitude impression of the failure probability.

The method where linearization is performed around the design point is often called a *first-order design point approach* (FDA).

The calculation of β_{HL} and the design point coordinates can be undertaken in a number of different ways. An iterative method must be used when the failure surface is non-linear. In the following a simple method is introduced.

Let θ denote the distance from the origin to any point at the failure surface given in the normalized coordinate system

$$\begin{cases} \theta = \left[\sum_{i=1}^n z_i^2 \right]^{\frac{1}{2}} \\ g(z_1, z_2, \dots, z_n) = 0 \end{cases} \quad (54)$$

Construct the multiple function (Lagrange function)

$$\begin{aligned} F &= \theta + K_1 g \\ &= \left[z_1^2 + z_2^2 + \dots + z_n^2 \right]^{\frac{1}{2}} + K_1 g(z_1, z_2, \dots, z_n) \end{aligned} \quad (55)$$

where K_1 is an unknown constant (multiplier).

Maximum or minimum of θ occurs when

$$\begin{cases} \frac{\partial F}{\partial z_i} = \left[z_1^2 + z_2^2 + \dots + z_n^2 \right]^{-\frac{1}{2}} \cdot z_i + K_1 \frac{\partial g}{\partial z_i} = 0 \quad i = 1, 2, \dots, n \\ g(z_1, z_2, \dots, z_n) = 0 \end{cases} \quad (56)$$

Assume that only one minimum exists and the coordinates of the design point D are given by

$$\left(z_1^d, z_2^d, \dots, z_n^d \right) = \left(\beta_{HL}\alpha_1, \beta_{HL}\alpha_2, \dots, \beta_{HL}\alpha_n \right) \quad (57)$$

Then

$$\theta_{min} = \beta_{HL} = \left[\sum_{i=1}^n (\beta_{HL}\alpha_i)^2 \right]^{\frac{1}{2}} \quad \text{and consequently}$$

$$\sum_{i=1}^n \alpha_i^2 = 1 \quad (58)$$

Eq. (56) becomes

$$\begin{cases} \alpha_i + K_1 \frac{\partial g}{\partial z_i} = 0 & i = 1, 2, \dots, n \\ g(\beta_{HL}\alpha_1, \beta_{HL}\alpha_2, \dots, \beta_{HL}\alpha_n) = 0 \end{cases} \quad (59)$$

or

$$\begin{cases} -K_1 \frac{\partial g}{\partial z_i} = \frac{-\frac{\partial g}{\partial z_i}}{K} \\ g(\beta_{HL}\alpha_1, \beta_{HL}\alpha_2, \dots, \beta_{HL}\alpha_n) = 0 \end{cases} \quad (60)$$

Inserting eq. (60) into eq. (58) gives

$$K = \left[\sum_{i=1}^n \left(\frac{\partial g}{\partial z_i} \right)^2 \right]^{\frac{1}{2}} \quad (61)$$

The α -values defined by (57) are often called *sensitivity factors* (or influence factors) because α_i^2 provides an indication of the relative importance on the reliability index β_{HL} of the random variable X_i . If α_i^2 is small it might be considered to model X_i as a deterministic quantity equal to the median value of X_i . In such case the relative change in the reliability index by assuming X_i deterministic can be approximated by

$$\frac{\beta_{HL}(X_i : \text{deterministic})}{\beta_{HL}(X_i : \text{random})} \simeq \frac{1}{\sqrt{1 - \alpha_i^2}} \quad (62)$$

The corresponding change in failure probability can be found from eq. (39) or from Table 1. Eq. (62) is used for the evaluation of a simplification of a failure function by reducing the number of random variables.

The sensitivity of β_{HL} to change in the value of a deterministic parameter b_i can be expressed by

$$\frac{d\beta_{HL}}{db_i} = \frac{1}{K} \frac{\partial g}{\partial b_i} \quad (63)$$

where K is given by eq. (36) and the partial derivative of g with respect to b_i is taken in the design point.

Eq. (63) is useful when it is considered to change a deterministic parameter (e.g. the

height of wave wall) into a stochastic variable.

EXAMPLE 1

Consider the hydraulic stability of a rock armour layer given by the Hudson equation formulated as the failure function, cf. eqs. (1) and (2)

$$g = A \Delta D_n (K_D \cot\alpha)^{\frac{1}{3}} - H_s \quad (64)$$

all the parameters are regarded uncorrelated random variables X_i , except K_D which signifies the *failure criterion*, i.e. a certain damage level here chosen as 5% displacement corresponding to $K_D \simeq 4$. The factor A is also a random variable signifying the uncertainty of the formula.

All random variables are assumed normally distributed with known mean values and standard deviations, cf. Table 2. The normal distribution can be a bad approximation for H_s which is usually much better approximated by an extreme distribution, e.g. a Weibull or Gumbel distribution as will be discussed later. The normal distribution of H_s is used here due to the simplicity involved but might be reasonable in case of depth limited wave conditions.

Table 2. Basic variables.

i	X_i	μ_{X_i}	σ_{X_i}	coefficient of variation σ_{X_i}/μ_{X_i}
1	A	1	0.18	18%
2	D_n	1.5 m	0.10 m	6.7%
3	H_s	4.4 m	0.70 m	16%
4	Δ	1.6	0.06	3.8%
5	$\cot\alpha$	2	0.10	5.0%

The failure surface corresponding to the failure function (64) reads for $K_D = 4$

$$A \Delta D_n (\cot\alpha)^{\frac{1}{3}} 1.59 - H_s = 0$$

or

$$X_1 X_4 X_2 X_5^{\frac{1}{3}} 1.59 - X_3 = 0 \quad (65)$$

By use of the transformation eq. (52) the failure surface in the normalized coordinate

system is given by

$$(1 + 0.18 z_1) (1.6 + 0.06 z_4) (1.5 + 0.10 z_2) (2 + 0.10 z_5)^{\frac{1}{3}} 1.59 - (4.4 + 0.70 z_3) = 0$$

In order to make the calculations in this illustrative example more simple we neglect the small variational coefficients of Δ and $\cot\alpha$ and obtain

$$(1 + 0.18 z_1) \cdot 1.6 \cdot (1.5 + 0.10 z_2) \cdot 2^{\frac{1}{3}} \cdot 1.59 - (4.4 + 0.70 z_3) = 0 \quad (66)$$

or

$$0.864 z_1 + 0.32 z_2 + 0.058 z_1 z_2 - 0.70 z_3 + 0.40 = 0 \quad (67)$$

$$0.864 \beta_{HL} \alpha_1 + 0.32 \beta_{HL} \alpha_2 + 0.058 \beta_{HL}^2 \alpha_1 \alpha_2 - 0.70 \beta_{HL} \alpha_3 + 0.40 = 0$$

$$\beta_{HL} = \frac{-0.40}{0.864 \alpha_1 + 0.32 \alpha_2 + 0.058 \alpha_1 \alpha_2 \beta_{HL} - 0.70 \alpha_3}$$

By use of eq. (60)

$$\alpha_1 = -\frac{1}{K} (0.864 + 0.058 \beta_{HL} \alpha_2)$$

$$\alpha_2 = -\frac{1}{K} (0.32 + 0.058 \beta_{HL} \alpha_1)$$

$$\alpha_3 = \frac{0.7}{K}$$

By eq. (61)

$$K = \sqrt{(0.864 + 0.058 \beta_{HL} \alpha_2)^2 + (0.32 + 0.058 \beta_{HL} \alpha_1)^2 + (0.7)^2}$$

The iteration is now performed by choosing starting values for β_{HL} , α_1 , α_2 and α_3 and calculating new values until small modifications are obtained. This is shown in Table 3. The convergence is faster if a positive sign is used for α -values related to loading variables and a negative sign is used for α -values related to resistance variables.

Table 3.

	Iteration No.			
	start	1	2	3
β_{HL}	3.0	0.438	0.342	0.341
K		1.144	1.149	1.149
α_1	-0.50	-0.744	-0.747	-0.747
α_2	-0.50	-0.263	-0.266	-0.266
α_3	0.50	0.612	0.609	0.609

The probability of failure is then

$$P_f = \Phi(-\beta_{HL}) = \Phi(-0.341) = 0.367$$

cf. Table 1 for some corresponding values of β and P_f .

The design point coordinates in the normalized z coordinate system are

$$\begin{aligned} (z_1^d, z_2^d, z_3^d) &= (\beta_{HL}\alpha_1, \beta_{HL}\alpha_2, \beta_{HL}\alpha_3) \\ &= (-0.255, -0.091, 0.208) \end{aligned}$$

Expression (58) $\beta_{HL} = \left(\sum_{i=1}^3 (z_i^d)^2 \right)^{\frac{1}{2}}$ provides a check on the design point coordinates.

Using the transformation

$$X_i^d = \mu_{X_i} + \sigma_{X_i} z_i^d$$

and the values of μ_{X_i} , σ_{X_i} given in Table 2 the design point coordinates in the original x coordinate system are found to be

$$(x_1^d, x_2^d, x_3^d) = (0.954, 1.491, 4.546)$$

The relative importance of the random variables to the failure probability is evaluated through the α^2 -values. Table 4 shows that the uncertainty related to D_n is of minor importance compared to the uncertainties on A and H_s .

Table 4.

i	X_i	α_i	α_i^2 (%)	$\frac{\beta_{HL}(X_i : \text{deterministic})}{\beta_{HL}(X_i : \text{random})}$ $\simeq \frac{1}{\sqrt{1-\alpha_i^2}}$	$\frac{P_f(X_i : \text{deterministic})}{P_f(X_i : \text{random})}$
1	A	-0.747	55.8	1.50 *)	0.831 *)
2	D_n	-0.266	7.1	1.04	0.989
3	H_s	0.609	37.1	1.26 *)	0.899 *)
			100.0		

*) The assumption of validity only for small α -values is not fulfilled

If all 5 parameters in the Hudson formula was kept as random variables with mean values and standard deviations as given in Table 2 then the corresponding values would be as shown in Table 5.

Table 5.

i	X_i	α_i	α_i^2 (%)	$\frac{\beta_{HL}(X_i : \text{deterministic})}{\beta_{HL}(X_i : \text{random})}$ $\simeq \frac{1}{\sqrt{1-\alpha_i^2}}$	$\frac{P_f(X_i : \text{deterministic})}{P_f(X_i : \text{random})}$
1	A	-0.705	49.7	1.41 *)	0.857 *)
2	D_n	-0.275	7.6	1.04	0.986
3	H_s	0.631	39.8	1.29 *)	0.896 *)
4	Δ	-0.154	2.3	1.01	0.999
5	$cot\alpha$	-0.068	0.5	1.00	1.000
			100.0		

*) The assumption of validity only for small α -values is not fulfilled

It is clearly seen why Δ and $cot\alpha$ can be regarded as constants.

If the normally distributed basic variables \bar{X} are *correlated* the procedure given above can be used if a transformation into non-correlated variables \bar{Y} is performed before normalizing the variables.

The correlation between any pair of the random variables \bar{X} is expressed by the covariance

matrix

$$\bar{C}_{\bar{X}} = \begin{bmatrix} Var[X_1] & Cov[X_1, X_2] & \cdots & Cov[X_1, X_n] \\ Cov[X_2, X_1] & Var[X_2] & & \vdots \\ \vdots & & \ddots & \vdots \\ Cov[X_n, X_1] & & & Var[X_n] \end{bmatrix} \quad (68)$$

If $\bar{C}_{\bar{Y}}$ is a diagonal matrix

$$\bar{C}_{\bar{Y}} = \begin{bmatrix} Var[Y_1] & \cdots & \cdots & 0 \\ \vdots & Var[Y_2] & & \vdots \\ \vdots & & \ddots & \\ 0 & & & Var[Y_n] \end{bmatrix} = \begin{bmatrix} \sigma_{Y_1}^2 & & 0 \\ \vdots & \sigma_{Y_2}^2 & \vdots \\ \vdots & & \ddots \\ 0 & & & \sigma_{Y_n}^2 \end{bmatrix} \quad (69)$$

then no correlation between any pair of random variables \bar{Y} exists.

A set of uncorrelated variables \bar{Y} can be obtained by the transformation

$$\bar{Y} = \bar{A}^T \bar{X} \quad (70)$$

where \bar{A} is an orthogonal matrix with column vectors equal to the orthonormal eigenvalues of $\bar{C}_{\bar{X}}$.

The diagonal elements of $\bar{C}_{\bar{Y}}$, i.e. $\sigma_{Y_1}^2 \cdots \sigma_{Y_n}^2$, are equal to the eigenvalues of $\bar{C}_{\bar{X}}$.

After determination of \bar{Y} and $\sigma_{\bar{Y}}$ the following transformation, analog to (52), into uncorrelated and normalized variables \bar{z} is performed

$$z_i = \frac{Y_i - \mu_{Y_i}}{\sigma_{Y_i}} \quad (71)$$

The reliability index β_{HL} , defined in the z -coordinate system as given in Fig. 10 and eq. (53), can be determined by the described iterative procedure of eqs. (60) and (61).

3.2.3 Non-linear failure functions containing non-normal distributed random variables

It is not always a reasonable assumption to consider the random variables normally distributed. This is for example the case for parameters such as H_s characterizing the sea state in long-term wave statistics. H_s will in general follow extreme distributions (e.g. Gumbel

and Weibull) quite different from the normal distribution, and cannot be described only by the mean value and the standard deviation.

For such cases it is still possible to use the reliability index β_{HL} but an extra transformation of the non-normal basic variables into normal basic variables must be performed before β_{HL} can be determined as described above.

A commonly used transformation is based on the substitution of the non-normal distribution of the basic variable X_i by a normal distribution in such a way that the density and distribution functions f_{X_i} and F_{X_i} are unchanged at the design point.

If the design point is given by $x_1^d, x_2^d, \dots, x_n^d$ then the transformation reads

$$F_{X_i}(x_i^d) = \Phi\left(\frac{x_i^d - \mu'_{X_i}}{\sigma'_{X_i}}\right) \quad (72)$$

$$f_{X_i}(x_i^d) = \frac{1}{\sigma'_{X_i}} \varphi\left(\frac{x_i^d - \mu'_{X_i}}{\sigma'_{X_i}}\right)$$

where μ'_{X_i} and σ'_{X_i} are the mean and standard deviation of the approximate (fitted) normal distribution.

From eq. (47) is obtained

$$\sigma'_{X_i} = \frac{\varphi\left(\Phi^{-1}\left(F_{X_i}(x_i^d)\right)\right)}{f_{X_i}(x_i^d)} \quad (73)$$

$$\mu'_{X_i} = x_i^d - \Phi^{-1}\left(F_{X_i}(x_i^d)\right) \sigma'_{X_i}$$

Eq. (47) can also be written

$$F_{X_i}(x_i^d) = \Phi\left(\frac{x_i^d - \mu'_{X_i}}{\sigma'_{X_i}}\right) = \Phi(z_i^d) = \Phi(\beta_{HL}\alpha_i)$$

Solving with respect to x_i^d gives

$$x_i^d = F_{X_i}^{-1}\left[\Phi(\beta_{HL}\alpha_i)\right] \quad (74)$$

The iterative method presented above for calculation of β_{HL} can still be used if for each step of iteration the values of σ'_{X_i} and μ'_{X_i} given by eq. (48) are calculated for those variables where the transformation (47) has been used.

For correlated random variables the transformation given by eq. (70) is used before normalization.

EXAMPLE 2

The same failure function and non-correlated normal-distributed variable as in Example 1 are considered except that H_s now follows a Gumbel distribution but with the same average and standard deviation as given in Table 2.

The Gumbel distribution function and density function are

$$F_G(x_3) = e^{-e^{-A(x_3-B)}} \quad (75)$$

$$f_G(x_3) = \frac{dF_G(x_3)}{dx_3} = A e^{[-e^{-A(x_3-B)} - A(x_3-B)]}$$

The distribution parameters A and B can be determined by the following expressions for the mean and the standard deviation

$$\mu_{x_3} = B + \frac{0.57722}{A} \quad (76)$$

$$\sigma_{x_3} = \frac{\pi}{\sqrt{6}} \frac{1}{A}$$

Using the Table 2 values $\mu_{x_3} = 4.4$ m and $\sigma_{x_3} = 0.7$ m gives $A = 1.83 \text{ m}^{-1}$ and $B = 4.08$ m.

In the normalized coordinate system the failure surface is then (compared with eq. (66))

$$(1 + 0.18z_1) \cdot 1.6 \cdot (1.5 + 0.1z_2) \cdot 2^{\frac{1}{3}} \cdot 1.59 - (\mu'_{x_3} + \sigma'_{x_3}z_3) = 0$$

$$0.864z_1 + 0.32z_2 + 0.058z_1z_2 - \sigma'_{x_3}z_3 + (4.8 - \mu'_{x_3}) = 0$$

$$\beta_{HL} = \frac{-(4.8 - \mu'_{x_3})}{0.864\alpha_1 + 0.32\alpha_2 + 0.058\alpha_1\alpha_2\beta_{HL} - \sigma'_{x_3}\alpha_3}$$

By eq. (60)

$$\alpha_1 = -\frac{1}{K} (0.864 + 0.058\beta_{HL}\alpha_2)$$

$$\alpha_2 = -\frac{1}{K} (0.32 + 0.058\beta_{HL}\alpha_1)$$

$$\alpha_3 = \frac{\sigma'_{x_3}}{K}$$

By eq. (61)

$$K = \sqrt{(0.864 + 0.058\beta_{HL}\alpha_2)^2 + (0.32 + 0.058\beta_{HL}\alpha_1)^2 + (\sigma'_{x_3})^2}$$

By eq. (74)

$$x_3^d = F_G^{-1} [\Phi(\beta_{HL}\alpha_3)]$$

By eq. (48)

$$\sigma'_{x_3} = \frac{\varphi(\Phi^{-1}(F_G(x_3^d)))}{f_G(x_3^d)}$$

$$\mu'_{x_3} = x_3^d - \Phi^{-1}(F_G(x_3^d)) \cdot \sigma'_{x_3}$$

The results from each step of iteration are shown in Table 6.

Table 6.

	Iteration No.							
	start	1	2	3	4	5	6	7
β_{HL}	3.0	1.717	0.553	0.569	0.463	0.461	0.457	0.457
K		1.295	1.363	1.165	1.155	1.144	1.143	1.143
α_1	-0.5	-0.629	-0.629	-0.735	-0.742	-0.749	-0.749	-0.750
α_2	-0.5	-0.199	-0.220	-0.254	-0.260	-0.262	-0.262	-0.263
α_3	0.5	0.772	0.754	0.627	0.619	0.609	0.608	0.607
x_3^d		5.359	4.568	4.525	4.475	4.471	4.469	4.469
σ'_{x_3}	1.0	1.027	0.731	0.715	0.697	0.695	0.694	0.694
μ'_{x_3}	3.0	4.033	4.139	4.264	4.270	4.275	4.276	4.276

The probability of failure is then

$$P_f = \Phi(-\beta_{HL}) = \Phi(-0.457) = 0.324$$

The coordinates of the design point D in the normalized z -coordinate system are

$$(z_1^d, z_2^d, z_3^d) = (\beta_{HL}\alpha_1, \beta_{HL}\alpha_2, \beta_{HL}\alpha_3)$$

$$= (-0.342, -0.12, 0.277)$$

Note that $\beta_{HL} = \left(\sum_{z=1}^3 (z_i^d)^2 \right)^{\frac{1}{2}}$.

The coordinates of the design point D in the original x -coordinate system are calculated by the transformation

$$x_i^d = \mu_{x_i} + \sigma_{x_i} z_i^d \quad i = 1, 2 \quad (\text{cf. Table 2 for } \mu_{x_i} \text{ and } \sigma_{x_i})$$

$$x_3^d = \mu'_{x_3} + \sigma'_{x_3} z_3^d \quad (\text{cf. Table 6 for } \mu'_{x_3} \text{ and } \sigma'_{x_3})$$

to be

$$(x_1^d, x_2^d, x_3^d) = (0.934, 1.474, 4.468)$$

The reliability index is now $\beta_{HL} = 0.457$ which is larger than $\beta_{HL} = 0.341$ from Example 1. However, the failure probability does not change so much (from 36.7% in Example 1 to 32.4% in this example).

A more widely used method of calculating β_{HL} is

1. Select some trial coordinates of the design point in the z -coordinate system

$$\bar{z}^d = (z_1^d, z_2^d, \dots, z_n^d)$$

2. Calculate $a_i \quad i = 1, 2, \dots, n$ by

$$a_i = \left. \frac{\partial g}{\partial z_i} \right|_{\bar{z}=\bar{z}^d}$$

3. Determine a better estimate of \bar{z}^d by

$$z_i^d = a_i \frac{\sum_{i=1}^n (a_i z_i^d) - g|_{\bar{z}=\bar{z}^d}}{\sum_{i=1}^n (a_i)^2}$$

4. Repeat 2) and 3) to achieve convergence

5. Evaluate β_{HL} and α_i by

$$\beta_{HL} = \left[\sum_{i=1}^n (z_i^d)^2 \right]^{\frac{1}{2}}, \quad \alpha_1 = z_i^d / \beta_{HL}$$

The method is based on the assumption of the existence of only one minimum. However, several "local" minima might exist. In order to avoid convergence against such local minima (and thereby overestimation of β_{HL} and the reliability) several different sets of trial coordinates might be tried.

EXAMPLE 3

A monolithic vertical breakwater designed according to deterministic Japanese design guidelines are considered in this example, where the reliabilities related to the failure modes sliding (Section 2.2.1), foundation failure in the rubble mound and clay subsoil (Section 2.2.2) and foundation failure in the rubble mound (Section 2.2.3) are calculated.

The uncertainties (physical, statistical and model) related to the above failure modes are modelled as stochastic variables. The failure functions given in Section 2 are used. The wave loads are estimated using the Goda formula with model uncertainty included. For the foundation failure modes the strength of the soil is modelled as a stochastic field.

The probability of failure of the failure modes are estimated using a First Order Reliability Methods (FORM). Associated with these estimates sensitivities of the probability of failures with respect to important parameters are obtained.

Characterization of the variables

All the mentioned parameters are in principle stochastic variables. In a level II reliability analysis such parameters should as a minimum be defined by a mean value and a standard deviation if the actual distribution is unknown. Some of the parameters have very small variational coefficients and can be regarded as deterministic parameters. In the present example this holds for all the geometrical parameters. The variables applied in the example are described in the following.

The *Goda formula* might, according to van der Meer et al. (1992), be regarded as a good central approximation for the maximum wave force in a sea state with duration of approximately 2500 waves. The variational coefficient of the resultant horizontal force calculated by the formula is estimated to 0.20 ($= \frac{0.25}{1.2}$), cf. van der Meer et al. (1992). This is taken into account by a stochastic parameter with mean value = 1 and standard variation = 0.20.

The *deep water wave climate* characterized by H_s is assumed to follow a Weibull distribution. The maximum significant wave height within T years is then given by

$$F_{H_{so}^T}(h_{so}) = \left[1 - \exp \left(- \left(\frac{H_{so} - B}{A} \right)^k \right) \right]^{\lambda T} \quad (77)$$

where λ is the average number of H_{so} data values per year. B is in this example for simplicity regarded a deterministic threshold value = 2.69 m.

A and k are taken as normal distributed stochastic variables with the following mean values and standard deviations signifying the statistical uncertainty

	mean	standard deviation, σ
k	1.14	$\simeq \sqrt{\frac{1}{N}}$ (approximation)
A	0.58 m	$\left[\frac{A^2}{N} \left(\frac{\Gamma(1+2/k)}{\Gamma^2(1+1/k)} - 1 \right) \right]^{0.5} = A \left(\frac{0.3}{N} \right)^{0.5}$

(78)

N is the number of available H_{so} -values, here taken as 30.

The uncertainty from the error on H_{so} might be taken into account by combining it with the statistical uncertainty on A . However, better ways of implementation are under consideration.

$$\sigma[A] \simeq A \sqrt{\frac{0.3}{N}} = 0.058 \quad \text{for } N = 30 \quad (79)$$

$$\sigma[k] \simeq \sqrt{\frac{1}{N}} = 0.18 \quad \text{for } N = 30 \quad (80)$$

λ is set equal to 1.

When A and k are modelled by stochastic variables the distribution function in (77) should be considered as a conditional distribution function $F_{H_{so}}(h_{so}|A, k)$.

The *wave direction* is assumed head-on to the breakwater.

Shoaling of the waves are neglected for simplicity.

The *design wave height* H_{design} to be applied in the Goda formula is in case of no surf zone in front of the structure taken as $1.8 \cdot H_{so}$.

In case of a surf zone in front of the structure the breaker height is taken as (Goda, 1985)

$$H_b = L_0 0.18 \left(1 - \exp \left(-1.5 \frac{\pi h_b}{L_0} \left(1 + 15 \tan^{4/3} \theta \right) \right) \right) \quad (81)$$

where h_b is the water depth at a distance $5H_s$ seaward of the structure. Consequently, $H_{design} = \min[H_{so}, H_b]$.

The *deep water wave steepness* is fixed to $H_{so}/L_o = 0.035$, i.e. $L_o = L = H_{so}/0.035$.

The *tidal elevation* ζ is assumed given by a cosine function with the probability distribution

function

$$F_{\zeta}(\zeta) = -\frac{1}{\pi} \arccos \left(\frac{\zeta}{\zeta_a} - 1 \right) - 1 \quad (82)$$

where ζ varies between $\pm\zeta_a = \pm 0.75$ m.

The *storm surge* is neglected. This simplification is not acceptable in calculations related to real structures in shallow water.

The *average mass density of the caisson* including sand ballast is assumed normal distributed with mean value $\rho_c = 2.15 \text{ t/m}^3$ and a coefficient of variation of 5%.

The *effective friction angle* is according to F. Nadim et al. (1994), assumed log normal distributed with a mean value $\tan \varphi' = 0.9$ and a standard deviation 0.09.

The *friction coefficient* between the base plate and rubble is assumed normal distributed with a mean value $\tan \xi = 0.636$ and a coefficient of variation of 10 %, Takayama (1992).

The *angle of dilation* of the rubble mound material is assumed normal distributed with a mean value $\psi = 0.279$ and a coefficient of variation of 10 %.

The *undrained shear strength of the clay* is modelled by a log-Gaussian stochastic field $\{c_u(x, z)\}$ where x is the horizontal coordinate and z the vertical coordinate. The mean value function and covariance function are in this paper assumed to be

$$E[c_u(x, z)] = 90 + 3z \quad (83)$$

$$Cov[c_u(x_1, z_1), c_u(x_2, z_2)] = 31^2 \exp\left(-\left|\frac{z_1 - z_2}{3.0}\right|\right) \exp\left(-\left(\frac{x_1 - x_2}{30.0}\right)^2\right) \quad (84)$$

where c_u is in kPa and x, z are in metres and $(x, z) = (0, 0)$ is taken in point B cf. Fig 4.

Applying the formula by Goda and Tanimoto to the above parameter values gives

$$F_H = U \left[\frac{1}{2} (p_1(H_{design}, \zeta) + p_2(H_{design}, \zeta)) h_c + \frac{1}{2} (p_1(H_{design}, \zeta) + p_3(H_{design}, \zeta)) h' \right] \quad \text{KN/m} \quad (85)$$

$$F_U = U \cdot \frac{1}{2} p_u(H_{design}, \zeta) \cdot B_r \quad \text{KN/m} \quad (86)$$

$$F_G = F_G(\zeta, h_w, B_r) \quad \text{KN/m} \quad (87)$$

U is the stochastic variable signifying the uncertainty on the Goda formula for wave induced pressure (mean value 1 and standard deviation 0.2). Application of U with standard deviation 0.2 on F_U is an approximation which has not been verified.

Deterministic design

A vertical breakwater is designed according to Goda's pressure formulation (Section 2.2.4), considering recommended Japanese design guidelines for sliding (safety factor 1.2), overturning (safety factor 1.2) and max heel pressure (700 kN/m^2) and friction coefficient between base plate and rubble (0.6).

The breakwater is placed on a high rubble mound, cf. Fig. 11. The following data are used: $h_s = 17 \text{ m}$, $d = 9.0 \text{ m}$, $h_c = 2.5 \text{ m}$, $h_w = 11.5 \text{ m}$, berm width on the seaward side and rear side is 8 m , tidal elevation is taken as zero and $H_{design} = 1.8H_{50y} = 1.8 \cdot 4.61 = 8.3 \text{ m}$. This results in a caisson width $B_r = 13.14 \text{ m}$ and the following safety factors and heel pressure:

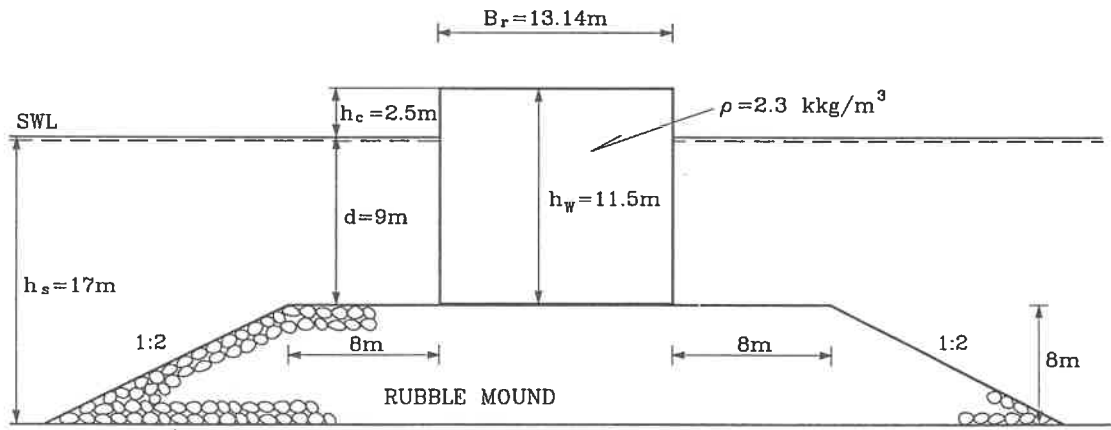


FIG. 11. Deterministic design of a monolithic vertical wall structure on high rubble.

- Safety against horizontal sliding = 1.20
- Safety against overturning around heel = 2.11
- Max soil pressure under base plate = 294 kN/m^2

Reliability analysis of the deterministic design

With a design lifetime of $T_L = 50$ years and a width of the caisson of $B_r = 13.14 \text{ m}$ a reliability analysis with the stochastic parameters from the beginning of the example gives the results presented in Table 7. It is seen that foundation failure in the rubble mound is the most important failure mode in this example. The reliability levels are seen to be rather low compared with conventional civil engineering structures. But compared with observed failure rates for breakwaters the reliability levels are realistic. For sliding failure, rubble foundation failure and rupture failure in clay the uncertainties related to the wave climate and to Goda's formula are dominating, cf. the α^2 -values in Table 7. Also shown in Table 7 are sensitivities of β with respect to changes in T_L and B_r .

Table 7. Failure probabilities and related relative influence of the stochastic parameters.

	sliding	rubble mound failure	rupture in clay
reliability index β	0.38	0.28	1.13
failure probability P_f	0.35	0.38	0.13
$\alpha_{H_{so}}^2$	0.24	0.25	0.25
α_k^2	0.20	0.19	0.24
α_A^2	0.04	0.04	0.03
α_ζ^2	0.09	0.14	0.05
α_U^2	0.28	0.31	0.17
$\alpha_{\rho_c}^2$	0.05	0.03	0.02
$\alpha_{\phi'}^2$	0	0.03	0
α_ψ^2	0	0.01	0
$\alpha_{u_w}^2$	0	0	0
α_ξ^2	0.10	0	0.24
Σ	1.00	1.00	1.00
$\frac{d\beta}{dB_r}$	0.163	0.293	0.112
$\frac{d\beta}{dT_L}$	-0.0080	-0.0083	-0.0070

3.2.4 Time-variant random variables

The failure functions within breakwater engineering are generally of the form

$$g = f_1(\bar{r}) - f_2(H_s, W, T_m) \quad (88)$$

where \bar{R} represents the resistance variables and H_s , W and T_m are the load variables signifying the wave height, the water level and the wave period. The random variables are in general time-variant.

Discussion of Load Variables:

The most important load parameter in breakwater engineering is the *wave height*. It is a time-varying quantity which is best modelled as a stochastic process. Distinction is made between *short-term* and *long-term* statistics of the wave heights. The first one deals with the distribution of the wave height H during a stationary sequence of a storm, i.e. during a period of constant H_s (or any other characteristic wave height). The short term wave height distribution follows the Rayleigh distribution in case of deep-water waves and some truncated distribution in case of shallow water waves.

The long term statistics deals with the distribution of the storms which are then characterized by the max value of H_s occurring in each storm. The storm history is given as the sample $(H_{s1}, H_{s2}, \dots, H_{sn})$ covering a period of observation Y . Extreme value distributions like the Gumbel and Weibull distributions are then fitted to the sample. For strongly depth limited wave conditions a normal distribution with mean value as a function of water depth might be considered.

The distribution of H_s can be substituted by the distribution of the maximum value within T years, i.e. the distribution of H_s^T . The calculated failure probability then refers to the period T (which in practice might be the lifetime of the structure) if distribution functions of the other variables in (88) are assumed unchanged during the period T .

As an example consider a sample of n independent storms, i.e. $H_{s1}, H_{s2}, \dots, H_{sn}$, obtained within Y years of observation. Assume that H_s follows a Gumbel distribution

$$F(H_s) = \exp[-\exp(-\alpha(H_s - \beta))] \quad (89)$$

i.e. the distribution of H_s within a period of average length between the observations Y/n .

The distribution parameters α and β can be estimated e.g. by the maximum likelihood method or the methods of moments. Moreover, the standard deviations of α and β signifying the statistical uncertainty due to limited sample size can be estimated too.

The sampling intensity is $\lambda = n/Y$. Within a T -years reference period the number of data will be λT . The probability of the maximum value of H_s within the period T is then

$$F(H_s^T) = (F(H_s))^{\lambda T} = [\exp[-\exp(-\alpha(H_s - \beta))]]^{\lambda T} \quad (90)$$

The estimate on the T -year event is given by

$$H_s^T = \beta - \frac{1}{\alpha} \ln \left[-\ln \left(1 - \frac{1}{\lambda T} \right) \right] \quad (91)$$

and the standard deviation of H_s^T - in case of maximum likelihood estimates - is

$$\sigma_{H_s^T} = \left(\frac{1}{n\alpha^2} \left[1.109 + 0.514 \left(-\ln \left(-\ln \left(1 - \frac{1}{\lambda T} \right) \right) \right) \right. \right. \\ \left. \left. + 0.608 \left(-\ln \left(-\ln \left(1 - \frac{1}{\lambda T} \right) \right) \right)^2 \right] \right)^{0.5} \quad (92)$$

This expression includes the statistical uncertainty due to limited sample size. Some uncertainty is related to the estimation of the sample values $H_{s1}, H_{s2}, \dots, H_{sn}$ due to measurement errors, errors in hindcast models etc. This uncertainty corresponds to a coefficient of variation $\frac{\sigma_{H_s}}{\mu_{H_s}}$ in the order of 5-20%. The effect of this might be implemented in the calculations by considering a total standard deviation of

$$\sigma = \left(\sigma_{H_s^T}^2 + \sigma_{H_s}^2 \right)^{0.5} \quad (93)$$

In the level II calculation eq. (90) is normalized around the design point and eqs. (91) and (92) or (93) are used for the mean and the standard deviation, cf. the procedure given in Example 2.

Instead of substituting H_s in eq. (88) with H_s^T the following procedure might be used: Consider T in eqs. (90) to (92) to be 1 year.

The outcome of the calculations will then be the probability of failure in a 1 year period, $P_f(1 \text{ year})$. If the failure events of each year are assumed independent for all variables then the failure probability in T years is

$$P_f(T \text{ years}) = 1 - [1 - P_f(1 \text{ year})]^T \quad (94)$$

However, for typical resistance variables such as concrete strength it is not realistic to assume the events of each year to be independent. The calculated values of the failure probability in T -years using $H_s^{1 \text{ year}}$ and H_s^T will be different. The difference will be very small if the variability of H_s is much larger than the variability of other variables.

The *water level* W is also an important parameter as it influences the structural *freeboard* and limits the wave heights in shallow water situations. Consequently, for the general case it is necessary to consider the joint distribution of H_s , W and T_m . However, in case of deep-water waves W is often almost independent (except for barometric effects) of H_s and

T_m and might therefore be taken as a non-correlated variable and might be approximated by a normal distribution with a certain standard deviation. The distribution of W is assumed independent of the length of the reference period T .

The *wave period* T_m is correlated to H_s . As a minimum the mean value and the standard deviation of T_z and the correlation of T_z with H_s should be known in order to perform a level II analysis. However, the linear correlation coefficient is not very meaningful as it gives an insufficient description when the parameters are non-normal distributed. Alternatively the following approach might be used: From a scatter diagram of H_s and T_m a relationship of the form $T_m = Af(H_s)$ is established in which the parameter A is normal distributed (or some other distribution) with mean value $\mu_A = 1$ and a standard deviation σ_A which signifies the scatter. T_m can then be substituted by the variable A in eq. (88). A is assumed non-correlated to all other parameters. Generally, the best procedure to cope with the correlations between H_s , W and T_m is to work on the conditional distributions. Assume the distribution of the maximum value of H_s within the period T given as $F_1(H_s^T)$. Further, assume the conditional distributions $F_2(W|H_s^T)$ and $F_3(T_m|H_s^T)$ to be known. Let Z_1 , Z_2 and Z_3 be independent standard normal variables and

$$\Phi(z_1) = F_1(H_s^T)$$

$$\Phi(z_2) = F_2(W|H_s^T)$$

$$\Phi(z_3) = F_3(T_m|H_s^T)$$

The inverse relationships are given by

$$H_s^T = F_1^{-1}[\Phi(z_1)]$$

$$W = F_2^{-1}[\Phi(z_2)|H_s^T]$$

$$T_m = F_3^{-1}[\Phi(z_3)|H_s^T]$$

Let the resistance variables \bar{R} be converted into standard normal variable \bar{z}_o . The resistance term is written $f_1(\bar{r}) = f_3(\bar{z}_o)$. Then the failure function eq. (88) becomes

$$g = f_3(\bar{z}_o) - f_2\left(F_1^{-1}[\Phi(z_1)], F_2^{-1}[\Phi(z_2)|H_s^T], F_3^{-1}[\Phi(z_3)|H_s^T]\right) = 0$$

Because g now comprises only independent standard normal variables the usual iteration methods for calculating β_{HL} can be applied.

Discussion of Resistance Parameters

The service life of coastal structures is in most cases a span of years, say 20 to 100 years. During periods of that length a decrease in the structural resistance is to be expected due

to various types of material deterioration. Chemical reaction, thermal effect, and repeated loads (fatigue load) can cause deterioration of concrete and natural stone leading to disintegration and rounding of elements. Consequently, the resistance against displacements of armour layers made of randomly placed armour units will decrease with time. Consequently, for armour layers it means a reduction of D_n and K_D with time, cf. the Hudson equation.

Although of great importance in some cases, it is not easy to account for the material effects in reliability calculations. The main problem is the assessment of the variation with time which depends a lot on the intrinsic characteristics of the applied rock and concrete. However, only fairly primitive methods are available for assessment of the relevant characteristics. Moreover, the variation with time depends very much on the load-history which can be difficult to estimate for the relevant period of structural life.

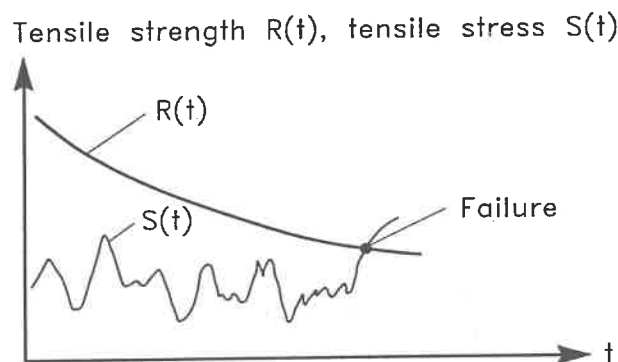


FIG. 12. Illustration of a first-passage problem.

Fig. 12 illustrates a situation where a resistance parameter $R(t)$, e.g. signifying the tensile strength of concrete armour units, decreases with time t . $R(t)$ is assumed to be a deterministic function. The load $S(t)$, e.g. the tensile stress caused by wave action, is assumed to be a stationary process. The probability of failure, i.e. $P(S > R)$, within a period T is

$$P_f(T) \simeq 1 - \exp \left[- \int_0^T \nu^+ (R(t)) dt \right] \quad (95)$$

where $\nu^+ (R(t))$ is the mean-upcrossing rate (number of up-crossings per unit time) of the level $R(t)$ by the process $S(t)$ at time t . ν^+ can be computed by Rice's formula

$$\nu^+ (R(t)) = \int_{\dot{R}}^{\infty} (\dot{S} - \dot{R}) f_{S\dot{S}} (R(t), \dot{S}) d\dot{S}$$

in which $f_{S\dot{S}}$ is the joint density function for $S(t)$ and $\dot{S}(t)$.

Implementation of time-variant variables into level II analyses is rather complicated. For explanation reference is given to Wen and Chen, 1987.

4 Failure probability analysis of failure mode systems

It is clear from Fig. 1 that a breakwater can be regarded as a system of components which can either fail or function. Due to interactions between the components, failure of one component may impose failure of another component and even lead to failure of the system. A so-called *fault tree* is often used to clarify the relations between the failure modes.

A fault tree describes the relations between the failure of the system (e.g. excessive wave transmission over a breakwater protecting a harbour) and the events leading to this failure. Fig. 13 shows a simplified example based on some of the failure modes indicated in Fig. 1.

A fault tree is a simplification and a systematization of the more complete so-called cause-consequence diagram which indicates the causes of partial failures as well as the interactions between the failure modes. An example is shown in Fig. 14.

The failure probability of the system, e.g. the probability of excessive wave transmission in Fig. 13, depends on the failure probability of the single failure modes and on the correlation and linking of the failure modes.

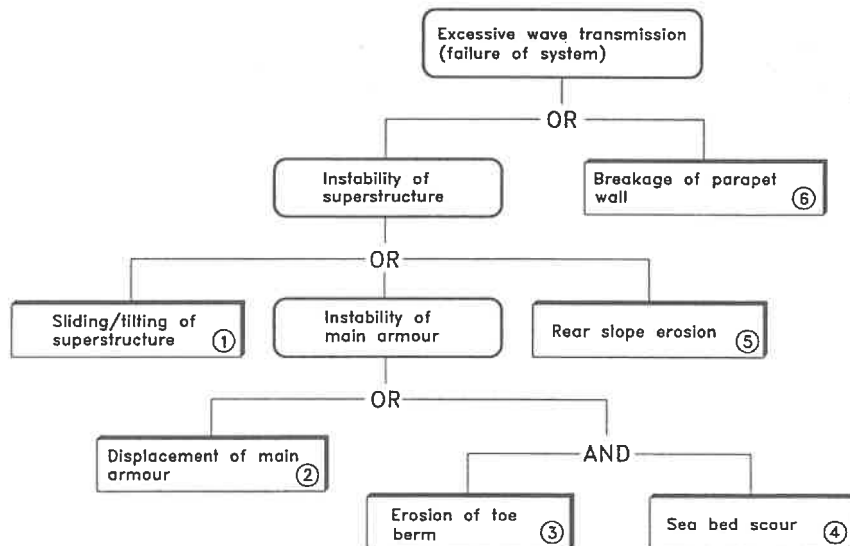
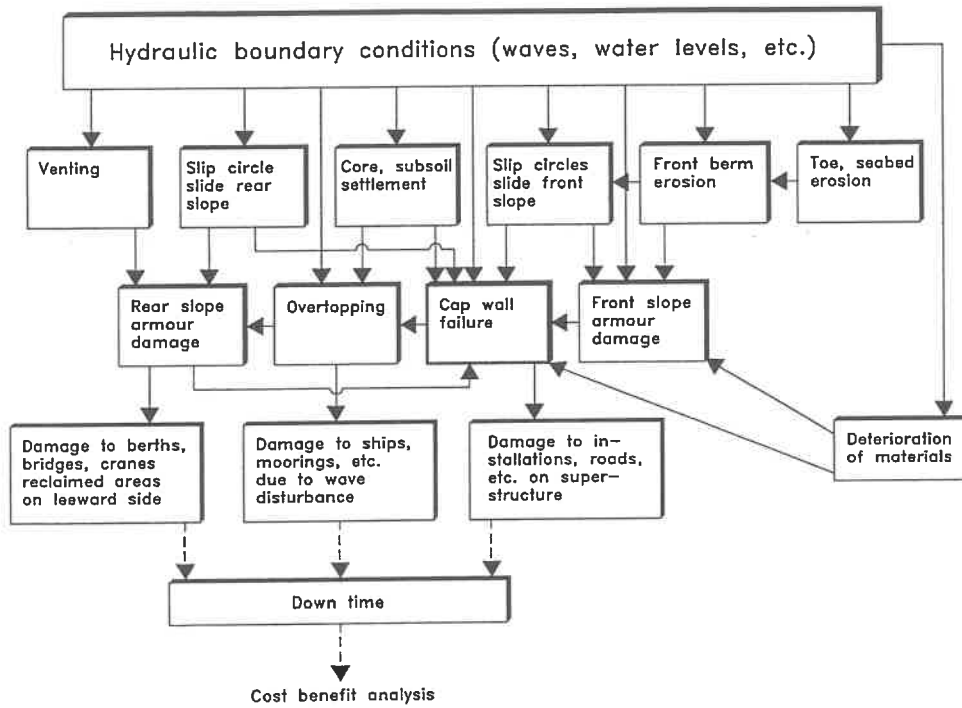


FIG. 13. Example of simplified fault tree for a breakwater.

The failure probability of a single failure mode can be estimated by the methods described in chapter 3. Two factors contribute to the correlation, namely *physical interaction*, such as sliding of main armour caused by erosion of a supporting toe berm, and *correlation through common parameters* like H_s . The correlations caused by physical interactions are



Only hydraulic loads are shown. Other types of loads are for example: SHIP COLLISION - SEISMIC ACTIVITY - AGGRESSIVE HUMAN ACTION (SABOTAGE, WAR, Etc.)

FIG. 14. Example of cause-consequence diagram for a rubble mound breakwater.

not yet quantified. Consequently, only the common-parameter-correlation can be dealt with in a quantitative way. However, it is possible to calculate upper and lower bounds for the failure probability of the system.

A system can be split into two types of fundamental systems, namely series systems and parallel systems, Fig. 15.

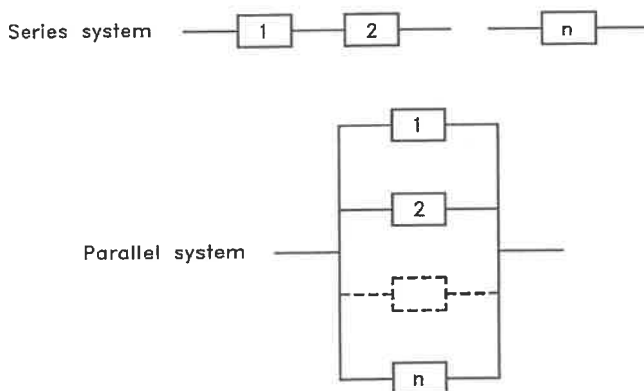


FIG. 15. Series and parallel systems.

Series systems

In a series system failure occurs if any of the elements $i = 1, 2, \dots, n$ fails. The upper and lower bounds of the failure probability of the system, P_{fS} are

$$\text{Upper bound } P_{fS}^U = 1 - (1 - P_{f1})(1 - P_{f2}) \dots (1 - P_{fn}) \quad (96)$$

$$\text{Lower bound } P_{fS}^L = \max P_{fi} \quad (97)$$

where $\max P_{fi}$ is the largest failure probability among all elements. The upper bound corresponds to no correlation between the failure modes and the lower bound to full correlation. Eq. (96) is sometimes approximated by $P_{fS}^U = \sum_{i=1}^n P_{fi}$ which is applicable only for small P_{fi} because P_{fS}^U should not be larger than one.

The OR-gates in a fault tree corresponds to series components. Series components are dominating in breakwater fault trees. Really, the AND-gate in Fig. 13 is included for illustration purpose and is better substituted by an OR-gate.

Parallel systems

A parallel system fails only if all the elements fail.

$$\text{Upper bound } P_{fS}^U = \min P_{fi} \quad (98)$$

$$\text{Lower bound } P_{fS}^L = P_{f1} \cdot P_{f2} \dots P_{fn} \quad (99)$$

The upper bound corresponds to full correlation between the failure modes and the lower bound to no correlation.

The AND-gates in a fault tree correspond to parallel components.

In order to calculate upper and lower failure probability bounds for a system it is convenient to decompose it into series and parallel systems. Fig. 16 shows a decomposition of the fault tree, Fig. 13.

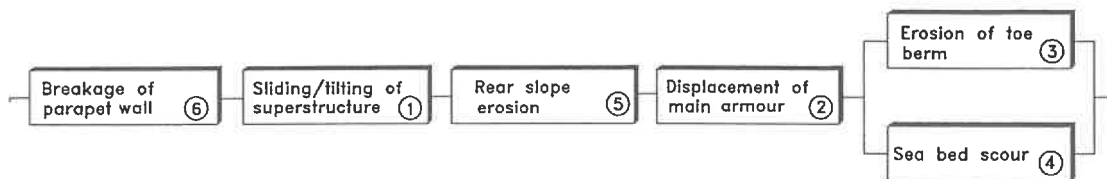


FIG. 16. Decomposition of the fault tree Fig. 8 into series and parallel systems.

EXAMPLE 4

The level II analysis of the single failure modes for a specific breakwater schematized in Figs. 13 and 16 revealed the following probabilities of failure in a 1-year period

i	1	2	3	4	5	6
P_{fi} %	3	6	4	3	0.5	1

Note that these P_{fi} -values cannot be used in general because they relate to a specific structure. However, they are typical for conventionally designed breakwaters with respect to order of magnitude and large variations.

The simple failure probability bounds for the system are, cf. eqs. (96), (97), (98) and (99):

Upper bound (no correlation):

$$P_{fS}^U = 1 - (1 - P_{f6})(1 - P_{f1})(1 - P_{f5})(1 - P_{f2})(1 - \min. \text{ of } [P_{f3}, P_{f4}]) = 12.9\%$$

or for small values of P_{fi}

$$P_{fS}^U = P_{f6} + P_{f1} + P_{f5} + P_{f2} + \min. \text{ of } [P_{f3}, P_{f4}] = 13.5\%$$

Lower bound (full correlation):

$$P_{fS}^L = \max \text{ of } [P_{f6}, P_{f1}, P_{f5}, P_{f2}, P_{f3} \cdot P_{f4}] = 6\%$$

The simple bounds corresponding to T -years structural life might be approximated by the use of eq. (58) *)

	Structure life in years		
	20	50	100
P_{fS}^U %	94	100	100
*) P_{fS}^L %	71	95	100

*) It is very important to notice that the use of eq. (58), which assumes independent failure events from one year to another, can be misleading. This will be the case if some of the parameters which contribute significantly to the failure probability are time-invariant, i.e. are not changed from year to year. An example would be the parameter signifying a large uncertainty of a failure mode formula, e.g. A in eq. (2). If all parameters were time-invariant then the correct lower bound would be $P_{fS}^L = \max_{i=1-n} [P_{fi}]$ independent of T , i.e. 6% for all T in the example. It follows that use of eq. (58) leads to too large values of P_{fS}^L for $T > 1$ year.

In order to obtain correct P_{fS} -values it is very important that the fault tree represents precisely the real physics of the failure development. This is illustrated by Example 4 where a fault tree alternative to Fig. 13 is analysed, however, containing the same failure mode probabilities as given in Example 3.

EXAMPLE 5

Fig. 17 shows the fault tree which differs from the fault tree in Fig. 13 in that in Fig. 17 only failure mode 6 can directly cause system failure, while in Fig. 13 each of the failure modes 6, 5, 1, 2 and (3+4) can cause system failure.

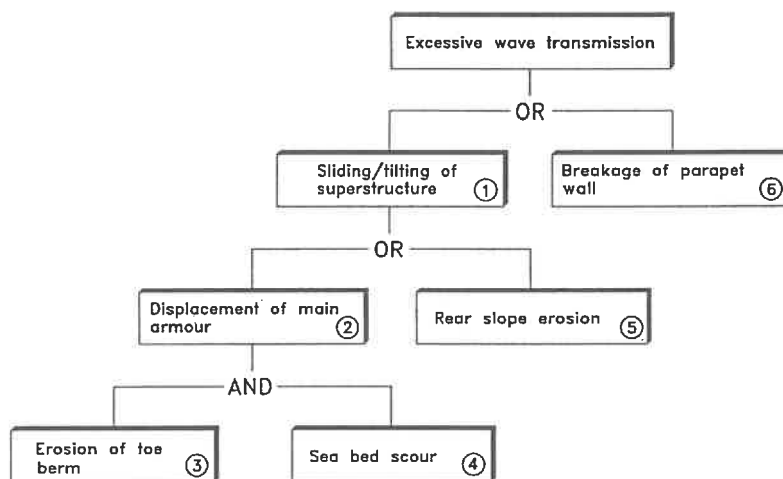


FIG. 17. Example of simplified fault tree for a breakwater.

The decomposition of the fault tree is shown in two steps in Fig. 18. Note that the same failure mode can appear more than once in the decomposed system.

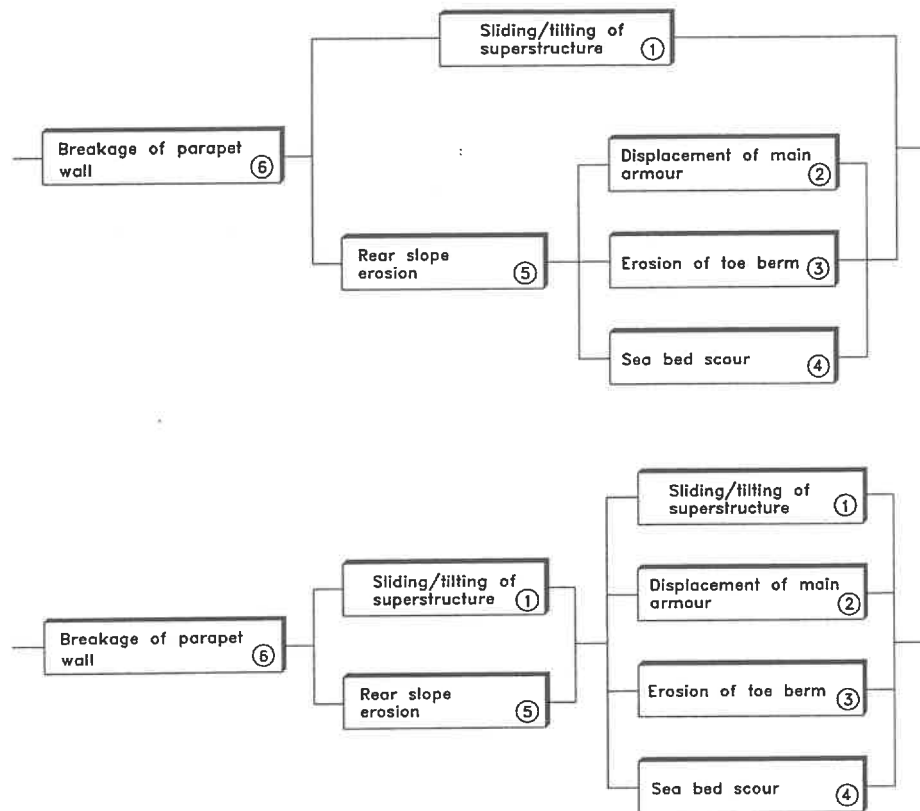


FIG. 18. Decomposition of the fault tree Fig. 17 into series and parallel systems.

The simple bounds for the system are, cf. eqs. (96), (97), (98) and (99):

Upper bound:

$$P_{fS}^U = 1 - (1 - P_{f6})(1 - \min. \text{ of } [P_{f1}, P_{f5}])(1 - \min. \text{ of } [P_{f1}, P_{f2}, P_{f3}, P_{f4}]) = 4.5\%$$

or for smaller values of P_{fi}

$$P_{fS}^U = P_{f6} + \min. \text{ of } [P_{f1}, P_{f5}] + \min. \text{ of } [P_{f1}, P_{f2}, P_{f3}, P_{f4}] = 4.5\%$$

Lower bound:

$$P_{fS}^L = \max. \text{ of } [P_{f6}, P_{f1} \cdot P_{f5}, P_{f1} \cdot P_{f2} \cdot P_{f3} \cdot P_{f4}] = 1\%$$

Using the same P_{fi} -values and procedure as given in Example 3 the following system failure probabilities are obtained

	Structure life in years		
	20	50	100
P_{fS}^U %	60	90	99
*) P_{fS}^L %	18	39	63

These values are quite different from the values of Example 4 which underlines the importance of a correct fault tree. *) see note on page 43.

The real failure probability of the system P_{fS} will always be in between P_{fS}^U and P_{fS}^L because some correlation exists between the failure modes due to the common sea state parameters, e.g. H_s .

It would be possible to estimate P_{fS} if the physical interactions between the various failure modes were known and described by formulae and if the correlations between the involved parameters were known. However, the procedure for such correlations are very complicated and are in fact not yet fully developed for practical use.

The probability of failure cannot in itself be used as the basis for an optimization of a design. This is because an optimization must be related to a kind of measure (scale) which for most structures is the economy, but other measures such as loss of human life (without considering some cost of a life) are also used.

The so-called *risk*, defined as the product of the probability of failure and the economic consequences is used in optimization considerations. The economic consequences must cover all kind of expenses related to the failure in question, i.e. cost of replacement, down-time costs etc.

5 Uncertainties related to parameters determining the reliability of the structure

Calculation of reliability or failure probability of a structure is based on formulae describing its response to loads and on information about the uncertainties related to the formulae and the involved parameters.

Basically, uncertainty is best given by a probability distribution. Because the distribution is rarely known it is common to assume a normal distribution and a related coefficient of variation

$$\sigma' = \frac{\sigma}{\mu} = \frac{\text{standard deviation}}{\text{mean value}} \quad (100)$$

as the measure of the uncertainty.

The word uncertainty is here used as a general term referring both to errors, to randomness and to lack of knowledge.

5.1 Uncertainty related to failure mode formulae

The uncertainty of a formula can be considerable. This is clearly seen from many diagrams presenting the formula as a nice curve shrouded in a wide scattered cloud of data points (usually from experiments) which are the basis for the curve fitting. Coefficients of variation of 15-20% or even larger are quite normal.

The range of validity and the related coefficient of variation should always be considered when using a formula.

5.2 Uncertainty related to environmental parameters

The sources of uncertainty contributing to the total uncertainties in environmental design values are categorized as:

1. Errors related to instrument response (e.g. from accelerometer buoy and visual observations)
2. Variability and errors due to different and imperfect calculations methods (e.g. wave hindcast models, algorithms for timeseries analysis)
3. Statistical sampling uncertainties due to short-term randomness of the variables (variability within a stochastic process, e.g. two 20 min. records from a stationary storm will give two different values of the significant wave height)

4. Choice of theoretical distribution as a representative of the unknown long-term distribution (e.g. a Weibull and a Gumbel distribution might fit a data set equally well but can provide quite different values of a 200-year event).
5. Statistical uncertainties related to extrapolation from short samples of data sets to events of low probability of occurrence.
6. Statistical vagaries of the elements

Distinction is to be made between *short-term* sea state statistics and *long-term* (extreme) sea statistics. Short-term statistics ~~is~~ ^{are} related to the stationary conditions during a sea state, e.g. wave height distribution within a storm of constant significant wave height, H_s . Long-term statistics deal with the extreme events, e.g. the distribution of H_s .

Related to the *short-term* sea state statistics the following aspects must be considered:

- The distribution for individual wave heights in a record in *deep water* and *shallow water* conditions, i.e. Rayleigh distribution and some truncated distributions, respectively.
- Variability due to short samples of single peak spectra waves in deep and shallow water based on theory and physical simulations.
- Variability due to different spectral analysis techniques, i.e. different algorithms, smoothing and filter limits.
- Errors in instrument response and influence of location of measurement. Floating accelerometer buoys tend to underestimate the height of steep waves. Characteristics of shallow water waves can vary considerably in areas with complex sea bed topography. Wave recordings at positions with depth limited breaking waves cannot produce reliable estimates of the deep water waves.
- Imperfection of deep and shallow water numerical hindcast models and quality of wind input.

Estimates on overall uncertainties for short-term sea state parameters covering items 1 - 3 given above, are presented in Table 8 for use when no more precise site specific information is available.

Table 8. Typical variational coefficients $\sigma' = \sigma/\mu$ (standard deviation over mean value) for measured and calculated sea state parameters (Burcharth, 1989).

Parameter	Methods of determination	Estimated typical values		Comments
		σ'	Bias	
Significant wave height, OFFSHORE	Accelerometer buoy, pressure cell, vertical radar	0.05-0.1	~ 0	
	Horizontal radar	0.15	~ 0	
	Hindcast, num. models	0.1-0.2	0-0.1	Very dependent on quality of weather maps.
	Hindcast, SMB method	0.15-0.2	?	Valid only for storm conditions in restricted sea basins.
	Visual observations from ships	0.2	0.05	
Significant wave height NEARSHORE determined from offshore significant waveheight taking into account typical shallow water effects (refraction, diffraction, shoaling, ...)	Numerical models	0.1-0.20	0.1	σ' can be much larger in some cases
	Manual calculations	0.15-0.35		
Mean wave period off-shore on condition of fixed significant wave height	Accelerometer buoy records	0.02-0.05	~ 0	
	Estimates from amplitude spectra	0.15	~ 0	
	Hindcast, num. models	0.1-0.2	~ 0	
Duration of sea state with significant wave height exceeding a specific level	Direct measurements	0.02	~ 0	
	Hindcast, num. models	0.05-0.1	~ 0	
Spectral peak frequency offshore	Measurements	0.05-0.15	~ 0	
	Hindcast, num. models	0.1-0.2	~ 0	
Spectral peakedness offshore	Measurements and hindcast, num. models	0.4	~ 0	
Mean direction of wave propagation offshore	Pitch - roll buoy	Degrees 5°		
	Measurements η , u, v or p, u, v *)	10°		
	Hindcast, num. models	15 - 30°		
Astro tides	Prediction from constants	σ' 0.001-0.07	~ 0	
Storm surge	Numerical models	0.1-0.25	± 0.1	

*) two horizontal velocity components and water level elevation or pressure.

Evaluation of the uncertainties related to the *long-term* sea state statistics and its use for design involves considerations of the following aspects:

- The encounter probability
- Estimation of the standard deviation of a return-period event for a given extreme distribution
- Estimation of extreme distributions by fitting to data sets consisting of uncorrelated values of H_s from
 - frequent measurements of H_s equally spaced in time
 - identification of the largest H_s in each year (annual series)
 - maximum values of H_s for a number of storms exceeding a certain threshold value of H_s (POT, peak over threshold, analysis)

(The methods of fitting are the maximum likelihood method, the method of moments, the least square method and visual graphical fit.)

- Uncertainty on extreme distribution parameters due to limited data sample size.
- Influence on the extreme value of H_s of the choice of threshold value in the POT analysis. (The threshold level should exclude all waves which do not belong to the statistical population of interest.)
- Errors due to lack of knowledge about the true extreme distribution. Different theoretical distributions might fit a data set equally well, but might provide quite different return period values of H_s . (The error can be estimated only empirically by comparing results from fits to different theoretical distributions.)
- Errors due to applied plotting formulae in case of graphical fitting. ^{wg}Dependent on the applied plotting formulae, quite different extreme estimates can be obtained. The error can only be empirically estimated.
- Climatological changes.
- Physical limitations in extrapolation to events of low probability. The most important example might be limitations in wave heights due to limited water depths and fetch restrictions.
- The effect of measurement error on the uncertainty related to an extreme event.

It is beyond the scope of this contribution to discuss in more detail the mentioned uncertainty aspects related to the environmental parameters. Reference is given to Burcharth (1989).

5.3 Uncertainty related to structural parameters

The uncertainties related to material parameters (like density) and geometrical parameters (like slope angle and size of structural elements) are generally much smaller than the uncertainties related to the environmental parameters and to the design formulae.

6 Introduction of a partial coefficient system for implementation of a given reliability in the design

The following presentation explains in short the partial coefficient system developed and proposed by Subgroup-F under the PIANC PTC II Working Group 12 on Rubble Mound Breakwaters. For more details reference is made to Burcharth (1991).

6.1 Introduction to partial coefficients

The objective of the use of partial coefficients is to assure a certain reliability of the structures.

The partial coefficients, γ_i , are related to characteristic values of the stochastic variables, $X_{i,ch}$. In conventional civil engineering codes the characteristic values of loads and other action parameters are often chosen to be an upper fractile (e.g. 5%), while the characteristic values of material strength parameters are chosen to be the mean values. The values of the partial coefficients are uniquely related to the applied definition of the characteristic values.

The partial coefficients, γ_i , are usually larger than or equal to one. Consequently, if we define the variables as either load variables X_i^{load} (as for example H_s) or resistance variables X_i^{res} (as for example the block volume), then the related partial coefficients should be applied as follows to obtain the design values

$$X_i^{design} = \gamma_i^{load} \cdot X_{i,ch}^{load} \tag{101}$$

$$X_i^{design} = \frac{X_{i,ch}^{res}}{\gamma_i^{res}}$$

The magnitude of γ_i reflects both the uncertainty on the related parameter X_i , and the relative importance of X_i in the failure function. A large value, e.g. $\gamma_{H_s} = 1.4$, indicates a relatively large sensitivity of the failure probability to the significant wave height, H_s . On the other hand, $\gamma_i \simeq 1$ indicates no or negligible sensitivity in which case the partial

coefficient should be omitted. It is to be stressed that the magnitude of γ_i is not – in a mathematical sense – a stringent measure of the sensitivity of the failure probability to the parameter, X_i .

When the partial coefficients are applied to the characteristic values of the parameters in eq. (2) we obtain the **design equation**, i.e. the definition of how to apply the coefficients.

The partial coefficients can be related either to each parameter or to combinations of the parameters (overall coefficients). In the first case we obtain the design equation

$$G = \frac{Z_{ch}}{\gamma_z} \frac{\Delta_{ch}}{\gamma_\Delta} \frac{D_{n,ch}}{\gamma_{Dn}} \left(K_D \frac{\cot\alpha_{ch}}{\gamma_{\cot\alpha}} \right)^{1/3} - \gamma_{H_s} H_{s,ch} \geq 0$$

or

(102)

$$D_{n,ch} \geq \gamma_z \gamma_\Delta \gamma_{Dn} \gamma_{\cot\alpha}^{1/3} \gamma_{H_s} \frac{H_{s,ch}}{Z_{ch} \Delta_{ch} K_D \cot\alpha_{ch}}$$

In the second case we could for example have only γ_{H_s} and an overall coefficient γ_z related to the first term on the right hand side of eq. (2). The design equation would then be

$$G = \frac{Z_{ch}}{\gamma_z} \Delta_{ch} D_{n,ch} (K_D \cot\alpha)^{1/3} - \gamma_{H_s} H_{s,ch} \geq 0$$

or

(103)

$$D_{n,ch} \geq \gamma_z \gamma_{H_s} \frac{H_{s,ch}}{Z_{ch} \Delta_{ch} (K_D \cot\alpha_{ch})^{1/3}}$$

Eqs. (66) and (67) express two different “code formats”. By comparing the two equations it is seen that the product of the partial coefficients is independent of the chosen format, other things equal. It is desirable to have a system which is as simple as possible, i.e. as few partial coefficients as possible, but without invalidating the accuracy of the design equation beyond acceptable limits.

Fortunately, it is very often possible to use overall coefficients, like γ_z in eq. (67), without losing significant accuracy within the realistic range of combinations of parameter values. This is the case for the system proposed in this paper where only two partial coefficients, γ_{H_s} and γ_z , are used in each design formula.

Usually several failure modes are relevant to a design. The relationship between the failure modes are characterized either as series systems or parallel systems. A fault tree can be used to illustrate the complete system. The partial coefficients for failure modes being in a system with failure probability, P_f are different from the partial coefficients for the single failure modes with the same failure probability, P_f . Therefore, partial coefficients for single failure modes and multi failure mode systems are treated separately.

6.2 Overall concept of the proposed partial coefficient system

In existing civil engineering codes of practise, e.g. for steel and concrete structures, it is a characteristic of them that

- partial coefficients are related to combinations of basic variables rather than to each of them in order to reduce the number of coefficients.
- the partial coefficients reflect the safety level inherent in a large number of well proven designs. Two sets of coefficients covering permanent and preliminary structures are usually given, but the related average probabilities of failure are not specified. In other words, it is not possible by means of the normal structural codes to design a structure to a predetermined failure probability.

However, it is not advisable to copy this concept in safety recommendations for rubble mound breakwaters for the following reasons:

- For coastal structures and breakwaters there is no generally accepted tradition which reflects one or more levels of failure probability. On the contrary it is certain that the safety level of existing structures varies considerably and is often very low. Besides, it is very difficult to evaluate the safety level of existing coastal structures and breakwaters because of lack of information, especially on the environmental conditions, e.g. the water level variations and the wave climate. Consequently, it is not possible to produce sets of partial coefficients which, in a meaningful way, are calibrated against existing designs.
- Due to the very nature of coastal engineering where design optimization dictates considerable variations in the safety level of the various structures it is necessary (advisable) to have sets of partial coefficients which correspond to various failure probabilities. In other words the designer and the client decide on the basis of optimization and cost benefit analyses that the structure should be designed for a specific safety level (for example 20% probability of failure ($P_f = 20\%$) within a structural lifetime of $T = 80$ years, where failure is defined as a certain degree damage). The code should then contain a set of partial coefficients corresponding to this failure probability.
- Because the quality of information about the long term wave climate (the dominating load) varies from very unreliable (uncertain) wave statistics based on few uncertain data sets to very reliable statistics based on many years of high quality wave recordings and hindcast values it is necessary that the partial coefficients must be a function of the quality of the available information on the wave climate. This means that the statistical uncertainty due to limited number of wave data and errors in the wave data should be implemented.

Extensive calculations, performed at University of Aalborg, of partial coefficients for armour layer stability formulae demonstrated that it was possible to develop a concept which satisfies these demands.

6.3 Method of determining the partial coefficient

The overall procedure for the development of a partial coefficient system was as follows

- Define the failure modes and the failure element structure (single element analysis and/or system analysis)
- Select the code format (design equations)
- Define intervals of the parameters, their statistical properties and combinations
- Select target probabilities of failure
- Calculate the partial coefficients
- Optimize and calibrate the system
- Verify the partial coefficient system against the observed behaviour of existing structures.

The partial coefficients γ_i are determined from a so-called level II reliability analysis. The applied computer programmes BWREL (Break Water RELiability programme) and BWCODE (Break Water CODE) were developed at the University of Aalborg by Dr. John Dalsgaard Sørensen especially for the reliability analysis of breakwaters. For further explanation reference is made to the Sub-group F report.

6.4 Breakwater types and failure modes

The Working Group set out to study five different types of breakwaters and considered a wide range of failure modes. During the work it became clear that sufficiently well documented failure formulae were only available to justify recommendations of partial coefficients for conventional multi-layer rubble mound breakwaters with armour carried over the crest – and for the following Failure modes:

- Hydraulic instability of front face armour
- Instability of low crested rock breakwaters
- Hydraulic instability of rock toe berm
- Run-up on rock armoured slopes

The formulae for these failure modes are given in section 6.8 in the form of design equations, which shows how to apply the partial coefficients.

6.5 Partial coefficient system format for single failure modes

For each failure mode only two partial coefficients γ_{H_s} and γ_z are used, cf. the example given by eq. (67). The partial coefficient are determined from formulae. Three different concepts for these formulae have been evaluated and the following were chosen as being acceptable with respect to deviations from the target probability of failure.

$$\gamma_{H_s} = \frac{\hat{H}_s^{T_{P_f}}}{\hat{H}_s^T} + \sigma'_{F_{H_s}} \left(1 + \left(\frac{\hat{H}_s^{3T}}{\hat{H}_s^T} - 1 \right) k_\beta P_f \right) + \frac{k_s}{\sqrt{P_f N}} \quad (104)$$

$$\gamma_z = 1 - k_\alpha \ln P_f \quad (105)$$

where

\hat{H}_s^T is the central estimate of the T -year return period value of H_s , where T is the structural lifetime ($T = 20, 50$ and 100 years were used for the code calibration). γ_{H_s} is applied to \hat{H}_s^T (the characteristic value of H_s , cf. the design equations).

\hat{H}_s^{3T} is the central estimate of the $3T$ -year return period value of H_s .

$\hat{H}_s^{T_{P_f}}$ is the central estimate of H_s corresponding to an equivalent return period T_{P_f} defined as the return period corresponding to a probability P_f that $\hat{H}_s^{T_{P_f}}$ will be exceeded during the structural lifetime T . T_{P_f} is calculated from the encounter probability formula $T_{P_f} = \left(1 - (1 - P_f)^{\frac{1}{T}} \right)^{-1}$, cf. Fig. 19.

$\sigma'_{F_{H_s}}$ is the variational coefficient of a function F_{H_s} modelled as a factor on H_s . F_{H_s} signifies the measurement errors and short term variability of H_s and has the mean value 1.0. $\sigma'_{F_{H_s}}$ is equal to σ' for H_s in Table YY. The statistical uncertainty on H_s is not included in F_{H_s} .

N is the number of H_s data, used for fitting the extreme distributions. The statistical uncertainty depends on this parameter.

k_α, k_β and k_s are coefficients which are determined by optimization. $k_s \simeq 0.05$ for all failure modes. The k_α and the k_β values are given in Tables 9-12.

The first term in eq. (104) gives the correct γ_{H_s} provided no statistical uncertainty and measurement errors related to H_s are present. The middle term in eq. (104) signifies the measurement errors and the short term variability related to the wave data. The last term

in eq. (68) signifies the statistical uncertainty of the estimated extreme distribution of H_s . The statistical uncertainty depends on the total number of wave data, N , but not on the length of the period of observation, as might be expected. The 10 largest values of H_s over a 15 years period provides a much more reliable estimate of the extreme distribution than the 10 largest values of H_s over 1 year. However, in the statistical analysis it is assumed that the data samples are equally representative of the true distribution. In other words it is assumed that the data, besides being non-correlated, are sampled with a frequency and over a length of time which ensures that periodic variations (e.g. seasonal) are not biasing the sample. The designer must be aware of these restrictions.

If the extreme wave statistics is not based on N wave data, but for example on estimates of H_s from information about water level variations in shallow water, then the last term in eq. (104) disappears and instead the value of σ'_{FH_s} must account for the inherent uncertainty.

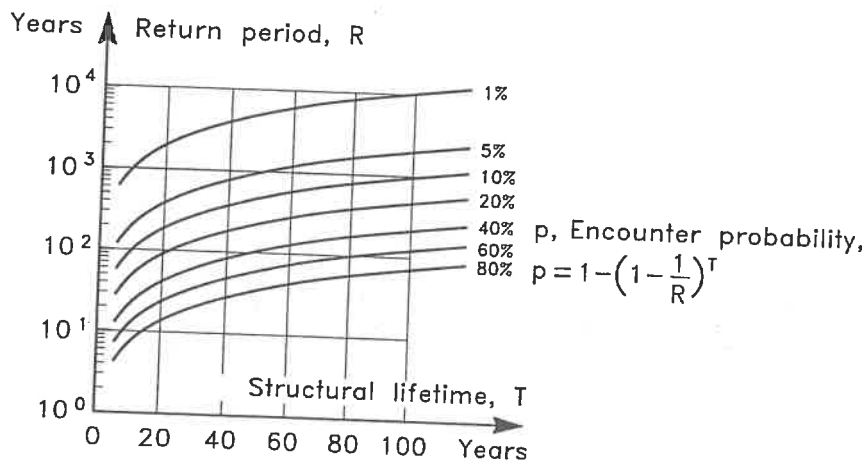


FIG. 19. Encounter probability, i.e. the probability p that the R -year return period event will be exceeded during a T -year structural life (based on annual observations).

6.6 Format for multi failure modes

A simple series system is considered, cf. chapter 4. The reliability of the system depends on the correlation between the failure modes. Two factors contribute to the correlation, namely the physical interaction, e.g. the erosion of a toe berm triggering a slide in the main armour layer, and the correlation through common parameters like H_s . The physical correlations are not yet generally known. Consequently, only the common parameter correlations have been implemented in the present work.

A simple system is to treat each failure mode, $i = 1, 2, 3, \dots, n$ separately using the single failure mode models. The upper and lower bounds of probability of the system, P_f^s could then be estimated as

$$\text{Upper bound } P_f^s = 1 - (1 - P_f^1)(1 - P_f^2) \dots (1 - P_f^n) \quad (106)$$

$$\text{Lower bound } P_f^s = \max P_f^i \quad (107)$$

Max P_f^i is the largest of the failure probabilities of the failure modes.

Eqs. (106) and (107) correspond to no correlation and full correlation, respectively. Due to the common parameters there will always be a correlation of some size which can be estimated from the sensitivity factors related to the parameters for the individual failure modes. Taking this into account some more narrow bounds can be found. However, closer bounds must await further work on the physical interaction and correlation between failure modes.

6.7 Investigated ranges of parameter variations

The optimization of the partial coefficients is based on calculations where all combinations of realistic values of the failure formula parameters are considered.

The resistance parameters are modelled as normally distributed stochastic variables given by mean values and standard deviations. An example of these values and the related range of parameter variations is given below for the Hudson equation applied to rock armour

$$\text{Hudson formula } \frac{H_s}{\Delta D_n} = (K_D \cot \alpha)^{1/3}$$

$$\text{Design equation : } G = \frac{1}{\gamma_Z} \hat{Z} \hat{\Delta} \hat{D}_n (K_D \cot \hat{\alpha})^{1/3} - \gamma_{H_s} \hat{H}_s^T \geq 0$$

Notation

- $D(p)$ indicates a deterministic value, p .
- $N(x_1, x_2)$ indicates a normally distributed parameter with mean value x_1 and standard deviation, x_2 .
- z is the design parameter
- \bar{p} defines the ranges of application of the code for this failure mode.
- \hat{X} expected value (mean value) of X .
- F_{H_s} error function on H_s .
- \hat{H}_s^T central estimate of the significant wave height which on average is exceeded once every T years.

Parameters for the stochastic variables:

parameter	distribution	variation of \bar{p}
Δ	$N(p_1, p_2)$	$(p_1, p_2) = (1.4, 0.03), (1.6, 0.06)$
D_n	$N(z, pz)$	$p = 0.01, 0.05$
$\cot\alpha$	$N(p, 0.1)$	$p = 1.5, 2, 3$
K_D	D	
F_{H_s}	$N(1, p)$	$p = \sigma_{F_{H_s}} = (0, 0.10, 0.20)$
Z	$N(1.0, 0.18)$	
H_s	Extreme distribution fitted to local wave data	

The statistical model for the load parameter H_s was described by three of the commonly used theoretical extreme distributions: Weibull, Gumbel and Exponential. The distributions are given below expressing the non-exceedence probability within T years. λ is the average number of H_s -data per year and N is the total number of data available for fitting the distribution.

The statistical uncertainty of the distributions is included through the parameters α and β which are modelled as stochastic normally distributed variables with variances based on the maximum likelihood estimates of α and β . It should be noted that no quality measure (correlation coefficient or X^2 -test) of the fit of a distribution to a data sample, is included in the analyses that were carried out.

The considered distribution functions are listed below.

$N(x_1, x_2)$ indicates a normally distributed parameter with mean value x_1 and standard deviation, x_2 .

Gumbel $F_{H_s^T}(H_s) = [\exp(-\exp(-\alpha(H_s - \beta)))]^{\lambda T}$

$$\alpha : N\left(\alpha, \alpha\sqrt{\frac{0.608}{N}}\right) \quad \beta : N\left(\beta, \frac{1}{\alpha}\sqrt{\frac{1.109}{N}}\right)$$

Weibull $F_{H_s^T}(H_s) = \left[1 - \exp\left(-\left(\frac{H_s - H'_s}{\beta}\right)^\alpha\right)\right]^{\lambda T}$

$$\alpha : N\left(\alpha, \sqrt{\frac{1}{N}}\right) \quad \beta : N\left(\beta, \left(\frac{\beta^2}{N} \left[\frac{\Gamma(1 + 2/\alpha)}{\Gamma^2(1 + 1/\alpha)} - 1\right]\right)^{\frac{1}{2}}\right)$$

$\text{var}[\alpha] = \frac{1}{N}$ is an assumption since it has not been possible to find an analytical expression. Γ is the gamma function.

Exponential $F_{H_s^T}(H_s) = \left[1 - \exp\left(-\frac{H_s - H'_s}{\alpha}\right)\right]^{\lambda T} \quad \alpha : N\left(\alpha, \alpha\sqrt{\frac{1}{N}}\right)$

The H_s data samples used in the analysis are real deep water and shallow water data set from the North Sea, the Atlantic Ocean, the Bay of Biscaya and the Mediterranean Sea. Table 9 shows the distribution parameters for the data sets.

Table 9. Distribution parameters for H_s -data samples.

	N	λ	Gumbel		Weibull		Exp.	
			α	β	α	β	H'_s	α
Bilbao	50	4.17	1.95	5.55	1.39	1.06	4.9	0.97
Sines	15	1.25	0.88	8.75	1.78	2.53	7.1	2.27
Tripoli	15	0.75	0.74	5.06	1.83	3.24	2.9	2.91
North Sea	30	1.88	1.30	6.65	1.28	1.48	5.7	1.39
Follonica	46	5.94	3.14	3.04	1.14	0.58	2.69	0.55
Pozzallo	22	6.94	3.62	2.48	1.05	0.48	2.20	0.47

The statistical uncertainty described through the variance of α and β does not include uncertainties

- lack of knowledge about the true extremal distribution
- climatological changes
- measurement errors
- variability due to imperfect calculations of H_s and short term randomness

The last two points are incorporated in the analysis by the multiplication term F_{H_s} on H_s . F_{H_s} is modelled as a normally distributed variable with a mean value of unity and a specified coefficient of variation, $\sigma'_{F_{H_s}}$, the size of which depends on the quality of the available information, cf. Table 7.

The first two points cannot be treated through F_{H_s} , but in a design situation the designer must try the different models for the extreme wave height and thereby select the most appropriate. A partial coefficient system cannot take these problems into account.

Moreover, it is assumed inherent in the analysis that the N values of H_s represent the statistical population to which H_s belongs. This sets limits to minimum length of the period of observation N/λ and N in order to prevent seasonal changes from biasing the results.

For the calibration of the system the following target values of $\sigma'_{F_{H_s}}$ and P_f were used:

$$\sigma_{F_{H_s}} = 0.00, 0.10 \text{ and } 0.20 \quad , \quad P_f = 0.01, 0.05, 0.10, 0.20 \text{ and } 0.40.$$

6.8 Example of design equations and recommended values of k_α and k_β

The values of k_α and k_β which have been obtained by carrying out optimization for each failure modes are presented as well as the related design equations in Tables 10 - 13. Note that limitations related to the equations are not given here.

Table 10. Main armour hydraulic stability.

Formula	Design equation	k_α	k_β
Hudson, rock	$\frac{1}{\gamma_z} \Delta D_{n50} (K_d \cot \alpha)^{1/3} \geq \gamma_{H_s} H_s^T$	0.036	151
Van der Meer, rock			
Plunging waves	$\frac{1}{\gamma_z} 6.2 S^{0.2} P^{0.18} \Delta D_{n50} \cot \alpha^{0.5} s_m^{0.25} N_z^{-0.1} \geq \gamma_{H_s} H_s^T$	0.027	38
Surging waves	$\frac{1}{\gamma_z} S^{0.2} P^{-0.13} \Delta D_{n50} \cot \alpha^{0.5-P} s_m^{-0.5P} N_z^{-0.1} \geq \gamma_{H_s} H_s^T$	0.031	38
Van der Meer			
Tetrapods $\cot \alpha = 1.5$	$\frac{1}{\gamma_z} \left(3.75 \frac{N_{od}^{0.5}}{N_z^{0.25}} + 0.85 \right) s_m^{-0.2} \Delta D_n \geq \gamma_{H_s} H_s^T$	0.026	38
Van der Meer			
Cubes $\cot \alpha = 1.5$	$\frac{1}{\gamma_z} \left(6.7 \frac{N_{od}^{0.4}}{N_z^{0.3}} + 1.0 \right) s_m^{-0.1} \Delta D_n \geq \gamma_{H_s} H_s^T$	0.026	38
Burcharth			
Dolos $\cot \alpha = 1.5$	$\frac{1}{\gamma_z} \Delta D_n (17 - 26r) \varphi_{n=2}^{2/3} N_{od}^{1/3} N_z^{-0.1} \geq \gamma_{H_s} H_s^T$	0.025	38
	r Dolos waist ratio		
	φ packing density		
	N_{od} number of displaced units within a width of one equivalent cubic length D_n		

Table 11. Hydraulic stability of low crested rock breakwaters.

Formula	Design equation	k_α	k_β
Van der Meer, rock	As for main armour with factor $f_i = \left[1.25 - 4.8 \frac{R_c}{H_s^T} \left(\frac{S_m}{2\pi} \right)^{0.5} \right]^{-1}$ applied to D_{n50}	0.035	42

Table 12. Hydraulic stability of rock toe berm.

Formula	Design equation	k_α	k_β
Van der Meer, rock	$\frac{1}{\gamma_z} 8.7 \left(\frac{h_t}{h} \right)^{1.43} \Delta D_{n50} \geq \gamma_{H_s} H_s^T$	0.087	100

Table 13. Run-up on rock armoured slopes.

Formula	Design equation	k_α	k_β
Hunt	for $(\cot\alpha)^{-1} s_m^{-0.5} < 1.5$ $\frac{1}{\gamma_z} R_u a^{-1} \cot\alpha s_m^{0.5} \geq \gamma_{H_s} H_s^T$	0.036	44
	for $(\cot\alpha)^{-1} s_m^{-0.5} > 1.5$ $\frac{1}{\gamma_z} R_u b^{-1} [\cot\alpha s_m^{0.5}]^c \geq \gamma_{H_s} H_s^T$	0.018	36

6.9 Examples of the use of the partial coefficient system

The following examples will illustrate how the partial coefficient system is applied for design purpose.

Example 1

Objective:

Determination of the average mass, or the nominal diameter D_{n50} , of quarry rock armour corresponding to the following design conditions:

- Case 1. Moderate to severe damage with a probability $P_f = 0.2$ within a structural life of $T = 50$ years.
- Case 2. As Case 1 but $P_f = 0.1$
- Case 3. Very severe damage (failure) with a probability $P_f = 0.2$ within a structural life of $T = 100$ years.
- Case 4. Moderate to severe damage with a probability $P_f = 0.1$ within a structural life of $T = 100$ years.

The Van der Meer formulae for rock given in Table 9 are assumed valid.

Design parameters:

Densities: Rock 2.8 t/m^3 , water 1.03 t/m^3 , $\Delta = 1.72$

Slope: $\cot\alpha = 1.5$, porosity $P = 0.4$

Wave climate: Weibull distribution of H_s with the site specific coefficients $(\alpha, \beta, H'_s) = (1.39, 1.06, 0.44)$ determined by fitting to a hindcasted H_s -data set consisting of the $N = 50$ largest values within a 12 years period, i.e. $\lambda = 50/12 = 4.17$. σ'_{FH_s} is estimated to 0.2 for the hindcasted H_s values. Wave steepness $s_m = 0.04$, number of waves $N_z = 2500$.

Damage: Moderate to severe damage $S = 6$, very severe damage (failure) $S = 14$.

Procedure:

The procedure and the partial coefficient formulae described in section 6.5 are used.

Calculations:

In case of a Weibull distribution the central estimate of the significant wave height with an average return period of T years is given by

$$\hat{H}_s^T = H'_s + \beta (\exp[\ln(\ln(\lambda T))/\alpha])$$

$$= 0.44 + 1.06 (\exp[\ln(\ln(4.17T))/1.39])$$

The equivalent return period is given by

$$T_{P_f} = (1 - (1 - P_f)^{\frac{1}{T}})^{-1}$$

From this is obtained

Case	T (year)	P_f	T_{P_f} (year)	\hat{H}_s^T (m)	\hat{H}_s^{3T} (m)	$\hat{H}_s^{T_{P_f}}$ (m)
1	50	0.2	225	3.98	4.49	4.67
2	50	0.1	475	3.98	4.49	5.00
3	100	0.2	449	4.30	4.80	4.97
4	100	0.1	950	4.30	4.80	5.29

From Table 9 (for plunging waves)

$$k_\alpha = 0.027, \quad k_\beta = 38$$

From the formulae

$$\gamma_{H_s} = \frac{\hat{H}_s^{T_{P_f}}}{\hat{H}_s^T} + \sigma_{FH_s}^j \left(1 + \left(\frac{\hat{H}_s^{3T}}{\hat{H}_s^T} - 1 \right) k_\beta P_f \right) + \frac{0.05}{\sqrt{P_f N}}$$

$$\gamma_Z = 1 - k_\alpha \ln P_f$$

and the Van der Meer design equation is obtained

	Case	γ_{H_s}	γ_Z	D_{n50} (m)	Average mass (t)
$S = 6$	1	1.22	1.04	1.56	10.6
	2	1.35	1.06	1.76	15.2
	3	1.21	1.04	1.67	13.1
	4	1.33	1.06	1.87	18.4

	Case	γ_{H_s}	γ_Z	D_{n50} (m)	Average mass (t)
$S = 14$	1	1.22	1.04	1.32	6.39
	2	1.35	1.06	1.48	9.16
	3	1.21	1.04	1.41	7.86
	4	1.33	1.06	1.58	11.1

Example 2

Objective:

Determination of the average mass, or the equivalent cubic length D_n of Dolos armour units corresponding to the above mentioned 4 design conditions:

The Burcharth formula for Dolosse given in Table 9 is assumed valid.

Design parameters:

Densities: Concrete 2.3 t/m^3 , water 1.03 t/m^3 , $\Delta = 1.23$

packing density $\varphi_{n=2} = 0.83$

waist ratio $r = 0.37$

Slope: $\cot\alpha = 1.5$

Wave climate: Weibull distribution of H_s with the site specific coefficients $(\alpha, \beta, H'_s) = (1.39, 1.06, 1.44)$ determined by fitting to a hindcasted H_s -data set consisting of the $N = 50$ largest values within a 12 years period, i.e. $\lambda = 50/12 = 4.17$. σ'_{FH_s} is estimated to 0.2 for the hindcasted H_s values. Number of waves $N_z = 2500$.

Damage: Moderate damage $N_{od} = 2$.

Procedure:

The procedure and the partial coefficient formulae described in section 6.5 are used.

Calculations:

In case of a Weibull distribution the central estimate of the significant wave height with an average return period of T years is given by

$$\begin{aligned} \hat{H}_s^T &= H'_s + \beta (\exp[\ln(\ln(\lambda T))/\alpha]) \\ &= 1.44 + 1.06 (\exp[\ln(\ln(4.17T))/1.39]) \end{aligned}$$

The equivalent return period is given by

$$T_{P_f} = (1 - (1 - P_f)^{\frac{1}{T}})^{-1}$$

From this is obtained

Case	T (year)	P_f	T_{P_f} (year)	\hat{H}_s^T (m)	\hat{H}_s^{3T} (m)	$\hat{H}_s^{TP_f}$ (m)
1	50	0.2	225	4.98	5.49	5.67
2	50	0.1	475	4.98	5.49	6.00
3	100	0.2	449	5.30	5.80	5.97
4	100	0.1	950	5.30	5.80	6.29

From Table 9

$$k_\alpha = 0.025 \quad , \quad k_\beta = 38$$

From the formula

$$\gamma_{H_s} = \frac{\hat{H}_s^{TP_f}}{\hat{H}_s^T} + \sigma'_{FH_s} \left(1 + \left(\frac{\hat{H}_s^{3T}}{\hat{H}_s^T} - 1 \right) k_\beta P_f \right) + \frac{0.05}{\sqrt{P_f N}}$$

$$\gamma_Z = 1 - k_\alpha \ln P_f$$

and the Burcharth design equation is obtained

Case	γ_{H_s}	γ_Z	D_{n50} (m)	Average mass (t)
1	1.20	1.04	1.34	5.56
2	1.31	1.05	1.48	7.45
3	1.19	1.04	1.42	6.54
4	1.30	1.06	1.58	9.02

The examples illustrates how easy it is to calculate the size of the armour for various design conditions. The system facilitates economical optimization of a design.

The system can be used also for the evaluation of the failure probability of existing structures.

6.10 Conclusions

A concept for the calculation of partial coefficients corresponding to given failure probability within given structure life is presented. These partial coefficients γ_{H_s} and γ_z are applied to a design formula. These partial coefficients are calculated from formulae (104) and (105) in which two failure mode specific coefficients, k_α and k_β , are used together with characteristic return period values of H_s , extracted from the site specific long term distribution of H_s .

So far the k_α , k_β coefficients have been calculated only for the failure modes which are described by existing uncertainty evaluated formulae . However, it is easy to expand the system as more failure mode formulae appear. It is important to notice that the reliability of the formulae must be documented, e.g. in terms of a standard deviation, in order to implement them in the partial coefficient system.

7 Acknowledgement

The useful help from Dr. Zhou Liu and Dr. J. Dalsgaard Sørensen are greatly acknowledged.

8 References

- Andersen, E.Y. & B.S. Andreasen & P. Ostensfeld-Rosenthal (1992). *Foundation Reliability of Anchor Block for Suspension Bridge*. Proc. IFIP WG7.5, Lecture notes in Eng. Vol. 76, Springer Verlag, 1992 pp. 131-140.
- Burcharth, H.F. (1989) Uncertainties related to environmental data and estimated extreme events. Report of Subgroup-B, PIANC PTCII Working Group 12 on Rubble Mound Breakwaters. (In print by PIANC 1992.)
- Burcharth, H.F. (1992). *Reliability evaluation of a structure at sea*. Proceedings of the Short Course on Design and Reliability of Coastal Structures. Venice, Scuola di S. Giovanni Evangelista, 1992. 23rd International Conference on Coastal Engineering.
- Burcharth, H.F. (1992). *Design of Breakwaters*. Aalborg University, Aalborg, Denmark.
- Burcharth, H.F. & J.D. Sørensen & E. Christiani (1994). *On the Evaluation of Failure Probability of Monolithic Vertical Wall Breakwaters*. Proc. "Wave Barriers in Deep-water", Port and Harbour Research Institute, Yokosuka, Japan, 1994, pp. 458-466. 469
- Burcharth, H.F. (1991). *Development of a Partial Coefficient System in the Design of Rubble Mound Breakwaters*. Report Subgroup F, PIANC PTC II Working group 12 on Rubble Mound Breakwaters, 1991.
- Burcharth, H.F. & J.D. Sørensen & E. Christiani (1995). *Application of reliability analysis for optimal design of monolithic vertical wall breakwaters*. COPEDEC, Rio, Brazil, 1995.
- Goda, Y. (1974). *A new method of wave pressure calculation for the design of composite breakwater*. Proc. 14th Int. Conf. Coastal Eng., Copenhagen, Denmark.
- Goda, Y. (1985). *Random Seas and Design of Maritime Structures*. University of Tokyo Press.
- Goda, Y. and T. Fukumori (1972). *Laboratory investigation of wave pressures exerted upon vertical and composite walls*. Coastal Engineering in Japan, Vol. 15. pp 81-90, 1972.
- Hallam, M.G., Heaf, N.I. and Wootos, I.R. (1977). *Rationalization of Safety and Serviceability factors in Structural Codes*. CIRIA report No. 63, London.
- Hansen, B. (1979). *Definition and use of friction angles*. Proc. Int. Conf. VII ECSMFE, Brighton, UK, 1979.
- Jacobsen M. (1989). *Brud i jord*. University of Aalborg, Denmark. (In Danish).
- Keaveny, J.M. & F. Nadim & S. Lacasse (1989). *Autocorrelation Function for Offshore Geotechnical Data*. Proc. ICOSSAR89, 1989, pp. 263-270.

- Madsen, H.O., S. Krenk & N.C. Lind (1986). *Methods of Structural Safety*. Prentice-Hall, 1986.
- Nadim, F. & S. Lacasse, and T.R. Cuttormsen (1994). *Probabilistic foundation stability analysis: Mobilized friction angle vs available shear strength approach*. Structural Safety & Reliability, 1994, Balkema, Rotterdam.
- van der Meer, J.W., Juhl, J. and G. van Driel (1993). *Probabilistic calculation of wave forces on vertical structures*. Proc. of Final overall workshop MAST I - G6S, Lisbon.
- Sørensen, J.D., H.F. Burcharth and E. Christiani (1994). *Reliability analysis and optimal design at monolithic vertical wall breakwaters*. Proc. 6th IFIP WG7.5 Assisi, Italy. Chapman & Hall.
- Takahashi, S., Tanimoto, K., and K. Shimosako (1994). *Dynamic Response and Sliding of Breakwater Caisson against Impulsive Breaking Wave forces*. Rept. of Port and Harbour Research Inst. 1994.
- Takayama, T. (1992). *Estimation of sliding Failure Probability of present Breakwaters for Probabilistic Design*. Report of Port and Harbour Research Inst., Vol. 31, No. 5, 1992.
- Thoft-Christensen, P. and Baker, M.J. (1982). *Structural Reliability Theory and its Application*. Springer Verlag. Berlin.
- Wen, Y.K. and Chen, H.C. (1987). *On fast integration for time variant structural reliability*. *Probabilistic Engineering Mechanics*, Vol.2, 1987, pp 156-162.